

Shawn X. Wang (Ed.)  
**Current Trends in Computer Science and Mechanical Automation**  
**Selected Papers from CSMA2016 - Volume 2**



Shawn X. Wang (Ed.)

# Current Trends in Computer Science and Mechanical Automation

---

Selected Papers from CSMA2016 - Volume 2

ISBN: 978-3-11-058498-1  
e-ISBN: 978-3-11-058499-8



This work is licensed under the Creative Commons Attribution-NonCommercial-NoDerivs 3.0 License.  
For details go to <http://creativecommons.org/licenses/by-nc-nd/3.0/>.

**Library of Congress Cataloging-in-Publication Data**

A CIP catalog record for this book has been applied for at the Library of Congress.

© 2017 Shawn X. Wang (Ed.) and chapters contributors  
Published by De Gruyter Open Ltd, Warsaw/Berlin  
Part of Walter de Gruyter GmbH, Berlin/Boston  
The book is published with open access at [www.degruyter.com](http://www.degruyter.com).

[www.degruyteropen.com](http://www.degruyteropen.com)  
Cover illustration: © cosmin4000 / iStock.com

# **Contents**

**Preface — XIII**

**Introduction of keynote speakers — XIV**

## **Part IV: Sensors, Instrument and Measurement II**

Liang GUO, Bi-fu QIAN, Gao-xiang LIN, Ben-ren PAN

**Design of Remote Real-Time Measuring System of Temperature and Humidity based on Raspberry Pi and Java Language — 1**

Da-peng Li, Xin-an Ge

**Design of Emotional Physiological Signal Acquisition System — 18**

Yao-peng PAN

**EMC Effects On High-Resolution Spaceborne SAR Image — 26**

Ke-ke GU, Yue-fang DONG, Zhe ZHOU, Min LIU, Shi CHEN, Wei-wei FU

**Real-time Pupil Detection based on Contour Tracking — 31**

Ning GUO, Yao-he LIU, Ming-hui YAN

**Chip Manufacturing, Data Integration and Transmission — 41**

Qing-qing WEI, Ru-chun CUI, Zi-chao CHEN, Ya LI

**A DCT-domain-based Research and Application of the Algorithm of Digital Audio Watermark — 52**

Yi XU, Wei-wei FU, Shi CHEN, Yue-fang DONG, Ke-ke GU, Li-ping WANG

**Detection of Placido rings fracture based on ECC image registration — 62**

Ying-qiao KONG, Jian-kang ZHAO, Xuan XIA, Cheng-guang ZHU

**Research on High-precision Calibration and Measurement Method based on Stereo Vision — 72**

Zhong-min LI, Guo-wei ZOU

**Comparison of Three Weak Small Moving Target Detection Methods  
based on Time Domain Filtering — 85**

Gong QIN, Jun ZHOU

**Breath Sounds Detection System based on SOPC — 93**

Bao Kai ZHANG, Chun Hua TAN

**A Novel Fiber-optic Sensor for the Determination of Melting Point of Solids — 105**

Bin ZHANG, Yue-Juan WEI, Wen-Yi LIU, Zong YAO, Yan-Jun ZHANG, Ji-Jun XIONG

**Method for Measuring Internal Liquid Level of Sealed Metal Container  
by Ultrasonic — 113**

Zhan-she GUO, Yan-shan WANG, Man-guo HUANG, Chao LU, Mei-ju ZHANG, Xin LI

**Design of Silicon-on-Sapphire Pressure Sensor For High Temperature And High  
Pressure Applications — 121**

Lang-shu LI, Hong-zhuan QIU, Hua SONG, Chun-ling WEI

**The Federated Filtering Algorithm based on the Asynchronous  
Multisensor System — 129**

Heng LI, Shi-bing WANG, Jun LI, Huai-min LI

**A Kind of Self-tuning Kalman Filter for the High Maneuvering Target  
Tracking System — 139**

Cun-qun FAN, Xian-gang ZHAO, Man-yun LIN, Li-zi XIE, You MA, Xiao-hu FENG

**A Multitasking Run Time Prediction Method based on GBDT in Satellite  
Ground Application System — 145**

Wen-zhi XING, Zhu-ping WANG

**Unmanned Ground Vehicle Behavior Decision via Improved Bayesian Inverse  
Reinforcement Learning — 151**

Qi YANG, Bin DENG, Yu-liang QIN, Hong-qiang WANG

**Analysis of the High Frequency Vibration on Radar Imaging in the Terahertz  
Band — 162**

Yu-jia SUN, Bo DU, Chen WU, Xian-quan HAN

**Object Tracking for Satellite Video based on Kernelized Correlation Filters  
and Three Frame Difference — 173**

Fan LI, Rui MO, He-lun SONG , Yao-hui ZHANG

**Noise Removal and Detail Enhancement of Passive Infrared Image Pretreatment  
Method for Robot Vision — 183**

Guang-chao ZHANG, Yuan GAO, Bing WANG, Yong-hui LAI

**Failure Mechanism and Support Strategy of Deep Roadway with  
High Horizontal Stress and Broken Rock Masss — 191**

Xian HUANG, Yue QIN, Jia-li LIANG, Yang LIU

**Design of a Climbing Robot for Nuclear Environmental Monitoring — 201**

## **Part V: Mechatronics and Electrical Engineering I**

Yu-heng HE, Kai FENG, Heng JU, Cheng-xin LIN

**The design and simulation of the new Space Release Device — 213**

Tao ZHAN, Guang-you YANG, Xue-hai CHEN, Wen-sheng LIU

**The Adjusting Method of Box Girder Pose based on Spatial Coordinate  
Transformation — 228**

Xiao-geng FANG, Yan-hui CHEN, Wan-feng LIU, Xi-rong LUO,  
Guo-jin XIE

**Application of Discrete Element Method in the Analysis of Loader Shovel  
Loading Process — 239**

Jian QIN, Liang FENG, Jun CHEN, Jian-cheng WAN

**Application of Piecewise Catenary Method in Length Calculation of Soft Busbar i  
n Ultra-high Voltage Substation — 250**

Jian QIN, Liang FENG, Jun CHEN, Jian-cheng WAN, Liang QIAO,Yi-min MA

**Calculation Method of Stiffness Matrix in Non-linear Spline Finite Element for  
Suspension Cable — 259**

Dong-xu WANG, Xue ZHENG, Xi YE, Wei CAI, Zhi-chun YANG

**A Load Outage Judgement Method Considering Voltage Sags — 267**

Juan WEI, Liang-liang GUI, Pan LU

**Macro Program Application on Non-circular Curve Machining in CNC Lathe — 279**

Qiu-wei HE, Chao-peng ZHANG, Mei FENG, Xing-tian QU, Ji ZHAO

**Singular Configuration Analysis for the Structure of Hybrid Grinding and Polishing Machine — 288**

Sha-na WANG

**Static Analysis and Size Optimization for the Bed of Gantry Milling Machine based on ANSYS Workbench — 298**

Da-xian HAO, Chao YUN, Hui JIN, Gang WANG

**Research and Optimization of Clip Type Passive Manipulator — 305**

Qiu-wei HE, Xu YANG, Xiao-hui WU, Xing-tian QU, Ji ZHAO

**Research on Material Removal of Belt Polishing for Blade Complex Surface — 319**

Chao LI, Chu-qing CAO, Yun-feng GAO

**Visual Servoing based object pick and place manipulation system — 334**

Hai-Sheng XIONG, De-Xing ZHANG

**Research on Wind Loads of Container Ship based on CFD — 342**

Qiang LUO, Ping ZHOU, Wen GAI, Fei LIAO

**Design and Research of Model Sting Support Control System of Icing Wind Tunnel — 356**

Ping ZHOU, Qiang LUO, Wei-kai HUANG, Zheng-hua GU

**Development of Control System of Icing Wind Tunnel — 369**

Chen LU, Hai-min YU, Zhen-wei YU, Kun-jie CHEN

**Railway Track Collapse Monitoring System in Mining Area based on KALMAN Filter — 385**

Xiao-ming LI, Jia-yue YIN, He-zuo QU, Cheng-qiong BI, Hao-jun XU, Li ZHU  
**The Method of Harmonic Source Identification in Power Supply System — 392**

Chun-yu WEI, Shuai LIU, Wen-da YU, Zhan WANG  
**Optimization for the Balancing Cylinder of a 3-DOF Planar Manipulator — 398**

En-de ZHOU, Xi-shun WANG, Hai-tao FANG, Kai HE, Ru-xu DU  
**Finite Element Modal Analysis of an Eight-axis Industrial Robot Painting System Applied to Boarding Bridge Painting — 408**

Ming YU, Meng-xin LI, Hai WANG, Cang-hua JIANG, Hao XIA, Si CHEN  
**Bayesian based Fault Identification for Nonlinear Mechatronic System with Backlash — 418**

Chi ZHOU, Li-hua FANG, Jun-jie DENG, Wen-tao ZHANG  
**A CAD/CAE Integrated Optimization of Hot Runner System — 428**

Wei LI, Zhi-gang SUN, Kai HE, Qi-yang ZUO, Qing-yin LIU, Ru-xu DU  
**Study On Tool Path Design for a Novel Incremental Sheet Metal Bending Process — 437**

Fan-yi MENG, Xiao-feng GONG, Xu KANG  
**Research on Tribological Characteristics of 316L Stainless Steel against PEEKHPV under Water Lubrication — 449**

Ning-shan WANG, Yong-sheng YANG  
**Turbofan Engine Controller Optimal Design based on Grey Wolf Optimizer — 458**

## **Part VI: Mechatronics and Electrical Engineering II**

Jian-Hua LI, Ting-Ting RAO, Wei-Hua WANG, Wei-Bo ZHU  
**Research of the EMI Suppression Circuit in the ASM Power — 471**

Yun-na WU, Ge-di JI, Ji WANG  
**Research on the Relationship Identification and Governance Countermeasures of Stakeholder in Two Phases of Thermoelectric Projects — 482**

Zhong-hua ZHANG, Yan-hai XU, Dao-jie JU, Xu-qiang QIAO

**Study on the Fluctuating Pressure and Aerodynamic Noise at Car Rearview Mirror Zone — 493**

Hongyan Yu, Jianjiang Chen, Zhengwei Dong, Guitang Liu

**Model and Simulation of Vehicle Based on Modelica Language — 502**

Le HE, Xiaoming LI, Xianyong MU, Ying LIU, Kunjie WANG

**Research on Asynchronous Starting Characteristics of Synchronous Motors Based on TSC Reactive Power Compensator — 510**

Yun-de SHEN, Jing-yi ZHANG, Su-jie ZHOU, Lei WANG, Dong-ji XUAN

**Motorcycle Engine Controller Design and Matlab/Simulink Simulation — 518**

Wenyu HU, Zhao WANG, Xiaosong YANG, Jian J. ZHANG

**An Efficient Bilinear Factorization based Method For Motion Capture Data Refinement — 533**

Zheng RAN, Hua YAN, Yun LI

**Reliability Evaluation of Embedded Real-time System based on Error Scenario — 548**

Chun-xiang XU, Wei SHI, Dong-mei CHEN, Xiang-wei WU

**Coordinate Transformation on CNC Machining of Quasi-Hypoid-Gear — 561**

Yan-wei TAN, Sheng-ya LI, Yan-hai XU, Ke-qi LI

**Study on the Influence of Rolling Wheels on Car External Flow Field and Aerodynamic Noise — 568**

Jian-xian ZHANG, Duan ZHOU, Xue-hong QIU, Rui LAI

**Hardware/Software Partitioning Algorithm under Multi-Constraints for the Optimization of Power Consumption — 578**

Zhi XIE, Jia-ju WANG, Chen LIU, Wei-min CHEN

**Research of Metering Arithmetic for Distortion Power — 590**

Gui-tian GONG, Hai-feng CHEN

**Study of the Influence of the Diode Ideality Factor on the Si Solar Cell — 598**

Wei SONG, Huai-yuan LIU, Bin XIANG, Hong HU, Cheng-jiang WANG, Ling-yun WAN

**Application of the Haar Classifier in Obstacle Target Detection — 605**

Qiu-wei HE, Yu-peng ZHANG, Xing-tian QU

**Virtual Assembly Process Simulation for Hybrid Car Battery  
based on DELMIA — 615**

Yu-fei WANG, Jian-ming FU, Yan LIN, Wei-xia LI

**Information Flow Integrity of ECPS based on Domain Partition — 624**

Hai-Tao CHEN, Hao HU

**Simulating the Time-Domain Response for Monopole Antennas Excited  
by DC Voltage Source — 638**

Xiao-long ZHOU, Wei SOHG, Xin-ping LI

**Permanent Magnet Brushless DC Motor Driver Base On DSP56F8346 — 645**

Qing ZHOU, Bang-fei DENG, Cheng-jiang WANG, Qian-bo XIAO, Hai-bing ZHANG,  
Xiang-ming LIU

**The Study on the Power Transmission Line Icing Image Edge Detection  
based on DTW Measure Cluster Analysis — 653**



## Preface

The 2nd International Conference on Computer Science and Mechanical Automation carried on the success from last year and received overwhelming support from the research community as evidenced by the number of high quality submissions. The conference accepted articles through rigorous peer review process. We are grateful to the contributions of all the authors. For those who have papers appear in this collection, we thank you for your great effort that makes this conference a success and the volume of this proceeding worth reading. For those whose papers were not accepted, we assure you that your support is very much appreciated. The papers in this proceeding represent a broad spectrum of research topics and reveal some cutting-edge developments.

Chapter 1 and 2 contain articles in the areas of computer science and information technology. The articles in Chapter 1 focus on algorithm and system development in big data, data mining, machine learning, cloud computing, security, robotics, Internet of Things, and computer science education. The articles in Chapter 2 cover image processing, speech recognition, sound event recognition, music classification, collaborative learning, e-government, as well as a variety of emerging new areas of applications. Some of these papers are especially eye-opening and worth reading.

Chapter 3 and 4 contain papers in the areas of sensors, instrument and measurement. The articles in Chapter 3 cover mostly navigation systems, unmanned air vehicles, satellites, geographic information systems, and all kinds of sensors that are related to location, position, and other geographic information. The articles in Chapter 4 are about sensors and instruments that are used in areas like temperature and humidity monitoring, medical instruments, biometric sensors, and other sensors for security applications. Some of these papers are concerned about highly critical systems such as nuclear environmental monitoring and object tracking for satellite videos.

Chapter 5 and 6 contain papers in the areas of mechatronics and electrical engineering. The articles in Chapter 5 cover mostly mechanical design for a variety of equipment, such as space release devices, box girder, shovel loading machines, suspension cables, grinding and polishing machines, gantry milling machines, clip type passive manipulator, hot runner systems, water hydraulic pump/motor, and turbofan engines. The articles in Chapter 6 focus on mechanical and automation devices in power systems as well as automobiles and motorcycles.

This collection of research papers showcases the incredible accomplishments of the authors. In the meantime, they once again prove that the International Conference on Computer Science and Mechanical Automation is a highly valuable platform for the research community to share ideas and knowledge. Organization of an international conference is a huge endeavor that demands teamwork. We very much appreciate everyone who is involved in the organization, especially the reviewers. We are looking forward to another successful conference next year.

Shawn X. Wang  
CSMA2016 Conference Chair

## **Introduction of keynote speakers**

### **Professor Lazim Abdullah**

School of Informatics and Applied Mathematics, Universiti Malaysia Terengganu, Malaysia

Lazim Abdullah is a professor of computational mathematics at the School of Informatics and Applied Mathematics, Universiti Malaysia Terengganu. He holds a B.Sc (Hons) in Mathematics from the University of Malaya, Kuala Lumpur in June 1984 and the M.Ed in Mathematics Education from University Sains Malaysia, Penang in 1999. He received his Ph.D. from the Universiti Malaysia Terengganu, (Information Technology Development) in 2004. His research focuses on the mathematical theory of fuzzy sets and its applications to social ecology, environmental sciences, health sciences, and manufacturing engineering. His research findings have been published in over two hundred and fifty publications, including refereed journals, conference proceedings, chapters in books, and research books. Currently, he is Director, Academic Planning, Development and Quality of his University and a member of editorial boards of several international journals related to computing and applied mathematics. He is also a regular reviewer for a number of local and international impact factor journals, member of scientific committees of several symposia and conferences at national and international levels. Dr Abdullah is an associate member, IEEE Computational Intelligence Society, a member of the Malaysian Mathematical Society and a member of the International Society on Multiple Criteria Decision Making.

### **Professor Jun-hui Hu**

State Key Lab of Mechanics and Control of Mechanical Structures, Nanjing University of Aeronautics and Astronautics, China

Dr. Junhui Hu is a Chang-Jiang Distinguished Professor, China, the director of Precision Driving Lab at Nanjing University of Aeronautics and Astronautics, and the deputy director of State Key Laboratory of Mechanics and Control of Mechanical Structures, China. He received his Ph.D. Degree from Tokyo Institute of Technology, Tokyo, Japan, in 1997, and B.E. and M.E. degrees in electrical engineering from Zhejiang University, Hangzhou, China, in 1986 and 1989, respectively. He was an assistant and associate professor at Nanyang Technological University, Singapore, from 2001 to 2010. His research interest is in piezoelectric/ultrasonic actuating technology. He is the author and co-author of about 250 papers and disclosed patents, including more than 80 full SCI journal papers and one editorial review for an international journal, and the sole author of monograph book “Ultrasonic Micro/Nano Manipulations” (2014, World Scientific, Singapore). He is the editorial board member of two international journals. Dr. Hu won the Paper Prize from the Institute of Electronics, Information and Communication Engineers (Japan) as the first author in 1998, and was once awarded the title of valued reviewer by Sensors

and Actuators A: Physical and Ultrasonics. His research work has been highlighted by 7 international scientific media.

### **Professor James Daniel Turner**

College of Engineering, Aerospace Engineering, Texas A&M University (TAMU), America  
Dr. James Daniel Turner is a research professor in College of Engineering, Texas A&M University (TAMU) from 2006 to current. In 1974, he received his B.S. degree in Engineering Physics in George Mason University. In 1976, he received his M.E. degree in Engineering Physics, University of Virginia. And he received his Ph.D. Degree from Engineering Science and Mechanics, Virginia Tech in 1980.

He has broad experience in public, private, and academic settings for working with advanced engineering and scientific concepts that are developed from first principles; modeled and simulated to understand the limits of performance; developed as hardware proto-types; tested in operationally relevant environments; and transitioned through partnering with industry and government to missions of critical national interest. Dr. James Daniel Turner is engaged in exploratory research where the goal is to transition aerospace analysis tools to bioinformatics. This research consists of applying multibody dynamics for drug design problems in computational chemistry, and most recently working with the immunological group at Mayo Clinic for exploring the development of generalized predator-prey models for analyzing melanoma cancer in Human cell behaviors.

### **Professor Rong-jong Wai**

Department of Electronic and Computer Engineering, National Taiwan University of Science and Technology, Taiwan

Rong-jong Wai was born in Tainan, Taiwan, in 1974. He received the B.S. degree in electrical engineering and the Ph.D. degree in electronic engineering from Chung Yuan Christian University, Chung Li, Taiwan, in 1996 and 1999, respectively. From August 1998 to July 2015, he was with Yuan Ze University, Chung Li, Taiwan, where he was the Dean of the General Affairs Office from August 2008 to July 2013, and the Chairman of the Department of Electrical Engineering from August 2014 to July 2015. Since August 2015, he has been with National Taiwan University of Science and Technology, Taipei, Taiwan, where he is currently a full Professor, and the Director of the Energy Technology and Mechatronics Laboratory. He has authored more than 150 conference papers, near 170 international journal papers, and 51 inventive patents. He is a fellow of the Institution of Engineering and Technology (U.K.) and a senior member of the Institute of Electrical and Electronics Engineers (U.S.A.).

### **Professor Zhen-guo Gao**

Dalian University of Technology, China

Zhen-guo Gao had been a visiting professor in University of Michigan, Dearborn with full financial support from China Scholarship Council. He has been working as a

visiting professor in University of Illinois at Urbana-Champaign in 2010. He received his Ph.D. degree in Computer Architecture from Harbin Institute of Technology, Harbin, China, in 2006 and then joined Harbin Engineering University, Harbin, China. His research interests include wireless ad hoc network, cognitive radio network, network coding, game theory applications in communication networks, etc.

He is a senior member of China Computer Federation. He is serving as a reviewer for project proposals to National Science Foundation of China, Ministry of Education of China, Science Foundation of HeiLongJiang Province, China, etc. He is also serving as a reviewer for some important journals including IEEE Transactions on Mobile Computing, Wireless Networks and Mobile Computing, Journal of Parallel and Distributed Computing, Journal of Electronics (Chinese), Journal of Computer (Chinese), etc.

### **Professor Steven Guan (Sheng-Uei Guan)**

Director, Research Institute of Big Data Analytics, Xi'an Jiaotong-Liverpool University, China

Steven Guan received his M.Sc. & Ph.D. from the University of North Carolina at Chapel Hill. Prof. Guan has worked in a prestigious R&D organization for several years, serving as a design engineer, project leader, and department manager. After leaving the industry, he joined Yuan-Ze University in Taiwan for three and half years. He served as deputy director for the Computing Center and the chairman for the Department of Information & Communication Technology. Later he joined the Electrical & Computer Engineering Department at National University of Singapore as an associate professor. He is currently a professor in the computer science and software engineering department at Xi'an Jiaotong-Liverpool University (XJTLU). He created the department from scratch and served as the head for 4.5 years. Before joining XJTLU, he was a tenured professor and chair in intelligent systems at Brunel University, UK. Prof. Guan's research interests include: machine learning, computational intelligence, e-commerce, modeling, security, networking, and random number generation. He has published extensively in these areas, with 130 journal papers and 170+ book chapters or conference papers. He has chaired and delivered keynote speeches for 20+ international conferences and served on 130+ international conference committees and 20+ editorial boards.

### **General Chair**

Prof. Wen-Tsai Sung, National Chin-Yi University of Technology, Taichung, Taiwan

Prof. Shawn X. Wang, Department of Computer Science, California State University, Fullerton, United States

## **Editors**

Prof. Wen-Tsai Sung, National Chin-Yi University of Technology, Taichung, Taiwan  
 Prof. Hong-zhi Wang, Department of Computer Science and Technology, Harbin Institute of Technology, China  
 Prof. Shawn X. Wang, Department of Computer Science, California State University, Fullerton, United States

## **Co-editor**

Professor Cheng-Yuan Tang, Huafan University, New Taipei City, Taiwan

Prof. Wen-Tsai Sung, Department of Electrical Engineering, National Chin-Yi University of Technology, Taichung, Taiwan, songchen@ncut.edu.tw  
 His main research areas are Electrical Engineering and Wireless Sensors Network.

Prof. Shawn X. Wang, Department of Computer Science, California State University, Fullerton, United States, xwang@fullerton.edu  
 His main research areas are Mathematics, Computer and Information Science.

Prof. Hong-zhi Wang, Department of Computer Science and Technology, Harbin Institute of Technology, China, whz\_hit@qq.com  
 His main research area is Dig data.

Professor Cheng-Yuan Tang, Department of Information Management, Huafan University, New Taipei City, Taiwan, cytang@cc.hfu.edu.tw, chengyuantang@outlook.com. His main research areas are Computer Science and Information Engineering.

## **Technical Program Committee**

Prof. ZhihongQian, Jilin University, Changchun, Jilin, China  
 Prof. Jibin Zhao, Shenyang Institute of Automation, Chinese Academy of Science, China  
 Prof. LixinGao, Wenzhou university, China  
 Prof. HungchunChien, Jinwen University of Science and Technology, New Taipei City, Taiwan  
 Prof. Huimi Hsu, National Ilan University, Yilan, Taiwan  
 Prof. Jiannshu Lee, Department of Computer Science and Information Engineering, National University of Tainan, Tainan, Taiwan  
 Prof. Chengyuan Tang, Huafan University, New Taipei City, Taiwan

**XVIII** — Introduction of keynote speakers

- Prof. Mingchun Tang, Chongqing University, Microwave Electromagnetic and Automation, China
- Dr. Jing Chen, Computer School of Wuhan University, China
- Dr. Yinghua Zhang, Institute of Automation, Chinese Academy of Sciences, China
- Dr. Lingtao Zhang, College of Computer Science and Information Technology, Central South University of Forestry and Technology, China
- Dr. Kaiming Bi, School of Civil and Mechanical Engineering, Curtin University, Perth, Australia
- Dr. Jingyu Yang, Faculty of Aerospace Engineering, Shenyang Aerospace University Shenyang, China
- Dr. Dong Wang, School of Information and Communication Engineering, Dalian University of Technology, Dalian, China
- Dr. Kang An, College of Communications Engineering, PLA University of Science and Technology, Nanjing, China
- Dr. Kaifeng Han, Department of Electrical and Electronic Engineering (EEE), The University of Hong Kong, Hong Kong
- Dr. Sri YulisBinti M Amin, UniversitiyTun Hussein Onn Malaysia, BATU PAHAT, Malaysia
- Dr. Longsheng Fu, Northwest A&F University, Yangling, China
- Dr. Hui Yang, Beijing University of Posts and Telecommunications, Beijing, China
- Dr. T. BhuvanEswari, Faculty of Engineering and Technology, Multimedia University, Melaka, Malaysia
- Dr. Xiangjie Kong, School of Software, Dalian University of Technology, Dalian, China
- Dr. Kai Tao Nanyang, Technological University, Singapore
- Dr. Lainchyrr Hwang, Dept. of Electrical Engineering, I-Shou University, Kaohsiung, Taiwan
- Dr. Yilun Shang, Department of Mathematics, Department of Mathematics, Shanghai, China
- Dr. Thang Trung Nguyen, Ton Duc Thang University, Ho chi Minh, Vietnam
- Dr. Chichang Chen, Department of Information Engineering, I-Shou University, Kaohsiung, Taiwan
- Dr. Tomasz Andrysiak, Technology and Science University, Bydgoszcz, Poland
- Dr. Rayhwa Wong, Department of Mechanical Eng., Hwa-Hsia University of Technology, New Taipei City, Taiwan
- Dr. Muhammad Naufal Bin Mansor, KampusUnicitiAlam, Universiti Malaysia Perlis (UniMAP), Sungai Chuchuh, Malaysia
- Dr. Michal Kuciej, Faculty of Mechanical Engineering, Bialystok University of Technology, Bialystok, Poland
- Dr. Imran Memon, Zhejiang university, Hangzhou, China
- Dr. Yosheng Lin, National Chi Nan University, Nantou, Taiwan
- Dr. Zhiyu Jiang, University of Chinese Academy of Sciences, Beijing, China

- Dr. Wan'anXiong, School of Electronic Engineering, University of Electronic Science and Technology of China(UESTC), Chengdu, China
- Dr. Dandan Ma, University of Chinese Academy of Sciences, Beijing, China
- Dr. ChienhungYeh, Department of Photonics, Feng Chia University, Taichung, Taiwan
- Dr. Adam Głowacz, AGH University of Science and Technology, Cracow, Poland
- Dr. Osama Ahmed Khan, Lahore University of Management Sciences, Lahore, Pakistan
- Dr. Xia Peng, Microsoft, Boston, United States
- Dr. Andrzej Glowacz, AGH University of Science and Technology, Cracow, Poland
- Dr. Zhuo Liu, Computer Science and Software Engineering Department, Auburn University Auburn, United States
- Dr. ZuraidiSaad, Universiti of Teknologi MARA, Shah Alam, Malaysia
- Dr. Gopa Sen, Institute for Infocomm Research, Agency for Science Technology and Research (A\*STAR), Singapore
- Dr. Minhthai Tran, Ho Chi Minh City University of Foreign Languages and Information Technology, Ho Chi Minh City, Vietnam
- Dr. FatihEmreBoran, Department of Industrial Engineering, Faculty of Engineering, Gazi University, Ankara, Turkey
- Prof. SerdarEthemHamamci, Electrical-Electronics Engineering Department, Inonu University, Malatya, Turkey
- Dr. Fuchien Kao, Da-Yeh University, Zhanghua County, Taiwan
- Dr. NoranAzizan Bin Cholan, Faculty of Electrical and Electronics Engineering, UniversitiTun Hussein Onn Malaysia, BATU PAHAT, Malaysia
- Dr. Krzysztof Gdawiec, Institute of Computer Science, University of Silesia, Sosnowiec, Poland
- Dr. Jianzhou Zhao, Cadence Design System, San Jose, United States
- Dr. Malka N. Halgamuge, Department of Electrical & Electronic Engineering, Melbourne School of Engineering, The University of Melbourne, Melbourne, Australia
- Dr. Muhammed EnesBayrakdar, Department of Computer Engineering, Duzce University, Duzce, Turkey
- Dr. DeepaliVora, Department of Information Technology, Vidyalankar Institute of Technology, Mumbai, India
- Dr. Xu Wang, Advanced Micro Devices (Shanghai), Co. Ltd, Shanghai, China
- Dr. Quanyi Liu, School of Aerospace Engineering, Tsinghua University, Beijing, China
- Dr. YiyouHou, Department of Electronic Engineering, Southern Taiwan University of Science and Technology, Tainan City, Taiwan
- Dr. Ahmet H. ERTAS, Biomedical Engineering Department, Karabuk University, Karabuk, Turkey
- Dr. Hui Li, School of Microelectronics and Solid-State Electronics, University of Electronic Science and Technology of China, UESTC, China
- Dr. Zhiqiang Cao, Institute of Automation, Chinese Academy of Sciences multi-robot systems, intelligent robot control, China

**XX** — Introduction of keynote speakers

Dr. Hengkai Zhao, School of Communication And Information Engineering, Shanghai University, China

Dr. Chen Wang, School of Electronic Information and Communications, Huazhong University of Science and Technology, China

---

## **Part IV: Sensors, Instrument and Measurement II**



Liang GUO\*, Bi-fu QIAN, Gao-xiang LIN, Ben-ren PAN

## **Design of Remote Real-Time Measuring System of Temperature and Humidity based on Raspberry Pi and Java Language**

**Abstract:** In order to improve the temperature and humidity monitoring level in substations, a remote real-time measuring system of temperature and humidity based on Raspberry Pi and Java language is developed. This system consists of three layers of hardware architecture, including client, server and temperature and humidity measurement module. The client and server are connected to the Internet or LAN, using Java language programming, and there are four modes of communication between the client and the server, while the client can display the visual control interface and measurement results. The system in operation shows high efficiency and fast speed, and it can greatly improve the temperature and humidity monitoring level, with great flexibility and a strong scalability.

**Keywords:** Raspberry Pi; embedded system; java language; remote measurement of temperature and humidity; multi thread; GUI interface

### **1 Introduction**

Temperature and humidity are the main indicators of the environment. In the traditional power system substation, temperature and humidity need to be monitored on many occasions (such as secondary screen cabinet, outdoor terminal box). At the present stage, the main means of monitoring is on-site inspections, depending on the human observation, feeling or artificial use of temperature-humidity measurements, which is not accurate enough, large workload, low efficiency and unable to know historical changes, and cannot view the data of temperature and humidity remotely either.

At present, the research on remote monitoring of the temperature and humidity in the transformer substation is few. Literature [1] developed a temperature and humidity real-time control system in substation. The system realizes the remote viewing of temperature and humidity data and the monitoring of historical data. However, since the field of hardware is implemented based on MCU (MicroControllerUnit), where the

---

\*Corresponding author: Liang GUO, Power Grid Technology Center, State Grid Jiangxi Electric Power Science Research Institute, Nanchang, China, E-mail: guoliangxinyu@126.com

Ben-ren PAN, Power Grid Technology Center, State Grid Jiangxi Electric Power Science Research Institute, Nanchang, China

Bi-fu QIAN, Gao-xiang LIN, Substation maintenance department, State Grid Wenzhou power supply company, Wenzhou, China

database is unable to establish, the monitoring client must constantly be connected with each measurement device to update the database, and the measuring data will be lost in the time period of disconnection. When the number of field measurement devices is large, the workload of connection and database operation for monitoring client machine will be very hard, which will make the measuring system slow and even wrong. What's more, the client of this system must be acted by computers with external conversion equipment. There are quite a lot of complex equipments in the whole system and it's difficult to implement the system. With the development of science and technology, temperature and humidity monitoring systems are researched and developed in other places such as greenhouse of vegetables, warehouses, piggeries in recent years [2-5]. Controllers of measurement of these methods are mostly also MCUs, unable to achieve the site data storage. In order to handle the storage of the field data and access from the clients, some others set a server in addition, but that greatly increased the cost and complexity of the system.

A remote real-time measuring system of temperature and humidity based on Raspberry Pi and Java language is developed. In this system, there is one Raspberry Pi set in each measuring point, as a measurement controller and server in the same time. Clients are acted by the ordinary computers, and both server and client are programmed using Java language, which is excellent in cross platform features. There are a variety of communication modes between clients and Raspberry Pi servers, and in each kind of communication mode and even when the client exit, the Raspberry Pi server can still store measuring results, without data loss. And the connection efficiency is greatly improved by flexible switching of various communication modes. The clients realize the visual control interface and the data vivid display with Java program, making the operation simple and the result clear at a glance.

The Raspberry Pi, whose processor is ARM-controller and operating system bases on Linux, is an open type of embedded system developed by a British small charities “The Raspberry Pi Foundation”. The size of one Raspberry Pi is merely equal to credit card, cheap, with small size and wide community. However it has all the functions of the host computer, provides a variety of interface, and can achieve powerful functions.

## 2 Overall Structure

The temperature and humidity remote real-time measurement system has a three-layer hardware architecture including client, server, and temperature and humidity measurement module, as shown in Figure 1. The client can be acted by the computer, and interact with the human through the custom GUI interface, obtaining the command and sending it to the server through the network. The server is acted by the embedded system Raspberry Pi. It accesses network, receives instructions from the client and completes the corresponding operation, controls the temperature and humidity measurement module, and sends the data to the client. The temperature and

humidity measurement module contracts with Raspberry Pi through a general IO port, and makes the measurement in accordance with the requirements of communication.

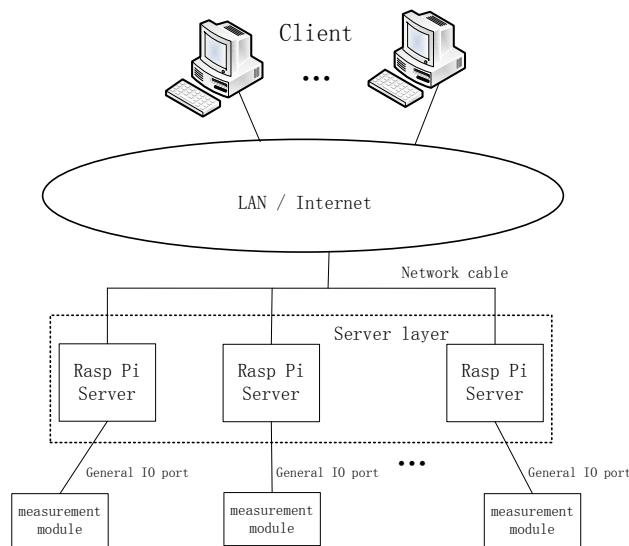


**Figure 1.** Architecture of temperature and humidity remote real-time measurement system

## 2.1 Client

Client uses java graphical user interface (GUI) technology to generate visual control interface. The interface can be input the server IP and port number to be connected, and provides a plurality of keys, each of which achieve a specific function. The client realizes the connection and communication with the server by network programming technology based on TCP/IP protocol. It also achieves the data operation and real-time data and historical data display using database technology and JfreeChart module.

## 2.2 Server

The server uses the network multi-thread programming technology to enables the server to be able to realize the real-time monitoring to the network port when executing the command, which is called multi-tasks executing simultaneously. It contracts the temperature and humidity measurement module for data and instructions exchange through the general IO port, processing received data, storing it in the database, and uploading data or database files to the client according to the need.

### 2.3 Temperature and humidity measurement module

The temperature and humidity measurement module is connected with Raspberry Pi through IO port pins to interactive data and instructions. The module is integrated by temperature and humidity sensor and single chip. It can output high and low level flow to Raspberry Pi pins receiving a correct start command, when it is provided the power supply. The high and low level flow, which represents the value of temperature and humidity, is encoded using a specific encoding mode. The program in Raspberry Pi processes the level flow by converting it into digital signals, according to the coding mode of data, and further transforms it into specific temperature and humidity values.

## 3 Realization of communication between client and Raspberry Pi server

### 3.1 Communication mode

Four communication modes are adopted in this system.

1. *Real time measurement mode.* The client sends a command on behalf of the “real time measurement” to the server. After receiving the command, the server starts the temperature and humidity measurement module connecting with it to continuously measure the temperature and humidity. When a value is measured, it is first stored in the database in a certain format, and then sent to the client. The process is carried out in a loop.
2. *Background measurement mode.* The client sends a command on behalf of the “background measurement” to the server. After receiving the command, the server starts the temperature and humidity measurement module connecting with it to continuously measure the temperature and humidity. When a value is measured, it is stored in the database in a certain format, but is not sent to the client.
3. *Access to historical data mode.* The client sends a command on behalf of the “getting historical data” to the server. After receiving the command, the server starts the file transfer command, and sends the database file of the stored data to the client.
4. *Client exit mode.* The client sends a command on behalf of the “client exit” to the server. After receiving the command, the server detects the current communication mode, and will stop the current mode and transferred to the background measurement mode if the current mode is “real time measurement” mode. If the current mode is “access to historical data” mode, the server will transfer to background measurement mode after the completion of file transmission, and if it is in “background measurement mode”, then continues to keep on.

### 3.2 The function of the server side

The Raspberry Pi server has the following functions:

- The server keep on listening signal from the client when it has started.
- Each time it receives an order or request, start a thread to process, and continue to listen to new requests at the same time.
- After receiving the command “real time measurement”, the server start the temperature and humidity measurement module connecting with it to continuously measure the temperature and humidity. When a value is measured, it is first stored in the database in a certain format, and then sent to the client. The process is carried out in a loop.
- After receiving the command “background measurement”, the server starts the temperature and humidity measurement module connecting with it to continuously measure the temperature and humidity. When a value is measured, it is stored in the database in a certain format, but is not sent to the client.
- After receiving the command “getting historical data”, the server starts the file transfer command, and sends the database file of the stored data to the client.
- After receiving the command “client exit”, the server will detect the current communication mode, and transfer to the background measurement mode.

### 3.3 The function of the client side

The client has the following functions:

- When the program is started, a control panel is open, and there are a server IP and port data frame, the state status bar, buttons of “connecting”, “real-time measurement”, “do not display / background measurement”, “access to historical data” and “quit” on the panel.
- Enter the Port and IP and press the “connection” button, the client is ready to connect to the server.
- When “real-time measurement” button is pressed, the client commands the server to start measuring, and is prepared to accept the data of measuring. After obtaining the data, two rectangular boxes with different colors to display real-time temperature and humidity values appear in the center of the control interface, and a JfreeChart real-time window is open, showing the recent changes of the data within 300 seconds.
- When “background measurement” button is pressed, the client sends the command to the server, the temperature and humidity value in the center of the control interface stop updating, and the real-time window of JfreeChart is close.
- When “access to historical data” button is pressed, the client is ready to accept data document sent by the server. When the document is completely received, a new data display window, which shows all the data, is generated.

- When “exit” button is pressed, all the windows disappear, and the server is commanded to transfer to “background measurement” mode.

### 3.4 Achieving network communications based on the TCP/IP protocol using Java language

Because operating system of the Raspberry Pi server is Linux, and that of the client computer is Windows, so the TCP/IP protocol, which can realize the interconnection of different hardware, different operating systems, different network systems [6], is used. In the network program of Java language, “Socket” is abstracted into a class for connecting applications with the network port, so the Socket class can be used to write communication programs. The interaction between the server and the client using Socket is shown in Figure 2.

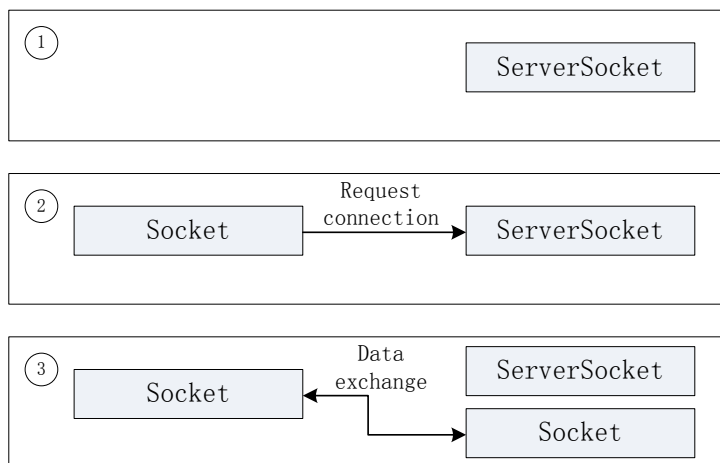


**Figure 2.** Interaction between client and Raspberry Pi server

There are three steps for the server and client to establish connection. Step 1, the server program creates a ServerSocket class, then call the accept () method waiting for a client to connect. Step 2, the client program create a socket to request to establish a connection with the server. Step 3, the server receives the client connection requests, and creates a new socket with the client to establish a connection, and in the same time the server continues to wait for new connections.

When the client and server have established a connection, they can carry on the exchange of instructions, data and data files, completing the corresponding communication tasks.

## 4 Key technology of remote measurement system

### 4.1 Start and setting of the Raspberry Pi server

To start the Raspberry Pi, the following is needed: (1) a Raspberry Pi (B type of second generation is used here); (2) USB or wireless mouse and keyboard; (3) display; (4) 16g SD card (the capacity can be increased according to the actual demand); (5) 5V DC power supply [7].

Before starting Raspberry Pi, the OS raspbian must be installed in it. There is a wide range of community resources for Raspberry Pi, providing lots of convenience for applications. The SD card should be formatted before installing operating system, and operating system installation file compression package NOOBS should be downloaded from the Raspberry Pi official website (URL: [www.raspberrypi.org](http://www.raspberrypi.org)). After decompression, the NOOBS files are copied into the SD card by card-reading device. Then insert the SD card into the card slot of the Raspberry Pi, connect mouse, keyboard, display, and the 5V power supply. After that, the Raspberry Pi will automatically start the installation program of operation system. When the operating system installation completed, Raspberry Pi can start.

The Raspbian operating system comes with the Java programming environment, which makes Java programming possible. Since this program requires database, taking into account the limited resources of embedded system, the light SQLite3 database is chosen for database of the server in this system. In the case of networking, open the command line interface, enter the following statement one after another to obtain the latest update, and to install the SQLite3.

```
sudo apt-get update
sudo apt-get upgrade
sudo apt-get SQLite3
```

In addition, the SQLite database driver package is needed to download for Java programming (the latest version of this paper is “sqlitejdbc-v056.jar”), and should be placed under the Java project folder.

### 4.2 Control of temperature and humidity measurement module from Raspberry Pi

#### 4.2.1 Hardware connection of temperature and humidity module

The type of temperature and humidity measurement module used in the system is DHT11. The module includes a resistive type humidity sensitive element and a NTC temperature sensor, and they are connected with a high-performance 8-bit microcontroller. The temperature and humidity sensors and the microcontroller are integrated together in a package, with high reliability and stability. Just providing the working power and control signal, then it can measure and output the temperature and humidity data of the digital signal.

DHT11 has 4 pins: (1) VCC power supply 3.3 ~ DC 5.5V; (2) DATA serial data, single bus; (3) NC air foot; (4) GND grounding.

The B type of second generation Raspberry Pi has 40 pins. For a pull-up resistor have been integrated between the power supply and the data interface inside the DHT11 module, the data export can be connected directly to Raspberry Pi GPIO port pin. The VCC, DATA, GND pins of DHT11 module should be respectively connected with Raspberry Pi 5V power pin and the GPIO pin and GND pin, while NC port can be suspended, as shown in Figure 3.

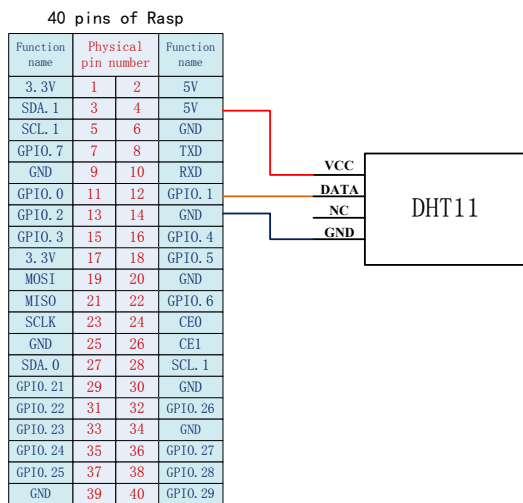


**Figure 3.** Wiring diagram between the DHT11 module and the PI pins

#### 4.2.2 Control program of temperature and humidity module

Since Python language for Raspberry Pi has a rich library, it is convenient to achieve control of Raspberry Pi pins using Python [8]. In this paper, Python language is used to write the program of data exchange with DHT11 module, and when DHT11 measurements are needed by Raspberry Pi, Java language program is run to call the python scripts. The measurement principle of DHT11 is as follows:

- After power up, DHT11 waits for 1s to cross the unstable state, and then measures the ambient temperature and humidity, and records data, while the data line of it has been pull-up by resistance and maintained at a high level. At this time, the DATA pin is in the input state, constantly detecting external signals.
- The microprocessor I/O port connected with DHT11 is set as output state and outputs low level for more than 18ms, and then is set as input state. Due to the pull-up resistor, the microprocessor I/O which is the same level to DHT11 data line, becomes high, waiting for DHT11 answer signal.

- c) When DHT11 data pin detects the external sustained 18ms low level ends into a high level, it delays for a short time and turn as the output state, and immediately outputs low level signal for 80 microseconds as a response signal, followed by the another output of 80 microseconds high level, to notice peripheral ready to receive data. At the same time, the microprocessor I/O should be in the input state, and when it detects low level (DHT11 response signal), begin to receive data after waiting for 80 microseconds of high level.
- d) The DHT11 starts to output 40 bit data through the DATA pin, while the microprocessor starts to receive 40 bits of data according to the change of the I/O level. 50us low level and 26~28us high level stand for data “0” and 50us low level plus 70us high level stand for data “1”. The flow chart of the program according which microprocessor controls DHT11 is shown in Figure 4.

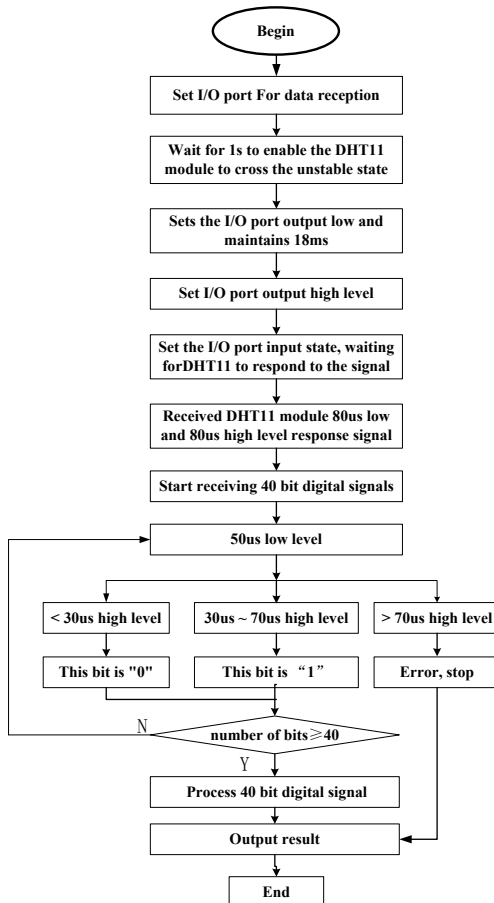


**Figure 4.** Program flow chart of DHT11 temperature and humidity measurement module

#### 4.2.3 Java language calls Python program

Java language has excellent cross platform characteristics, so that it can call any program. The Java program can be simplified by calling the Python program which has been completely written. If the temperature and humidity control program is named dht11.py, and stored in the Java project file, the following Java statement section is used to achieve the call to the program, and the operation results is displayed on Java interface.

```
try{
    Process pr = Runtime.getRuntime().exec("python dht11.py");
    BufferedReader in = new BufferedReader
        (new InputStreamReader(pr.getInputStream()));
    String str;
    while ((str = in.readLine()) != null){
        System.out.println(str);
    }
    in.close();
    pr.waitFor();
} catch (Exception e) { e.printStackTrace(); }
```

After the Java program is compiled, enter “java dht11 (dht11 is the name of Java program of this system)” directly in the command line interface, the running results will be the same as the results of running Python program.

#### 4.3 Java multi thread programming for Raspberry Pi server

The server works in a variety of modes. When there is no command from the client, the server will measure the temperature and humidity and store the result in database continuously. When the server receives the “real-time measurement” command, it begins to measure the temperature and humidity according to the timing of the client, and sends the data to the client. When the client receives the “access to historical data” command, the server will transmit the data file to the client at the same time of measurement. For the realization of these functions above, there is a prerequisite that the server can simultaneously carry on the work of the temperature and humidity measurement, the network port monitor, the data document transmission and so on. As a result, the server program needs to have the ability to perform multiple tasks at the same time.

Java language provides a multi-threaded concurrency mechanism, which makes it possible to execute multiple threads in the program, each thread to complete a function, and concurrent with other threads.

In this paper, the server program constructs the multi thread function of the server through the realization of the java.lang.Runnable interface. The specific process is as follows. First, create a “Runnable” object, and declare a class object

named HandleATask through the statement “HandleATask implements Runnable{} class”, in which the corresponding receiving instruction and the function of the corresponding instruction are set up to realize the specific communication mode. Then use the statement “new Thread(new HandleATask(socket)).start();” to create a thread instance and calls the “Start ()” method to start the thread, where “socket” is the server socket that has been started. The flow chart of the realization of the multi thread function of the server is shown in Figure 5.

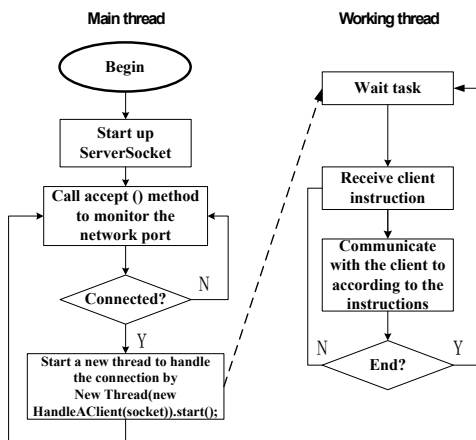


**Figure 5.** Multi-threaded program diagram of Raspberry Pi server

The main program thread realizes real-time monitoring the client's request through ServerSocket, if there is a connection, a new thread is started to process the connection, without affecting the following new connections, so the implementation of multiple tasks can be achieving at the same time.

#### 4.4 Database design

In order to store the measured data of the temperature and humidity, and obtain historical data, it is necessary to establish a database.

After setting the Raspberry Pi server as mentioned earlier, Java program in Raspberry Pi server can process database operation. First, refers to a SQLite database driven by using the statement “Class.forName(“org.sqlite.JDBC”);”, then set up database files and data table, the data will be stored in the database file according to the format of the data table after every measurement. The format and content of each data in the data table can be set according to the actual needs. The data table of this paper includes four parts: server identification, serial number, temperature, humidity and the corresponding time.

## 4.5 Client GUI interface design

### 4.5.1 Client program flow

The system client needs to communicate with human through visual GUI interface where control interface and measurement results are shown. There are, in Java language, rich GUI graphical user interface programming libraries which makes it capable to achieve displaying control interface and measurement results. The system Java program flow chart of client is shown in Figure 6. The communication model 1~4 in the program flow chart respectively indicates the real-time measurement model, the background measurement model, the access to historical data mode, the client exit mode, which are mentioned before.

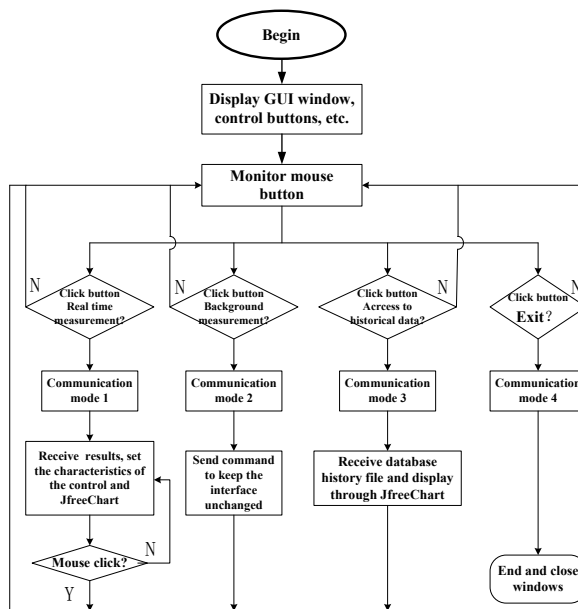


Figure 6. Java program flow chart of client

### 4.5.2 Visual interface and dynamic display of measurement results

Using java GUI tool can realize the visualization window, and displaying real-time data update. The JavaFX stage, scene class and pane class can realize visualized GUI interface [9-13] and convenient control command input. Data dynamic update can be implemented through timeline class. In this paper, the size of the widths of rectangle frames filled with two different colors is used to mean temperature and humidity, and the digital results of temperature and humidity are displayed in the same time.

#### 4.5.3 Clicking mouse to control temperature and humidity measurement

Issuing commands to control the temperature and humidity sensors to start or stop, is achieved through adding the mouse button driver event class to the button. For example, there is a Java statement blow which can be used for adding mouse button driver event class (where “animation” is an example of the Timeline class). In the statement, after adding mouse button driver event class to button named “btMeasure1” (real-time measurement), click the button by mouse, then the system displays prompt “Real-time Measuring...” and starts the dynamic display.

```
btBegin.setOnAction(e ->{
    System.out.println("Real-time Measuring...");
    animation.play();});
```

#### 4.6 Design of JFreeChart graphic

JFreeChart is a widely-used chart library for Java, which can be easily used for Java applications to show the charts of professional quality. In this paper, JFreeChart is used to display real time measurement data and historical data.

In this paper, the realization of real-time data displaying method is as follows. Firstly, construct a JfreeChart chart through the implementation of the Runnable interface, and join real-time data into the timeSeries sequence. Then secondly, create a JFrame object, and add the chart into the JFrame object, and finally start the instantiate Runnable object to realize real-time display. This thread is added in the communication mode 1.

The realization of historical data displaying method is as follows. Firstly, construct a JfreeChart chart through the implementation of the Runnable interface, and query the database files, add all the specified temperature and humidity data into the XYSeries sequence of the chart. Then secondly, create a JFrame object, and add the chart into the JFrame object, and finally start the instantiate Runnable object to realize real-time display. This thread is added in the communication mode 3.

Due to the chart for real-time and historical data display is achieved by starting the instantiate Runnable object, the chart can be shown simultaneously with the other functions of the Java program.

## 5 Operation results

Raspberry Pi server is connected to the Internet/Intranet by network cable and connected with DHT11 temperature and humidity module through the GPIO port. The physical map is shown in Figure7. Before work, Raspberry Pi server must be started, waiting for client connection requests.

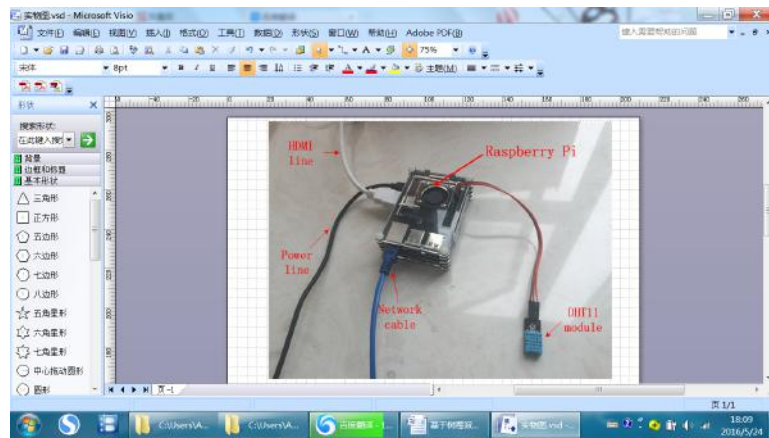


Figure 7. Picture of Raspberry Pi server and DHT11 module

The client of this measurement system is a computer connected to the net. When the application is started, the client computer displays initial interface, and on the top of the interface, there are four buttons on behalf of the four kinds of network model respectively. The left side is the server IP and port input box, and the intermediate region for the schematic real-time displaying, while the State bar below is for the prompt displaying. As shown in Figure 8.

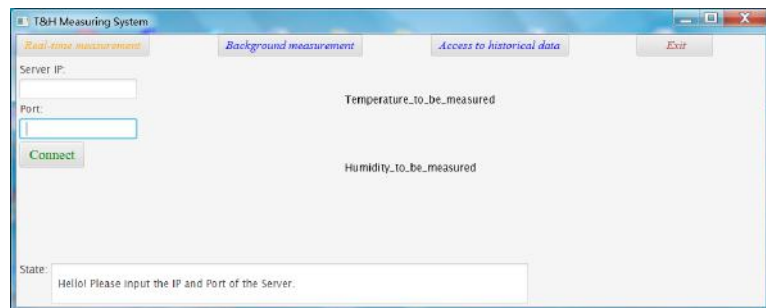
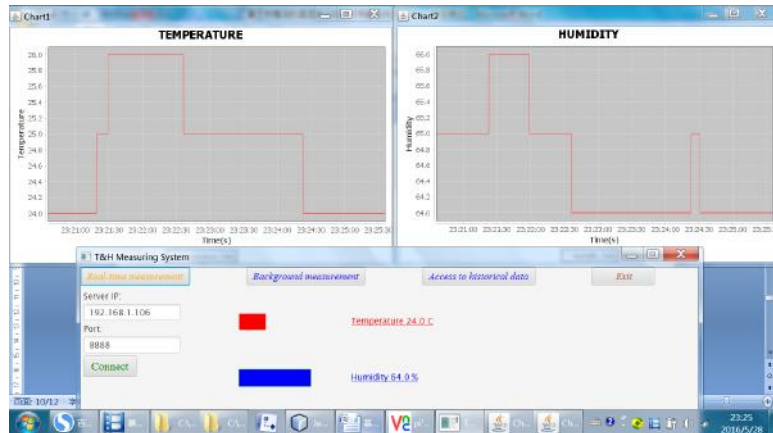


Figure 8. The client initial interface of temperature and humidity measurement system

Input the server IP and port number, click the connection button, State bar will display the prompt language “Client has get the address, waiting for demand...”.

When “Real-time measurement” button is pressed, program will start real-time measurement. The middle part of control interface is blank., before starting measurement, and now the region display two rectangular boxes with different colors for sketching the size of temperature and humidity. Meanwhile, two JfreeChart windows are generated to display the real-time measurement graphs. The graphs

show the recent 300s temperature and humidity real-time changes, as shown in Figure 9.



**Figure 9.** The client interface state of “real time measurement” mode

When the “Background measurement” button is pressed, the program will start the server to automatically process measuring in the background and store data in the database. If real-time measurement have started before, the JfreeChart window will hide and the center temperature and humidity display area diagram will stop updating, being in the last state. As shown in Figure 10.

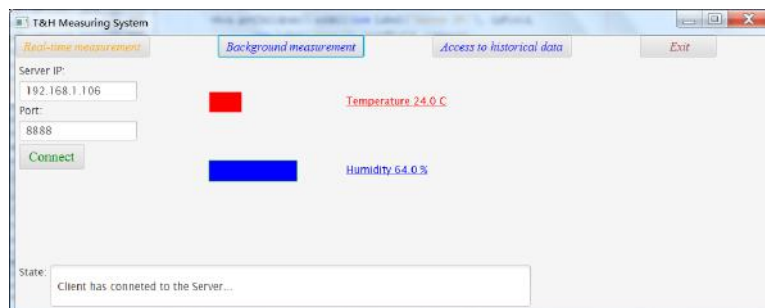


**Figure 10.** The client interface state of “background measurement” mode

When the “access to historical data” button is pressed, the program will start the server to upload the database file, which contains all measuring data in the Raspberry Pi server. A new JfreeChart window will be started to display all the data of temperature and humidity, and status bar will show the time period for the historical data. This

button can be executed concurrently with other tasks, without affecting previous operations. Temperature and humidity changes of a secondary screen cabinet in 3 days time is shown in Figure 11. It can be seen in the Figure that the temperature change is little, and humidity change is great. The humidity was once more than 70%, indicating that the operation and maintenance personnel should take timely measures to control the over-limit humidity.

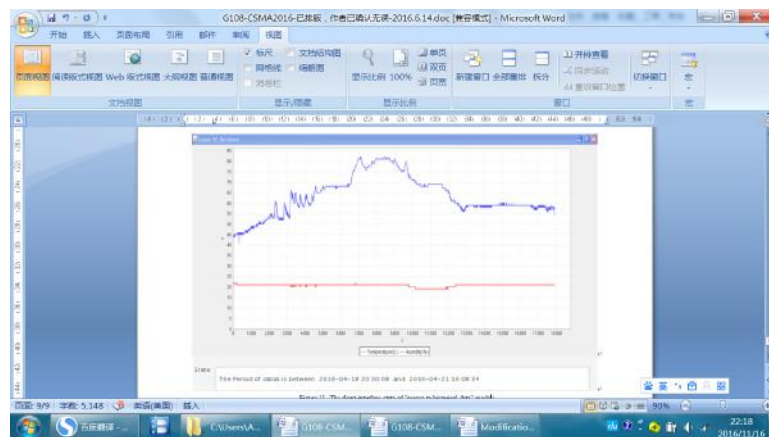


**Figure 11.** The client interface state of “access to historical data” mode

When the “exit” button is pressed, all the displaying windows withdraw, and the program send commands to the server to get into the state of automatic continuous measurement, storing data in the database and waiting for a new connection in the same time.

Operation results show that the system has rapid response, complete data, clear graphics, reliable measurement results, which can greatly facilitate the operation and maintenance personnel to monitor the temperature and humidity of key places of substation.

## 6 Conclusion

In this paper, a temperature and humidity remote real-time measurement system is designed based on Raspberry Pi and Java language, and it realizes the data continuously measured and database generated on-site. Because the system uses Raspberry Pi, which can act as both on-site measurement controller and server, as a controller, so the database operation is assigned to each measurement server, thereby reducing the operation burden of client and thus improving the efficiency of the connection.

This system is composed of client and server side, and can add multiple clients and servers according to need, so it has with great flexibility. The server uses multi thread programming, which can achieve communication between multiple clients and one server. While the client can also achieve communicate with multiple servers by inputting different IP and port. As a result, the system can realize the multi-directional flow of information. The client interface uses java visualization interface and JfreeChart for programming, and the interface can be changed according to need, with a strong scalability.

The system can also be used in other places where the temperature and humidity monitoring is needed. The communication architecture and programming method used in this system can also be used in other measurement and monitoring fields.

## References

- [1] Xu Tong. Research and development of temperature and humidity observe and control in substation[D], North China Electric Power University, 2012
- [2] Yang Liu, Mao Zhihuai, Jiang Zhijie, Ren Zhijun. Remote monitoring system of grain temperature and humidity based on wireless transmission [J], Chinese Journal of Agricultural Engineering, 2012, 28 (4).
- [3] Zhu Junguang, Gao Jian, Tian Jun, Zhao Min, Qi Haifeng, Xie Yaquan, et al. Long-distance temperature and humidity monitoring system based on Internet of things technology[J], Experimental Technology and Management, 2014, 33 (11).
- [4] Guo Dongping. Research and development of greenhouse temperature and humidity monitoring alarm device based on single chip microcomputer [D]. Northwest Agriculture and Forestry University, 2015
- [5] Sun Qianwen. Design of piggery humidity monitoring system based on Wireless Sensor [D]. Anhui University of Technology, 2014
- [6] Ming Rikeji. Java from entry to the master [M]. Tsinghua University press, 2012
- [7] Carrier Anne Philbin. Adventures in Raspberry Pi[M]. People's Posts and Telecommunications Press, 2015
- [8] Alex Bradbury. Learning Python with Raspberry Pi [M]. Beijing: Mechanical Industry Press, 2015.
- [9] Y.Daniel Liang. Introduction to Java Programming. Mechanical Industry Press, Beijing: 2016.
- [10] Song Kai, Yao Jia Ming, Li Jing, Wang Sheng. Research on Intelligent Home Furnishing control switch based on Raspberry Pi[J]. Electronic Technology and Software Engineering, 2015 (21).
- [11] Lai Jiang, Li Yingxiang, He Qi, Su Kai. Elevator colorful display system based on Raspberry Pi[J]. Single chip microcomputer and embedded system application, 2014 (5).
- [12] Li Wensheng. Embedded Linux development teaching exploration based on Raspberry Pi [J]. Electronic technology and software engineering, 2014 (9).
- [13] Bird brother. The Linux private kitchens based learning of Bird brother [M]. People's Posts and Telecommunications Press, 2010

Da-peng Li, Xin-an Ge

# Design of Emotional Physiological Signal Acquisition System

**Abstract:** Emotional physiological signal is non-controlled by man's subjective emotion, and is more objective and suitable for emotion calculation. In this paper, human physiological signal acquisition system for emotion recognition based on data acquisition card was designed. For collecting physiological signal in different emotion status, we used a video induction method on subjects participated the experiments. The EMG, body temperature and pulse signal of upper arm muscle were collected when subject was angry, happy, fear, sad, surprise and disgust. Collected signal can be shown and processed in PC to study the connection between the emotional and physiological signal characteristics. Experiments showed that this system correctly collected physiological signals and could be used for emotion recognition.

**Keywords:** Emotional physiological signal; Pulse signal; Electromyographic (EMG); Data Acquisition

## 1 Introduction

With the rapid development of Internet, especially the mobile Internet, people day and night play with computers and cell phones. Human-human Interaction gradually reduced, and human-machine interaction increased. People put forward higher requirements in the human-computer interaction technology and emotional needs. As the affective computing continuously developed, emotional interaction has become the main development trend of high-level information era of human-computer interaction. Emotion recognition is a key problem in affective computing and is the foundation of establishing harmonious man-machine environment.

At present there are two ways for emotion recognition, one is to detect physiological signals such as ECG, EEG, the other is to detect the emotional behavior such as facial expression recognition, speech emotion recognition and gesture recognition. Currently, the latter is used more. Psychology on the commonly used questionnaire investigation, the result is usually affected by subjects and subjective factors of the experiment. And physiological changes only controlled by the autonomic nervous system and endocrine system, is not controlled by man's subjective. The physiological

---

\*Corresponding author: Da-peng Li, School of Mechanical and Electronic Engineering, Tianjin Polytechnic University, Tianjin, China, E-mail: ldp513@163.com

Xin-an Ge, School of Mechanical and Electronic Engineering, Tianjin Polytechnic University, Tianjin, China

signal measurement method and data is more objective. People found that different emotions can produce different muscle motion mode. We can according to the different EMG signal of extraction of feature to identify the emotion [1].

Emotion needs certain physiological activation energy. The energy comes from the activation of human physiological functions, including the changes of neurocrine, increased blood pressure, heart rate, dilated pupils, muscle contraction, etc. People laughed and the cheek raised, for example, and the muscles around the eye heaped up, and the electrical activity in the left hemisphere increased. EMG can well reflect the strength of muscle activity level, local level of fatigue, motor unit excited conduction velocity and muscle coordination and so on.

MIT media team led by professor Picard proved that application of physiological signal for emotion recognition method is feasible. They collected 1 actors deliberately to perform 8 kinds of emotional physiological signals, extracted statistical characteristic value by Fisher. The projection got 83% of the emotion recognition rate [2].

This paper collected EMG signal, temperature, pulse signal of the human body as an emotional identification signal. Figure 1 shows the block diagram of the emotion recognition system [3].

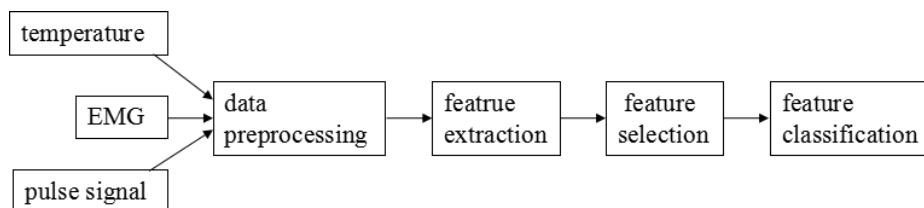


**Figure 1.** Emotion recognition system

## 2 Data acquisition system

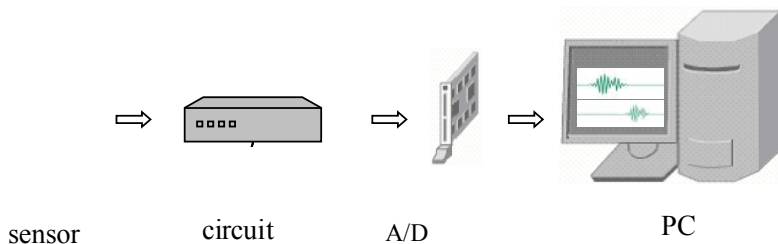
### 2.1 EMG circuit

In order to study surface EMG, body temperature and pulse signal well, a data acquisition system was constructed. Figure 2 shows the construction of the system. Emotional signals could be displayed and analyzed real time, and can be stored in the PC.

The electrodes used in the EMG collection design are silver/silver chloride electrodes with a very low DC offset potential, minimal motion artifact and good low frequency response.

The electrode for disposable sticky Ag/AgCl snap electrode, can guarantee the quality and convenience of the application of the signal, specially used in the surface

EMG measurement in medical or scientific research. It's special viscose texture can prevent skin allergy test before. It only need a few skin preparation and the area is not large. The size of each viscous region is 4cm by 2.2cm, each circular conductive area diameter is 1cm. Its two electrodes are fixed and the center distance is 2 cm, thus avoiding the change detection results from the change of the center electrode distance for each measurement.



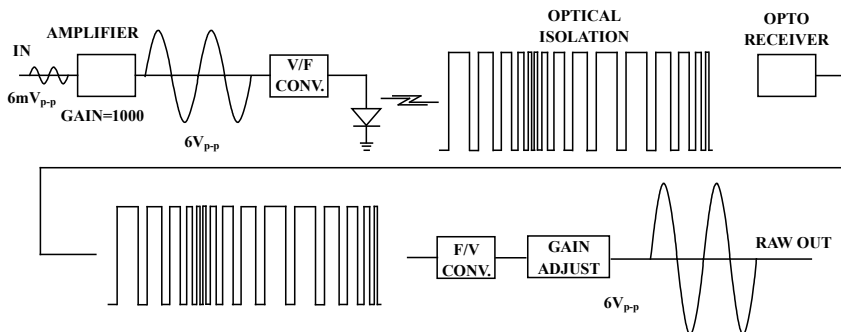
**Figure 2.** Surface EMGs detection system block diagram

Figure 3 shows EMGs detection electrodes stuck to the arm.



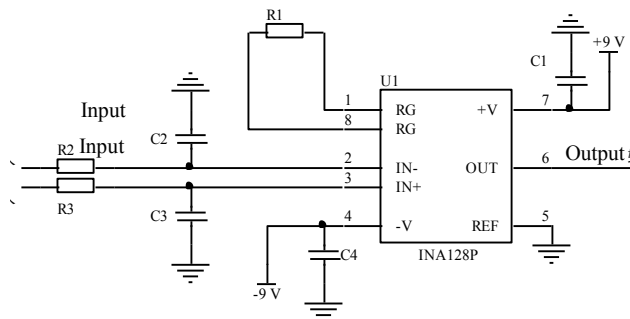
**Figure 3.** Surface EMGs detection electrodes

Figure 4 shows a single channel EMG signal treatment block diagram. EMG signal was amplified in amplifier with gain=1000, and then converted by V/F converter with pulse width of the input voltage changes the size of the optical pulse. The optical pulse is received by the light receiver and then through frequency / voltage converter (F/V) demodulation, gain adjusted as the original output signal output [4].



**Figure 4.** Block diagram of single channel SEMG treatment

Figure 5 shows the preamplifier circuit. An instrumentation amplifier INA128 is used to compare both of the signals to give an output of the difference between them. And it can adjust gain by change the value of R1 [5].



**Figure 5.** Schematic circuit of preamplifier

## 2.2 Pulse signal sensor circuit

Due to people's heart beat, blood flow in blood vessels occur a series of periodic change. The monitoring of the pulse signal is through the collection and the change of blood flow in blood vessels. We will select a simple and convenient, practical, low cost, good performance, high sensitivity of the pulse sensor. Acquisition pulse signal is presented in this paper by selecting sc0073 pulse micro pressure sensor, which has piezoelectric thin film that can change dynamic pressure signal into an electrical signal. And more importantly, this kind of sensor is high sensitivity, small volume, convenient operation and low cost. In addition, sc0073 sensor can better withstand shock wave and overload phenomenon, anti-jamming performance is also better. Therefore they are widely used in all aspects of human society. Figure 6 is the Schematic circuit of pulse signal sensor.

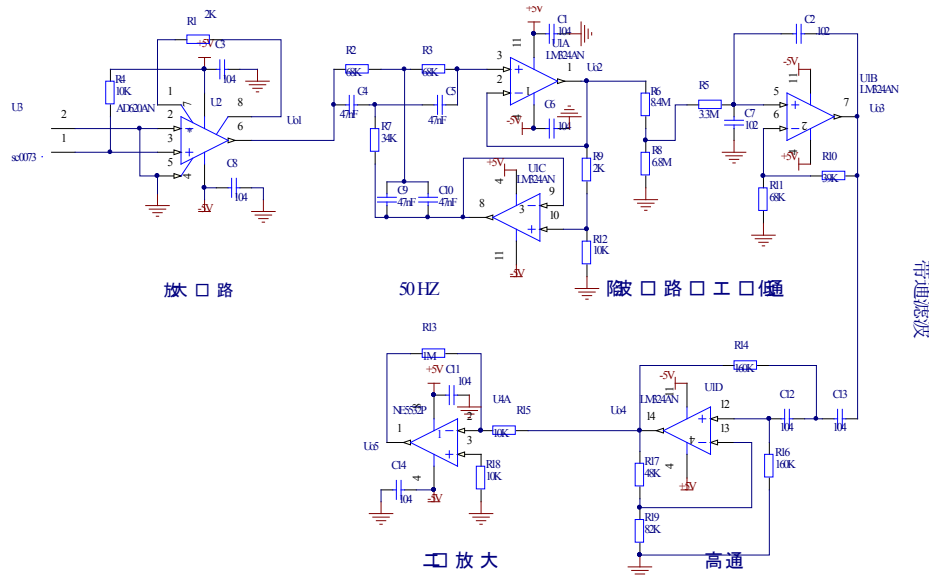


**Figure 6.** Schematic circuit of pulse signal

### 2.3 Temperature circuit

There are various temperature sensors on the market and are widely used at present. But for this system, the temperature accuracy needed is higher. Therefore, we use the latest high precision MF-52E thermistor temperature sensor. MF-52E temperature sensor is not only of high precision, and is low cost, simple and convenient to use. Figure 7 is the Schematic circuit of temperature sensor.

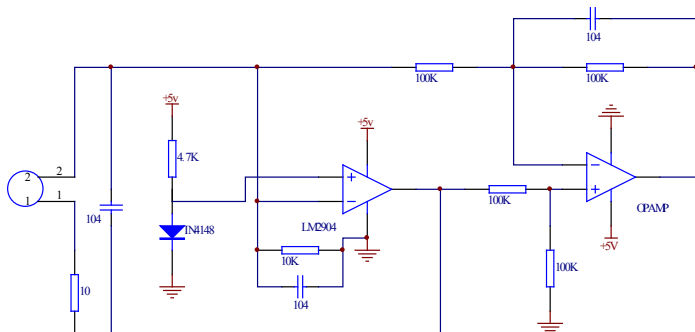


**Figure 7.** Schematic circuit of temperature

## 2.4 Data acquisition card and the interface

Acquisition system was based on acquisition card, Labview and PC. M series DAQ is NI a new generation of multifunctional data acquisition equipment with 16 analog input, can provide DC measurement with above 5.5 bit resolution. Connection mode of the data acquisition card can be divided into single input mode and differential input mode. The single input mode is more easily coupled into the electromagnetic noise than differential mode. So differential mode is used if there is no restriction on the number of connections.

We used the DAQ assistant in LabView, set the voltage value of channel 1 and sampled with N sampling. The corresponding waveform was displayed in PC. Acquisition system as shown in Figure 8.



**Figure 8.** Schematic circuit of pulse signal

## 2.5 Signal collection interface

Visualization interface at the same time was realized in Labview. The corresponding function was shown in Figure 9.

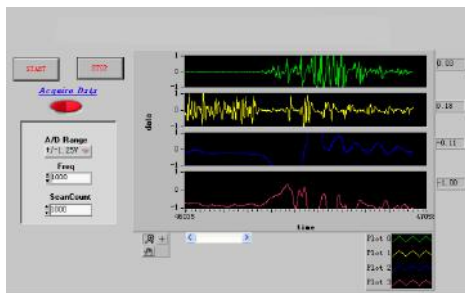


**Figure 9.** Signal collection interface

### 3 Experiment Result

In our experiment, we have chosen a quiet laboratory, we have locked all the doors and windows. Natural light was chosen as the ambient light. We have selected ten participants to take turns into the laboratory. After everyone stayed calm, pulse sensor was fixed on their right hand wrist. The temperature sensor was under his arm and EMG sensor was stuck on the arm. Exercises were necessary to the subjects to train them not to be disturbed. After the preparations, video that could cause anger, happiness, fear, sadness, surprise and disgust was shown by computer. The emotional signal file was stored in the computer. The EMG data collected was shown in Figure 10.

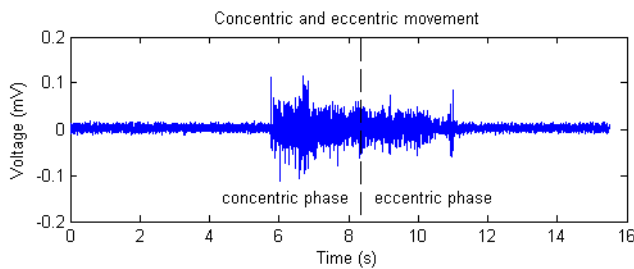


**Figure 10.** Raw Surface EMG

### 4 Conclusion

Acquisition system was designed in this paper for emotional physiological signals. The relationship between the emotional and physiological signals was studied by means of signal processing and computational analysis. Emotional physiological signal recognition system is being designed in the PC. In the future, the wavelet transform method will be used to decompose the collected EMG signals. Through the extraction of EMG signal, the features which may reflect the change of emotion will be extracted. In the reduced feature space, Fisher classifier will be used for further search to select the best subset of features for classification of emotion.

Experiment showed that the system can collect a variety of signals and can be used in the emotion, rehabilitation medicine and psychological research.

**Acknowledgment:** This research was supported by Tianjin High School Science and Technology Development Fund Planning Project 20140405.

## References

- [1] Mahdi Khezri, Mohammad Firoozabadi, Ahmad Reza Sharafat, Reliable emotion recognition system based on dynamic adaptive fusion of forehead biopotentials and physiological signals, Computer Methods and Programs in Biomedicine, Volume 122, Issue 2, November 2015, Pages 149-164
- [2] Rosalind W Picard, affective computing [M]. Beijing university of science and technology press, 2005
- [3] Johannes Wagner, Jonghwa Kim, From Physiological Signals to Emotions: Implementing and Comparing Selected Methods for Feature Extraction and Classification. Proceedings of the 2005 IEEE International Conference on Multimedia and Expo, ICME 2005, July 6-9, 2005, 1-4
- [4] Li Dapeng, Zhang Yaxiong, Artificial neural network prediction of angle based on surface electromyography, 2011 International Conference on Control, Automation and Systems Engineering, CASE 2011:1–3.
- [5] Li Dapeng, Li Xingfei. STUDY ON REAL-TIME CONTROL OF HUMANOID ROBOT USING SURFACE EMGS, International Technology and Innovation Conference 2006, p1999-2002

Yao-peng PAN\*

## EMC Effects On High-Resolution Spaceborne SAR Image

**Abstract:** Due to the complex structures and the wide frequency bandwidth applied for high resolution, the electromagnetic compatibility (EMC) design has significant effects on synthetic aperture radar (SAR) images. In this paper, the characteristics of SAR system are analyzed first. Based on the analysis, the model of noise caused by EMC design is built, which is used for research the effects on SAR images. Finally, computer simulation results illustrate the effects on the SAR images.

**Keywords:** EMC; SAR; noises; image

### 1 Introduction

Spaceborne synthetic aperture radar (SAR) has played an irreplaceable role in remote sensing, and has been used in many area, such as ship detection, environment monitoring, agriculture, resource survey, and so on [1-4]. With the development of the SAR technique, high-resolution, multifunction and miniaturization are the future development trends of spaceborne SAR, which arise a new challenge for electromagnetic compatibility (EMC) design. Because radar itself has both high power emitting device and sensitive receiving device, it is hard to make a good electromagnetic protection in space environment. Moreover, as for SAR, in order to obtain high resolution SAR image, it transmits a linear frequency modulation (LFM) signal, which has a very large frequency range. For example, for 0.5m resolution, 600MHz signal bandwidth is need. Due to so wide signal bandwidth, signal is very easy to be interfered, which consequently affects the quality of the SAR images.

Effects caused by EMC on radar system have been analyzed and discussed in [5-7]. A measurement model is built for radar electromagnetic compatibility analysis in [5], and describes the relationship of the attenuation coefficient of radar maximum range. Moreover, in [6,7], several features of airborne radar and shipborne radar are introduced by using the electromagnetic compatibility, especially the discussion of the effects on wideband signal. However, compared with the traditional radar, SAR is different because of the super-wide frequency bandwidth. Furthermore, due to the requirement of miniaturization and the complex space electromagnetic environment, it is a challenge for EMC design to guarantee the quality of SAR image.

Aim at the problem mentioned above, EMC effects on high-resolution spaceborne SAR image are researched as follow in this paper. Section I gives a general introduction

---

\*Corresponding author: Yao-peng PAN, School of Electronics and Information Engineering, BeiHang University, Beijing, China, E-mail: [pyp@buaa.edu.cn](mailto:pyp@buaa.edu.cn)

of the background. Section II reviews the composition of SAR system and the signal mathematic formula. Section III addresses the effects of EMC on SAR signal. Section IV shows some simulations by using the true SAR images. Section IV draws the conclusions of this paper.

## 2 SAR System And Signal Formula

Synthetic aperture radar is composed of the Linear FM source, transmit device, receive device, Low noise receiver, power amplifiers, and so on. In order to get high-resolution and high gain, LFM signal is applied in SAR system. As for LFM signal, its phase is quadratic, and the frequency is changed linearly, which cover a wide range in frequency domain. The mathematical formula of LFM is given as follow:

$$S(\tau) = A \cdot \text{rect}\left[\frac{\tau}{T}\right] \cdot \exp\left\{-j\pi \frac{B_w}{T} \tau^2\right\} \quad (1)$$

Where  $A$  is the amplitude of LFM signal,  $\text{rect}[\cdot]$  is rectangular envelope,  $T$  is the pulse length of LFM signal,  $B_w$  is the frequency bandwidth, and  $\tau$  is time parameter.

According to the formula (1), the phase of LFM signal should obey quadratic. So, by applying the principle of stationary phase (POSP), we can transform LFM signal to frequency domain, which is given as follows:

$$L(f) = A'(f) \cdot p\left[\frac{f}{f_s}\right] \cdot \exp\left\{j\pi \frac{T}{B_w} f^2\right\} \quad (2)$$

Where,  $f$  is frequency parameter,  $p[\cdot]$  is envelope in frequency domain, and  $A'(f)$  is amplitude of frequency response.

Figure 1 shows an example of LFM signal, and illustrates phase in time domain and amplitude in frequency domain, which has the 30us width and 300MHz frequency bandwidth with a 350MHz sampling rate. From the Figure 1, it is obvious that the signal is very easy disturbed by noise caused by EMC, when the radio-frequency signal is down-conversion to baseband signal. And, noise intensity defines the degree of influence on SAR images.

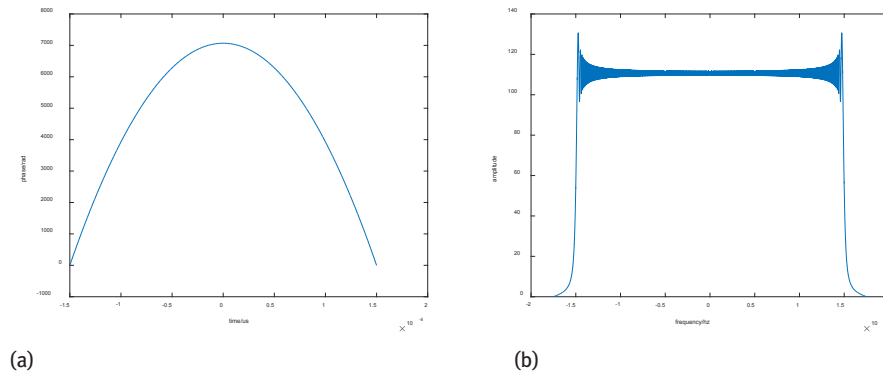


**Figure 1.** LFM signal in time domain and frequency domain:(a) in time domain (b) in frequency domain

### 3 EMC Effects Analysis

In this section, the model of noise will be discussed and analyzed. As mentioned in section II, SAR system is composed with different components, and each component have their own characteristics. For example, some of them work with low-pass frequency characteristic, and some of them work with high-pass frequency characteristic. Moreover, their dynamic range and attenuate are also different, which lead to a complex effect on signal in frequency domain.

High-resolution SAR have a super wide frequency bandwidth. However, different components have different frequency band range and different modulation mode, so the piecewise functions can be used to describe the EMC effects on signal. There will be  $n$  kinds of interference sources, and the whole frequency range is divided into  $m$  segment.

$$L(f) = \begin{cases} L(\Delta f_1) + a_{11}N_1(\Delta f_1) + a_{21}N_2(\Delta f_1) + \dots + a_{n1}N_n(\Delta f_1) \\ L(\Delta f_2) + a_{12}N_1(\Delta f_2) + a_{22}N_2(\Delta f_2) + \dots + a_{n2}N_n(\Delta f_2) \\ \vdots \\ L(\Delta f_i) + a_{1i}N_1(\Delta f_i) + a_{2i}N_2(\Delta f_i) + \dots + a_{ni}N_n(\Delta f_i) \\ \vdots \\ L(\Delta f_m) + a_{1m}N_1(\Delta f_m) + a_{2m}N_2(\Delta f_m) + \dots + a_{nm}N_n(\Delta f_m) \end{cases} \quad (3)$$

Where  $L(\Delta f_i)$  represents the signal without interference,  $\Delta f_i$  represents  $i$ th segment of frequency band,  $N_i$  represents the  $i$ th interference source, and  $a_{im}$  represents the amplitude of effects on  $m$ th segment frequency band caused by  $i$ th interference source.

As for the arbitrary interference source, the amplitude obeys the Gauss distribution, and phase obeys the uniform distribution. Moreover, for different interference sources, their amplitude and phase are statistically independent. Formula (4) give the amplitude statistically distribution.

$$f(x) = \frac{1}{\sqrt{2\pi}\sigma_i} \exp\left\{-\frac{x^2}{2\sigma_i^2}\right\} \quad (4)$$

Where  $\sigma_i^2$  represents the variance of  $i$ th interference source, and the average is zero.

### 4 Simulation

In order to illustrate the effects on the SAR images, we carried out some experiments by using TerraSAR-X image product. The parameters are listed in Table 1.

**Table 1.** Parameters Of Simulations

Parameter	Value
wavelength(m)	0.03
Resolution(m)	1.0
Pulse length(us)	33.6
Bandwidth(MHz)	300
Sampling rate(MHz)	330

And, Figure 2 shows the SAR images results with different noise levels. From Figure 2, the larger the noise level is, the bigger the effect is. And, some weak targets are even submerged by noise caused by EMC, which will decline the image quality and lead a wrong decision based on SAR images. Moreover, in the case of high noise level, SAR images become blurred. So, it is very important to consider the effects caused by EMC, when we design the SAR system, especially for the high-resolution system.

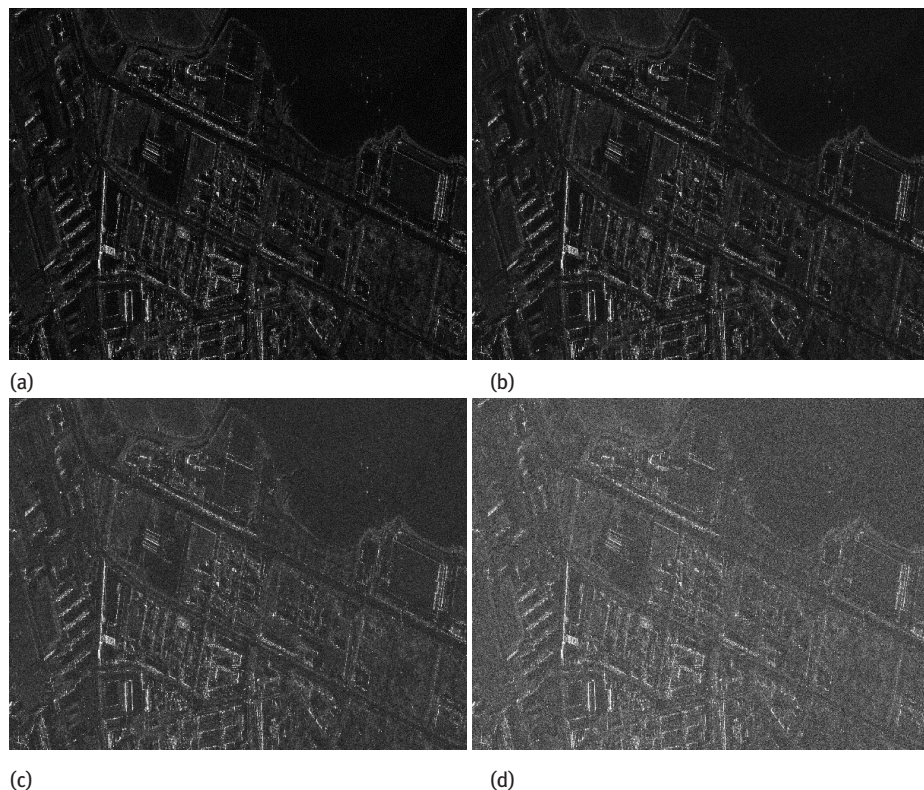


**Figure 2.** EMC effects on SAR images with different noise level:(a) original image (b) image with low noise level (c) image with middle noise level (d) image with high noise level

## 5 Conclusion

To guarantee the quality of SAR image, especially in the case of high-resolution images, the EMC effects should be taken into account. In this paper, combined with the characteristic analysis of LFM signal, the effects on high-resolution SAR images were addressed and verified by simulations using TerraSAR-X image. According to the simulation results, the noise caused by EMC will degrade the SAR image quality, which should be avoided in SAR system design.

**Acknowledgment:** The authors would like to thank to Dr. Yang and Dr. Dai for giving some suggestions for this paper, and some reviewers for their comments that greatly improved the quality of this paper.

## References

- [1] F. Mazzarella, M. Vespe and C. Santamaria, SAR ship detection and self-reporting data fusion based on traffic knowledge, *Geoscience and Remote Sensing Letters*, IEEE, vol. 12, no. 8, pp. 1685-1689, Aug 2015
- [2] G. Suresh, G. Heygster, C. Melsheimer and G. Bohrmann, Natural oil seep location estimation in SAR images using direct and contextual information, *Geoscience and Remote Sensing Symposium (IGARSS)*, 2014 IEEE International, pp. 1678-1681, July 2014.
- [3] G. G. Ponnurangam, T. Jagdhuber, I. Hajnsek, Y. S. Rao. Soil moisture estimation using hybrid polarimetric SAR data of RISAT-1, *IEEE Transaction on Geoscience and Remote Sensing*, vol. 54, no. 4, pp. 2033-2049, April 2016.
- [4] S. Solberg, G. Riegler, , P. Nonin. Estimating forest biomass from TerraSAR-X stripmap radargrammetry, *IEEE Transaction on Geoscience and Remote Sensing*, vol. 53, no. 1, pp. 154-161, January 2015.
- [5] G. Y. Li, H. Zhang, X. Yin, H. L. Tian. Study on Measurement Model for Radar Electromagnetic Compatibility Analysis, *ICMMT*, pp. 1559-1562, 2010.
- [6] X. Chen, K. F. Cui, X. X. Rong. Study on Electromagnetic Compatibility for Airborne Radar, *Modern Radar*, vol. 27, no. 1, pp.55-57, 2005.
- [7] C. Y. Min. Study on Electromagnetic Compatibility for Airborne Radar, *Shipboard Electronic Countermeasure*, vol. 25, no. 1, pp.40-42, 2002.

Ke-ke GU, Yue-fang DONG, Zhe ZHOU, Min LIU, Shi CHEN,  
Wei-wei FU\*

## Real-time Pupil Detection based on Contour Tracking

**Abstract:** A new method for pupil detection was proposed on the basis of contour tracking in this paper. The method scans the binary pupil image to find the starting point of the contour, and then find the complete contour from the starting point. Calculate the contour area to judge if it is eyelash or pupil area. Continue to search until the pupil contour is found and then calculate its diameter and center. According to the pupil information of the previous frame, narrow the detection region for binaryzation and track the contour to get the pupil information of the current frame. Threshold for binarization can be fixed, which is the threshold of the first frame of the cropped image. Experimental results show that the method has high accuracy, stable performance, and can meet the real-time detection speed.

**Keywords:** contour tracking; pupil detection; narrow detection region; real-time detection

### 1 Introduction

Human pupil diameter changes from 2mm to 8mm in general. Regardless of its shape, margin and reflection, pupil has important academic and clinical research value in the human visual system because of its special sensitivity. Therefore, pupil detection is often used for clinical diagnosis [1]. Real-time pupil detection and tracking is an important research topic in the field of computer vision, and is related to many subjects such as physiology, artificial intelligence, pattern recognition, computer vision, image analysis and processing. Meanwhile, it has huge potential application value in the field of health care, traffic security [2], public security guarantee, military affairs, criminal investigation and so on.

Currently, manual inspection is mainly used for the detection of the pupil size, only can give positive diagnosis of the patients with dramatic symptoms. Missed diagnosis of mild symptoms will lead to missed treatment opportunities. If we can detect the above indicators objectively and quantitatively, small changes will be found in the early stage of the disease and postoperative monitoring for timely treatment, and will save more physiological function of patients.

---

\*Corresponding author: Wei-wei FU, Suzhou Institute of Biomedical Engineering and Technology

Chinese Academy of Sciences, Suzhou, China, E-mail: fuww@sibet.ac.cn

Ke-ke GU, Yue-fang DONG, Zhe ZHOU, Min LIU, Shi CHEN, Suzhou Institute of Biomedical Engineering and Technology Chinese Academy of Sciences, Suzhou, China

As a part of the iris recognition detection, the current commonly used pupil localization methods are circular detection operator proposed by Daugman [3] and binarization combined with Hough transform proposed by Wildes [4]. The calculus algorithm proposed by Daugman has high accuracy and robustness, but has long detection time due to the blind search, resulting in a waste of computation. Wildes's algorithm has been improved in the localization speed, but also has the problem of long computation time. Then in order to improve the speed and precision of the Hough transform, the scholars put forward the improved algorithm of Hough transform, such as the point Hough transform [5,6]. These methods are based on circle detection, so the least square method is used to fit the ellipse when pupil is not perfect circle [7]. In addition, other people put forward methods like morphological reconstruction [8], template matching [9], regional growth [10] for pupil detection and pupil extraction based on image feature [11].

This paper realized real-time detection for pupil parameters under light stimulation, mainly using contour tracking to locate the pupil. As the contour tracking has nothing to do with the pupil shape, it is applicable to the irregular pupil. The scope of application can be wider.

## 2 Contour tracking method

Contour tracking, also called boundary tracking, is a method used to extract the boundary information in digital images, which can be used in the segmentation of gray images or binary images. So far, scholars have proposed a variety of contour tracking and other improved methods. Square tracking method, Moore neighborhood tracking method, radial scan method, Theo Pavlidis method and so on are comparatively classical [12]. Each method has its own advantages and defects, and can not apply to all the image conditions.

The basic steps of contour tracking methods are as following: Firstly, determine a point on the object contour as starting point according to some criterions; secondly, find new boundary points in turn from the starting point according to the criteria of tracking; finally, stop tracking according to the conditions for termination. If the image has more than one connected boundary, repeat tracking steps to search for new contours.

## 3 Pupil image processing

### 3.1 Pupil Imaging

Infrared light is generally used in pupil detection. Near-infrared spectrum between 850nm and 950nm has no stimulation to human eyes, and the retina can reflect the

incident light up to eighty or ninety percent. The edge between pupil and iris can be very clear, so the part of the pupil is highlighted. However, there is an unavoidable interference of light source and eyelash in pupil images. Figure 1 shows the pupil image of 450\*275 pixels acquired under the illumination of 850nm infrared.

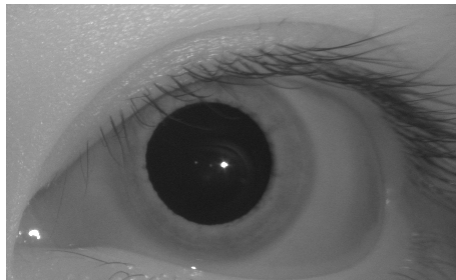


**Figure 1.** Pupil image

In this paper, the flow chart of pupil detection is shown in Figure 2. Firstly, choose the suitable threshold for binarization, then contour track to get the precise contour. Finally get the information such as diameter and the center of the pupil. According to the position of the center of pupil, narrow the search range for the next frames to speed up the detection speed.

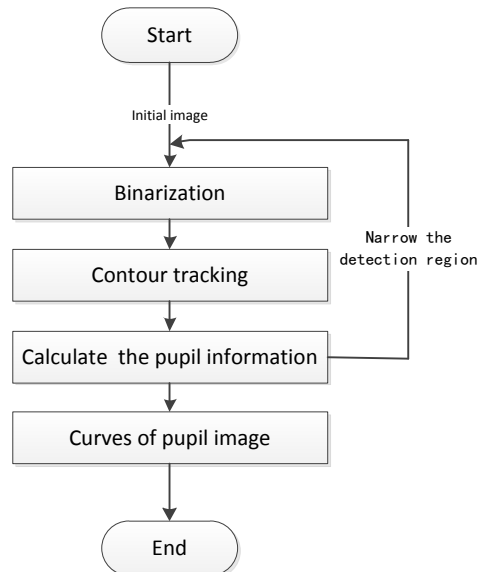


**Figure 2.** Process of pupil detection

### 3.2 Image Binarization

In pupil detection, the aim of binarization is to divide the pupil image into two parts, the pupil and the background. The key is to find the appropriate threshold. As a commonly used method in image processing, a variety of binarization methods have been proposed up to now, such as Otsu method, optimal interactive threshold method, global threshold method based on minimum error and so on. For pupil images, these methods can not be used to segment the pupil perfectly. According to the characteristics of pupil images, binarization based on the histogram is used to find the appropriate threshold.

As shown in Figure 1, the gray value of the pupil part in infrared image is significantly lower than the other parts. The large difference between the pupil and the background will form two peaks on the histogram. As shown in Figure 3, pupil region is located around the first peak and the background is located around the second peak. Setting the corresponding gray level of trough between two peaks as the threshold can separate the pupil from the background as much as possible. Choose the gray level of the trough right to the first peak as threshold for binarization, the result is shown in Figure 4.

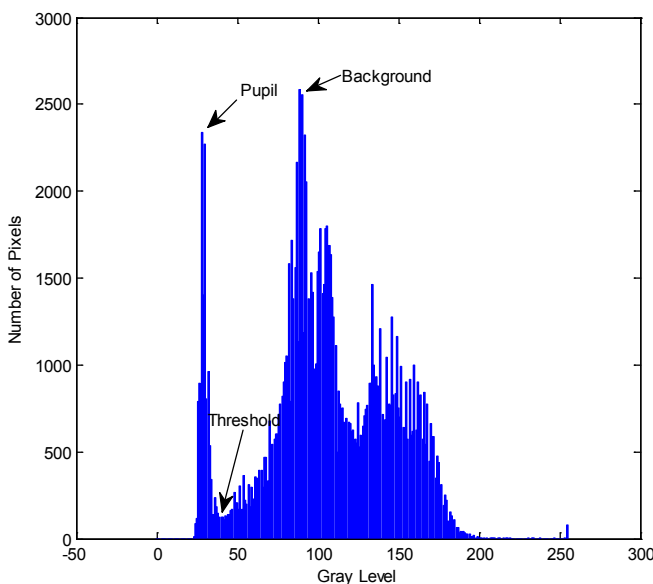


**Figure 3.** Histogram of pupil image

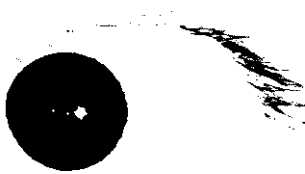


**Figure 4.** Binary Image of pupil image

### 3.3 Eyelash Removal and Contour Tracking

As the light spot falls inside the pupil, contour tracking of the outer boundary of the pupil will not affect the integrity of the pupil, thus will not affect the calculation of pupil size, center and diameter. However, due to the gray level of eyelash and pupil are close, not only pupil but also eyelash are existed in the binary image. Only avoid the eyelashes can find the real pupil contour. In pupil detection, the morphological methods such as erosion and dilation are used to preprocess the pupil gray image [10], and then after binarization the eyelashes can be removed. However, this method will greatly reduce the calculation speed, and may cause the distortion of the pupil's edge easily. Therefore, eyelashes will be removed in the process of contour tracking in this paper.

The pupil image is approximately circular, and it is a complete connected domain, which will not be cut off or 8-connected. So simple and fast tracking method is enough to meet the requirement. Firstly, find the first boundary pixels: Search from top to bottom, left to right. Every time meet a black pixel, search its 8 neighborhood. If the number of black pixels in 8 neighborhood is greater than or equal to 3, confirm that it is not isolated noise, but the starting point of the first boundary. Secondly, search for the neighboring boundary points from the starting point: Define the initial search direction along the top right. If the top right point is black, it is the new boundary point, otherwise the search direction rotate 45 degrees clockwise until the first black pixel is found. Then set the black pixel as the new boundary point, rotate 90°counterclockwise based on the current search direction. Continue to search for the next black pixel with the same approach. Finally, when the initial boundary point is found, once contour tracking ends. The contour tracking process is shown in Figure 5.

Due to the binary image of pupil has a few eyelash noise located above the pupil, although the isolated noise have been skipped while looking for the first boundary pixel, the first boundary be tracked may also be large eyelash region. Therefore, calculate the area surrounded by the contour, if less than a certain value, it is not regarded as the pupil, continue to look for new contours, until the pupil contour is

found. For the images processed in this paper, the value can be 1500. The contour tracking process of this paper is shown in Figure 6.

After the contour tracking of binary image, store the contour points of the pupil in an array, and finally calculate the center and diameter of the pupil.

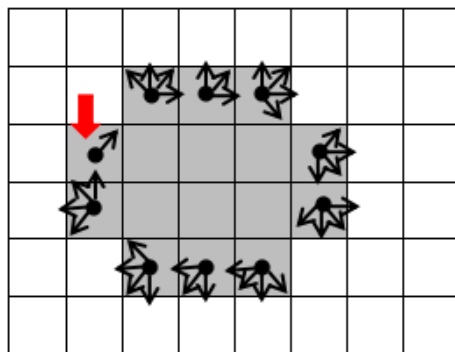


**Figure 5.** Sketch of contour tracking

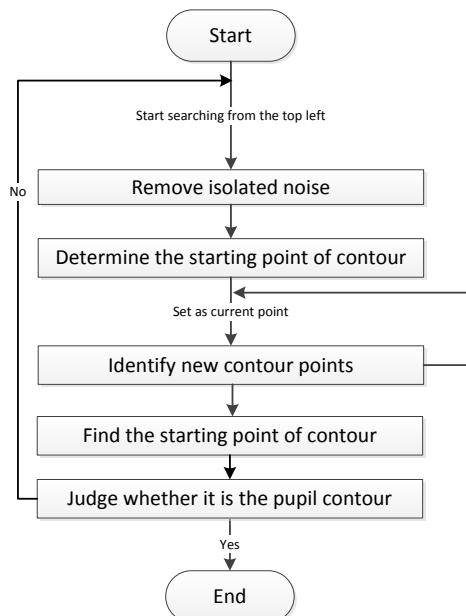


**Figure 6.** Flow chart of contour tracking

### 3.4 Calculation of Pupil Information

According to the contour array got by contour tracking, add up the number of points surrounded by pupil contour as the pupil area. Then calculate the radius of the pupil according to the formula of circle area. The center of the pupil is calculated by the formula of mass center:

$$x = \sum x_j / n$$

$$y = \sum y_j / n$$

In the formula,  $x$  and  $y$  are the horizontal and vertical coordinates of the pupil center, and  $x_j$  and  $y_j$  are the horizontal and vertical coordinates of the pupil pixels respectively,  $n$  is the number of pupil points.

## 4 Simplification of method

### 4.1 Narrow the Search Range

Pupil is only a part of eye, in the process of localization, if the approximate location of the pupil is known according to a priori knowledge, you can narrow the search range to improve the detection rate further. Some papers use gray projection method [13] in pupil detection for coarse positioning on the pupil. However, if illumination is uneven and image range is large, the overall gray value of the tail side of the eye is low relatively, gray projection in the column direction will be impacted, thus resulting errors in the coarse positioning.

As in the acquisition process of images, the pupil will not move casually, the pupil position of two adjacent frames are basically the same. After calculation to the previous frame for the information of pupil, Set the pupil center as the new center of the current frame, cut area of 160\*160 pixels as shown in Figure 7. Operate binarization and contour tracking on the narrowed area in the square to get the pupil information of this frame. Then repeat operation to the next frame according to this pupil center until all the images are tested. Narrowing the search scope can greatly reduce the amount of computation and speed up the detection rate.

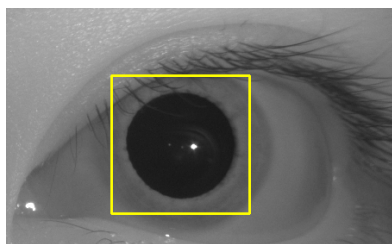


**Figure 7.** Reduced effective area

## 4.2 Using Fixed Threshold

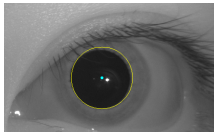
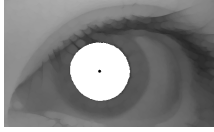
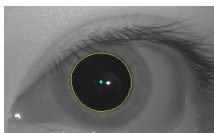
As the acquisition of pupil images is under the dark condition, environment changes little, set the threshold of the first narrowed frame as the fixed threshold can also reduce the computation and speed up the detection rate.

## 5 Experiment results

In order to verify the effectiveness and real-time of the method, 600 images acquired continuously are processed. The pupil image is 450\*275 pixels, 8-bit gray. Experiment is under the hardware environment of i5 CPU, 4GB memory, 64-bit operating system and software environment of VS2008 in C++ language.

Compare three methods of Hough transform, regional growth method in literature [10] and this paper. Table 1 shows the positioning results of these three methods. It can be seen that the pupil center and the diameter of these methods are basically consistent. However, as the pupil is not a perfect circle, pupil positioning of Hough transform vary slightly.

**Table 1.** Location results of three methods

Methods	Result	Pupil Center	Diameter
Hough Transform		(206,156)	130
Region Growing		(202,158)	124.101
This Paper		(202,158)	123.040

Process the images acquired continuously. As the diameters calculated by Hough transform are statistical results, and if deviation between the pupil shape and the perfect circle is great, the error of pupil centers and diameters detected will be large, so do the curve. Region growing method and the method of this paper do not need to take into account the pupil shape, the results are close and the curves are smooth.

The changes of pupil diameters under flash stimulation of three methods are shown in Figure 8.

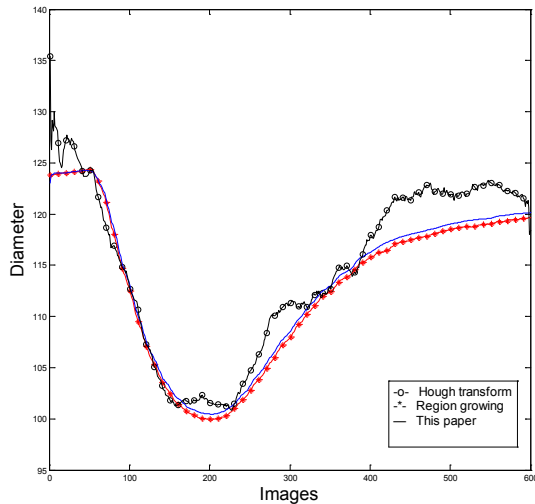


**Figure 8.** Pupil diameter curves of three methods

Statistics of running time of three methods shown that Hough transform has large amount of computation, so it is longest; literature[10] increases the operation time due to the use of dilation and erosion; the proposed method is fastest, the more images are detected, the more obvious advantages are, shown in Table 2. The results show that the proposed method can meet the requirements of real-time pupil detection.

**Table 2.** Comparison of method efficiency

Method	Running time/ms		
	10 frames	100 frames	600 frames
Hough Transform	138	1334	7909
Region Growing	78	799	4713
This Paper	16	138	773

## 6 Conclusion

A new method for pupil detection was proposed on the basis of contour tracking in this paper to locate pupil center. The effect of isolated noise and eyelashes are removed in the process of contour tracking. In the method, reduce the processing range according to the initial image and set the threshold of the first frame of the reduced image as the fixed threshold for subsequent treatment. The method can speed up the image processing rate of pupil detection on the basis of accurate location of the pupil center and can finally meet the requirements of real-time pupil detection. Because it is suitable for the detection of irregular pupil, it can be applied to the objective and quantitative detection of some eye diseases.

**Acknowledgment:** Project of key research and development plan (Social Development) of Jiangsu Province in 2016 (SBE2016740249)

## References

- [1] YAN H J. Design and application research of eye dynamic detection system[D]. 2011, 6.
- [2] WU C ZH, HE W, TANG R S, et al. Adaptive illumination detection system for fatigue driving[J]. Journal of Electronic Measurement and Instrument, 2012, 26(1):60-66.
- [3] JOHN G. DAUGMAN. High confidence visual recognition of persons by a test of statistical independence[J]. IEEE TRANSACTIONS ON PATTERN ANALYSIS AND MACHINE INTELLIGENCE, 1993, 15(11):1148-1161.
- [4] RICHARD P. WILDES. Iris Recognition:An emerging biometric technology[J]. PROCEEDINGS OF THE IEEE, 1997, 85(9): 1348-1363.
- [5] WANG C Y, ZHANG J, LI J J. Research on algorithm for pupil-center rapid localization[J]. Computer Engineering and Applications, 2011. 47(24):196-198.
- [6] LIN J L, SHI Q Y. Circle recognition through a point Hough transformation[J]. Computer Engineering, 2003. 29(11):17-18, 160.
- [7] CHEN J, ZHENG S H, PAN L, YU L. Pupil detection method based on ellipse fitting and parameter passing[J]. Chinese Journal of Scientific Instrument, 2014. 35(8):1890-1899.
- [8] TIAN Y, WANG H J, FANG Z L. The pupil diameter precise measurement based on morphological reconstruction algorithm [J]. Journal of Optoelectronics-Laser, 2008, 19(3):409-411.
- [9] MAO S B. Exact pupil detection algorithm combining Hough transformation and contour matching[J]. Journal of Computer Applications, 2016, 36(5):1415-1420.
- [10] LUO Y H, ZOU Y W, XIA X. Real-time pupil parameter detection for infrared image using OpenCV[J]. Computer and Modernization, 2013. 6:71-75.
- [11] CHEN J, ZHEN S H, PAN L, YU L. Fast pupil extraction algorithm based on image feature[J]. Journal of Electronic Measurement and Instrumentation, 2014. 28(2):203-210.
- [12] LV Y F. An Object Boundary Following Algorithm[D]. Dalian:Dalian Maritime University, 2014:10-12.
- [13] WU J H, ZOU D X, LI J H. Iris location algorithm based on small-scale searching[J]. Chinese Journal of Scientific Instrument, 2008. 29(8):1704-1708.
- [14] MU K Z, SHI Y K. Applying research of the threshold methods in pupil detection[J]. Institute of Mechanical and Electrical, 2005. 12, 24(6):443-445.

Ning GUO\*, Yao-he LIU, Ming-hui YAN

## Chip Manufacturing, Data Integration and Transmission

**Abstract:** With the wide spread application of Chip in daily life, like Smartphone, tablet PC, biochip, etc. Chip manufacturers have been raising their requirements on the Chip manufacturing data transmission. In this paper, under the concept of cloud manufacturing, the manufacturing data transmission platform is assumed established, with the application of jQuery technology, the way to realize lightweight design of Chip data interface is explored.

**Keywords:** Chip Manufacturing; Cloud Manufacturing; Data Transmission; jQuery Technology

### 1 Introduction

Due to the rapid development of science and technology, the replacement rate of smart phones, tablet PCs and other products are also growing fast, therefore, electronic products are increasingly demanding on chip, the global semiconductor market is getting more and more prosperous. At the same time, consumer electronics and mobile Internet are closely connected, which will continuously expand the application surface of network accessible terminal products like smart phones, tablet PCs, smart TVs, etc. Based on the soaring demand of electronic products, the demand for chips will continuously rising; undoubtedly, it will enhance the chip manufacturing front and rear ends' data transmission in the cloud platform.

Regarding the chip manufacturing process, concerning of varying demand of different users, faster replacement of chip is needed. In order to obtain greater profits, chip manufacturers have to introduce new technologies and equipments constantly, therefore, the cost for manufacturing will be increased [1]. During the manufacturing of chip, huge amount of date will be produced, this paper concentrates on the research of establishing a data cloud platform during the manufacturing data's transmission process, which will enables manufacturers to achieve Chip Manufacturing Front-data in a more efficient way, compared with before.

---

\*Corresponding author: Ning GUO, School of Mechanical Engineering, Hubei University of Technology, Wuhan, China, E-mail: ningcountry@163.com

Yao-he LIU, Ming-hui YAN, School of Mechanical Engineering, Hubei University of Technology, Wuhan, China

## 2 Chip manufacturing data storage and retrieval

The manufacturing process of chip is divided into two parts: Front End and Back End. Front End, meaning the front process of chip manufacturing, which including Lithography, etching machines working, washing machines working, ion implantation, chemical mechanical planarization, etc. Back End, meaning the back process of chip manufacturing, it mainly contains separating the device on wafer, SMT assembling and encapsulation, etc.

Development of economic globalization has led to the development of the globalization of production, a joint production of the product value chain can be completed by different companies in different countries. The process of chip manufacturing, is also such a process. That is, the Front End manufacturing and Back End manufacturing is conducted in different places, even for Front End manufacturing, different parts can be done in different places. However, in the chip manufacturing process, the Back End manufacturing depends on the Front End manufacturing data. Without Front End Manufacturing date, it would be difficult for the Back End Manufacturers to conduct the following producing.

Nowadays, with the rapid development of manufacturing industry, Cloud Manufacturing is gradually introduced into modern manufacturing, especially semiconductor industry. Taking reference to cloud computing thinking, Cloud Manufacturing is developed based on the concept of “manufacturing as a service” [2]. The purpose of rising the idea of Cloud Manufacturing is to lower manufacturing waste of resources, make use of information technology to achieve a high degree of shared manufacturing resources. The establishment of shared manufacturing resources in the public service platform, can contribute to putting social resources in the public service platform, providing needed manufacturing services for users, in this way, business users can on the one hand saving the cost of buying processing equipment, reducing the waste of resources, on the other hand, manufacturing service is obtained. Under assumed circumstance, cloud manufacturing can achieve a product life circle’s Related Resources Integration [3]. In this way, users can easily get access to variety of manufacturing service, just like using water, electricity and gas. Thus, when Front End semiconductor manufacturers input the manufacturing date into cloud platform, Back End semiconductor manufacturers will be able to download the date according to their demands, does not need to get access into all the data. This will not only reduce the occupation of funds for enterprises on information investment, but also it will substantially help them to save cost.

As a matter of fact, the development of the semiconductor industry is relatively slow in China, though benefits from economic globalization, the export limiting of some technologies and equipments to us have been relieved, however, the key technology and equipments of chip manufacturing is still blocked. So that, the developments of China’s semiconductor industry is slow, still unable to meet the domestic demand for the chip industry. Among the manufacturing process of chip,

the Front End's date storage is pre-recorded during overseas production environment, and the equipment to input the chip date is also produced overseas. Therefore, as most of the manufacturing equipments cannot be produced in domestic, we have to fully adopt foreign advanced countries' equipment, while the imported equipment is extremely expensive. If not introducing overseas advanced equipments, without the Front End manufacturing data, when manufacturing chip Back End in domestic, it will cause some problems like chip size error, and electrical characteristics instability, etc. Thus, the domestic semiconductor industry's technical level is difficult to achieve transcendence, which greatly effects the development of domestic semiconductor industry.

In order to solve the problems in Front End date transmission, a cloud manufacturing platform is called to be built up. As showing in Figure 1.

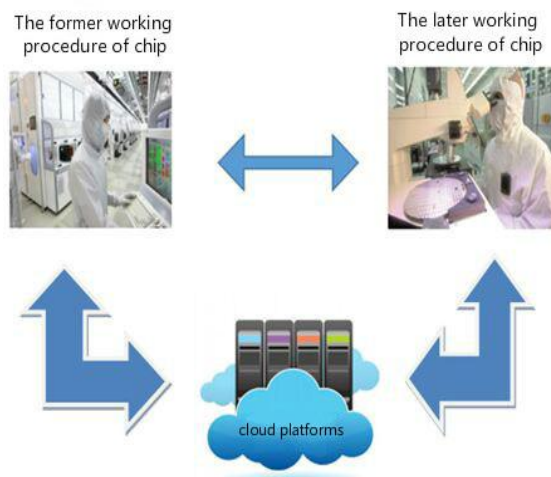


**Figure 1.** The cloud platforms for chip manufacturing data

### 3 Chip manufacturing data extraction size adaptation

Data transmission and Integration during the chip manufacturing process is like the current Mobile Internet date transmission. Result of the rapid development of Mobile Internet and smart mobile devices (for example, Smart Phone), the traditional network infrastructure is gradually shift in the direction of Cloud Computing. In order to realize automated on-demand, Cloud Computing needs to configure fast on Terminal Device, under the facility of Data centers, servers, storage, Lightweight design software and

operating system. Data size adaption, means the Front end and Back end data should match each other [4]. To better understand the data size adaption, here is a simple sample, see Figure 2. From Figure 2, we can find obviously, the firefighter's gun should be connected to the hydrants, while general household faucets should not be connected to the hydrants, otherwise, it is not match. In the design of things, there is also data size adaptation problems existed among the mobile terminal and back-end. Which means, if the Cloud drive cache is oversized (data transmission fluent or bandwidth flow abundant), perhaps there will be a resource waste problem; on the contrary, if the Cloud drive cache is too small, it may cause date transmission uneasy or even blocked.



**Figure 2.** Civil piped water supply adaptation

The biggest challenge for Internet of Things mobile terminal design is that the hardware design cannot be completed independently, it must rely on back end software interaction model adaptation. The mobile terminal design system is huge and complicate, result in the uneasy to fine balance point in design. Besides, mobile search needs optimization, the mobile search is very different with traditional Internet search. Moreover, traditional Internet date cannot be fully displayed on a smart mobile device, there must be a conversion process to help resolving the fast refreshing by users, so as to provide better user experience. However, traditional Internet data is normally stored in relative date base, when the date base reach a huge level, it easily cause searching time consuming. Therefore, it is necessary to introduce Lightweight Database and some related technology, such as Mongodb and Restful Web Service. Foreseeable, this will lead to a challenge on technology innovation for software designers.

Nowadays, along with the rapid growing of Internet and the wide spread of 4G technology, mobile terminals have been increasingly common used in daily life. There are mainly two problems existed in mobile terminal application: firstly, due to the

need of meeting with different application logic, the exploring is very complicated; secondly, facing with verified mobile terminal application, the adaption workload is huge and facing great pressure. Thence, based on the concept of traditional middleware and mobile middleware, an mobile middleware architecture which can adapt varied of mobile terminal is designed. Also, the specific supporting method including key visual development environment, simulation running engine, application generation engine and cross-device support engine should be provided, so that the exploitation of mobile application can be more easy to handle and visible. Self adaption can be achieved depends on different model of mobile terminals, hence, the key problem of terminal support in mobile application popularizing is resolved [5].

## 4 The wcf framework for chip manufacturingdata

### 4.1 Brief Introduction of WCF

SECS/GEM is the common used standard in Semiconductor Industry, also in China, this standard is adopted by our chip manufacturing enterprises. In highly automated chip manufacturing plants, the manufacturing procedure and whole process is controlled and monitored by CIM (Computer Integrated Manufacturing) system, this will help to reduce errors during the manufacturing process, further, it will lower the cost and improve products quality. However, because the manufacturing process are different, not only the equipments used for production are verified, also equipments from different manufacturers are not in the same parameter. As a result, this will make CIM Automation Management conduction even difficult and complex. Under normal circumstances, when supplying Semiconductor Equipments, equipments suppliers will also provide SECS/GEM software interface. But for Automation Software Integration, different equipments suppliers do not have communication protocol as a common principle [6]. Equipments suppliers can sometimes do not open communication protocol and interface software to semiconductor manufacturers, so semiconductor manufacturers have to build up their own software connection, leading to a huge increase on the program expense [7]. Besides, facing with different manufacturers' equipments, only SECS/GEM can be used to comply the management of recipe as well as each different parameter. However, as the recipe format are settled verified by different suppliers, lots of equipments encryption is unable to be resolved, this will called for another exploitation by semiconductor manufacturers, referring to the SECS/GEM protocol.

WCF (Windows Communication Foundation) is an application framework exploited by Microsoft, being used to support data communication. So WCF can be translated as Windows Communication Development Platform. Integrated original Windows communication mechanism, knowing as.NET Remoting, Web Service and Socket, and merged the related technology of HTTP and FTP, WCF is the best practice to develop distributed applications on Windows platform.

The advantages of WCF are as below: Firstly, the unity of development. WCF united the technology of Enterprise Services, Messaging, .NET Remoting, Web Service, and WSE, contributed to the development and deployment, reduced development complexity. Secondly, WCF can achieve Multi interoperate. It applied the SOAP communication mechanism, which ensured the system to be interoperable, controlled, even under different development languages, cross-process and cross-machine and even cross-platform communication can be conducted. Thirdly, it can provide higher level safety and reliance. The last but not least, WCF can support multi-vessel message exchange patterns, for example, request-response, Simplex, duplex, etc. The WCF framework model shown as Figure 3.

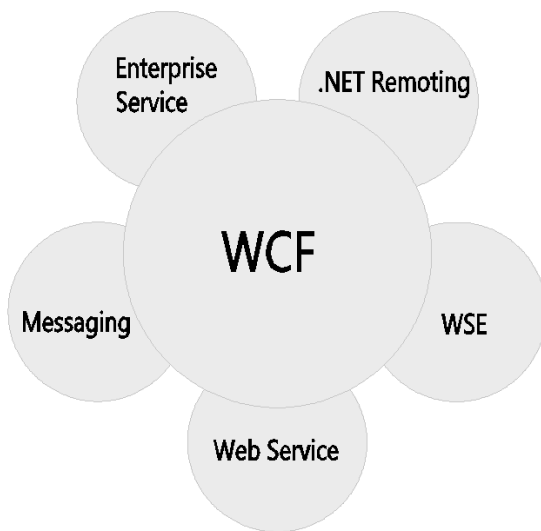


**Figure 3.** WCF frame model

To sum up, WCF is a good option to comply SOA. With the adoption of WCF, Cross-platform and cross-language connection can be realized seamlessly, thus will enable Web service to be mutual transferred cross-platform and cross-language. The technology can overcome the problems encountered in chip manufacturing during cloud data transmission; it is facilitative to large application program development.

## 4.2 WCF Framework

Same as traditional distributed communication frameworks, WCF essentially provides a cross-process, cross-machine cross- network service call [8]. Here below to create a simple WCF service and users program, and use WCF to test the users program.

**Step 1:** To start the development Web server, load the WCF service information, expand the reference and click OK to add the service reference, as shown in Figure 4.

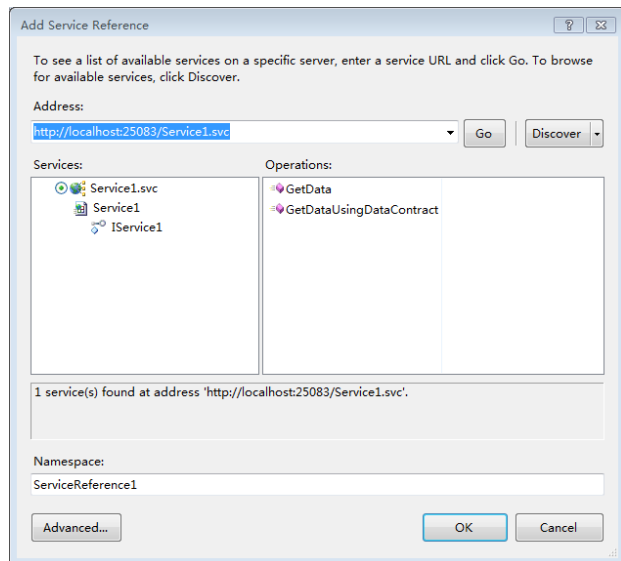


Figure 4. Add Service Reference

**Step 2:** Using WCF to test users program. See Figure 5: The request and response when using WCF to test users program.

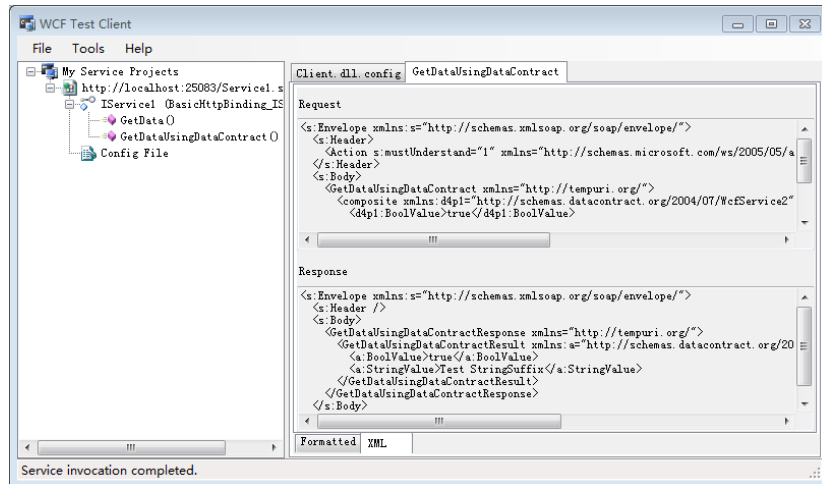


Figure 5. WCF Test Client

Part of the code is as following:

```

the file Program.cs in Client program
using System;
using System.Collections.Generic;
using System.Linq;
using System.Text;
using System.Threading.Tasks;
using Client.ServiceReference1;

namespace Client
{
    class Program
    {
        static void Main(string[] args)
        {
            string numericInput = null;
            int intParam;
            do
            {
                Console.WriteLine ("Enter an integer and press enter to call the WCF
service.");
                NumericInput=Console.ReadLine ();
            }
            while (!int.TryParse(numericInput, out intParam));
            Service1Client client = new Service1Client();
            Console.WriteLine(client.GetData(intParam));
            Console.WriteLine("Press any key to exit");
            Console.ReadKey();
        }
    }
}

```

This example creates a simple Web service and console users application program residing on the Web server, and use the WCF Test Client Program to inspect and invoke the service created. The default VS template was applied for WCF project, the operating defined by the default template can be used without any need to adding new code. And in the file IService1.cs to define the data agreement Composite Type which can be provided to the client application through the metadata. In IService1.cs file it also contains the service agreement and the agreement is defined as an interface with Service Contract characteristics. WCF service departs the implement classes from service interface, so that users does

not need any information about the classes, and the functions that classes may contain is far more than the function of service implementation, or even a class can implement multiple service agreements. The configuration files Web.config of the WCF service is a feature extracted from the .NET remote technology and it can handle all types of WCF services and the client program WCF serves. The test client allows input of parameters to be used, calls the method, and then displays the results, all of which do not require customers to write any code. We have also checked the XML we send and receive for obtaining the results, and find the information has very strong technicality. This is why we select WCF as an application program framework of data communications.

## 5 The interface design of the chip manufacturing data

### 5.1 jQuery Page Design

In the process of chip manufacturing, we need to extract data of former procedure from a cloud platform and display it on the terminal page. Today, jQuery has become the most popular java script library and in the world's top 10,000 sites which are visited most, more than 55% of the users are using jQuery [9]. Compared with other page design technology, jQuery technology has the following advantages: first, jQuery is a lightweight java script library compatible with multiple browsers. It's easy to handle and allows the application developer to get the most interface design by writing the least codes, providing the developers with different effects and features. Second, jQuery has a wide variety of document instructions and very detailed applications, and it also has a number of optional plug-ins, and the developers can select the appropriate characteristics according to different needs. Third, jQuery enables on the user's html page that the code and html content keep separated, bringing the visitors totally different browsing experience.

Due to jQuery's wide application and its unique advantage, to better display the chip data, hereby we use jQuery technology to proceed page design. Figure 6 shows the basic data table designed with the use of jQuery.

### 5.2 jQuery Mobile Interface

With smart phones, tablet PCs widely used, the mobile data terminal display has also become an important part of the front end data presentation, and this article proceed the design of mobile terminal interface by using jQuery mobile. The features of jQuery Mobile are: small frame, containing 12KB of JavaScript library, 6KB CSS and few icons, and supporting both low-end and high-end equipment at the same time.

Product parameters							
	Wafer ID	Product Name	Time	Diameter	Address	Attribute	Status
	0001	Koi	0.01	300	China	Large	P
	0002	Dalmation	0.01	300	China	Spotted Adult Female	P
	0003	Rattlesnake	0.02	300	China	Venomless	P
	0014	Rattlesnake	0.01	300	China	Rattleless	P
	0105	Iguana	0.02	300	China	Green Adult	P
	0106	Manx	0.03	300	China	Tailless	P
	0115	Manx	0.01	300	China	With tail	P
	0116	Persian	0.05	300	China	Adult Female	P
	0117	Persian	0.01	300	China	Adult Male	P

**Figure 6.** The chip manufacturing data page based on jQuery

By using the jQuery mobile framework and Restful Web Service method, chip manufacturers can query and access into real-time business in the mobile terminal (such as smart phones) anywhere and anytime, for example checking the chip's size, thickness, diameter, etc. before chip manufacturing, and sending the data to chip's production and processing center, which can greatly improve the chip production efficiency. This dynamic, real-time data acquisition can make the chip makers timely, comprehensively and accurately grasping the information of chip, and also making the workers, technical administrators and other specific executors better obtaining the chip's information.

## 6 Conclusion

As the demand for smaller, thinner and lighter mobile devices continues growing, and the intelligent internet-work equipment, data and video content expanding explosively, the needs of mobile data transmission promotes rapidly, which will inevitably bring for the chip makers challenges and opportunities. Data size adaption plays an important role in the data integration and transmission of chip manufacturing. With the adoption of WCF, Cross-platform and cross-language connection can be realized seamlessly. To study the data integration and transmission in chip manufacturing is of great significance for the development of China's semiconductor industry.

## References

- [1] Yang Zhang, The Process Semiconductor Manufacturing[M].Beijing:China Machine Press.2011
- [2] Chaohui Deng, Wei Liu, Researchand Application of Intelligent Grinding Cloud Platform Based on Cloud Computing[J]. China Mechanical Engineering:2012(1)p.65–68, 84.

- [3] Zheqi Zhu, The Research on Resource Matching in Cloud Manufacturing[D], Chongqing:Chongqing University2014
- [4] Yaohe Liu. The Optimum Design of the Internet of Things and the Technology of Data Adaptation[M].Beijing:Science press.2014, 14-15
- [5] Hao Xu, Design and Implementation of Mobile Middleware for Adapting Multi-terminal[J]. Computer and Modernization, 2011(9), p.65-68, 77
- [6] Ji Wang. Bing Wang, Application of GEM in Semiconductor Equipment[J], Journal of Mechanical & Electrical Engineering, 2008(7)p. 34-36, 55.
- [7] Bo Liu, The Standard Way to Implement Semiconductor Devices Interface A Based on WebService[D], Shanghai:Fudan University, 2012
- [8] Jinnan Jiang, The Analysis of WCF Technology, Beijing:Publishing House of Electronics Industry, 2009, p2-6
- [9] Guofei Ji, The Detail Explanation of Jquery Development Technology, Beijing: Publishing House of Electronics Industry, 2010, p102-106

Qing-qing WEI\*, Ru-chun CUI, Zi-chao CHEN, Ya LI

## A DCT-domain-based Research and Application of the Algorithm of Digital Audio Watermark

**Abstract:** Digital watermarking technology has important application value in the aspect of authenticity identification, covert communication, hidden identification and electronic identity authentication. Digital watermarking is the important means to solve the problem of copyright protection of audio media. Through the analysis of the basic characteristics and basic methods of audio digital watermark embedding and extraction technology, the paper further discusses the domain audio digital watermarking algorithm that is based on the discrete cosine transform (DCT) and with the aid of MATLAB tool, A specific implementation method of the algorithm based on the two valued gray image as a watermark is proposed. This approach implements the copyright identification of specific application Settings for audio signal.

**Keywords:** audio digital watermarking; DCT domain algorithm; watermarking embedded; watermarking extraction

### 1 Introduction

Discrete Cosine Transform (DCT) is the best way for image conversion. And it has lots of advantages. First, DCT is a change of orthogonal, and it can convert 8\*8 spatial expression to a frequency domain, which only needs a small number of data points to present the image; Second, DCT coefficient can easily be quantified, so it can get a good block compression; Third, DCT algorithms performs very well, and it has a fast algorithm, such as fast Fourier Transform for efficient operation, so it is easy to implement, whether in hardware or software; Fourth, DCT algorithm is symmetrical, so inverse DCT algorithm can be used to unzip image [1].

Digital watermarking system consists of digital watermark generation, digital watermark embedding, watermark detection, digital watermark extraction and the attack on the part of the digital watermarking system [2]. The paper mainly focuses on the watermark generation, embedding, detection and extraction process.

---

\*Corresponding author: Qing-qing WEI, Department of Computer Science, Foshan University, Foshan, Guangdong, China, E-mail: fswqq@126.com

Ru-chun CUI, Ya LI, Department of Computer Science, Foshan University, Foshan, Guangdong, China  
Zi-chao CHEN, Department of Educational Information Technology, Foshan University, Foshan, Guangdong, China

## 2 The Construction of Watermark

### 2.1 the Generation of Watermark

Suppose that watermark is a binary image of  $m_1 \times m_2$ , it can be expressed as  $W = \{w(i,j), 0 \leq i < M_1, 0 \leq j < M_2\}$ , in which  $w(i,j) \in \{0,1\}$ . In order to embed the two dimensional binary image into the one dimensional audio signal, we take it into dimension reduction processing, then two dimensional will be reduced to one dimensional:

$$V = \{v(k) = w(i,j), 0 \leq i < M_1, 0 \leq j < M_2, k = iM_2 + j\} \quad (1)$$

In order to eliminate the sequence  $V$  in adjacent element correlations (and) improve the watermark embedding stability, Arnold scrambling transform is used to generate pseudo random sequence of  $V$  in all the elements of the pseudo-random sequence:

$$V_p = \text{Arnold}(V) = \{V_p(k) = V(k'), 0 \leq k, k' < M_1 M_2\} \quad (2)$$

Through the pseudo random sorting operation, the  $v'$  elements in  $V$  sequence is moved to the position of the  $k$ -th in  $V_p$  sequence. In order to further improve the resistance of the watermark damage, the watermark sequences spreads spectrum modulation, with Key for random seed producing  $m$  series  $\{m(k)\}$ . Use  $\{m(k)\}$  and watermark sequences  $\{V_p(L)\}$  to spread spectrum modulation and get a sequence  $\{s(k)\}$ , spread spectrum factor for  $m$ ,  $S(k) = V_p(\lfloor k/m \rfloor) \Lambda m(k), V_p(k), m(k) \in \{0,1\} (0 \leq k < M_1 M_2 - 1)$ , type in “ $\Lambda$ ” for XOR operator,  $[x]$  for not more than  $x$  nearest integer. To spread the spectrum modulation is to use the bandwidth for signal-to-noise ratio and, to use the increase of watermark channel capacity for the improvement of the stabilization algorithm [3].

### 2.2 the Processing of Watermark Embedded

Watermark embedded process can be divided into three steps: DCT transformation, embedded watermark weight and DCT inverse transform. If  $A$  is set as the original digital audio signal, and the number of data as  $K$ , it can be expressed as:

$$A = \{a(k), 0 \leq k \leq K - 1\} \quad (3)$$

In this formula,  $a(k) \in \{1, 2, \dots, (a-1)\}$  is the range of data value of No.  $K$ , and  $P$ , the number of bits used for each hat data. For the sake of argument, the original digital audio signal is put into two parts:

$$A = Ae + Ar \quad (4)$$

In the expression,  $Ae$  is relevant to watermark while  $Ar$  not.

Because watermark is embedded into the original digital audio signal as noise, such embedding should not interfere with the use of digital audio signals as the

prerequisite. Generally, to improve the robustness of the embedded watermark, one embedding needs at least N audio data [4].

In consideration of the spread spectrum of modulation factor of spread spectrum m, if all the  $M_1 \times M_2$  pixels of the watermark is embedded, the size of Ae relevant to the embedded watermark is N.

### 2.2.1 DCT Transformation

The processing of the audio data related to the embedded watermark and divided into segments of  $M_1 \times M_2$  and the DCT Transformation of each segment results in  $Dk(u)$  expressed as follows:

$$Dk(u) = DCT(Ar(k)) = \{dk(x), 0 \leq x \leq N-1, 0 \leq k \leq M_1 \times M_2\} \quad (5)$$

In the expression,  $dk(x)$  is the factor of No. x in the discrete cosine transformation of the audio data segment of No. k [5].

### 2.2.2 Watermark Weight Embedding

First of all, confirm the area for digital audio embedding in the discrete cosine transformation. That is, choose DC component and  $(m-1)$  low frequency AC coefficient as the embedding point in  $Dk(u)$  to embed m values of modulation sequence  $\{S(k)\}$ , namely, a pixel.

And then modify the selected wavelet coefficients  $dk(x)$  and embed in a sequence of modulation element  $S(k)$ :

$$dk'(x) = dk(x) + \beta S(k) \quad (6)$$

$\beta$  is predetermined quantitative coefficient, which is used to regulate the embedding depth and whose value should be given according to the specific conditions of the embedded watermark because the watermark robustness will be poorer if the value is too small or otherwise will reduce excessively the value of original digital audio signal [6].

### 2.2.3 DCT Inverse Transformation

The digital audio signal containing watermark information is achieved when the inverse transformation of the embedded watermark to audio data section d (u) in the discrete cosine is finished. The expression is as follows:

$$A'e = IDCT(D'k(u)) = \{d' k(u), 0 \leq k \leq M_1 \times M_2\} \quad (7)$$

The digital audio signals containing watermark is obtained when Ae is substituted by  $A'e'$  and in (7). The expression is  $As = A'e + Ar$ .

### 2.3 The Extraction and Detection of Watermark

Only when the expected watermarking information can be tested and extracted in the watermark embedded into audio signal can the protection of copyright and the integrity be protected.

Watermark extraction can be expressed as  $W = F(I', I)$ , in which  $F$  is the function of watermarking extraction. Original audio signal is an option for watermark extraction and detection. It will be difficult for watermark technology to achieve its product release and network communication as the use of original audio signal in watermark detection is a defect, which explains why current watermark detection algorithm is carried out without the participation of original audio signal.

Still, the original digital audio signal and the watermarked signal need to be preserved for testing use. The detection process and the watermark embedded process are on the opposite.

If  $Aw$  is the digital audio signal to be tested, the inspection process of watermark extraction can be described as follows:

Segment the digital audio signals  $Aw$ , namely,  $Aw = Awe + Awr$ , then transform the discrete cosine containing watermark segments:

$$Dwk(u) = DCT(Awe(k)) = \{dwk(x), 0 \leq x \leq N-1, 0 \leq k \leq M_1 \times M_2\} \quad (8)$$

As for the DC component and  $(m-1)$  AC frequency components, use the original audio signal to find the hidden  $m$  binary image sequences of spread spectrum positions, which results in  $(k) = [k(x)-dk(x)]/\beta$

According to the  $m$  sequence produced by the individual key, the solution to and the expansion of  $\{(k)\}$  results in another sequence of  $\{p(k)\}$ , which is done in way of taking exclusively or operation, namely:

$$r'p(k) = S'(k) \Lambda M_1 m(k) \quad (9)$$

Transform the dimension of  $\{p(k)\}$ , that is, change the sequence of 1d into binary images of 2d:

$$Ws = \{ws(i,j) = V' p(k), 0 \leq i < M_p, 0 \leq j < M_2, k = i M_2 + j\} \quad (10)$$

Compare the detected image of watermark  $Ws$  with the original one  $W$  to discern the false from the genuine watermark through the following formula:

$$\text{sim}(W, Ws) = (W^* Ws) / \text{SQRT}(W^* Ws) \quad (11)$$

## 3 DCT Algorithm

Discrete Cosine Transform (DCT) is one of mathematical operations that is closely related to Fourier transform. In Fourier series expansion, if an unfolded function is an even one, it only contains cosine term in the Fourier series, and is called discrete cosine transform when discretized [7].

### 3.1 DCT algorithm analysis

The specific process of the extraction and detection of the embedded watermark through DCT algorithm is shown in Figure 1 and Figure 2.

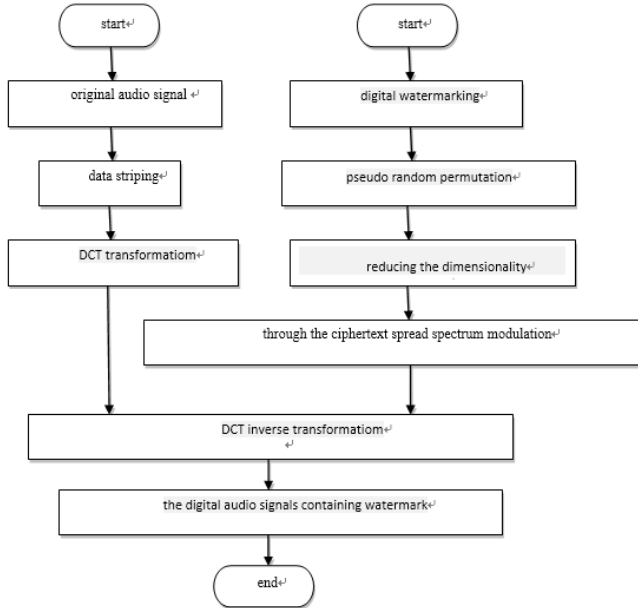


**Figure 1.** DCT watermark algorithm

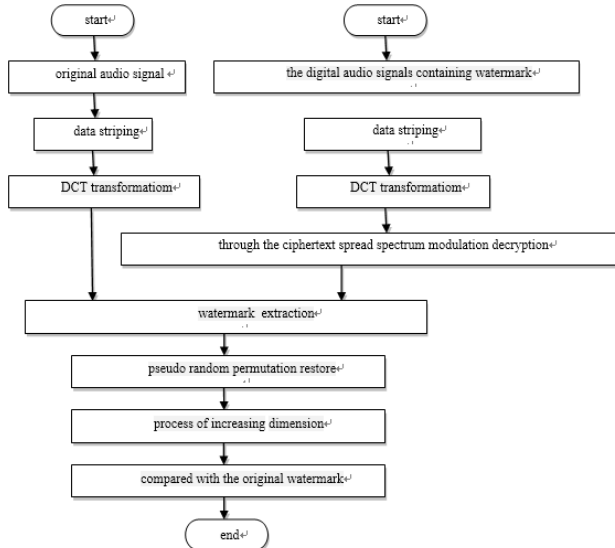


**Figure 2.** DCT Algorithm for watermark extraction and detection

### 3.2 Simulation and Testing

In the study, the binary gray image used as a watermark (as shown in Figure 3) is a 278\*278 pixel grayscale one. The procedures to improve the robustness and the anti-interpolation of the embedded watermark are as follows:

1. Valuing the quantitative coefficient of  $\beta$  in function 1-6 1.5;
2. Using proper Arnold transform.

The watermark image become illegible when the pictures

Undergo six times of Arnold transform (as shown in Figure 4 and Figure 5), but they restitute when undergone adequate iteration cycles. Because the watermark image size is 278\*278, the restitution will be achieved after 24 times of iteration [8].



Figure 3. Binary gray watermark

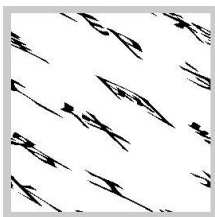


Figure 4. The watermark undergone one Arnold scrambling

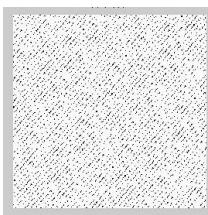
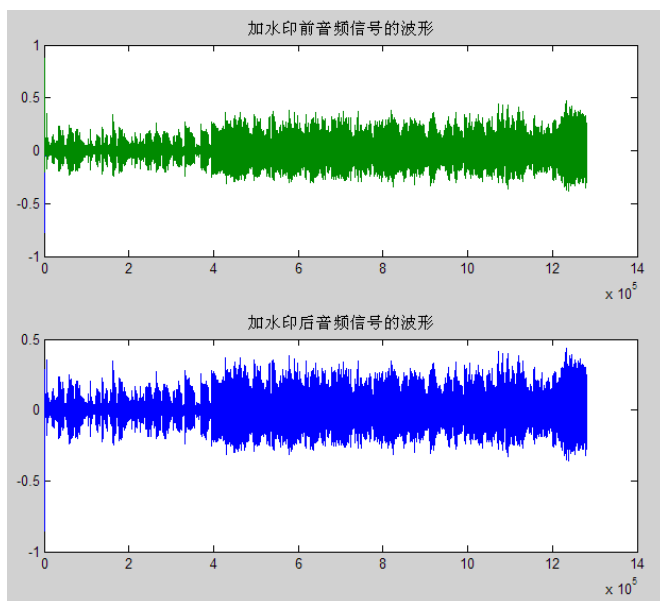


Figure 5. The watermark undergone six times of Arnold scrambling

3. In addition, we can use the digital audio signal of 1411 kbps in the wav format as the original one. First, the original digital audio signal ( $A = Ae + Ar$ ) is divided into two parts:  $Ae$  and  $Ar$ , in which  $Ae$  is the embedded watermark, and  $Ar$  is the redundancy part. The embedding of watermark has no effect on  $Ar$ . Second, divide  $Ae$  into  $M1 * M2 N$ -bytes of audio data segment ( $M1$  is the watermark image pixels, and  $M2$ , the width watermark image pixels). In this paper, value the watermark image 8 and size of  $278 * 278$ ). The audio signals containing digital watermark can be achieved when the watermark undergoes six times of Arnold scrambling and receives a dimensional decrease of one dimension binary sequences and all audio data segments each embedded with a watermark pixel undergo both discrete cosine and reverse discrete cosine transform [9].

The results of the experiments are shown in Figure 6. It is clear that the audio signals embedded with watermark become a bit stronger than the original ones. There is little significant distortion of sound quality when such signals are normally played, which shows the anti-effect and the concealment of watermark.



**Figure 6.** Figure of waveform in experiment

In the process of watermark extraction and inspection, MATLAB is used to extract a 1d binary watermarking signal which becomes a 2d one that has previously undergone six times of Arnold scrambling transformation and the original watermark is obtained when the 2d binary watermark signal undergoes 18 times of replacement. The

experiment results shown in Figure 7 show that the watermark has been successfully embedded in the audio and can be correctly extracted [10].

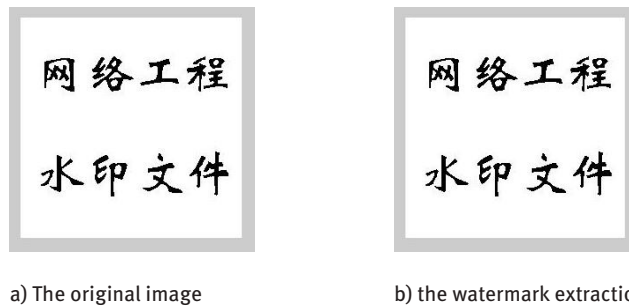


**Figure 7.** Contrast of extracted experiment watermark

### 3.3 Audio Attack

Compact the audio file embedded with watermark into wma form before transform it into wav one.

The signal waveform obviously change if the audio file is compacted, as shown in Figure 8. The watermark extracted from the compacted audio file is quite different from the original one as shown in Figure 9.

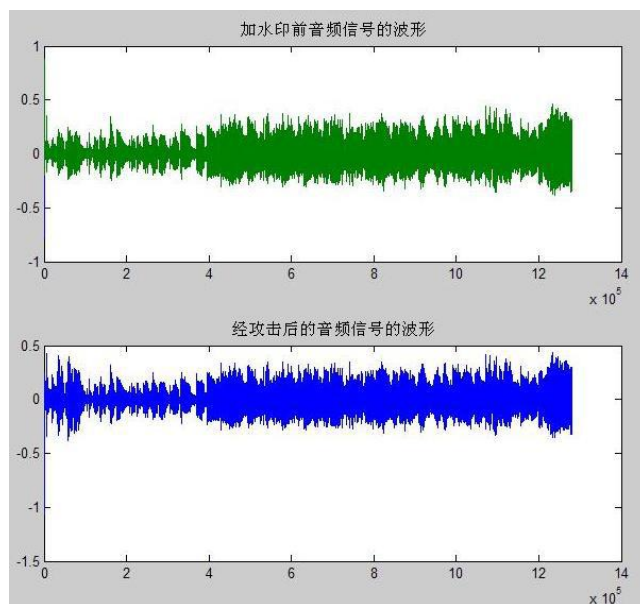


**Figure 8.** The different waveform of audio signal before and after compact attack



a) the original watermark image      b) the watermark image after being attacked

**Figure 9.** The different watermark before and after compact attack

## 4 The Experimental Results and Analysis

In light of the characteristics of embedding watermark into audio signal and the outstanding advantages of the discrete cosine transform used in audio data processing, a solution to the embedding of binary gray 2d image watermark by using discrete cosine transform (DCT). The advantage of image watermark is to offer users an intuitive and friendly analytical result while that of discrete cosine transform (DCT) is to provide users with software implementation that reflects the superior performance of digital and audio signals [11].

1. Because the watermark is, in the form of noise, embedded into audio signal, the embedding of watermark into audio signal should be based on a number of audio signals or the audio quality will be damaged because of the effect of watermark noise on the audio signals. It has been proved in this paper that the proportion between the watermark and the audio signals should not be higher than 1:8 – that is, the watermark image resolution is 278\*278, and the shortest value of audio signal is  $L = 278*278*8 = 618272$  – or the shortest length of audio signals will be limited if such proportion is too low and the length of watermark signals are limited. That's why an additional analysis of the length of audio signals before the embedding of watermark.
2. The spreading spectrum and encryption of digital watermark is to improve the robustness of digital watermarking, but in practice, the robustness of digital watermarking provided by the software suggested in the paper does not perform well, this is basically because of the contradictory choice of abandoning the higher signal-to-noise ratio to reserve the integrity and the origin of the audio signals and prevent the audio signals from excessive distortion when they are embedded with watermark.

## 5 Conclusion

Through the analysis of the algorithm and simulation tests, it can be seen that using the audio digital watermark algorithm based on discrete cosine transform (DCT), with the aid assistant of MATLAB tool, it is effective to embed audio signals with watermark which is based on binary gray image, whose corresponding algorithm and application are illustrated in the paper for setting copyright marks by using audio signals.

## References

- [1] Jia Yong-Hong. Computer image processing and analysis [M]. Wuhan: Wuhan University Press.. 2001.9
- [2] Xu Wen-Li, Wang Ming-Yu. Digital watermarking technology and its application[M]. Beijing: Publishing House of Electronics Industry. 2013.1
- [3] Sun Sheng-He, Liu Zhe-Ming, Niu Xia-Mu etc. Digital watermarking technology and application [M]. Beijing: Science Press. 2004.
- [4] Zhong Hua, Zhang Xiao-Hua, Xiong Li-Cheng. Digital watermarking and image authentication algorithm and its application [M]. Xian: Xian University of Electronic Science and Technology Press, 2006.
- [5] Yang Yu. Information hiding and digital watermarking experiment tutorial [M]. Beijing: National Defense Industry Press. 2010.1
- [6] Wang Yu-Ming, Li Hui, Liang Chuan-Jia. Information theory and coding theory [M]. Beijing: Higher Education Press. 2005
- [7] Yang Yi-Xian, Niu Xin-Xin. Theory and applications of Digital watermarking [M]. Beijing: Higher Education Press.2006.3
- [8] Zhang Xian-Ming. MATLAB language and its application cases [M]. Nanjing: Southeast University Press. 2010.9
- [9] Zhang Liang, Guo Shi-Jian Wang Bao-Shun etc. MATLAB7.X system modeling and simulation [M]. Beijing: Posts & Telecom Press. 2006.
- [10] Meng Yi-Zheng. MATLAB and technique [M]. Beijing: Science Press. 1999.11
- [11] Qiu Zhi-Cong. Encryption and decrypt skill practice [M], Beijing: China Railway Publishing House). 2005.1

Yi XU, Wei-wei FU, Shi CHEN, Yue-fang DONG, Ke-ke GU,  
Li-ping WANG\*

## Detection of Placido rings fracture based on ECC image registration

**Abstract:** In this paper, a new detection algorithm for tear film rupture based on Placido ring is proposed based on image registration and region segmentation. The algorithm divides the image into local regions, analyzes the joint entropy of the relevant local image, and judges the correlation between the joint images. The image registration of ECC is a kind of method based on Mutual Information. We judge the correlation between images by analyzing the entropy of relevant images. In this algorithm of ECC, we improve it by dividing the original image into local area regularly. It would improve the contrast of local region. The test results of proposed method can accurately mark the change of Placido rings' position.

**Keywords:** Placido Rings; ECC; image registration; local contrast

### 1 Introduction

Dry eye is a kind of chronic ocular surface diseases in the clinical. Most of people use their eyes for a long time. It becomes the most common reason for the dry eye. At the same time, some diseases of the eyes would also bring the complication of dry eye. Studies have shown that the incidence of dry eyes is increasing. Along with the social aging, the professional of the women and the popularity of cornea contact lens, the diagnosis and treatment of dry eye make everyone pay attention to it [1].

At present, most of the dry eye detection equipment are based on corneal topography. This kind of devices of dry eye is all using the Placido rings for their lighting source. This type of lighting source is extremely special so that it is significant for making up the broken corneal topography. But in this process, we need to fit a series of circular as well as analyze the contour consist of circles. Although the kind of detection for dry eye is already comprehensive, it is too complex and unpractical to the clinical medicine compared with the theoretical study. In clinical practice, we need a more simple and efficient method of detecting dry eye. In this article, we talk

---

\*Corresponding author: Li-ping WANG, Nanjing University of Science and Technology, Nanjing, China,  
E-mail: wangliping@njust.edu.cn

Yi XU, Ke-ke GU, Nanjing University of Science and Technology, Nanjing, China  
Shi CHEN, Wei-wei FU, Yue-fang DONG, Suzhou Institute of Biomedical Engineering and Technology  
Chinese Academy of Sciences, Suzhou, China

about how to use the changes of Placido rings to demarcate the location of broken tear film in direct.

## 2 The relationship between the broken placido rings and dry eye

Tears distributed evenly in the conjunctival sac and form a layer of liquid membrane. It is called tear film in medicine name. There are three parts of tear film, including the layer of mucin, water liquid layer and lipid layer. There are some causes for the patients of dry eye that the tear film of dry eye spread unevenly because of the less tears made by dry eye. This kind of tears secretes less than normal eyes, but they evaporate faster. When we light upon the normal eyes using the Placido rings, it would appear a series of whole and perfect rings. On the contrary, we have the same condition to apply on the bad eyes; the projection of Placido rings becomes distorted, eventually broken. In normal conditions, we use the slit lamp to examine dry eye. In this method, we must make the tear film in some specified color. When the tear film changed, we could find the changing out under the slit lamp by watching lost color. In the imaging, the method of Placido rings has the same principle with slit lamp. We merely find out the changing of rings. In addition, the method of using Placido rings would not injure the patient eyes because the tester's eye would not be colored. This new technology is called non-invasive. And non-invasive tear break-up time (NIBUT) has been widely admitted by the medical profession [2].

In ring rupture process, it can easily distinguish the rupture by human eyes. But the tear film appears to cover on the colored cornea, and it appears as the transparent color. Under normal conditions, we cannot see the process of the rupture. After rigorous medical research, it has shown that the rupture of Placido rings has a certain linear relationship with broken tear film. Therefore, we can make the process of rupture of tear film visible by corresponding the changing of Placido rings with the rupture of tear film [3,4].

## 3 Image registration based on ECC

### 3.1 The theory of image registration based on ECC

ECC is the abbreviation of entropy related coefficient [5]. Image registration based on ECC is a member of registration calculated by mutual information. Entropy is an important concept in information theory. Entropy is used to describe the uncertainty measurement system and reflects the amount of information that a system itself can provide. The greater the information entropy of a variable, so does he appeared. The mathematical expression of information entropy is:

$$H(X) = -\sum_{j=1}^N p(a_j) \log p(a_j)$$

In the image, we translate the computational expressions of entropy as follows:

$$p_i = h_i / \left( \sum_{i=1}^{N-1} h_i \right)$$

$$H(Y) = -\sum_{i=0}^{N-1} p_i \log p_i$$

$h_i$  represents the gray image value to 5 of the total number of pixels in image Y. And N represents gray level in image Y. So we can find the probability is where the gray value is i. Gray-level is a shape of measure in representing the gray histogram [6]. When the image histogram has one or more of the peak, there is a smaller entropy; Conversely, the greater the entropy value represents that the histogram is flat.

Entropy has special properties [7]:

1. The negative:  $H(X) \geq 0$  ;
2. The certainty: When the probability is  $H(X) = 0$ . The certain events do not carry any information;
3. The symmetry:  $H(p_1, p_2, p_3, \dots, p_N) = H(p_2, p_1, p_3, \dots, p_N) = H(p_3, p_1, p_2, \dots, p_N)$
4. Maximum entropy theorem:

$$H(X) \leq H\left(\frac{1}{N}, \frac{1}{N}, \frac{1}{N}, \dots, \frac{1}{N}\right) = \log_2 N$$

When all equal to the probability of events, source of entropy is the maximal;

5. The additive properties:  $H(X, Y) = H(X) + H(Y | X)$

The properties fully reflect the knowledge that can be accumulated, on the other hand, they reflect that any complex problem can also be solved step by step.

Joint entropy, reflects the correlation of two random the variables X and Y. If there are two random variables X and Y, X and Y of the joint entropy is expressed as:

$$H(X, Y) = -\sum_{x,y} p_{X,Y}(x, y) \log p_{X,Y}(x, y)$$

In this formula, X and Y respectively behave two images. According to the entropy calculation of single image, we can take the advantage of the joint histogram to calculate the joint entropy between them [8].

Define the size of  $M \times N$  matrix  $\text{Hist}[M, N]$ . M, N, respectively, are on behalf of the reference image F and floating image R gray-scale series.

Take reference images and floating image the same coordinates of pixels in the image for a and b. The gray value of a is r and the gray value of b is f. These two gray levels of pixels on forming a new coordinates [r, f]. Then calculate the following operations:

$$\text{Hist}[r, f] = \text{Hist}[r, f] + 1$$

Wherein,  $\text{Hist}[r, f]$  represents the number of reference image having a number of gray scale value r and a floating point image with associated gray value of f after traversing

the two images corresponding to all the pixels. Hist [M, N] matrix, represent two joint gray histogram of the image. Thus, we can calculate the joint probability density of two images [9]:

$$p_{\text{J}}(r, f) = \frac{\text{Hist}[r, f]}{\sum_{r, f} \text{Hist}[r, f]}$$

Mutual information (MI), is an important concept in information theory describing the correlation between the two systems [10]. MI could also be understood as comprising each case information. Guidelines for the use of mutual information image is to use two images of entropy and joint entropy to reflect the extent of the information contained in each other. For two images X, Y whose mutual information is represented as:

$$M(X, Y) = H(X) + H(Y) - H(X, Y)$$

As to X as well as Y, the higher the degree of similarity, namely high degree of overlap, the greater its relevance, the smaller the joint entropy and the greater their mutual information MI.

Learn more related content understanding, we shall find the template matching criteria exist FIG mutual information in the original sub-image.

But when the picture is similar in intensity distribution, FIG template may be the same mutual information of a plurality of sub-graph. This makes mutual information error-prone match. Meanwhile, the mutual information of two images is sensitive to the overlap region. If the two images overlapping area is too small, resulting in mutual information is very small, thus reducing our registration accuracy.

To avoid these drawbacks mutual information, mutual information has been improved by Mares:

$$\text{ECC}(R, F) = \frac{2M(R, F)}{H(R) + H(F)}$$

### 3.2 Based on the local contrast enhancement

Since lighting Placido rings are special, so we need to identify the region as a whole has a certain ring brightness changes. Due to changes in brightness caused by uneven gray scale image, so we set a single gray stretch scope that we lose a lot of gray scale information. In this paper, a regional division of the local gray contrast enhancement methods is raised [11]. After matching, we will offset the corresponding pixel gray; the rest will be part of the two images changes. In order to solve the whole gradation changes that are not uniform, we want to focus on the identified region which is divided into a plurality of pixels uniformly small area. In each small area which we were set gray stretch the scope of each region, so that we can change the whole image area more specific manifested enhance local contrast without losing information or change the excessive amplification change information [12].

Figure 1 shows an image at a single threshold range conditions on the global image contrast after stretching. Figure 2 shows the rear area were taken for each individual corresponding threshold range of contrast stretch in all regions revert to the original image composed of images. For comparison, we can clearly find that the single threshold range will lose a lot of gray area of the region changed significantly after contrast stretch process, so that we recognize the annular rupture area has a great influence. After local area contrast stretching, changes in the area of each region can be shown. This improves the accuracy of the detection area of land.



**Figure 1.** Under a single threshold



**Figure 2.** Multi-threshold

### 3.3 Image registration and identification process

In this paper, testing steps:

1. Image matching based on ECC;
2. Get picture and image matching diagram corresponding changes;
3. We will approximate the curvature of the ring and into the approximate size of the area. The area is divided into 8 equally large rectangle for the convenience of our calculations;
4. Respectively, for each small area contrast stretching, in order to highlight change region;

5. Make binary image, marked change region;
6. Calculate changes in the regional area. Thresholds defined medical screening to calibrate the tear film break area;
7. Mark the screened area on the original.

## 4 Experimental verification

In this paper, we make the 400\*400 grayscale image which image format is jpg as the original registration and take the 240\*240 grayscale image which image format is jpg as a registration template. Ultimately, we cut the registration into two equally large images, as shown on Figure 3 and 4.

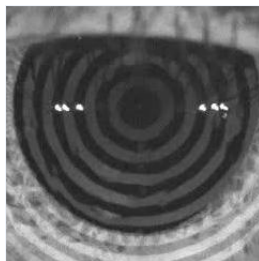


**Figure 3.** Registration picture

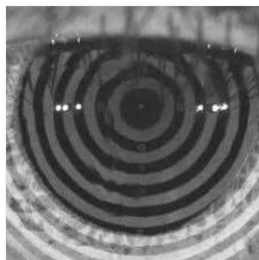


**Figure 4.** Matching template

Since this image taken in infrared light, we identify the major changes under the black pupil area. So we cut out the main pupil area. We can clearly distinguish the human eye changes in the two images of the ring. We also found that the brightness of the white ring region two images has changed. This is due to the special lighting conditions caused by unavoidable. But the change in position that we need to get there will be more substantial changes in brightness. We will cut a good image

corresponding to the pixel positions after registering two subtraction image obtained (shown on Figure 5).

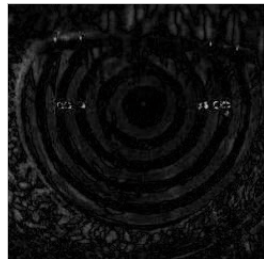


**Figure 5.** Difference image after matching

In Figure 5 we can see the variation in the amplitude of the gray area by the naked eye. But it is difficult to distinguish changes in specific details. Therefore, by dividing the region, we will need to identify areas were calibrated eight other large rectangular area. We were eight in this area of the rectangle window width and position of the contrast stretch. First, we were to observe the situation of local branches gray area. Figure 6 is a partial rectangular region we selected:

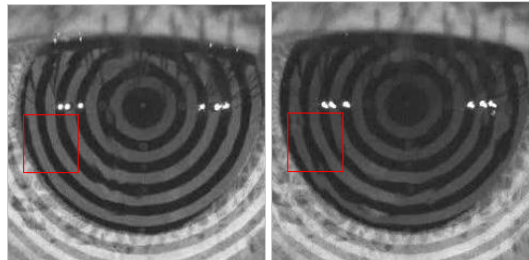


**Figure 6.** Choose gray stretch zones

By observing Figure 6, we can see a clear ring local region changes. Here is the gray area of analysis:

The histogram can be seen that the gray area which is mainly concentrated in the range of [0,100]. Next, we need to change us into the gray area through a “window frame” box. Here, we choose the box in the grayscale range [37, 42] of the area, and we block the gray level stretch the entire gray scale. We can make changes in the region to identify more clearly:

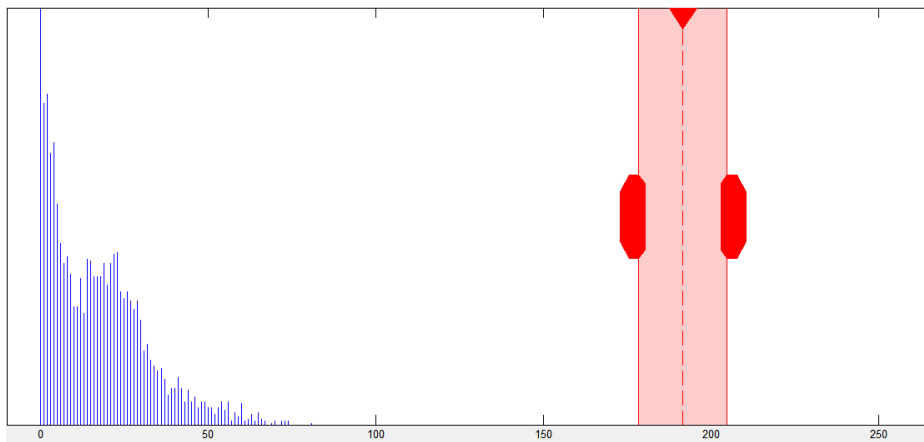


Figure 7. Histogram in a rectangular area

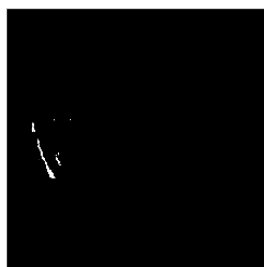


Figure 8. After the rectangular area gray stretch

Through the observation of a rectangular area, we divided area while eight were gray stretch. According to the distribution histogram of each area, the change in tensile selection “window frame” area. Eventually we demarcate the areas of the respective changes.

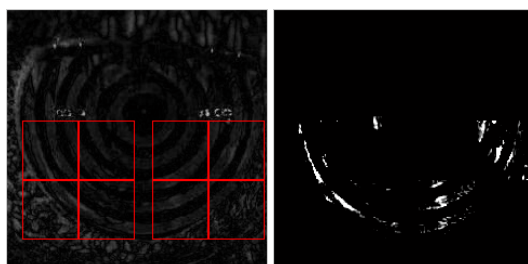
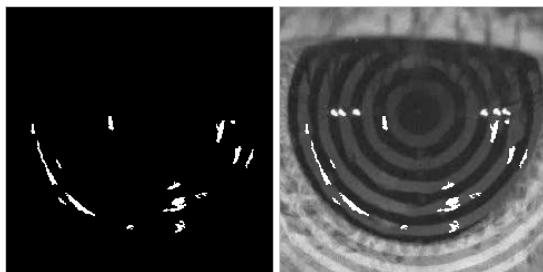


Figure 9. Divided rectangular area divided areas, and the contrast stretching results

After a single stretch, we can clearly see the gray-scale changes in the two images. Due to the small changes will not be easy to identify the human eye, at the same time, through the current detecting dry eye study finds more than a certain range when the change in the size of the tear film that is broken to a certain extent before it can be recognized criteria. Therefore, we set a standard threshold value, the removal of an area less than the area threshold value changes. Here we set the threshold value Th 10. By regional standards in line with tear breakup following results:



**Figure 10.** After the removal of less than a threshold area and the nominal position resulting image

After the final treatment, we will change the area marked on the template showing the change region.

## 5 Conclusion

This paper presents an ECC image registration method based on the detection ring rupture. In the algorithm implementation process, by comparing the local area for analysis and processing, the overall image of the image is divided into several local areas. And to detect changes in the area of the local area, the final summary to the whole global picture of them. This method can avoid the global image intensity distribution is uneven, as well as single threshold range contrast stretch resulting in the loss of an image change information.

**Acknowledgment:** Project of key research and development plan (Social Development) of Jiangsu Province in 2016 (SBE2016740249)

## References

- [1] Chinese Medical Association Ophthalmology Branch corneal disease group. The consensus of dry eye clinical diagnosis and treatment experts. Chin J Ophthalmol, January 2013, vol.49, No1.

- [2] SHAPIRO A, MERIN S. Schirmer test and break-up time of tear film in normal subjects. *Am J Ophthalmol*, 1979, 88:752-757.
- [3] CHO P and DOUTHWAITE W. The relation between invasive and noninvasive tear break-up time. *Optom Vis Sci*, 1995, 72:17-22.
- [4] GuoYan-wen. An Improved Pretreatment Algorithm of Corneal Topography. *Journal of North University of China(Natural Science Edition)*. Vol.35, No5, 2014.
- [5] HanYucan, YangYanning, Chenglinkui.Clinical analysis of patients with dry eye tear breakup time of non-contact measurement results.*Journal of Clinical Ophthalmology*, 2015.23(3):238.
- [6] ChenXianyi, ZhouKaili.Medical image registration and classification of common methods[J]. *Information Technology*, 2008.7:17—19
- [7] WOODS R P, MAZZIOTTA J C, CHERRY S R. MRI-PET registrtrion with automated algorithm[J]. *Journal of Computer Assisted Tomography*, 1993, 17(4): 536-546.
- [8] Nathan D.Cahill, Cranos M.Williams, eta1. Incorporating spatial information into entropy estimates to improve multimodal image registration[J]. *IEEE* 2006, 8(06), pp:832-835.
- [9] CHIHOUB, A., BANSAL, R., etc. Performance comparisons of multi-modal medical image registration algorithms[C]. *Proc of IEEE conference on Image Process*. 2002, 125-128.
- [10] Li Ke. Medical Image Registration Based on Mutual Information[D]. Shan Dong University, 2006.
- [11] Yang Jin-bao, Liu Chang-chun, Hu Shun-bo. Generalized entropy in medical image registration[J]. *Computer Engineering and Applications*, 2008, 44(8): 34-36
- [12] Zitova, B., Flusser, J.: Image registration methods: a survey. *J. Image vis. comput.* 21, 977–1000
- [13] J.MATINZ, M.VIERGEVER. A Survey of Medical Image Registration[J]. *Medical Image Analysis*, 1998, (2): 1-16.

Ying-qiao KONG, Jian-kang ZHAO\*, Xuan XIA, Cheng-guang ZHU

## **Research on High-precision Calibration and Measurement Method based on Stereo Vision**

**Abstract:** In stereo vision measurement system, distortion caused by the optical system makes images of targets deviate from theoretical imaging points, which results in measurement error of the system. In order to improve the measurement accuracy of the system, a quartic polynomial on the whole image plane is obtained through fitting the pixel resolution of each angular point on calibration board, the coefficient of which is proportional to the distance from the object to the camera. Then, we utilize binocular vision technology to calculate the distance of the detected object, and monocular vision to measure its transverse dimension. Experimental results show that, when the distance between the object and the camera is within 10m, the distance error can be reduced to less than 5%. And when the object is 1 meter away from the camera, the measuring error of the transverse width of the object is within 0.5mm, which approaches to the theoretical highest resolution.

**Keywords:** calibration; pixel resolution; distortion equation; fitting; measuring distance by binocular model; measuring size of monocular vision

### **1 Introduction**

As an emerging test technology, computer vision measurement technology utilizes some functions of the optical or electronic device, based on the biological vision, to obtain the information of the detected object, and complete the real-time measurement of three-dimensional information of the object. With the development of modern science and technology, vision inspection technology has been more important in the field of non-contact measurement, and widely adopted in various fields such as industry, medical industry and aviation.

Measurement accuracy is an important factor in weighing measurement technology which is related to many factors, such as calibration error of the camera and the selected measurement method [1-10]. In recent years, many domestic and overseas scholars have been trying to improve the measurement accuracy. The traditional calibration method [5,6] has the advantage of high precision, while with a complicated process. Self-calibration method [7,8] relies on the relationship between

---

\*Corresponding author: Jian-kang ZHAO, School of Electrical Information and Electrical Engineering, Shanghai Jiao Tong University, Shanghai China, 200240, E-mail: zhaojiankang@sjtu.edu.cn

Ying-qiao KONG, Xuan XIA, Cheng-guang ZHU, School of Electrical Information and Electrical Engineering, Shanghai Jiao Tong University, Shanghai China, 200240

corresponding points of some images, which is flexible but has strong robustness. Calibration method upon active vision [9,10] solves parameters through controlling the camera to move by the given way, which calculates simply and has strong robustness, but requires using high-precision mobile platforms.

Hereby, this paper proposes a measurement method based on stereo vision. We will establish a new type of camera calibration model, which utilizes binocular vision technology to calculate the distance of the object, and monocular vision to measure its transverse dimension. And the calibration template uses the conventional liquid crystal display, which does not need professional production and can be placed and adjusted easily.

## 2 Measurement model

### 2.1 Binocular Vision Model

Binocular vision model [11] is shown in Figure 1: two cameras which image planes are exactly coplanar with each other, with exactly parallel optical axes that are a known distance apart, and with equal focal lengths. And the paper has assumed that the principal points-  $c_x^{\text{left}}$  and  $c_x^{\text{right}}$  have been calibrated and have the same pixel coordinates in their respective left and right images. Usually, the center of an image is not on the optical axe, so we use  $c_x$  and  $c_y$  to imitate the shift of the center.

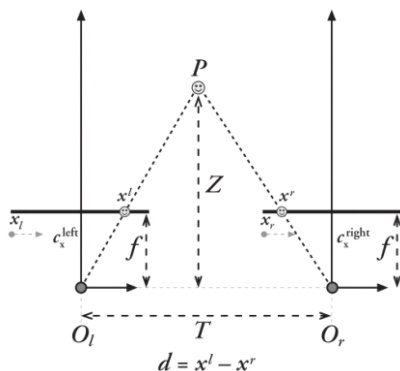


**Figure 1.** Binocular vision model of parallel transverse mode

For describing the model quantitatively, we define the world coordinate system, the camera coordinate system and the pixel coordinate system [12]. A world coordinate system is defined as a spatial 3D coordinate. The camera coordinate system takes the optical center to the coordinate origin, and usually defines the optical-axis direction

as Z-axis which is perpendicular to the image plane. And we take the point  $O$ - the intersection of the optical axis of the image plane to the main point. A pixel coordinate system is a cartesian coordinate system on the image plane which is in pixels. The upper left corner is seen as the origin, and the pixel coordinate  $(x, y)$  represents the number of columns and rows of the point on the image.

Moving on, let's further assume a point  $P$  in the left and the right image views as  $p_l$  and  $p_r$  which have the respective horizontal coordinates  $x_l$  and  $x_r$ . And the coordinate of  $P$  in the world coordinate system is  $(X, Y, Z)$ . Take the left camera coordinate system to the world coordinate system  $O\text{-}XYZ$ , and the left pixel coordinate system is  $O_l\text{-}x_l y_l$ , while the right is  $O_r\text{-}x_r y_r$ . The disparity is defined simply by  $d = x_l - x_r$ . As the situation shown in Figure 1, we can easily derive the following formulas by using similar triangles:

$$x_l = f_x \frac{X}{Z} + c_x \quad (1)$$

$$x_r = f_x \frac{X - T}{Z} + c_x \quad (2)$$

$$\frac{Z - f}{Z} = \frac{T - (x_l - x_r)}{T} \rightarrow Z = \frac{fT}{x_l - x_r} \quad (3)$$

where  $f$  represents the focal length of the camera, and  $T$  is the length between two cameras.

According to Eq.(3), the depth is inversely proportional to disparity, and obviously there is a nonlinear relationship between them: when disparity is near zero, small disparity differences make for large depth differences. When disparity is large, small disparity differences do not change the depth by much. Therefore, the binocular vision system is with high precision when the object is relatively near the camera.

In the experiment, we adopt SAD [11] to find matching points between the left and right stereo rectified images. SAD means the sum of square of absolute error of accumulated data in the given window, which is shown as Eq. (4).

$$SAD(x, y) = \text{Sum}\{|Left(x, y) - Right(x, y)|\} \quad (4)$$

The window with the minimum value of SAD in the searching area is the best matching block of pixels in the left and right image.

## 2.2 Monocular Model of Measuring Width

As shown in Figure 2 is the schematic diagram of the perspective, and only objects among the area of  $W$  and  $Z$  can be precisely imaged on the photosensitive sheet sensor. The angle formed by  $WC$  and  $ZD$  is the maximum range to observe objects, and that is

the perspective. The focal length is  $F$  mm, and the length of the photosensitive device is  $l$  mm. According to the triangular relations, the perspective can be calculated as

$$\tan \frac{\alpha}{2} = \frac{l/2}{F} \rightarrow \alpha = 2 \tan^{-1} \frac{l}{2F} \quad (5)$$

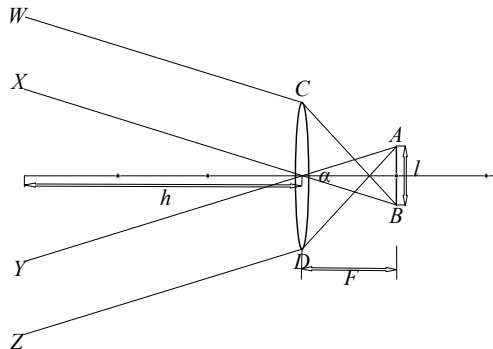


**Figure 2.** Range of single camera

In the meantime, the resolution accuracy which refers to the actual physical width of a pixel can be calculated as

$$s = \frac{2h \cdot \tan \frac{\alpha}{2}}{p} = \frac{2h \cdot \frac{l/2}{F}}{p} = \frac{hl}{pF} \quad (6)$$

where  $h$  is the real distance between the target and the camera, and  $p$  is the number of pixels on the photosensitive sheet in the longitudinal direction.

Moving on, let's process the target's image and count the number  $n$  of pixels ready to be measured, so the transverse width is

$$W = ns = n \cdot \frac{hl}{pF} \quad (7)$$

### 3 Error analysis

In visual detection system, measurement accuracy is a key indicator which runs through the design process of the system. The application field and worth of the system depend on the level of its measurement accuracy. Measurement accuracy of the system is influenced by various factors. Figure 3 mainly analyzes several key steps in the image processing process and the main factors that affect the accuracy of the transverse width and longitudinal distance.

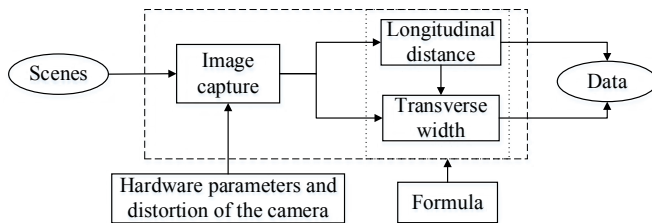


**Figure 3.** Image processing and factors affecting the accuracy of detection

As can be seen from the above figure, followings are the factors affecting measurement accuracy of the camera [13]:

The natural parameters of the object itself or the changes of characteristics.

- Various factors in the process of capturing images, which mainly refer to the influence of camera hardware parameters, including distortion, installation accuracy of the camera, physical focal length, baseline, as well as the size and resolution of CCD.
- Different measurement methods and calculation formulas.
- Interference caused by noise or something else in processing and analyzing image.

In the meantime, according to Eq. (7), the horizontal width of the object is directly proportional to the actual distance between the object and the camera. Therefore, the measurement accuracy of the distance also significantly affects the transverse measurement accuracy.

As seen from the above analysis, the main factors affecting the accuracy of the measurement system originate in both hardware and software. Among them, natural parameters of the object itself or changes of characteristics are not controllable. Then, we will focus on optimizing the calibration model and measurement method. Some hardware parameters of the camera, such as distortion and accuracy of installing the camera, and some noise caused by the software will not be discussed in this paper.

## 4 High-precision camera calibration and measurement

### 4.1 Pixel Resolution Calibration

The classic binocular camera calibration, such as the calibration method proposed by Zhang [5], is a process to determine the mapping matrix of points from three-dimensional to two-dimensional space. The projection matrix is determined by the internal and external parameters obtained by the camera calibration. Internal parameters refer to distortion coefficients of the camera, while external parameters

indicate rotation coefficients and offset coefficients of the camera coordinate system relative to the world coordinate system. In object vision measurement, since the calibration template and the measured object are not in the same image plane, online fine adjustment needs to be carried out respectively in calibration and measurement so as to make the imaging clearer. Because the system is adjusted in measurement, parameters of the camera need to be calibrated again which is difficult to maintain the consistency of calibration results of the lens. Moreover, the calibration is tedious and complex.

Image processing based on machine vision is to convert actual size of the object through the number of pixels. Therefore, the calibration model proposed in this paper will directly calibrate the pixel resolution of the camera, namely the relationship between the pixel and the actual size. The measurement result is the superposition of the resolution of each pixel. The accuracy of the measurement results can be greatly improved through accurate calibration of pixel resolution.

The calibration and measurement process throughout the experimental system is shown in Figure 4.

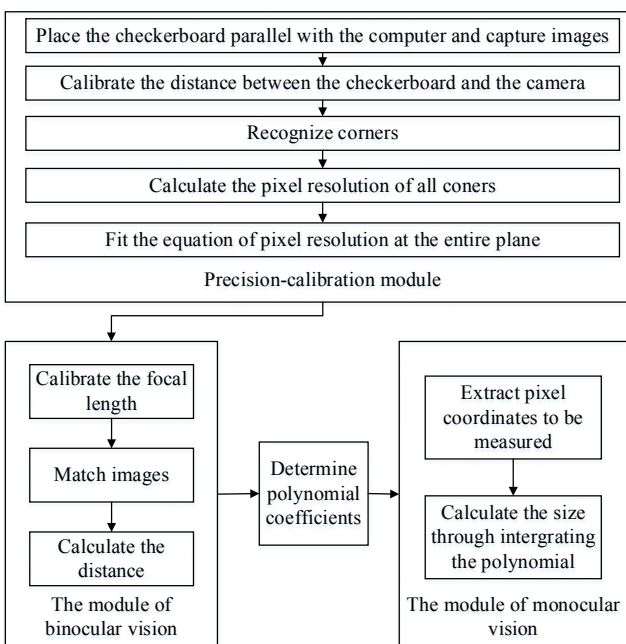


**Figure 4.** The process of experimental calibration and measurement

## 4.2 Fitting the Calibration Model

The optimum fitting of a plane can be interpreted as the minimum sum of errors' squares of existing data. When a polynomial is defined as the fitting surface, the polynomial least square fitting can be carried out [14,15]. Theoretically, the selected order of the polynomial is arbitrary. However, high-order polynomial will lead to poor numerical characteristics. Furthermore, with the increase of the order of polynomial, the fitting surface will become not smooth enough. Therefore, polynomial of which the order is higher than the required should not be selected. Generally speaking, the precision of cubic polynomial established through the calibration proposed by Zhang [5] is limited. Consequently, this paper will establish a quartic polynomial fitting model for the measured data, which is shown as Eq. (8).

$$f(x, y) = k(\sum p_{ij}x^i y^j)(i + j \leq 4) \quad (8)$$

According to Eq. (6), it can be known that the resolution of pixel points is not only related to hardware parameters of the camera, such as the focal length, the number of pixels on the photosensitive sheet, and the length of sheet, but also proportional to the actual distance from the camera to the object to be measured. Therefore, the proportionality coefficient between the distance from the object to the camera and the calibrated standard distance is the coefficient  $k$  required to be multiplied by the pixel resolution equation at this distance.

## 4.3 Calibration of Focal Length of the Camera

As shown in Figure 5,  $l$  is a resolution fitting curve when image coordinate  $y$  and depth  $Z$  are fixed.  $c_x$  represents offset of original point in the image.  $x_1$  is the pixel coordinates of point  $X$  on the imaging plane. Take into account the distortion of the camera, the rectified pixel coordinate  $x$  can be obtained when the areas of quadrangle  $ABCD$  and  $ABFE$  are equal.

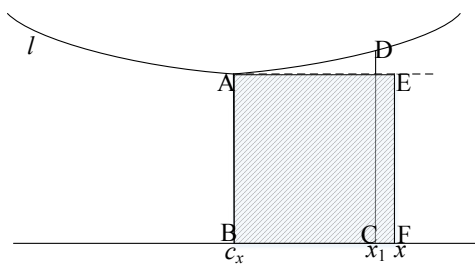


**Figure 5.** The correction of pixel coordination

The focal length of the camera can be calculated according to the model of pinhole camera proposed above. The rectified pixel coordinates of points on the image can be denoted as  $(x, y)$ , the depth of standard template as  $Z$ , the actual length as  $(X, Y)$  and the offset of the origin point in the actual image as  $(c_x, c_y)$ , so the focal length  $f_x$  and  $f_y$  of the camera on  $x$  and  $y$  direction can be calculated, as shown in Eq. (9). Moreover,  $c_x$  and  $c_y$  are just the coordinates of the central point in the fitting model.

$$f_x = Z \cdot \frac{x - c_x}{X}, f_y = Z \cdot \frac{y - c_y}{Y} \quad (9)$$

## 5 Experimental scheme and result

### 5.1 Resolution Model

The experiment is implemented with two aims. Firstly, it aims to verify the feasibility of the proposed detection method in the scheme. Secondly, it purposes to analyze the measurement accuracy of the method. The experimental system consists of a group of binocular cameras, with the resolution of 1920\*1080, the focal length of 15mm, the photosensitive sheet's length of 7.52mm, and the length between two cameras of 200mm. The experiment shows that the targeted accuracy of the system in distance measurement is for 5%, while the transverse dimension measurement for 0.5mm.

The checkerboard is placed 100cm away from the camera to capture images. Make sure that the checkerboard is filled with the entire imaging plane, as shown in Figure 6. The camera is calibrated based on the method which has been described, with the fitting model shown in Figure 7. And the calibration result of the focal length is 4345 pixels.

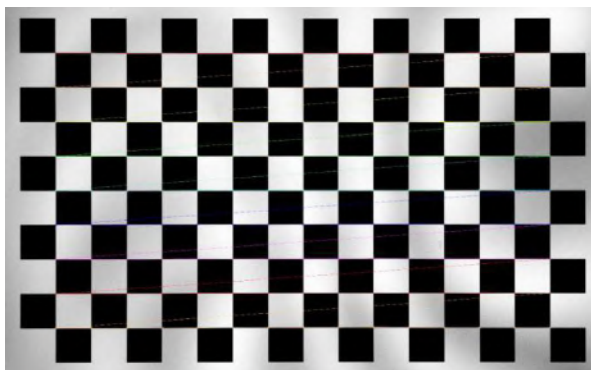


**Figure 6.** The calibration image

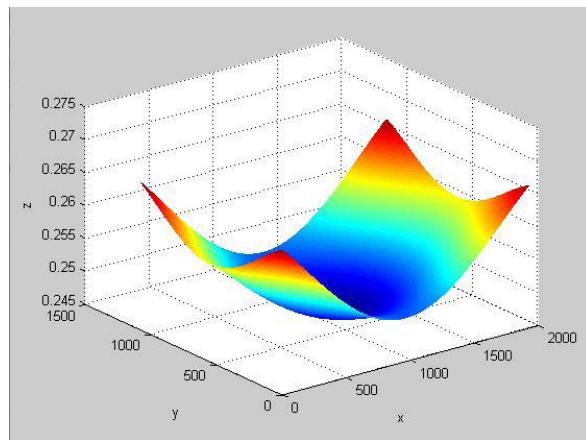


**Figure 7.** The fitting model of pixel resolution

## 5.2 Distance Measurement by Binocular Vision

In order to maintain whether the system can calculate the target distance accurately, the distance of the object will be calculated by binocular vision, comparing with the actual distance while the object is 1m to 5m away from cameras. The measurement results are shown in Table 1. A relative error curve is gained based on the results in Table 1, from which the measurement error is within 5% when the object is away from the camera within 10 m.

**Table 1.** Measure results of distance

True distance/m	Measured result/m	Error/m	Relative error
100	99.5	-0.5	0.5%
150	147.75	-2.25	1.5%
200	195.96	-4.04	2.02%
250	243.75	-6.25	2.5%
300	291.48	-8.52	2.84%
350	338.8	-11.2	3.2%
400	386.2	-13.8	3.45%
450	432.9	-17.1	3.8%
500	479.75	-20.25	4.05%

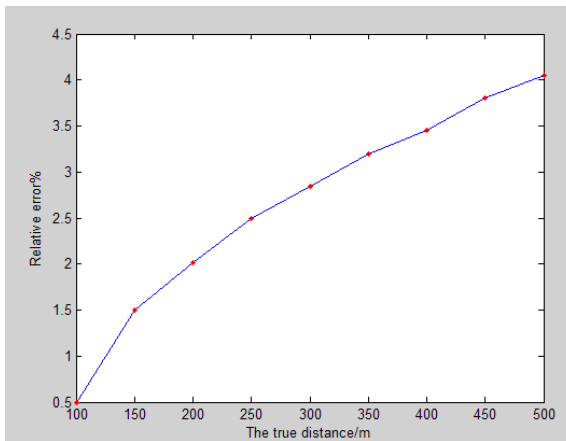


**Figure 8.** Relative error curve of the distance by binocular system

### 5.3 Width Measurement by Monocular Vision

In order to test the accuracy of transverse dimension measurement by the system, the length of any section of a scale will be measured to be compared with the actual size. For eliminating the influence of the distance on the transverse width, we will fix the distance between the scale and the camera of 100cm, which is the standard distance when calibrating. Therefore the proportionality coefficient of the quartic polynomial will be 1. The pixel coordinates of the two ends of the scale are adopted to calculate the length by means of the integration for the quartic polynomial which has been fitted.

The theoretical pixel resolution accuracy of the experimental system based on Eq.(6) is 0.245mm. Any section of the measurement scale is taken to be measured, and the result is shown in Table 2 where  $(x_1, y_1)$  and  $(x_2, y_2)$  represent respectively pixel coordinates of the two end points in any section of the scale.

**Table 2.** Measurement results of transverse width

x1	y1	x2	y2	Measured width/mm	True width/mm	Error/mm
60	412	213	412	39.7620	40	-0.238
213	412	409	412	50.2449	50	0.2449
409	415	608	415	50.3446	50	0.3446
608	415	808	415	50.1071	50	0.1071
808	396	1009	396	50.1609	50	0.1609
1009	398	1210	398	50.2492	50	0.2492
1210	401	1407	401	49.6186	50	-0.3814
1408	422	1602	422	49.4122	50	-0.5878

#### 5.4 Analysis on the Experimental Results

From above, it can be seen that the measurement accuracy obtained by the two methods is high.

When measuring the distance, calculating the disparity has consumed lots of time. In order to improve the efficiency of the system, the resolution of the camera should be lowered and the disparity parameter should be adjusted. However, a pixel deviation might correspond to long distance in the actual situation. Theoretically, the system will measure the distance more accurately with higher resolution of the camera. Obviously, it is necessary to maintain a balance between the accuracy of the distance measurement and the operation time of the algorithm.

As can be observed from Figure 8, with the distance of the object from the camera increasing, the measurement error of the system is also constantly increasing. It can be seen that the error appears an approximately parabolic relationship with the distance, which is related to the principle of distance measurement by the binocular vision. The distance of the object is inversely proportional to its pixel deviation in two photos. When the object is far away from the camera, a great distance movement corresponds to just a small deviation of pixels, so the system is not so sensitive to remote objects. In addition, the resolution of the camera is not high enough, leading to the difficulty of measuring remote objects.

In testing the transverse accuracy of the system, the measurement error is about 0.3mm within 0.8m to 1.5m away from the camera, which has achieved the target precision of 0.5mm. It can be found that the error in the system mainly comes from three aspects:

- The measurement of the distance

The distance between the object and the camera determines the coefficient of the fitting equation, so if we don't measure the distance accurately, the polynomial will change.

- Error itself of the fitting model

Firstly, the resolution of individual pixel is calculated by adopting the average distance of two points. What's more, a certain amount of optimization in the fitting model is possible to cause some errors. In order to decrease the error, the more accurate calibration boards are supposed to apply, and more images should be captured to cover all pixels when calibrating. And we have to look for the better curve fitting method.

- Camera Pixels

In the experiment, the pixel coordinates of the end points of the scale are manually extracted, and a pixel shift may correspond to a certain width deviation. Therefore, it is necessary to improve the accuracy of extracting pixel coordinates.

## 6 Conclusion

In this paper, fitting a polynomial is adopted to propose a new model of high-precision camera calibration. And establishing the general equation for the resolution of the entire field has been written into the program for real-time measurement. We will calculate the distance through binocular system as well as the monocular system to measure the transverse dimension of the object. While the calibration template uses the conventional liquid crystal display, which does not need professional production and can be placed and adjusted easily. The experimental results show that the four fitting equation can effectively improve the accuracy of the object measurement. In the meantime, further improvement of extracting pixel coordinates and measuring remote objects has an important role in high-precision measurement, and we will make further exploration in the future studying.

## References

- [1] QU Xue-jun, ZHANG Lu, ZHANG Ling-yun. Camera calibration and 3D reconstruction based on a new imaging model[J]. Chinese Journal Scientific Instrument, 2011, 32(8): 1830-1836.
- [2] Mei C, Rives P. Single view point omnidirectional camera calibration from planar grids[C]// Proceedings 2007 IEEE International Conference on Robotics and Automation. IEEE, 2007: 3945-3950.
- [3] Herrera D, Kannala J, Heikkilä J. Joint depth and color camera calibration with distortion correction[J]. IEEE Transactions on Pattern Analysis and Machine Intelligence, 2012, 34(10): 2058-2064.
- [4] TIAN Yuan-yuan, HUANG He-cheng, TAN Qing-chang, ZHANG Hai-bo, SHI Zhi-biao. Research on camera lens distortion[J]. Computer Engineering and Applications, 2009, 45(26): 49-52.
- [5] Zhang Z. A flexible new technique for camera calibration[J]. Pattern Analysis and Machine Intelligence, IEEE Transactions on, 2000, 22(11): 1330-1334.
- [6] WEI Zheng-liang, ZHONG Yue-xian, YUAN Chao-long, JIAO Wei. Calibration of a 3D measurement system having one camera and one projector[J]. Journal of Tsinghua University(Science and Technology), 2009(2): 202-205.
- [7] ZHANG Hu, DA Fei-peng, LI Qin. Self-calibration using two same circles[J]. Chinese Journal of Scientific Instrument, 2010(3): 618-624.
- [8] WU Fu-chao, WANG Guang-hui, HU Zhan-yi. A linear approach for determining intrinsic parameters and pose of cameras from rectangles[J]. Journal of Software, 2003, 3.
- [9] ZHANG Wei-zhong, ZHAO Zhi-gang, YOU Shi-ming, YUAN Cui-mei. Calibrating camera using planar pattern on LCD with a rotating camera[J]. Chinese Journal of Scientific Instrument, 2011, 32(1): 120-125.
- [10] PEI Ming-tao, JIA Yun-de. Linear self-calibration technique based on active vision[J]. Transaction of Beijing Institute of Technology, 2006, 26(1): 27-35.
- [11] Bradski G, Kaehler A. Learning OpenCV: Computer vision with the OpenCV library[M]. O'Reilly Media, Inc., 2008.
- [12] Zhang Cheng-wei, WANG Biao, XU Gui-li. A study on classification of camera calibration methods[J]. Computer Technology and Development, 2010, 26(1): 27-35.
- [13] SHI Yong-jie. Research on high precision vision inspection system[D]. Jilin University, 2007.

- [14] QIAO Yan-feng, GAO Feng-duan, WANG Zhi-qian, ZHAO Yan, LI Jian-rong. Distortion correction for the photoelectricity measuring System Based on the Cubic Fitting Equation[J]. Opto-Electronic Engineering, 2008, 35(6): 28-31.
- [15] CHEN Lan-feng, YANG Jing-yu, CUI Song, PAN Qing-chao, LI Liu. Simulation of fitting least-square curve based on MATLAB[J]. Journal of Shenyang Normal University(Natural Science Edition), 2014, 32(1): 75-79.

Zhong-min LI\*, Guo-wei ZOU

## Comparison of Three Weak Small Moving Target Detection Methods based on Time Domain Filtering

**Abstract:** The weak small moving target detection method based on time domain filtering can be seen as a background suppression method in time domain. In this paper, aiming at three commonly used time domain filtering methods – the time domain average filtering, the time domain median filtering, and the time domain minimum value filtering, we analyze the weak small targets detection performance of them by observing their images after filtering. The experimental results show that although the time domain minimum value filtering method in target brightness is the highest, but produces the more false alarm points, and the number of false alarm areas using the time domain average filtering method is obviously less than using the time domain median filtering method and the time domain minimum value filtering method. The performance using the time domain average filtering method is better than the other two, so the time domain average filtering method is more suitable for weak small moving target detection than the time domain median filtering methods and the time-domain minimum value filtering method.

**Keywords:** moving target detection; time domain filtering; background suppression

### 1 Introduction

Background filtering and suppression actually uses a variety of the image preprocessing algorithms to enhance the target and suppress the background of infrared image. In this way, the SNR of image is improved. The background of infrared image is generally considered as spatial correlation, stability in the time domain and on the low frequency part of the image in frequency domain. The target is generally considered irrelevant to the background; it occupies the high frequency part of the image in the frequency domain [1]. Therefore, we can detect the target directly from the image except the background. We also can predicate the background firstly, and then eliminate the image background to calculate the residual image. Image preprocessing methods mainly includes the time domain filtering method, the spatial domain filtering method and the transform domain filtering method.

---

\*Corresponding author: Zhong-min LI, School of Information Engineering, Nanchang Hangkong University, Nanchang, China, E-mail: zhongmli@163.com, 824206587@qq.com

Guo-wei ZOU, School of Information Engineering, Nanchang Hangkong University, Nanchang, China

The time domain filtering method estimates global motion parameters for registration to the background before the time domain filtering, Bin Wu et al. put forward the infrared background suppression algorithm based on third order cumulates [2]; Yan Xing et al. put forward the frame of nonlinear filtering algorithm; reference [3] proposed a multiple frames integrated detection algorithm in time domain based on the point estimation. Due to the need for three dimensional signal processing, the computational complexity of these methods is very large, and they would occupy lots of storage space. It is difficult to accurately estimate the global motion parameters of the non-stationary background. Therefore, they are mainly used to inhibit the short-time stationary background.

The spatial domain filtering method has good real-time performance and it is easy to implement, so it is widely used in practical engineering [4]. Hat transform method is a kind of practical nonlinear background prediction technology [5]. In order to enhance the adaptability of the algorithm, some scholars introduced the adaptive filter technology to image preprocessing, such as the two-dimensional minimum mean square error filter [6], the minimum mean square support vector machine [7], Karman filters [8] and Wiener filters [9], etc. Ming Li put forward a three-dimensional bidirectional filter to inhibit the complex background [10]. Ch. O. Goo put forward a kind of infrared small target detection method based on variable structure tensor [11]; Siguang Zhong et al. used gradient operator to describe the target area of the “gray singularity” to implement the background suppression [12]; Biyin Zhong et al. set up first-order field spatial distribution model of infrared dim-small target image, and used the neat filter to realize background suppression adaptive and target enhancement [4,13]; Yanhua Wang and others used anisotropic diffusion filter to separate the target and gradient feature of background to improve the image of the SNR [14]; Jin Liu et al. put forward a kind of infrared background prediction and suppression algorithm based on improved M estimate of the current residual error [15]; Jin Qin put forward weak small targets detection method based on the optical flow estimation and adaptive background suppression [16]; Rimeng Liu et al. proposed an adaptive region growing algorithm that could automatically extract the small target from infrared image [17]. Without the statistical properties of the backgrounds and assumption of the gray feature, the structures of these methods are very simple, and widely used in engineering application. However, they would residue much strong background texture, and it is not enough to improve the SNR of image as for detecting the weak small target in complex background.

The transform domain filtering method firstly maps the image to transform domain, and then detects the target in the transform domain. Yang Yong et al. used Butterworth high-pass filter in the preprocessing of infrared dim-small target image [18]; Thayaparan T. et al. found the frequency domain algorithm based on the fast Fourier transform [19]. But these methods are not suitable for the weak small target detection in the low SNR infrared image. S. Liu and Z. Cao proposed an improved visual attention algorithm to detect SAR image target in complex environments [20];

M. S. Islam and U. Chong presented an improvement in moving target detection based on Hough Transform and Wavelet [21]; Zhicheng Wang et al. proposed a detection method of fusion the infrared small target based on support vector machine in the wavelet domain [22]. The performance of these methods mainly depends on the design of wavelet basis. Liu Riming and others extracted high order statistical characteristic of the image by Fukunaga - Koontz nuclear transformation to implement the background suppression and enhancement the target [23]. Yong Yang et al. used two-dimensional general S transformation to obtain the information of background [24]. In order to solve the structured background suppression, Xiang Zhang et al. put forward an infrared weak small target background suppression method based on dual tree complex wavelet transform [25]. Yiquan Wu et al. put forward a test method of inhibition the original image, based on nonnegative matrix decomposition and independent component analysis and complex contoured transform [26]. Y. Wu, and D. Yin put forward a kind of background prediction test method based on the next sampling transform and fuzzy c-means clustering multi-model least squares support vector machine (SVM) [27]. All in all, the transform domain filtering method need to implement two transformations, so its computational complexity generally become larger and its real-time is reduced.

## 2 Basic Principles

The weak small moving target detection method based on the time domain filtering can be seen as a background suppression method in time domain. In this paper, aiming at three commonly used time domain filtering methods –the time domain average filtering, the time domain median filtering, and the time domain minimum value filtering, we compare their performance by using them to detect the weak small target in IR images.

### 2.1 The Time Domain Average Filtering

The time domain average filtering uses the average of the pixel  $(i, j)$  in the time window K as its background prediction value. The residual signal  $f_r(i, j, k)$  of the pixel  $(i, j)$  after average filtering can be represented as follows.

$$f_r(i, j, k) = f(i, j, k) - \mu_{i,j}, k = 1, 2, \dots, K \quad (1)$$

The steps of time domain average filtering are described as follows.

1. Read K frames of infrared images into memory, and store in imk ( $k=1, 2, \dots, K$ ).
2. Put imk combined by function imadd(), stored in matrix I, and make matrix I divided by K, then we get the matrix J, which contains the time domain average of each point.

3. Make each frame of image minus the mean value matrix, and then get the residual signal.
4. Select an appropriate threshold for binarization.
5. The points which gray values are greater than threshold are candidate targets, and then the others are background points.

## 2.2 The Time Domain Median Filtering

The time domain median filtering uses the median of the pixel  $(i, j)$  in the time window  $K$  as its background prediction value. The residual signal  $f_r(i, j, k)$  of the pixel  $(i, j)$  after median filtering can be represented as follows.

$$f_r(i, j, k) = f(i, j, k) - \text{med}(i, j) \quad k = 1, 2, \dots, K \quad (2)$$

The steps of the time domain median filtering are similar to the steps of the time domain average filtering. Only the step (2) need to be changed to remove the gray value of each pixel in the array, then get the median of each point by function `median(a)`, which deposited in corresponding position of the matrix  $b$  which has the same size to the image matrix.

## 2.3 The Time Domain Minimum Value Filtering

The time domain minimum value filtering uses the minimum value of the pixel  $(i, j)$  in the time window  $K$  as its background prediction value. The residual signal  $f_r(i, j, k)$  of the pixel  $(i, j)$  after median filtering can be represented as follows.

$$f_r(i, j, k) = f(i, j, k) - \min(i, j) \quad k = 1, 2, \dots, K \quad (3)$$

The steps of the time domain minimum value filtering and the time domain average filtering are almost similar. Only the step (2) need to be changed to remove the gray value of each pixel in the array, then get the median of each point by function `min(a)`, which deposited in corresponding position of the matrix  $b$  which has the same size to the image matrix.

## 3 Experimental Results and Analysis

The experimental results for the first frame image in infrared sequence images using the time domain average filtering, the time domain median filtering, and the time-domain minimum value filtering are shown in Figure 1.

As shown in Figure 1, the three time domain filtering methods can detect the target, but they all produce some false alarm points. These false alarm points are generally produced by cloud edge or random noise.

In Figure 1b, 1c and 1d, the false alarm points using the time domain average filtering are mainly produced by cloud edge, and the number of the false alarm areas using the time domain average filtering is obviously less than the other two methods.

Seen in Figure 1c and 1d, the number of the false alarm areas using the time domain median filtering is similar to the number of the false alarm areas using the time-domain minimum value filtering, but the number of the false alarm pixels using the time domain median filtering is obviously less than the number of the false alarm pixels using the time-domain minimum value filtering.

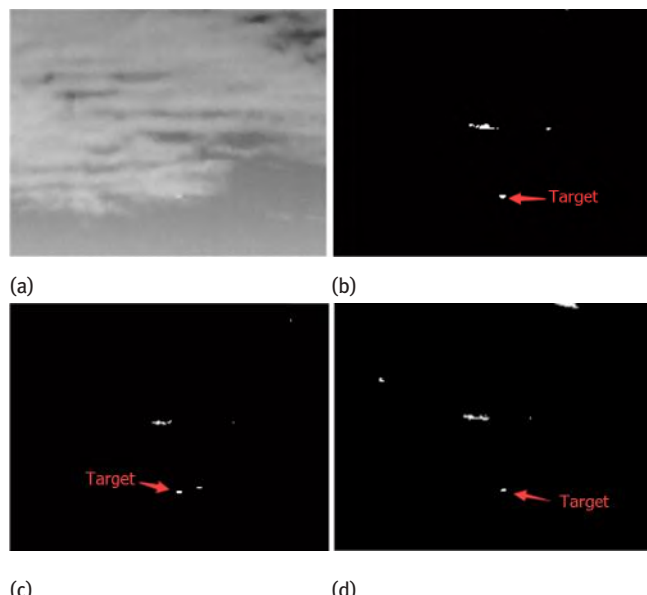


**Figure 1.** The results of the three time domain filtering methods: (a) the original infrared image, (b) the binary image by using the time domain average filtering, (c) the binary image by using the time domain median filtering, (d) the binary image by using the time domain minimum filtering.

Only considering the false alarm points by using the three time domain filtering methods, it is not enough to judge which method is the best one of them. We want to find more information using the three dimensional histograms. The three dimensional histograms of the binary images by using three time domain filtering methods are shown in Figure 2.

The three dimensional histogram of the binary image by using the time domain average filtering method is shown in Figure 2a. It shows that the ordinate of the target is around 44, and the ordinates of false alarm points remain 10 -15.

As shown in the three dimensional histogram of the binary image by suing the time domain median filtering method (seen in Figure 2b), the ordinate of the target is about 47, and the ordinates of most of the false alarm points maintain 20-30.

As shown in the three dimensional histogram of the binary image by suing the time domain minimum value filtering method (seen in Figure 2c), the ordinate of the target is around 62, and the ordinates of most of the false alarm points remain 35-47. Furthermore, the number of false alarm points by using the time domain minimum filter ing method is more than the other two.

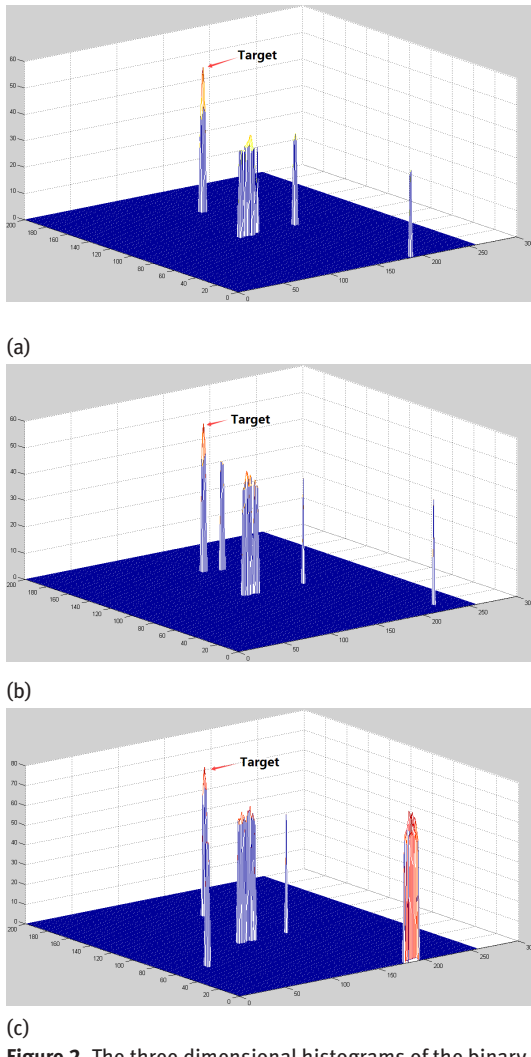


**Figure 2.** The three dimensional histograms of the binary images by using three time domain filtering methods: (a) get the binary image of the three dimensional histogram, (b) median filter to get the binary image of the three dimensional histogram, (c) the minimum filter to get the binary image of the three dimensional histogram.

In short, comprehensive consideration, the time domain average filtering method is more suitable for weak small moving target detection than the time domain median filtering methods and the time-domain minimum value filtering method.

## 4 Conclusion

In this paper, we introduce three time domain filtering methods, and apply the three time domain filtering methods in weak small moving target detection. By comparing the number of the false alarm points and the three dimensional histograms by using the three time domain filtering methods to detect the weak small target in infrared image, we can see that although the time domain minimum value filtering method is the highest in target brightness, but it produces the biggest number of the false alarm points. The performance of the time domain average filtering method is better than the other two, so it is the most appropriate method to detect weak small moving target in the time domain filtering.

**Acknowledgment:** This work was financially supported by the Programs of the National Natural Science Foundation of China (Grant No. 61263040).

## References

- [1] M. Wan, F. Zhang, and J. Li, Infrared weak small targets detection method based on local window, *Journal of Arrows of the Guidance*, vol. 31, no. 5, 2011, pp. 237-240.
- [2] B. Wu, G. Ji, and P. Li, A new method of infrared small moving targets detection based on the third order cumulate, *Journal of Infrared and Millimeter Wave*, vol. 25, no. 5, 2006, pp. 364-367.
- [3] YiSiKa, The key techniques of infrared search and tracking system, Chengdu: University of Electronic Science and Technology Ph.D. Thesis, 2003.
- [4] B. Zhang, T. Zhang, Z. Cao, et al., Fast new small-target detection algorithm based on a modified partial differential equation in infrared clutter, *Optical Engineering*, vol. 46, no.10, 2007, pp. 106-110.
- [5] R. C. Gonzalez, and R. E.Woods, *Digital image processing*, 2nd Edition, USA: Prentice Hall, 2003.
- [6] H. Fan, and C. Wen, Two-dimensional adaptive filtering based on projection algorithm, *IEEE Trans on Signal Processing*, vol. 52, no. 3, 2004, pp. 832-838.
- [7] P. Wang, J. W. Tian, and C. Q. Gao, Infrared small target detection using directional highpass filters based on LS-SVM, *Electronics Letters*, vol. 45, no. 3, 2009, pp. 156-158.
- [8] H. Sang, X. Shen, C. Chen, Architecture of a configurable 2-D adaptive filter used of small object detection and digital image processing, *Optical Engeering*, vol. 43, no. 8, 2003, pp. 2182-2198.
- [9] H. Nie, and Z. Shen, The infrared background suppression method based on A Winer filter, *Journal of National University of Defense Technology*, vol. 25, no. 3, 2003, pp. 51-54.
- [10] M. Li, T. Zhang, W. Yang, and X. Sun, Moving weak point target detection and estimation with three-dimensional double directional filter in IR cluttered background, *Optical Engineering*, vol. 44, no. 10, 2005, pp. 145-148.

- [11] C. Q. Gao, J. W. Tian and P. Wang, Generalised-structure-tensor-based infrared small target detection, *Electronics Letters*, vol. 44, no. 23, 2008, pp.1349-1351.
- [12] S. Zong, J. Wang, and Q. Chen, New algorithm of infrared target detection under sea and aircomplicated background, *Journal of Electrical Engineering*, vol. 32, no. 4, 2005, pp. 9-12.
- [13] B. Zhang, T. Zhang, S. Nong etc., Neat filter method of infrared small moving targets in real time detection, *Journal of Infrared and Millimeter Wave*, vol. 27, no. 2, 2008, pp. 95-100.
- [14] Y. Wang, W. Liu, Dim Target enhancement algorithm for low-contrast image based on anisotropic diffusion, *Opto-Electronic Engineering*, vol. 35, no. 6, 2008, pp. 15-19.
- [15] J. Liu, and G. Ji, Infrared small target detection based on non-stationary background, *Journal of Electronics & Information Technology*, vol. 32, no. 6, 2010, pp. 1295-1300.
- [16] W. Qian, J. Qin, and Q. Chen, Weak small targets detection based on optical flow estimation and adaptive background suppression, *Journal of Photons*, vol. 40, no. 3, 2011, pp. 476-482.
- [17] R. Liu, L. Yang, E. Liu and J. Yang, Automatic extraction of infrared small target based on support vector regression and adaptive region growing algorithm, *Optical Engineering*, vol. 46, no. 4, 2007, pp. 046402.
- [18] L. Yang, J. Yang, and K. Yang, Adaptive detection for infrared small target under sea-sky complex background, *Electronics Letters*, vol. 40, no. 17, 2004, pp. 1083-1085.
- [19] T. Thayaparan, S. Kennedy, Detection of a maneuvering air target in sea-clutter using joint time-frequency analysis techniques, *IEEE Proceedings, Radar, Sonar and Navigation*, 2004, vol. 151, no. 1, pp. 19-30.
- [20] S. Liu and Z. Cao, SAR image target detection in complex environments based on improved visual attention algorithm, *EURASIP Journal on Wireless Communications and Networking*, 2014, no. 1, pp.1-8.
- [21] M. S. Islam and U. Chong, Improvement in moving target detection based on Hough Transform and Wavelet, *IETE Technical Review*, 2015, vol. 32, no. 1, pp. 46-51.
- [22] Z. Wang, J. Tian, J. Liu and S. Zheng, Small infrared target fusion detection based on support vector machines in the Wavelet domain, *Optical Engineering*, 2006, vol. 45, no. 7, pp. 076401.
- [23] R. Liu, E. Liu, and J. Yang, Infrared weak target detection base on nuclear Fukunage - Koontz transform, *Journal of Infrared and Millimeter Wave*, vol. 27, no. 1, 2008, pp. 47-51.
- [24] Y. Yong, X. Yang, B. Wang, et al., A small target detection method based on generalized S-transform, *International Conference on Apperceiving Computing and Intelligence Analysis*, 2008, pp. 189-192.
- [25] X. Zhang, J. Qin, H. Liu, Infrared weak small targets background suppression based on dual tree complex wavelet transform, *Journal of Photons*, 2010, vol. 39, no. 9, pp. 1672-1677.
- [26] Y. Wu, S. Ji, and D. Yin, Infrared small target detection based on NMF, ICA and complex Contourlet transform, *Journal of Aerospace*, 2011, vol. 32, no. 8, pp. 1833-1839.
- [27] Y. Wu, and D. Yin, Infrared small target detection based onNSCT, KFCM and model of LS – SVM, *Journal of Instruments and Meters*, 2011, vol. 32, no. 8, pp. 1704-1709.

Gong QIN\*, Jun ZHOU

## Breath Sounds Detection System based on SOPC

**Abstract:** The core of the SOPC development platform named DE2 was the Altera's FPGA with embedded soft core of NIOS II CPU. This system used audio codec chip WM8731 to complete signal sampling and playback of breath sounds, and also determined the start-stop of breath sounds with the use of short-time energy and short-time zero-crossing rate, and short-term autocorrelation analysis, and then took advantage of digital filter and FFT transform and linear prediction analysis technology to extract related parameters of breath sounds, matching with DTW algorithm for identification. The experimental results show that the system can efficiently identify various breath sounds. The function of the system can be used in the clinical auxiliary diagnosis of lung disease and identification of different lung sounds. It also can facilitate medical teaching and remote diagnosis.

**Keywords:** breath sounds detection; the SOPC; digital signal processing; pattern recognition

### 1 Introduction

An important clinical index of lung physiology and pathology is lung sounds, which is often said that breath sounds [1,2]. Breath sounds detection through the stethoscope preliminary diagnosis of lung disease is the most basic and most rapid method, but it need a doctor with personal accumulated rich clinical experience to judge. Due to the low resolution and narrow frequency response range of the stethoscope and different auscultation level of different doctors, the listening content is difficult to be described objectively in text and language. So both learning and mastering auscultation technology is considerable difficult for doctors who had less clinical experiences [3,4].

This paper tries to research a breath sounds auscultation system on SOPC platform. With the help of modern signal processing technology, this system can realize objective record, storage, playback, analysis, comparison, identification, and so on for the physiological and pathological characteristics of lung index. The function of the system can be used in the clinical auxiliary diagnosis and identification of lung disease, it also can facilitate medical teaching and remote diagnosis [10].

---

\*Corresponding author: Gong QIN, School of Physics and Information Engineering, Jiang han

University, Wuhan, Hubei, China, E-mail: 497839993@qq.com

Jun ZHOU, School of Physics and Information Engineering, Jiang han University, Wuhan, Hubei, China

## 2 Design of the system

System consists of front-end analog signal processing circuit and DE2 development board. The front-end circuit realizes signal acquisition and conversion of breath sounds through the sensor, and amplifying, filtering. Then, through A/D conversion of the WM8731, the audio signal of original breath sounds is digitized. Then, DE2 part, NIOS II as the core, is used to store and analyse digital signal, to extract the feature parameters, used for matching and recognition, and to display information on the LCD screen. The system structure is shown in Figure 1.

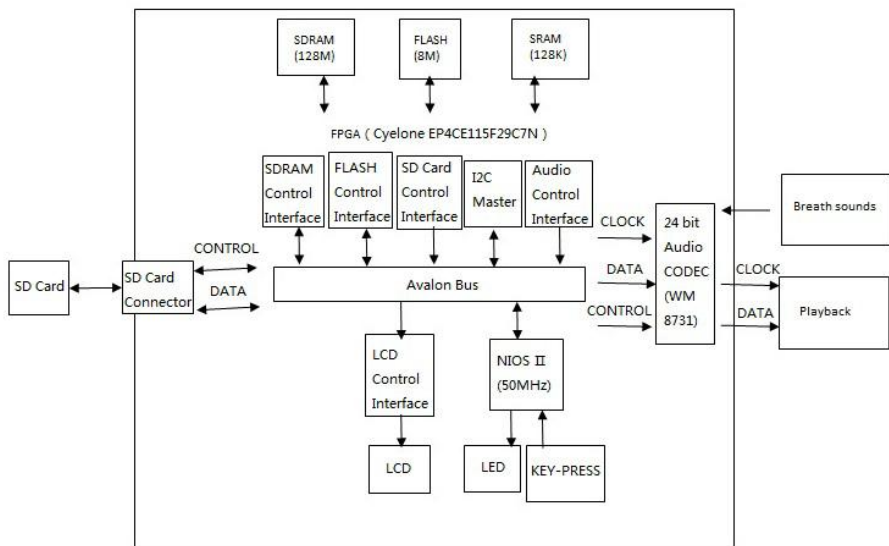


**Figure 1.** System structure diagram

### 2.1 Hardware Resource Configuration

Through the SOPC Builder, we can build and implement the system flexibly, Figure 2 and Figure 3 shows the basic setup of the system in the SOPC Builder

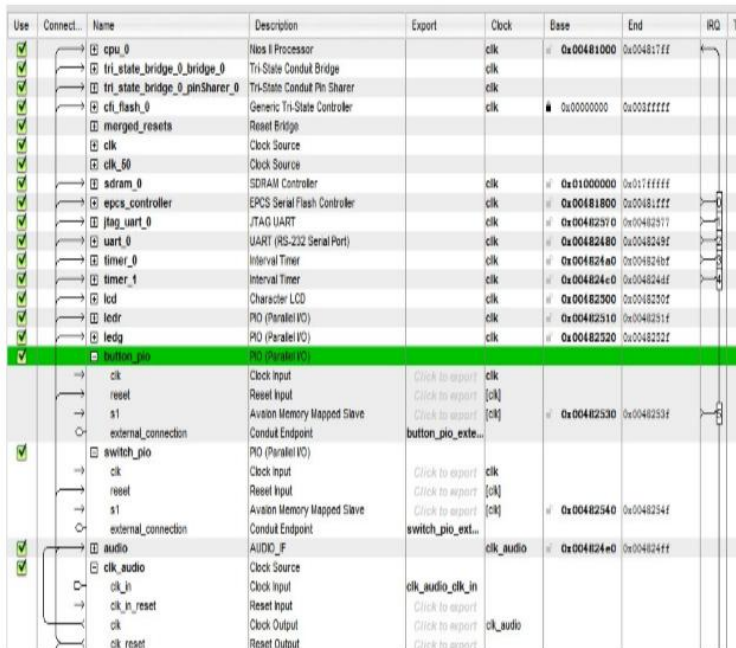


Figure 2. SOPC Builder configuration (1)

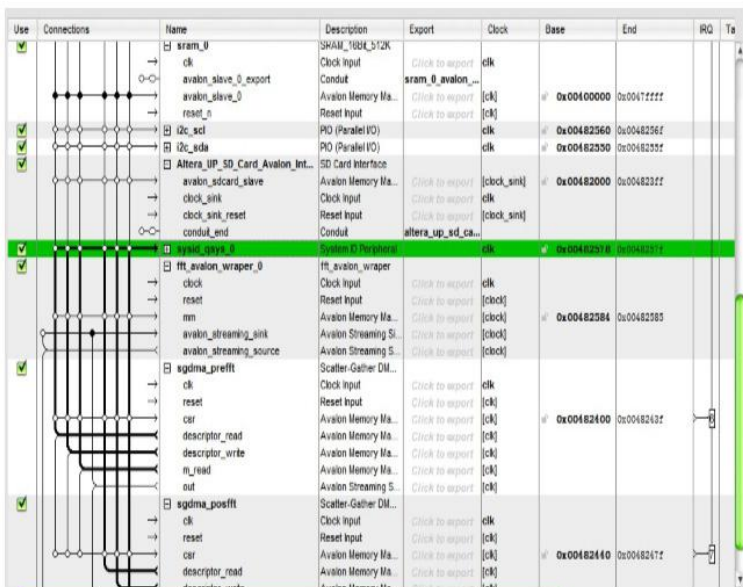
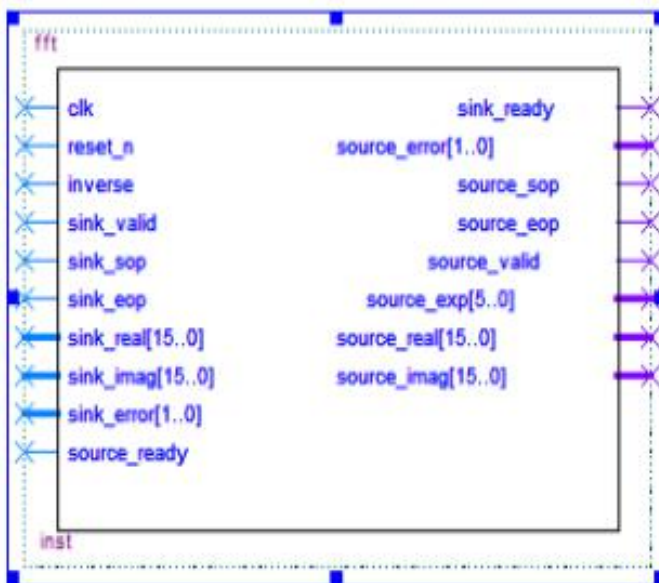


Figure 3. SOPC Builder configuration (2)

## 2.2 FFT Configuration

FFT algorithm adopts high performance Fast Fourier Transform (FFT) processing IP core of Altera company. Because the frequency of breath sounds mainly ranges from 50 to 2000 Hz [8], we reduce the sampling rate into 22.05 kHz, and choose 512 as transform length for the high-speed complex FFT algorithm, which is equivalent to 23 ms in short period, the frequency resolution is 44.1 Hz, so the frequency resolution and time resolution can satisfy most application. Because the original signal is recorded by 44.1 kHz, in the future we can also realize different analysis and inter-comparison through a variety of sampling rate and window lengths.

Figure 4 is the FFT principle diagram. According to the timing, we write files that generated FFT IP core that can hang avalon bus, what enhanced the flexibility of the system and real-time processing capacity of the data [6].



**Figure 4.** FFT principle diagram

## 2.3 SGDMA Configuration

FFT algorithm is used in Avalon - ST bus, the Avalon - ST bus can be set by Scatter gather DMA Controller of Altera, as shown in Figure 5.

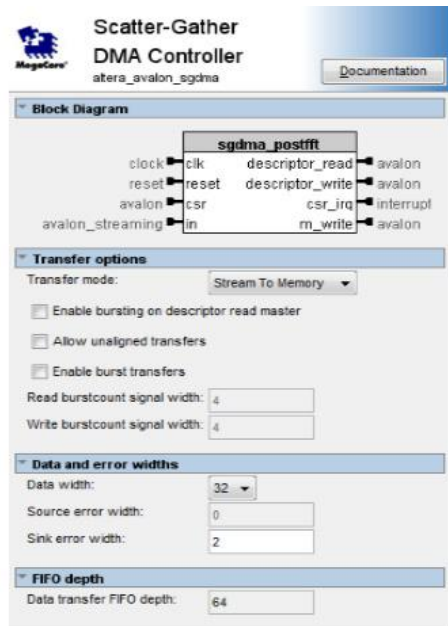


**Figure 5.** Scatter gather DMA controller IP core

## 2.4 External Resource Configuration of the System

Breath sounds are collected by the sensor. After amplified and filtered, the analog signal that is set between -1V to +1V inputs to the WM8731. Controlling the WM8731 can realize A/D and D/A conversion. A/D conversion is mainly applied to the sample signal acquisition, and D/A conversion is mainly applied to replay breath sounds through loudspeaker. WM8731 makes configuration through the I<sup>2</sup>C bus [5-7]. The working frequency of I<sup>2</sup>C cannot be set too high. If the working frequency is set too high, WM8731 is too late to response after it receives the data, then cannot judge the ACK correctly. So, I<sup>2</sup>C bus clock is set to 20 KHz by frequency division of 50 MHz system clock.

The system uses the SD card to storage breath sounds data and analysis results. The NIOS II system is added to PIO control port and data port of operating the SD card.

The NIOS II system is added to the control port of operating LED and key-press. The main function of LED is real-time displaying of input audio signal energy. The main function of key-press is to realize the human-computer interaction function by manipulating.

In QSYS platform, we add PIO port what driving graphic dot matrix LCD, and write underlying device driver of LCD, and write API function as help module. According to the prompt of the menu interface, the system inputs breath sounds, recording the

breath frequency and displaying the breath frequency, then displaying recognition results after completing the system processing.

### 3 Breath sounds detection algorithm

Through short-time energy and short-time zero-crossing rate, and short-term autocorrelation analysis, the system determines the start-stop of breath sounds digital signal, then to realize the endpoint detection. Using digital filter and FFT transform and linear prediction analysis technology to extract characteristic parameters of the breath sounds signal, then combining medical principle, synthetically matching by the DTW (dynamic time warping) algorithm [9], to realize the breathing sound detection and recognition. The algorithm flow chart is shown in Figure 6.

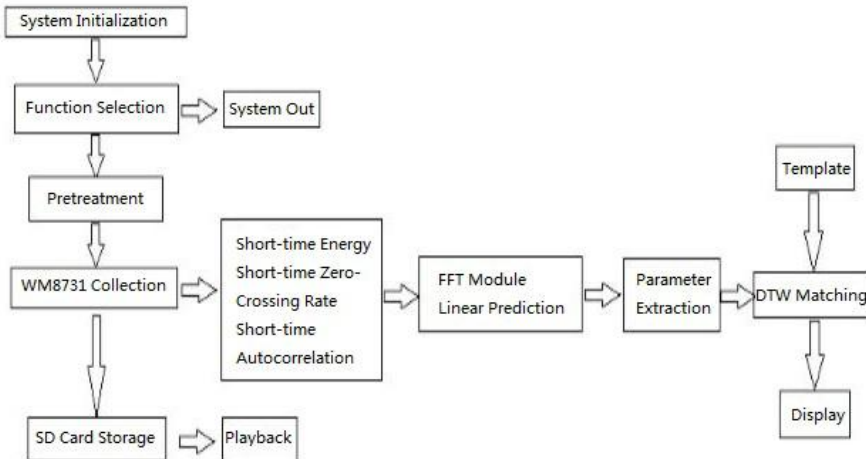


**Figure 6.** System algorithm flow chart

#### 3.1 Pretreatment

Pretreatment including preemphasis, framing, adding window and etc.

First we enter into preemphasis to the original breath sounds signal, the purpose is to enhance the high frequency component of the signal. Usually by a transfer function  $H(Z) = 1 - \alpha Z^{-1}$  to filter, among them,  $0.9 < \alpha < 1.0$  for preemphasis coefficient, it always be 0.95, 0.97, 0.98, we take 0.95.

Assuming that sampling value of breath sounds is  $x(n)$  in the  $n$  time, then after dealing with the pre-emphasis, as in

$$y(n) = x(n) - \alpha x(n-1) \quad (0.9 < \alpha < 1) \quad (1)$$

Breath sounds signal has the characteristics of short time smooth and long time period, through framing operation, it can improve the short-term features, so as to facilitate the establishment of the model. General, frame length is set to 20 ms, at this time, frame shift is set to 10 ms.

Then each frame signal is multiplied by using Hamming window, in order to reduce discontinuous signal in the frame start and t the frame end, the Hamming window function is here

$$w(n) = 0.54 - 0.46 \cos\left(\frac{2\pi n}{N-1}\right) \quad (1 \leq n \leq N-1) \quad (2)$$

Where N is the sampling number of current data frame.

### 3.2 Parameter Extraction in Time Domain

#### 3.2.1 Short-time energy and short-time amplitude

After the body spread, the waveform of breath sounds signal is similar to voice signal waveform, its energy change is also very obvious in short period. After framing and adding window, the nth frame breath sounds signal is  $X_n(m)$ , its short-time energy is set to  $E_n$ , as in

$$E_n = \sum_{m=0}^{N-1} |x_n(m)|^2 \quad (3)$$

$E_n$  is a function of the variable quantity on voice signal amplitude value, but it is very sensitive to high level, because it is used to the square of the signal in computing. For this, using the short-time average amplitude function  $M_n$  describes the variable quantity, it is defined as

$$M_n = \sum_{m=0}^{N-1} |x_n(m)| \quad (4)$$

Through the short-time energy and short-time average amplitude function, we can get the change of strength that is similar to auditory sense, to obtain the part of breath sounds signal parameters. By the analysis, signal energy is affected by airflow speed and ventilation volume. Through literature, found that the strength mainly were positively correlated to the airflow speed square and local ventilation volume.

#### 3.2.2 Short-time zero-crossing rate

By the analysis of breath sounds signal, found that some breath sounds, such as vesicular sound, while energy is lower, but its zero-crossing rate is higher. So zero-crossing rate have also been used as one of analysis parameters, which also reflects the spectrum composition in some way. Zero-crossing rate  $Z_n$  of the signal  $X_n(m)$  is defined as

$$Z_n = \frac{1}{2} \sum_{m=0}^{N-1} |sgn[x_n(m)] - sgn[x_n(m-1)]| \quad (5)$$

Where  $sgn[]$  is symbol function, namely

$$sgn[x] = \begin{cases} 1, & (x \geq 0) \\ -1, & (x < 0) \end{cases} \quad (6)$$

### 3.2.3 Short-time autocorrelation function

Short-time autocorrelation analysis is a kind of commonly analysis methods on the time domain waveform, it can be used to obtain cycle value of periodic sequence, etc. Breath sounds signal is similar to the periodic voice signal, so its analysis in short-time autocorrelation function is applied, at the same time, the short-time autocorrelation algorithm is also one of operation in extracting the linear prediction coefficients.

Near the Nth sample point, intercepting a signal with short-time window, the result of doing autocorrelation calculation is short-time autocorrelation function, as in

$$R_m(k) = \sum x(n)x(n-k) \quad (7)$$

Where  $n$  said that window function begins to join from the nth point.

### 3.2.4 Linear prediction coefficient

This method based on linear prediction theory is a kind of very effective audio signal analysis method, also is a kind of feature parameter extraction technology widely. It is because a established model is correspond to man's vocal tract model, and the model has high computing precision and speed.

The analysis of linear prediction (LPC) is that linear combination of the past output signal value estimate the upcoming output value for a given discrete linear system. For the solution of the LPC prediction coefficients, we can adopt the Durbin algorithm to recursive computation.

## 3.3 Parameter Extraction in Frequency Domain

In a broad sense, the frequency domain analysis of breath sounds signal include signal spectrum, power spectrum, spectral envelope analysis, etc., and the common methods of frequency analysis have band-pass filter group, Fourier transform, linear prediction and so on. Because breath sounds having the same as the audio signal is a nonstationary process [2], so signal spectrum analysis of breath sounds cannot be used by direct Fourier transform, and should be used by short-time Fourier transform (STFT), the corresponding spectrum is called a "short-time spectrum". From the point of power spectrum, a variety of breath sounds energy distribution has obvious

difference, for example, high frequency component of asthma sound and rale sound is richer than alveolar sound's.

### 3.3.1 Short-time spectrum

The short-term spectrum of breath sounds can be obtained by using short-time Fourier transform. After adding window processing on breath sounds signal, the resulting nth frame signal  $X_n(m)$  is used to DTFT, as in

$$X_n(e^{j\omega}) = \sum_{m=0}^{N-1} x_n(m) e^{-j\omega m} \quad (8)$$

Usually, in frequency domain analysis, to choose hamming window is more suitable than rectangular window. In the actual signal processing, the discrete Fourier transform  $X_n(k)$  instead of  $X_n(e^{j\omega})$ , and can be done with fast Fourier transform (FFT). In general, the calculation of FFT can complete the corresponding algorithm by computer software, this way can only realize the real time operation. In order to complete the real time operation, it can use digital signal processing chip or special FFT chips, then, the SOPC platform is easier to do at this point.

### 3.3.2 Short-time power spectrum

Short-time power spectrum of breath sounds can be directly obtained by short-time Fourier transform, its formula is

$$S_n(k) = X_n(k) \cdot X_n^*(k) = |X_n(k)|^2 \quad (9)$$

## 3.4 Breath Sounds Recognition

DTW algorithm is that a global optimization problem is converted into a local optimization algorithm, and being a nonlinear warping technique that combining time warping and distance measure to calculate. Ensure that under a certain path to limit the algorithm can find the best matching module. The waveform on N axis is template waveform, the waveform on M axis is collected waveform. Because there is a length difference between the collected breath sounds and breath sounds template identified on the time domain, then, the waveforms on M and N axis need to vector quantization. Using the DTW (dynamic time warping) algorithm, insert or delete syllable, and template matching, to get the distance measure between this syllable and the system the template, so as to determine its type. DTW algorithm diagram as shown in Figure 7.

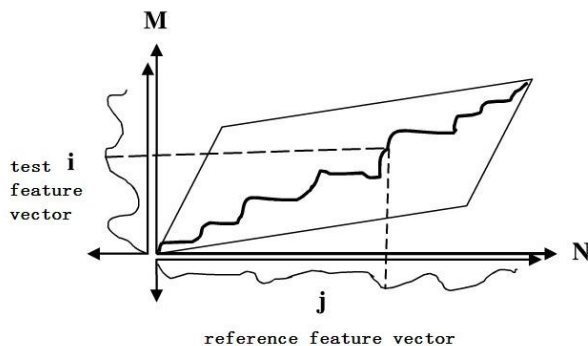


**Figure 7.** DTW algorithm

For recognition of different breath sounds, choose different parameter combination for vector quantization, it can further improve the recognition effect.

#### 4 System experimental analysis

3 KHz sine signal is as a test, the signal spectrum is shown in Figure 8. Normal breathing sounds is alveolar sound, and its frequency is focused on the 20 Hz ~ 100Hz, as shown in Figure 9. Sick big wet rale sound is on 100Hz ~ 200 Hz frequency, as shown in Figure 10. Sick pleural rub sound is on 400Hz ~ 600 Hz frequency, there were 2 KHz high frequency components, as shown in Figure 11.

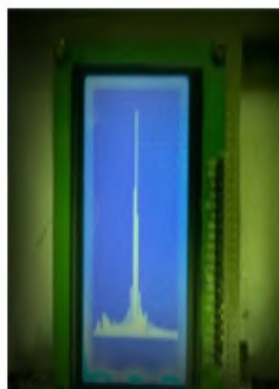


**Figure 8.** 3 KHz sine

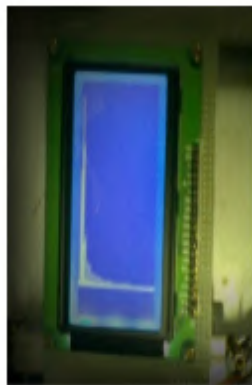


**Figure 9.** Alveolar sound

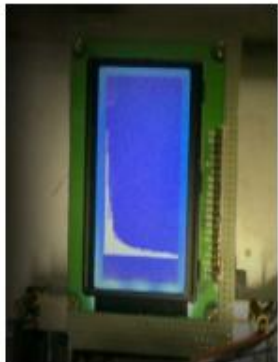


**Figure 10.** Big wet rale sound

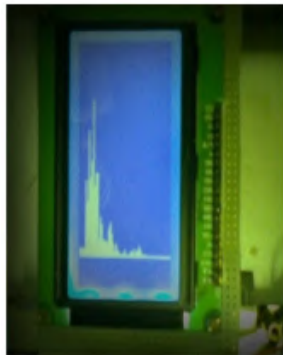


**Figure 11.** Pleural rub sound

Other breath sounds recognition results such as Table 1.

**Table 1.** Contrast table of 5 kinds of breath sounds recognition

breath sounds	accuracy of breathing frequency detection	rate of identification
alveolar sound	98%	92%
pleural rub sound	90%	90%
big wet rale sound	92%	85%
medium wet rale sound	90%	75%
snoring sound	80%	85%

## 5 Conclusion

This paper shows a breathing sounds detection system using SOPC platform design. With the front-end acquisition circuit and output devices, the system design completely gets implementation in a FPGA. It has the advantage of miniaturization, lower power consumption and increasing stability. The small breathing sound detection and analysis system, which helps doctors to identify a variety of breath sounds quickly and accurately, as well as some fuzzy sounds that the human ear is difficult to distinguish, can help to improve the diagnostic accuracy.

## References

- [1] YAO Xiao-jing, WANG Hong, LI Yan and CUI Jian-guo, The research advance of analysis and identification method of lung sound signals, Journal of Chongqing university of technology (Natural Science), VOL.27, NO.12, DEC.2013, pp.95-100
- [2] Marshalla A, Boussaktab S. Signal analysis of medical acoustic sounds with application to chest medicine, Journal of the Franklin Institute, 2007, 344 (3), pp.230-242
- [3] LI Zhen-zhen, WU Xiao-ming, Research progress of adventitious respiratory sound signal processing, Journal of BiomedicalEngineering, VOL.30, NO.5, Oct.2013, pp.1131-1135
- [4] Abbas A, Fahim A. An automated computerized auscultation and diagnostic system for pulmonary diseases, J MedSyst, 2010, 34(6), pp.1149-1155
- [5] LI Ying-hong, ZHAO Jun-tao, Design and realization of the embedded audio processing system based on SOPC, Modern ElectronicsTechnique, VOL.289, NO.2, 2009, pp.33-35
- [6] FFT MegaCore Function User Guide, July 2010, Altera Corporation
- [7] ZENG Fan-zheng, WANG Ming-juan, QU Yi, LI Li-li, Voice recording and playback system based on FPGA, Modern ElectronicsTechnique, VOL.327, NO.16, 2010, pp.66-68
- [8] XIN Xiao-feng, YIN Kai-sheng, HUANG Xiao-ping, Establish and application of a lung sounds recording and spectral analysis system, Chinese Journal of Biomedical Engineering, VOL.19, NO.2, June 2000, PP.236-39
- [9] YANG Jie, KANG Ning, Research of Dynamic Time Warping, Science and Technology & Innovation, vol. 4, pp. 11-12, Apr. 2016.
- [10] Maria Barbarosou, Ioannis Paraskevas, Amr Ahmed, Military aircrafts' classification based on their sound signature, Aircraft Engineering and Aerospace Technology, Vol. 88(1), pp. 66-72, 2016.

Bao Kai ZHANG, Chun Hua TAN\*

## A Novel Fiber-optic Sensor for the Determination of Melting Point of Solids

**Abstract:** A novel, rapid and automatic computer-controlled equipment based on the two-channel fiber optic refractive index sensor for determining the melting point of minute quantities of solid substances is described. The technique uses two optical fiber heads as serve sample holder and temperature sensor, respectively. Principle of the method is that there is a linear relationship between the temperature and the refractive index of the simethicone. The refractive index-time curve was recorded by the sensor, and the abrupt change point of the curve indicated liquidus and solidus transition. Combined of the two curves of the refractive index and the refractive index-time of simethicone, the melting point can be calculated easily. The results obtained with this new method showed good agreement with the results acquired from other methods, with relative standard deviations (RSDs) less than 2%. The automatic method based on fiber optic sensing has the following advantages: clever design, easy operation, good repeatability, accurate result, implying its potential for industrial application.

**Keywords:** Simethicone; Melting point; Refractive index sensor; Fiber optic

### 1 Introduction

The melting point is the most fundamental parameter influencing the properties and behaviors of materials, and it also plays a vital role in technical applications. Therefore, it is important to have a simple, accurate and rapid method for the determination of the melting point. In the past decades, many methods have been developed to determine the melting point [1,2], visual observation is used to determine the melting point, but its large errors are inevitable, the use of the optical instrument can make its results more accurate [3,4]. The capillary-tube methods by means of a thermometer immersed in the melt sample is usually used, but it is a tedious work, and the results of different observers, using the same apparatus and the same specimen, may suffer a large errors. Differential thermal analysis (DTA), differential scanning calorimetry

---

\*Corresponding author: Chun Hua TAN, Laboratory of Nanophotonic Functional Materials and Devices, School for Information and Optoelectronic Science and Engineering, South China Normal University, Guangzhou, China, E-mail: tch@scnu.edu.cn

Bao Kai ZHANG, Laboratory of Nanophotonic Functional Materials and Devices, School for Information and Optoelectronic Science and Engineering, South China Normal University, Guangzhou, China

(DSC) [5-9], derivative thermogravimetry(DTG) [10], noise thermometry [11,12] were also applied to determine the melting point. Thermal analysis methods are rapid but less accurate [13], because they are subject to systematic errors coming from the small sample volumes [14]. Noise thermometry, which the mean square of the noise voltage developed in a resistor is proportional to T, can be variously applied at both high and low temperatures, and the temperature of this melting point depends on the surrounding atmosphere and its uncertainties are relatively high. A few new optical methods such as laser ultrasonic [15], step-shift method [16], and absolute spectral radiometric [17,18], infrared thermal camera technology [19], high-field electron paramagnetic resonance spectroscopy [20] are proposed for the determination of the melting point. Laser ultrasonic has a advantage of non-contact samples, the step-shift method can be determined by direct observation, the measurements of the absolute spectral radiometric are absolute. However, expensive equipments, complicated procedures and high-qualified staff limit their applicability for serial measurements. As a result, the determination of the exact melting point of a substance is a matter of some little difficulty and trouble.

An urgent need to find a method for determining melting-points of minute quantities of solid substances which is rapid and accurate, capable of giving strictly comparable and reproducible results, and potential for application by a relatively unskilled operator. Unfortunately, at present, no existing method can satisfy all above-mentioned criteria.

The objective of our work is to research a novel method for determining the melting points with lower price, easy to operation, precise and suitable to unskilled operator. What is more, the technique can be applied in industry.

In this paper, we present a novel and automatic method to determine the melting point of substances based on fiber optic refractive index sensing to detect the solid/liquid transition. One of two fiber optic heads holds minute quantities of solid sample, little simethicone is coated to another optic fiber head as a temperature sensor. Theory analyses and the experimental setup of the method are introduced in detail. With our method, melting point values of three kinds of substances were determined and compared with the results from other methods.

## 2 Principle of operation

In this paper, the temperature was measured using a fiber sensor based on a two-channel Fresnel reflection technique. The measurement principle of the sensor can be found in the literature [21]. Figure 1 is the set-up diagram.

The fiber head A is the reference arm, which is exposed to the air environment, used to eliminate the influence of light source fluctuation. In addition, the undesirable effects or the errors coming from the different losses of fibers and couplers and

environment temperature can be also decreased. There is a calibration process to get the constant K before formal test.

In this paper, the refractive index of air is 1.0003. The effective index  $nf$  of the fiber mode  $nf$  is 1.44961 at  $\lambda = 1550$  nm.

### 3 Materials and Methods

#### 3.1 Apparatus

Figure 1 shows the general arrangement of the apparatus. A schematic diagram of the electric heating chamber is also shown in Figure 1. The home-built heating chamber is made of copper, 10cm in high, 2cm in diameter, round the cylindrical surface is the heating coil inside asbestos. The heating current which pass through the heating coil is under micro-transformer control. The heating chamber is supported on a iron stand, the optic fiber heads pointing upwards are inserted into the chamber and heated in air.

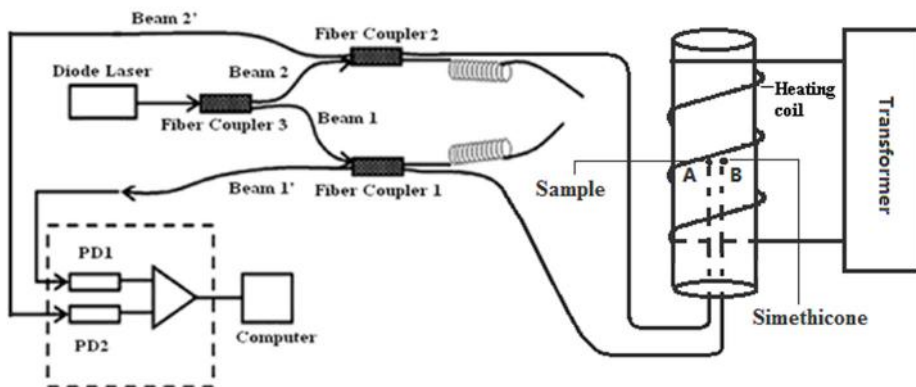


**Figure 1.** Schematic diagram of the melting point determining system.

Two Lightcomm OPM2012AA optical power meters connected to the computer via the RS-232C port is used for monitoring and collecting the reflective intensity-time (R-t) data. The appratus is controlled by a MS Windows computer and home-built software written in C++, the signals are collected data in fixed intervals (can be adjusted), corresponding refractive indices are calculated and saved it as the excel format for further processing.

### 3.2 Materials

Simethicone and other samples were used for experiments and supplied by tianjin kemiou chemical reagent Ltd (China). All other analytical reagent grade chemicals and distilled water were used.

### 3.3 Methods

To carry out a determination, a minute quantity of the finely powdered solid, which was spread in the head A as thin as possible, the head B was coated a thin layer of simethicone. Then, the two heads located in the center of the chamber was heated in air atmosphere to the appropriate temperature by means of the heating coil at the rate of approximately 5–10°C per minute, the rise of temperature of the system may be easily regulated by applied voltage. The system was ensured a gradual and regular rise of temperature all the time. When the system approached certain temperature (approximately 5°C below the melting point, acquired by preliminary experiments), the heating rate was reduced to about 1°C per minute.

In order to obtain the relationship between the refractive index and temperature, the refractive indices of simethicone corresponding to a series of known temperatures were determined firstly, and a calibration curve can be obtained. A linear equation relating temperature and refractive index can be established. The temperature corresponding to a given refractive index was then calculated by aid of the equation.

At the melting-point, the molten substance spreaded the head A, the head A-molten substance interface was replaced by the head A –air interface, the light intensity reflected at the head A-molten substance interface occurred a sudden change, causing a abrupt change in the refractive index-time curve, the temperature corresponding to the refractive index of the abrupt point indicated the melting point.

## 4 Results and Discussion

Before the determination of the melting point, the refractive indices of simethicone versus temperature were measured, the results are shown in Figure 2. The straight line is the linear fit to measured data. It can be seen that the linear fit is in very good agreement with the experimental data.

It will be noticed that the relationship between the refractive index of simethicone and the temperature is a straight line, and for the fitting equation:  $n=1.34448-T\times1.87881E-4$ , where n is the refractive index and T is the temperature. By the help of the equation, the apparatus is once set up, the melting-points of the sample may be readily obtained by simply measuring the refractive index of simethicone, the

inflection point of the refractive index-time indicates the temperature at which the sample begins to dissolve.

The measurement of the melting points were carried out for three kinds of samples (with different melting point) and the curve of refractive index vs time of diphenylamine is shown in Figure 3. The curve having two inflexion points and three line segments can be observed. The melting point is found by the first intersection of the two lines. The first segment corresponds to the curve of refractive index vs temperature of simethicone, the second rapid descending branch refers to the melting of solids. Combined with Figure 2, the temperatures can be determined from the refractive index of the first intersection. It can be seen from Figure 3, the observed transition is quite clear.

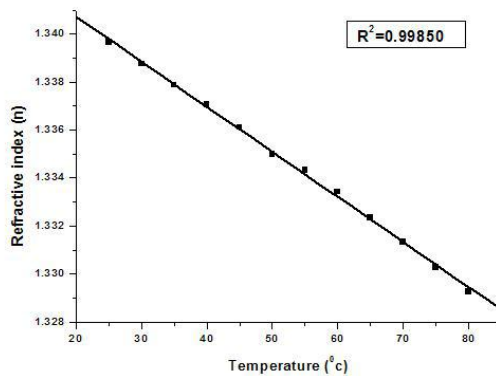


**Figure 2.** Plot of change in reflective index  $n$  of simethicone as a function of change in temperature  $T$ , fitted with a linear function. The fitted equation and  $R^2$ s of fit are indicated.

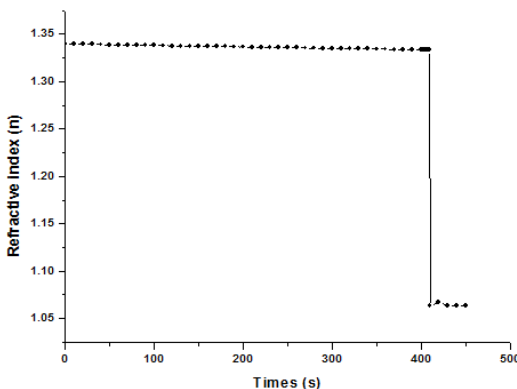


**Figure 3.** Under the experimental conditions, plot of change in reflective index  $n$  of diphenylamine as a function of change in time.

The results obtained for diphenylamine, paraffin, benzil are given in the following Table 1.

**Table 1.** Melting points T for the investigated substances compared with their literature values

Materials	<sup>a</sup> This work	<sup>b</sup> Literature
Diphenylamine	53.42°C±1.3%	53.00°C [21]
Paraffin	52.28°C±1.5%	52.52°C [capillary-tube method]
Benzil	93.75°C±1.9%	94.40°C [22]

<sup>a</sup>All values are the means of seven determinations ± relative standard deviation

<sup>b</sup>The mean of three determination, by standard capillary tube method, the heating rate of the bath was 1°C/min at the beginning, when approaching the melting point, the rate reduced to 0.5°C/min until the sample began to melt.

Seven determinations of the melting-point of each substance were made, and the values recorded above represent the mean of these results.

A comparison with literature data suggests a satisfactory overall performance of this fiber-optic sensing technique. The agreement between the values determined by this technique and these measurements, such as DSC, DTG, and capillary-tube method is rather good and demonstrates that the melting point can be easily determined in a wide range of samples for solids.

Conventional melting point analyses should be avoided those methods, which subject to large error, complex, tedious, expensive. Classical methods, such as thermal analysis, are accurate, but prone to system error coming from a little sample volume, spectral methods involves expensive equipment and professional operators, their applications have been limited. In this report, we describe a method that is fast and easy to use, testing requires only a small amount of sample and the melting can be obtained easily. The method is useful for labor and time savings to yield reliable results of the melting points.

In this paper, it was found from Table 1 that the relative standard deviations of the melting point of the three samples were never more than 2%, which shows that good reproducibility can be obtained and the performance of this technique is very stable, the reason is that the reference signal received by reference head A can be used to eliminate the influence of light source fluctuation, the undesirable effects can be also decreased. Thus, in this paper, long term stability can be effectively guaranteed.

## 5 Conclusion

A new automatic computer-controlled device for convenient and accurate determination of melting points is described. Its reliability evaluated by comparison with other methods.

Some advantages of the fiber optic sensing technique can be identified.

- The great advantage of the method is the automatic determination and the melting point can be obtained easily.
- A thermometer is not required.
- Unskilled observers can obtain results with a small error.
- Air bath instead of liquid bath and stir is cancelled.
- The two optic fiber heads being touched by the sample and the simethicone respectively, and the temperature of the sample is certain to be of exactly the same as the simethicone's. So the Results are close to the actual melting point.

One apparent limitation of the technique is that the melting range cannot be obtained.

The experimental results illustrate that this approach is capable of providing melting point measurements that are in good agreement with the data from other methods.

This paper shows the high potential of the technique to study liquidus and solidus transition, and it opens a new way to determining the melting points in industrial application.

**Acknowledgement:** The authors gratefully acknowledge the financial support for this work from the Science and Technology Plan of Guangdong Province (2009B050700011)

## References

- [1] Owen W S., Reid W M., Apparatus for the determination of melting points and boiling points, *Microchim Acta* 44, 1956, pp. 1373-1376.
- [2] Deman J M.. Deman L., Blackman B., Melting-point determination of fat products, *Journal of the American Oil Chemists Society* 60, 1983, pp. 91-94.
- [3] Kravchenko I N., Lobskii M I., Yatsiv D M., 1975., *Chemistry and Technology of Fuels and Oils* 11, 1975, pp. 820-821.
- [4] Rimington C., Symons P., Determination of the melting point of porphyrins and other darkly coloured substances with the use of polarized light, *Microchim Acta* 3, 1938, pp. 4-6.
- [5] Ding M S., Xu K., Jow T R., Phase diagram of EC-DMC binary system and enthalpic determination of its eutectic composition, *Journal of Thermal Analysis and Calorimetry* 62, 2000, pp. 177-186.
- [6] Ding M S., Xu K., Jow T R., Liquid-solid phase diagrams of binary carbonates for lithium batteries, *Journal of The Electrochemical Society* 147, 2000, pp. 1688-1694.
- [7] Ding M S., Xu K., Zhang S., Jow T R., Liquid/solid phase diagrams of binary carbonates for lithium batteries part II, *Journal of The Electrochemical Society* 148, 2001, pp. A299-A304.

- [8] Arsac A., Carrot C., Guillet J., Determination of primary relaxation temperatures and melting pointd of ethylene vinyl acetate copolymers, *Journal of Thermal Analysis and Calorimetry* 61, 2000, pp. 681-685.
- [9] Giordano F., Rossi A., Pasquali I., Bettini R., Frigo E., Gazzaniga A., Sangalli M E., Mileo V., Catinella S., Thermal degradation and melting point determination of diclofenac, *Journal of Thermal Analysis and Calorimetry* 73, 2003, pp. 509-518.
- [10] O'Connell C., Dollimore D., Determination of the melting point using derivativethermogravimetry, *Instrumentation Science & Technology Instrum* 27, 1999, pp. 13-21.
- [11] Crovini L., Actis A., Noise thermometry in the range 630-962degC, *Metrologia* 14, 1978, pp. 69-78.
- [12] Edler F., Kuhne M., Tegeler E., Noise temperature measurements for the determination of the thermodynamic T8mperature of the melting point of palladium, *Metrologia* 41, 2004, pp. 47-55.
- [13] Skau E L., Arthur C A., Weissberger A., Rossiter B W(Eds.), *Physical Methods of Chemistry*, Part V, Wiley-Interscience, New York. 1, 1971, pp. 105–197.
- [14] Wachter P., Schweiger H G., Wudy F., Gores H J., Efficient determination of crystallisation and melting points at low cooling and heating rates with novel computer controlled equipment, *Journal of Chemical Thermodynamics* 40, 2008, pp. 1542-1547.
- [15] Nadal M H., Hubert C., Chapuis G R., Shear modulus determination versus temperature up to the melting point using a laser-ultrasonic device, *Journal of Alloys and Compounds* 444, 2007, pp. 265-267.
- [16] Bloembergen P., Dong W., Zhang H., Wang T., A new approach to the determination of the liquidus and solidus points associated with the melting curve of the eutectic Co–C, taking into account the thermal inertia of the furnace, *Metrologia* 50, 2013, pp. 295-306.
- [17] Fox N P., Martin J E., Nettleton D H., Absolute spectral radiometric determination of the thermodynamic temperatures of the melting/freezing points of gold, silver and aluminium, *Metrologia* 28, 1991, pp. 351-374.
- [18] Gregor G., Ruslan K., Dirk U., Heinz S., Andreas S., Emissivity and temperature determination on steel above the melting point, *Weld World*, 2013, 57, 595-602.
- [19] Kohsaku K., Parallel Thermal Analysis Technology Using an Infrared Camera for High-Throughput Evaluation of Active Pharmaceutical Ingredients: A Case Study of Melting Point Determination, *AAPS PharmSciTech*, 2010, 11:1202-1205.
- [20] Massa C A., Pizzanelli S., Berzu V., Pardi L., Bertoldo M., Leporini D., A High-Field EPR Study of the Accelerated Dynamics of the Amorphous Fraction of Semicrystalline Poly(dimethylsiloxane) at the Melting Point, *Applied Magnetic Resonance*, 2014, 45:693-706.
- [21] Su H., Huang X G., Fresnel-reflection-based fiber sensor for on-line measurement of solute concentration in solutions, *Sensor Actuator B-Chemical* 126, 2007, pp. 579-582.
- [22] Rogers H., Holmes W C., Lindsay W L., The melting point of diphenylamine, *Journal of Industrial and Engineering Chemistry* 13, 1921, pp. 314-316.
- [23] Charsley E L., Laye P G., Palakollu V., Rooney J J., Joseph B., DSC studies on organic melting point temperature standards, *Thermochim Acta* 446, 2006, pp. 29-32.

Bin ZHANG, Yue-Juan WEI, Wen-Yi LIU, Zong YAO, Yan-Jun ZHANG,  
Ji-Jun XIONG

## Method for Measuring Internal Liquid Level of Sealed Metal Container by Ultrasonic

**Abstract:** The liquid level measurement method considers only the echoes energy inside the metal wall detected directly. By analyzing the sound field distribution and the characteristics of the round piston transducer in the metal wall, we proposed the concept of “energy circle” and calculated the two critical positions automatically. Finally, we achieved the accurate calibration of the inner liquid level from the outside of the sealed metal container.

**Keywords:** liquid level measurement; sealed; metal; ultrasonic

### 1 Introduction

The accurate measurement of liquid level in the sealed metal container is an important guarantee for the realization of the production process detection and real-time control [1]. Especially in aviation, petroleum and chemical industry and other special areas of production, the liquid in metal sealed container mostly are volatile, flammable, explosive, corrosive mixtures. At present, there are several kinds of ultrasonic measurement methods have been widely used, but all of them have some deficiency more or less which affect the precision of liquid level measurement.

First, in the ultrasonic penetrative method [2,3], sound waves must penetrate the liquid medium and is easily affected by internal impurities and bubbles in liquid which will lead to more errors. In addition, if the measured liquid medium is poor transmittance or the diameter of container is larger, then the echoes signal may be very weak or undetectable. It will lead to a very small difference in strength of the echoes signal in different cases which is not easy to distinguish, and ultimately will make the determination of the liquid level become difficult.

---

\*Corresponding author: Wen-Yi LIU, Key Laboratory of Instrumentation Science & Dynamic Measurement, Ministry of Education, North University of China, Taiyuan 030051, China, E-mail: liuwenyi\_nuc@126.com

Bin ZHANG, Zong YAO, Yan-Jun ZHANG, Ji-Jun XIONG, Key Laboratory of Instrumentation Science & Dynamic Measurement, Ministry of Education, North University of China, Taiyuan 030051, China

Bin ZHANG, Wen-Yi LIU, Zong YAO, Yan-Jun ZHANG, Ji-Jun XIONG, Science and Technology on Electronic Test & Measurement Laboratory, North University of China, Taiyuan 030051, China  
Yue-Juan WEI, Software School of North University of China, Taiyuan 030051, China

Second, the ultrasonic measurement methods which have been proposed in recent years are more advanced and accurate, but the equipment for determining the liquid level are increasingly complex and expensive [4-6].

Therefore, in this paper, we will avoid the deficiencies and research how to easily resolve and simply improve the measuring method of the liquid level in sealed metal container.

## 2 Theory

According to the knowledge of ultrasound [7-9], the length of the near field  $N$  and the diffusion angle  $\theta$  are given by Eq. (1) and Eq. (2) respectively [10].

$$N = \frac{a^2}{\lambda_c} \quad (1)$$

$$\sin \theta = \frac{1.22\lambda_c}{2a} \quad (2)$$

Normally, the geometry size is much larger than the wave length for the plane round piston transducer. Its beam shape comprises two different regions in the medium [11], which are near-field and far-field region or called cylindrical and diverging region shown as Figure 1.

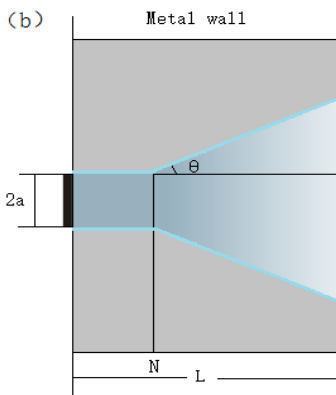


**Figure 1.** Beam shape and the acoustic characteristics of the plane round piston transducer

Furthermore, since the sound intensity is proportional to the square of amplitude, the sound intensity along the central axis has the same distribution characteristics.

The wall of metal container is regarded approximately as semi-infinite isotropic solid medium, and the ultrasonic propagation complies with the laws of reflection and refraction of sound waves [8]. The reflection coefficient  $R$  is given by the Eq. (3).

$$R = \frac{R_2 - R_1}{R_2 + R_1} = \frac{\rho_2 c_2 \cos \theta_i - \rho_1 c_1 \cos \theta_t}{\rho_2 c_2 \cos \theta_i + \rho_1 c_1 \cos \theta_t} \quad (3)$$

Where:  $\rho$  is the medium density,  $c$  is the speed of sound in the medium,  $\theta_i$  is the incidence angle,  $\theta_t$  is the transmission angle.

Assuming the thickness of the wall is  $L$ , the detector is a round piston transducer which has the function of receiving and transmitting, its center frequency is  $f$  and the radius is  $a$ , perpendicular to the outer surface of the wall of the metal container, the transducer is excited to transmit a ultrasonic beam into the wall which will be projected onto the inner surface of the wall and will form a circular area in which the energy is concentrated relatively.

In this paper, we called the projected circular area as “energy circle”. Assuming the “energy circle” diameter is  $h$  and according to Eq. (2), the value of  $h$  is given by Eq. (4).

$$\begin{cases} h = 2a & (L \leq N) \\ h = 2[a + (L - N) \tan \theta] & (L > N) \end{cases} \quad (4)$$

In the actual detecting process, when the detection transducer moved from bottom to top along the outer surface of the metal container wall, the “energy circle” will locate in three different states.

Assuming that the attenuation coefficient of ultrasonic wave in the metal container wall is  $P_o$ , the incident sound pressure in an excitation period is, the acoustic impedance of the metal container wall is  $Z_m = \rho_m c_m$ , the acoustic impedance of gaseous medium is  $Z_g = \rho_g c_g$ , the acoustic impedance of liquid medium is  $Z_l = \rho_l c_l$ .

It is assumed that the energy of the reflection has been decayed to a very small amount after  $n$  times in the metal wall.

When the “energy circle” below the interface of the liquid level, the total energy  $P_{tl}$  received by the receiving transducer is given by Eq. (5):

$$P_{tl} = \sum_{i=1}^n \frac{(P_0 R_{ml}^i R_{ma}^{i-1} e^{-2i\alpha L})^2 \pi a^2}{2Z_m} \quad (5)$$

In the same way, when the “energy circle” above the interface of the liquid level, the total energy  $P_{tg}$  received by the receiving transducer is given by Eq. (6):

$$P_{tg} = \sum_{i=1}^n \frac{(P_0 R_{mg}^i R_{ma}^{i-1} e^{-2i\alpha L})^2 \pi a^2}{2Z_m} \quad (6)$$

When the “energy circle” is divided into two parts by the liquid level shown as Figure 2, In this state, the calculation of the “energy circle” will be the superposition of two states:

$$P_t = \sum_{i=1}^n \frac{(P_0 R_{ml}^{i-1} e^{-2i\alpha L})^2 \pi a^2 [(R_{ml}^{2i}(1-r_A) + R_{mg}^{2i}r_A)]}{2Z_m} \quad (7)$$

In the Eq. (7), if the  $\Delta h$  are critical value 0 or 1, the Eq. (7) will become to the Eq. (5) and Eq. (6) respectively.

Therefore, with the increasing of the  $\Delta h$  from 0 to  $h$ , the “energy circle” is moved from the state below the liquid level to the state above the liquid level. In

this process, and the total energy  $P_t$  received by the receiving transducer is linear with the ratio  $\Delta h$ .

For a given testing environment and the transducer locates a fixed position, the values of the  $P_t$  are constant. Therefore, we can find the two critical height of  $h_d$  and  $h_u$  corresponding to the two critical states, the actual liquid level  $h_l$  will be given by the Eq. (8).

$$h_l = \frac{h_d + h_u}{2} \quad (8)$$

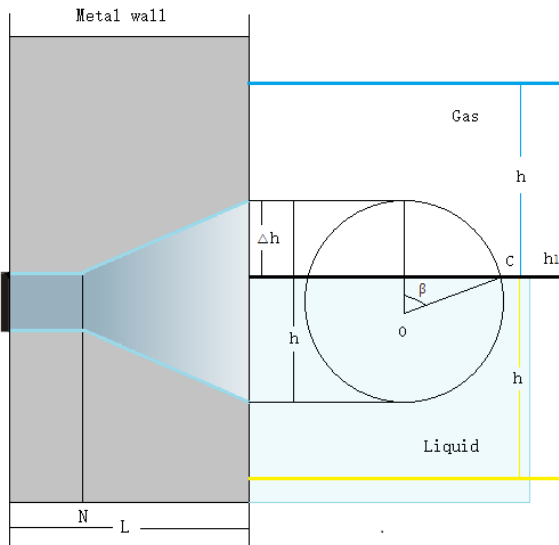


**Figure 2.** The “energy circle” is divided into two parts by the liquid level

### 3 Experimental

In the experiments, we use a sealed metal container for homogeneous aluminum alloy, the length, the width and the height of which are designed respectively for 500mm, 300mm, 400mm, the wall thickness of the four side plates of which are respectively 50mm, 40mm, 25mm, 8mm, the bottom and the cover thickness of which are 150mm, the liquid medium and the gaseous medium in which are water and air.

Considering the propagation characteristics of the ultrasonic in the metal container wall, we selected two kinds of round piston transducers whose center frequency  $f$  are 1MHz and whose diameters are 10mm and 20mm respectively. Excitation voltage used in the experiment  $u$  is 225V, the repetition frequency of excitation pulse is, the repetition period is.

According to the analysis in the second section, we measured the position of the liquid level under the conditions of different thickness of the metal wall, and take L=50mm as an example.

The echoes signals shown in Figure 3 are the two states that the “energy circle” are above and below the liquid level respectively within a transmission period 0.01s.

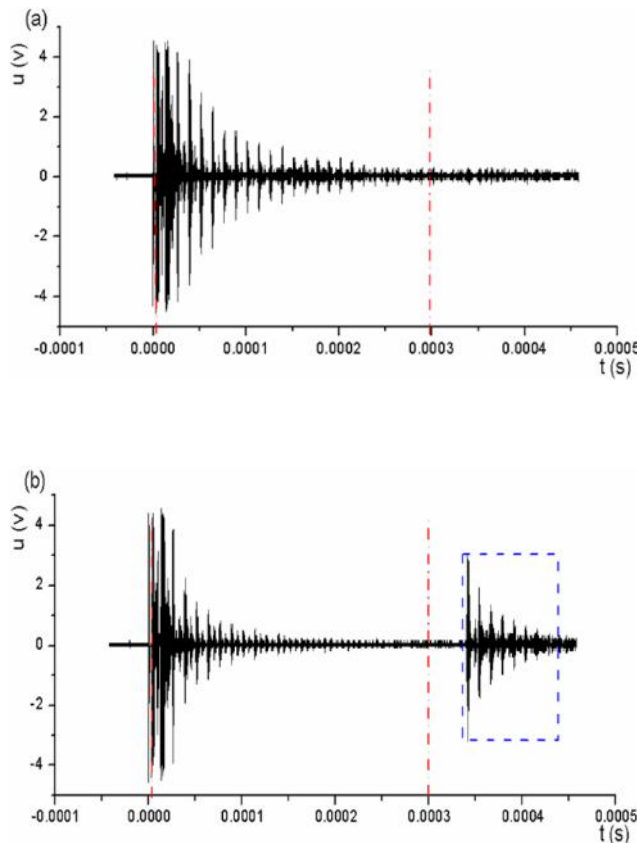


**Figure 3.** The echoes signals in the metal wall as the thickness L=50mm, (a) the energy circle is above the liquid level, (b) the energy circle is below the liquid level

In addition, in Figure 3b, the signals in the dashed blue box are the echoes signals that the transmitting ultrasonic beam passing through a gas or a liquid medium was reflected by the opposite inner surface of the metal container wall, which is not adapted in this contribution.

From Figure 3a and 3b, we can see that the echoes signals in the metal wall measured disappeared about after the time of s when the “energy circle” is below the liquid level; and after the time about s, the echoes signals in the metal wall measured

also disappeared when the “energy circle” is above the liquid level. About s later, the signals penetrating the gaseous or liquid medium were reflected back from the opposite wall of the metal container.

In Figure 3, the time section from 0.000008s to 0.0003s could be used as effective regional to calculate echoes energy. Based on the detection environment and conditions, there are,,,.

In Figure 4, the vertical axis represents the energy received by the receiving transducer, the horizontal axis shows the radius of “energy circle”, and it can be seen that the change of the energy is consistent with the change law of the theoretical analysis in section 2.2. Table 1 shows the actual measurement results under different wall thickness.

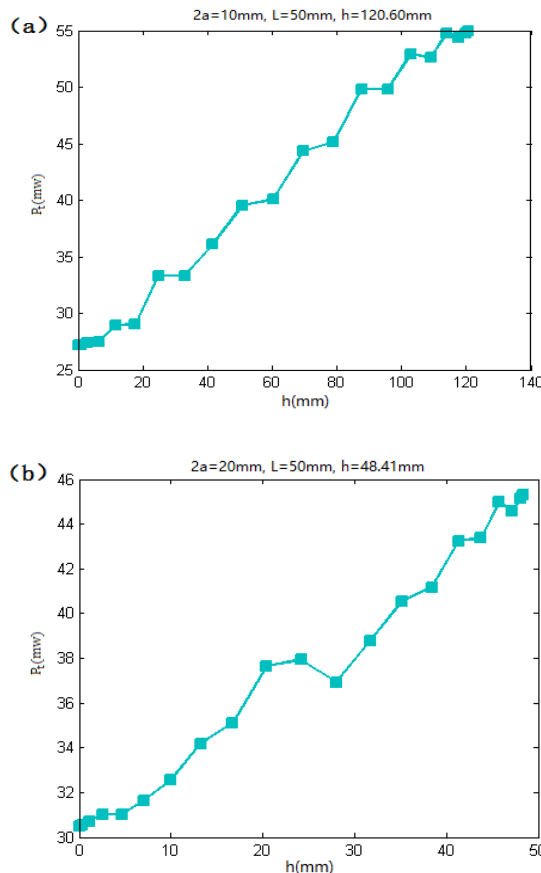


**Figure 4.** The change law of the actual total energy received by the receiving transducer under the 50mm thickness of the metal container wall.

From the experimental data in Table 1 it can be seen that the bigger the diameter of the transducer, the more concentrated the ultrasonic beam, the smaller the divergence angle, the longer the near-field length, the smaller the interval between two critical positions, high sensitivity and lower resolution; the smaller the diameter of the transducer, the more scattered the ultrasonic beam, the greater the divergence angle, the smaller the length of the near-field, the larger the interval between two critical positions, low sensitivity and high resolution.

**Table 1.** The results of measurements (mm)

L	2a	actual	hd	hu	hl
8	10	150	141.11	161.32	151.215
25	10	150	121.43	181.33	151.38
40	10	150	103.27	199.98	151.625
50	10	150	90.81	213.3	152.055
8	20	150	141.63	160.51	151.07
25	20	150	135.69	166.795	151.2425
40	20	150	131.21	172.04	151.625
50	20	150	127.795	176.53	152.1625

#### 4 Discussion and conclusion

The selection of initial conditions in the experiment of the third section, such as the center frequency and the radius of the detection transducer and the voltage of the excitation pulse, needs according to the actual testing environment, the material of metal container and the physical characteristics of the medium measured in the container, considering the discussion of ultrasonic sound field in the first section, and programming to achieve the automatic optimization of parameters selected to avoid using the experimental value directly. It will be more conducive to simplify the detection process and improve the measuring accuracy.

**Acknowledgements:** This work is supported by the internal research funding of North University of China, the authors would like to thank the technical staff in our library for their valuable suggestions to this project.

## References

- [1] D.P. Huang, Y.M. Luo, Research and Design on an Intelligent Level Measurement System [J]. Journal of Sichuan University of Science & Engineering (Natural Science Edition), 2009, 22(5): 108-110.
- [2] J. Xie, J. LIU, G. Tian, Impact of pressure and temperature upon ultrasonic velocity in two sorts of hydraulic oil [J]. Technical Acoustics, 2007, 26(6): 1155-1160.
- [3] J.X. Peng, G.P. Zhou, Z.F. Liang, Effect of Bubble Volume Fraction on Distribution of Ultrasonic Field in Liquid [J]. Journal of South China University of Technology (Natural Science Edition), 2008, 36(8): 128-131.
- [4] Y Zhang, X Du, Influences of non-uniform pressure field outside bubbles on the propagation of acoustic waves in dilute bubbly liquids, Ultrasonics sonochemistry, vol. 26, pp. 119-127, March 2015.
- [5] P Li, Y Cai, X Shen, S Nabuzaale, An Accurate Detection for Dynamic Liquid Level Based on MIMO Ultrasonic Transducer Array, IEEE Transactions on Instrumentation and Measurement, vol. 64, no. 3, pp. 582-595, September 2014.
- [6] KV Santhosh, Blessy Joy. Analysis of additive in a liquid level process using multi sensor data fusion. 2016 10th International Conference on Intelligent Systems and Control (ISCO). Pages: 1 - 6, DOI: 10.1109/ISCO.2016.7726924
- [7] Schmerr, L. W., 1998, Fundamentals of Ultrasonic Nondestructive Evaluation: A Modeling Approach, Plenum Press, New York.
- [8] Vezzetti, D. J., 1985, Propagation of Bounded Ultrasonic Beams in Anisotropic Media, J. Acoust. Soc. Am., 78(3), pp. 1103–1108.
- [9] Schmerr, L. W., and Sedov, A., 1989, An Elastodynamic Model for Compressional and Shear Wave Transducers, J. Acoust. Soc. Am., 86(5), pp. 1988–1999.
- [10] Bass, R., 1958, Diffractions Effects in the Ultrasonic Field of a Piston Source, J. Acoust. Soc. Am., 30(7), pp. 602–605.
- [11] S. Roa-Prada, H. A. Scarton, G. J. Saulnier, D. A. Shoudy, J. D. Ashdown, P. K. Das, A. J. Gavens, An Ultrasonic Through-Wall Communication (UTWC) System Model. Journal of Vibration and Acoustics. FEBRUARY 2013, Vol. 135.

Zhan-she GUO, Yan-shan WANG, Man-guo HUANG, Chao LU\*,  
Mei-ju ZHANG, Xin LI

## Design of Silicon-on-Sapphire Pressure Sensor For High Temperature And High Pressure Applications

**Abstract:** In this paper, a design scheme of high pressure and high temperature piezoresistive pressure sensor is presented. In order to meet the design requirements, SOS(silicon on sapphire) technology and circular flat diaphragm structure are adopted. Through theoretical analysis, the geometric dimensions of the diaphragm and the position of the piezoresistors on the SOS wafer are optimized for high sensitivity and linearity. A circle flat diaphragm with a radius of 2.5mm and a thickness of 0.8mm is designed, which enables the sensor to operate in high pressure condition (such as 28 MPa). The design is verified by the FEM (finite element method), and the simulation results are consistent with the theoretical results. It is also proved that the design of circular diaphragm has higher sensitivity compared to the square and rectangular diaphragm. With the advantages of high temperature resistance, wide operation range, high sensitivity and good linearity, the design ought to be an ideal candidate for high temperature and high pressure sensing in real application.

**Keywords:** pressure sensor; silicon-on-sapphire; circular flat diaphragm

### 1 Introduction

Pressure sensor is one of the most commonly used sensors in industrial field, which plays an important role in process controls, petrochemical and other industries [1]. With the development of measurement technique, high pressure and high temperature pressure sensor for measurements in harsh environments has become a hot research topic [2]. Due to the influence of temperature, it is very strict in material selection and structure design to ensure good sensitivity and linearity. Nowadays the commonly used pressure sensors include strain gauge, capacitance transducer, optical fiber grating sensor, piezoelectric transducer, and piezoresistive sensor, etc., among which the piezoresistive sensor is the maturest in application [3]. Piezoresistive pressure

---

\*Corresponding author: Chao LU, School of Instrument Science and Opto-electronics Engineering, Beihang University, Beijing, China, E-mail: bhluchao@163.com

Zhan-she GUO, School of Instrument Science and Opto-electronics Engineering, Beihang University, Beijing, China

Yan-shan WANG, Man-guo HUANG, Mei-ju ZHANG, Xin LI, AVIC Beijing Changcheng Aeronautical Measurement and Control Technology Research Institute

Yan-shan WANG, Man-guo HUANG, Mei-ju ZHANG, Xin LI, Aviation Key Laboratory of Science and Technology on Special Condition Monitoring Sensor Technology, Beijing, China

sensor generally utilizes the periphery fixed circular flat diaphragm or square flat diaphragm [4]. In order to overcome the influence of high temperature, the diaphragm material includes polysilicon, sapphire, SiC, diamond, etc. [5].

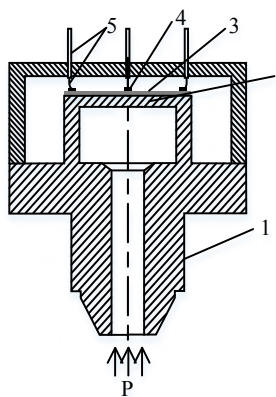
Through the selection of different materials and diaphragm structures, some research institutions have put forward designs of piezoresistive pressure sensors. Zhe Niu et al. [3] adopted rectangular membrane and thick film structure and designed a SOI(silicon-on-insulator) pressure sensor with an operation range of 0~150MPa. The fabricated sensor achieved a favorable linearity of 0.13% and a high sensitivity of 1.1126mV/MPa. S. Santosh Kumar et al. [6] evaluated the sensitivity and non-linearity of polysilicon piezoresistive pressure sensors with different diaphragm sizes. Experimental results indicated that the sensor with a diaphragm edge length of 1,280 $\mu$ m was found to have optimum characteristics, and sensitivity of 3.35–3.73 mV/Bar and non-linearity of <0.3 % were obtained in the pressure range of 0–30 Bar.

After analyzing the advantages and disadvantages of various materials and diaphragm structures, this paper designs a high pressure and high temperature SOS pressure sensor based on circular flat diaphragm structure. In order to achieve high linearity and sensitivity, while obeying the rules of allowable stress, the optimal design of diaphragm size and position of the resistors is made through theoretical analysis and verified by finite element simulation software. Compared with the conventional piezoresistive pressure sensor, this design has the advantages of high temperature resistance, wide operation range, high sensitivity and good linearity.

## 2 Analysis and Design

Since the p-n junction which isolates the piezoresistor and substrate is easy to get damaged at high temperature, traditional diffused silicon piezoresistive pressure sensors fail to work at a high temperature above 100 °C. The SOS structure is a monocrystalline silicon film (0.1-0.5 $\mu$ m) grown on single-crystal sapphire ( $\text{Al}_2\text{O}_3$ ) by heteroepitaxy technology. The evident advantage of SOS usage is a significant extension of the operating temperature range due to the absence of a p-n junction. This design enables the sensor to operate in a wide temperature range (from -272 to +350°C), as well as bringing a lot of advantages such as high precision, wide measuring range, small hysteresis, corrosion resistance, etc.

Figure 1 is a schematic of SOS pressure sensor. The design includes a bilayered elastic element made from a titanium-alloy diaphragm and a SOS sensing element. The pressure applied to the sensor causes a deformation of the bilayered elastic element, which leads to the changes of silicon piezoresistors in the Wheatstone bridge. The bridge circuit outputs a voltage signal proportional to the pressure, thus realizing the measurement of pressure.



1-metal shell; 2-titanium-alloy diaphragm;  
3-sapphire diaphragm; 4-piezoresistors; 5-lead wire

**Figure 1.** Schematic of SOS pressure sensor.

The sensing element of the sensor is the bilayered elastic element, in which the titanium-alloy diaphragm plays the main role. Figure 2 shows the schematic of an edge-clamped circular flat diaphragm with a radius of  $R_0$  and a thickness of  $H$ .

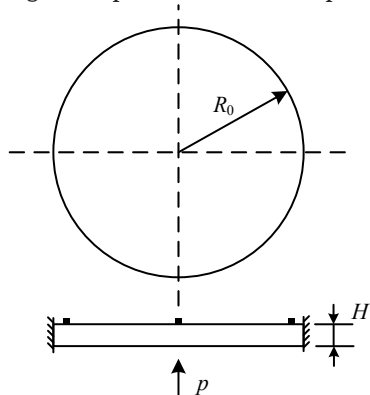


**Figure 2.** Schematic of an edge-clamped circular flat diaphragm.

When the diaphragm is deformed under the pressure of  $p$ , the upper surface of the diaphragm will be subjected to stress. The maximum stress lies at the edge of the diaphragm:

$$\sigma_{\max} = \sigma_r(R_0) = -\frac{3pR_0^2}{4H^2} \quad (1)$$

Where  $\sigma_{\max}$  is the maximum stress on the diaphragm, and  $\sigma_r(R_0)$  represents the stress at the edge of the diaphragm. To improve the sensitivity of the sensor, it is appropriate to increase the value of  $\sigma_{\max}$ . But there will be a nonlinear relationship between the measured pressure and the strain of diagram when the value of  $\sigma_{\max}$  increase to a

certain extent. According to the mechanical properties, following rule should be obeyed to ensure the stability of the sensor:

$$K_s \sigma_{\max} \leq \sigma_b \quad (2)$$

Where  $K_s$  is the safety factor, and  $\sigma_b$  represents the allowable stress for the material. Take the safety factor of 1.7, the allowable stress of 441MPa and the maximum pressure of 28MPa into calculation, boundary relationship between  $R_0$  and  $H$  must fit:

$$\left( \frac{R}{H} \right)_{\max} = 3.515 \quad (3)$$

The  $R$  is designed as 2.5mm to meet the design requirements of the sensor. According to the formula, the minimum value of  $H$  is 0.711mm. So, 0.8mm is selected as the thickness of the diaphragm. The design ensures the stability of the diaphragm, as well as good sensitivity and linearity.

In order to convert the pressure signal into a voltage signal, four piezoresistors are fabricated on the SOS wafer by bulk-micromachining technology. During the design of the resistors, some rules must be obeyed as follows:

- (a) The initial resistances should be equal;
- (b) When pressure is applied, two resistors should have an increase in resistance, while the other two are the opposite. It is a necessary condition for the composition of Wheatstone bridge;
- (c) The change value of the four resistors must be equal and as large as possible, which will ensure a good sensitivity and linearity.

Implanting resistors at the edge of the diaphragm ( $r=R_0$ ) is proved to get the largest stress, which will also result in the largest change value of resistors. Taking into account the size of the resistor, the design of  $r=2.3\text{mm}$  is made. For the (100) P-type silicon, it has the largest piezoresistive coefficient along the crystal direction <011>. Besides, longitudinal piezoresistive coefficient is opposite to the transverse piezoresistive coefficient in this direction ( $\pi_a = -\pi_n = 1/2\pi_{44}$ ). Thus, the position of the resistors can be set in accordance with the method in Figure 3.

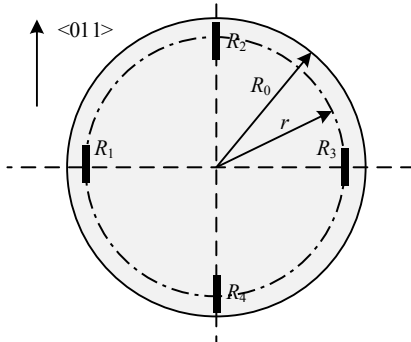


Figure 3. The distribution of piezoresistors.

When pressure is applied,  $R_1$  and  $R_3$  increase, while  $R_2$  and  $R_4$  decrease. According to the piezoresistive effect, all of them have the same rate of change:

$$\frac{\Delta R}{R} = \frac{1}{4} \pi_{44} (\sigma_r - \sigma_\theta) \quad (4)$$

Where  $\pi_{44}$  is the shear piezoresistive coefficient.  $\sigma_r$  and  $\sigma_\theta$  represent the radial stress and tangential stress. The Wheatstone bridge circuit is shown in Figure 4. The output of the bridge is

$$U_{\text{out}} = U_{\text{in}} \frac{\Delta R}{R} \quad (5)$$

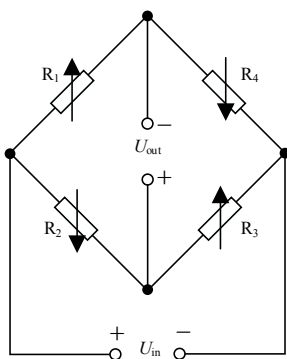


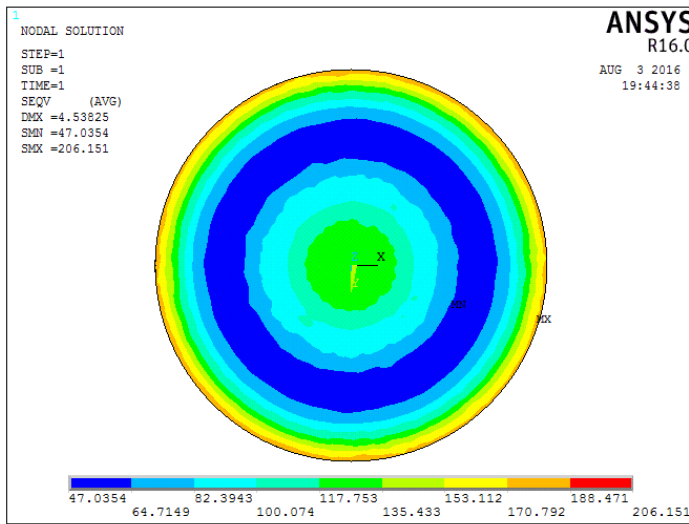
**Figure 4.** Wheatstone bridge circuit.

The input pressure signal is finally converted into output voltage signal. The design can get a high sensitivity as well as ensure a good linear relationship between the measured pressure and output voltage. However, due to the thickness of the diaphragm and other reasons, the stress condition of the diaphragm is different from the theoretical value. In order to guarantee the feasibility of the design, a series of analyses based on the finite element method (FEM) are made in Section 3.

### 3 FEM Analysis

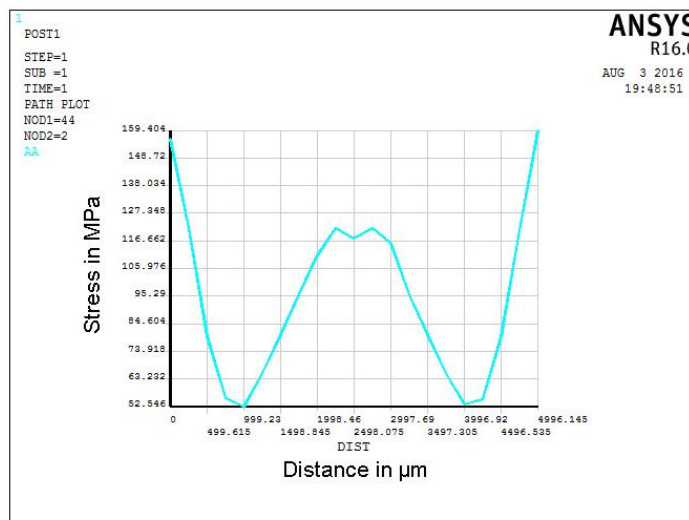
Based on the ANSYS, a circular flat diaphragm with 5mm diameter and 0.8mm thickness is created. The elastic modulus of titanium-alloy is 108GPa, and the poisson ratio is 0.33. A fixed boundary condition is applied surrounding the diaphragm, and the pressure applied to the lower surface is set as 28 MPa. A path is made across upper surface to find out the relationship between the stress and the distance. Figure 5 is the simulation result of the von-Mises stress distribution for the diaphragm. From Figure 5,

conclusion can be drawn that the stress on the upper surface of the diaphragm only varies with the distance from the position to the center.



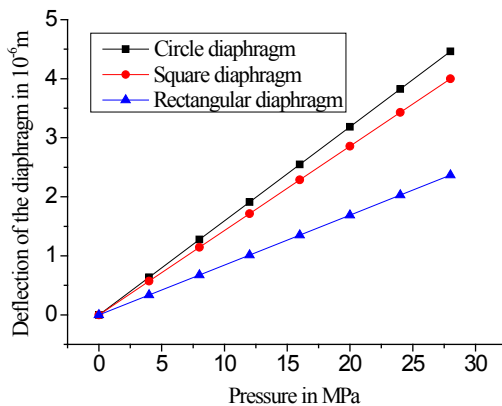
**Figure 5.** Von-Mises stress distribution.

Figure 6 shows the von-Mises stress along the path. It indicates that the maximum stress lies at the edge of the diaphragm, which is consistent with the theoretical result. The design to arrange resistors at the edge of the diaphragm will result in a highest sensitivity.



**Figure 6.** Von-Mises stress along the path.

Figure 7 shows the simulation results of deflections of the diaphragm under various pressures. In the figure, square flat diaphragm ( $4.43 \times 4.43 \times 0.8$  mm), rectangular flat diaphragm ( $6.26 \times 3.13 \times 0.8$  mm) and circular flat diaphragm ( $R_0=2.5$  mm,  $H=0.8$  mm) are compared. The size is decided based on keeping equal area and thickness for the three diaphragm. It can be seen from Figure 7 that the circular flat diaphragm has the largest deflection, which means it achieves the highest sensitivity. The results also demonstrate that the linearity is very good for this design.



**Figure 7.** Deflections of the diaphragm under various pressures.

## 4 Conclusion

This article proposes a design method for SOS pressure sensor working in high pressure and high temperature environment. The work focuses on the optimal design of geometric dimensions of the diaphragm and positions of the piezoresistors. In order to achieve high sensitivity and linearity, silicon on sapphire technology and circular flat diaphragm structure are adopted, and optimal design is made by analysing the stress distribution. The design is verified by the finite element method, and the results prove it to be fully feasible. With the advantages of high temperature resistance, wide operation range, high sensitivity and good linearity, the design ought to have a wide range of applications.

**Acknowledgment:** This work was supported by the Aviation Research Foundation with grant No.: 20153451023 and Technology Innovation Foundation of AVIC with grant No.: 2013F63447R.

## References

- [1] C. C. Hsieh, C. C. Hung and Y. H. Li, Investigation of a pressure sensor with temperature compensation using two concentric wheatstone-bridge circuits, *Mod. Mech. Eng.*, vol. 3, May. 2013, pp. 104-113, doi: 10.4236/mme.2013.32015.
- [2] J. Yang, A Harsh Environment Wireless Pressure Sensing Solution Utilizing High Temperature Electronics, *Sensors*, vol. 13, Feb. 2013, pp. 2719-2734, doi: 10.3390/s130302719.
- [3] Z. Niu, Y. Zhao and B. Tian, Design optimization of high pressure and high temperature piezoresistive pressure sensor for high sensitivity, *Rev. Sci. Instrum.*, vol. 85, Jan. 2014, pp. 015001, doi: 10.1063/1.4856455.
- [4] M. Molla-Alipour and B. A. Ganji, Analytical analysis of mems capacitive pressure sensor with circular diaphragm under dynamic load using differential transformation method (DTM), *Acta Mech. Solida Sin.*, vol. 28, Aug. 2015, pp. 400-408, doi: 10.1016/S0894-9166(15)30025-2.
- [5] H. D. Ngo, B. Mukhopadhyay, O. Ehrmann and K. D. Lang, Advanced liquid-free, piezoresistive, SOI-based pressure sensors for measurements in harsh environments, *Sensors*, vol. 15, Aug. 2015, pp. 20305-20315, doi: 10.3390/s150820305.
- [6] S. S. Kumar, A. K. Ojha and B. D. Pant, Experimental evaluation of sensitivity and non-linearity in polysilicon piezoresistive pressure sensors with different diaphragm sizes, *Microsyst. Technol.*, vol. 22, Jan. 2016, pp. 83-91, doi: 10.1007/s00542-014-2369-3.

Lang-shu LI\*, Hong-zhuan QIU, Hua SONG, Chun-ling WEI

## The Federated Filtering Algorithm based on the Asynchronous Multisensor System

**Abstract:** This paper is concerned about the asynchronous multisensor dynamic system and an asynchronous fusion algorithm is proposed, which is depended on the federated Kalman filter. Each sub filter is updated on the rate that is associated with the local sensors. Then outputs of sub filters are propagated to the next fusion time. These propagated values are to be combined with the time update value of the main filter and the fusion results are fed back to each sub filter. This algorithm effectively solves the problem that sub filters may not able to provide data to be fused at the fusion time for the asynchronous sensor system. The detailed process of the new algorithm is introduced. The simulation results for the satellite autonomous navigation system is given to demonstrate its validity.

**Keywords:** asynchronous fusion algorithm; autonomous navigation for satellite; navigation sensor

### 1 Introduction

Data fusion is a new technology in the information science field. It uses multiple information sources or multiple sensors to get, process and synthesize information. The purpose is to get more accurate and more complete estimation and judgement [1,2]. With the development of modern science and technology, the structure of various devices is more and more complex and it's common to use devices which have different sampling time and different sampling period. In particular, many navigation sensors work asynchronously because of their operation mode, range of action, inherent delay and system transmission delay.

Most researches about the multi sensor information fusion aim at the synchronous situation. But considering that many devices work asynchronously, it's necessary to research asynchronous information fusion algorithm. Alouani and Rice proposed a suboptimal asynchronous fusion algorithm in paper [3] based on the linear minimum mean square error. But this algorithm artificially rewrites the measurements and leads the noises in the new system to be correlated. Aiming at the shortcoming, in paper [4]

---

\*Corresponding author: Lang-shu LI, School of Automation Science and Electrical Engineering, Beihang University, Beijing, China, E-mail: liliash1993@buaa.edu.cn

Hong-zhuan QIU, Hua SONG, School of Automation Science and Electrical Engineering, Beihang University, Beijing, China

Chun-ling WEI, National Key Laboratory of Space Intelligent Control Technology, Beijing, China

Wang Jie proposed an asynchronous fusion algorithm focused on the measurement noises which are correlated after discretization. In paper [5] Wen Chenglin proposed a distributed prediction fusion algorithm. In a filtering period, all the sensors do time updating and measurement updating according to their respective measurements and do one step prediction to the fusion time after the last measurement updating. Then weighted fusion is implemented under the condition that the trace of the fusion variance matrix should be the minimum. However, in the algorithm, each sensor filters independently throughout and the result after fusion will not be used to correct the sub filters.

To deal with the asynchronous data fusion problem, a new algorithm based on the federated filter is discussed in the paper. Each sub filter is dedicated to a separate sensor. In one filtering period, the estimated values of sub filters are obtained by the time updating and measurement updating depended on their own measurements respectively. Then the optimal state estimate of each sub filter is propagated from the last measurement time to the next fusion time. Finally, all the estimated values are combined with the predicated values of the main filter and the results are fed back to each sub filter. In this paper, the system description is presented in Section II, the algorithm is introduced in Section III, and the simulation result is given in Section IV. Section V contains conclusion.

## 2 System description

A satellite autonomous system composed by the ultraviolet sensor and the receiver of GNSS is considered. The direction vector pointing to the earth center and the apparent radius are provided by the ultraviolet sensor. The apparent radius is the included angle of the tangent between the edge of the earth and the ultraviolet sensor and the line between the earth's core and the ultraviolet sensor. The pseudo range and pseudo range rate are provided by the receiver of GNSS. These data are used as the measurement data. Based on the Earth Centered Inertial Frame, the measurement equation can be written as follows,

$$z(t) = \begin{bmatrix} \frac{\mathbf{r}}{|\mathbf{r}|} \\ \arcsin\left(\frac{R_e}{|\mathbf{r}|}\right) \\ |\mathbf{r} - \mathbf{r}_s^i| + \delta t_u \\ (\mathbf{v}_s^i - \mathbf{v}) \frac{\mathbf{r}_s^i - \mathbf{r}}{|\mathbf{r}_s^i - \mathbf{r}|} + \delta f_u \\ \vdots \end{bmatrix} + \begin{bmatrix} \dot{\mathbf{a}}_e \\ \varepsilon_\theta \\ \varepsilon_p \\ \varepsilon_{\dot{p}} \\ \vdots \end{bmatrix} \quad (1)$$

where  $\mathbf{r} = [x, y, z]^T$  is the position vector from the satellite to the earth's core.  $\mathbf{r}_s = [x_s, y_s, z_s]^T$  is the position vector from the earth's core to the navigation satellite.

$\dot{\boldsymbol{a}} = [\varepsilon_e, \varepsilon_\theta, \varepsilon_p, \varepsilon_{\dot{p}}, \dots]^T$  is the observation noise. Considering that there may have more than one navigation satellite which is visible, the observation dimension is not fixed and depends on the number of the navigation satellite.

Let the state vector be  $\boldsymbol{x} = [\mathbf{r}^T, \mathbf{v}^T, \delta t_u, \delta f_u]^T$  where  $\mathbf{v} = [v_x, v_y, v_z]^T$  is the velocities of the satellite,  $\delta t_u$  and  $\delta f_u$  are the clock correction and clock drift. The effects of J2 perturbation and the solar and lunar gravitational perturbation are considered in the dynamical model. The state equation is

$$\dot{\boldsymbol{x}} = \boldsymbol{f}(\boldsymbol{x}) + \boldsymbol{w} \quad (2)$$

where

$$\boldsymbol{f}(\boldsymbol{x}) = \begin{bmatrix} v_x \\ v_y \\ v_z \\ -\frac{\mu}{|\mathbf{r}|^3}x + \frac{\mu R_e^2 J_2}{2} \left( -\frac{3}{|\mathbf{r}|^5} + \frac{15z^2}{|\mathbf{r}|^7} \right)x \\ + \mu_s \left( \frac{x_s - x}{|\mathbf{r}_s - \mathbf{r}|^3} - \frac{x_s}{|\mathbf{r}_s|^3} \right) + \mu_m \left( \frac{x_m - x}{|\mathbf{r}_m - \mathbf{r}|^3} - \frac{x_m}{|\mathbf{r}_m|^3} \right) \\ -\frac{\mu}{|\mathbf{r}|^3}y + \frac{\mu R_e^2 J_2}{2} \left( -\frac{3}{|\mathbf{r}|^5} + \frac{15z^2}{|\mathbf{r}|^7} \right)y \\ + \mu_s \left( \frac{y_s - y}{|\mathbf{r}_s - \mathbf{r}|^3} - \frac{y_s}{|\mathbf{r}_s|^3} \right) + \mu_m \left( \frac{y_m - y}{|\mathbf{r}_m - \mathbf{r}|^3} - \frac{y_m}{|\mathbf{r}_m|^3} \right) \\ -\frac{\mu}{|\mathbf{r}|^3}z + \frac{\mu R_e^2 J_2}{2} \left( -\frac{9}{|\mathbf{r}|^5} + \frac{15z^2}{|\mathbf{r}|^7} \right)z \\ + \mu_s \left( \frac{z_s - z}{|\mathbf{r}_s - \mathbf{r}|^3} - \frac{z_s}{|\mathbf{r}_s|^3} \right) + \mu_m \left( \frac{z_m - z}{|\mathbf{r}_m - \mathbf{r}|^3} - \frac{z_m}{|\mathbf{r}_m|^3} \right) \\ \delta f_u \\ -\frac{1}{\tau} \delta f_u \end{bmatrix} \quad (3)$$

The system process noise  $\boldsymbol{w}$ , is the gaussian white noise with zero mean and covariance Q.  $\mu_s$  is the solar gravitational constant and  $\mu_m$  is lunar gravitational constant.  $\mathbf{r}_s = [x_s, y_s, z_s]^T$  and  $\mathbf{r}_m = [x_m, y_m, z_m]^T$  are the position vectors of the solar and lunar in the inertial coordinate system.

### 3 Algorithm description

The federated filtering algorithm is a decentralized processing algorithm which uses two stage parallel structure. The navigation devices can make up multiple subsystems and use a main filter to fuse the data of each subsystem. According to the principle of information distribution, by reasonably distributing the state information to the main filter and the sub filters, it's effective to eliminate the correlation of all the sub

filters and make local estimations independently in the sub filters [6,7]. The basic flow Figure is illustrated in Figure 1.

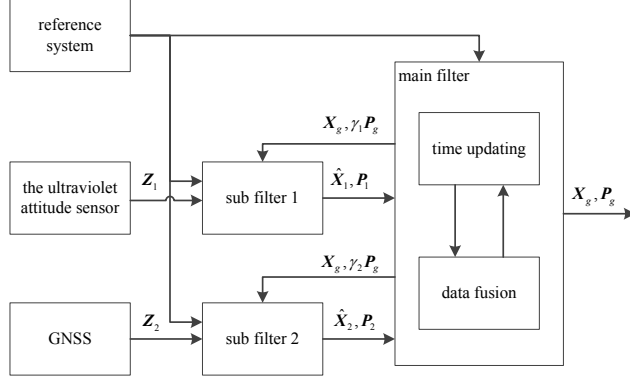


**Figure 1.** The basic flow Figure of federated filter algorithm

The reference system is represented by the dynamic equation of the satellite.

When the sensors operate asynchronously, some sensor may not provide data at the fusion time. Aiming at solving the problem that the sampling time is not synchronize and the sampling period is not consistent, this paper designs a new algorithm named *Federated Predictive Filtering Algorithm*. Its core idea is to use the predicted values of the sub filter from last measurement updating time to fusion time to be the contribution values of the sub filter at fusion time.

Assuming that the number of the sub filters is  $N$ , which depends on the number of navigation sensors, and the filtering period is  $T$ .

During the time period  $t_k \square t_k + T$ , the number of measurements for the  $i$ th sub filter is represented by  $n_i$ . Letting  $t_{n_i}$  be the time that the last measurement is taken.

The steps of the algorithm are as follows:

(1) The sub filters and main filter are reset by the fused value at time  $t_k$ , i.e.,

$$\hat{x}_i(t_k | t_k) = x(t_k | t_k) \quad (4)$$

$$P_i(t_k | t_k) = \gamma_i P(t_k | t_k) \quad (5)$$

Where  $0 \leq \frac{1}{\gamma_i} \leq 1$  and  $i = 1, 2, \dots, N, N+1$ . The following condition must be satisfied,

$$\frac{1}{\gamma_1} + \dots + \frac{1}{\gamma_N} + \frac{1}{\gamma_{N+1}} = 1 \quad (6)$$

Where the factor  $\gamma_{N+1}$  is associated to the main filter.

(2) The process noise covariance values of the sub filters and the main filter are assigned by the common process noise covariance value. By variance amplification, it's effective to make local estimations independently in the sub filters, i.e.,

$$Q_i = \gamma_i Q \quad (7)$$

- (3) The estimated values of  $\hat{x}_{N+1}(t_k | t_k)$  and  $P_{N+1}(t_k | t_k)$  are propagated from  $t_k$  to  $t_k + T$  by the main filter.
- (4) If  $n_i = 0$ , the predicted values of the  $i$ th sub filter at time  $t_k + T$  is obtained by the time updating from  $t_k$  to  $t_k + T$ . Otherwise,  $n_i$  times time updating and measurement updating are processed by the  $i$ th sub filter. Then the predicted values of  $\hat{x}_i(t_k + T | t_{n_i})$  and  $P_i(t_k + T | t_{n_i})$  are obtained by the time updating from  $t_{n_i}$  to  $t_k + T$ .
- (5) The predicted values of sub filters are combined with those of the main filter by the following fusion algorithm,

$$\begin{aligned} P^{-1}(t_k + T | t_k + T) &= P_1^{-1}(t_k + T | t_{n_1}) \\ &\quad + \cdots + P_N^{-1}(t_k + T | t_{n_N}) + P_{N+1}^{-1}(t_k + T | t_k) \end{aligned} \quad (8)$$

$$\begin{aligned} P^{-1}(t_k + T | t_k + T) \hat{x}(t_k + T | t_k + T) &= \\ P_1^{-1}(t_k + T | t_{n_1}) \hat{x}_1(t_k + T | t_{n_1}) + \cdots + P_N^{-1}(t_k + T | t_{n_N}) x_N(t_k + T | t_{n_N}) \\ + P_{N+1}^{-1}(t_k + T | t_k) \hat{x}_{N+1}(t_k + T | t_k) \end{aligned} \quad (9)$$

- (5) Repeat the above steps.

## 4 Simulation

Based on the established model, the validity of the algorithm is tested by simulating and analyzing. The simulation time is set to 86400s and the filtering period is set to 0.9s. The sampling periods of the ultraviolet sensor and the receiver of GNSS are respectively set to 1.1s and 1s. The sensor specification is shown in the Table 1.

**Table 1.** The sensor specification

sensor	specification	value
<b>ultraviolet sensor</b>	measurement precision of the earth direction vector	0.02°
	measurement precision of apparent radius	0.02°
<b>the receiver of GNSS</b>	measurement precision of pseudo range	5m
	measurement precision of pseudo range rate	0.1m/s

The mean values of the error and rootmean square error(RMSE) are chosen to represent the algorithm precision. The simulation results of 50 Monte Carlo simulation are shown in Figure 2 to Figure 5.

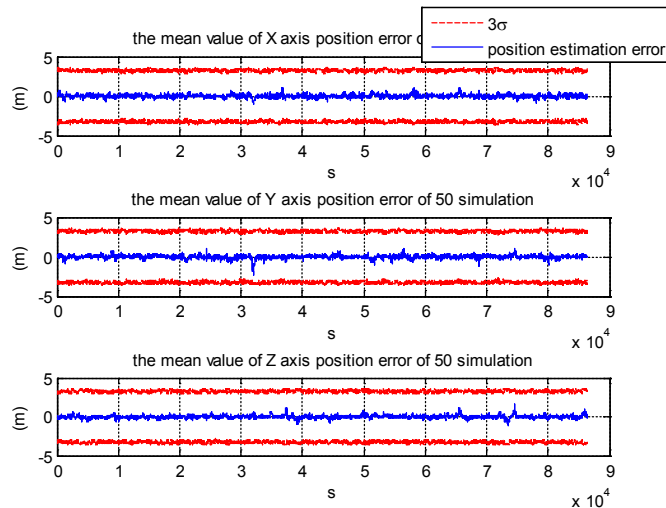


**Figure 2.** The mean value of position error of 50 asynchronous simulation

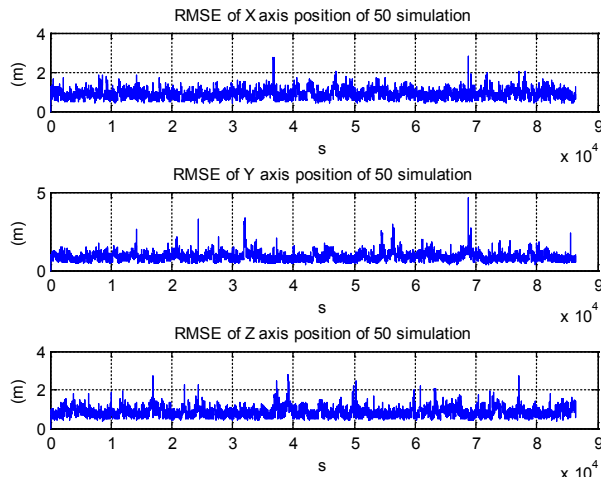


**Figure 3.** RMSE of position of 50 asynchronous simulation

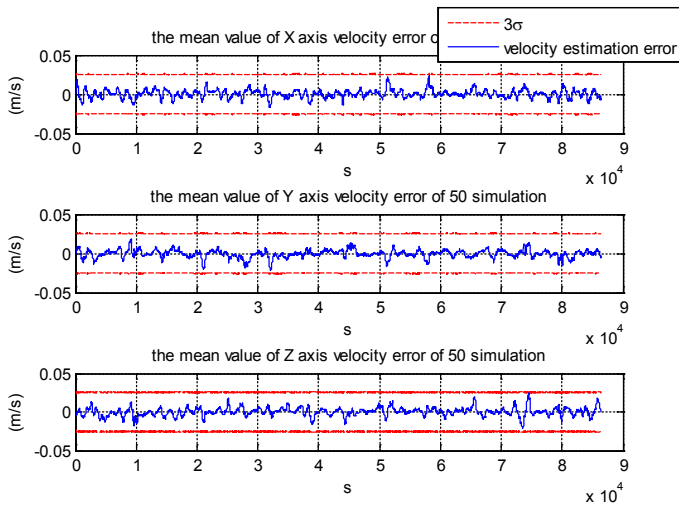


**Figure 4.** The mean value of velocity error of 50 asynchronous simulation

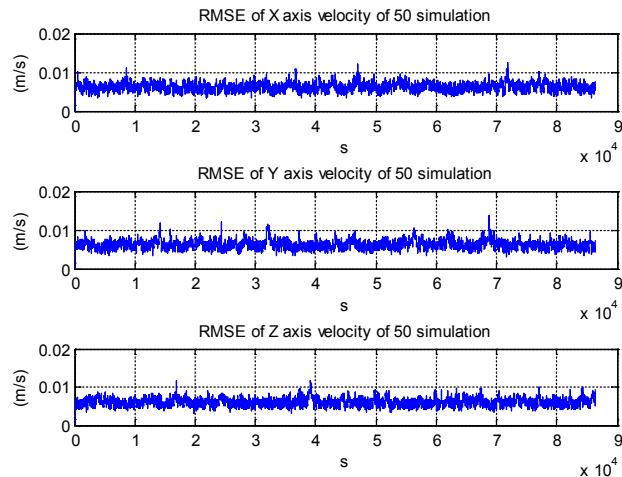


**Figure 5.** RMSE of velocity of 50 asynchronous simulation

From the above figures, it can be shown that the position and velocity have high estimation accuracy. The accuracy can meet the navigation demand. Further validation, set the sampling period of the ultraviolet sensor and GNSS to 1s and the

filtering period to 1s, too. Simulate again and the simulation results of 50 Monte Carlo simulation are shown in Figure 6 to Figure 9.

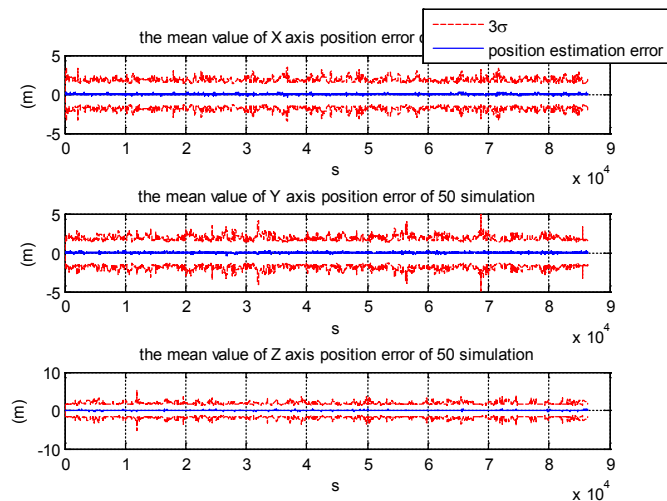


**Figure 6.** The mean value of position error of 50 synchronous simulation

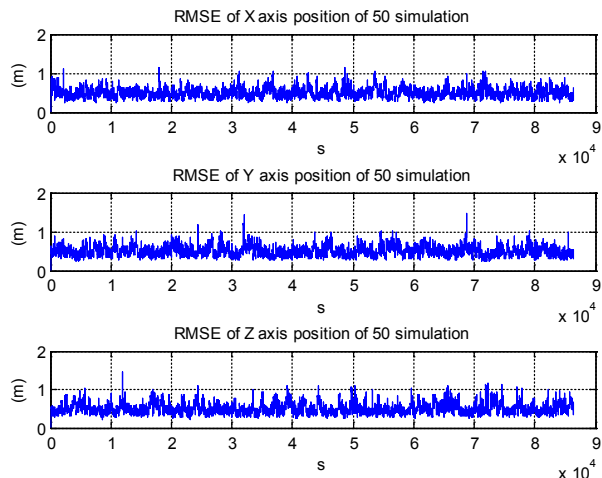


**Figure 7.** RMSE of position of 50 synchronous simulation

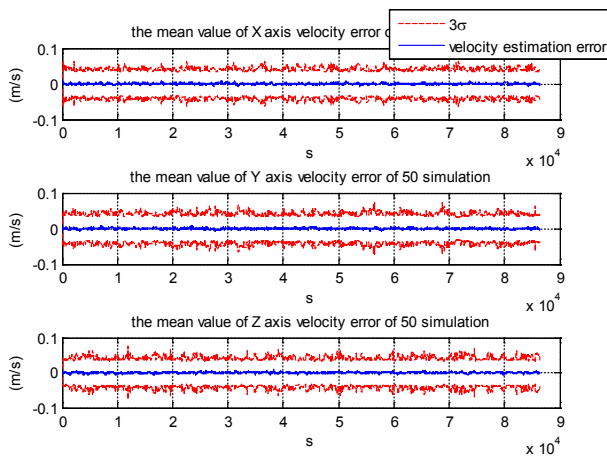


**Figure 8.** The mean value of velocity error of 50 synchronous simulation

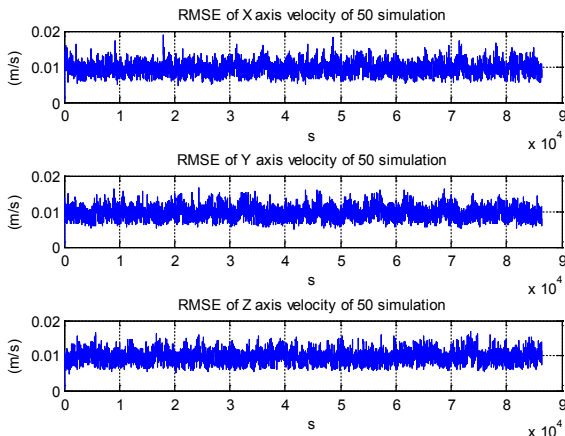


**Figure 9.** RMSE of velocity of 50 synchronous simulation

From the above figures, it can be verified that the accuracy of the asynchronous federated filtering algorithm can reach the accuracy of the synchronous federated filtering algorithm. It is shown that the new algorithm can usefully deal with the asynchronous problem and can still reach high accuracy. So the new asynchronous algorithm is feasible.

## 5 Conclusion

This paper designs a new asynchronous federated filtering algorithm based on an actual project. The new algorithm can be used in the case that the sampling time is not synchronize or the sampling period is not consistent.

Through the simulation results based on the new algorithm and the synchronous algorithm, the conclusion can be gotten that the new asynchronous algorithm is feasible.

## References

- [1] HE You, WANG Guo-hong, LU Da-Jin, PENG Ying-ning. Multi-sensor Information Fusion with Application [M]. Peking; Electronic Industry Publishing House. 2000.
- [2] Y.B. Shalom, X.R. Li, T. Kirubarajam. Estimation with Application to Tracking and Navigation [M]. New York: John Wiley&Sons, INC, 2001.
- [3] A.T. Alouani, T.R. RICE. On asynchronous data fusion[A]. Proceedings of the Annual Southeastern Symposium on System Theory[C]. Athens, 1994: 143-146.
- [4] WANG Jie, Han Chong-zhao, LI Xiao-rong. Asynchronous Multisensor Data Fusion [J]. Control and decision, 2001, 16(6): 877-881.
- [5] WEN Cheng-lin, GE Quan-bo. The Step by Step Prediction Fusion Based On Asynchronous Multisensor System[A]. Proceedings of the Proceedings of the 2015 Chinese Intelligent Automation Conference[C], Qingdao, 2005: 917-922.
- [6] CARLSON, A. Neal. Federated square root filter for decentralized parallel processors [J]. IEEE Transactions on Aerospace and Electronic Systems, 1990, 26(3): 517-525.
- [7] QIU Hong-zhuan. Decentralized Filtering Techniques and its Application to Integrated Navigation System [D]. Peking; Beihang University, 2004.

Heng LI\*, Shi-bing WANG, Jun LI, Huai-min LI

## A Kind of Self-tuning Kalman Filter for the High Maneuvering Target Tracking System

**Abstract:** For the high maneuvering target tracking system,in order to solve the filtering problem with unknown noise statistics, based on the jerk model, a kind of self-tuning filter is presented in this paper. System identification method is used to estimate the noise statistics information which is substituted into the optimal Kalman filter to get the self-tuning Kalman filter. It's proved that this self-tuning Kalman filter converges to the optimal Kalman filter in this paper. A simulation example shows the effectiveness of this kind self-tuning filter.

**Keywords:** Jerk model; unknown noise statistics information; self-tuning Kalman filter

### 1 Introduction

Kalman filter has been proved to be the best method to deal with the filtering problem in the target tracking field [1]. In order to get the optimal convergence of the filter, noise statistics information should be precisely known. But in the practical applications, especially in the early stage of the filtering process, noise statistics information is always unknown [2]. In order to solve the filtering problem with unknown noise statistics, self-tuning filter was presented in [3]. Its basic principle is to estimate the unknown parameters and noise statistics information by system identification method. The estimations could be used to replace the real values in the Kalman filter [4]. Based on the Dynamic Error System Analysis (DESA) method [5], it has been proved that the self-tuning filter has good convergence to the optimal Kalman filter. Deng presented self-tuning  $\alpha$ - $\beta$  filter [6] and  $\alpha$ - $\beta$ - $\gamma$  filter [7], which could deal with the models with unknown parameters and noise ststistics information. In these filters, the target state vector includes position, velocity and acceleration. But when the target has high maneuverability, the tracking ability of these filters will be declined. Jerk model is known to be a accurate model with high order in these years. To get more accurate estimations, the acceleration rate was considered in the Jerk model filter [8], which could deal with the system with acceleration rate. This paper try to give a kind

---

\*Corresponding author: Heng LI, School of Computer and Information Engineering, Fuyang Teachers' College, Fuyang, China, E-mail: shenzhou5hao0519@163.com

Shi-bing WANG, Jun LI, Huai-min LI, School of Computer and Information Engineering, Fuyang Teachers' College, Fuyang, China

of self-tuning filter based on Jerk model to deal with the vector with acceleration rate. The convergence of this kind self-tuning filter is proved in this paper. An example shows the good convergence of this kind self-tuning Kalman filter.

## 2 Problem formulation

Consider the time-invariant system

$$X(t+1) = FX(t) + \Gamma w(t) \quad (1)$$

$$y(t) = HX(t) + v(t) \quad (2)$$

where  $t$  is the discrete time,  $X(t)$  is state vector,  $X(t) = [x(t), \dot{x}(t), \ddot{x}(t), \dddot{x}(t)]^T$ ,  $x(t)$  is the position of the target,  $\dot{x}(t)$  is the speed of the target,  $\ddot{x}(t)$  is the acceleration of the target,  $\dddot{x}(t)$  is the acceleration rate(jerk  $j(t)$ ) of the target.  $F$ ,  $\Gamma$  and  $H$  are constant matrices.  $T$  is sampling period.

**Assumption 1.**  $w(t)$  and  $v_i(t)$  are uncorrelated white noises with zeros mean and variances  $\sigma_w^2$  and  $\sigma_{vi}^2$  respectively, the values of  $\sigma_w^2$  and  $\sigma_{vi}^2$  are both unknown.

**Assumption 2.** The observational processes  $y(t)$  is bounded,  $|y(t)| \leq c_1$ .

The jerk's self-correlation function

$$r_j(\tau) = E[j(t)j(t+\tau)] = \sigma_j^2 \exp(-\alpha|\tau|) \quad (3)$$

$\tau$  is the interval of two discrete time,  $\sigma_j^2$  is the variance of  $j(t)$ ,  $\alpha$  is the constant of the self-correlation function, when  $\alpha$  is very small,  $\alpha \rightarrow 0$ ,  $j(t)$  can be treated as a constant value,  $F$  has the form

$$\lim_{\alpha \rightarrow 0} F = \begin{pmatrix} 1 & T & T^2/2 & T^3/6 \\ 0 & 1 & T & T^2/2 \\ 0 & 0 & 1 & T \\ 0 & 0 & 0 & 1 \end{pmatrix} \quad (4)$$

$$\Gamma = \left[ \begin{matrix} T^3/6 & T^2/2 & T & 1 \end{matrix} \right]^T \quad (5)$$

The covariance of  $w(t)$  is

$$Q = \Gamma \sigma_w^2 \Gamma^T = \begin{pmatrix} T^6/36 & T^5/12 & T^4/6 & T^3/6 \\ T^5/12 & T^4/4 & T^3/2 & T^2/2 \\ T^4/6 & T^3/2 & T^2 & T \\ T^3/6 & T^2/2 & T & 1 \end{pmatrix} \sigma_w^2 \quad (6)$$

$$H = [1 \ 0 \ 0 \ 0]^\top \quad (7)$$

$\sigma_v^2$  is recorded as R. With the assumption 1-2, the objective is to get the self-tuning Kalman filter and its convergence analysis.

### 3 Noise Variance Estimation

Define backward shift operator  $q^{-1}$  and  $q^{-1}X(t+1) = X(t)$ , From (1) we have

$$X(t) = (I - Fq^{-1})^{-1} \Gamma w(t-1) \quad (8)$$

Substituting (8) into (2), we can get

$$y(t) = H(I - Fq^{-1})^{-1} \Gamma w(t-1) + v(t) \quad (9)$$

Assume  $I - Fq^{-1}$  is non-singular matrix, we can get

$$\det(I - Fq^{-1})y(t) = \text{Hadj}(I - Fq^{-1})\Gamma w(t-1) + \det(I - Fq^{-1})v(t) \quad (10)$$

From (3)-(5), we can get

$$\det(I - Fq^{-1}) = (1 - q^{-1})^4 \quad (11)$$

From (10), we can get

$$\begin{aligned} & (2q^{-7} - 14q^{-6} + 42q^{-5} - 70q^{-4} + 70q^{-3} - 42q^{-2} + 14q^{-1} - 2)y(t) = \\ & (-T^3q^{-6} + 3T^3q^{-5} - 2T^3q^{-4} - \frac{3}{2}T^3q^{-3} + \frac{19}{6}T^3q^{-2} - \frac{5}{6}T^3q^{-1} + \frac{1}{6}T^3)w(t-1) + \\ & (2q^{-7} - 14q^{-6} + 42q^{-5} - 70q^{-4} + 70q^{-3} - 42q^{-2} + 14q^{-1} - 2)v(t) \end{aligned} \quad (12)$$

According to the Assumption 1, we define

$$\begin{aligned} r(t) &= \det(I - Fq^{-1})y(t) \\ &= \text{Hadj}(I - Fq^{-1})\Gamma w(t-1) + \det(I - Fq^{-1})v(t) \end{aligned} \quad (13)$$

$r(t)$  has the relationship

$$r(t) = (2q^{-7} - 14q^{-6} + 42q^{-5} - 70q^{-4} + 70q^{-3} - 42q^{-2} + 14q^{-1} - 2)y(t) \quad (14)$$

We define

$$M(q^{-1}) = -T^3q^{-6} + 3T^3q^{-5} - 2T^3q^{-4} - \frac{3}{2}T^3q^{-3} + \frac{19}{6}T^3q^{-2} - \frac{5}{6}T^3q^{-1} + \frac{1}{6}T^3 \quad (15)$$

$$N(q^{-1}) = 2q^{-7} - 14q^{-6} + 42q^{-5} - 70q^{-4} + 70q^{-3} - 42q^{-2} + 14q^{-1} - 2 \quad (16)$$

$M(q^{-1})$  and  $N(q^{-1})$  are both the polynomial matrices with the form

$$X(q^{-1}) = x_0 + x_1q^{-1} + \dots + x_{n_x}q^{-n_x} \quad (17)$$

$n_x$  is the highest order of  $X(q^{-1})$ . From (13)-(16) we can get

$$r(t) = M(q^{-1})w(t-1) + N(q^{-1})v(t) \quad (18)$$

The correlation function of  $r(t)$  could be estimated by sampling method

$$\hat{R}_r^t(k) = \frac{1}{t} \sum_{u=1}^t r(u)r(u-k) \quad (19)$$

Which has the recursive formula

$$\hat{R}_r^t(k) = R_r^{t-1}(k) + \frac{1}{t} [r(t)r(t-k) - R_r^{t-1}(k)] \quad (20)$$

From (18) we can get the correlation function

$$\hat{R}_r^t(k) = \sum_{i=k}^{n_m} m_i Q m_{n_m-i} + \sum_{i=k}^{n_n} n_i R n_{n_n-i}, k = 0, 1, \dots, 7 \quad (21)$$

Equation (21) can be treated as linear functions with unknown variables  $Q$  and  $R$ , this linear functions are compatible, so the estimations  $\hat{Q}(t)$  and  $\hat{R}(t)$  at time t could be obtained.

## 4 Self-tuning Kalman filter

Substituting  $\hat{Q}(t)$  and  $\hat{R}(t)$  ( $\hat{Q}$  and  $\hat{R}$ ) into the optimal Kalman filter, we have the self-tuning Kalman filter

$$\hat{x}(t | t) = \hat{\Psi}(t)x(t-1 | t-1) + K(t)y(t) \quad (22)$$

In (22), we can get Riccati function

$$\Sigma = F[\Sigma - \Sigma H'(H\Sigma H' + \hat{R})^{-1} H\Sigma]F' + \hat{Q} \quad (23)$$

When  $t$  is renewed, the values of the variables are renewed in (22)-(23).

## 5 The Convergence analysis

Applying the ergodicity of stationary stochastic process, we can get

$$\hat{R}_r^t(k) \rightarrow R_r(k), t \rightarrow \infty, w.p.1 \quad (24)$$

w.p.1 is in short for “with probability 1”, In(19), the estimations of  $Q$  and  $R$  are consistent, they converge to the real values, we can get

$$\hat{Q}(t) \rightarrow Q, \hat{R}(t) \rightarrow R, t \rightarrow \infty, w.p.1 \quad (25)$$

$$\hat{K}(t) \rightarrow K, \hat{\Psi}(t) \rightarrow \Psi, t \rightarrow \infty, w.p.1 \quad (26)$$

We can get  $\|\hat{K}(t)\| \rightarrow \|K\|, t \rightarrow \infty, w.p.1$ , there must be a constant  $c_2$  to satisfy  $\|\hat{K}(t)\| \leq c_2, \forall t$ , according to the Assumption2, we can get  $|y(t)| \leq c_1$ . Dynamic Error System Analysis method [9,10] can be used to get the below Eq. 27.

$$\|\hat{x}(t|t) - x(t|t)\| \rightarrow 0, t \rightarrow \infty, w.p.1 \quad (27)$$

So self-tuning Kalman filter could converge to the optimal Kalman filter.

## 6 Simulation Example

We take sampling period  $T = 1$  s, input noise variance  $\sigma_w^2 = 0.8$ , measurement noise variance  $\sigma_v^2 = 0.2$ . The self-tuning Kalman filter presented in this paper is used, Figure 1 is the comparison curve of self-tuning Kalman filter and optimal Kalman filter. In Figure 1, the curved line denotes the optimal Kalman filter, spots denote self-tuning Kalman filter. It can be seen that self-tuning Kalman filter converges to the optimal filter. Figure 2 is the error curve, the curved line means the difference between the self-tuning Kalman filter and optimal filter. It has convergence to 0 as (27) is satisfied.

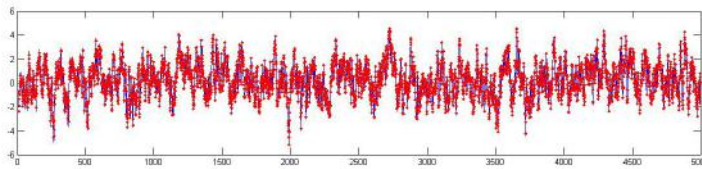


**Figure 1.** The self-tuning Kalman filter and optimal Kalman filter

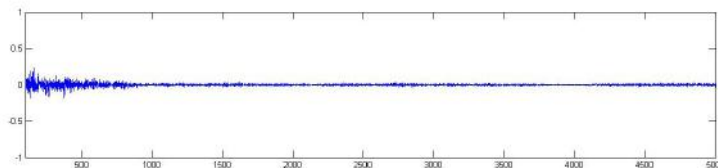


**Figure 2.** The difference between the self-tuning Kalman filter and optimal filter

## 7 Conclusion

This paper presents a kind of self-tuning Kalman filter, which could deal with the target tracking model with accelerate rate. Jerk model is used to fit the state equations. The convergence of this algorithm is proved. The simulation example shows the good convergence of this algorithm. This kind of self-tuning Kalman filter could improve

the tracking ability of the high maneuvering target, but the disadvantage is that the calculation is complicated. In the future, we can use the dimension reduction method to deal with the matrices to reduce the amount of computation.

**Acknowledgment:** This paper is supported by Fuyang Teachers' College Science Research Project (2015FSKJ11,2016FSKJ16). This paper is supported by Electronic technology excellent resources sharing curriculum (2013gxk063).

## References

- [1] Singer R A.Estimating optimal tracking filter performance for manned maneuvering targets.IEEE Transcations on Aerospace and Electronic System, vol.AES-6, no.4, pp.473-483, 1970.
- [2] P. J. Dua, S. C. Liu, J. S. Xia and Y. D. Zhao, Information fusion techniques for change detection from multi-temporal remote sensing images, *Information Fusion*, vol. 14, no. 1, pp. 19-27, 2013.
- [3] B.Wittenmark.A self-tuning predictor[J].*IEEE Transactions on Automatic Control*, vol.19, no.5, pp.848-851, 1974.
- [4] Gao Y, Ran C J, Sun X J, et al.Optimal and self-tuning weighted measurement fusion Kalman filters and their asymptotic global optimality.*International Journal of Adaptive Control and Signal Processing*, vol.24, no.1, pp.982-1004, 2010.
- [5] Ran C J, Deng Z L.Self-tuning weighted measurement fusion Kalman filter and its convergence. *Journal of Control Theory and Applications*, vol.8, no.4, pp.435-440, 2010.
- [6] Deng Z L.Self-tuning  $\alpha$ - $\beta$ - $\gamma$  Tracking Filter[J].*Control and Decision*, vol.6, no.5, pp.384-387, 1992.
- [7] Deng Z L.Self-tuning  $\alpha$ - $\beta$  Tracking Filter[J].*ACTA Automatica SINICA*, vol.18, no.6, pp.720-723, 1993.
- [8] Kishore Mehrotra, Pravas R.Mahapatra.A Jerk Model for Tracking Highly Maneuvering Target[J]. *IEEE Transactions on Aerospace and Electronics Systems*, vol.33, no.4, pp.1094-1105, 1997.
- [9] Gao Y, Ran C J, Sun X J, et al.Optimal and self-tuning weighted measurement fusion Kalman filters and their asymptotic global optimality.*International Journal of Adaptive Control and Signal Processing*, vol.24, no.1, pp.982-1004, 2010.
- [10] Ran C J, Deng Z L.Self-tuning weighted measurement fusion Kalman filter and its convergence. *Journal of Control Theory and Applications*, vol.8, no.4, pp.435-440, 2010.

Cun-qun FAN, Xian-gang ZHAO, Man-yun LIN, Li-zi XIE, You MA\*,  
Xiao-hu FENG

## A Multitasking Run Time Prediction Method based on GBDT in Satellite Ground Application System

**Abstract:** In satellite ground application system, it will cause resource constraints when running multiple tasks. To accurately measure out the task run time, this paper proposed a task running time estimation method based gradient boosting decision tree (GBDT). Firstly, according to various features of the time series variables classify applications. The predicted values are given for each node in the tree according to GBDT algorithm. Then through the establishment of multiple trees, the loss function is minimized. Finally, the most accurate predictions are calculated. After analysis, the proposed algorithm has a high accuracy ground.

**Keywords:** task run time; gradient boosting decision tree; various feature; loss function

### 1 Introduction

Fengyun meteorological satellite ground application system receives satellite data from the satellites, and depending on the business needs, according to the different levels and types of meteorological satellite data product to generate and distribute. At present, satellites are widely used in communications, meteorology and geology. Satellites have a large number of data and products. Satellite ground application system will face carry more tasks. Due to the limitations of the overall resources, often resulting in a decline multitasking operating efficiency. How to accurately estimate the task run time, thus providing support for the scheduling of the current study is needed to solve a problem.

Certain task run prediction methods have been proposed in the literatures. The paper [1] described and evaluated the Running Time Advisor (RTA), a system that can predict the running time of a compute-bound task on a typical shared, unreserved commodity host. The prediction is computed from linear time series predictions of host load and takes the form of a confidence interval that neatly expresses the error associated with the measurement and prediction processes, error that must be

---

\*Corresponding author: You MA, National Satellite Meteorological Centre, Beijing, China,  
E-mail: mayou@cma.gov.cn

Cun-qun FAN, Xian-gang ZHAO, Man-yun LIN, Li-zi XIE, Xiao-hu FENG, National Satellite Meteorological Centre, Beijing, China

captured to make statistically valid decisions based on the predictions. In paper [2], they proposed a method for predicting run-time resource consumption in multi-task component based systems based on a design of an application. The paper [3] proposed a running time prediction method for Grid tasks based on our previous work, which is a novel CPU load prediction method. The paper [4] proposed a novel approach that enables the construction models for predicting task running-times of data-intensive scientific workflows. Ensemble Machine Learning techniques are used to produce robust combined models with high predictive accuracy. Information derived from workflow systems and the characteristics and provenance of the data are exploited to guarantee the accuracy of the models. The paper [5] considered three objectives: expected time, long-run average, and timed (interval) reachability. Expected time objectives focus on determining the minimal (or maximal) expected time to reach a set of states. Long-run objectives determine the fraction of time to be in a set of states when considering an infinite time horizon. Timed reachability objectives are about computing the probability to reach a set of states within a given time interval. The paper [6] proposed two approaches utilizing some a priori knowledge and estimating it from scratch via a sparse structure assumption.

Although the researches of the cloud environment resource scheduling achieved good results, but there are still insufficient in error estimation. So, this paper introduces the GBDT algorithm, the prediction process as far as possible down to the minimum loss function, thereby enhancing the overall prediction accuracy.

## 2 Gradient Boosting Decision Tree Algorithm

GBDT is a very broad application of the algorithm, can be used for classification, regression. In many data prediction has a very good effect. GBDT decision is an iterative algorithm, the algorithm is composed by a number of trees tree, and the conclusion of all the trees make the final decision.

### 2.1 Algorithm Principle

The GBDT regression tree analysis resource consuming task to run time series to predict the various features of the task run time. GBDT algorithm based on time-series variables various features and applications to classify each node in the tree gives the predicted value. The GBDT algorithm by establishing multiple trees, to minimize the loss function, to get the most accurate predictions.

At the time of the beginning of the algorithm for each sample assigned a weight value, the initial time, each sample is the same important. At each step of the training obtained in model will make the estimated data points have to be wrong. We are at the end of each step, increase the weight of misclassification point weight, and reduce

weight division right on point. This makes is always some point if misclassification, it will be “serious concern.” It will be assigned a high weight on the right. Then after  $N$  iterations (specified by the user), user will get  $N$  simple classification. The final model may be obtained by a linear combination of ways.

If there is a sample  $x$ , it may belong to  $K$  categories, the estimated values are  $F_1(x) \cdots F_k(x)$ . Logistic transformation is a smooth and standardized data process (such as the length of the vector is 1). The probability  $p_k(x)$  of the result belonging to category  $K$  is as follows:

$$p_k(x) = \exp(F_k(x)) / \sum_{l=1}^k \exp(F_l(x)) \quad (1)$$

After logistic transformation, the loss function is as follows:

$$L\left(\{y_k, F_k(x)\}_1^K\right) = -\sum_{k=1}^K y_k \log p_k(x) \quad (2)$$

Where,  $y_k$  is the estimated function of the input sample data. And its derivative, there is the gradient of loss function:

$$\begin{aligned} y_{ik} &= -\left[ \frac{\partial L\left(\{y_{il}, F_l(x_i)\}_{l=1}^K\right)}{\partial F_l(x) = F_{l,m-1}(x)} \right] \\ &= y_{ik} - p_{k,m-1}(x_i) \end{aligned} \quad (3)$$

## 2.2 Loss Function Gradient Analysis

The input data  $x$  may belong to five categories  $(c_1, c_2, c_3, c_4, c_5)$ . If  $x$  belongs to category  $c_3$ , there is  $y = (0, 0, 1, 0, 0)$ . The resulting model estimation is  $F(x) = (f_1, f_2, f_3, f_4, f_5)$ , Then after logistic transformation can be  $p(x) = (p_1, p_2, p_3, p_4, p_5)$ . After the above, the conclusions can be as follows.

If  $g_k$  is the sample when the gradient of a dimension.

When  $g_k > 0$ ,  $g_k$  smaller, the probability  $p(x)$  of this dimension should be greater. It should belong to the “right direction” forward. This estimate represents the smaller the more “accurate.”

When  $g_k < 0$ ,  $|g_k|$  greater, the probability  $p(x)$  of this dimension should be smaller. It should belong to the “wrong direction” forward. This estimate represents the smaller the more “accurate.”

In general, for a sample of the best gradient is closer to 0.

## 3 Run Time Prediction Based on GBDT

GBDT regression tree based on the training set of feature vector sequence characteristics were divergent. Task run time as GBDT classification entropy, that is, the tree will try to make the crossing task to run every time the minimum entropy.

This approach makes the degree of aggregation run tasks on each node in the tree relatively high. Make the final decision based on the time relatively easy to predict the characteristics of the input operation time.

There are four tasks sample points in Figure 1. The running time of them are  $(t_a, t_b, t_c, t_d)$ . If  $t_a < t_b < t_y < t_c < t_d$ , the running time can be divided into two sets  $(t_a, t_b)$  and  $(t_c, t_d)$ . And  $(t_a, t_b)$  can be divided into two sets  $(t_a)$  and  $(t_b)$ ,  $(t_c, t_d)$  can be divided into two sets  $(t_c)$  and  $(t_d)$ .

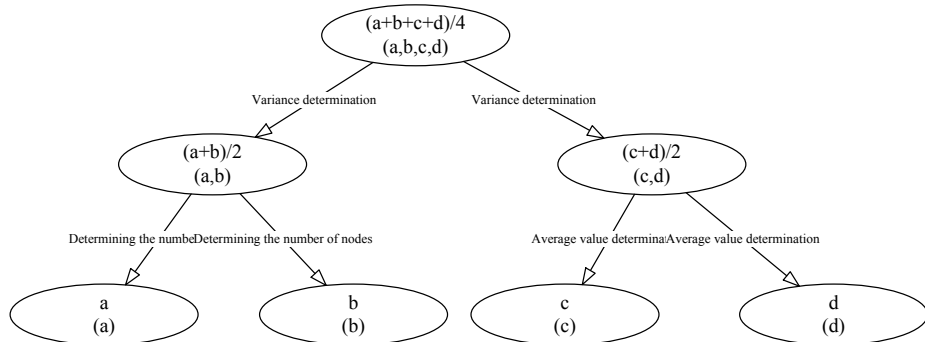


**Figure 1.** Multi node sample flow.

In the process of forecasting tasks running, we can go from the root all the way down the final decision condition according to the root node, and get the task running time of the root node. In GBDT workflow, there are M decision trees, obtained from the M trees like tree algorithm running time and the final prediction is GBDT run time.

As shown in Figure 2, tree generated every time according to the last tree prediction residuals of the tree all the variables residuals negligible so far. Multi-tree prediction value obtained by adding the result of addition makes forecasting more precise.

The main purpose of this section is based on the task of running time sequence characteristics to estimate the run time of the task. Enter the program requires the input feature time-series set. We need the help of feature extraction feature extraction module, but also need to use the features described above and converting the characteristic variable generation module.

Generate GBDT prediction module comprises two steps, the matrix (the training set) time series feature to generate variable GBDT decision tree and decision tree based on the task run time prediction.

When the estimated time sequence time, all the features need to enter a variable time series. By M trees forecasting and time series to generate the final run time.

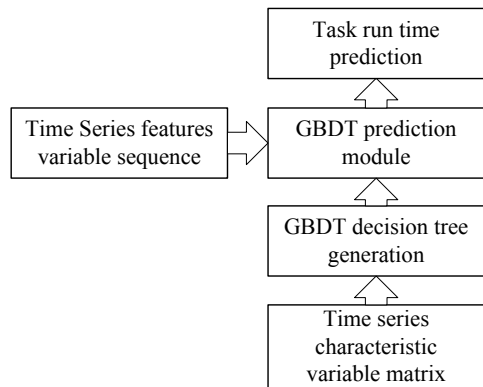


**Figure 2.** GBDT prediction task flow chart.

## 4 Simulation

In order to verify the effectiveness of the proposed algorithm, we use the Visual Studio 6.0 platform to achieve our algorithm based on GBDT, and compare with the run time prediction algorithm based on fixed weights (FWA).

The simulation environment of PC configuration is: CPU Core i5-6500 3.20GHz, RAM=4GB, Windows 7 system. The simulation system through the C++ language, math calculations involved in the experiment were analyzed by calling math.h math library to calculate. Figure 3 shows the prediction accuracy of 10 experiments.

The proposed GBDT algorithm is higher than the FWA algorithm on prediction accuracy.

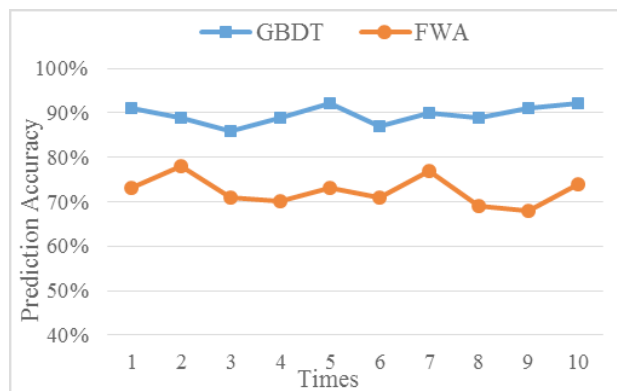


**Figure 3.** Prediction accuracy.

## 5 Conclusion

To accurately measure out the task run time, this paper proposed a task running time estimation method based gradient boosting decision tree (GBDT). Firstly, according to various features of the time series variables classify applications. The predicted values are given for each node in the tree according to GBDT algorithm. Then through the establishment of multiple trees, the loss function is minimized. Finally, the most accurate predictions are calculated. After analysis, the proposed algorithm has a high accuracy ground.

**Acknowledgment:** The work presented in this study is supported by National High-tech R&D Program (2011AA12A104) and the National Natural Science Foundation of China (NSFC61602126).

## References

- [1] P. Dinda, Online prediction of the running time of tasks, IEEE International Symposium on High PERFORMANCE Distributed Computing. IEEE Computer Society, 2001, pp. 383-394.
- [2] J. Muskens, M. Chaudron, Prediction of run-time resource consumption in multi-task component-based software systems, Component-Based Software Engineering, International Symposium, Cbse 2004, Edinburgh, Uk, May 24-25, 2004, pp. 162-177.
- [3] Y. Zhang, W. Sun, Y. Inoguchi, Predict task running time in grid environments based on CPU load predictions, Future Generation Computer Systems, 2008, vol. 6, pp. 489-497.
- [4] D. Monge, M. Holec, F. Železný, and C. Garino, Ensemble Learning of run-time prediction models for data-intensive scientific workflows, High Performance Computing. 2014, pp. 83-97.
- [5] D. Guck, H. Hatifi, H. Hermanns, Analysis of timed and long-run objectives for markov automata. Logical Methods in Computer Science, 2014, vol. 10, pp. 930-942.
- [6] Y. Zhang, W. Cheung, J. Liu, A unified framework for epidemic prediction based on poisson regression, IEEE Transactions on Knowledge & Data Engineering, 2015, vol. 1, pp. 1-10.

Wen-zhi XING, Zhu-ping WANG\*

## Unmanned Ground Vehicle Behavior Decision via Improved Bayesian Inverse Reinforcement Learning

**Abstract:** In this paper, we address an improved Bayesian inverse reinforcement learning (BIRL) algorithm for behavior decision making problem of unmanned ground vehicle through learning from teaching sequences. It is demonstrated that in this paper how the autonomous driving vehicle executes optimal action under current state according to expert's demonstration by using the proposed approach. Simulation tests show that the proposed improved BIRL can make reasonable decisions for the driverless car.

**Keywords:** Inverse reinforcement learning; decision-making; unmanned ground vehicle.

### 1 Introduction

In recent years, unmanned ground vehicle as a important research topic for decreasing traffic accidents in intelligent transportation system has been mentioned gradually. It is very important to design an effective autopilot system for UGV. Generally speaking, the autopilot system of unmanned ground vehicle can be divided into three parts. As Fig. 1 shows, the first part is the environment recognition that will capture all the information from surroundings and be seen as "eyes". The module of decision-making is the part which is regarded as "brain". This part's main task is to decide the vehicle's actions according to current information provided by environment recognition system. The third part is called control module that is to plan optimal path and implement the decision made in the second part. From this framework, we can find that the decision-making module has played a central role in autopilot system.

To the best of our knowledge, the current researches about decision-making have obtained some achievements. For example, Multiple Criteria Decision Making (MCDM) [1] and Multiple Attribute-Based Decision Making (MADM) [2] can provide a better decision in the simple external environment that has less states defined by human. In paper [1], a maneuver decision making method for autonomous vehicle in urban environment is studied. The algorithm can be decomposed into three steps. The first step is to select all possible logical maneuvers and the second step to remove the maneuvers which break the traffic rules. At the last step, Multiple Attribute Decision

---

\*Corresponding author: Zhu-ping WANG, Department of Control Science & Engineering, Tongji University, Shanghai, China, Corresponding Author Email: elewzp@tongji.edu.cn  
Wen-zhi XING, Department of Control Science & Engineering, Tongji University, Shanghai, China

Making methods are used in the process of selecting the optimal driving maneuver in the scenario considering safety and efficiency. In paper [2], the stage of decision making is also to select and execute the most appropriate alternative from those driving maneuvers which have been determined to be feasible in the current traffic situation. More precisely, this method breaks general objective into a lower hierarchy level containing more specific objectives, which specify how to achieve the objective of the higher level.

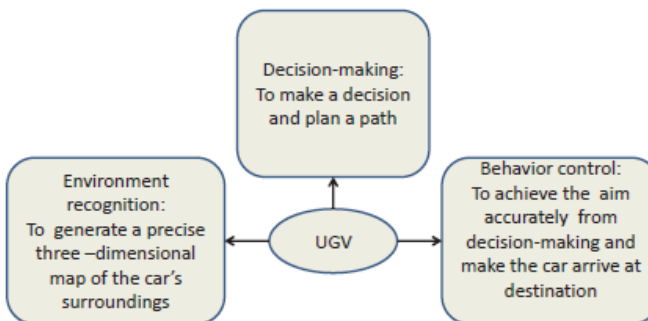


**Figure 1.** Autopilot system

Inverse reinforcement learning (IRL) [3] has been proposed to solve the decision-making problem. As pointed out in paper [3], IRL problems are of great interests for a wide range of application, from basic science [4,5] to optimal control of aircraft [6] and more recently aerobatic helicopter flight [7] within the robotic community. Supervised learning approaches such as [8-12] that learn a direct mapping from the states to the actions and directly mimic the demonstrator will do not work for highway driving or more complex driving situations. The inverse learning algorithm, to some extent, will be the most succinct and robust way to explain expert behavior. In addition, the algorithm has better generalization ability in the domain of the features. Bayesian inverse reinforcement learning [13] is one inverse reinforcement learning algorithm of all. The algorithm will update a prior on reward functions and we learn the process for recovering expert's actions by this posterior. However, the algorithm still has serious problem in driving behavioral decision, especially for the poor rate of convergence. It means that we will need more time to get ideal reward function if the algorithm is not good enough. This case will be danger when applying this algorithm to recover expert's driving behaviors. What's more, to a large extent, the learning process does not take into account existing noise problem. That is to say, in driving environment, it is hard to derive good policy in short time. So, new solutions to solving this problem will be necessary. This paper attempts to propose a improved algorithm.

In this paper, we apply improved Bayesian inverse reinforcement learning to learn optimal expert's policy. The improved algorithm will have fast convergent speed

and high accuracy for recovering expert's driving behaviors. From the perspective of engineering, it is very important to improve these two points above when compared to traditional BIRL. First, assuming expert's policy is stationary stochastic policy can get reward function's posterior distribution combining with Bayesian theory. Finally, using sampling method estimates the mean of the posterior distribution as our predictive value. We will improve existed Bayesian reinforcement learning algorithm to derive a better performance and learn expert's policy from making full use of demonstration information. This algorithm can let the driverless car has more security decision-making behaviors in environment and execute the relative optimal actions. Besides, we will give the simulation experiment's results to verify the algorithm.

The rest of this paper proceeds as follows. In section II, we will give a brief introduction for Markov decision process (MDP) basic properties and inverse reinforcement learning algorithm. Section III reviews BIRL algorithm and introduces improved BIRL algorithm. Our main contribution in revising the algorithm's potential function and adding the fitting process will be presented. The simulation and experimental test will be showed in section IV. In this section, we will also analyze those results' data. We conclude in section V with a brief discussion of opportunities for future work.

## 2 Preliminaries

### 2.1 Markov Decision Process

The inverse reinforcement learning problem is generally described by the Markov decision process formalism. A Markov decision process has five elements  $(S, A, \{P_{sa}(\cdot)\}, \gamma, R)$ , wherein:

$S$  is a finite set of  $n$  states;

$A = \{a_1, \dots, a_k\}$  is a set of  $k$  actions;

$\{P_{sa}(\cdot)\}$  are the state transition probabilities upon taking action in state ;

$\gamma \in [0, 1]$  is the discount factor;

$R$  is the reward.

A policy is defined as any state map to action:  $S \rightarrow A$ , notates  $\pi$ . The value function for describing a policy, evaluated at any state  $S_i$  is given by:

$$V^\pi(s_1) = E[R(s_1) + \gamma R(s_2) + \gamma^2 R(s_3) + \dots | \pi]. \quad (1)$$

In the same way, we have the Q-function according to

$$Q^\pi(s, a) = R(s) + \gamma E_{s' \sim P_{sa}(\cdot)}[V^\pi(s')] \quad (2)$$

The optimal value function is:

$$V^* = \sup_{\pi} V^{\pi}(s). \quad (3)$$

And the optimal Q-function is:

$$Q^*(s, a) = \sup_{\pi} Q^{\pi}(s, a). \quad (4)$$

To solve the IRL problem, the two basic properties concerning MDP are needed. The two basic properties can be characterized as following [14]:

Theorem 1 (Bellman Equation) Let an MDP  $M = (S, A, \{P_{sa}(\cdot)\}, y, R)$  and a policy  $\pi: S \rightarrow A$  be given. Then, for all  $s \in S, a \in A$ ,  $V^{\pi}$  and  $Q^{\pi}$  satisfy:

$$V^{\pi}(s) = R(s) + \gamma \sum_{s'} P_{s \in \pi(s)}(s') V^{\pi}(s'), \quad (5)$$

$$Q^{\pi}(s) = R(s) + \gamma \sum_{s'} P_{sa}(s') V^{\pi}(s') \quad (6)$$

Theorem 2 (Bellman Optimality) Let an MDP  $M = (S, A, \{P_{sa}(\cdot)\}, y, R)$  and a policy  $\pi: S \rightarrow A$  be given. Then that is an optimal policy for  $M$  if and only if, for all

$$\pi(s) \in \operatorname{argmax}_{a \in A} Q^{\pi}(s, a). \quad (7)$$

According to the two basic properties above, an important theorem can be derived to explain expert behavior in MDP using reward function. We can think this theorem that is the core for inverse reinforcement learning. The theorem is written:

Theorem 3 Let a finite state space  $S$ , a set of actions  $A = \{a_1, \dots, a_k\}$ , transition probability matrices  $P_{sa}$ , and a discount factor  $\gamma$  be given. Then the policy  $\pi$  given by  $\pi(s) = a_1$  is optimal if and only if, for all  $a = a_2, \dots, a_k$ , the reward satisfies:

$$(P_{a1} - P_{az})(I - \gamma P_{a1})R \geq 0. \quad (8)$$

This result characterizes the set of all reinforcement functions that are solutions to the inverse reinforcement learning problem. Using this equation we can recover expert behavior via reward function for finite-state MDP. For further problem about the criteria of choosing reward and how to approximate for reward function in large scale state space will be found in paper [15].

## 2.2 Problem Formulation

In considering the decision-making problem of autonomous driving vehicles, we think that the car can be taught by expert. So, our aim is to design a more efficient algorithm to learn a reward function from sample trajectories. The reward function can capture the state's features and help the driverless car make decision no matter whether the state ever emerged or not. Our algorithm applied in decision-making can be seen as Fig. 2. In training process, this framework will be repeated again and again. Once we capture the partial states' reward function that can explain expert's behaviour, these

process will terminate. Then, the value function can choose appropriate action from current state to next state.

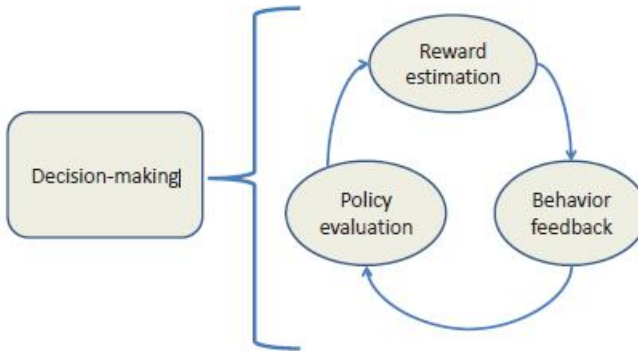


**Figure 2.** Decision-making framework

### 3 Improved Bayesian Inverse Reinforcement Learning

#### 3.1 Bayesian Reinforcement Learning

We recall some basic definitions and assumptions relating to Bayesian reinforcement learning. We can assume expert's demonstration that equals to a reward function from posterior distribution. Then an agent according to this reward function implements optimal policy. Expert's a trajectory expresses as:  $O = \{(s_1, a_1), (s_2, a_2), \dots, (s_k, a_k)\}$ , which means that the expert was in state  $s_i$  and took action  $a_i$ . The two assumptions have guaranteed that the problem is defined in Markov decision framework and does not abandon problem's mathematic's essence. Because demonstrator employs stationary policy, the problem can make a further independence assumption, giving

$$P(O|R) = P((s_1, a_1|R), \dots, (s_k, a_k|R)). \quad (9)$$

Expert's goal is to maximize the total accumulated reward and the goal amounts to every step the agent that executes the action with maximum action function  $Q(s, a)$ . Therefore the larger  $Q(s, a)$  is, the more likely it is that the demonstrator would choose action  $a_i$  at state  $s_i$ . So we can model this problem's distribution as this potential function:

$$P((s_i, a_i)|R) = \frac{1}{Z} \exp(\alpha Q(s_i, a_i, R)). \quad (10)$$

Then the likelihood of the entire evidence is:

$$P(O|R) = \frac{1}{Z} \exp(\alpha E(O, R)), \quad (11)$$

where

$$E(O|R) = \sum_i Q^*(S_i, a_i, R), \quad (12)$$

and  $Z'$  is the appropriate normalizing constant. Finally, the posterior probability of reward function by applying Bayes theorem can rewrite as following:

$$P(R|O) = \frac{P(O|R)P(R)}{P(O)} = \frac{1}{Z'} \exp(\alpha E(O, R)) P(R). \quad (13)$$

Detailed derivation of these equations and its complete algorithm can be found in prior work [13].

### 3.2 Improved Bayesian Reinforcement Learning

In the original BIRL algorithm, to maximize demonstrator trajectories' likelihood equation is regarded as to maximize the sum of  $E(O, R)$ . The model will tend to increase all weights' value during the process of iteration. From this point of view, the reward function with weight vector  $\omega$  multiplying by  $\beta$  cannot influence original policy while such a change like this will be not good for reducing the times of iteration and lead to a new potential function  $\beta E(O, R)$  and a new likelihood equation. As a result, the algorithm will select a new reward function to replace last reward function. This case however, must be hard to stop in short time. That means that we cannot get better proper reward function. If so, the reward function recovered by unimproved BIRL will lead to an overfitting problem.

This part will introduce a series of efforts to improve the Bayesian inverse reinforcement learning. To reconstruct the potential function is to be the main method in this section and then to design a new algorithm frame combined with linear function from states' features mapping to reward. The first modified potential function is giving:

$$E(O|R) = \sum_{(s_i, a_i) \in O} (Q(s_i, a_i) - Q(s_i, a_{\pi(s_i)})), \quad (14)$$

where  $\pi(s_i)$  is a random policy. The policy is to sample an action randomly that is different from expert's action in every state, following  $\pi(s_i) \in A \setminus a_i$ . The meaning of this kind of potential function is to maximize the distance of the expert's policy and random policy. It is also easy to express it in linear return function and prove its convergence. Nevertheless, on the original algorithm performance improvement is not particularly significant because of its performance depending on the start policy.

We rewrite the potential function again like:

$$E(O, R) = \sum_{(s_i, a_i)} \left[ Q(s_i, a_i) - \max_{a \in A \setminus a_i} Q(s_i, a) \right]. \quad (15)$$

This equation tries to maximize the difference between optimal and suboptimal strategy. From the experimental results, the potential function for ascension algorithm performance is better than the first one. But it still tends to choose a larger weight vector. In order to solve the problem, we made a further attempt. So the new equation is described as this:

$$Q(s_i, a_i) - \max_{\alpha \in A \setminus a_i} Q(s_i, a) = \frac{1}{1 + \exp(-\alpha(Q(s_i, a_i) - \max_{\alpha \in A \setminus a_i} Q(s_i, a)))} \quad (16)$$

The function can be intuitive understanding as the probability of expert's action. If  $Q(s_i, a_i) - \max_{\alpha \in A \setminus a_i} Q(s_i, a)$  is larger positive value, we can think that the probability of carrying out optimal action is very close to 1 under the current state. Under this kind of understanding the new potential function is the expectation of expert's optimal actions. The potential function is rewritten formally:

$$E(O|P) = \sum_{(s_i, a_i) \in O} \left( \text{sigmoid} \left( Q(s_i, a_i) - \max_{\alpha \in A \setminus a_i} Q(s_i, a) \right) \right). \quad (17)$$

There is no need to increase the reward function value for the actions that has been defined as optimal actions with maximum probability. The algorithm will tend to increase the probability of other actions that are included in sample trajectories. Our improved learning algorithm is as follows:

$P$        $M$        $\rightarrow_\delta$ , features' vector , threshold value  
a random weight' vector , reward vector  $R \in R^{|S|}/\rightarrow_\delta$ , expect threshold value for

$\pi_E$

$$\| - \pi_E \|_2 > \varepsilon$$

Pick a reward vector uniformly at random from the neighbours of  $R \in R^S/\rightarrow_\delta$

$:= \text{policyInternation}(M, R)$

$$Q^\pi(s, a, \bar{R}) \quad (s, a) \in S, A.$$

$$\exists (s, a) \in (S, A), Q^\pi(s, \pi(s), \bar{R}) < Q^\pi(s, a, \bar{R})$$

$\bar{\pi} := \text{policyInternation}(M, \bar{R}, \pi)$

$$R := \bar{R} \quad \bar{\pi} := \bar{\pi} \text{ with probability } \min \left\{ 1, \frac{P(\bar{R}, \pi)}{P(R, \pi)} \right\}$$

$R$

$$\min ||R - \bar{\omega}^T||_{p \in \{1, 2, \dots, N\}} < \varepsilon$$

$$:= \bar{\omega}$$

Upon termination, the algorithm returns

## 4 Simulation Results

We evaluated the algorithm on more concrete behaviors in the context of a simple highway driving simulator as Fig. 3 shows, similar evaluations in other work [3]. The task is to navigate a car on a three-lane highway, where all other vehicles move at a constant speed with different level. From the leftmost to rightmost lane, the speed level of vehicle is set to 90km/s, 60km/h and 30km/s randomly. Target car has added two kinds of behavior that are acceleration and deceleration. Under such settings, we assume that has a special random driving style to avoid collision and then is able to drive as fast as possible. For example the car will be the leftmost lane and its speed is 120km/s. If there is another car ahead, the target car will change its current lane to the middle lane when the middle lane has nothing. Further, the target car will decrease its speed to 90km/h and keep going in the left lane when another car emerges in the middle lane.



**Figure 3.** The simulation environment

In real world, driving style is very complex and popular. Naturally, complex driving styles are very hard to train. So we will evaluate the algorithm by random driving styles. At first, we show the rate of converge between previous algorithm and improved algorithm by comparison in three-lane simulator. Then we will show all features' weight values to analyze the algorithms' performance for recovering reward function one by one.

Our improved BIRL algorithm that is applied to the problem of driving decision will have less iteration times and faster converged speed from Table 1 and Table 2. The median of iteration for improved BIRL is less than BIRL. The success rate in 500 steps is 100%, but the unimproved BIRL is only 42%. These comparisons are obvious for algorithms' performance.

**Table 1.** Key Parameters for Birl

Driving Style Nice	Nice
Median of Iteration 87	87
Success Rate in 500 Steps 42%	42%

**Table 2.** Key parameters for improved birl

Driving Style	Nice
Median of Iteration	28
Success Rate in 500 Steps	100%

Similarly, we can also present the results between previous algorithm and improved algorithm by comparison in three-lane simulator for reward function's weight values. Owing to more states, it is hard to guarantee the demonstrators optimality. For unimproved BIRL algorithm, that will be facing a bigger challenge to recover a reward function with proper weight value vector.

**Table 3.** Key features' weight value

Features' Name	BIRL	Improved BIRL
Left Lane	0.156	0.041
Middle Lane	-0.022	0.029
Right Lane	-0.016	-0.021
30km/h	-0.110	-0.027
60km/h	0.045	0.035
90km/h	-0.061	0.045
120km/m	0.516	0.184
Collision	-0.020	-0.388
Distance 30 to 60	0.024	-0.094
Distance 60 to 120	-0.190	0.001

We have made a comparison for our improved BIRL and initial BIRL. All features have emerged in our sample data except "Collision". All features' weight values observed from Table 3 have two larger values for left lane and 120km/h. It is interesting to see that collision's weight value for improved BIRL is smaller than initial BIRL. To explain this phenomenon, we have to repeat again about the advantage of the improved BIRL algorithm that is relative insensitive to these features that have not ever emerged in demonstrator' strategies. The reward function will became smaller when the environmental states data have included collision's feature. Besides, improved BIRL algorithm can also make the features' weight values be positive when comes to "Middle lane" and "90km/h". The weight values for "Distance 60 to 120" and "30km/h" have increased a little respectively. Other features included in sample data will give proper weight values according to the scale in sample trajectories. For example, the weight values for "Right Lane" and "Distance 30 to 60" have decreased a little respectively because of less data included in sample data. These changes show that the improved

algorithm has made full use of existing data information to get reward function. The main features are described as follows:

Left lane: Running at the left lane when avoiding collisions with other cars as many as possible;

Middle lane: Running at the middle lane when avoiding collisions with other cars as many as possible;

Right lane: Running at the right lane when avoiding collisions with other cars as many as possible;

30km/h, 60km/h, 90km/h, 120km/h: Driving at a constant speed;

Safe distance from 30/60 to 60/120: Keeping a safe distance from other cars;

Collision: Hitting other cars.

## 5 Conclusion

In this paper, it is assumed that driving demonstrations by an expert can be quantified by a reward function to solve the decision-making problem for the driverless car in more states' environment, and an improved algorithm for Bayesian reinforcement learning is presented. The proposed method is based on Markov decision process, terminates in less iteration, and guarantees that the policy found has similar performance comparable to that of the expert.

The proposed algorithm is applied to unmanned ground vehicle's behavioral decisions through simulation and experimental validation. From the viewpoint of input data, the proposed algorithm can improve the effectiveness of using the sample data. From the viewpoint of output data, the proposed algorithm can derive the reward function that is very possible to recover expert's demonstration. In this work, the reward is considered as a linear combination of known features. To explore unmanned vehicle's behavioral decision under more realistic conditions, the reward function as a nonlinear form will be a more meaningful work in the future. In today's world, deep learning has promoted the application of intelligent systems in speech recognition, image classification and natural language processing. There is no doubt about that we can do more solid work in decision making for unmanned ground vehicle combined with deep learning in the near future.

**Acknowledgement:** This work is partially supported by project of National Natural Science Foundation of China (91420103, 91120308).

## References

- [1] J. J. Chen, P. Zhao, H. W. Liang and T. Mei, A multiple attribute-based decision making model for autonomous vehicle in urban environment, In proc. IEEE Intelligent Vehicles Symposium (IV), 2014, pp.480-485.
- [2] A. Furda, and L. Vlacic, Enabling safe autonomous driving in realworld city traffic using multiple criteria decision making, IEEE Intelligent Transportation System, vol.3, no.1, pp.4-17, 2011
- [3] P. Abbeel, and A.Y. Ng, Apprenticeship learning via inverse reinforcement learning, In proc. International Conference on Machine Learning, 2004, pp.1-8.
- [4] M. Y. Kuniyoshi, M. Inaba, and H. Inove, Learning by watching: Extracting reusable task knowledge from visual observation of human performance, IEEE transaction on robotics and automation, vol. 10, no.6, pp.799-822, 1994
- [5] J. Demiris, and G. Hayes, A robot controller using learning by imitation, In proc. International Symposium on Intelligent Robotic Systems, 1994, pp.198-204.
- [6] E. Todorov, Optimality principles in sensorimotor control, Nature Neuroscience, vol.7, no.9, pp.907-915, 2004
- [7] P. Abbeel, A. Coates, and A.Y. Ng, Autonomous helicopter aerobatics through apprenticeship learning, International Journal of Robotics Research, vol.29,no.13, pp.1608-1639, 2010
- [8] R. Amit, and M. Mataric, Learning movement sequences from demonstration, In proc. International Conference on Development and Learning, 2002, pp.203-208.
- [9] C. Sammut, S. Hurst, D. Kedzier, and D. Michie, Learning to fly, In proc. International Conference on Machine Learning, 1992, pp.385-393.
- [10] D. Pomerleau, An autonomous land vehicle in a neural network, In proc. Advances in Neural Information Processing Systems 1, 1989, pp.305-313.
- [11] K. Kording, and D. Wolpert, The loss function of sensorimotor learning, National Academy of Sciences of the United States of America, vol.101, no.26, pp.9839-9842, 2004
- [12] M. Krstic, and P. Tsotras, Inverse optimal stabilization of a rigid spacecraft, IEEE Transactions on Automatic Control, vol.44, no5, pp.1042-1049, 1999
- [13] D. Ramachandran, and E. Amir, Bayesian inverse reinforcement learning, In proc. International Joint Conference on Artificial Intelligence, 2007, pp.2586-2591.
- [14] R. S. Sutton, and A. G. Barto, Reinforcement Learning, 1998, pp.66-80.
- [15] A.Y. Ng, and S. Russell, Algorithms for inverse reinforcement learning, In proc. International Conference on Machine Learning, 2000, pp. 663-670

Qi YANG\*, Bin DENG, Yu-liang QIN, Hong-qiang WANG

## Analysis of the High Frequency Vibration on Radar Imaging in the Terahertz Band

**Abstract:** High frequency vibration of the platform or the targets is an inevitable problem in the field of radar imaging, and it has significant effects on the image quality. A theoretical model of the high frequency vibration of the platform in the turntable imaging mode is established in this paper, and it shows that effects of the high frequency vibration in the terahertz band are more obvious than that in the microwave band. In addition, a 0.22 THz imaging radar system is introduced and imaging experiments on a corner reflector are carried out in this paper to verify the theory analysis.

**Keywords:** terahertz radar; high frequency vibration; turntable imaging; imaging resolution; phase autofocus

### 1 Introduction

Terahertz (THz) waves usually refer to electromagnetic waves with frequencies between 0.1-10 THz. The terahertz band lies between the millimeter wave and infrared, which is a transitional band from electronics to photonics [1,2]. With breakthroughs in the terahertz sources, signal detectors and other devices in recent years, the terahertz radar technology has developed rapidly, and the terahertz synthetic aperture radar (SAR) and inverse synthetic aperture radar (ISAR) imaging has been receiving more and more attention [3,4]. The high frequency vibration of the platform often considered in the microwave band radar imaging is still problem in the terahertz band, and it may be even more obvious. The high frequency vibration in radar applications mainly includes: the high frequency vibration of the target while moving in the ISAR field, the high frequency vibration of the carrier aircraft and vehicles in the SAR field, or both. However, no matter in the SAR field or in the ISAR field, the essential effect of the high frequency vibration is a modulation of the echo phase, which will result in the deterioration of the imaging resolution. The high frequency vibration of the platform or the targets has been extensively studied and several suppression methods are discussed [5-7]. However, researches on this problem in the terahertz band are insufficient.

---

\*Corresponding author: Qi YANG, College of Electronic Science and Engineering, National University of Defense Technology, Changsha, China, E-mail: yangqi\_nudt@163.com

Bin DENG, Yu-liang QIN, Hong-qiang WANG, College of Electronic Science and Engineering, National University of Defense Technology, Changsha, China

A theoretical model of high frequency vibration of the platform in the turntable imaging is established in this paper, and its effects on imaging quality are analyzed in detail. After that, a 0.22 THz imaging radar system is adopted to verify the theory analysis. The paper is organized as follows: the motion model and the echo model of a scattering center in the turntable imaging mode are established in section II, and expressions of the range profile and the ISAR image are obtained through the theoretical deduction. In section III, a 0.22 THz imaging radar system is introduced and experiments on a corner reflector and a plane model are presented. The resolution deterioration induced by the high frequency vibration is analyzed and a phase autofocus algorithm is introduced to reduce the effects of the high frequency vibration. The conclusions are presented in section IV.

## 2 Theory analysis

### 2.1 The echo model

The paper takes the turntable imaging mode as example to build the motion model and the echo model, and they are also applicable to SAR and ISAR mode due to the relativity of motions. It is generally known that SAR/ISAR achieves high range resolution by the large bandwidth of the transmitting signal, while the high azimuth resolution depends on the Doppler effect caused by a relative movement between radar and the target. Suppose there is a scattering center on the target located at  $(x_{p,0}, y_{p,0})$ , and it rotates a small angle  $\delta\theta$  round the coordinate origin  $O$ , as shown in the Figure below.

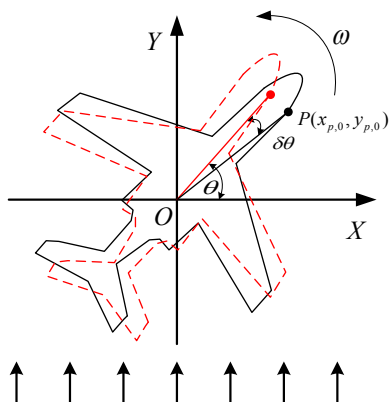


**Figure 1.** A diagram of turntable imaging

The imaging radar mentioned in this paper utilizes frequency modulated continuous wave (FMCW) signal. Its bandwidth of the transmitting signal is  $B$ , the carrier frequency is  $f_c$ , the frequency-sweep period is  $T_p$ , the chirp rate is  $\gamma$ . Then the transmitting signal can be expressed as:

$$s(\hat{t}, t_m) = \text{rect}\left(\frac{\hat{t}}{T_p}\right) \exp\left[j2\pi\left(f_c t + \frac{1}{2}\gamma t^2\right)\right] \quad (1)$$

where  $\hat{t}$  and  $t_m$  represent the range fast-time and azimuth slowtime respectively. Suppose the initial distance between the radar and the target is  $R_0$ , and the vibration of the platform can be viewed as a simple harmonic motion. The actual distance considering the vibration is:

$$R = R_0 + a_v \sin(2\pi f_v t_m) \quad (2)$$

where  $a_v$  and  $f_v$  are the amplitude and frequency of the vibration respectively. In general, it can be called high frequency vibration when  $|f_s \cdot T_m| \geq 1$  is satisfied ( $T_m$  is the synthetic aperture time). The expression of the echo signal is:

$$s_r(\hat{t}, t_m) = \text{rect}\left(\frac{t - 2R/c}{T_p}\right) \exp\left[j2\pi\left(f_c(t - \frac{2R}{c}) + \frac{1}{2}\gamma(t - \frac{2R}{c})^2\right)\right] \quad (3)$$

The transmitting and receiving signal possess large product of time-width and bandwidth, which requires high performance for hardware if sampling and processing directly according to Nyquist sampling theorem. Consequently, the dechirp method is often adopted, that is, mixing the echo signal with a reference signal, which usually refers to the echo signal of a target located at the reference distance  $R_{ref}$  and it can be expressed as:

$$s_{ref}(\hat{t}, t_m) = \text{rect}\left(\frac{t - 2R_{ref}/c}{T_p}\right) \exp\left[j2\pi\left(f_c(t - \frac{2R_{ref}}{c}) + \frac{1}{2}\gamma(t - \frac{2R_{ref}}{c})^2\right)\right] \quad (4)$$

The intermediate frequency signal after dechirp is :

$$\begin{aligned} s_{if}(\hat{t}, t_m) &= s_r(\hat{t}, t_m) \cdot s_{ref}^*(\hat{t}, t_m) \\ &= \text{rect}\left(\frac{\hat{t} - 2R/c}{T_p}\right) \exp\left[-j\frac{4\pi}{c}\gamma\left(\hat{t} - \frac{2R_{ref}}{c}\right)R_\Delta - j\frac{4\pi}{c}f_cR_\Delta + j\frac{4\pi\gamma}{c^2}R_\Delta^2\right] \end{aligned} \quad (5)$$

where  $R_\Delta = R - R_{ref}$ .

## 2.2 Resolution analysis

The range profile can be obtained by the Fourier transform of Equation (5) to the range fast-time:

$$\begin{aligned} S_{if}(f_i, t_m) &= T_p \sin c\left[T_p\left(f_i + 2\frac{\gamma}{c}R_\Delta\right)\right] \cdot \\ &\quad \exp\left(-j\left(\frac{4\pi f_c}{c}R_\Delta + \frac{4\pi\gamma}{c^2}R_\Delta^2 + \frac{4\pi f_i}{c}R_\Delta\right)\right) \end{aligned} \quad (6)$$

where  $\sin c(a) = \sin(\pi a) / (\pi a)$ . The last two phase terms in Equation (6) are the residual video phase (RVP) term and the range skew term respectively, and they are easy to be compensated because the range profiles are Sinc functions with very narrow widths. After phase compensation, the Equation (6) can be rewritten as:

$$S_{if}(f_i, t_m) = T_p \sin c \left[ T_p \left( f_i + 2 \frac{\gamma}{c} (R_0 - R_{ref} + a_v \sin(2\pi f_v t_m)) \right) \right] \cdot \exp \left( -j \frac{4\pi f_c}{c} (R_0 - R_{ref} + a_v \sin(2\pi f_v t_m)) \right) \quad (7)$$

According to characteristics of the Sinc function, it has a peak at  $f = -2\gamma R_\Delta / c$ , and its 3 dB width is  $0.886 / T_p$ . Consequently, the range resolution of the radar system is:

$$\rho_r = \frac{0.886}{T_p} \cdot \frac{c}{2\gamma} = \frac{0.886c}{2B} \approx \frac{c}{2B} \quad (8)$$

It could be seen from the range profile in Equation (7) and the range resolution in Equation (8) that: vibration of the platform or the targets has no effect on the range resolution, but a position modulation of the range profiles, and the modulation amplitude and the modulation frequency just equal to the amplitude and frequency of the vibration. The range resolution of a microwave radar is commonly on the decimeter level, and vibrations on the level of millimeter or even micrometer are usually can be neglected. However, the terahertz radar can reach a range resolution of centimeter or even millimeter level due to the large bandwidth of the transmitting signal. In this situation, compensation or correction operations are often necessary if high quality imaging results are required. Considering that  $t_m \in [-T_m / 2, T_m / 2]$  and  $R_0 - R_{ref} = y_{p,0}$ , the Equation (7) can be written as:

$$S_{if}(f_i, t_m) = T_p \sin c \left[ T_p \left( f_i + 2 \frac{\gamma}{c} R_\Delta \right) \right] \cdot \text{rect} \left( \frac{t_m}{T_m} \right) \exp \left( -j \frac{4\pi f_c}{c} (x_{p,0} \omega t_m + y_{p,0} + a_v \sin(2\pi f_v t_m)) \right) \quad (9)$$

If no phase term associated with vibration existed, the ISAR image can be written as:

$$\begin{aligned} S_{if}(f_i, f_m) &= K \cdot FT_{t_m} \left( \text{rect} \left( \frac{t_m}{T_m} \right) \exp \left( -j \frac{4\pi f_c}{c} x_{p,0} \omega t_m \right) \right) \\ &= K T_m \sin c \left[ T_m \left( f_m + \frac{2f_c}{c} \omega x_{p,0} \right) \right] \end{aligned} \quad (10)$$

where  $K = T_p \sin c \left[ T_p \left( f_i + 2 \frac{\gamma}{c} R_\Delta \right) \right] \exp \left( -j \frac{4\pi f_c}{c} y_{p,0} \right)$  is the part unrelated to  $t_m$  in Equation (9). The azimuth resolution is:

$$\rho_a = \frac{0.886}{T_m} \cdot \frac{c}{2f_c \omega} = \frac{0.886c}{2f_c \delta\theta} \approx \frac{c}{2f_c \delta\theta} \quad (11)$$

If the phase term associated with vibration is considered, it can be decomposed as follow according to the Jacobi-Anger expansion.

$$\exp\left(-j\frac{4\pi f_c}{c}a_v \sin(2\pi f_v t_m)\right) = \sum_{-\infty}^{\infty} J_n\left(-\frac{4\pi f_c}{c}a_v\right) \exp(j2\pi n f_v t_m) \quad (12)$$

where  $J_n(\cdot)$  is the n-order Bessel function. The ISAR image can be expressed:

$$\begin{aligned} S_{if}(f_i, f_m) &= K \cdot FT_{t_m} \left\{ \begin{aligned} &\text{rect}\left(\frac{t_m}{T_m}\right) \exp\left(-j\frac{4\pi f_c}{c}x_{p,0}\omega t_m\right) \cdot \\ &\left( \sum_{-\infty}^{\infty} J_n\left(-\frac{4\pi f_c}{c}a_v\right) \exp(j2\pi n f_v t_m) \right) \end{aligned} \right\} \\ &= K \cdot \sum_{-\infty}^{\infty} J_n\left(-\frac{4\pi f_c}{c}a_v\right) T_m \sin c\left(T_m\left(f_m + \frac{4\pi f_c \omega}{c}x_{p,0} - 2\pi n f_v\right)\right) \end{aligned} \quad (13)$$

As can be seen from the comparison between Equation (10) and Equation (13), the azimuth expression is no longer a Sinc function, but the sum of series of Sinc functions modulated by Bessel functions because of the influence of the vibration. The azimuth resolution in this situation will deteriorate, and the deterioration factor is proportional to the carrier frequency. So the deterioration factor in the terahertz band is much greater than that in the microwave band. Besides that, interference signals in azimuth will emerge.

### 3 Imaging experiments

#### 3.1 The terahertz radar system

The imaging radar system adopted in this paper is based on the FMCW principle and has 221 GHz of carrier frequency with a synthetic bandwidth of 12.8 GHz, thereby realizing a 1.17 cm theoretical range resolution. The 0.22 THz radar system consists of five modules: the signal source, transmitting and receiving chains, cone-shaped horn antennas, the intermediate frequency (IF) module, and the data collection module. The terahertz signal is transmitted by a horn antenna after 16 times frequency multiplication of a Ku-band (13.45-14.25 GHz) sweeping generator in the transmitting chain, and the transmitting power is greater than 3 mW. The differential frequency in sweeping generators between the transmitting chain and the receiving chain is 60MHz. Through harmonic mixing, the received terahertz signal is down-converted to IF for super heterodyne reception. A photo of the 0.22 THz radar system's transmitting/receiving front-ends is shown in Figure 2.

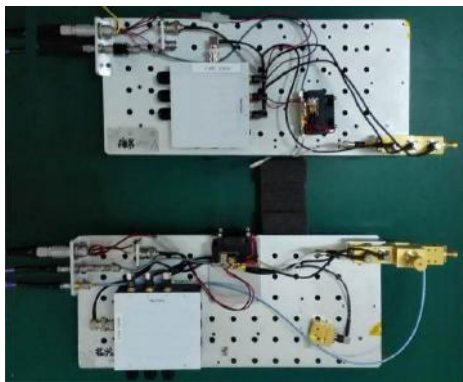


**Figure 2.** The transmitting/receiving front-ends

### 3.2 Imaging experiments

The target is placed on a turntable at a distance of 4m from the radar system, and the reference distance is 4m as well. The angular velocity of the turntable is  $30^\circ/\text{s}$ . The synthetic aperture time  $T_m$  is 0.1s, which realizes a 1.3 cm theoretical range resolution. The radar system and the targets are placed in an absorbing chamber during the experiments. The experiment scene is shown in Figure 3, and the imaging results of a corner reflector at different vibration situations are shown in Figure 4.

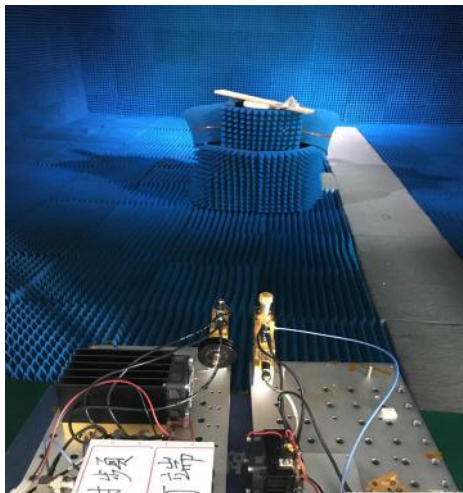
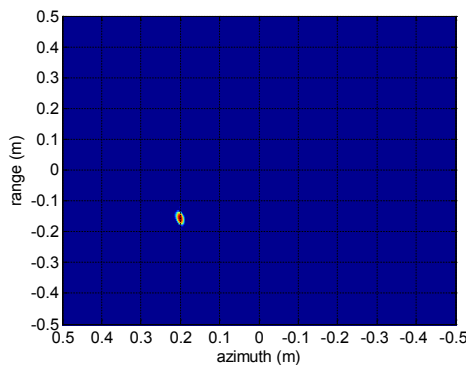
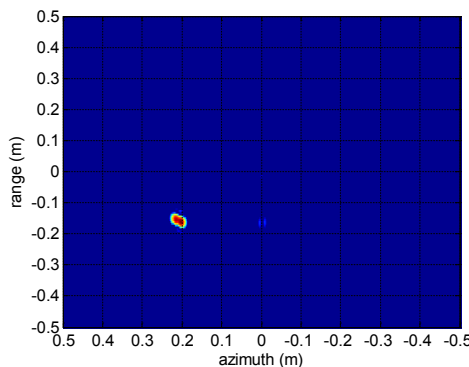


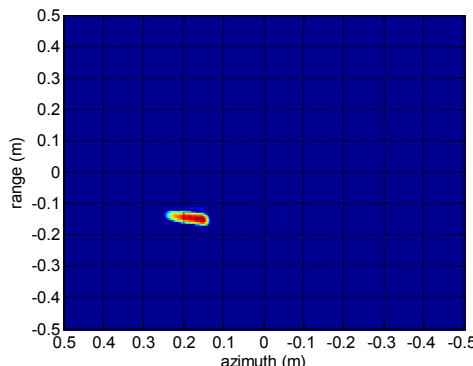
**Figure 3.** The experiment scene



(a)



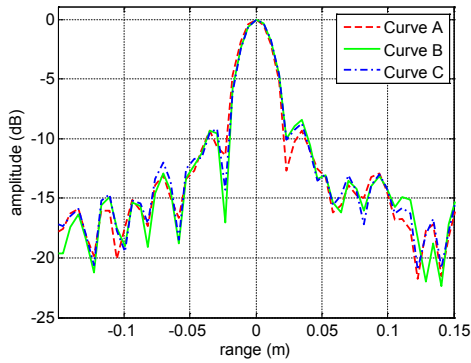
(b)



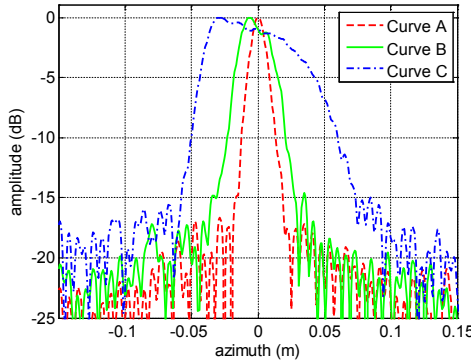
(c)

**Figure 4.** The imaging results of a corner reflector: (a) is the imaging result when the platform doesn't vibrate. (b) is the imaging result when the platform vibrates on the micrometer level. (c) is the imaging result when the platform vibrates on the millimeter level.

The range and azimuth resolutions of the imaging result in Figure 4 are shown below, and it validates the conclusion that: vibration of the platform or the targets has no effect on the range resolution, but will deteriorate the azimuth resolution. Curve A, B and C in the Figure respectively correspond to the imaging results in Figure 4a, 4b and 4c.



(a)



(b)

**Figure 5.** The range and azimuth resolutions of the imaging result in Figure 4: (a) is the range resolution, (b) is the azimuth resolution.

For the above problem, the phase gradient autofocus (PGA) algorithm is adopted in this paper. PGA algorithm has been widely used in the SAR/ISAR field since it was proposed in 1989 due to its good robustness and fast convergence [8,9]. The azimuth resolutions of a corner reflector vibrating at different vibration situations in Figure 4 after PGA process are shown in Figure 6, and it is obvious that the azimuth resolutions after PGA are close to that when the platform doesn't vibrate.

Furthermore, experiments on a plane model are carried out and the results are shown in Figure 7 and Figure 8. The platform vibrates on the micrometer level and millimeter level in Figure 7 and Figure 8 respectively. The results show that: for

multiple scattering center targets, the performance of the PGA algorithm is very limit in the terahertz band and other high performance algorithms are a subject urgent to be studied presently.

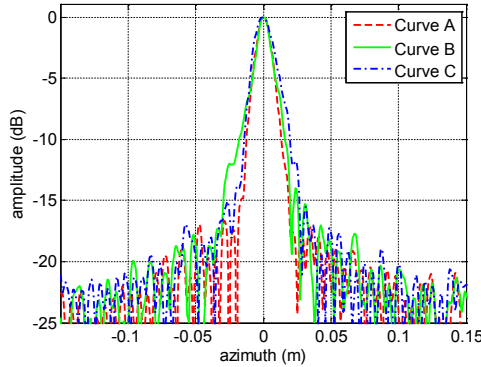


**Figure 6.** The azimuth resolution after PGA

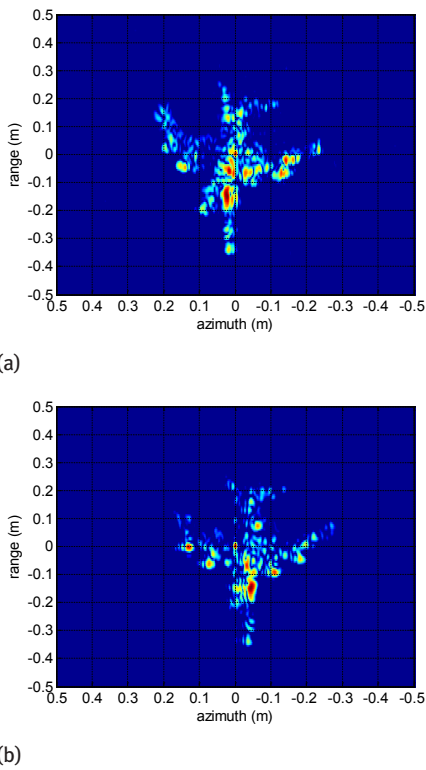


**Figure 7.** The imaging results of a plane model when the platform vibrates on the micrometer level:  
(a) is the initial imaging result, (b) is the imaging result after PGA.

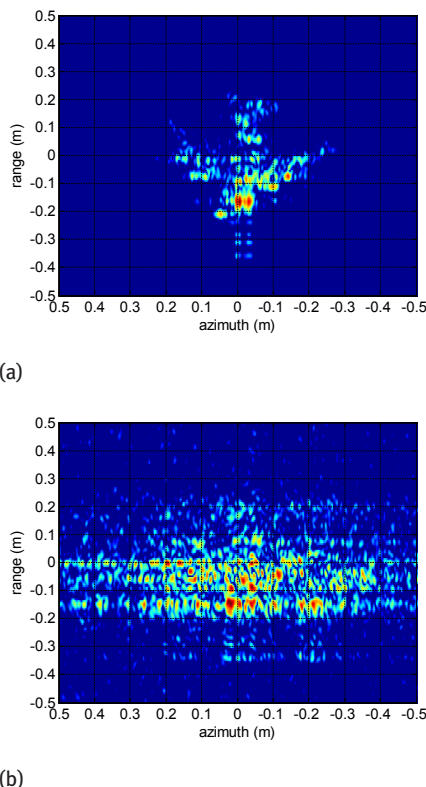


**Figure 8.** The imaging results of a plane model when the platform vibrates on the millimeter level: (a) is the initial imaging result, (b) is the imaging result after PGA.

## 4 Conclusion

The high frequency vibration is very common in the radar imaging field, and it effects more significantly in the terahertz band. In this paper, a theoretical model of the high frequency vibration of the platform in the turntable imaging mode was established, and the effects on imaging resolutions were analyzed in detail. In addition, a 0.22 THz imaging radar system is introduced and imaging experiments on a corner reflector and a plane model were presented to verify the theory analysis. Finally the PGA algorithm commonly used in the microwave radar was tried in the experiments.

## References

- [1] I. Hosako, N. Sekine, M. Patrashin, et al., At the dawn of a new era in terahertz technology, Proceedings of the IEEE. 2007; 95(8): 1611-1623.
- [2] P. H. Siege, Terahertz technology and applications, Asia Pacific Microwave Conference, Kyoto, Japan, 2002.
- [3] J. A. Trischman, J. R. Bennetta, K. A. Melendeza, B. F. Summersa, J. Sorensena and K. B. Cooperb, et al., Inverse synthetic aperture radar Imaging at 580 GHz, International Conference on Infrared. 2008: 1-2.
- [4] H. Wang, Z. Yuan, B. Wang, J. Sun, A novel helicopter-borne terahertz SAR imaging algorithm based on Keystone transform, International Conference on Signal Processing. 2014: 1958-1962.
- [5] BC. Barber, Some effects of target vibration on SAR images, European Conference on Synthetic Aperture Radar. 2008:1-4.
- [6] Q. Wang, M. Pepin, A. Wright, R. Dunkel, et al., Reduction of vibration-induced artifacts in synthetic aperture radar imagery, IEEE Transactions on Geoscience & Remote Sensing. 2014; 52(6): 3063-3073.
- [7] Y. Zhang, J. Sun, G. Wang, Moving target vibration estimation in SAR Using Chirp Modulation and Autofocus, Radar Conference. 2014; 33(5): 1311-1320.
- [8] DE. Wahl, PH. Eichel, DC. Ghiglia, CV. Jakowats, Phase gradient autofocus — a Robust Tool for High Resolution SAR Phase Correction, IEEE Transactions on Aerospace & Electronic System. 1994; 30(3): 827-835..
- [9] KS. Kim, EJ. Yang, HK. Chan, SC. Park, Impovement of ISAR autofocusing performance based on PGA, Journal of the Korea Institute of Military Science & Technology. 2014; 17(5): 680-687.

Yu-jia SUN\*, Bo DU, Chen WU, Xian-quan HAN

# Object Tracking for Satellite Video based on Kernelized Correlation Filters and Three Frame Difference

**Abstract:** Recently, correlation filters have yielded lots of promising results in the field of target tracking. However, when dealing with object tracking in satellite video, KCF tracker achieves poor results, because the size of the target is too small compared with the whole image, and the target and background are exactly similar. So, in this paper, we introduce the KCF tracker to the satellite video and propose the three frame difference algorithm to improve the performance of KCF tracker. For the purpose of reducing the probability of drifting in KCF tracker, a simple but effective target detection method: three frame difference algorithm is utilized to locate the target every once a few frames. Based on combining the KCF tracker and three frame difference algorithm, the proposed tracker achieves outperform top ranking trackers such as Struck and TLD on two datasets.

**Keywords:** correlation filters; satellite video; object tracking; frame difference

## 1 Introduction

Remote sensing satellite image processing has attracted lots of attention, and has been widely used in many applications [1-3]. Recently, commercial satellite has achieved great process in using the remote sensing devices to capture VHR satellite videos. Remote sensing videos have great potentials in traffic flow detection, forest cover dynamic monitoring, flood disaster monitoring, etc. According to 2016 IEEE GRSS Data Fusion Contest, a high-definition video with the spatial resolution of 1m from the International Space Station (ISS) was released [4], and has drawn much attention about object recognition and tracking for the cars, vessels and buildings. The Jilin No.1 commercial satellite produced by China can provide VHR satellite videos at 0.74-m spatial resolution. Those advancements prove that it is possible to research object tracking in satellite video.

Generally, tracking algorithms can be categorized into two classes, which are generative model [5-8] and discriminative model [9-14,18,19] based on their

---

\*Corresponding author: Yu-jia SUN, School of Computer, Wuhan University, Wuhan, China, E-mail: 1527927373@qq.com

Bo DU, School of Computer, Wuhan University, Wuhan, China

Chen WU, International School of Software, Wuhan University, Wuhan, China

Xian-quan HAN, Changjiang River Scientific Research Institute, Wuhan, Wuhan, China

representation schemes. In generative model, tracking is treated as a problem of searching for the region within a neighborhood, which is most similar to the target object. A variety of search algorithms based on generative model have been employed to estimate object state. For instance, 11-tracker [5] used a sparse linear combination of the target and the trivial fragmental templates to establish a target model. Adam et al. [6] designed an appearance model by utilizing some information fragments to deal with pose variation and partial occlusion. When compared with the generative algorithms, the discriminative methods have attracted wider attention due to their exploitations to the information of target and background. They treat object tracking as a binary classification problem. Hare et al. [9] utilized a large number of image features to train a classifier based on the Structured Output Support Vector Machine and Gaussian kernels. Z. Kalal. [11] uses a set of structure constraints to guide the sampling process of a boosting classifier.

Recently, tracking methods based on the correlation filters have been proved to obtain good performance in object tracking problem. Henriques et al. [14] proposed kernelized correlation filter (KCF) algorithm to conduct dense sampling in the area around the target, and transformed the computation into Fourier domain. It can take advantage of abundant information of negative samples by dense sampling. Besides, KCF transforms the computation from the spatial domain into the Fourier domain by constructing a circulant matrix. As a result, the computational cost is reduced substantially. Many following studies show that trackers based on KCF are far ahead of other trackers evaluated on CVPR 2013 OOTB.

For a VHR image, the total number in a frame can be up to six million pixels, more than 100 times of the normal frame, and the resolution of satellite imagery is much less than natural image. Those factors will lead to higher probability for tracking window drift. Due to the fact that the surroundings in satellite video suffer less changes, we utilize the three frame difference method to detect moving objects. With assistance from three-frame-difference method, the drift offset caused by KCF in object tracking can be reduced.

So, in this paper, we propose a novel tracker algorithm based on the KCF and three frame difference. KCF tracker is employed for it takes full advantage of negative samples in VHR image and high speed in object tracking. To reduce drift error, a simple but efficient target detection algorithm, three frame difference, is used to detect the target. The flowchart of the proposed method is shown in Figure 1.

The rest of this paper is organized as follow. In Section II, we introduce the proposed algorithm. Section III provides experimental results. A conclusion is given in Section IV.

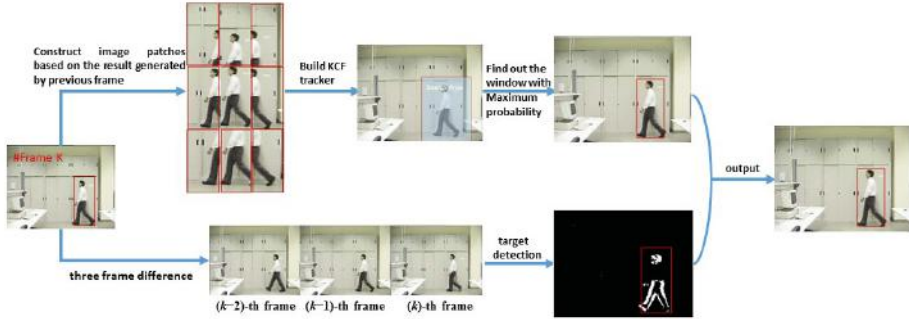


**Figure 1.** A system flowchart of the proposed algorithm. We can generate many image patches by circulant matrix based on the result from prior frame. KCF tracker is built by training the image patches, and then searches the area around the base image sample. It will Find the target location according to the maximum response value of the classifier. Besides, three-frame-difference is utilized to detect the target every given frames. Combine the KCF and three-frame-difference, the proposed tracker is able to get a good performance in object tracking

## 2 Methodology

### 2.1 Three Frame Difference

For a given video sequences, we mark the current frame as k-th frame and the previous frame as (k-1)-th frame. A binary image will be acquired by the formula (1):

$$D(x, y) = \begin{cases} 1, & |f_k(x, y) - f_{k-1}(x, y)| \geq T \\ 0, & |f_k(x, y) - f_{k-1}(x, y)| < T \end{cases} \quad (1)$$

T is a threshold, which is manually set according to experiment result. If T is set oversize, the target may be miss-detected. If T is set undersize, too much noise will be detected.

Wojcik and Kaminski [15] proposed the three frame difference method. For three sequential frames: (k-1)-th, k-th and (k+1)th, firstly we calculate the  $D_1(x, y)$  through the k-th frame subtracting the (k-1)-th frame, and  $D_2(x, y)$  through the (k+1)th frame subtracting the k-th frame. And then, we get the result  $D(x, y)$  through  $D_1(x, y) \cap D_2(x, y)$ . This method is shown as follows:

$$D_1(x, y) = \begin{cases} 1, & |f_k(x, y) - f_{k-1}(x, y)| \geq T \\ 0, & |f_k(x, y) - f_{k-1}(x, y)| < T \end{cases} \quad (2)$$

$$D_2(x, y) = \begin{cases} 1, & |f_{k+1}(x, y) - f_k(x, y)| \geq T \\ 0, & |f_{k+1}(x, y) - f_k(x, y)| < T \end{cases} \quad (3)$$

$$D(x, y) = \begin{cases} 1, & D_1(i, j) \cap D_2(i, j) = 1 \\ 0, & D_1(i, j) \cap D_2(i, j) = 0 \end{cases} \quad (4)$$

Compared with the two-frame-difference method, three-frame-difference method can deal with the occlusion more effectively and reduce the irrelevant noise points. Besides, three frame difference method is not sensitive to illumination variation. Figure 2 has shown the therapy of three-frame-difference method:

Comparing Figure 2d, 2e with Figure 2f, we can conclude that Figure 2f generated by three frame difference has achieved much better result than Figure 2d and 2e. For the object outline is more clear and unbroken.

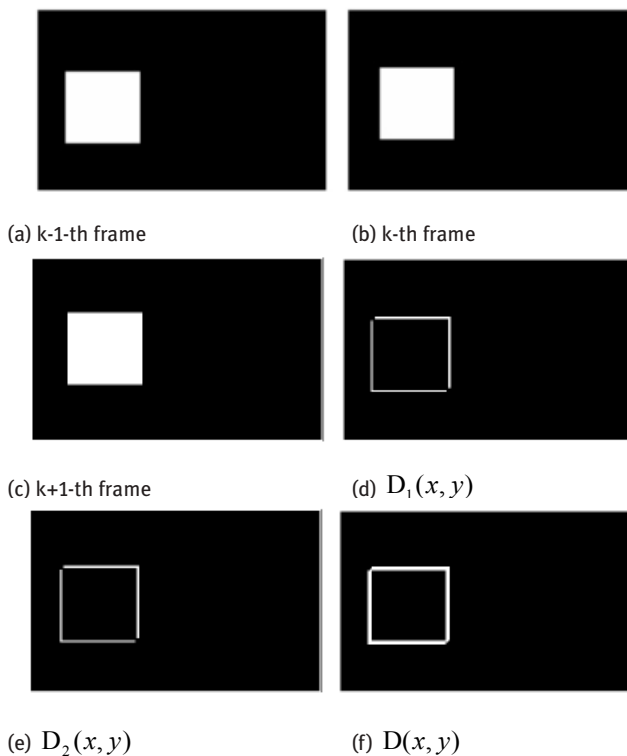


**Figure 2.** Visualization of the three frame difference.

## 2.2 Kernelized Correlation Filters Tracking

The core component of most modern trackers is a discriminative classifier, tasked with distinguishing between the target and the surrounding environment. To cope with natural image changes, this classifier is typically trained with translated and

scaled sample patches. Such sets of samples are riddled with redundancies — any overlapping pixels are constrained to be the same. Based on the simple observation, KCF [14] was proposed to take full advantages of negative samples and reduce the redundancies. Besides, KCF regards the tracking problems as regression rather than classification. For each sample, instead of labeling the positive samples as 1 and the negative samples as 0, KCF gives a value ranging in [0,1]. Similarly, Struck [9] utilizes a loss function assigning a continuous value for each sample.

A typical tracker based on correlation filter trains the classifier with a target region sample image  $X$ , and set its size to  $I \times J$ . Through circularly shifting  $X$ , shown in the (5), the method obtains numerous training samples  $x_{i,j}$ , where  $(i, j) \in \{0, 1, \dots, I-1\} \times \{0, 1, \dots, J-1\}$ .

$$X = C(x) = \begin{bmatrix} x_1 & x_2 & x_3 & \dots & x_n \\ x_n & x_1 & x_2 & \dots & x_{n-1} \\ x_{n-1} & x_n & x_1 & \dots & x_{n-2} \\ \vdots & \vdots & \vdots & \ddots & \vdots \\ x_2 & x_3 & x_4 & \dots & x_1 \end{bmatrix} \quad (5)$$

where  $x$  represents the base sample, and  $X$  represents the training samples through circularly shifting  $x$ . Figure 3 has shown the process of creating training samples based on the target region sample, which represent the 2D image. KCF utilizes a classifier to map them to the Gaussian function label  $y_{i,j}$ . Then, the algorithm models the target with the filter  $W$ . It can be achieved by searching for the minimum value using the following formula (6):

$$\min_W \sum_{i,j} |\varphi(x_{i,j} \square W - y_{i,j})|^2 + \lambda \|W\|^2 \quad (6)$$

where  $\varphi$  denotes the kernel function mapping features into a kernel space, and  $\lambda$  is a regularization parameter. Following [14], we know that  $w = \sum_{i,j} \alpha_{i,j} \varphi(x_{i,j})$ , where:

$$A = F(\alpha) = \frac{F(y)}{F(k^{xx}) + \lambda} \quad (7)$$

In (7),  $k^{xx}$  stands for the kernelized correlation [14],  $F$  is defined as the discrete operator. In this paper, we adopt a Gaussian kernel function, as:

$$k^{xx'} = \exp\left(-\frac{1}{\sigma^2} (\|x\|^2 + \|x'\|^2 - 2F^{-1}(F(x) \square F^*(x')))\right) \quad (8)$$

where  $F^{-1}$  represents the inverse Fourier transformation,  $F^*(x')$  stands for the conjugate of  $F(x')$ , and  $\square$  is the Hadamard product of the matrix.

In detecting phase, we firstly take the target location in the former frame as the central position, clip an image patch  $z$  of the size  $I \times J$  in the new frame, and compute the response value of the classifier based on (9):

$$\hat{y} = F^{-1}(A \square F(k^{\hat{x}})) \quad (9)$$

where  $\hat{x}$  is the learned target appearance model. The response value  $\hat{y}$  stands for the similarity between the candidate target and the real target. Therefore, the current position of the target can be detected by searching for the maximum value of  $\hat{y}$ , that is:

$$L = \max(\hat{y}) \quad (10)$$

Finally, we output the target location in the current frame, and take the output window as the base sample for next frame.

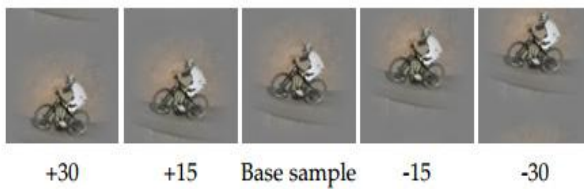


**Figure 3.** Examples of vertical cyclic shifts of a base sample. Our Fourier domain formulation allows us to train a tracker with all possible cyclic shifts of the base sample, both vertical and horizontal, without iterating them explicitly.

### 2.3 Model Update

Algorithm 1. The procedure of the proposed algorithm

---

**Input:** video frame ( $t$ ) and  $l_{t-1}$

---

Method:

1. Sample a set of image batches based on  $l_{t-1}$ , where  $l_{t-1}$  is the tracking result at previous frame.
  2. Each image patch is imposed a weighting factor for showing the similarities with the result at previous frame based on distance between the pixels.
  3. Build the KCF tracker by training the image patches in step (b) In order to reduce the probability of overfitting, we add a 2-norm to control kernel function.
  4. Every a few frames, three frame difference is utilized to detect the target and output  $l_t$  and  $l_t$  will be used as input for step 1).
  5. Find out the maximum value of  $\hat{y}$ , Image patch with the max value L will be selected as tracking result. Combine the step (4) to output  $l_t$ .
- 

**Output:** tracking location  $l_t$

---

For the most time, KCF tracker is employed for its high speed and reluctant accuracy in satellite video. KCF tracker will drift and lost its target for two factors. First, the target in VHR image contains less information, for its size is too small compared with

the whole image. Second, target and background is exactly similar in VHR image. In this paper, we introduce the three frame difference to correct the drifting error caused by KCF tracker. The specific strategy is that every a few frames or the tracking window drifts drastically, three frame difference is used to detect the target and outputs the result. The output window will be used as the input window for KCF tracker. Repeat this process, proposed tracker will track the target at high accuracy and acceptable speed (50fps).

Generally, the proposed tracker utilize three frame difference to correct the error generated by KCF tracker. The basic procedure of our algorithm is presented in the following table Algorithm 1, and Figure 1 shows the pseudo-code of the proposed algorithm.

## 3 Experiment

### 3.1 Implementation Details

Since the satellite video data is relatively scarce, we acquire two videos generated from the 2016 IEEE Data Fusion Contest, Deimos Imaging and UrtheCast, and Chang Guang Satellite CO., LTD. The first video describes the traffic conditions of a harbor in Canada, and the second video describes the traffic conditions of New Delhi. The scene sizes of the three videos are all  $3840 \times 2160$  pixels. Both the two videos contains 1024 frames. To make our work more meaningful, we select the moving trains as the targets. Figure 4 shows the detail of two datasets. Besides, we initialize the position of the first frame, and evaluate the proposed algorithm by comparing the output window with the ground truth window. For comparison, 3 state-of-art tracking algorithm, TLD [11], STRUCK [9] and KCF [14] are employed to evaluate the proposed algorithm. The three trackers have been proved achieving top performances in CVPR 2013 OOTB datasets.

The proposed algorithm is implemented in C++ Opencv library on 8G memory with 3GHz desktop. The speeds of the proposed algorithm with HARR-LIKE feature [17] and raw pixels are 40 fps and 50 fps. The size of the searching window is set 1.5 times of the target size. The  $\sigma$  used in Gaussian function is set to 0.5, the cell size of HARR is  $4 \times 4$  and the orientation bin number of HARR is 9. The regularization  $\lambda$  is set  $10^{-4}$ . We set  $T$  in (2), (3) as 10 to apply the three frame difference method to reduce the probability of drifting.

### 3.2 Evaluation

Bounding box overlap and the average center location error referring to [16] are provided to make more quantitative comparisons. Table 1 shows the average center

location errors (in pixel). Table 2 shows the average bounding box overlap score (%). Figure 5 shows some representative screenshots about the two video sequences.

To make the comparisons more quantitative, Table 1 and Table 2 show the accurate results according to the CLE and OS. The best performance was marked with red bold digits and second best performance was marked with blue bold digits. The character “X” in the Table 1 and Table 2 represents the tracker fails on the dataset completely. On all the two datasets, the proposed algorithm ranks first and second. TLD and STRUCK didn’t perform well, even losing the target completely, although these three algorithms have achieved outstanding results in the CVPR 2013 OOTB.

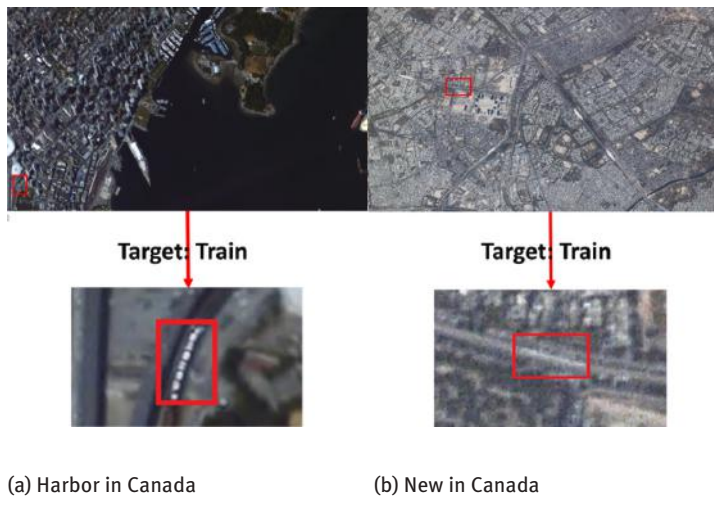


**Figure 4.** Details of Two datasets evaluated in our experiments are listed.

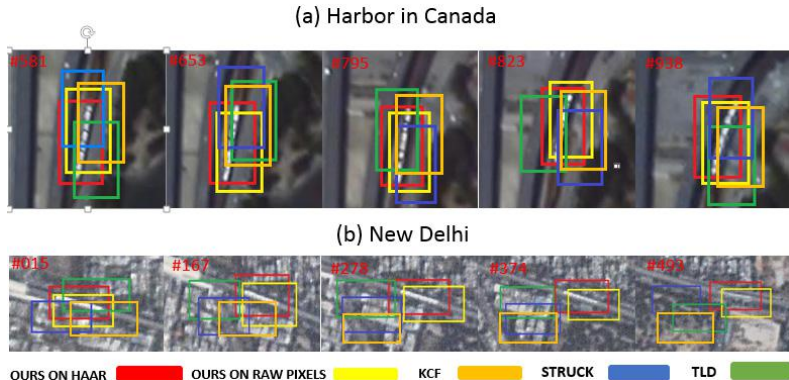


**Figure 5.** Screenshots of Some Three Videos Tracking Results

**Table 1.** Average Center Location Errors (in pixel)

	<b>OURS ON HAAR-LIKE</b>	<b>OURS ON RAW PIXEL</b>	<b>KCF</b>	<b>TLD</b>	<b>STRUCK</b>
Canada	<b>12</b>	<b>13</b>	17	18	15
New Delhi	<b>9</b>	<b>11</b>	X	X	X
Average CLE	<b>11</b>	<b>14</b>	X	X	X

**Table 2.** Average Bounding Box Overlap Score (%)

	<b>OURS ON HAAR-LIKE</b>	<b>OURS ON RAW PIXEL</b>	<b>KCF</b>	<b>TLD</b>	<b>STRUCK</b>
Canada	<b>68.46</b>	<b>57.37</b>	48.21	48.46	57.34
New Delhi	<b>61.38</b>	<b>51.64</b>	X	X	X
Average CLE	<b>64.91</b>	<b>53.85</b>	X	X	X

## 4 Conclusion

In this paper, a new algorithm based on kernelized correlation filters and three frame difference is proposed for object tracking in satellite video. Given the speed and accuracy of the tracker, for the first time, we introduce the kernelized correlation tracking to high resolution satellite video, and combine three frame difference method to reduce the drift raising by the original KCF tracker. Combining KCF and three frame difference, we can deal with the satellite video tracking accurately at the acceptable speed, such as 40 fps on HARR feature and 50 fps on raw pixel. Three satellite video datasets were used to evaluate the proposed algorithm with three state-of-the-art trackers. The experiments show that proposed algorithm on HARR feature ranks first, and the proposed algorithm on raw pixel ranks second according to the CLE and OS. Therefore, it is proved that the proposed algorithm is a robust and efficient method to deal with tracking in the satellite video.

**Acknowledgment:** The authors would like to thank Deimos Imaging and Chang Guang Satellite CO., LTD. for acquiring and providing the data used in this study, and the IEEE GRSS Image Analysis and Data Fusion Technical Committee. This work was supported by the China Postdoctoral Science Foundation under Grant 2015M580667, the Fundamental Research Funds for the Central Universities under Grant 20420.

16kf0034, National Natural Science Foundation of China under Grant No.41301434 and Open Foundation of Basic Scientific Research Operating Expenses of Central-Level Public Academies and Institutes (CKSF2015020/GC).

## References

- [1] Chen, Xueyun, Vehicle detection in satellite images by hybrid deep convolutional neural networks. In GRSL, vol. 11, no. 10, pp. 1797-1801, 2014.
- [2] Li X, Liu Y, Aircraft Detection Based on Shadow Affect in Optical Remotely Sensed Imagery in CSMA, pp. 215-222, 2015.
- [3] Li, Yansheng, et al. Unsupervised multilayer feature learning for satellite image scene classification. In GRSL, vol. 13, no. 2, pp. 157-161, 2016.
- [4] 2016 IEEE GRSS Data Fusion Contest. Online: [www.grss-ieee.org/community/technical-committees/data-fusion](http://www.grss-ieee.org/community/technical-committees/data-fusion).
- [5] X. Mei and H. Ling, Robust visual tracking and vehicle classification via sparse representation, in TPAMI, vol. 33, no. 11, pp. 2259–2272, Nov. 2011.
- [6] A. Adam, E. Rivlin, and I. Shimshoni, Robust fragments-based tracking using the integral histogram, in CVPR, Jun. pp. 789–805, 2006.
- [7] D. Ross, J. Lim, R. Lin, and M. Yang, Incremental Learning for Robust Visual Tracking, in IJCV, vol. 77, nos. 1-3, pp. 125-141, Aug. 2007.
- [8] Ding, J., et al. Severely Blurred Object Tracking by Learning Deep Image Representations. In TCSV, Feb. 2015.
- [9] S. Hare, A. Saffari, and P. Torr, Struck: Structured output tracking with kernels, in ICCV, 2011.
- [10] K. Zhang, L. Zhang, and M.-H. Yang, Real-time compressive tracking, in ECCV., pp. 864–877, 2012.
- [11] Z. Kalal, K. Mikolajczyk, and J. Matas, Tracking learning detection, in TPAMI, vol. 34, no. 7, pp. 1409–1422, Jul. 2012.
- [12] Grabner, M. Grabner, and H. Bischof, Real-Time Tracking via Online Boosting, in BMVC, pp. 47-56, 2006.
- [13] B. Babenko, M.-H. Yang, and S. Belongie, Visual Tracking with Online Multiple Instance Learning, in TPAMI, pp. 983–990, 2009.
- [14] Henriques, João F., et al. High-speed tracking with kernelized correlation filters. in TPAMI, pp. 583-596, 2015.
- [15] Grzegorz M. Wojcik, Wieslaw A. Kaminski. Liquid state machine built of Hodgkin-Huxley neurons and pattern recognition. Neurocomputing. pp. 245-251, 2004.
- [16] Y. Wu, J. Lim, and M.-H. Yang, Online Object Tracking: A Benchmark, in CVPR, pp. 2411–2418, 2013.
- [17] Lienhart R, Maydt J. An extended set of Haar-like features for rapid object detection [J]. vol.1. 2002.
- [18] Y. Wu, B. Shen, and H. Ling, Online robust image alignment via iterative convex optimization, in CVPR, pp. 1808–1814, 2012.
- [19] D. S. Bolme, J. R. Beveridge, B. A. Draper, and Y. M. Lui, Visualobject tracking using adaptive correlation filters, in CVPR, pp. 2544–2550, 2010.

Fan LI, Rui MO, He-lun SONG \*, Yao-hui ZHANG

## **Noise Removal and Detail Enhancement of Passive Infrared Image Pretreatment Method for Robot Vision**

**Abstract:** In order to explore the usefulness of thermal infrared imaging as a mobile robot sensing modality and to make feature extraction more effective and accurate, an algorithm for noise removal and detail enhancement of the blurred infrared image based on Guided filter has been raised in this paper. We first used a guided filter to smooth the input image and separate it into a base layer and a detail layer. Then constraining the gradient of the detail will get a reliable halo free detail layer and using gain mask to enhance it later. Meanwhile, the base layer controls the gray scale contrast which also needs to be processed with adaptive histogram equalization. Finally, the two parts of the image combined with weighted coefficients will be exported into the second guided filter. This method has the advantages of computational simplicity and a great performance. Many experiments and illustrations have been made to prove its effectiveness in improving the perception ability of vision system for a mobile robot.

**Keywords:** infrared thermal image; guided filter; detail enhancement; noise removal; robot vision

### **1 Introduction**

The properties of infrared thermal imaging technology make it not only visually display the object surface temperature field in the form of pictures, but also enable it to show the environment and identify targets highly robustly to changing lighting conditions and other environmental effects. It is a relatively new field to exploit the thermal infrared imaging as a mobile robot sensing modality, such as being used for mobile robot object Identification [1], Simultaneous Localization And Mapping (SLAM) [2].

However, compared with a visible light camera, the context of infrared images in the video-based SLAM system has some most serious challenges:

- Limited resolution
- High noise
- Low contrast
- Poor texture distribution

---

\*Corresponding author: He-lun SONG, Suzhou Institute of Nano-Tech and Nano-Bionics, Chinese Academy of Sciences, Suzhou, China, E-mail: hlsong2008@sinano.ac.cn

Fan LI, Rui MO, Yao-hui ZHANG, Suzhou Institute of Nano-Tech and Nano-Bionics, Chinese Academy of Sciences, Suzhou, China

The four listed disadvantages of infrared thermal imaging have a great influence in achieving a large number of reliably tracked features between frames in a thermal-infrared video sequence [3]. Therefore, infrared image pretreatment method is meaningful and necessary for robot vision.

Most researchers' work about passive infrared image pretreatment is for the purpose of human vision, which is different from robot vision. Moreover, we need to not only deal with the higher temperature object of the infrared image, but also focus on the blurred infrared image with no significant difference in temperature or the background part of the heat source object. In this paper, we introduce a pretreatment method that aims at enhancing the details, preventing noise amplification and removal unwanted halo artifacts effectively.

## 2 The principle of the proposed algorithm

The basic strategy of our proposed algorithm is that a guided filter could smooth the input image and separate it into the base layer and the detail layer. Then high frequency information is enhanced by our modified certain strategy in the detail layer. Meanwhile, the base layer controls the gray scale contrast which also needs to be processed with histogram equalization. Finally, the two parts of the image combined with weighted coefficients, the assembled image will more smooth and less noisy after exported into the second guided filter. The completed processing pipeline is schematically illustrated in Figure 1. Since the GIF is the key to our algorithm, we first give a fast review on how the GIF works.

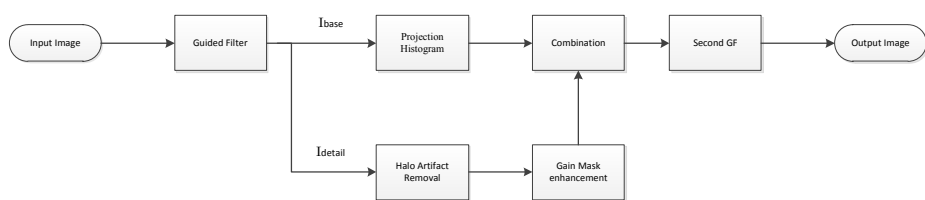


**Figure 1.** The proposed method block diagram

### 2.1 Guided Image Filtering [4]

The guided Image filter smooths an input image  $p$  under the guided image  $I$ . A local linear model assumes that filtered output  $q$  is expressed by a linear function of  $I$  in a window  $\omega_k$  centered at pixel  $k$ :

$$q_i = a_k I_i + b_k, \forall i \in \omega_k \quad (1)$$

where  $(a_k, b_k)$  are some linear coefficients assumed to be constant in window  $\omega_k$ . A square window is used in the original formula of 2D guided filtering. We can determine the linear coefficients by minimizing the difference between  $q$  and  $p$ .

$$E(a_k, b_k) = \sum_{i \in w_k} ((ak_i + b_k - p_i)^2 + \epsilon a_k^2) \quad (2)$$

The least squares solution of (2) is given as:

$$a_k = \frac{\frac{1}{|w|} \sum_{i \in w_k} l_i p_i - \mu_k \bar{p}_k}{\sigma_k^2 + \epsilon} \quad (3)$$

$$b_k = \bar{p}_k - a_k \mu_k \quad (4)$$

where  $\mu_k$  and  $\sigma_k^2$  are the mean and variance of  $I$  in  $w_k$ ,  $|w|$  is the number of pixels in,  $w_k$  and  $\bar{p}_k$  is the mean of  $p$  in  $w_k$ . Because each pixel lies in the overlapping windows, then a pixel's smooth result is the average of multiple estimates, we rewrite the final Equation:

$$q_i = \bar{a}_i I_i + \bar{b}_i \quad (5)$$

where  $\bar{a}_i = \frac{1}{|w|} \sum_{k \in w_i} a_k$  and  $\bar{b}_i = \frac{1}{|w|} \sum_{k \in w_i} b_k$  are the average coefficients of all windows overlapping  $i$ .

## 2.2 Histogram Redistribution for base component

A projection histogram is very suitable in image dynamic range compression [5]. Because the basic level of detail is less, and the dynamic range is large, so it can be compressed directly without taking into account the loss of details. In this paper, we use the improved projection histogram technique.

Firstly, with statistical image histogram information  $H(x)$ , the histogram of the base layer is binarized by a threshold  $T$ . The number of pixels in the histogram is greater than the gray value of  $T$  marked as 1, otherwise marked as 0. Then the cumulative histogram distribution is obtained by the histogram  $D(x)$ :

$$H(x) = \begin{cases} 0, & n_x < T \\ 1, & n_x \geq T \end{cases} \quad (6)$$

$$D(x) = \begin{cases} 0, & x = 0 \\ \frac{\sum_{y=0}^{x-1} H(y)}{n_{\text{valid}}}, & \text{other} \end{cases} \quad (7)$$

The maximum range of output image  $R$  as:

$$R = \min(n_{\text{valid}}, D) \quad (8)$$

where  $n_{\text{valid}}$  denotes the total number of the valid gray levels and  $D$  is the dynamic range of a monitor. This limit ensures that the output image gray level range does not exceed the display effective display range. Taking into account it that the image background

is relatively simple and effective gray level is relatively small, the histogram could be distorted and full of noise. Here we focus on how to raise the output value in a better and more effective way. The histogram projection output is modified as follows:

$$I_{BP} = \frac{D-R}{Pare} + \frac{D(I_B)*R}{n_{valid}} \quad (9)$$

Pare is a controllable parameter for fine tuning the output brightness. To ensure that the output gray level is less, then the output image will not be compressed to a very low brightness.  $I_{BP}$  is the basic layer after histogram redistribution.

### 2.3 Removal of halos Artifacts

Though the guided filter is better than bilateral filter about avoiding the gradient reversal artifacts may appear in detail enhancement detail enhancement for high-dynamic-range infrared images which have been run through a Guided Filter produce halos near some edges [6]. The problem is more acute when enhance the Larger multiples of details, so requires a reliable halo free detail layer.

In [7] prevent gradient reversal by directly constraining the gradient of the detail. We also force the detail derivatives and the input derivatives to have the same sign. However, For the Guided filter's better edge preserving performance avoid gradient reversal, we modify the detail's gradient by an amplification parameter:

$$\frac{\partial p'}{\partial x} = \begin{cases} 0 & \text{if } \text{sign}(\frac{\partial p}{\partial x}) \neq \text{sign}(\frac{\partial q}{\partial x}) \\ \frac{\partial q}{\partial x} & \text{else if } \left| \frac{\partial p}{\partial x} \right| > \delta \left| \frac{\partial q}{\partial x} \right| \\ \frac{\partial p}{\partial x} & \text{otherwise} \end{cases} \quad (10)$$

in which  $\frac{\partial p}{\partial x}$  is the x directions' gradient of original details,  $\frac{\partial q}{\partial x}$  is the x direction's gradient of input image.  $\frac{\partial p'}{\partial x}$  is the modified x directions' gradient. According to next process, the gain mask enhancement,  $\delta = 1.5$  can give out a good result. The y component is defined similarly. After modifying the gradient of detail layer, the corrected detail layer is obtained by solving the reconstruction Poisson equation:

$$\frac{\partial I}{\partial t} = \nabla I - \text{div}(v) \quad (11)$$

Here,  $I$  is the reconstructed image,  $v$  is a 2D field of 2D vectors.  $\nabla I$  is the gradient of  $I$ .

### 2.4 Gain mask enhancement for detail component

The edge-preserving filtering property of guided filter explained intuitively help us to design the gain mask [4]. Consider the case where  $I = p$ .

- |                         |                   |
|-------------------------|-------------------|
| Case 1: "High variance" | $a_k \approx 1$ . |
| Case 2: "Flat patch"    | $a_k \approx 0$ . |

We simplify the gain mask as follows:

$$T = (KH - KL)\bar{a}_i + KL \quad (12)$$

The parameter KH(the max), KL: (the min) can modify the masking function, which makes the detail enhancement more controllable. With this function we are able to enhance the detail region as much as we need, and directly using save a number of computation.

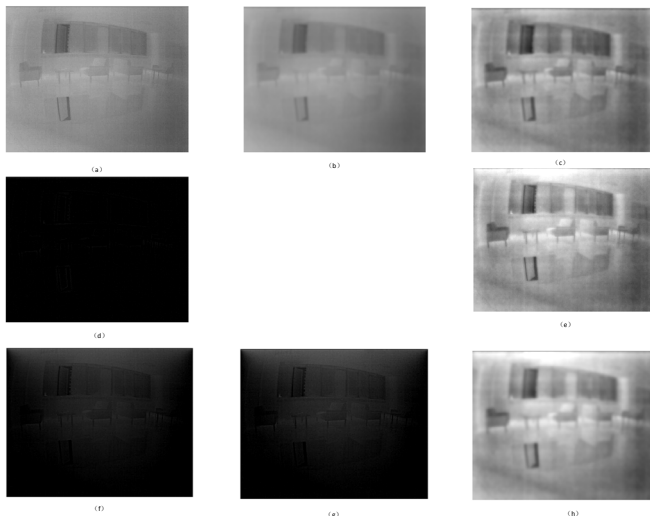


**Figure 2.** The proposed method flow chart on test image. (a) Original IR image. (b) The base layer by GF. (d) The detail layer by GF. (c) The projection histogram of base layer. (f) The halo removal of detail layer. (g) The Gain mask enhancement of (f). (e) The combination of (c) and (g). (h) The second GF of (e).

### 3 Experimental results

#### 3.1 Test images and the process of the method

The workflow of the method displays in Figure 2. In Figure 2a is the original IR image. Figure 2b and 2d are the base layer and detail layer after filtering original image by GF. Then, we first project histogram the base layer's gray levels distribution and get Figure 2c, and it can be noticed that the brightness of Figure 2c is brighter than Figure 2b. Meanwhile, we process the detail layer. As shown in the detail layer Figure 2d, there is very dark and blurry of the details because the temperature of objects in original IR image is very small. It is necessary to make sure that the detail derivatives and the input derivatives have the same sign. After applying the technique

removal of halos artifacts, the correction result in Figure 2f. Then the gain mask enhancement of Figure 2f is shown in Figure 2g. After dealing with the base layer and detail layer, Figure 2e is the combination of them. Finally, Figure 2h is the output of the second GF of Figure 2e.

The bright of the enhancement shows the details clearly. The contrast is better than original images, and the local details are perceived well. The parameters setting are as follow: the twice of GF is same as:  $r = 4$ ;  $\text{eps} = 0.5^2$ . The Gain Mask is  $KL = 1$ ;  $KH = 3$ ;

### 3.2 Comparison with two Guided filter output image

Why use a guided filter twice? This is because after the first filtering of original image, the result of the flow of process until the combination of the base layer and the detail layer is often used for human observation. However, it is not necessarily suitable for robot vision. In the process of detail enhancement will inevitably enhance some noise or interference light intensity difference the details are not needed, and micro texture are strengthened. Then the second filter not only effectively erases the increased noise and the unnecessarily details, but also highlights the key edge. We use the “canny” edge extraction algorithm for verification.

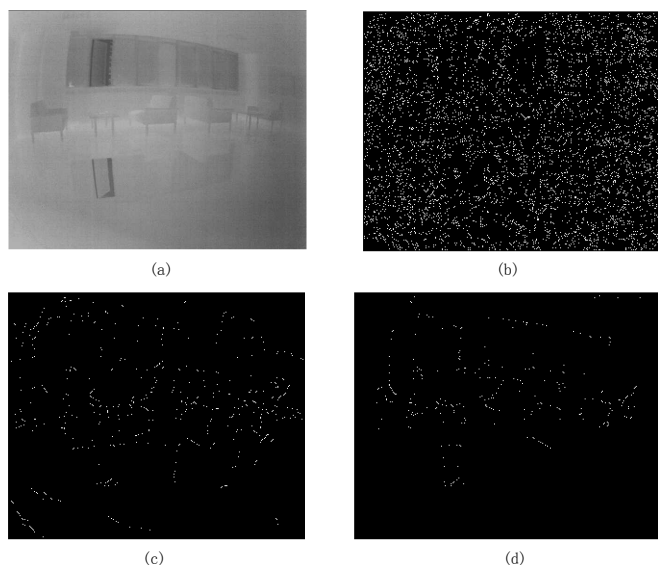


**Figure 3.** The “canny” algorithm on test image inside the hall. (a) Original IR image. (b) the edge of Original Image. (c) The edge of the first GF process. (d) The edge of the second GF.

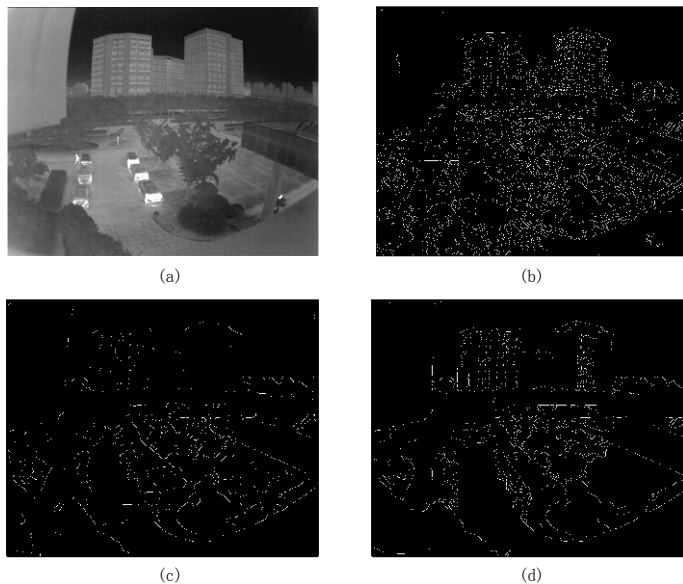


**Figure 4.** The “canny” algorithm on test image the square. (a) Original IR image. (b) The edge of Original Image. (c) The edge of the first GF process. (d) The edge of the second GF.

The results of comparison are the output edges images of three images. It is very obvious that the noise of the original image is terrible, especially the less the temperature difference is in an indoor environment. Then, the first GF has good noise removal, but the edges are cluttered and there are too many. The last edge image has a good effect to use for robot vision, and to a number of works such as SLAM.

## 4 Conclusion

In this paper, a novel HDR IR image enhancement approach is presented. Firstly, the guided filter is utilized to separate the input image into the base layer and the detail layer. Then the projection histogram to make the distribution of the base layer more evenly. Then we constrain the gradient of the detail to get a reliable halo free detail layer and using gain mask to enhance it. Finally, the two parts of the image combined can be used for human observation. In order to get less noise and only main details of image, the arranged image will be to exported into the second guided filter. The performance of HDR IR image detail enhancement of the proposed method has been demonstrated can improve the contrast, enhance the scene details effectively with less artifacts. This approach can be useful in many applications for robot vision.

## References

- [1] Fehlman Li, William L., and M. K. Hinders. Passive infrared thermographic imaging for mobile robot object identification, *Journal of Field Robotics* 1211.1(2010):2076-2083.
- [2] G. Klein and D. Murray. Parallel tracking and mapping for small AR workspaces, In International Symposium on Mixed and Augmented Reality (ISMAR), 2007.
- [3] S. Vidas and S. Sridharan, Hand-held monocular SLAM in thermalinfrared, in International Conference on Automation, Robotics, Controland Vision (ICARCV), 2012.
- [4] K. He, J. Sun, X. Tang, Guided image filter, *IEEE Trans. Pattern Anal. Mach. Intell.* 35 (6) (2013) 1397–1409.
- [5] Zhang F, Xie W, Ma G, et al. High dynamic range compression and detail enhancement of infrared images, in the gradient domain[J]. *Infrared Physics & Technology*, 2014, 67:441-454.
- [6] N. Liu, D. Zhao, Detail enhancement for high-dynamic-range infrared imagebased on guided image filter, *Infrared Phys. Technol.* 67 (2014) 138–147.
- [7] Song Q, Wang Y, Bai K. High dynamic range infrared images detail enhancement based on local edge preserving filter, *Infrared Physics & Technology*, 2016, 77:464-473.

Guang-chao ZHANG\*, Yuan GAO, Bing WANG, Yong-hui LAI

## **Failure Mechanism and Support Strategy of Deep Roadway with High Horizontal Stress and Broken Rock Masss**

**Abstract:** Stability control of deep roadways with broken surrounding rock masses is a long-standing issue for deep coal seam extraction. This paper presents an integrated investigation of failure mechanism and control strategy of such gate road based on the field investigation, numerical calculation, laboratory tests. The results demonstrated that the broken characteristic of the rock masses and the high horizontal stress are main factors for the failure of the roadways. Based on this, a new combined support strategy, incorporating high strength bolts/cables, large-tonnage yieldable long ring supports, and delayed grouting measures, was proposed and successfully applied for the field test. Field monitoring results indicated that the new combined support strategy can be treated as an effective measure for such roadway support.

**Keywords:** roadway; surrounding rock; horizontal stress; deep mine; yieldable support;

### **1 Perface**

With the exhaustion of shallow coal resources, many mines are moving deep. Deep coal roadway supports have become an important restricting subject. Among them, the high-horizontal stress fractured roadways are special in deep mines. Because of the extremely developed fault and fold, the surrounding rocks are cut by the primary structure and mining-induced fractures, the horizontal stress convert into the maximum principal stress [1]. There are problems of surrounding rock dilatancy, large bulking deformation, caving and support system damage in this kind of roadways after construction. It is hard to ensure the roadway long-term stability by the usage of the conventional support technique and operating models [2]. Through investigation, the problem of high horizontal stress and broken roadway surrounding rock control was found that it was pervasive in many deep mines. Therefore, analyzing the mechanism of deformation and failure of roadway, and finding rational and scientific surrounding rock control measures are important for the realization of safe and efficient production in such roadways.

---

\*Corresponding author: Guang-chao ZHANG, China University of mining and technology (Beijing), Beijing, China, E-mail: 874557858@qq.com

Yuan GAO, Yong-hui LAI, China University of mining and technology (Beijing), Beijing, China  
Bing WANG, Shandong energy Xinwen Mining Group Zhaoguan Coal Mine, Dezhou, China

In recent years, experts and scholars have done numerous researches and practices in deformation and failure control of surrounding rock in deep roadways, and have made a variety of control techniques and support theories. In deep high horizontal stress broken roadways, the deformation and failure characteristics and mechanism change obviously. Special support theory and control measures should be taken in this condition.

In order to ensure that the -980 roadway will be stable longer, this paper combine the complex geological conditions of the high horizontal stress broken surrounding rock in -980 roadway. Analyzing the deformation and failure characteristics, a comprehensive control system consisting of bolting and shotcreting combined support technique and large tonnage yieldable long ring support and delayed grouting reinforcement was proposed.

## 2 Engineering Background

### 2.1 Engineering Conditions

Xing Dong mine -980 roadway buried in -1040m deep is a permanent main roadway. The roadway passes through the limestone, 2# coal seam, silt and other geological layers, lithology and thickness change a lot, the fissure develops well but incomplete, and the engineering activities cause large deformation. The roadway is located at the second horizontal where has dense structures, more than ten faults have the gap above 5m. The stress test shows that the maximum principal stress is about 45MPa (horizontal direction), intermediate principal stress is about 25MPa (vertical direction), the minimum one is about 25MPa (horizontal direction), the lateral pressure coefficient is 1.5~2.0.

### 2.2 Original support pattern and strata behavior

The -980 roadway is 383m long, the straight wall arch section, 4.5\*3.5m, the initial support is bolting and shotcreting, with MG335 threaded steel bolt, and the space between the bolts is 800\*800mm, the  $\Phi=14\text{mm}$  steel bar ladder beam and  $\Phi=6\text{mm}$  cold-drawn metal mesh, C20 concrete are used as the grouting material.

There are significant squeezing and fractured belt caused by horizontally compressive movement in roof surrounding rock. The broken belt along the roadway to extend the 10~34m, swelling deformation of the surrounding rock significantly, the maximum settlement is 1.0~2.0m, many complex sections have vicious collapse, the maximum roof fall is 5~8m, resulting in a full obstruction. The deformation by sides is serious, the maximum deformation is 1.0m. The whole floor heave is serious, the maximum deformation is more than 0.5m, the middle part became a circular-

arc after the deformation. Bolt twisting, shedding, pallet damage, reinforced girder, steel mesh tearing, lining cracking happen. Roadway section is only 3.1\*1.8m. There are no choices but to arrange the maintenance team to repair the roadway because of the damaged support.

### 3 Failure mechanism analysis

#### 3.1 Broken Characteristics of Surrounding Rocks

The fractured, low mechanical strength and more susceptible surrounding rock is the direct reason of the failure of the -980 roadway. According to the boring data, part of the immediate roof is inter-bedded marl, 1.1m thick, and the uniaxial compressive strength is 35.97MPa. The roof contains plant fossils' fragments, developed joint fissures, unstable and easy caving. The main roof is 8.4m thick muddy siltstone with developed joint fissures, and it causes separation and deformation easily. The floor is sandy shale. With the effect of high-concentrated stress caused by the excavation, surrounding rocks become broken immediately; simultaneously with the obvious creep characteristics, the deformation lasts about a half year, the broken-expand surrounding rock deformation is large, and fracture depth is high.

Although MG335 high-strength fully grouted bolts has been used, considering the condition of the extreme broken surrounding rock, the bolts are not enough. Most bolts in the broken area fails. In the process of the rock deformation, the bolts move along the surrounding rock, and the rock still broken. Besides, according to the analysis of the mineral composition of the surrounding rock, there are illite and montmorillonite which are water-swelling; the water spraying and seeping, resulting in the swelling and deformation, and imposing deformation compressive stress on the support, causing the tearing of steel-mesh and the lining crack.

#### 3.2 Effect of High Horizontal Stress on Surrounding Rock Stability

As an important part of the stress of primary rocks, tectonic stress is almost horizontal. Engineering, deformation and failure of supporting, rock burst, serious floor heave, coal and gas outburst etc. dynamic disasters have a close relationship with the tectonic stress [3]. Under the condition of that, the mechanism of the failure and deformation of surrounding rock is different with the normal.

Using the FLAD<sup>3D</sup> analyses the influence law of horizontal stress on the -980 roadway surrounding rock displacement and plastic area. The model size is 40\*30\*32m, and the section of three-center arch is 5.1\*4.3m. There are displacement constraints at the bottom and horizontal direction in the model. Considering the intensity weakening during the process of the deformation of the deep surrounding

rock, strain-softening model was used in the coal seam and roof and floor [4], Mohr-Coulomb model was used for calculation, and the mechanical parameters are in Table 1.

**Table 1.** Mechanical parameters of strata

stratum	density /kg/m <sup>3</sup>	bulk/GPa	shear/Gpa	cohesion /MPa	friction/(°)
shale	2800	7.87	3.38	2.26	28
2#coal	2690	6.87	3.30	1.00	28
siltstone	2800	8.95	4.88	2.50	30
mudstone	2350	3.55	2.10	1.80	24
coal	1350	2.35	1.47	1.00	20
medium sandstone	2750	9.95	4.92	2.56	30

Research scheme: vertical stress  $\sigma_z = 25\text{ MPa}$  on the top of the model, horizontal stress  $\lambda\sigma_z$  on the horizontal direction, lateral pressure coefficients  $\lambda=1.0, 1.2, 1.4, 1.6, 1.8, 2.0$  in turn. Monitor the dynamic response pattern of the plastic area and the displacement under the condition of various horizontal stresses, and analysis the response pattern of surrounding rock stability with the horizontal stress in deep mines.

In Figure 1 when  $\lambda=1.0, 1.2$ , the plastic failure range differences among roadway's roof and floor and sides' surrounding rock are small, and the shallow surrounding rock in roof experiences tensile failure; while the sidewalls' shallow rock experiences tension-shear failure, and shear failure is the main failure for deep surrounding rock; when  $\lambda=1.4, 1.6$ , the plastic failure in sidewalls transfers to the roof and floor, and the failure range in roof and floor is larger than that in sidewalls, the shallow surrounding rock experiences the tension-shear failure, and the sidewalls shallow area experiences tensile failure; when  $\lambda=1.8, 2.0$ , the shear failure range of roof and floor rock greatly increases, and the effect of shear failure is obvious. Thus, with the increase of horizontal stress, the surrounding rock plastic failure transfers from sidewalls to roof and floor, and the depth of the roof and floor failure is large, which corresponds to the characteristics of in-situ engineering; and the plastic failure area is almost an arch. With the increase of horizontal stress, the width and height increase.

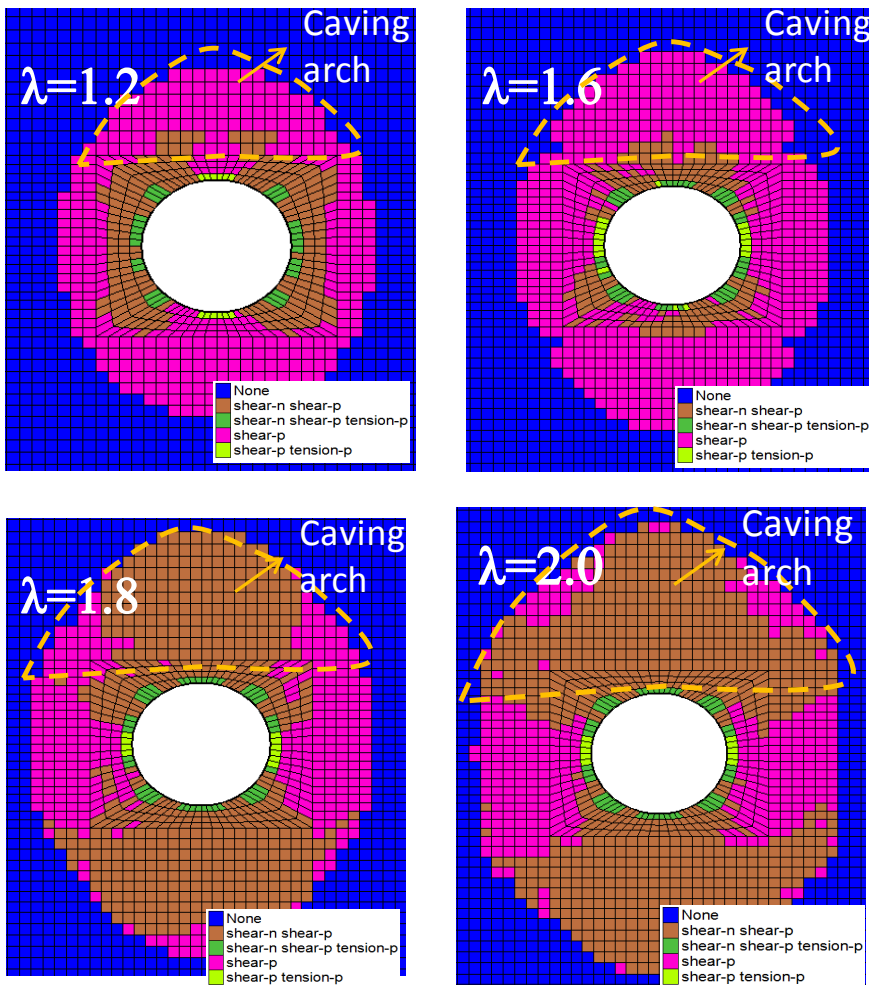


**Figure 1.** Plastic area distribution under different side coefficient

Figure 2 shows the surrounding rock failure depth curve under different lateral coefficients. The relationship presents a linear growth, while the sides' surrounding rock failure depth's effect on the horizontal stress is weak. The lateral pressure coefficient in the high-horizontal stress area of -980 roadway reaches 2.0; contrast to the low-horizontal stress roadway (1.0), the failure depth in the roof has a 1.12 times increase; and the failure depth in the floor has a 0.81 times increase; while the failure depth in sidewalls stays at 3.7m, the failure depth of all parts of the roadway is over the acting area of bolt supporting, which corresponds to the conclusion of borehole observation. The several collapse accidents in -980 roadway have close relationship with the deep failure of the surrounding rock. Moreover, even the sidewalls' effect on

the horizontal stress is weak, the failure depth stays over 3.0m. Attention should be paid to the stress caused by the rock movement for it is a threat to the safety of roof.

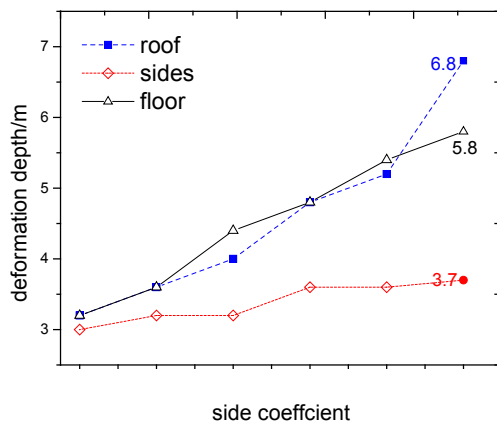


Figure 2. Relationships between the depths of surrounding rock failure and side coefficient

Place sensors in roof, floor and the middle of the sides to monitor the roadway's surface displacement; Figure 3 presents the relationship between surrounding rock surface displacement and lateral pressure coefficient. As shown in the Figure 3, with the increase of horizontal stress, the roof surface displacement increases in an exponential function, while the floor and sidewalls' displacement increases in a linear growth. Contrast to the low-horizontal stress roadway (1.0), in -980 roadway's high-horizontal stress area (2.0) the displacement of roof-floor and sidewalls increased by 1.72 times, 2.04 times, 2.50 times, from 441mm to 1200mm, 351mm to 1068mm, 285mm to 998mm respectively. It is obvious that high-horizontal stress is the main factor on -980 roadway displacement.

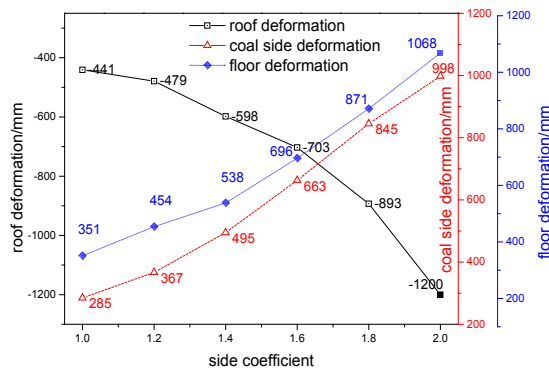


Figure 3. Relationships between displacements and side coefficient

According to the numerical analysis, the high-horizontal stress influence on -980 roadway roof and floor's plastic failure and displacement distribution is over that on the sidewalls; with the increase of horizontal stress, the depth of roof and floor's failure and displacement presents a linear or exponential increase. Thus, the roof and floor are the key factors, meanwhile, the larger depth of sides' failure which affects the safety of roof.

## 4 Control technology

### 4.1 Stability Principle

After the roadway excavation, the surrounding rock stability is extremely low, and large scale broken area appeared in a short time; with the outstanding horizontal stress and the unreasonable roadway section and other factors, the deformation of shallow area become larger. The conventional anchor-net-shotcrete support did not work, which causes the transfer of high horizontal stress to roof and floor and the failure of deep surrounding rock, even roof caving; and finally results in the instability destruction of the roadway full section. Therefore, applying reasonable support system and improving the carrying capacity and restricting the deep surrounding rock damage are the key factors to ensure the long term stability of -980 roadway.

This paper proposes the control stratagem of the -980 roadway: high-intensity support should be put into practice to tackle the strong deformation of the initial stage of roadway excavation and form a bearing structure with some strength and stiffness, and participate in the adjustment process of surrounding rock stress and restrict the surrounding rock's initial large deformation. Secondary supporting is used after the release of deformation to provide the final support strength and to restrict the permanent deformation and the development of failure and to ensure the stability. Strength enhancement measures of the fragmented surrounding rocks are used to improve the whole strength and provide effective support and improve the whole stability of the support structure.

### 4.2 Control Technology

1. High strength bolts/ *cables support technique*. The high pre-stressed and high strength bolts in the surrounding rock improve the surrounding rock inherent shear strength, and strictly restrict the surrounding rock shear deformation along the preexisting fractures and epigenetic fissures [5], and high stiffness pre-stressed bearing structure forms in the anchorage area. Cables impose high compressive stress on the surrounding rock, which combines with the compressive stress area caused by bolts into framework net structure, then forms large scale high stability

surrounding rock bearing structure. The surrounding rock residual strength and peak strength has been improved significantly, which effectively restrict the development of surrounding rock deformation and reduce the early decrease of surrounding rock strength.

2. Secondary support measures with large tonnage yieldable ring support. Considering the -980 roadway surrounding rocks' complicated characteristics and the roadway's long service time, employ the large tonnage yieldable supports to reinforce the surrounding rock. The yieldable ring supports provide enough support resistance, improve the surrounding rock strength, and ensure the effective transfer of the horizontal stress. The ring supports can transfer the local deformation stress to the whole support. Through the connection between the support and the surrounding rock the high-horizontal stress in the floor can transfer and diffuse to the low stress area in the sidewalls. These characteristics of the supports can decrease the floor stress concentration degree [6].
3. Delayed grouting measures. The -980 roadway surrounding rock has developed joint fissures and experienced several fractures. In order to ensure the long term roadway stability, deep and shallow grouting holes should be applied to reinforce the surrounding rock; the main function is as follows [7,8]: improving the deformation rigidity and shear strength; the function of the slurry concretion network skeleton: the surrounding rock collapse condition transferred from the fracture weak plane strength condition to the rock strength condition; transfer of the surrounding rock failure mechanism: the fissures full of solidified materials or compacted transferred from two-dimensional stress state to three-dimensional stress state, strength improved, brittleness weakened, plasticity improved.

## 5 Industrial Tests

### 5.1 Support Scheme and Construction Technique

Enlarge the roadway section into a three-center-arch with a 5.095\*4.361 section. Employ the Φ22\*3000mm grouted bolts that with a space of 800\*800mm. Employ the Φ21.8\*8500mm cable, and the row-line space is 2000\*800mm. Yieldable support is made by 36U steel, and every pillar has four parts, and lap length is 450mm. Employ clamp as the connector and the space is 80mm; and the space between supports is 800mm. Grouting holes are in a row and the row-line space is 1500\*3200mm. There is a hole every 5 supports, and the depth of the holes are 1m, 2m, 8m respectively, and the length of the grouting pipes are 0.6m, 1.2m, 2.0m respectively. There are eight pipes in each row. Deep and shallow holes are in staggered layout, and the dip of the grouting hole in the roof and floor is 35. The deep grouting hole is close to roof and floor, while the shallow ones are close to sidewalls. The grouting materials are No.42.5

cement and sodium silicate. The first shallow hole grouting pressure is 1.0MPa, and the second is 2.5MPa, and the deep hole grouting pressure is 6.0 MPa.

## 6 Conclusion

1. With the increase of horizontal stress, the plastic broken areas in the sidewalls transfer to the roof and floor, and the depth of the presents a linear increase. The depth of the sidewalls changes little, and the roof displacement presents an exponential function increase. The floor and sidewalls' displacement presents a linear increase.
2. The failure mechanism of such roadway surrounding rock are as follows: developed and low strength surrounding rock fracture, large scale fracture, high-horizontal stress and unreasonable section and failure support, aggravated shallow surrounding rock deformation, the transfer of high-horizontal stress, failure of the deep surrounding rock and roof caving.
3. High-strength cable support forms high intensity and large thickness pre-stressed bearing structure in the surrounding rock. The yieldable ring support ensures the transfer and diffusion of high stress to low stress area, and implements the even distribution of surrounding rock stress. Grouting improves the intensity of the surrounding rock and ensures its integrity. The engineering experiments show that this technique effectively solves the problem of high horizontal stress surrounding rock control.

**Acknowledgement:** This study was supported by the National Natural Science Foundation of China (No. 51574243) and the Fundamental Research Funds for the Central Universities (No.2010YZ02).

## References

- [1] KANG Hong-pu, WU Zhi-gang, GAO Fu-qiang, et al. Effect of geological structures on in-situ stress distribution in underground coal mines[J]. Chinese Journal of Rock Mechanics and Engineering, 2012;31) :2674-2680.
- [2] LIU Quan-sheng, KANG Yongshui, BAI Yun-qiang. Research on supporting method for deep rock roadway with broken and soft surrounding rock in Guqiao Coal Mine[J]. Rock and Soil Mechanics, 2011;32(10): 3097-3104.
- [3] SUN Yu-fu. Effects of in-situ horizontal stress on stability of surrounding rock roadway[J]. Journal of China Coal Society, 2010;35 (6) : 891-895.
- [4] CHEN Kun-fu. Research on failure evolution and control mechanism of surrounding rock of deep roadways and its application[D]. Jiangsu: China university of mine and technology press, 2009: 78-80.
- [5] REN Li, Xie He-ping, Zhu Zhe-ming, et al. Failure analysis of cracked rock specimen under tension[J]. Journal of China Coal Society, 2012(1):21-27.

- [6] QIAN Ming-gao, SHI Ping-wu. Mine pressure and strata control[M]. Jiangsu: China university of mine and technology press, 2003: 256-259.
- [7] WANG Cheng, WANG Liang-hai, ZHANG Nian-chao. Research on the dynamic evolutionary of rock rheology in soft rock with high ground stress[J]. Journal of Mining & Safety Engineering, 2013, 30(1): 14-18.
- [8] HAN Li-jun, ZONG Yi-jiang, HAN Gui-lei, et al. Study of shear properties of rock structural plane by grouting reinforcement[J]. Rock and Soil Mechanics, 2011(9): 2570-2576.
- [9] QIAO Jian-yong. Complex Dynamics of Renormalization Transformations, Science Press, Beijing, 2010.

Xian HUANG, Yue QIN, Jia-li LIANG, Yang LIU \*

## Design of a Climbing Robot for Nuclear Environmental Monitoring

**Abstract:** As nuclear science and technology develop, robotic applications are becoming common and important in nuclear islands and beyond. Climbing robots designed to replace human workers for nuclear environmental monitoring at high altitudes with dangerous working conditions offer security and efficiency. This paper proposes a feasible design of a ladder-climbing robot, including the mechanical structure, the control system and a human-machine interface, and a feasible gait planning based on the designed robot.

**Keywords:** nuclear robot; climbing robot; gait planning

### 1 Introduction

With the enormous development of the nuclear power industry, the demand for nuclear robot applications in NPP (nuclear power plants) is constantly rising. Numerous specially designed robots have been developed according to different working purposes, which cover the operation, the inspection, the maintenance and the decommissioning either inside or outside of nuclear islands [1-4].

Inside nuclear islands, robots are often required to operate under water, in high temperature, or under strong radiation. For this kind of operation, the ‘Pegasys’ robot has been designed by Westinghouse Electric Company for plugging tubes in PWR steam generators [5]. For instrument inspection, in nuclear reactor vessels, the Korea electric power research institute developed an underwater robotic system, which is already applied in the PWR in Yonggwang nuclear power plant [6,7]. In primary circuit feeder pipes, a snake-arm robot system designed by OC Robotics in Britain is applied in CANDU reactors in Canada [8,9]. For instrument maintenance, an underwater welding technique, including an underwater welding system developed by Toshiba [10] and the YAG-laser repair welding robot developed by Ishikawajima-Harima Heavy Industries Company [11], is important to use to fix stress corrosion cracking [12]. For instrument decommissioning, the excavator-like robot “Brokk 180” designed by Brokk Company is used in decommissioning nuclear facilities at Dounreay [13].

---

\*Corresponding author: Yang LIU, Sino-French Institute of Nuclear Engineering and Technology, Sun Yat-Sen University, Zhuhai, China, E-mail: LIUY338@mail.sysu.edu.cn

Xian HUANG, Yue QIN, Jia-li LIANG, Sino-French Institute of Nuclear Engineering and Technology, Sun Yat-Sen University, Zhuhai, China

Outside nuclear islands, robots have fewer requirements connected radiation and temperature, but more with the architecture. For environment inspection under a normal nuclear environment, the robot “Warrior” [14] uses tracks to obtain mobility. Under a nuclear accidental situation, the “Quince” robot [15] was also equipped with crawlers designed with tracks to overcome obstacles and steps.

Structure climbing is one of the common actions required for the operation, inspection and maintenance both inside and outside the nuclear island. A climbing robot with efficiency performance and high accuracy could serve as a good platform to replace a human’s manual operations. The design of a climbing robot is specialized according to the features of different working conditions. Robots equipped with suction cups, such as the “ROMA” robot [16], can move omni-directionally on slick wall, while a high dryness, slickness and flatness is required for the wall. On the contrary, robots equipped with spines, such as the “CLIBO” robot [17], can climb on a rough wall, but a high roughness of the wall is needed. Robots with clampers usually use a paralleled structure to climb tubes or rods, such as the “TREPA” robot [18], however, crossing obstacles is difficult for these robots. As shown by “Quince”, and “Warrior”, robots with track can easily cross obstacles. Moreover, this kind of robot can also climb stairs with a large load [19], even though the stairs will not have a great slope. Robot with limbs and claws, such as the “ASTERISK” robot [20], can also afford a large load to climb ladders, while the motion is complicated so that the climbing efficiency will not be as high as the other types of robot.

Another structure that can serve as a potential consideration for climbing robot design is the ladder. A ladder is a common auxiliary tool that stands everywhere especially for vertical architectures with high altitudes, such as nuclear environmental monitoring towers. A well designed robot which is able to climb a ladder will have a wide application range to assist humans working in high altitude architecture. In this paper, a ladder-climbing robot is designed as the working platform for automatic instrument maintenance and decommissioning to replace humans working in such a dangerous working environment. In consideration of the ladder structure, a climbing strategy and the corresponding mechanical structures, a remote control system and the human machine interface are proposed together with a performance analysis.

## 2 System configuration

The robot system includes a mechanical structure, a control system and a human-machine interface.

## 2.1 Mechanical Structure

The robot has a car-like structure for the feasibility of ground moving with two degrees of freedom. More precisely, using a structure with two front unidirectional driving wheels and two back omni-directional wheels, the adjustment to the moving direction of the robot can be controlled by the rotational directions and the difference between the rotational speeds on the driving wheels. A DC (direct current) motor is chosen as the driving motor for the front wheels.

When the robot climbs on the ladder, these four wheels act as the supporter that keep the robot hands grabbing on the rungs of the ladder properly. Four guiding wheels are installed to maintain the movement direction. Figure 1 shows a sketch of the robot's mechanical structure.

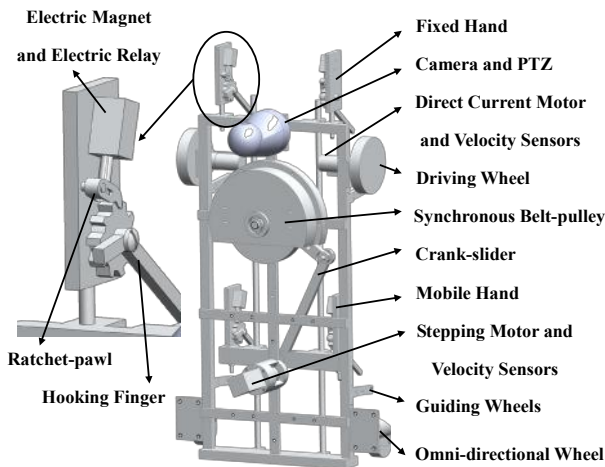


**Figure 1.** Mechanical structure of the robot

The robot uses four grabbing hands to preserve the balance on the ladder: two front symmetric hands fixed on the frame of the robot and two back symmetric hands as mobile hands, which are mobile compared with the fixed hands. The two fixed hands grab on the same rung of the ladder, so as two mobile hands on another rung. To climb, the distance between the fixed hands and the mobile hands should change periodically. A crank-slider structure imposed with a motor can offer the mobile hands such a periodical displacement without breaking the motor's continuous rotation. A selection of a stepping motor assures accuracy for the climbing movement and a synchronous belt-pulley is used to improve the output torque of the stepping motor.

The climbing mechanism demands the hands not only grab on rungs for the robot's balance, but also cross over rungs for the augmentation or the diminution of altitude. A hand with three working positions is composed of a hooking finger, an

electric magnet and a ratchet-pawl structure. With a suitable control of the electric magnet, the state of the hand is able to be switched between crossing upward a rung, crossing downward a rung and grabbing on a rung.

In order to diminish the self-load of the robot, the geometry parameters of the mechanical components are optimized by using a finite element method. Almost all the mechanical components are built with aluminum alloy except some important loading components such as the shaft and the key of the pulley.

## 2.2 Control System

The control system of the robot (Figure 2) is consisted of an Arduino board, a couple of wireless RF (radio frequency) modules, DC motors with driver, a stepping motor with driver, photoelectric velocity sensors, photoelectric position sensors, electric magnets, electric relays, a WIFI camera with PTZ (pan-tilt-zoom) control platform and a computer. The computer is the host-computer and the Arduino board with necessary circuits is its slave-computer. The camera and its PTZ platform form a visual system.

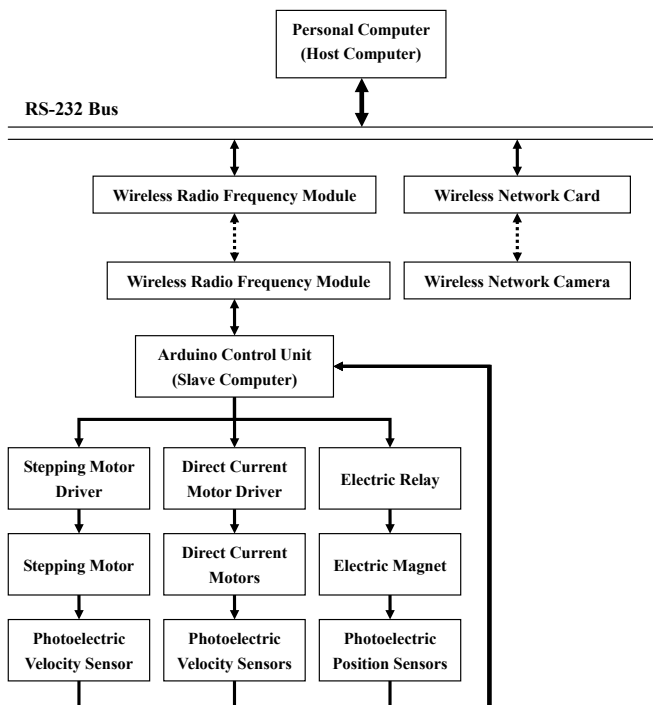


**Figure 2.** Control system of the robot

Data transmission is realized by two independent ways respectively: a, the real-time video and the command and feed-back signal between the camera and the host-computer are transmitted by WIFI through the Internet Protocol; b, the command and feed-back signal between the slave-computer and the host-computer are transmitted RF through the RS232 Protocol. The separation of visual system data from the control command guarantees the transmission bandwidth and improves the reliability of system.

During the motion of the robot, the host-computer keeps sending orders to the slave-computer until the robot reaches its aimed position. Within each command period, which can be chosen from 0.1s to 1s, the slave-computer enables motors. Consequently, the robot will be stopped automatically without any order. It assures that the robot can still be stopped even under a bad communication environment.

### 2.3 Human-machine Interface

On the consideration of the Windows system, the interface is developed on the basis of MFC (Microsoft Foundation Classes) programming for the control and the inspection of the robot. The interface is composed of two modules: the real-time video module and the serial port communication module.

The real-time video module is developed to realize user login, PTZ control, real-time video display, video recording and image capture. That can support the camera integrated (DS-2CD3Q10FD-IW, HIKVISION®). The data transmission of video relies on the LAN (local area network) built by a portable router.

For the serial communication module, RS-232 communication protocol is adopted. The reading file and writing file function, the thread listening function and other files related to serial communication are considered as the fundamental part. With these basic files, the following functions are realized:

- accessible port selection;
- operation mode selection, including ground moving mode, ladder climbing mode and automatic climbing mode;
- relative parameters set, such as speed, sensibility, etc.;
- long press control by the virtual button and keyboard;
- display of the robot state.

To realize remote control, a wireless communication through RS-232 communication protocol between the robot and the human control software on the computer is realized with the help of the couple of radio frequency module. A string of numbers in a length of 8 or 15, whose first and last number is the check code, is sent to give orders or to feed back information.

### 3 Ladder climbing strategies

The crank-slider structure transforms the continuous rotational movement denoted by the motor into a periodical linear to-and-fro movement for the mobile hands. With the help of switching the state of the hands for grabbing or for crossing, the robot can climb up or down on the ladder. The climbing procedure is the cycling of three primary states shown in Figure 3. The robot starts the climbing from the initial state, shown in Figure 3a. At this state, the robot hangs on the ladder by keeping a long distance between the fixed hands and the mobile hands. To climb up on the ladder, the robot decreases the distance between the fixed hands and the mobile hands while the fixed hands grab the rung, retaining its old position. Consequently, the mobile hands move across one rung to grab the upper rung and reach its transitional state, shown as Figure 3b. Next, the distance is enlarged by keeping the mobile hands grabbing on the rung and moving the fixed hands across one rung to grab the upper one. At the end of this movement, the robot reaches its climbed-up state, shown as Figure 3c and finishes its climbing cycle one time. The robot climbs up one-rung distance in one climbing cycle. The distance between the fixed and mobile hands in the climbed-up state is the same as that in the initial state. The climbed-up state is the initial state of a new climbing cycle. The climbing down procedure is to cycle the climbing up process in adverse order.

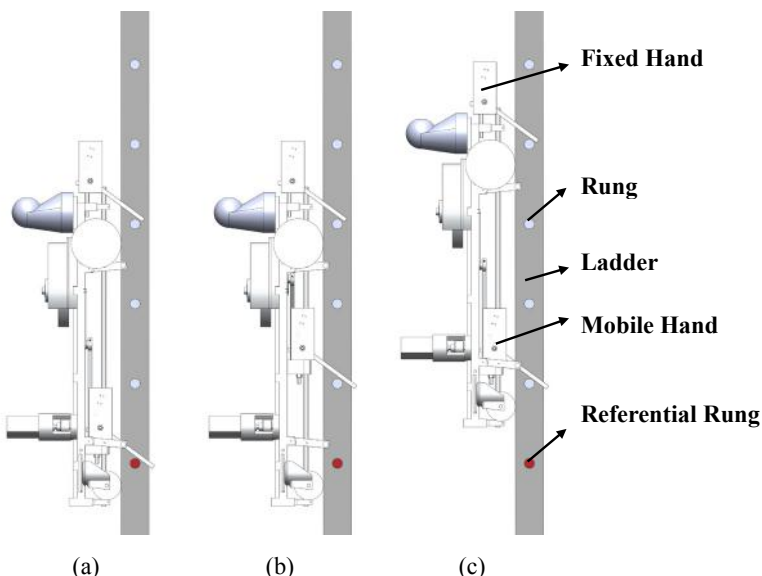


**Figure 3.** Climbing cycle of the robot states (side-view): a, initial state on lower altitude; b, transitional state; c, climbed-up state

In the climbing procedure, both fixed and mobile hands are required to grab the rung and to move over either the upper rung (for climbing up) or the lower rung (for climbing down). In order to satisfy this requirement, the robot hand is designed to integrate a ratchet with a pawl driven by an electric magnet and a rolling-up spring that provides the recovery stress. The working sequences of one hand for climbing up and climbing down the ladder are presented in Figure 4 and Figure 5 respectively.

By controlling the pawl and the relative position of the hands on the rungs, the robot can climb the ladder without breaking the continuous rotation of the loading motor. Consequently, the energy dissipation to change the rotation direction of the motor is avoided and the energy is used more efficiently for climbing. Furthermore, the accumulation of the rotational angle error due to the change of the rotational direction can also be avoided.

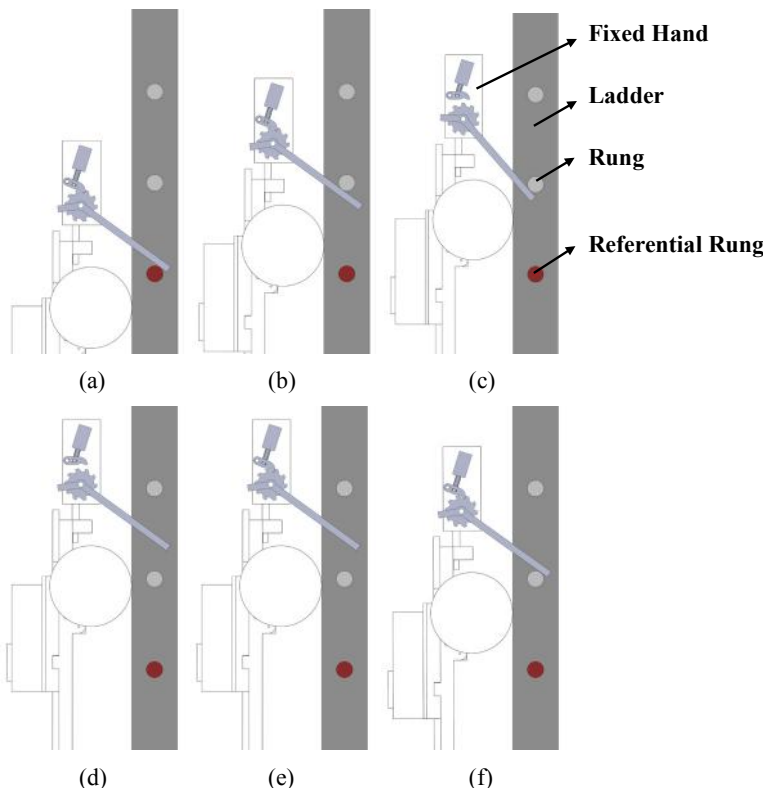


**Figure 4.** Hands' working position for climbing up (side-view): a, grabbing on rungs; b, crossing upper rungs; c, unlocking ratchets; d, having crossed upper rungs; e, locking ratchets; f, grabbing on upper rungs

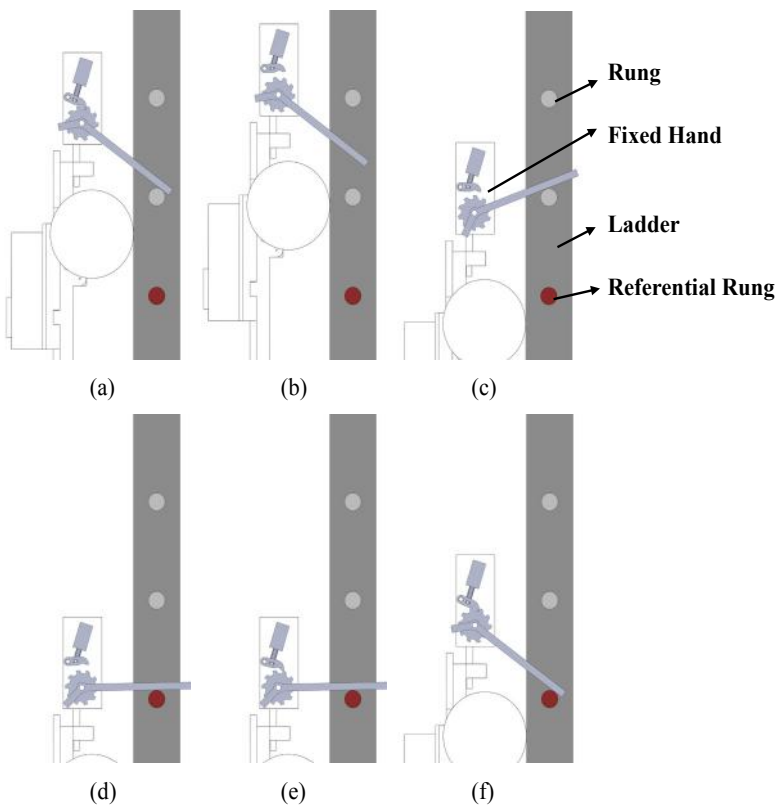


**Figure 5.** Hands' working position for climbing down (side-view): a, grabbing on rungs; b, unlocking ratchets; c, crossing under rungs; d, having crossed under rungs; e, locking ratchets; f, grabbing on under rungs

#### 4 Conclusion

The ladder-climbing robot is developed with the realization of the mechanical structure. The control system is constructed to realize the required motions. The human-machine interface is composed based on the need of operation and inspection. According to the specific design of the robot, the climbing mechanism and the gait planning are conceived.

## References

- [1] B. L. Luk, K. P. Liu, A. A. Collie, D. S. Cooke and S. Chen, Tele-operated climbing and mobile service robots for remote inspection and maintenance in nuclear industry, *Industrial Robot: An International Journal*, vol. 33, iss 3, pp. 194 – 204, 2006.
- [2] R. Bogue, Robots in the nuclear industry: a review of technologies and applications, *Industrial Robot: An International Journal*, vol. 38, iss 2, pp. 113 – 118, 2011.
- [3] W. F. Xu and Z. G. Mao, Research Status and Development Trend of Nuclear Power Plant Robots, *Robot*, vol. 33, iss 6, pp. 758-767, November, 2011.
- [4] C. Z. Liu, Z. Yan and J. S. Deng, Application Status and Performance Analysis of Robot in Nuclear Power Plants, *Nuclear Safety*, iss 4, pp. 72-76, 2012.
- [5] L. J. Pestrosky, Innovative robot for inspection of nuclear steam generators, 1st Joint Emergency Preparedness and Response/Robotic and Remote Systems Topical Meeting, pp. 461-465, 2006.
- [6] B. H. Cho et al., KeproVt : underwater robotic system for visual inspection of nuclear reactor internals, *Nuclear Engineering & Design*, vol. 231, iss. 3, pp. 327-335, 2004.
- [7] J. Y. Park, B. H. Cho and J. K. Lee, Trajectory-tracking control of underwater inspection robot for nuclear reactor internals using Time Delay Control, *Nuclear Engineering & Design*, vol. 239, iss 11, pp. 2543-2550, 2009.
- [8] R. O. Buckingham, and A. C. Graham, Dexterous Manipulators for Nuclear Inspection and Maintenance – Case Study, International Conference on Applied Robotics for the Power Industry, pp. 1-6, October, 2010.
- [9] R. O. Buckingham and A. C. Graham, Nuclear snake-arm robots. *Industrial Robot*, vol. 39, iss 1, pp. 6-11, 2012.
- [10] M. Yoda, et al., Laser-based maintenance and repair technologies for reactor components, *Proceedings of the International Conference on Nuclear Engineering*, vol. 1, pp. 39-46, 2004.
- [11] Y. Makihara, Y. Miwa, M. Hirose, S. Satoh and K. Ohwaki, The Application of the Welding Technique at Fillet Groove by the YAG-Laser Repair-Welding Robot for Underwater Environment, *International Conference on Nuclear Engineering*, pp. 149-155, 2004.
- [12] J. L. Zhu and X. D. Jiao, Applications of underwater laser welding in nuclear power plant maintenance, *International Conference on Mechanic Automation & Control Engineering IEEE*, pp. 2947-2950, 2011.
- [13] R. Bloss, How do you decommission a nuclear installation? Call in the robots, *Industrial Robot: An International Journal*, vol. 37, iss 2, pp. 133-136, 2010.
- [14] R. Q. Yang and K. W. Song, A ‘Warrior’ Teleoperated Mobile Robot, *High Technology Letters*, pp. 11-14, February, 1997.
- [15] E. Rohmer et al., Integration of a sub-crawlers’ autonomous control in Quince highly mobile rescue robot, *IEEE/SICE International Symposium on System Integration*, pp. 78-83, 2010.
- [16] C. Balaguer, A. Gimenez and A. Jordan, Climbing Robots’ Mobility for Inspection and Maintenance of 3D Complex Environments, *Autonomous Robots*, vol. 18, pp. 157–169, 2005.
- [17] A. Sintov, T. Avramovich and A. Shapiro, Design and motion planning of an autonomous climbing robot with claws, *Robotics and Autonomous Systems*, vol. 59, iss 11, pp. 1008-1019, 2011.
- [18] J. M. Sabater, R. J. Saltarén, R. Aracil, E. Yime and J. M. Azorín, Teleoperated parallel climbing robots in nuclear installations, *Industrial Robot: An International Journal*, vol. 33, iss. 5, pp. 381-386, 2006.
- [19] W. J. Tao, Y. Ou and H. T. Feng, Research on Dynamics and Stability in the Stairs-climbing of a Tracked Mobile Robot, *International Journal of Advanced Robotic Systems*, vol. 9, iss. 4, pp. 467-485, 2012.
- [20] S. Fujii, K. Inoue, T. Takubo, Y. Mae and T. AraiFujii, Ladder Climbing Control for Limb Mechanism Robot ‘ASTERISK’. *IEEE International Conference on Robotics and Automation*, pp. 3052-3057, 2008.



---

## **Part V: Mechatronics and Electrical Engineering I**



Yu-heng HE, Kai FENG, Heng JU, Cheng-xin LIN\*

## The design and simulation of the new Space Release Device

**Abstract:** For the reason that traditional space release device has the drawbacks of high shock and inflammability, this paper presents a new design of incomplete thread space release device. The structure of the release device was designed first, and the main parameters of the components were calculated. The strength check of the springs inside the release device and the dynamic of the device were obtained by the ADAMS software. What more, the static strength of main components was analyzed by the ANSYS software. The results indicated the release device possesses feasibility, and the designed parameters satisfy the theoretical requirements and the strength check. The device meets the purpose of fast release and low shock whose release time is 0.36s and the maximum velocity is 14.4121cm/s.

**Keywords:** Space release device; Incomplete thread; Dynamic simulation; Intensity check

### 1 Introduction

Space release device is widely used in the space missions, such as the separation of the satellite and rocket and the space expansion of large appendages. It can provide preload for the attachments' locking to ensure its completeness under the launching impact. What's more, it can release under the instruction of the space orbit state [1].

At present, the space release device is mainly pyrotechnical products, such as the pyrotechnic bolts which is a mature and reliable technology. Although the reliability of the pyrotechnics is checked out by countless tests, it is still inflammable, explosive, nonreusable and hard to store. Due to these reasons, the application of pyrotechnic bolt is limited on many conditions [2,3]. The United States, Russia and other countries have used memory alloys as the material of release mechanism in space fields since 1980s [4-6]. The Fast Acting, Shock less Separation Nut, developed by Strays Research Corporation, represents a kind of release devices with low-shock and non-pyrotechnic [7]. However, the structure of the separation nut is relatively complex.

For the reasons that traditional space release device has these shortcomings, the new design of incomplete thread space release device is presented. This paper

---

\*Corresponding author: Cheng-xin LIN, Department of Mechanical Engineering, Dalian Maritime University, Dalian, 116026, China, E-mail: lchxin@dltmu.edu.cn

Yu-heng HE, Kai FENG, Heng JU, Department of Mechanical Engineering, Dalian Maritime University, Dalian, 116026, China

introduced the structure and the release process of the new-type space release device, and it calculated the main parameters of the device. The dynamics of the incomplete thread space release device was simulated by the ADAMS software, verifying the feasibility of the device. Meanwhile, the main bearing components of the release device were also proceeded the strength check by the ANSYS software.

## 2 The Methods of Design and Simulation

### 2.1 The Structure Design and Working Mechanism of the Release Device

The structure diagram of the space release device is shown as Figure 1.

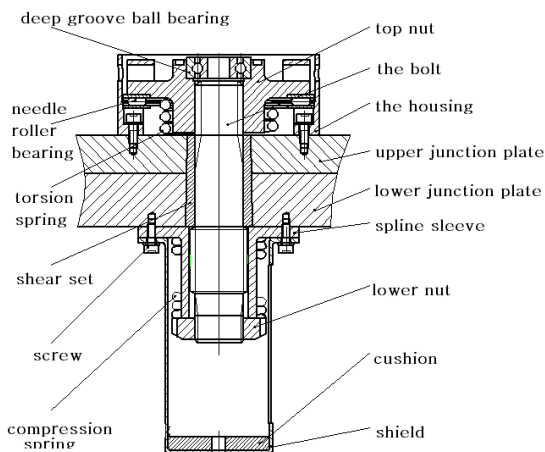


**Figure 1.** The structure diagram of the space release device

The bolt connects the upper and lower junction plate by the way of crossing the center of the hole, and the connection between the bolt and the upper nut is incomplete thread connection. On the upside platform of the upper nut, the circular ring groove which has a 60 degrees in radians is used to limit the upper nut's rotation. What's more, the upper nut's radial position is limited by the deep groove ball bearing. The needle roller bearing is used to support the upper nut's rotary, and the radial locating of the upper nut's lower part is guaranteed by the match between the upper nut and the needle bearing's top circle. The initial torque of the upper nut is applied by the torsion spring which at the bottom of the upper nut and fastened with the housing. Meanwhile, the shear set is adopted to ensure that the entire device can bear the shear force, the shear sleeve is adopted. Because of the connection of the spline sleeve and the bolt, the bolt can't rotate during upper nut's rotation. The compression spring

provides axial force for the bolt, so that the device can release successfully. The bolt's bottom part connects with the lower nut by the way of thread, which is used to apply initial pre-tightening load on the bolt. After completely releasing, the bolt and the lower nut will be held by the shield.

When the device got release instructions, the rotate limitation is relieving. Then the upper nut begins to rotate due to the non-locking feature of the thread and the initial torque of torsion spring. When the upper nut and the bolt's threads are fully staggered, the groove on the top of the upper nut contacts with the small cylinder of the trigger device to restrict the rotation of the upper nut. Then the bolt disconnect with the upper nut by the driving force of the compression spring, and the upper and lower junction plates separate to achieve the release.

## 2.2 The Dynamic Simulation of the Space Release Device

In order to obtain release time and release shock of the space release device, the dynamic was simulated by the ADAMS software. The ADAMS software (developed by MDI Company, the United States) uses the interactive graphics environment, the parts library and the constraints library to establish the fully parameterized geometry model. And the dynamic equations are used to simulate the dynamic by the virtual prototype [8].

### 2.2.1 The basic algorithm of the ADAMS software

The ADAMS software uses the Lagrange equation method to establish the system dynamics equations. It selects three rectangular coordinates of the mass center in each inertial reference frame and three Euler angles which determine the orientation of the rigid as Descartes generalized coordinates. The Lagrange first equation with a multiplier can handle complete restraint system or a complete restraint system of the redundant coordinates to export the kinetic equations which has the variable of Cartesian coordinate. The calculation program of the ADAMS software uses Jill rigid integral algorithm and sparse matrix techniques, and it greatly improves the computational efficiency [9].

### 2.2.2 The coordinates of ADAMS

Most of the mechanical system use rectangular coordinate system and the widely used Cartesian coordinate is a rectangular coordinate system which adopts right-hand rule. All vectors of kinematics and dynamics can be represented by the coordinates of the unit vectors along three components. The reasonable coordinate system can simplify the motion analysis of mechanical system. Three coordinates were often used in the ADAMS software, as follow.

- a) *Ground coordinate system.* The ground coordinate system is also called static coordinate system, and it is a coordinate system fixed on the ground. In the ADAMS software, the positions, directions and speed of whole members can express by the ground coordinate system.
- b) *Local part reference frame (LPRF).* This coordinate is fixed on the members and moved with it, and each member has a local reference coordinate system. The position and orientation of the member are determined by the way of the position and orientation of the local reference coordinate system on the ground coordinate system.
- c) *Marker system.* The marker system is also called marker, and it is an auxiliary coordinate system for simplifies the modeling and analysis. There are two types of marker system: fixed marker and floating marker. The fixed marker is fixed on the member and moved with the member. And the location and direction of the fixed marker can be determined through the position and orientation of the fixed marker in the partial elements coordinate. What more, the fixed marker are also used to define the shape of the member, the position of the centroid, the point of action and reaction, the connecting position of the members and so on. The floating marker moves relatively to the member, and some force and constrains are located by the floating marker in the motion analysis of mechanical system [10].

### 2.2.3 The solving equation of dynamics

The ADAMS software uses the Cartesian coordinates and Euler angles of the rigid body's ( $B_i$ ) centroid as generalized coordinates, that's  $q_i = [x, y, z, \psi, \theta, \phi]^T$ . For a system which includes severe ( $n$ ) rigid bodies, that's

$$q = [q_1^T, q_2^T, \dots, q_n^T]^T.$$

The ADAMS software uses Lagrange-multiplier method to establish the kinematic equations of the system, as Eq. (1) shows.

$$\frac{d}{dt} \left( \frac{\partial T}{\partial \dot{q}} \right)^T - \left( \frac{\partial T}{\partial q} \right)^T + \varphi_q^T \rho + \theta_{\dot{q}}^T \mu = Q \quad (1)$$

The complete constraint equation is shown as Eq. (2):

$$\varphi(q, t) = 0 \quad (2)$$

The incomplete constraint equation is shown as Eq. (3):

$$\theta(q, \dot{q}, t) = 0 \quad (3)$$

Where,  $T$  is the kinetic energy of the system,  $q$  is the generalized coordinates array of the systems,  $Q$  is the generalized force array,  $\rho$  is the Lagrange multiplier array of complete constraint,  $\mu$  is the Lagrange multiplier array of incomplete constraint.

The kinematic equation of the system is reduced-order to first-order algebraic differential equations and written into the general form, as Eq. (4) shows.

$$\begin{cases} F(q, u, \dot{u}, \lambda, t) = 0 \\ G(u, \dot{q}) = u - \dot{q} = 0 \\ \Phi(q, t) = 0 \end{cases} \quad (4)$$

Where  $\dot{q}$ ,  $u$  is the generalized velocity array,  $\lambda$  is the reaction forces and force array,  $F$  is the system dynamics and user-defined differential equations,  $\Phi$  is the constrained algebraic equations array.

If the state vector of the system is define as  $y = [q^T, u^T, \lambda^T]^T$ , then the above equations is written as  $g(y, \dot{y}, t) = 0$ .

These equations are Differential-Algebraic Equations (DAEs), and the ADAMS software uses two algorithms to solve DAEs:

- a) *The DAE is solved directly.* The software provides three powerful integration solutions of variable order and step size: GSTIFF integrator, DSTIFF integrator and BDF integrator. Those solutions are used to solve the nonlinear and sparsely coupling differential-algebraic equations, and this method is suitable for the simulation of stiff system.
- b) *The ABAM integrate solution of the procedure is used.* The ADAMS software decomposes generalized coordinates into independent or non-independent coordinate coordinates by constraint equations. Then the DAEs are curtailed into ordinary differential equations (ODE) for its solution. This method applies to the system which simulate eigenvalues undergo mutation or high frequency system [9].

#### 2.2.4 The analysis process of the ADAMS software

With the component library and the constraint library modules of the ADAMS software, the model of the system was established in accordance with the actual physical parameters of the system. (1) It checks the original input data first before the software analyzes, when the data doesn't have errors the software will judge the freedom of the whole system. If the degree of freedom is zero, it will simulate the kinematics of the release device. Otherwise it will begin its dynamics simulation or static analysis; (2) The software solves matrixes with its powerful integrators; (3) Before the end of the simulation, the simulation is success when the Jacobian matrix or matrix organization are not singular. The relevant parameters could be measured, and its curves could be drawn; (4) Otherwise, the simulation is fail. The model and the constrained conditions need to be re-examined, and the simulation time, steps or other parameters need to be re-setted until the simulation results are correct.

#### 2.2.5 The modeling of the release device

Firstly, the model of the space release device was built. Due to the poor capability of the automatically dynamics analysis software in the modeling of the mechanical system, it is unsuited for the modeling of complex construction. Thus the 3D design

software SolidWorks, a mechanical product design as the main object of the CAD/CAM/CAE integration, was used to establish the solid model. The solid model includes the upper nut, the bolt, the upper and lower junction plates and so on, and the entirety model of the space release device was shown in Figure 2.

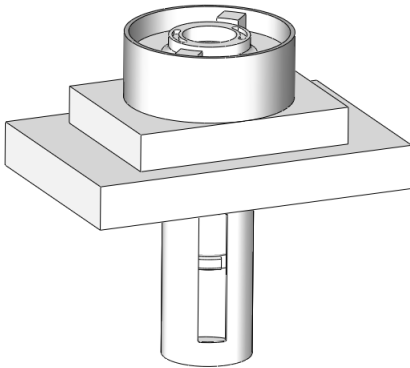


**Figure 2.** The model of the space release device in the Solidworks software

### 2.2.6 The simulation conditions

The system is simultaneously bore the axial force of the compression spring, the torque of torsion spring and the bolt's pre-tightening load before releasing. After receive the release signal, the bolt's pre-tightening load is released, and the system is only driven by the two springs. In the model, the limited post (the red part in Figure 3) which limits the rotary of the upper nut is simulated the trigger stop-action device for the system.

The upper and lower function plates in the model are assumed to be stationary. The upper and lower function plates were connected with the housing, the spline sleeve, the shield and the limited post in the whole system. The connections of the bolt and the spline sleeve, the upper nut and the housing are the sliding pair, the cylindrical pair, respectively.

There are 5 contacts in the model: the contact between the bolt and the upper nut is friction-type contact; the contacts between the upper nut and the limited post, the upper nut and the housing, the lower nut and the shield and the lower nut and the splined sleeve are both no frictional contact.

To accurately simulate the relationship between the upper nut and the bolt and provide a trigger signal, some assumptions are setting as follow. Firstly, in order to simulate the pre-tightening load before the releasing, sliding pair was applied between the upper nut and the housing, and a gap was set between the upper nut and the bolts' thread. The upper nut can only move along axis without rotation, and

its thread was pressed onto the bolt's thread by the moved down of the bolt with the axial force of the compression spring and the pre-tightening load. Secondly, in the release process the script file that the sliding pair will lose efficiency at 0.5s was built in the release process, and after that the upper nut rotates.

### 2.3 Intensity Check

In order to research the load conditions of the device, the ANSYS software was used to analyze the static strength of main components. The stress and strain contours were obtained from the software, verifying the reliability of the device.

Before the finite element analysis, the type of the finite element analysis unit must be determined first, which affects the meshing of the model and the accuracy of the analysis. The solid45 unit is often chosen to define the solid model. While the solid95 unit is more advanced than solid45 unit, and it is applied to the model of the curved boundary. The unit possesses plasticity, creep, stress stiffening, and capabilities of large deformation and large strain. What's more, this unit has 20 nodes, and each node has three translational degrees of freedom in the X, Y and Z directions. It can absorb irregularly shaped units without losing accuracy. Thus, considering the actual forces of the upper nut, the time for computing and other factors, solid95 unit was chosen for analyze.

Considering the feasibility of the simulation on the complex structure, the free mesh method was chosen. The material of the upper nut, the bolt, the spline sleeve, and the shear set are steel, their elastic modulus, Poisson ratio is 210GPa, 0.3, respectively. The contact surface of the upper nut and the needle roller bearing, the surface of the bolt contacted with the lower nut and the surface of the spline sleeve contacted with the lower nut were exerted 122.5kN axial surface load. And fully constrained in the direction of X, Y and Z were applied on the thread part of the upper nut and the bolt, and on the surface of the spline sleeve which connected with the lower junction plate. Meanwhile, the shear set was only bear the shear force. The surface of the set contacted with the lower junction plate was put constraint, the set could move along axis and rotate around the axis. The surface of the set contacted with the upper junction plate was exerted 20kN shear force.

## 3 Results and Discussions

### 3.1 The parameters of the springs

In order to increase the releasing, the connection styles of the upper nut and the bolt are trapezoidal thread, and the no self-lock feature should be insured. The thread parameters calculated is shown as Table 1.

**Table 1.** Parameters of the thread

Thread type	Thread angle	Pitch	Nominal diameter	Pitch diameter of thread
Double trapezoidal thread	$\alpha=30^\circ$	$P=4\text{mm}$	$d=18\text{mm}$	$d_2=16\text{ mm}$

For the reason to reduce the separation time, the initial torque and axial should provide for the upper nut and the bolt. While the torsion spring and compression spring couldn't bear big force, the parameters of those spring calculated by the formulas are shown in Table.2, Table.3.

**Table 2.** Parameters of the torsion spring

Spring Wire diameter	Number Of turns	Rotation angle	Pitch diameter	Spring rate
$d=4\text{mm}$	$n=2$	$\varphi=60^\circ$	$D=40\text{ mm}$	$T=179\text{ Nmm}/^\circ$

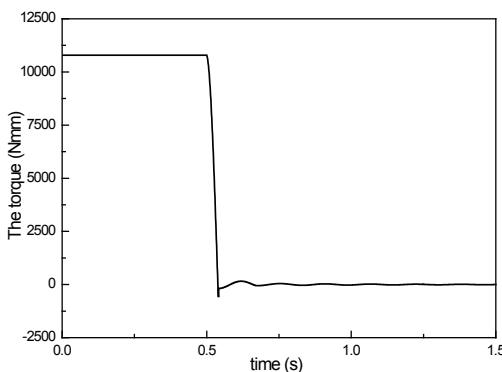
**Table 3.** Parameters of the compression spring

Material	Mean diameter of coil	Diameter	Pitch	Number of total coils
Carbon spring steel wire B	$D=32\text{mm}$	$d=3\text{mm}$	$p=9\text{ mm}$	$n_0=9$

### 3.2 Results and Analysis of the ADAMS Software

#### 3.2.1 The checkout of the springs' performance

The value of the torque and the output force were simulated to examine whether they corresponds with the value of the theoretical loading [12]. The torque curve of the torsion spring was shown as Figure 3.

**Figure 3.** The torque curve of the torsion spring

The Figure 4 indicates that the torque of the torsion spring is 10785.9Nmm within 0.5s, and this value is fully consistent with theoretical calculation. When received release signal at 0.5s, the torsion spring drove the upper nut rotating, and the torque reduce to 0 at 0.54s. This showed that the spring could be completely released within 0.04s.

The axial force curve of the compression spring was shown in Figure 4.

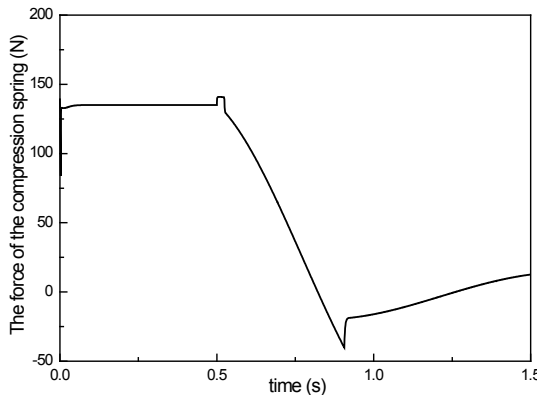


**Figure 4.** The axial force curve of the compression spring

The Figure 5 indicates that the axial force of compression spring is fluctuating within 0.0003s, and this is the instant effect of applied pre-tightening load. During 0.0003s to 0.5s, the spring is in compressed state. And due to the slight displacement of the bolt, the axial force of the spring can maintain around 135N which is less than the theoretical calculation (139.08N). Because of the effect of the thread on the upper nut, it would lead the bolt have a slight axial displacement during rotation when the system received release signal at 0.5s. Meanwhile, the spring is compressed, and the axial force is slightly larger. So the axial force of the compression spring will have a slight increase at 0.5s. At the same time, the upper nut and the bolts' threads was completely staggered. Then the bolt dropped down, and the compression spring stretched. Afterwards the process of the bolt was bottomed out and driven the compression spring stretching.

Therefore, the loading conditions of the torsion spring and compression spring was conformed to the requirements of the theoretical design, which would apply the foundation of the subsequent dynamics simulation.

### 3.2.2 Results and analysis of the dynamic simulation

The axial displacement curve of the bolt was shown in Figure 5.

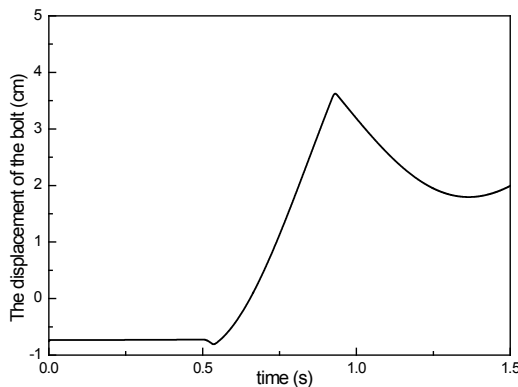


**Figure 5.** The axial displacement curve of the bolt

The Figure 6 indicates that the pre-tightening load between the upper nut and the bolt was stable, and the rotation of the upper nut was hold by the limited post during the time  $0s \sim 0.5s$ . So the bolts had no displacement during this period. When the device got a release signal at  $0.5s$ , the upper nut started to rotate, then the bolt have an inverse axial displacement. When the incomplete thread of the upper nut and the bolt stagger, the bolt left the upper junction plate at  $0.86s$ , and the device completely released. The subsequent displacement change of the bolt was caused by the bottomed out of the bolt and the shake with the compression spring. Consequently, the device can achieve the release, and the release time is  $0.36s$  which is lower than the time of the design requirements.

The velocity curve of the bolt was shown in Figure 6.

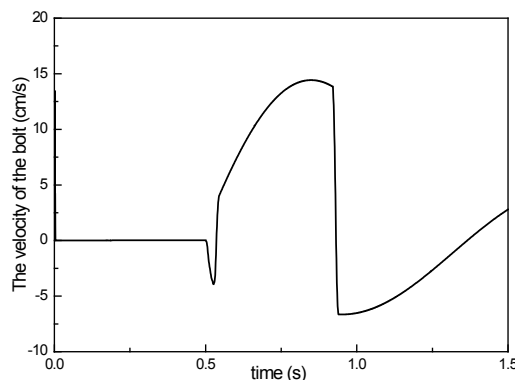


**Figure 6.** The bolt velocity curve

From the Figure 7, the velocity of the bolt changed in an instant because of the applied pre-tightening load within 0.004s, and then the velocity remained stable. The upper nut began to rotate when the device got a release signal at 0.5s, and the bolt possessed a reverse velocity. What's more, the bolt didn't drop down until the thread completely staggers. The maximum velocity of the bolt is 14.4121cm/s when the bolt nearly touched the shield. However, there's the cushion at the bottom of the shield, so the impact of the shock reduce gradually.

### 3.3 The Results of the Intensity Check by ANASY Software

The results of stress and strain contours of the upper nut are shown in Figure 7 and Figure 8.

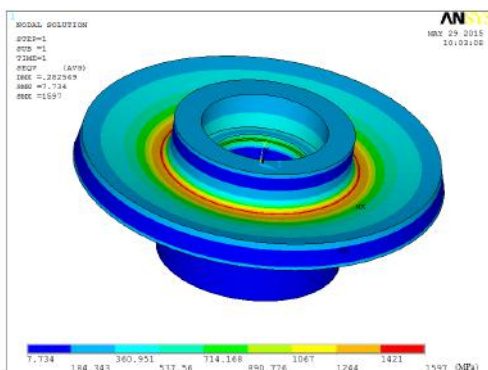


**Figure 7.** The stress contour of upper nut

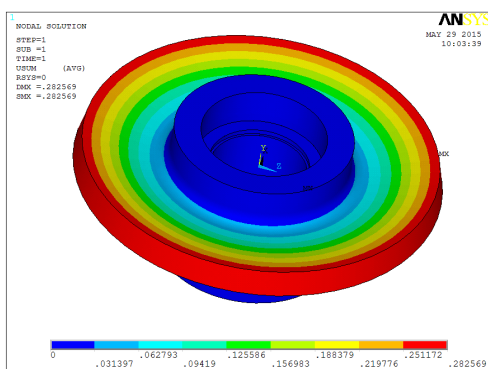


**Figure 8.** The strain contour of the upper nut

The maximum stress get from the software is 1597MPa, which appears on the end face of the upper nut and the lower end position. The upper nut material is steel TM210 and its yield strength is 1960MPa, so the upper nut's structure can meet the strength requirement. The maximum deformation of the structure is only 0.2826mm, which appears on the upper cylindrical of the upper nut, it also meet the design requirement.

The results of other parts are shown as follows, as shown in Figure 9 to Figure 14. Their strength and deformation also meet the requirement.

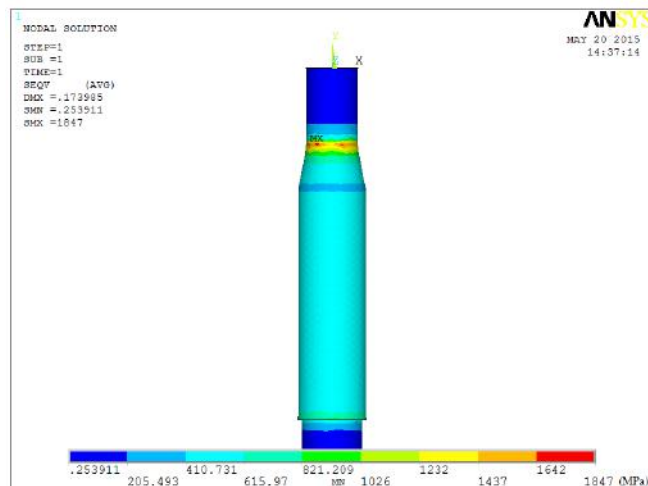


Figure 9. The stress contour of the bolt

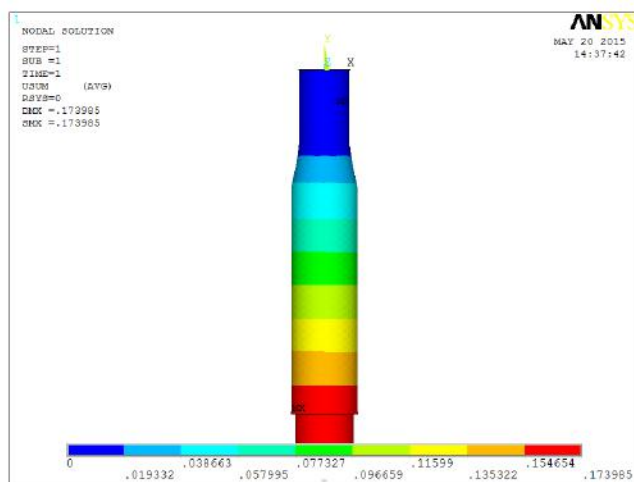
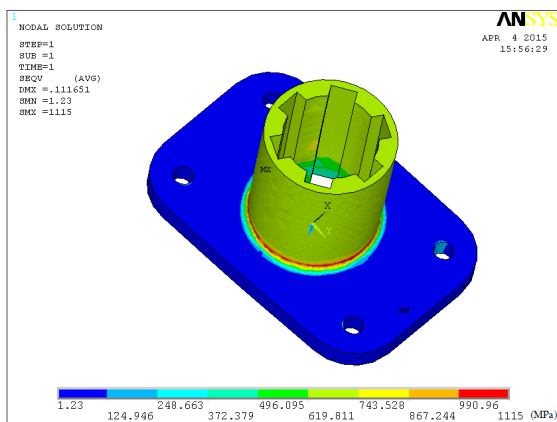
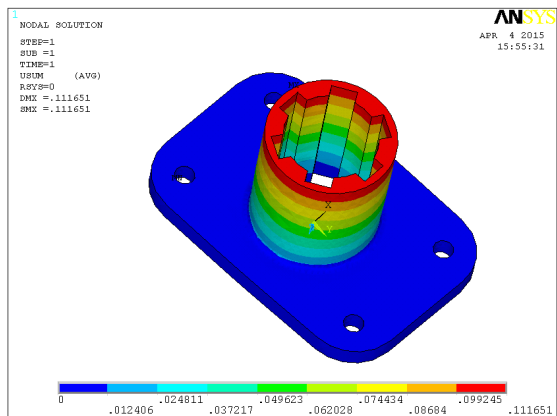


Figure 10. The strain contour of the bolt



**Figure 11.** The stress contour of the spline sleeve



**Figure 12.** The strain contour of the spline sleeve

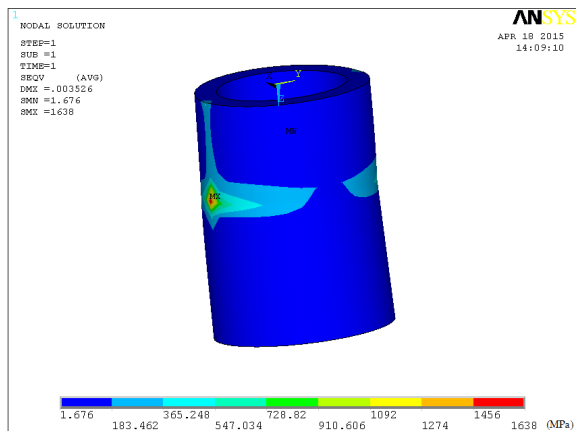


**Figure 13.** The stress contour of the shear set

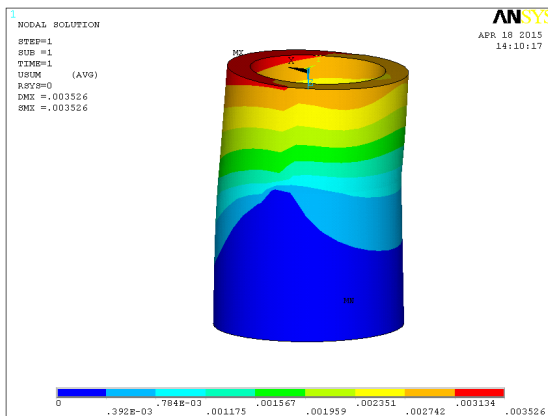


**Figure 14.** The strain contour of the shear set

## 4 Conclusion

This paper designed the structure of the incomplete thread space release device. The main parameters of the thread and the springs were also calculated.

The ADAMS software was used to carry on dynamic simulation and verify the force and the torque of the springs. The release time and the maximum velocity of the device got through the simulation is 0.36s, 14.4121 cm/s, respectively. The device releases fast and has a very low shock.

The ANSYS software was used for the intensity check of main components. The main components that the upper nut, the bolt, the spline sleeve, and the shear set were checked by the software. The maximum stresses got from the software were 1597MPA, 1847MPA, 1115MPA, and 1638MPA, respectively. Their strengths meet the load conditions.

**Acknowledgment:** This paper is supported by the Fundamental Research Funds for the Central Universities (3132016354).

## References

- [1] Wang Yuzhuo. Development and experiment of shape memory alloy rotary lock/ release mechanism[D]. Harbin Institute of Technology, 2013.
- [2] Li Zhiqiang. The explosive device used in spacecraft[J]. Spacecraft Recovery & Remote Sensing, 1997, 17(6):63-67.
- [3] Yang Mouxiang, Hao Fang. Space pyrotechnics devices[J]. Spacecraft Recovery & Remote Sensing, 1999, 19(4):37-40.

- [4] Leng J, Lan X, Liu Y, Du S. Shape-memory polymers and their composites: stimulus methods and applications. *Master Sci* 2011;26(7):1077-135.
- [5] Herbage E. Comparison of shape memory metals and polymers. *Adv Eng Master* 2006;8:101-6.
- [6] Huang W. On the selection of shape memory alloys for actuators. *Master Des* 2002; 23:11-9.
- [7] Hanqing Wei, Liwu Liu, Zhichun Zhang. Design and analysis of smart release devices based on shape memory polymer composites. *Composite Structures* 2015;133:642-651.
- [8] Yu Dianyong, Qian Yujin. Parameter settings for the dynamic simulation based on ADAMS[J]. *Computer Simulation*, 2006, 23(9):103-108.
- [9] Ma Yi. The study of virtual prototype technology on dynamics simulation of spacecraft deployable mechanism[D]. Chinese Academy of Science, 2006.
- [10] Chen Liping, Zhang Yunqing. *ADAMS mechanical system dynamics analysis and application tutorials*[M]. Beijing: Tsinghua University Press, 2005.
- [11] Xu Jinsu, Zhao Yun. Dynamic analysis of chilli block seeding transplanter based on ANSYS and ADAMS[J].*Zhejiang Sci-Tech University*, 2009, 26(5):731-733.
- [12] Zhao Ying. Development of the space release device based on shape memory alloy[D]. Harbin Institute of Technology, 2011.

Tao ZHAN\*, Guang-you YANG, Xue-hai CHEN, Wen-sheng LIU

## The Adjusting Method of Box Girder Pose based on Spatial Coordinate Transformation

**Abstract:** In the jacking construction of box girder at four points, in order to move the box girder to its design position people generally use artificial experience methods in which the labor intensity is great and the adjustment time is long. In this paper, the idea of spatial coordinate transformation is used to solve the adjustment quantity of three-direction jacks in the jacking construction, the principle of box girder adjustment is given, and the calculation formula of adjustment quantity of three-direction jacks is derived. For the adjustment quantity calculation of redundant three-direction jacks in practical application of engineering, a method based on coordinate transformation matrix and one based on geometric relation are presented respectively in this paper. In addition, in this paper, the influence factors on vertical adjustment quantity of jacks are analyzed, and the results show that when the initial and design coordinates of measuring points are given, under certain conditions it can be considered that the vertical adjustment quantity of three-direction jacks is only related to X and Y coordinates of the vertexes of three-direction jacks in the initial position, this conclusion helps to reduce the workload of measurement. This paper provides a multi-directional asynchronous jacking method based on the use of computer-controlled technology with a theoretical basis.

**Keywords:** Spatial coordinate transformation; Adjusting principle; Redundant three-direction jack; Vertical adjustment quantity

## 1 Introduction

In the hoisting construction of box girders, it is very difficult for them to reach their design position. In general, the position and orientation of box girders are adjusted by three-direction hydraulic jacks, so that the box girders are moved from their initial position to their design position. In the jacking construction of box girders at four points, the schematic diagram of three-direction jacks positioning is shown in Figure 1. At present, the manual adjustment method is often used in the project, which is time-consuming and laborious, and sometimes even seriously delays the progress of the

---

\*Corresponding author: Tao ZHAN, Institute of Agricultural Machinery, Hubei University of Technology, Wuhan, China, E-mail: 924635344@qq.com

Guang-you YANG, Xue-hai CHEN, Institute of Agricultural Machinery, Hubei University of Technology, Wuhan, China

Wen-sheng LIU, School of Civil Engineering and Architecture, Hubei University of Technology, Wuhan, China

project. Hydraulic synchronous jacking technology based on PLC can realize the translational synchronization of each hydraulic jack in [1], but it cannot realize the asynchronous adjustment of each hydraulic jack in all directions and cannot realize the adjustment of box girder pose. The idea of spatial coordinate transformation in [2] is used in this paper to study the adjustment method of box girder pose and solve the adjustment quantity of three-direction jacks, which provides a theoretical basis for the quick adjustment of three-direction jacks.

## 2 The adjustment principle of box girder pose

As shown in Figure 1, the box girder is supported by 4 three-direction jacks in its jacking construction. The known condition is that in the geodetic coordinate system the coordinates of the measuring points on the box girder in the initial and design position, and the coordinates of the vertexes of 4 three-direction jacks which support the box girder in the initial position. The problem is how to adjust the displacement in three directions of each three-direction jack to make the measuring points reach their design position, namely, to make the box girder reach its design position.

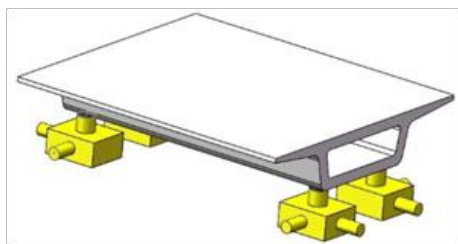


**Figure 1.** Schematic diagram of three-direction jacks positioning

### 2.1 Selection of measuring points

In engineering practice, the height of measuring pins on the box girder is different, and there is a certain error in the measurement. Therefore, it is necessary to select three ones from the four measuring points appropriately to reduce the error. The specific method is to eliminate the measuring point whose absolute value of the coordinate change between the design position and the initial position is maximum. In addition, the box girder is lifted by four jacks, although the more jacking points there are, the better rigidity the lifting surface has, the smaller the deformation is, and the better the stability is in [3], but four-point jacking will cause a redundancy problem in [4]. In this paper, we only select three from the four jacks to calculate,

and we assume the polyhedron composed of 4 measurement points and 4 vertexes of 4 three-direction jacks as a rigid body. Without a loss of generality, we assume that the bottom of the box girder is a plane. Thus the coordinates of the vertex of the fourth jack can be solved according to the shape of the box girder and the relative position of jacks. When the dynamic coordinate system is established on a box girder, the adjustment quantity of three-direction jacks can be solved according to the idea of spatial coordinate transformation.

## 2.2 Establishment of coordinate system

As shown in Figure 2, we assume that in the initial position of the box girder, the measuring points selected are  $A_{10}$ ,  $A_{20}$ ,  $A_{30}$ , and the corresponding vertexes of three jacks selected are  $B_{10}$ ,  $B_{20}$ ,  $B_{30}$ ; In the design position of the box girder, the measuring points are  $A_{11}$ ,  $A_{21}$ ,  $A_{31}$ , and the vertexes of the three jacks are  $B_{11}$ ,  $B_{21}$ ,  $B_{31}$ . The box girder is moved from the initial position  $\Delta A_{10}$ ,  $A_{20}$ ,  $A_{30}$  to the design position  $\Delta A_{11}$ ,  $A_{21}$ ,  $A_{31}$  by adjusting hydraulic jacks, namely, the correct positioning of the box girder is realized. Any coordinate system which is fixed to an object can be used as a reference coordinate system for describing the position and orientation of an object in [5]. First we create a dynamic coordinate system  $A_{10} - X_0 Y_0 Z_0$  at point  $A_{10}$ , the positive direction of  $X_0$ -axis is the same as the direction of vector  $\overrightarrow{A_{10}A_{20}}$  and the positive direction of  $Z_0$ -axis is the same as the direction of vector  $\overrightarrow{A_{10}A_{20}} \times \overrightarrow{A_{10}A_{30}}$ , thus the  $Y_0$ -axis can be determined based on the right-hand rule; Similarly, we create a dynamic coordinate system  $A_{11} - X_1 Y_1 Z_1$  at point  $A_{11}$ , the positive direction of  $X_1$ -axis is the same as the direction of vector  $\overrightarrow{A_{11}A_{21}}$ , and the positive direction of  $Z_1$ -axis is the same as the direction of vector  $\overrightarrow{A_{11}A_{21}} \times \overrightarrow{A_{11}A_{31}}$ , thus the  $Y_1$ -axis can also be determined based on the right-hand rule. By obtaining the coordinate transformation relations between the dynamic coordinate system and, as well as the geodetic coordinate system  $A_{10} - X_0 Y_0 Z_0$  and  $A_{11} - X_1 Y_1 Z_1$  the dynamic coordinate system  $A_{10} - X_0 Y_0 Z_0$ , we can convert the description in the coordinate system  $A_{11} - X_1 Y_1 Z_1$  of the vertexes of jacks in the design position to that in the geodetic coordinate system in [6].

## 2.3 Calculation of transformation matrix

As shown in Figure 2, we assume that in the coordinate system  $A_{10} - X_0 Y_0 Z_0$  created in the initial position whose direction vectors of  $X_0$ -axis,  $Y_0$ -axis,  $Z_0$ -axis are respectively assumed as  $a_0$ ,  $b_0$ ,  $c_0$ , the direction cosines of the vectors  $a_1$ ,  $b_1$ ,  $c_1$  which are assumed as the corresponding direction vectors of  $X_1$ -axis,  $Y_1$ -axis,  $Z_1$ -axis of coordinate system  $A_{11} - X_1 Y_1 Z_1$  created in the design position are respectively  $(n_1, n_2, n_3)$ ,  $(o_1, o_2, o_3)$ ,  $(a_1, a_2, a_3)$ , and the coordinates of the point  $A_{11}$  in the dynamic coordinate system  $A_{10} - X_0 Y_0 Z_0$  are

$(p_{x1}, p_{y1}, p_{z1})$ . According to the coordinate systems established in the previous section, we can have:

$$\begin{aligned}\vec{a}_0 &= \overrightarrow{A_{10}A_{20}} & \vec{c}_0 &= \overrightarrow{A_{10}A_{20}} \times \overrightarrow{A_{10}A_{30}} & \vec{b}_0 &= \vec{c}_0 \times \vec{a}_0 \\ \vec{a}_1 &= \overrightarrow{A_{11}A_{21}} & \vec{c}_1 &= \overrightarrow{A_{11}A_{21}} \times \overrightarrow{A_{11}A_{31}} & \vec{b}_1 &= \vec{c}_1 \times \vec{a}_1\end{aligned}$$

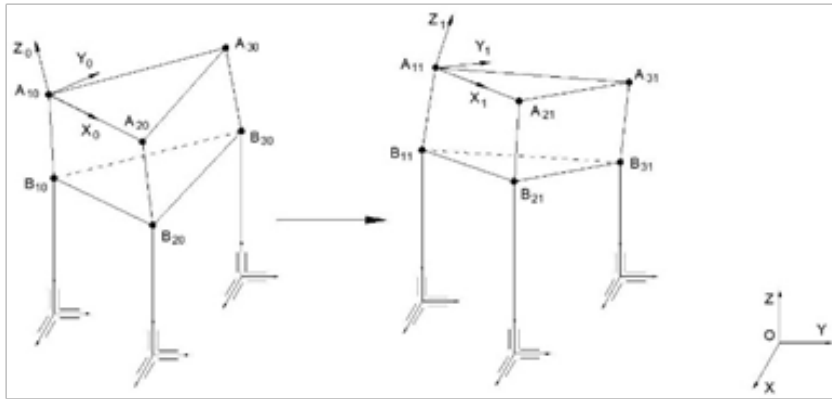


**Figure 2.** Coordinate systems established in the adjustment of box girder

The dynamic coordinate system  $A_{10}-X_0Y_0Z_0$  can be consistent with the dynamic coordinate system  $A_{11}-X_1Y_1Z_1$  through spatial coordinate transformation in [7], we assume that the transformation matrix which  $A_{11}-X_1Y_1Z_1$  is relative to  $A_{10}-X_0Y_0Z_0$  is:

$$T_1 = \begin{bmatrix} n_1 & o_1 & a_1 & p_{x1} \\ n_2 & o_2 & a_2 & p_{y1} \\ n_3 & o_3 & a_3 & p_{z1} \\ 0 & 0 & 0 & 1 \end{bmatrix}$$

We assume that in the initial position, the coordinates of the vertexes  $B_{10}, B_{20}, B_{30}$  of jacks in the dynamic coordinate system  $A_{10}-X_0Y_0Z_0$  are respectively  $B_{10}(x_{b_{10}}, y_{b_{10}}, z_{b_{10}})$ ,  $B_{20}(x_{b_{20}}, y_{b_{20}}, z_{b_{20}})$ ,  $B_{30}(x_{b_{30}}, y_{b_{30}}, z_{b_{30}})$ , then we can get:

$$x_{b_{10}} = \frac{\overrightarrow{A_{10}B_{10}} \cdot \overrightarrow{A_{10}A_{20}}}{|\overrightarrow{A_{10}A_{20}}|}, \quad y_{b_{10}} = \frac{\overrightarrow{A_{10}B_{10}} \cdot \vec{b}_0}{|\vec{b}_0|}, \quad z_{b_{10}} = \frac{\overrightarrow{A_{10}B_{10}} \cdot \vec{c}_0}{|\vec{c}_0|}$$

$$x_{b_{20}} = \frac{\overrightarrow{A_{10}B_{20}} \cdot \overrightarrow{A_{10}A_{20}}}{|\overrightarrow{A_{10}A_{20}}|}, \quad y_{b_{20}} = \frac{\overrightarrow{A_{10}B_{20}} \cdot \vec{b}_0}{|\vec{b}_0|}, \quad z_{b_{20}} = \frac{\overrightarrow{A_{10}B_{20}} \cdot \vec{c}_0}{|\vec{c}_0|}$$

$$x_{b_{30}} = \frac{\overrightarrow{A_{10}B_{30}} \cdot \overrightarrow{A_{10}A_{20}}}{|\overrightarrow{A_{10}A_{20}}|}, \quad y_{b_{30}} = \frac{\overrightarrow{A_{10}B_{30}} \cdot \vec{b}_0}{|\vec{b}_0|}, \quad z_{b_{30}} = \frac{\overrightarrow{A_{10}B_{30}} \cdot \vec{c}_0}{|\vec{c}_0|}$$

We assume that the coordinate transformation matrix which the dynamic coordinate system  $A_{10}-X_0Y_0Z_0$  is relative to the geodetic coordinate system O-XYZ is  $T_2$ , let

$$T_2 = \begin{bmatrix} n_{10} & o_{10} & a_{10} & p_{x10} \\ n_{20} & o_{20} & a_{20} & p_{y10} \\ n_{30} & o_{30} & a_{30} & p_{z10} \\ 0 & 0 & 0 & 1 \end{bmatrix}, \text{ then we have}$$

$$n_{10} = \frac{\vec{a}_0 \cdot (1, 0, 0)}{1 \cdot |\vec{a}_0|}, \quad n_{20} = \frac{\vec{a}_0 \cdot (0, 1, 0)}{1 \cdot |\vec{a}_0|}, \quad n_{30} = \frac{\vec{a}_0 \cdot (0, 0, 1)}{1 \cdot |\vec{a}_0|}$$

$$o_{10} = \frac{\vec{b}_0 \cdot (1, 0, 0)}{1 \cdot |\vec{b}_0|}, \quad o_{20} = \frac{\vec{b}_0 \cdot (0, 1, 0)}{1 \cdot |\vec{b}_0|}, \quad o_{30} = \frac{\vec{b}_0 \cdot (0, 0, 1)}{1 \cdot |\vec{b}_0|}$$

$$a_{10} = \frac{\vec{c}_0 \cdot (1, 0, 0)}{1 \cdot |\vec{c}_0|}, \quad a_{20} = \frac{\vec{c}_0 \cdot (0, 1, 0)}{1 \cdot |\vec{c}_0|}, \quad a_{30} = \frac{\vec{c}_0 \cdot (0, 0, 1)}{1 \cdot |\vec{c}_0|}$$

$$p_{x10} = x_{A_{10}}, \quad p_{y10} = y_{A_{10}}, \quad p_{z10} = z_{A_{10}}$$

Among them,  $(x_{A_{10}}, y_{A_{10}}, z_{A_{10}})$  are the coordinates of point  $A_{10}$  in the geodetic coordinate system O-XYZ.

#### 2.4 The adjustment quantity calculation of three-direction jacks

By adjusting three-direction jacks under the box girder, the coordinate system  $A_{10} - X_0 Y_0 Z_0$  coincides with the coordinate system  $A_{11} - X_1 Y_1 Z_1$ , namely, the adjustment of box girder from the initial position to the design position is completed. We assume that the adjustment quantity of the three jacks in the adjustment process is respectively  $(\Delta x_1, \Delta y_1, \Delta z_1), (\Delta x_2, \Delta y_2, \Delta z_2), (\Delta x_3, \Delta y_3, \Delta z_3)$ , we continue to assume that  $D_0$  is the initial position matrix of the vertexes of three-direction jacks in the coordinate system  $A_{10} - X_0 Y_0 Z_0$  and  $D_1$  is the initial position matrix of the vertexes of three-direction jacks in the geodetic coordinate system O-XYZ, namely,

$$D_0 = \begin{bmatrix} x_{b10} & x_{b20} & x_{b30} \\ y_{b10} & y_{b20} & y_{b30} \\ z_{b10} & z_{b20} & z_{b30} \\ 1 & 1 & 1 \end{bmatrix}, \quad D_1 = \begin{bmatrix} x_{B10} & x_{B20} & x_{B30} \\ y_{B10} & y_{B20} & y_{B30} \\ z_{B10} & z_{B20} & z_{B30} \\ 1 & 1 & 1 \end{bmatrix}$$

Then we can get:

$$\begin{bmatrix} \Delta x_1 & \Delta x_2 & \Delta x_3 \\ \Delta y_1 & \Delta y_2 & \Delta y_3 \\ \Delta z_1 & \Delta z_2 & \Delta z_3 \\ 0 & 0 & 0 \end{bmatrix} = T_2 \cdot T_1 \cdot D_0 - D_1. \quad (1)$$

Since the expression on the right side of (1) is consists of the known values which have been solved or obtained by measuring, the adjustment quantity of the three three-direction jacks in the adjustment process can be obtained, thus the box girder can be moved from the initial position to the design position.

### 3 Discussion on practical application of engineering

#### 3.1 The adjustment quantity calculation of redundant three-direction jack

During the installation construction of a box girder, the box girder is usually supported by 4 or more three-direction jacks. The position and orientation of the box girder regarded as a rigid body can be determined by a coordinate system. For the adjustment quantity calculation of the rest of the three-direction jacks, two ways can be adopted to deal with.

One way is to make the vertexes of the rest of the three-direction jacks and the ones of the three three-direction jacks which have been selected above (namely  $B_{10}$ ,  $B_{20}$ ,  $B_{30}$ ) have the same coordinate transformation, then we can get the coordinates of the vertex of each redundant three-direction jack in the design position in the geodetic coordinate system O-XYZ, so the corresponding adjustment quantity can be obtained. Here we take the fourth three-direction jack as an example, we assume that in the initial position, the coordinates of the vertex  $B_{40}$  of the fourth three-direction jack in the dynamic coordinate system  $A_{10} - X_0Y_0Z_0$  are  $(x_{b_{40}}, y_{b_{40}}, z_{b_{40}})$  and the ones in the geodetic coordinate system O-XYZ are  $(x_{B_{40}}, y_{B_{40}}, z_{B_{40}})$ , moreover we assume:

$$E_0 = [x_{b_{40}}, y_{b_{40}}, z_{b_{40}}, 1]^T, E_1 = [x_{B_{40}}, y_{B_{40}}, z_{B_{40}}, 1]^T$$

Then the adjustment quantity  $(\Delta x_4, \Delta y_4, \Delta z_4)$  of the fourth three-direction jack meet:

$$[\Delta x_4, \Delta y_4, \Delta z_4, 0]^T = T_2 \cdot T_1 \cdot E_0 - E_1. \quad (2)$$

Another way is to solve the adjustment quantity of the rest of the three-direction jacks by the geometric relation, namely, in the adjustment process of the box girder, the vertexes of the rest of the three-direction jacks are always kept in contact with the bottom of the box girder by only adjusting the Z coordinate. Without loss of generality, we assume there is a fourth jack under the box girder and the bottom of the box girder is a plane (If it is not a plane, the adjustment quantity can also be calculated by this method according to the relative position relation), the calculation procedures of the adjustment quantity are as follows.

We assume that in the initial position, the coordinates of the vertex  $B_{40}$  of the fourth three-direction jack in the geodetic coordinate system O-XYZ are  $(x_{B_{40}}, y_{B_{40}}, z_{B_{40}})$ , the normal vector of plane  $B_{11}, B_{21}, B_{31}$  is  $\vec{n}_1 = \overrightarrow{B_{11}B_{21}} \times \overrightarrow{B_{11}B_{31}} = (A, B, C)$ , thus the point norm form equation of plane  $B_{11}, B_{21}, B_{31}$  in the geodetic coordinate system O-XYZ is:

$$A(x - x_{B_{11}}) + B(y - y_{B_{11}}) + C(z - z_{B_{11}}) = 0. \quad (3)$$

Because the plane  $B_{11}, B_{21}, B_{31}$  cannot be in a vertical state,  $C \neq 0$ . Thus (3) can be converted into:

$$z = \frac{A}{C}(x_{B_{11}} - x) + \frac{B}{C}(y_{B_{11}} - y) + z_{B_{11}}. \quad (4)$$

From (4), we know that the adjustment quantity  $\Delta z_4$  of the Z coordinate of the fourth three-direction jack is:

$$\Delta z_4 = \frac{A}{C}(x_{B_{11}} - x_{B_{40}}) + \frac{B}{C}(y_{B_{11}} - y_{B_{40}}) + z_{B_{11}} - z_{B_{40}}. \quad (5)$$

The advantage of the second way is that only the Z coordinate of the redundant three-direction jack along the vertical direction need to be adjusted, the adjustment process is simplified and the work intensity is reduced.

After the adjustment quantity calculation of all three-direction jacks is accomplished, the multi-direction asynchronous adjustment of three-direction jacks can be realized by multi-axis motion control system, so that the box girder can be moved from its initial position to its design position.

### 3.2 Analysis of influence factors on the vertical adjustment quantity of three-direction jacks

After the initial position and design position coordinates of measurement points are given, the adjustment quantity of three-direction jacks along the vertical direction is less affected by Z coordinates of the vertexes of three-direction jacks in the initial position, that's to say, it can be considered that the adjustment quantity is only related to X and Y coordinates of the vertexes of three-direction jacks in the initial position. The analysis procedure is as follows:

We assume that  $T_2 \cdot T_1 = \begin{bmatrix} N_1 & O_1 & A_1 & P_{x1} \\ N_2 & O_2 & A_2 & P_{y1} \\ N_3 & O_3 & A_3 & P_{z1} \\ 0 & 0 & 0 & 1 \end{bmatrix}$ , thus the design position matrix of the vertexes of three-direction jacks in the geodetic coordinate system O-XYZ is:

$$\begin{aligned} & \begin{bmatrix} x_{B_{11}} & x_{B_{21}} & x_{B_{31}} \\ y_{B_{11}} & y_{B_{21}} & y_{B_{31}} \\ z_{B_{11}} & z_{B_{21}} & z_{B_{31}} \\ 1 & 1 & 1 \end{bmatrix} = T_2 \cdot T_1 \cdot \begin{bmatrix} x_{b_{10}} & x_{b_{20}} & x_{b_{30}} \\ y_{b_{10}} & y_{b_{20}} & y_{b_{30}} \\ z_{b_{10}} & z_{b_{20}} & z_{b_{30}} \\ 1 & 1 & 1 \end{bmatrix} \\ & = \begin{bmatrix} N_1 & O_1 & A_1 & P_{x1} \\ N_2 & O_2 & A_2 & P_{y1} \\ N_3 & O_3 & A_3 & P_{z1} \\ 0 & 0 & 0 & 1 \end{bmatrix} \cdot \begin{bmatrix} x_{b_{10}} & x_{b_{20}} & x_{b_{30}} \\ y_{b_{10}} & y_{b_{20}} & y_{b_{30}} \\ z_{b_{10}} & z_{b_{20}} & z_{b_{30}} \\ 1 & 1 & 1 \end{bmatrix}. \end{aligned} \quad (6)$$

Then, the adjustment quantity of the hydraulic cylinder in the vertical direction is respectively:

$$\Delta z_1 = z_{B_{11}} - z_{B_{10}} = N_3 \cdot x_{b_{10}} + O_3 \cdot y_{b_{10}} + A_3 \cdot z_{b_{10}} + P_{z1} - z_{B_{10}}. \quad (7)$$

$$\Delta z_2 = z_{B_{21}} - z_{B_{20}} = N_3 \cdot x_{b_{20}} + O_3 \cdot y_{b_{20}} + A_3 \cdot z_{b_{20}} + \\ P_{z1} - z_{B_{20}}. \quad (8)$$

$$\Delta z_3 = z_{B_{31}} - z_{B_{30}} = N_3 \cdot x_{b_{30}} + O_3 \cdot y_{b_{30}} + A_3 \cdot z_{b_{30}} + \\ P_{z1} - z_{B_{30}}. \quad (9)$$

We assume that  $\vec{c}_o = (d_1, d_2, d_3)$ ,  $\vec{b}_o = (d_4, d_5, d_6)$ . By separating the variable  $z_{B_{10}}$  from the expression on the right side of (7), we can get:

$$\Delta z_1 = K_{11} + K_{12} \cdot z_{B_{10}}, \text{ and}$$

$$K_{12} = \frac{(n_{30} \cdot n_1 + o_{30} \cdot n_2 + a_{30} \cdot n_3)(z_{A_{20}} - z_{A_{10}})}{\sqrt{(x_{A_{20}} - x_{A_{10}})^2 + (y_{A_{20}} - y_{A_{10}})^2 + (z_{A_{20}} - z_{A_{10}})^2}} + \\ \frac{d_6(n_{30} \cdot o_1 + o_{30} \cdot o_2 + a_{30} \cdot o_3)}{\sqrt{d_4^2 + d_5^2 + d_6^2}} + \frac{d_3(n_{30} \cdot a_1 + o_{30} \cdot a_2 + a_{30} \cdot a_3)}{\sqrt{d_1^2 + d_2^2 + d_3^2}} - 1. \quad (10)$$

Similarly, by separating respectively the variable  $z_{B_{20}}$  and  $z_{B_{30}}$  from the expression on the right side of (8) and (9), we can get:

$$\Delta z_2 = K_{21} + K_{22} \cdot z_{B_{20}}, \text{ and}$$

$$\Delta z_3 = K_{31} + K_{32} \cdot z_{B_{30}},$$

$$K_{22} = \frac{(n_{30} \cdot n_1 + o_{30} \cdot n_2 + a_{30} \cdot n_3)(z_{A_{20}} - z_{A_{10}})}{\sqrt{(x_{A_{20}} - x_{A_{10}})^2 + (y_{A_{20}} - y_{A_{10}})^2 + (z_{A_{20}} - z_{A_{10}})^2}} + \\ \frac{d_6(n_{30} \cdot o_1 + o_{30} \cdot o_2 + a_{30} \cdot o_3)}{\sqrt{d_4^2 + d_5^2 + d_6^2}} + \frac{d_3(n_{30} \cdot a_1 + o_{30} \cdot a_2 + a_{30} \cdot a_3)}{\sqrt{d_1^2 + d_2^2 + d_3^2}} - 1$$

$$K_{32} = \frac{(n_{30} \cdot n_1 + o_{30} \cdot n_2 + a_{30} \cdot n_3)(z_{A_{20}} - z_{A_{10}})}{\sqrt{(x_{A_{20}} - x_{A_{10}})^2 + (y_{A_{20}} - y_{A_{10}})^2 + (z_{A_{20}} - z_{A_{10}})^2}} + \\ \frac{d_6(n_{30} \cdot o_1 + o_{30} \cdot o_2 + a_{30} \cdot o_3)}{\sqrt{d_4^2 + d_5^2 + d_6^2}} + \frac{d_3(n_{30} \cdot a_1 + o_{30} \cdot a_2 + a_{30} \cdot a_3)}{\sqrt{d_1^2 + d_2^2 + d_3^2}} - 1$$

Thus  $K_{12} = K_{22} = K_{32}$ .

Let  $K_{12} = K_{22} = K_{32} = -K$ , then we can get:

$$\Delta z_1 = K_{11} - K \cdot z_{B_{10}} \quad (11)$$

$$\Delta z_2 = K_{21} - K \cdot z_{B_{20}} \quad (12)$$

$$\Delta z_3 = K_{31} - K \cdot z_{B_{30}} \quad (13)$$

Substituting multi-group actual data, for example, the initial position and design position coordinates of the measurement points as well as the initial position coordinates of the vertexes of three-direction jacks shown in Table 1, value K obtained is very small (value K obtained from the first set of data is less than  $10^{-7}$  and values K obtained from the second and third sets of data are both less than  $10^{-6}$ ), and the values of  $z_{B_{10}}$ ,  $z_{B_{20}}$ ,  $z_{B_{30}}$  are less than  $10^2$ (m), therefore, for a set of engineering data, if value K obtained indirectly by (10) is not more than  $10^{-6}$ , the linear part of (11), (12), (13) can be ignored, that's to say we can have:

$\Delta z_1 \approx K_{11}$ , error  $\delta_1 = |-K \cdot z_{B_{10}}| < 10^{-4}$   
 $\Delta z_2 \approx K_{21}$ , error  $\delta_2 = |-K \cdot z_{B_{20}}| < 10^{-4}$   
 $\Delta z_3 \approx K_{31}$ , error  $\delta_3 = |-K \cdot z_{B_{30}}| < 10^{-4}$

Table 1. Actual data and calculation results of value K

Groups	Axes	Measurement points	Vertexes of jacks						value K		
			The initial position coordinates (m)			The design position coordinates (m)			The initial position coordinates (m)		
		The first point	The second point	The third point	The first point	The second point	The third point	The first point	The second point	The third point	
The first group	X	79.586	78.08	78.148	79.588	78.081	78.147	79.4	78.2	78.3	
	Y	-13.676	-13.665	-6.052	-13.676	-13.667	-6.053	-11.1	-11.1	-8.6	3.68875E-08
	Z	18.496	18.487	18.648	18.494	18.485	18.644	16.06	16.06	16.06	
The second group	X	79.569	78.064	78.122	79.588	78.083	78.154	79.379	78.179	78.275	3.58714E-07
	Y	-13.675	-13.668	-6.05	-13.676	-13.667	-6.049	-11.098	-11.1	-8.6	
	Z	18.496	18.486	18.649	18.494	18.485	18.644	15.185	15.073	15.185	
The third group	X	79.573	78.08	78.149	79.588	78.095	78.225	79.363	78.163	78.243	3.582775E-07
	Y	-13.672	-13.675	-6.052	-13.676	-13.667	-6.045	-11.099	-11.108	-8.608	
	Z	18.497	18.489	18.645	18.494	18.485	18.645	16.062	16.062	16.061	

**Table 2.** Actual data and calculation results of value K

Groups	Axes	Measurement points			The design position coordinates (m)			The initial position coordinates (m)			Vertices of jacks	value K
		The first point	The second point	The third point	The first point	The second point	The third point	The first point	The second point	The third point		
The first group	X	79.586	78.08	78.148	79.588	78.081	78.147	79.4	78.2	78.3		
	Y	-13.676	-13.665	-6.052	-13.676	-13.667	-6.053	-11.1	-11.1	-8.6		3.68875E-08
The second group	Z	18.496	18.487	18.648	18.494	18.485	18.644	16.06	16.06	16.06		
	X	79.569	78.064	78.122	79.588	78.083	78.154	79.379	78.179	78.275		3.58714E-07
The third group	Y	-13.675	-13.668	-6.05	-13.676	-13.667	-6.049	-11.098	-11.1	-8.6		
	Z	18.496	18.486	18.649	18.494	18.485	18.644	15.185	15.073	15.185		
	X	79.573	78.08	78.149	79.588	78.095	78.225	79.363	78.163	78.243		
	Y	-13.672	-13.675	-6.052	-13.676	-13.667	-6.045	-11.099	-11.108	-8.608		3.58276E-07
	Z	18.497	18.489	18.645	18.494	18.485	18.645	16.062	16.062	16.061		

Therefore, after the initial position and design position coordinates of the measurement points are given, if value K obtained is not more than  $10^{-6}$ , it can be considered that the adjustment quantity of three-direction jacks along the Z-axis is only related to X and Y coordinates of the vertexes of three-direction jacks in the initial position, that is to say, it is not related to Z coordinate of the ones, this helps to reduce the workload of measurement.

## 4 Conclusion

In this paper, the idea of spatial coordinate transformation is used to calculate the adjustment quantity of three-direction jacks in the adjustment process of box girder pose, and these theoretical calculation values can be displayed intuitively with the use of graphical user interface software. The adjustment method studied in this paper is mainly aimed at the multi-axis motion control system which can realize the multi-direction asynchronous adjustment of three-direction jacks, it facilitates the adjustment of box girders with any pose and greatly saves time. In addition, the adjustment method is also applicable to the adjustment of the box girder pose where the vertexes of many three-direction jacks are not in the same plane.

**Acknowledgment:** This paper is supported by Collaborative Innovation Center of Southern Agricultural Machinery and Equipment, Hubei University of Technology.

## References

- [1] HOU ZH G, ZHAO ZH Q, WANG W P. Hydraulic Synchronous Bridge Jack-up System Based on PLC Control [J]. ROAD MACHINERY & CONSTRUCTION MECHANIZATION, 2011, 28(6):28-31.
- [2] CAI Z X. ROBOTICS [M]. Beijing: Tsinghua University Press, 2009:18-25.
- [3] DONG Y H. Research Situation and Application Prospect of Bridge Jack-up Technique [J]. ROAD MACHINERY & CONSTRUCTION MECHANIZATION, 2011, 28(6):21-27.
- [4] ZHANG A R. Discussion on the level adjustment of objects supported by four points [J]. Fire Control Radar Technology, 1995, 24(1):42-46.
- [5] John J. Craig. Introduction to robotics mechanics and control [M]. Beijing:CHINA MACHINE PRESS, 2006:14-29.
- [6] WANG Y, HAO Y M. A Coordinate Transformation Method by Means of Space Vector [J]. JOURNAL OF SHENYANG INSTITUTE OF TECHNOLOGY, 1999, 18(1):29-32.
- [7] ZHANG K, ZHANG D J, SHENG Y H, WANG P F, PANG Y T. Research on Two Methods of Three Dimensional Coordinate Transformation and Their Comparision [J]. MATHEMATICS IN PRACTICE AND THEORY, 2008, 38(23):121-128.

Xiao-geng FANG\*, Yan-hui CHEN, Wan-feng LIU, Xi-rong LUO,  
Guo-jin XIE

## **Application of Discrete Element Method in the Analysis of Loader Shovel Loading Process**

**Abstract:** Distinct element method is a numerical method which is applicable to the analysis of granular material system, and its theoretical model is more suitable for the discontinuous, large displacement material particles. In this paper, the application of the EDEM software based on the Discrete Element Method in the analysis of the loader bucket loading process is introduced. From the force curve of the simulation, it shows that the bucket resistance can be increased first, and then gradually decreased to a stable value. Through the analysis, the simulation results are in accordance with the engineering application, which has certain reference value.

**Keywords:** Distinct element method; EDEM simulation; Loader shoveling

### **1 Introduction**

Wheel loader (Figure 1) is a type of widely used transport equipment, mainly used in mining, construction, railways, roads, ports construction. Its main working process can be divided to shovel - Transport - unloading, is one of the main engineering machineries. The loader bucket in service, must meet the high loading efficiency, small operation resistance, low shovel wear etc. As the direct function parts with material, the size of the bucket working resistance directly affects the integral design of the loader. Therefore, in the design of bucket, it is very significant to study the interaction between the bucket and material.

However, the bucket is a continuum while the material is discontinuous, and material system of shoveling and unloading process is complex and changeable, moreover, the interaction force is dynamic, thus the traditional finite element analysis for the continuum can not satisfy the needs of bucket design analysis [1]. Therefore, it is necessary to explore the new technology which can be used in bucket force analysis.

---

\*Corresponding author: Xiao-geng FANG, College of Mechanic Engineering, Guangxi University of Science and Technology, Liuzhou, China, E-mail: 958096750@qq.com

Yan-hui CHEN, Wan-feng LIU, Xi-rong LUO, Guo-jin XIE, College of Mechanic Engineering, Guangxi University of Science and Technology, Liuzhou, China

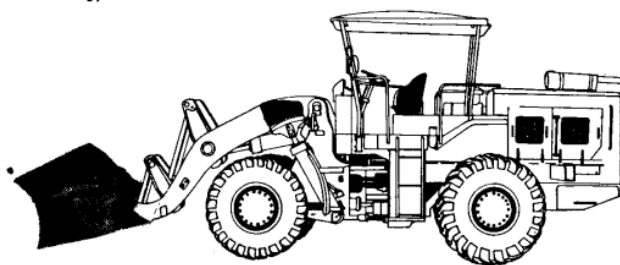


**Figure 1.** Wheel loader

Discrete element method is a numerical method mainly used for study of granular materials. It is proposed by Cundall and Strack after their study of the rock mass, using rigid element to simplify discontinuous system, and then Newton's second law motion equation and time-step iterative method to obtain the overall state of motion of discontinuous system. The calculation process can be summarized as follows: Firstly, contact force and the relative displacement are determined according to the interparticle contact model; secondly, unbalanced forces between particles were calculated on the basis of Newton's second law; finally, use the time-step iteration law and repeat the two process above until the final claiming iterations or system tends to force balance.

The choice of the particle contact model is the core part of the discrete element method. Cundall initially proposed a two-dimensional disk contact model shown in Figure 2, two spheres' contact was simplified as springs, dampers,  $K_n$  meant normal stiffness,  $d_n$  as the normal damping,  $K_t$  as the tangential stiffness,  $d_t$  as the tangential damping. Normal force and tangential force were respectively determined according to the Hertz theory [2] and Mindlin-Dereciewicz theory [3]. To achieve a more accurate model of the discrete material system, scholars improved contact model of discrete element method constantly. In literature[4-8], when the adhesion effect between unit was considered, Thorntond formed the Thorntond theory, in which tangential force was calculated based on Savkoor and Briggs theory [9], normal force combined with the adhesion force JKR (Johnson - Kendall - Rorberts) theory [10] on the basis of the original Hertz theory. In document [11], Rothenburg used a two-dimensional elliptic disk model for numerical simulation. In document [12], the effect of particle shape on the strength and deformation mechanism of the particle system was analyzed by Ting. In Document [13], Lin used the three-dimensional ellipsoid contact model, while in the literature [14], Oda took into account the rotation of the element, and improved the Cundall discrete element model on the basis of the Cundall model.

In short, the model DEM has been developed from simple 2D model to complex 3D model for the following 40 years since 1971, whose calculation results are getting closer to the actual situation. Gradually, it shows the advantage in certain areas.

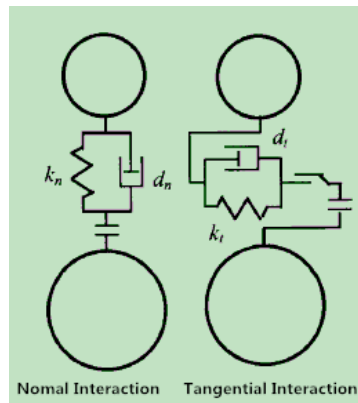


**Figure 2.** DEM model of Cundall

## 2 Domestic engineering applications of Discrete Element Method

With the development of the discrete element method, the related simulation software has emerged. EDEM is a Discrete Element Method analysis CAE software, mainly used in the simulation of industrial particles and manufacturing equipment. EDEM, having been launched by the Solutions DEM Company since 2002, is recognized by more and more users. EDEM simulation is mainly applied in agricultural engineering and mining engineering in China. In document [15], by simplifying soybean grain as tetrahedral configuration, the process of seed filling, retaining, cleaning, seeding and other movement in a mechanical soybean high speed precision metering device was simulated. In [16], researchers used EDEM to analyze movement law of rapeseed in a centrifugal metering device, as well as the related factors influencing the metering performance. Finally, the simulation results compared with the experimental results, proved the EDEM reliable. In the literature [17] and [18], authors used EDEM to simulate the movement of particles in the large capacity silo, and discussed the factors which influenced the material flow blockage in the process of using, which provided theoretical basis for optimizing the structure of the silo. In [19], the particle motion characteristics in the dense medium cyclone were obtained based on the coupling of EDEM and other CFD software.

## 3 The advantages of using discrete element method to analyze the bucket force

The materials that loaders load mainly include iron ore, sand, coal. These materials have rough surfaces, angular edges, a variety of shapes, and large size distribution

range. Besides, they are interconnected with each other, being very loose, belonging to the granular materials.

Granular materials are a complex systems consisting of a large number of discrete solid particles in which particle size  $d$  is greater than  $1\mu\text{m}$ , interstitial fluid viscosity is low and saturation is less than 1, the contact force between the particles is leading role, while the thermal motion of the particles and fluid action weak [20]. Bulk materials systems can be divided into micro-scale, meso-scale and macro-scale, their relationships [21] are shown in Figure 3. The micro-scale mainly refers to the contact force and adhesion between particles. Meso level mainly refers to the force chain formed by the inner contact force. Force chain is relatively stable, net distributed structure formed by granular material that contact with each other, which supports the gravity and external load of the whole system, but only afford small shear. Its main properties related to not only the granular material elastic modulus, surface friction coefficient, Poisson's ratio, but also to the particle system external conditions, such as boundary conditions, initial state, external load, bulk particles dispersion. Macro scale is the mechanical behavior of the whole particle system to the external environment.

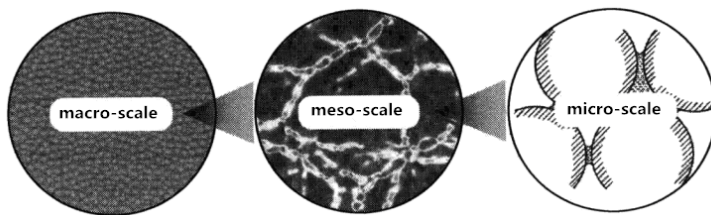


**Figure 3.** Multi-scale mechanics research framework of particle system

Theoretical model of the discrete element method fully takes account of the system discontinuity and large displacement. Therefore, the application in granular material system can perform its accuracy. Loading material is mainly ore, sand, coal. These materials are discrete, theoretically, it is feasible to adopt discrete element method for bucket force analysis. Discrete element method has been applied to the design of the loader bucket abroad, while China started relatively late in this field. Traditional method of mechanical structure analysis is using the patch to measure stress, and the bucket directly contacts with material when working, it is difficult to direct patch measurement. Only by indirect measurement method, can the force be measured. This is not only cumbersome operation, and experimental design of a great impact on the measurement accuracy. Through setting reasonable parameters, EDEM simulation can get the interaction force between the material and the bucket, providing qualitative reference for bucket design, which is conducive to shorten the design cycle and response to market demand rapidly.

## 4 The edem simulation of bucket shovelling process

EDEM mainly contains three modules: Creator, Simulator, analyst. EDEM has a powerful geometric modeling capability, allowing users to directly import mechanical structure CAD and particle CAD model, which can reduce the difficulty of its modeling, and also makes the particles model more accurately reflect the actual particle, improving simulation accuracy. What is more, EDEM software can also set the physical characteristics of the particle in the custom database, and thus reduce repeating operation.

EDEM software simulation module supports multiple operating system platforms, users can directly be offered by software contact model, and program custom contact model via the software interface; EDEM can be coupled with the CFD software simulation, to achieve a solid - liquid / gas two-phase analysis, in addition, EDEM can also be coupled with the FEA tool to complete the analysis of the structure of the manufacturing equipment. EDEM and other mainstream CAE tools coupled, which greatly expanded the discrete element method applications.

EDEM post processing module can achieve visualization and graphics operations, users can observe the physical quantity of the measurement that is not easy to measure, and can obtain 3D animation, to facilitate the dynamic display of simulation results. After calculated by EDEM, the users can get the speed and position of each particle, the interaction force chain between particles and the force between the particle and the manufacturing equipment. At last, users can get the information about the granular system behavior.

The realization of EDEM simulation in the manufacturing industry, we must determine the material properties of the granular system parameters, the relevant experiment can refer to the literature [22-24]. In theory, simulation parameters of EDEM are Poisson's ratio, shear modulus, coefficient of restitution, static friction coefficient and rolling friction coefficient. The following part describes EDEM simulation of loader shovel in loading process.

### 4.1 Setting global model parameters

Global model parameters need to be set are: global unit, contact model, gravity acceleration, material characteristics, material contact characteristics, and parameters were selected in Table 1, Table 2, Table 3.

**Table 1.** Main parameters

Name	Length	Angle	Quality	Acceleration of gravity	Contact Model
Parameter	mm	°	kg	-9.81 m/s <sup>2</sup>	Hertz-Mindlin(no slip)

**Table 2.** Material characteristics

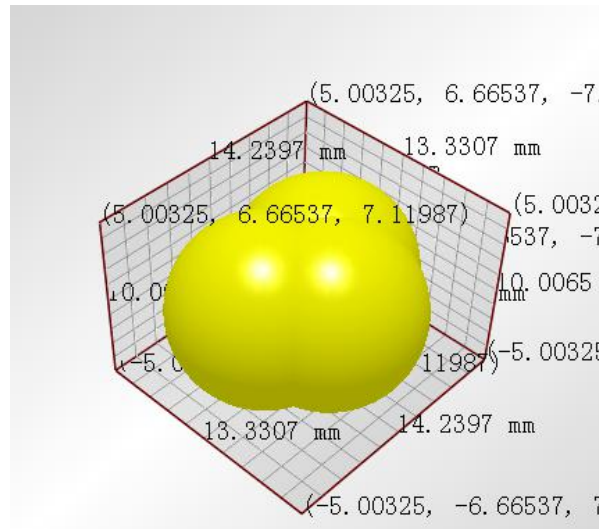
Material	Poisson ratio	Shear Modulus /GPa	Density / kg ·m <sup>-3</sup>
Stone	0.29	11.1	2090
Steel	0.3	79	7850

**Table 3.** Material contact properties

Interaction	Coefficient of restitution	Coefficient of static friction	Coefficient of rolling friction
Stone-Stone	0.5	0.84	0.002
Stone-Steel	0.45	0.47	0.002

#### 4.2 Defining the basic particles and geometry

Material particles shown in Figure 4 was defined as “stone”, size was 14\*13\*10m<sup>3</sup>. The bucket model shown in Figure 5 was created by the UG, and then imported into the EDEM, material selected for the “steel”, the movement of the bucket was set as following: 0s-2s, shoveled into material with uniform velocity of 0.12 m/s to the X-axis direction; 2s-3s for rotating bucket stage, the angular velocity was 25°/s; 3s-3.27s as backing stage with speed of 0.5m/s to negative X-axis direction; 3.27s-4s as lifting phase with velocity of 0.1 m/s to the Z-axis direction.

**Figure 4.** Particle model

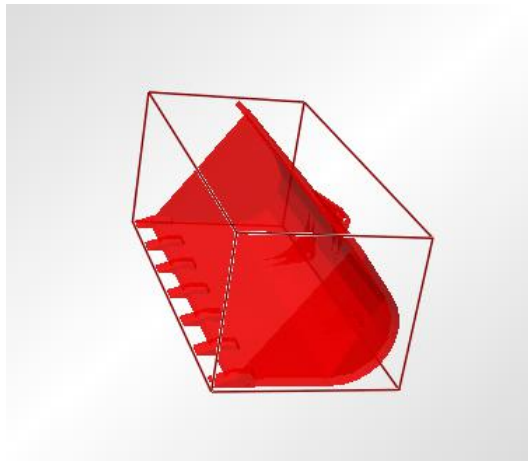


Figure 5. Bucket model

#### 4.3 Defining the particle factory

Factory type was set to generate statically, and the total number of simulation particles was 1000, generated at a rate of 1000 per second. The distribution of particles was normal distribution, the particle generation location was random, with the velocity of 0.1m/s to negative Z-axis. After generated, the particle factory was shown in Figure 6.

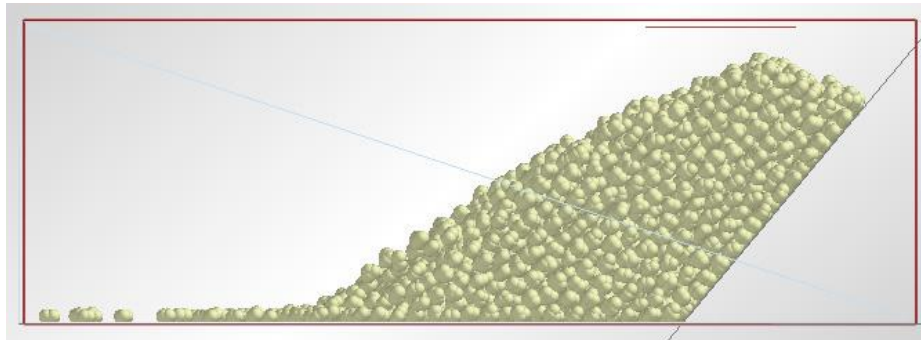


Figure 6. Particle factory

#### 4.4 Simulation parameter setting

The simulation step size was set to 20%, and the total simulation time was 4s, outputting interval was 0.01s.

#### 4.5 Analysis of simulation results

Simulation process was shown in Figure 7. After the simulation, by using EDEM post-processing tools, loading weight was measured to be 1.39 kg, shown in Figure 8. Eventually, changes of resistance force by bucket were presented in Figure 9.

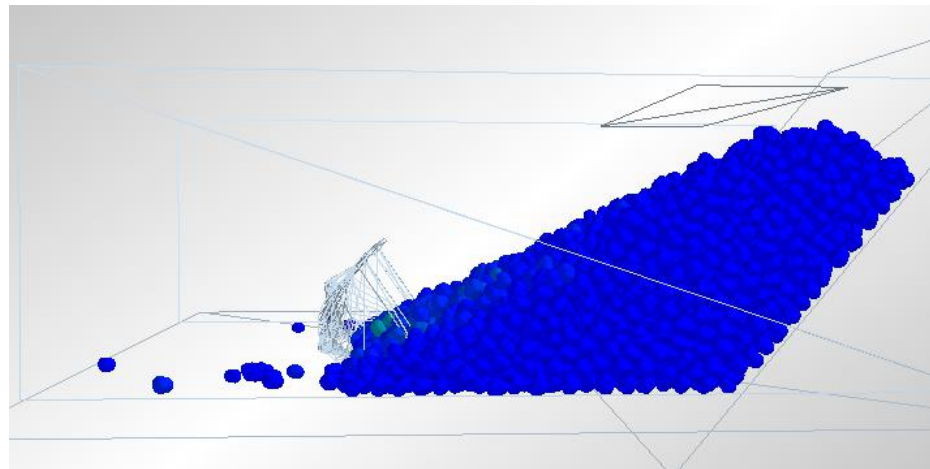


**Figure 7.** Simulation process

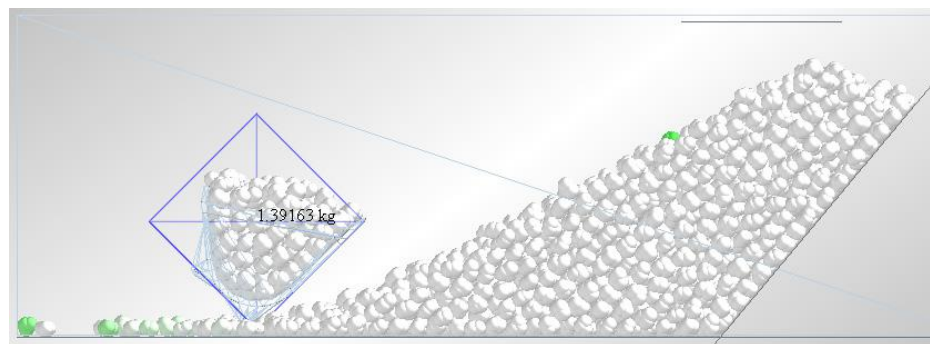


**Figure 8.** Loading quality

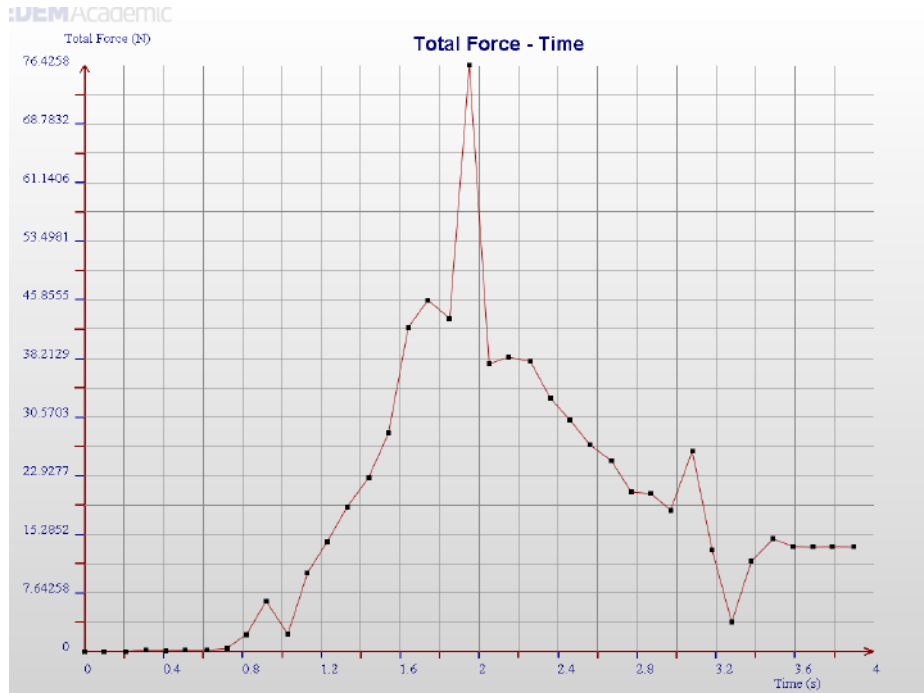


**Figure 9.** The resistance of bucket change with time

## 5 Conclusion

The simulation results showed that the bucket's resistance increased rapidly and reached the maximum value, and then decreased gradually to a stable value. Through the analysis, the simulation results were in accordance with the engineering application. Because the materials system was in a static state at the beginning, a stable force chain was formed inside. When the bucket was horizontally inserted into the bottom of the material system, the materials contacted with the bucket not only formed a force chain with the materials above but also with the rear materials. In this case, material system could withstand greater external force, so the resistance suffered by the bucket gradually increased. As the bucket rotated, the materials contacted with the bucket just formed a force chain with the materials above it. Thus, the bucket could shovel into the materials with less force, so the resistance force was reduced gradually. When the bucket was lifted at a uniform speed, the bucket would only be subjected to the gravity of the materials loaded, and its size would be fixed.

Bulk materials are abundant in agricultural and mining production. Loaders bucket traditional design method is the empirical formula calculation and experimental comparison. The interaction force between material elements and bucket is difficult

to be accurately measured, and test cycle is long and costly. Discrete element method is a numerical method to solve the problem of granular system. Compared with the finite element method, the discrete element method is still applicable to large displacement and discontinuous systems, which gives the discrete element method a unique advantage in specific fields. EDEM software based on discrete element method can facilitate the simulation of particle production process, reduce the prototype test and shorten the design cycle, which provides an effective tool for the design of bucket.

**Acknowledgment:** The work was funded by the Natural Science Foundation Program of Guangxi Province of China (Grant No. 2015GXNSFAA139271), Program of Guangxi Science and Technology innovation ability and condition construction plan (Grant No.1598021-2), and also supported by the Educational Commission of Guangxi Province of China (Grant No. ZD2014074).

## References

- [1] HOU Yajuan, WANG Jisheng, LI Aifeng, eta. Discrete Element Method and its application to Bucket Design[J]. Construction Machinery and Equipment, 2014, 45(4):23~29.
- [2] Johnson K L, Contact Mechanics[M]. London:Cambridge University Press, 1985:84~104.
- [3] Mindlin R D, Deresiewicz H. Elastic spheres in contact under varying oblique forces[J]. J Appl Mech, 1953, 20(3):327~344.
- [4] Thornton C. Interparticle sliding in the presence of adhesion[J]. J Phys D: Appl Phys, 1991, 24:1942~1946.
- [5] Thornton C, Yin K K. Impact of elastic spheres with and without adhesion[J]. Powder Technology, 1991, 65:153~166.
- [6] Thornton C. On the relationship between the modulus of particulate media and surface energy of the constituent particles[J]. J Phys D: Appl Phys, 1993, 26:1587~1591.
- [7] Thornton C, Ning Z. A theoretical model for the stick/bounce behaviour of adhesive, elastic-plastic spheres [J]. Powder Technology, 1998, 99:154~162.
- [8] Thornton C, Coefficient of restitution for collinear collisions of elastic-perfectly plastic spheres[J]. J Appl Mech, 1998, 64: 383~386.
- [9] Savkoor A R, Briggs G A D. The effect of tangential force on the contact of elastic solids in adhesion[J]. Proc R Soc Lond A, 1977, 356:103~114.
- [10] Johnson K L, Kendall K, Roberts A D. Surface Energy and the contact of elastic solids[J]. Proc R Soc Lond A, 1971, 324: 301~313.
- [11] Rothenburg L, Bethurst R J. Numerical simulation of idealized granular assemblies with plane elliptical particles[J]. Compute Geotech, 1991, 11:315~329.
- [12] Ting J M, Meachum L R, Rowell J D. Effect of particle shape on the strength and deformation mechanisms of ellipse-shaped granular assemblages[J]. Engineering Computations, 1995, 12(2): 99~108.
- [13] Lin X, Ng T-T. A three dimensional discrete element model using arrays of ellipsoids[J]. Geotechnique. 1997, 47(2):319~329.
- [14] Oda M, Iwashita K, Kakiuchi T. Importance of particle rotation in the mechanics for granular materials. In: Behringer R P, Jenkins J T, eds. Powder Grain 97, 1997:207~214.

- [15] WANG Fulin, SHANG Jiajie, LIU Hongxin, etal. Application of EDEM particles simulation technology on seed-metering device research[J]. Journal of Northeast Agriculture University. 2013, 44(2):110~114.
- [16] Liao Qingxi, Zhang Pengling, Liao Yitao, etal. Numerical Simulation on Seeding Performance of Centrifugal Rape-seed Metering Device Based on EDEM [J]. Transaction of the Chinese Society for Agricultural Machinery, 2014, 45(2):109~114.
- [17] Liu Zhen, Wang Xuewen, Yang Zhaojian. Simulation of lateral pressure during stewing and discharging in silos based on EDEM[J]. Journal of Chinese Agricultural, 2015, 36(2):104~106.
- [18] WANG Xue-Wen, QIN Yi, TIAN Yan-Kang, etal. Analysis on flow features of bulk coal during coal unloading period based on EDEM[J]. Coal Science and Technology, 2015, 43(5):130~134.
- [19] HUANG Bo, CHEN Jing-Jing. Characteristic Analysis and Numerical Simulation of Particle Motion in Dense Medium Cyclone [J]. Coal Engineering, 2015, 47(5):115~117.
- [20] SUN Qicheng, WANG Guangqian. Introduction to mechanics of particle matter [M]. Beijing, Science Press 2009:1~3.
- [21] SUN Qicheng, WANG Guangqian, HU Kaiheng. Thoughts on several key problems of granular material mechanics [J]. Progress in Natural Science, 2008, 18(10):1104~1110.
- [22] YANG Jie. Simulation study of particles flow on the vertical dryer based on DEM[D]. Huazhong Agricultural University, 2012.
- [23] Cui Tao, Liu Jia, Yang Li, etal. Experiment and simulation of rolling friction characteristic of corn seed based on high-speed photography [J]. Transactions of Chinese Society of Agricultural Engineeering, 2013, 29(15):34~41.
- [24] Gabriel K. P. Barrios, Rodrigo M. de Carvaho. Contact parameter estimation for DEM simulation of iron ore pellet handling[J]. Powder Technology, 2013, 248:84~93

Jian QIN\*, Liang FENG, Jun CHEN, Jian-cheng WAN

## **Application of Piecewise Catenary Method in Length Calculation of Soft Busbar in Ultra-high Voltage Substation**

**Abstract:** According to actual setting-up operation condition of the soft busbar in the ultra-high voltage substation, the nonlinear piecewise catenary equations are established including weight of the insulator string, elastic elongation of the busbar, weight load of the electrical fitting etc. several influence factors on basis of the elastic catenary equation. The initial value selection plan is also given out for Newton iteration method of the nonlinear equations. The method sets both the insulator string and the busbar as the catenary lines, and considers the weight of fitting of multiple split conductors in the final cable shape, which greatly improves calculation accuracy. Reliability of the method is validated through comparison between calculation result of the piecewise catenary method and actual data. The piecewise catenary calculation forwarded in this paper is simple in formation and small in calculation quantity, which is liable to realize by program. The sags corresponding to the different blanking length of the busbar are obtained according to calculation results. The method can provide the effective mean for the length calculation and engineering construction of the soft busbar in the ultra-high voltage substation.

**Keywords:** substation; busbar; insulator string; piecewise suspension catenary; nonlinear equations

### **1 Introduction**

At present, construction of the ultra-high voltage power transmission line is developing in great scale, and the corresponding construction technology of the busbar in the substation is changed greatly from the conventional 500kV and 750kV substation. In engineering process, the key factor affecting construction quality of the busbar is the blanking length of the conductor [1,2].

In the conventional substation, length and weight of the insulator string are far less than the corresponding parameters of the conductor during construction of the busbar, which makes blanking calculation of the busbar conductor as the simple suspension cable issue. Length of the insulator string is neglected in the busbar

---

\*Corresponding author: Jian QIN, China Electric Power Research Institute, Beijing, China, E-mail: mathmech@126.com

Liang FENG, Jun CHEN, Jian-cheng WAN, China Electric Power Research Institute, Beijing, China

calculation method of the conventional substation, the busbar is considered as one catenary line, the single catenary equation or its similar solution is applied to calculate blanking length [3].

In the ultra-high voltage substation, influence of the insulator string on the sag of the conductor is increased because length and weight of the insulator strings in the busbar are increased greatly; error is great when the catenary equation is directly applied to calculate the blanking length of the conductor, which can't meet with design requirement [4,5]. Therefore Hu Shenghui et al. put forward the *combined model method* [6], which considers the insulator string as the suspension catenary, and calculates the busbar as the parabola or the straight line. This method doesn't obtain the accurate cable shape of the soft conductor; it also doesn't consider the influence caused by weight or centralized loads on the sag.

For the above issue, a piecewise catenary method is put forward in this paper for the blanking length calculation of the conductor during construction of the busbar in the ultra-high voltage substation. This method can analyse the elastic elongation of the busbar and the influence of fitting and centralized loads on the sag. Through comparison calculation with the engineering calculation sample in the reference document, it is seen the results are in accordance with engineering design requirements, which have high engineering practicability.

## 2 Piecewise analysis of busbar

Lengths of the insulator string and the fitting in the 1000 kV ultra-high voltage substation are very great (about 13m), and weights are also greater. Therefore influence of the insulator string on the whole sag can't be neglected, in particularly influence is more obvious when the span is very small.

Because difference of the conductor and the insulator string is very great in line density and there is the spacer, fittings in the conductor, the space cable shape of the busbar is generally divided into several segments, such as the conductor sections and insulator string sections. The conductor section is split up by the fittings between the insulator strings at two ends, shown as Figure 1. The insulator string section and the conductor section are the catenary lines which only bear weight.

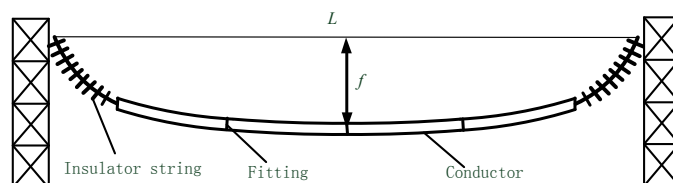


**Figure 1.** Diagram of segmented busbar.

For the split conductor, length changes of the conductors at upper and lower can be calculated according to connection conditions at two ends of the conductor.

### 3 Piecewise equation set of elastic busbar

In the busbar, both the insulator string section and the conductor section are catenary lines, set  $q$  as the cable density which is distributed along length of the arc,  $K$  is elastic constant of material,  $K = 0$  for the insulator string (i.e., elastic constant is 0), for the conductor  $K = 1/(EA_0)$ ,  $E$  is elastic module of the conductor,  $A_0$  is section area.

Shown as Figure 2, according to forcing conditions of the suspension cable micro-body, elastic catenary equations of height difference  $h$  and horizontal span  $l$  are obtained [7,8]:

$$\frac{H}{q}(a-b) + K \frac{H^2}{q} [\sinh(a) - \sinh(b)] = l \quad (1)$$

$$\frac{H}{q} [\cosh(a) - \cosh(b)] + \frac{KH^2}{2q} [\cosh^2(a) - \cosh^2(b)] = h \quad (2)$$

$$\frac{H}{q} [\sinh(a) - \sinh(b)] = s_0 \quad (3)$$

$$\begin{aligned} \frac{H}{q} [\sinh(a) - \sinh(b)] + \frac{KH^2}{4q} [\sinh(2a) - \sinh(2b)] \\ + \frac{KH^2}{2q} (a-b) = s \end{aligned} \quad (4)$$

In which:  $H$  is horizontal component of tangential tension;  $a = \sinh^{-1}(V_A/H)$ ,  $b = \sinh^{-1}(V_B/H)$ ,  $V_A$ ,  $V_B$  are vertical components of tangential tension at end points;  $s_0$  is initial cable length,  $s$  is length of the cable after elastic elongation.

For the above equation set, horizontal tension  $H$  in the cable and vertical force  $V_A$ ,  $V_B$  at end points can be calculated when  $l$ ,  $h$  and  $s_0$  are known.

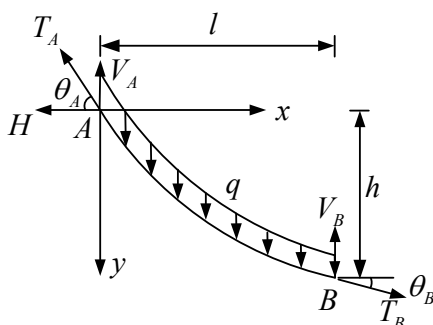


**Figure 2.** Forcing analysis of elastic cable section.

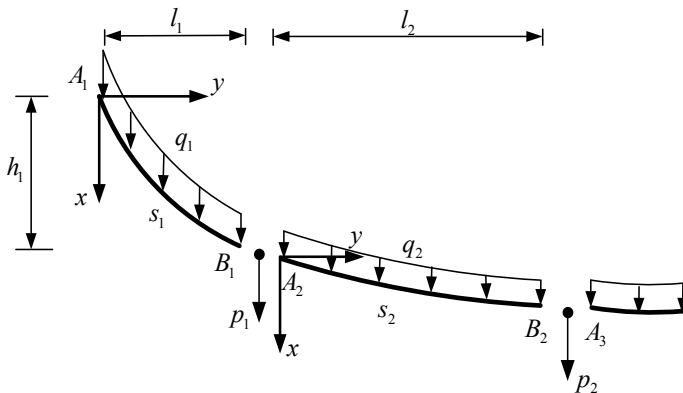


**Figure 3.** Forcing analysis of piecewise catenaries.

We will construct the cable equation set of the busbar which is applicable to different material and several concentrated loads according to this equation set, and calculate its horizontal tension  $H$  and the sag  $f$  in the cable.

The whole busbar can be considered as a combination of the Piecewise catenaries which are divided according to change point of the material quality, the centralized load action point, the suspension cable at every section only bears dead weight action. Assuming the suspension cable consists of  $n$  sections, the end points of every section are  $A_i, B_i$ , dead weight density is  $q_i$ , elastic constant is  $K_i$ , initial arc length is  $s_i$ , horizontal span is  $l_i$ , height difference is  $h_i$  ( $i = 1, 2, \dots, n$ ). There are  $n-1$  centralized loads on conductor sections, which are  $p_i$  ( $i = 1, 2, \dots, n-1$ ) respectively.

Establish the local coordinate system for every section of the suspension cable, and establish the non-linear equation set of the piecewise busbar under several centralized loads in every local coordinate system, shown as Figure 3.

### 3.1 Continuity condition of tension

For the connection point between every cable section, according to the force balance conditions at horizontal direction and vertical condition in Figure 4, there are  $H_i - H_{i+1} = 0$ ,  $V_{Ai} - V_{Bi} = p_i$  ( $i = 1, 2, \dots, n-1$ ). Therefore it is learnt horizontal tension  $H_i$  of every cable section is same, which is marked as  $H$ .

Establish the force balance equation of every load point according to  $V_A/H = \sinh(a)$  and  $V_B/H = \sinh(b)$ :

$$H[\sinh(b_i) - \sinh(a_{i+1})] = p_i \quad (i = 1, 2, \dots, n-1) \quad (5)$$

### 3.2 Section length

Length of the insulator string is generally a determined value during construction of the busbar in the substation, size of the sag is determined by the blanking length of the conductor. The sag which meets with design condition is reversely reckoned through adjusting the blanking length side of the conductor. The length equation of every section is obtained according to the equation (3):

$$\frac{H}{q_i} [\sinh(a_i) - \sinh(b_i)] = s_i \quad (i = 1, 2, \dots, n) \quad (6)$$

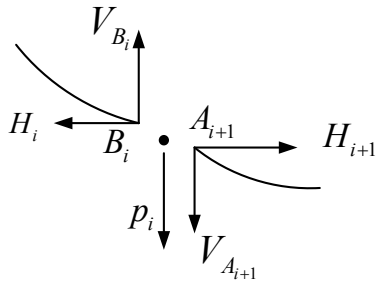


**Figure 4.** Forcing analysis of centralized load action location.

### 3.3 Compatibility condition

Every section of the busbar shall be in accordance with the whole compatibility equation of the horizontal span  $\sum_{i=1}^n l_i = l$ , obtain the following equation according to the equation (1):

$$H \sum_{i=1}^n \frac{(a_i - b_i)}{q_i} + H^2 \sum_{i=1}^n K_i \frac{[\sinh(a_i) - \sinh(b_i)]}{q_i} = l \quad (7)$$

There is deformation compatibility equation at height direction  $\sum_{i=1}^n h_i = h$ , the following equation is obtained according to the equation (2):

$$\begin{aligned} & H \sum_{i=1}^n \frac{[\cosh(a_i) - \cosh(b_i)]}{q_i} + \\ & \frac{H^2}{2} \sum_{i=1}^n K_i \frac{[\cosh^2(a_i) - \cosh^2(b_i)]}{q_i} = h \end{aligned} \quad (8)$$

### 3.4 Nonlinear equation set

Summarizing the above equation, the non-linear equation set of the elastic busbar under action the multiple centralized loads are obtained:

$$\begin{cases} H[\sinh(b_i) - \sinh(a_{i+1})] - p_i = 0 & (i = 1, 2, \dots, n-1) \\ \frac{H}{q_i}[\sinh(a_i) - \sinh(b_i)] - s_i = 0 & (i = 1, 2, \dots, n) \\ H \sum_{i=1}^n \frac{(a_i - b_i)}{q_i} + H^2 \sum_{i=1}^n K_i \frac{[\sinh(a_i) - \sinh(b_i)]}{q_i} - l = 0 \\ H \sum_{i=1}^n \frac{[\cosh(a_i) - \cosh(b_i)]}{q_i} \\ + \frac{H^2}{2} \sum_{i=1}^n K_i \frac{[\cosh^2(a_i) - \cosh^2(b_i)]}{q_i} - h = 0 \end{cases} \quad (9)$$

This equation set includes  $2n+1$  nonlinear equations, unknown numbers are  $a_i$  ( $i = 1, 2, \dots, n$ ),  $b_i$  ( $i = 1, 2, \dots, n$ ),  $H$ , there are  $2n+1$  unknown number. Therefore the nonlinear equation set is enclosed, and it can be expressed as:

$$F(X) = 0 \quad (10)$$

In which  $X = [a_1, a_2, \dots, a_n, b_1, b_2, \dots, b_n, H]^T$ .

Newton iteration method is applied to solve this nonlinear equation set [9].

When  $X$  is calculated, place into the basic catenary equation (1) and (2) of every section, and obtain every position coordination of the busbar, and then the sag is obtained.

#### 4 Initial value selection plan of Newton iteration method

Because calculation of Newton iteration method is very sensitive to selection of initial value, the iteration initial value  $X_0$  shall approach true solution as possible in order to ensure calculation convergence and calculation speed. This paper calculates approximate vector height  $f$  according to the parabola equation:

$$f = \sqrt{\frac{3(s_0 - l)}{8}} \quad (11)$$

And horizontal component  $H$  and  $a_1$  of tension under action of centralized load are further solved:

$$H = \frac{\bar{q}l^2}{8f} \quad (12)$$

$$a_1 = \sinh^{-1}(y'|_{x=0}) = \sinh^{-1}\left(\frac{h+4f}{l}\right) \quad (13)$$

In which,  $\bar{q}$  is average density of the section busbar:

$$\bar{q} = \left( \sum_{i=1}^{n-1} p_i + \sum_{i=1}^n q_i s_i \right) \quad (14)$$

And initial value  $X^0 = [a_1^0, a_2^0, \dots, a_n^0, b_1^0, b_2^0, \dots, b_n^0, H^0]^T$  of the nonlinear equation set  $F(X) = 0$  are calculated by the equations (5) and (6).

## 5 Validation of calculation sample

In order to validate accuracy of the piecewise catenary calculation of the busbar, data in [4] and [10] are compared.

During actual construction engineering of the busbar in the substation mentioned in [4], actual measured span  $L = 57.58\text{m}$ ; lengths of the insulator and the metal string at upper layer  $L_i = 13.42\text{m}$ , quality of the single string is  $503.15\text{kg}$ ; the conductor select the four split heat resistant aluminum alloy diameter expansion conductor, actual measured quality of every meter of the conductor is  $4.47\text{kg}$ . Carry out actual measurement of the sag according to the blanking length of the conductor.

**Table 1.** Comparison validation 1.

Conductor length /m	Sag/m		Error %
	Reference document value	Calculated value in this paper	
32.804	5.58	5.42	-2.87
33.004	5.86	5.68	-3.07

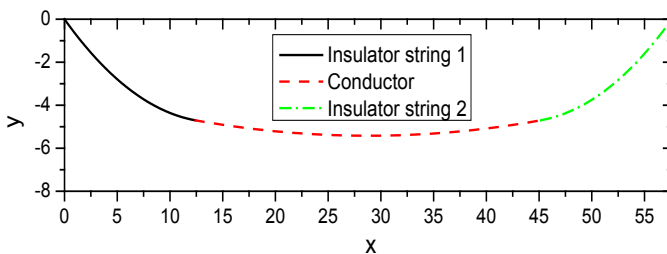


**Figure 5.** Diagram of cable shape when conductor length is 32.804.

Seen from comparison data in Table 1, the sag obtained through calculation of the piecewise catenary calculation is very close the actual measurement value, maximum error is 3.07%, which meets with design requirements. Rope shape is shown as Figure 5 when conductor length is 32.804m.

The calculation sample in [10] is the contour line span of 5 loads, and refers to table 2 for basic data.

Seen from comparison data in table 3, error of horizontal tension is 4.65%, error of distance of the lowest point to right end is 0.21%, which meet with design requirement. It is seen that shape calculation of the busbar with multiple centralized loads is more accurate by the piecewise catenary.

**Table 2.** Basic data.

Name	Value	Name	Value
Weight of insulator string /kg	266	Span /m	46.88
Length of insulator string /m	5.7	Weight of unit conductor /(kg·m <sup>-1</sup> )	5.932
Key weight of first load /kg	0	Distance to right end point /m	41.18
Key weight of second load /kg	113	Distance to right end point /m	38.38
Key weight of third load /kg	60	Distance to right end point /m	31.38
Key weight of fourth load /kg	60	Distance to right end point /m	8.38
Key weight of fifth load /kg	61	Distance to right end point /m	5.7

**Table 3.** Comparison validation 2.

Comparison item	Value in reference document	Calculated value in this paper	Error
Horizontal tension /kN	12.472	11.892	4.65%
Distance of lowest point to right end /m	27.180	27.238	0.21%

## 6 Conclusion

In the ultra-high voltage AC substation engineering, the insulator string of the busbar is long and weight is great, which affects the sag of the conductor greatly. This paper takes the whole busbar as combination of the multiple piecewise catenaries which are classified as change point of the material and centralized load action point. And tension continuity condition, height difference compatibility condition and the span compatibility conditions of every section of the catenaries are analyzed, and the balance equation set of the elastic piecewise catenary under action of the multiple centralized loads is established. Formation of the equation set is simple, structure is clear, which can be solved and calculated by Newton iteration method. Calculation quantity is small, and result accuracy is high.

The forwarded method is applicable to the cable shape calculation of the busbar with different height difference and considering weights of several fittings and length of the different insulator string, and accurate sag of the busbar is obtained. Accuracy of this calculation method is validated through 2 calculation samples. This calculation method provides theoretic basis for blanking length calculation of the busbar in the ultra-high voltage substation, which is helpful to improve construction efficiency of the busbar in the substation, which reduces engineering waste.

**Acknowledgment:** This research was supported by Science and Technology Research Project of State Grid (Study on the calculation method and selection test of cargo cableway of transmission line : GCB17201500105).

## References

- [1] LIU Hua, ZHANG Bin, et al. Installation Techniques of Large-Section Busbar in 1000kV UHV Transformer Substation[J]. Electric Power Construction, 2010, 31(6): 15–18.
- [2] GUO Shang-wei, GAO Jing, et al. Implementation of the Automatic Calculation and Forecast Analysis Using EXCEL for the Increments of Soft-bus Conductor Length in the Substations [J]. Northeast Electric Power Technology, 2003, (2): 31–33.
- [3] YAO Zhong-tian. Approach Installation of Flexible Bus in Substation [J]. Guangxi Electric Power, 2004, (4): 57–58.
- [4] ZHANG Bin, ZHANG Jun, et al. Discussion on the Calculation of Conductor Fitting Length in the Busbar Construction of 1000 kV UHV Transformer Substation[J]. Power System Protection and Control, 2008, 36(18): 81–83.
- [5] Cheng Wei, Zhang Jun, Zhang Bin, et al. Calculation of Conductor Blanking Length in Construction of Flexible Bus for V-Shape Insulator Strings of 1000 kV Substation[J]. Power System Technology, 2009, 33(13):24–26.
- [6] HU Sheng-hui, Song Guo-gui, et al. Development Study on Calculation Software for Large Cross-section Soft-bus Conductor Length in 1000kV UHV AC Substation[J]. Hubei Electric Power, 2009, 33(6): 5–10.
- [7] QIN Jian, XIA Yongjun. The matrix iteration method for analysis of suspension cable based on segmental catenary theory [J]. Chinese Journal of Engineering Design, 2013, 20(5): 404–408.
- [8] Zhang Zhiguo, Jin Mingjun, Zou Zhenzhu. Static solution of suspension cables under tare load [J]. China Railway Science, 2004, 25(3): 67–70.
- [9] Li Qingyang, Mo Zizhong, Qi Liqun. Numerical solution of nonlinear equations[M]. Beijing: Science Press, 1987.
- [10] GUO Shang-wei, GAO Jing. Exploration on the Methods of Measuring Sags of Soft Bus in the Interval of Unequal-height Frame Bents of Substation and Relative Calculations [J]. Northeast Electric Power Technology, 2002, (8): 23–25.

Jian QIN\*, Liang FENG, Jun CHEN, Jian-cheng WAN, Liang QIAO,  
Yi-min MA

## **Calculation Method of Stiffness Matrix in Non-linear Spline Finite Element for Suspension Cable**

**Abstract:** Through the characteristics of cubic B spline function, the stiffness matrix expression is obtained for the non-linear spline finite element of the suspension cable, and the three calculation method is put forward such as the integral by parts method, the matrix assembly method based on spline integral and the matrix assembly method based on Gauss integral, which are applied to calculate the non-linear stiffness matrix. The integral by parts method using the Leibniz formula as foundation can calculate every item of the stiffness matrix directly, but its efficiency is low when the matrix order is high. The matrix assembly method based on spline integral fully uses the local non-zero property of the spline function, converts the calculation of high order matrix into calculation of 4 order matrix and its assembly, with high efficiency and small storage in calculation. The matrix assembly method based on Gauss integral is similar with the method based on spline integral, but its workload is larger than the method based on spline integral when the matrix order is high. These calculation methods can all be processed by parallel algorithm to improve calculation efficiency, which can provide new ideas for high efficient numerical analysis works.

**Keywords:** non-linear stiffness matrix; spline function; integral by parts; matrix assembly

### **1 Introduction**

Performance of the modern computer with high speed provides strong technical support for solving the non-linear problems, such as the non-elastic material, the complicated contact issue and the large geometrical deformation of the structure etc. Following the enlargement and refinement of the structure, working quantity for non-linear numerical calculation is also increased greatly [1,2]. In order to improve calculation efficiency, solve the problems in structure design and analysis appeared during actual engineering, the more efficient and more accurate theoretical algorithm is necessary to be proposed.

---

\*Corresponding author:Jian QIN, China Electric Power Research Institute, Beijing, China, E-mail:

mathmech@126.com

Liang FENG, Jun CHEN, Jian-cheng WAN, Liang QIAO, Yi-min MA, China Electric Power Research Institute, Beijing, China

In the finite element, the expression formula and calculation of the stiffness matrix is a matter of prime importance [3-5]. The main method for stiffness matrix calculation is always numerical integral (generally Gauss integral). In order to ensure integral accuracy in non-linear issue, the order of numerical integral shall be improved 1-2 orders accordingly, so the calculated amount is greatly increased, especially in iteration process of Newton-Raphson method where the stiffness matrix shall be generated repeatedly. When free degree is more, time cost is extremely great [6,7].

On basis of the non-linear spline finite element method [8-10], the calculation methods of the stiffness matrix for the suspension cable are forwarded for the large geometrical deformation issue, which can effectively improve generation efficiency of the stiffness matrix.

## 2 Characteristic of non-linear spline element

The difference between the spline finite element and the common finite element method is that cubic B spline function is taken as the interpolation function. The spline function has high accuracy for calculating the angle, stress, strain and bending moment etc.

Nonzero parts of the cubic B spline basic function is generally expressed as 4 cubic polynomial  $d_1, d_2, d_3, d_4$  in unit sections during calculation, shown as Figure 1.

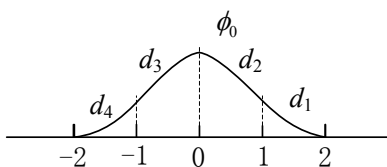


**Figure 1.** Figure cubic B spline function

The polynomial formulas of the spline function in  $[0, 1]$  are  $d_1 = (1 - 3t + 3t^2 - 3t^3) / 6$ ,  $d_2 = (4 - 6t^2 + 3t^3) / 6$ ,  $d_3 = (1 + 3t + 3t^2 - 3t^3) / 6$ ,  $d_4 = t^3 / 6$ ,  $t \in [0, 1]$ .

Cubic B spline base is expressed as tensor base of one dimension base  $V_\xi$ ,  $V = V_\xi = \phi_i(\xi)$ ,  $i = -1, \dots, n+1$ .  $V$  is  $n+3$  dimensions space.

So the arbitrary function in the interval  $[0, n]$  can be interpolated by the base and expressed as the product of spline function and coefficient.

$$x(\xi) = \Phi(\xi) \cdot A \quad (1)$$

The spline function vector is  $\Phi = [\phi_{-1}(\xi), \phi_0(\xi), \dots, \phi_n(\xi), \phi_{n+1}(\xi)]$  and coefficient vector is  $A = [a_{-1}, a_0, \dots, a_{n+1}]^T$ .

The non-linear spline finite element function forwarded in this paper sufficiently uses the advantage of the spline function in interpolation for calculation the integral function to reduce the calculated amount.

### 3 The stiffness matrix of suspension cable

For the suspension cable, the Green strain is

$$\varepsilon = \frac{dX^T}{ds} \cdot \frac{dU}{ds} + \frac{1}{2} \frac{dU^T}{ds} \cdot \frac{dU}{ds} \quad (2)$$

According to the constitutive relation and the principle of minimum potential energy, the potential energy function can be expressed as

$$\Pi_p = \int_s [A_0 (\frac{1}{2} E \varepsilon^2) - \mathbf{f} \cdot U] ds \quad (3)$$

The stiffness matrix can be expressed as combination of the following integral matrixes:

Here,  $A$  and  $B$  are the known constant vectors,  $A = [a_{-1}, a_0, \dots, a_{n+1}]^T$ ,  $B = [b_{-1}, b_0, \dots, b_{n+1}]^T$ .

And then

$$G(A, B) = G(B, A) = \int_0^n \frac{d\Phi^T}{d\xi} \frac{d\Phi}{d\xi} \cdot A \cdot B^T \cdot \frac{d\Phi^T}{d\xi} \frac{d\Phi}{d\xi} d\xi \quad (4)$$

So the importance matter of non-linear spline FEM is the calculate method of the matrix  $G(A, B)$ .

Set the matrix  $G(A, B)$ , the entry in the  $i$ -th row and  $j$ -th column of the matrix can be expressed as:

$$G_{ij} = \int_0^n \left( \sum_{k=-1}^{n+1} \sum_{l=-1}^{n+1} b_k a_l \phi'_k \phi'_l \right) \phi'_i \phi'_j d\xi = \sum_{k=-1}^{n+1} \sum_{l=-1}^{n+1} b_k a_l \int_0^n \phi'_k \phi'_l \phi'_i \phi'_j d\xi \quad (5)$$

It is seen that  $G_{ij}$  is the combination of integral of products of four spline functions. Calculated amount for the expansion of combination is great and efficiency is extremely low.

Three effective methods are proposed for the calculation of stiffness matrixes.

### 4 Integral by parts method

When  $\int_0^n \phi'_k \phi'_l \phi'_i \phi'_j d\xi$  ( $i, j, k, l = -1, \dots, n+1$ ) is calculated, the  $G_{ij}$  is obtained and then the stiffness matrix  $G$ .

For products of the 4 spline functions  $\phi_i^{(p)} \phi_j^{(q)} \phi_k^{(r)} \phi_l^{(s)}$  ( $p, q, r, s$  are derivatives respectively), it is carried out by integral by parts until the derivative of the product of the spline functions becomes zero.

$$\int_0^n \phi_i^{(p)} \phi_j^{(q)} \phi_k^{(r)} \phi_l^{(s)} d\xi = (-1)^m \sum_{m=0}^{12-p-q-r-s} \frac{\xi^{m+1}}{(m+1)!} \left[ \phi_i^{(p)} \phi_j^{(q)} \phi_k^{(r)} \phi_l^{(s)} \right]^{(m)} \Big|_0^n \quad (6)$$

From the differential Leibniz formula

$$\left[ \phi_i^{(p)} \phi_j^{(q)} \phi_k^{(r)} \phi_l^{(s)} \right]^{(m)} = \sum_{\substack{i_a + i_b + i_c + i_d = m \\ 0 \leq i_a, i_b, i_c, i_d \leq m}} \frac{m!}{i_a! i_b! i_c! i_d!} \phi_i^{(p+i_a)} \phi_j^{(q+i_b)} \phi_k^{(r+i_c)} \phi_l^{(s+i_d)} \quad (7)$$

So  $\int_0^n \phi_i^{(p)} \phi_j^{(q)} \phi_k^{(r)} \phi_l^{(s)} d\xi$  can be calculated.

The derivative of the cubic B spline function can be directly obtained at integral end 0 and n, therefore the integral by parts can be directly calculated. And the spline function is local nonzero, the product of the spline functions is zero when the interval between  $i, j, k$  and  $l$  is greater than 3.

Because the method needs repeatedly judge the continuity of derivative of the spline function and complete the multi-layer summation, it is inefficient in the computer.

## 5 Matrix assembly method

### 5.1 The matrix assembly method based on spline integral

Define  $\Phi' = \frac{d\Phi}{d\xi} = [\phi'_{-1}, \phi'_0, \dots, \phi'_n, \phi'_{n+1}]$  in the matrix  $G(A, B)$  of non-linear spline finite element method.

The matrix  $G(A, B)$  can be seen as the sum of integration in the interval:

$$\begin{aligned} G(A, B) &= \int_0^n (B^T \Phi'^T \Phi' A) \Phi' d\xi \\ &= \int_0^1 + \int_1^2 + \int_2^3 + \dots + \int_{n-2}^{n-1} + \int_{n-1}^n [(B^T \Phi'^T \Phi' A) \Phi'^T \Phi'] d\xi = M_1 + M_2 + \dots + M_n \end{aligned} \quad (8)$$

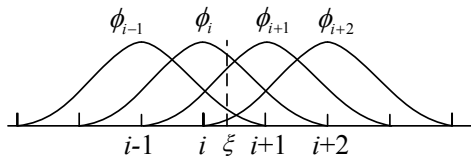


**Figure 2.** The nonzero terms of the spline function in the  $[i, i+1]$  interval

According to the compactness of spline function, the  $\Phi$  or  $\Phi'$  in any unit interval has at most 4 nonzero terms then the vectors can be simplified. For example, when  $\xi \in [i, i+1]$ ,  $\Phi(\xi) = [0, 0, \dots, 0, \phi_{i-1}(\xi), \phi_i(\xi), \phi_{i+1}(\xi), \phi_{i+2}(\xi), 0, \dots, 0, 0]$ , as shown in Figure 2.  $\Phi'$  has same features.

In this section, the function vector  $\Phi'$  can be expressed by  $d_1, d_2, d_3, d_4$ .

$$\Phi'(\xi) = [0, 0, \dots, 0, d'_1(\beta), d'_2(\beta), d'_3(\beta), d'_4(\beta), 0, \dots, 0, 0], \quad \beta = \xi - i \in [0, 1] \quad (9)$$

So in every unit interval, there is nonzero items from row  $i-1$  to row  $i+2$  and from column  $i-1$  to column  $i+2$  of the  $n+3$  order integral matrix  $M_i = \int_i^{i+1} (B^T \Phi'^T \Phi' A) \Phi'^T \Phi' d\xi$ , which compose a  $4 \times 4$  nonzero submatrix  $K_i$ .

In order to reduce the amount of calculation and memory space, the 4 order vectors  $R = [d'_1, d'_2, d'_3, d'_4]$ ,  $A^i = [a_{i-1}, a_i, a_{i+1}, a_{i+2}]$  and  $B^i = [b_{i-1}, b_i, b_{i+1}, b_{i+2}]$  are defined. The 4 order nonzero submatrix  $K_i$  can be expressed as:

$$K^i = \int_0^1 [(B^i)^T R^T R A^i] R^T R d\xi \quad (10)$$

When  $K_i$  is calculated, it can be assembled into the global matrix according to the order of coefficients, and the global stiffness matrix  $G$  is formed finally, shown in Figure 3 (the process is similar with the assembling of structure stiffness matrix in finite element, so this method can be regarded as the stiffness matrix assembly of spline finite element).

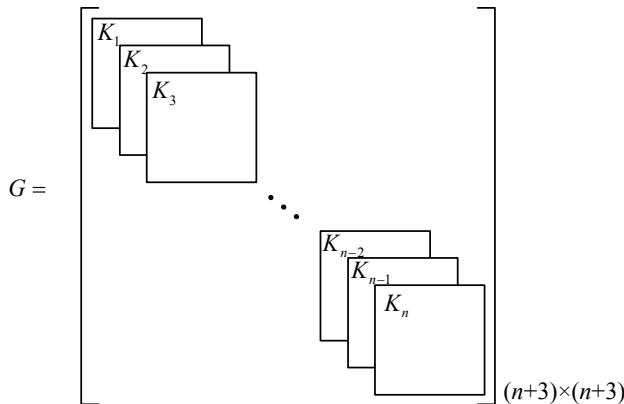


**Figure 3.** Assembly of stiffness matrix

The entry in the matrix  $K_i$  can be written as

$$K_{pq}^i = \sum_{k=1}^4 \sum_{l=1}^4 B_k^i A_l^i \int_0^1 (d'_k d'_l d'_p d'_q) d\xi \quad (11)$$

Let  $D_{pqkl} = \int_0^1 (d'_p d'_q d'_k d'_l) d\xi$ ,  $p, q, k, l \in [1, 2, 3, 4]$ , and then

$$K_{pq}^i = \sum_{k=1}^4 \sum_{l=1}^4 B_k^i A_l^i D_{pqkl} = B^{iT} \cdot D(\cdot, \cdot, p, q) \cdot A^i \quad (12)$$

$D_{pqkl}$  can be obtained by analytical calculation. Saving  $D_{pqkl}$  as a file and calling the file in the calculation procedure, the calculation efficiency can be extremely improved.

## 5.2 The matrix assembly method based on Gauss integral

Because the integral term in  $K_i$  is the product of the polynomials which is 8 orders polynomial,  $K_i$  can be accurately calculated by the Gauss integral of 5 integral points which can reach accuracy of  $2 \times 5 - 1 = 9$  order. So

$$K_i = \int_0^1 [(B^{iT} R^T R A^i) R^T R] d\xi = \sum_{m=1}^5 H_m [(B^{iT} R(\xi_m)^T R(\xi_m) A^i) R(\xi_m)^T R(\xi_m)] \quad (13)$$

Here  $H_m$  is integral coefficient and  $\xi_m$  is integral point in  $[0, 1]$  section.

Value of  $M = \int_0^n (\Phi A) \Phi'^T \Phi' d\xi$  at every Gauss integral point can be saved as the file and called in the calculation procedure to improve the calculation efficiency.

## 6 Example

For known constant vectors A and B with different orders, the stiffness matrix is calculated by integral by parts method, the matrix assembly method based on spline integral and the matrix assembly method based on Gauss integral respectively, the CPU time cost is shown as Figure 4. Results obtained by three methods are the same.

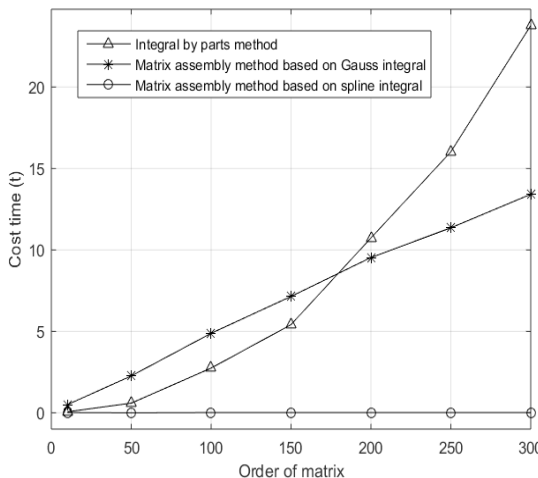


**Figure 4.** The cost time with different matrix order

It is seen that efficiency of the matrix assembly method based on spline integral is highest whose time cost is minimum with same matrix order, and no obvious change when the order of the matrix increases. This method has the calculation speed twice as high as the other two methods.

The cost time of the matrix assembly method based on Gauss integral is linearly increasing with the order of the matrix, its working quantity is mainly Gauss integral calculation of the function in every section. The time of integral by parts method is square growth with the matrix order, and the judgment of spline function boundary and summation of product of the spline function are the main workload. When the matrix order is small, efficiency is high, and efficiency decreases quickly when order increases.

## 7 Conclusion

The three calculation methods for the stiffness matrixes of suspension cable issues are put forward. It can be seen from the given example, the matrix assembly method based on spline integral has the highest efficiency and fastest calculation speed. The cost time of this method is two orders of magnitude larger than other methods when the matrix order is high, and this method can obtain the accurate result. Therefore the matrix assembly method based on spline integral is the best for calculation of the stiffness matrix. And the technique of this method can also be used in calculation of other matrixes, such as the load matrix in spline element method.

**Acknowledgment:** This research was supported by Science and Technology Research Project of State Grid (Study on the calculation method and selection test of cargo cableway of transmission line: GCB17201500105).

## References

- [1] Shen Pengcheng, He Peixiang. The Developments of Spline Finite Element Method in Computational Mechanics[J]. Advances in Mechanics, 2000, 30(2):191–199.
- [2] Qin Rong, Spline Function Method and Program for Structural Mechanics[M]. Beijing: Science Press, 2015.
- [3] Yao Zhong-tian. Approach Installation of Flexible Bus in Substation [J]. Guangxi Electric Power, 2004, (4): 57–58.
- [4] He Zhengjia, Chen Xuefeng. Advances in Theory Study and Engineering Application of Wavelet Finite Element[J]. Chinese Journal of Mechanical Engineering, 2005, 41(3):1–11.
- [5] Huang Yi, Han Jian-gang. Theory and Application of Wavelet Finite Element Method for Thin Plate[J]. Chinese Journal of Computational Mechanics, 2006, 23(1) :76–80.
- [6] Xia Yiming, Zhao Huilin, Zuo Xiaobao. Comparative Analysis of Earthquake Response of Suspension Structures[J]. Journal of Southeast University(Natural Science Edition), 2000, 30(4):33–38.
- [7] Zhang Le-le, Tan Nan-lin, Liu Cai. Simulation and Application of Spline Finite Strip Method in Process of Cold-roll Forming[J]. Journal of System Simulation, 2008, 20(7):1703–1706.
- [8] Qin Jian, Huang Ke-fu. B-Spline Finite Element Method for the Plane Problem of Arbitrary Region[J]. Engineering Mechanics, 2010(6):29–34.

- [9] Qin Jian, Zhang Qingdong, Huang Kefu. Nonlinear Spline Finite Element Method for Ribbing of Cold-Rolled Coils[J]. Journal of Iron & Steel Research International, 2012, 19(1):36–40.
- [10] Xie Jingzhong, Li Guoqiang. Method of Directly Integrating Nonlinear Frame Load Matrix Based on Integration Factors[J]. Chinese Journal of Computational Mechanics, 2003, 20(4):490–494.

Dong-xu WANG, Xue ZHENG\*, Xi YE, Wei CAI, Zhi-chun YANG

## A Load Outage Judgement Method Considering Voltage Sags

**Abstract:** Whether the load equipments of the power system will be outage considering voltage sags is analyzed in this paper. Reclassifying the load equipments because of the great impact on the sensitive loads due to the voltage sags. This paper has proposed a new Power Consumers Integrated Voltage Sensitive Curve and the Electrical Nodes Integrated Voltage Sensitive Curve based on the CBEMA and ITIC curves in order to characterize the sensitivity of the power consumers to voltage sags. The outage criterion for the sensitive loads is proposed based on the curves which has been described previously and can be used to get the probability curves of both amplitudes and durations of the voltage sags for different power users.

**Keywords:** Voltage sags; Power Quality; Load outage; Sensitive curves; Probability curves

### 1 Introduction

The electrical equipments and precision instruments which are based on the microprocessors are quite sensitive to the voltage sags and power outages. The economic losses caused by the voltage sags and other transient power quality problems has been growing all the time, so it's very necessary to put the voltage dips and other transient power quality problems into the power system reliability evaluation [1-4].

Whether the load equipments will be outage when the voltage sag occurs will be a key link considering the voltage sag in power system reliability analysis, then a correct load outage criterion will be particularly important. The literature [5] and [6] propose a load outage criterion method based on the SCBEMA curve, which put forward an average outage criterion contains amplitude and downtime. However, the curve cannot fully reflect the different important levels between the sensitive and non-sensitive loads as the load outage happens. The different levels of sensitive loads should also be taken into account. This paper proposes the IVSC and ENIVSC curve which are more comprehensive than any other curves, in order to determine whether the load equipment will be outage based on the IVSC curve.

---

\*Corresponding author: Xue ZHENG, Wuhan Electric Power Technical College, Wuhan, China, E-mail: dreamy\_zx@qq.com

Dong-xu WANG, Wei CAI, State Grid Wuhan Power Supply Company, Wuhan, China

Xi YE, School of Electrical Engineering, Wuhan University, Wuhan, China

Zhi-chun YANG, Electric Power Research Institute of Hubei Electric Power Company, Wuhan, China

## 2 Classification of load equipments for electric users

Because the sensitive loads have a very short tolerance time to the voltage sags, these loads may tend to be affected from different levels or even outage when the power system have the voltage sag problems. Generally speaking, the electric power users can be divided as the resident users, the commercial office users, the general industrial users and the major industrial users. The type and the percentage of the load equipments that each power user contains are not the same as well, they can be divided into the following four categories [7]:

1. General loads (non-sensitive loads). The general loads will not be significantly affected by the voltage sags, they will be affected only by the circumstances such as the longtime blackouts or a wide range of voltage fluctuations.
2. Little sensitive loads. This kind of loads will be influenced by a certain degree when faced with the power quality problems such as the voltage sags. It may also cause certain damage to the load equipments.
3. Sensitive loads. The sensitive loads will have more serious effects when faced with the power quality problems such as the voltages sags, we should take certain measures to ensure the quality of electric energy to avoid the load equipments damage.
4. The core loads. They are often in the central position of the load equipments, and they are very sensitive to the voltage sags and other power quality problems that may cause the outage of the power system directly, which can cause huge economic loss and negative social impact.

The above four kinds of loads will be of different types and in different proportions in each electric power user, the sensitive loads mentioned in this paper will refer to the three kinds of sensitive loads above.

## 3 Voltage sensitive curve

### 3.1 Definition of voltage sensitive curve

The voltage sensitivity curve generally has two branches--the up branch and down branch, which separately define the limit value of high voltage and low voltage that the equipments can bear. The voltage sensitivity of the equipments can be reflected intuitively in the curve. The abscissa of the curve is generally defined as the duration of the voltage disturbance, the ordinate is generally defined as the voltage amplitude or the percentage that the voltage deviates from the nominal value.

### 3.2 Traditional voltage sensitive curves

(1) CBEMA curve. As is shown in Figure 1, the curve was determined by the Computer Business Equipment Manufacturing Association because of the power quality requirements based on the mainframe computers, in order to prevent the maloperation and damage of the computers and control equipments cause by the voltage disturbance. The curve is a kind of the statistical curve, most CBEMA curves of the sensitive loads can be formulated according to the experimental data and historical data [8].

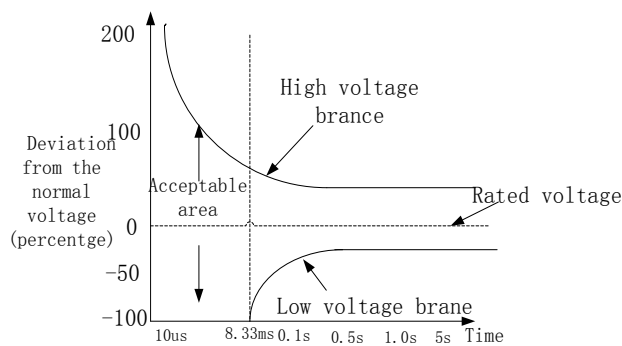


**Figure 1.** The CBEMA sensitive curve

This paper mainly discusses the influence on the power system reliability caused by voltage sags. Both the amplitude and the duration of voltage sags have to be taken into account. So we make the curve become to the polyline. Then the following typical load equipment CBEMA curve is obtained in Figure 2 by collecting the historical statistics [9].

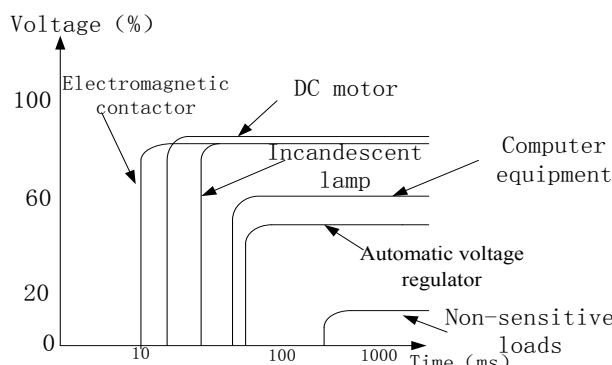


**Figure 2.** The CBEMA curve of the typical loads

(2) ITIC curve. The ITIC curve is formulated by the Information Technology Industry Council, it is based on the CBEMA curve, in order to characterize the disturbance rejection capability of the computers and other information industrial equipments under the voltage sag circumstance (Figure 3). The ITIC curve becomes polyline compared with the CBEMA curve, while the up and low tolerance value was changed to 110% and 90% and the starting time is changed from 8.33ms to 20ms.

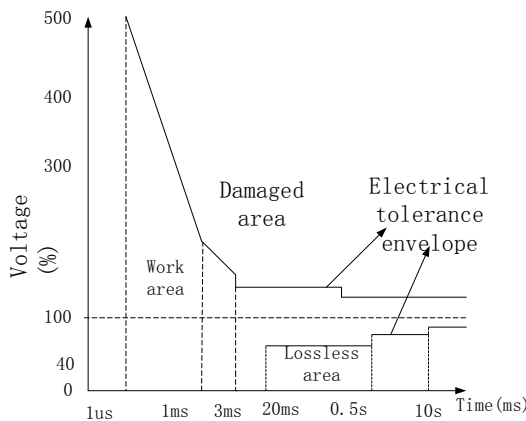


**Figure 3.** The ITIC curve

## 4 Load outage criterion

### 4.1 The integrated voltage sensitive curve of the power users

We get the traditional CBEMA curve by measuring the individual sensitive load, it can only reflect the effect that the individual load has under the voltage sags [10], and it can't be used to analyze the voltage sags' impact on the overall loads. So it's difficult to react the influence on the overall loads under the voltage sag circumstance. What's more, the same loads will not be in the same position when they are in different electric users. For example, when voltage sag happens in the resident users, we always focus on the little sensitive loads, but we will focus on the core loads when the same thing happens in the major industrial users. If we use CBEMA curve to analyze the electric users' sensitivity, then we can't know the difference between them.

In order to get the overall power outage criterion for amplitude and downtime of the power users, part of the literatures propose a SCBEMA curve (Specified Computer Business Equipment Manufacturer Association). To strike a SCBEMA curve we may first set the composition ratio of the load equipments in each power user, then we will

multiply the tolerance limit value from the CBEMA curve and the composition ratio, after having done this we accumulate the result to get the SCBEMA tolerance limit values for each user type [5]. Here is the formulas:

$$\begin{cases} X = \sum_{i=1}^j (X_i + K_i) + X_0 \times K_0 \\ Y = \sum_{i=1}^j (Y_i + K_i) + Y_0 \times K_0 \end{cases} \quad (1)$$

The  $X$  and  $Y$  represent the voltage sag duration and voltage sag amplitude in the SCBEMA curve; The  $X_0$  and  $Y_0$  represent the voltage sag duration and voltage sag amplitude of the non-sensitive loads in a certain power user; The  $K_i$  represents the composition ratio of the  $i$  type of sensitive loads in a certain power user; The  $K_0$  represents the composition ratio of non-sensitive loads.

Although the SCBEMA curve can describe the voltage sag outage probability more comprehensively compared with the CBEMA curve, we can still find some defects from the corresponding formulas: (1) The formula only considers the number ratio of the load equipments, the capacity ratio isn't mentioned. If a core load exists in the certain user, when it comes to be outage then the whole load equipments of the user will be outage, if we still use the above formula to calculate then the voltage sensitive curve we get will be quite different to the actual circumstances; (2) In the formula we can see that the importance of all load equipments are the same, but we can find that the non-sensitive loads have little effect on the outage of the power users when the voltage sag is happening, while the sensitive loads and the core loads can often play a decisive role.

For these reasons, this paper presents a Power Consumers Integrated Voltage Sensitive Curve, which referred to as the IVSC curve. The IVSC curve reflects a comprehensive concept, It will get a comprehensive criterion of outage amplitude and outage time by making statistical analysis of all kinds of load equipments for power users and considering the ratio of capacity and number for load equipments, at the same time we will create different weighting factors which will depend on the sensitivity level of the load equipments in the synthesis of the IVSC curve. When a voltage sag reaches a certain amplitude or duration, then we can believe that all the load equipments in this class of users will have power outage.

Here we will introduce the steps to calculate the IVSC curve: (1) To classify the load equipments according to the classification method which is mentioned previously and make sure the capacity and number of each kind of load equipment; (2) To determine the weighting factor of each load equipment and the weighting coefficients of the capacity ratio and number ratio according to the load equipments' sensitivity level; (3) We will multiply the different tolerance values by the corresponding ratios and weighting factors of each load equipments, and then accumulate them to get the tolerance values of the IVSC curve for the certain kind of power users.

The tolerance values of IVSC curve can be calculated by the following formula:

$$\begin{cases} T = \sum_{i=0}^j W_i X_i (\alpha \frac{N_i}{N} + \beta \frac{S_i}{S}) \\ U = \sum_{i=0}^j W_i Y_i (\alpha \frac{N_i}{N} + \beta \frac{S_i}{S}) \end{cases} \quad (2)$$

The  $T$  and  $U$  respectively represent the coordinate values of the corresponding duration and amplitude of the voltage sags; The  $X_i$  and  $Y_i$  represent the abscissa and ordinate values of the CBEMA curve which is belong to the certain kind of load equipment for an electric power use; The  $X_0$  and  $Y_0$  represent the coordinate values of the non-sensitive loads; The  $\alpha$  and  $\beta$  represent the weighting coefficients considering the number and capacity, which is determined by the actual composition of the load equipments; The  $W_i$  represents the weighting factor considering the load equipments' sensitivity; The  $N_i$  and  $S_i$  represent the number and capacity of the certain kind of load equipment; The  $N$  and  $S$  represent the total numbers and capacities of load equipments in the certain power user.

According to the types of users and the composition ratio of load equipments in Table 1 and the calculation from formula (2), we can get the IVSC curves for different types of power users which are shown in Figure 4.

**Table 1.** Different types of power users and composition ratio of load equipments

Loads	resident users		commercial office users		general industrial users		major industrial users	
	Number ratio	Capacity ratio	Number ratio	Capacity ratio	Number ratio	Capacity ratio	Number ratio	Capacity ratio
DC motor controllers	0	0	0.05	0.1	0.15	0.15	0.25	0.3
Electromagnetic contactors	0	0	0	0	0.15	0.2	0.25	0.2
Lights	0.1	0.1	0.1	0.15	0.2	0.2	0.1	0.15
Computer and communications equipment	0.15	0.2	0.3	0.15	0.2	0.15	0.2	0.15
Automatic voltage regulator	0	0	0	0	0.1	0.1	0.05	0.1
Non-sensitive loads	0.75	0.7	0.55	0.6	0.2	0.2	0.15	0.1

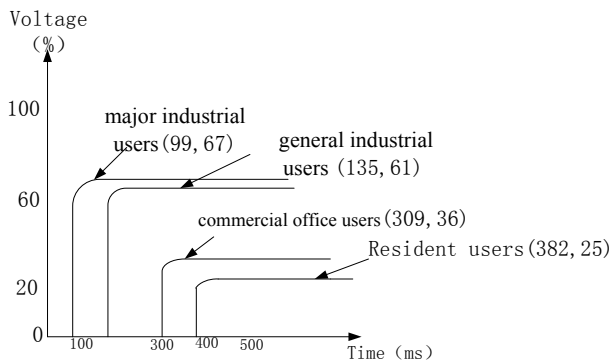


**Figure 4.** The IVSC curves for different types of power users

#### 4.2 The integrated voltage-sensitive curve for electrical nodes

Meanwhile, we should also think that there are many power users and load equipments in the power system, it's very difficult to collect the relevant data. Secondly, sometimes we don't need to know the voltage-sensitive situations for each power user for the viewpoint of power system, the only thing we need to do is to know the voltage-sensitive situation for one electrical node. Then the Electrical Nodes Integrated Voltage Sensitive Curve (ENIVSC curve) will be a good choice which can reflect the whole voltage-sensitive situation of the load equipments in one electrical node. The ENIVSC curve is a curve which is based on the IVSC curve, it can reflect the sensitivity of all power users in one node, the following formula will explain how we get it:

$$\begin{cases} T' = \sum_{m=1}^n W_m T_m (\alpha' \frac{N_m}{N'} + \beta' \frac{S_m}{S'}) \\ U' = \sum_{m=1}^n W_m U_m (\alpha' \frac{N_m}{N'} + \beta' \frac{S_m}{S'}) \end{cases} \quad (3)$$

The  $T'$  and  $U'$  represent the Abscissa and ordinate value of the curve; The  $T_m$  and  $U_m$  represent the Abscissa and ordinate value of the IVSC curve; The  $\alpha'$  and  $\beta'$  represent the weighting coefficients that considering the number and capacity ratio of electric power users in the electrical node; The  $W_m$  represent the weighting coefficient that considering the importance of the power users; The  $N_m$  and  $S_m$  represent the number and capacity of the certain kind of power users; The  $N'$  and  $S'$  represent the total number of load equipments and the total capacities.

### 4.3 The load outage probability curve of the voltage sags

The CBEMA curve we discussed earlier is essentially a kind of probability and statistics curve, the load equipments may be outage if the duration and amplitude value exceed the critical value of the curve. The IVSC curve is the curve which is obtained from the CBEMA curve, it also has the features of probability and statistics: When the voltage sag occurs inside the IVSC curve, part of the load equipments may be outage. what's more, different durations and amplitudes will have different effects on the power users, these two factors are interrelated in general. In order to get better smoothing feature, this paper will select a similar S-shaped curve as the outage probability curve of the load equipments under the voltage sag circumstance.

The time probability function of load outage:

$$P_{Tx} = \begin{cases} \frac{1}{2} \times \left(\frac{x}{a}\right)^2 & 0 < x < a \\ 1 - \frac{1}{2} \times \left(\frac{b-x}{b-a}\right)^2 & a \leq x < b \\ 1 & b \leq x \end{cases} \quad (4)$$

The  $P_{Tx}$  represent the time probability function value of load outage for voltage sags; The  $x$  represents the sag duration; The  $a$  and  $b$  represent the corresponding curve value when the probability value is 0.5 and 1. Generally, the value of  $a$  is often the tolerance value of the curve. The value of  $b$  will be 500ms, which represents most of the loads will be outage.

The amplitude probability function of load outage:

$$P_{Uy} = \begin{cases} 1 & y < 100 - b' \\ 1 - \frac{1}{2} \times \left(\frac{b'+y-100}{b'-a'}\right)^2 & 100 - b' < y < 100 - a' \\ \frac{1}{2} \times \left(\frac{100-y}{a'}\right)^2 & 100 - a' < y < 100 \end{cases} \quad (5)$$

The  $P_{Uy}$  represents the amplitude probability function value of load outage for voltage sags; The  $y$  represents the residual amplitude value after the voltage sag (in percent); The  $a'$  and  $b'$  represent the corresponding curve value when the probability value is 0.5 and 1. Generally, the value of  $a'$  is often the tolerance value of the curve; The value of  $b'$  will be 100%, when most of the loads will be outage.

After getting the two probability curves, we should taking two curves into account to determine the probability of load outage under voltage sag circumstance, that is:  
 $P = (P_{Tx} + P_{Uy}) / 2$

Taking example for the data of Figure 4 and referring the general industrial users' data of IVSC curve, we can calculate the time probability curve (as is shown in Figure 5) of load outage when voltage sag happens by using the formula (4):

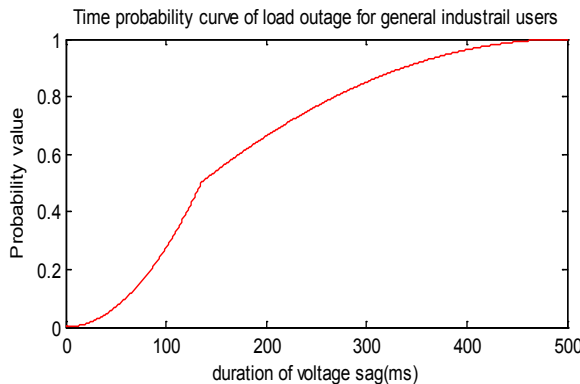


**Figure 5.** The time probability curve of load outage for general industrial users

We can calculate the amplitude probability curve (as is shown in Figure 6) of load outage when voltage sag happens.

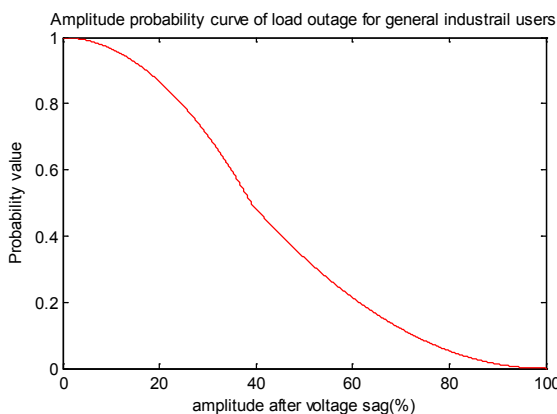


**Figure 6.** The amplitude probability curve of load outage for general industrial users

Similarly, by referring the tolerance value of IVSC curve for the resident users, we can respectively get the time and amplitude probability curve which is shown in Figure 7 and Figure 8.

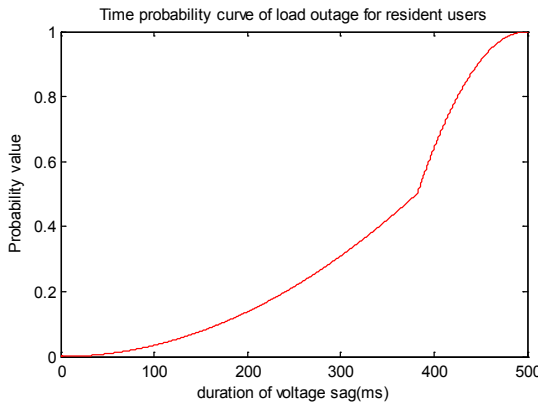


**Figure 7.** The time probability curve of load outage for resident users

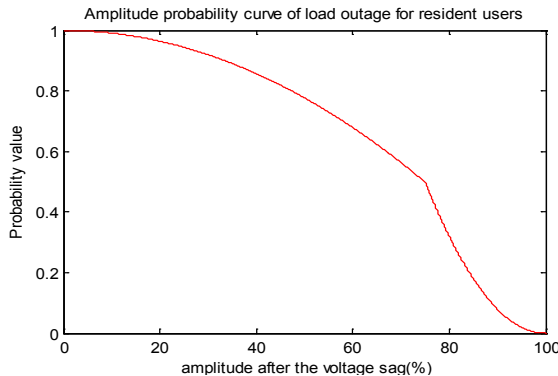


**Figure 8.** The amplitude probability curve of load outage for resident users

## 5 The total flow of load outage judgment

When a voltage sag happens in the power system, we can calculate the amplitude and duration data of the voltage sag by several ways, then we can know the load outage probability by comparing with the corresponding  $P_{Ix}$  and  $P_{Uy}$  curves, when it is greater than a set value, we can consider that the load will be outage. The same method can also be applied to determine whether the electrical nodes will be outage under the voltage sag circumstance. The flow chart of load outage judgment is as follows:

Taking the fifth bus of the RTS-6 bus test system for example, the load composition in the fifth bus has already be given in Table 1. Assuming that a voltage sag happens because of the three phase short circuit somewhere in this bus, for a certain power user, such as the general industrial user on the 14<sup>th</sup> node, we first set an outage

probability threshold  $P_0 = 45.6\%$ , according to the short circuit flow calculation and protection device operating time we can calculate the drop amplitude and duration are 24% and 153ms when the voltage sag happens. Compared with Figure 5 and Figure 6 we can know the amplitude probability and time probability value are  $P_1 = 10.8\%$  and  $P_2 = 75.3\%$ . The power user's comprehensive outage probability value is  $P = (P_1 + P_2)/2 = 43.05\%$ , it is obvious that  $P < P_0$ , so we believe that the loads of the power user can still work in the period of three phase short circuit. If we find  $P > P_0$  in practice, it shows that the loads of the power user will be outage in the period of three phase short circuit.

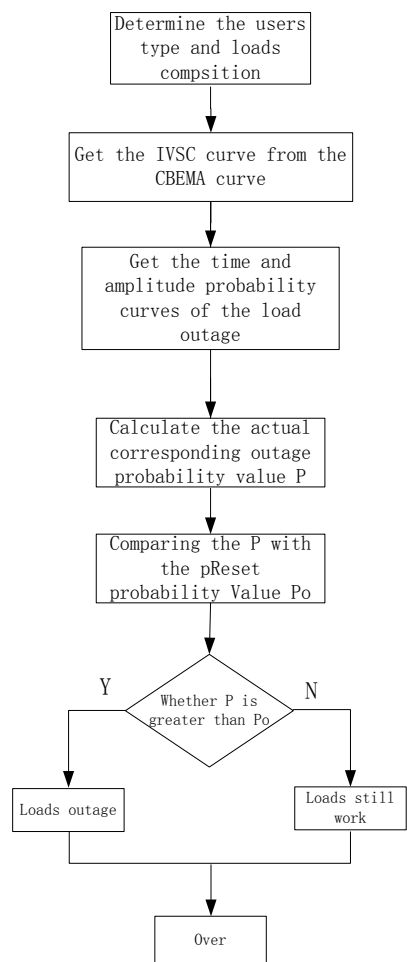


**Figure 9.** The flow chart of load outage judgment

## 6 Conclusion

This paper has re-classified the load equipments as the different sensitivities of loads; analyzing the CBEMA curve which was mentioned in part of the articles and pointing out its shortcomings; Proposing the IVSC and ENIVSC curves based on the CBEMA curve; Proposing a sensitive load outage criterion based on the IVSC curve considering the voltage sags; Using the ambiguity function to get the outage amplitude and duration probability curves, when the voltage sag happens, we can get the load outage probability value by using the voltage sag amplitude and duration values. Comparing the calculated outage probability value with the outage probability threshold, if the calculated value is greater than the set value, it can be judged that the load equipments will be outage.

## References

- [1] Zhang Guohua, Yang Jingyan, Zhang Jianhua, etc. Arithmetic of Distribution Network Reliability Calculation in Consideration of Voltage Sags and Protective Relays[J]. Proceedings of the CSEE, 2009, 29(1): 28-34
- [2] Wang Bin, Pan Zhencun, Xu bingen. Analysis of Voltage Sags in Distribution System[J]. Power System Technology2004, 14(2): 56-59
- [3] Lin Yan, Yu Xinmei, Xiong Xinliang, etc. A Survey on Calculation And Analysis Methods of Voltage Sag[J]. Power System Technology, 2004, 28(14): 74-78
- [4] Wang Bin, Pan Zhencun, Xu Wenyuan. Voltage Sags Profile Estimation for Power Distribution Systems[J]. Proceeding of the CSEE, 2005, 25(13): 29-34s
- [5] Yang Jingyan, Ni Wei, Xiao Xiangning, etc. Reliability Evaluation of Distribution Network Considering Voltage Sags[J]. Proceeding of the CSEE, 2005, 25(21): 63-69
- [6] Tao Shun, Xiao Xiangning, Liu Xiaojuan. Study on Distribution Reliability Considering Voltage Sags and Acceptable Indices[J]. Proceeding of the CSEE, 2005, 25(21): 63-69
- [7] Ni Wei. Probability Evaluation of Distribution Network Taking Into Account Voltage Sags[D]. Beijing: North China Electric Power University, 2003: 29-31
- [8] Liu Lingqun, The Analysis of Voltage Sags and Short Interruptions and Reliability Evaluation of Distribution System[D]. Beijing: North China Electric Power University, 2003: 29-31
- [9] Carl Becker, William Braun Jr. Proposed Chapter 9 for Predicting Voltage Sags(Dips ) [R].in Revision to IEEE Std 493, the Gold book, IEEE Transactions on Industry Applications, 1994, 30(3): 808-812
- [10] Xiao Yao, Li Shushen, Voltage Dip in Power Supply Network[J]. Power System Technology, 2001, 25(1): 73-77

Juan WEI, Liang-liang GUI\*, Pan LU

## Macro Program Application on Non-circular Curve Machining in CNC Lathe

**Abstract:** A programming method of the macro program is studied in this paper, a part with complex surface contain of a parabola, an ellipse and some lines as a case, it's CNC machining program is design using macro program, and the part complete machining process is simulated by virtual simulation system of TK 36 CNC lathe is that the accuracy of the program is validated, at the same time proof the macro program can come true the CNC machining of complex surface and program simple and high universality.

**Keywords:** Macro program; non-circle curve; CNC lathe; VERICUT simulation

### 1 Introduction

In CNC lathe machining, external contour is elliptic, parabolic and the non-circular curve of parts are often met. These complex surface parts of the processing, if we adopt the traditional CAD/CAM software programming, not only make the workload and the complexity of the process but also the processing parameters are not easy to modify and the poor of accuracy. But using macro programming, not only can shorten the programming cycle, simplify the calculation, the program easy to understand, improve the processing accuracy and processing efficiency, but also can be repeated machining similar parts of different size in which realize the function of ordinary programming is hard to realize of improve the use function of machine tool.

This paper adopts FAUNC Oi CNC system. The macro program of the non circular curve turning parts with parabola and ellipse, the part machining is verified by the simulation software VERICUT.

### 2 The Basic Principle Of A Macro Programming

Macro program is a special programming function of FANUC CNC system, its greatest feature is that the user macro program ontology can be used to programming of variables, and has calculated, assignment, selection, jumps and circulatory functions.

---

\*Corresponding author: Liang-liang GUI, College of Mechanical Engineering, Xi'an University of Science and Technology, Xi'an, China, E-mail: 1632567848@qq.com

Juan WEI, Pan LU, College of Mechanical Engineering, Xi'an University of Science and Technology, Xi'an, China

It can be divided into four types of variables: empty variables (#0), local variables (#1-#33), public variables (#100-#199, #500-#599), system variables (#1000-#5335). User macro program is divided into macro program A and B, macro program A is G65 Hxx P#xx Q#xx R#xx; the format of the input, it needs to remember more instruction. Macro program B is based on formulas and direct language input and is similar to C languages, it is mainly used in FANUC Oi system, this paper uses the macro program B programming [1,4].

## 2.1 The Macro Programming Ideas

Macro processing of non-circular curved contour of the basic programming idea is to use a linear approximation method outline node. Specifically, in order to guarantee the accuracy of parts, generally in 0.1 or smaller values for an interval. Using the function of the non circular curve, the definition of a letter in the expression as the independent variable, the other is the dependent varia. Coordinates of each point was determined by the function which the equation, then the points are connected together to form a non-circular contour final. Due to the macro program can define variables and assigned, it also can undertake operation and condition judgment which is constitute a loop transfer, this can be for those use mathematical function relational expression of non-circular curve to continuous “fitting” processing [9], so as to realize the programming.

## 2.2 The Macro Program of Instruction Format

In the program, the use of GOTO statements and IF statements can realize the CNC program logic judgment, comparison, jump and various operation, also can effectively solve the complex of the non-circular curve parts CNC programming problem [3].

### 2.2.1 The JMP (GOTO statement)

Instruction format: GOTO + target segment number (without N);

JMP for unconditional jump to the specified program segment number start executing program section.

For example: GOTO10; (transfer to the serial number for the N10 program section).

### 2.2.2 The JNE (IF statement)

Instruction format: IF + [expression] condition + GOTO target segment number (without N).

When the condition is met, segment that is transferred to the specified procedures section, If the condition is not satisfied, the next program is executed.

For example: N10 IF [#1GT10] GOTO100;

Judge whether the value of the variable # 1 is more than 10.

N20 G00 X70 Y20; If not, then execute program segment N20.

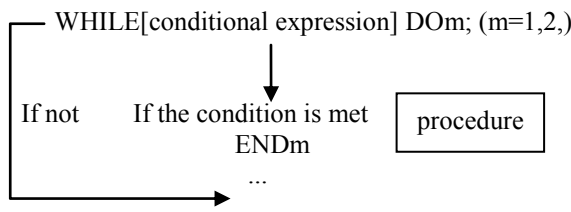
...

N100 G00 X90; If so, then transfer to the serial number for the N100 program section.

### 2.2.3 Loop (WHILE statement)

Specify a conditional expression after WHILE, when the specified condition is satisfied, the program is executed from DO to END, otherwise, the program is transferred to END.

For example:



## 3 Application Examples Of Macro Programs

As shown contains for parabolic and elliptic contour of parts and size for 40×120mm of LY12 in Figure 1. Try the macro programming parts with parabola and ellipse.

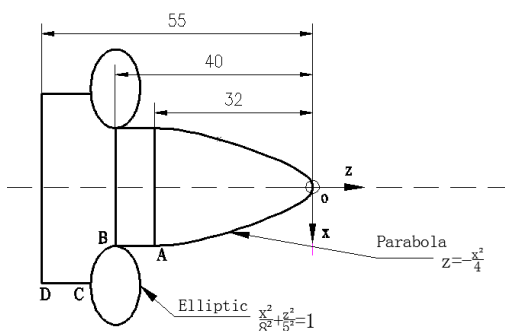


Figure 1. Contains The Parabola And Elliptic Contour Parts.

### 3.1 Analysis of Programming Ideas

As shown in the above parts, assuming that the workpiece origin is located in intersection point of the right end face of artifacts and axis, then establish workpiece coordinate system that is programmed coordinate system is done by adjusting tool. In order to ensure the machining accuracy, and 0.1 for an interval, and as the independent variables, X as a function of Z. When processing a parabola in which the coordinates of each point is calculated according to the equation. However the center of the ellipse coordinates are not the origin of the coordinate system programming is that need to coordinate transformation in which the coordinates of each point on the elliptic arc transition to the programming system for processing. Determine its coordinates of each point, eventually connecting the points together to form a parabolic and elliptical outline. Therefore, the general idea of programming is to use a fixed cycle instructions G71 rough machining of parabolic, then machining of oval and cylindrical surface, last parts for finishing [2].

### 3.2 Mathematical Model

A mathematical model is established by the standard equation of parabolic and elliptic [5,6].

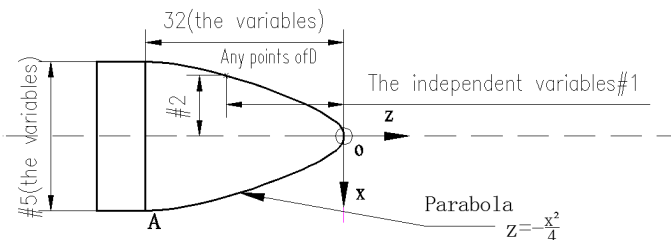


**Figure 2.. Diagram Of Parabola Curve.**

As shown in Figure 2, the Z (#1) value of an arbitrary point D is used in the NC program to express the value of the X (#2) value. By the equation concluded that (unilateral value). Using the straight line fitting for take 0.1mm as a step distance and take Z as the independent variable, the X as a function of Z in which the independent variable range for. The definition of Z and X respectively are #1 and #2, and macro program formats: #2=SQRT[-4\*#1].

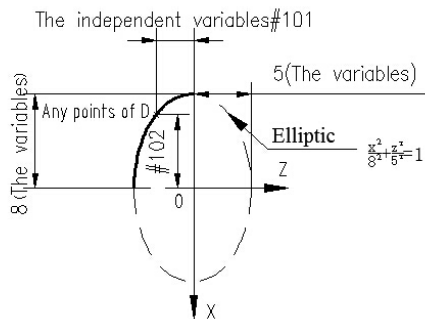


**Figure 3.. Diagram Of Elliptic Curve.**

As shown in Figure 3, the Z (#101) value of an arbitrary point D is used in the NC program to express the value of the X (#102) value. By the equation concluded that (unilateral value), Using the straight line fitting for take 0.1mm as a step distance and take Z as the independent variable, the X as a function of Z in which the independent variable range for. The definition of Z and X respectively are #101 and #102, and macro program formats: #102=8\*[1-#101\*#101/25]. Due center of the ellipse is not programmed coordinates origin (0,0), the need for coordinate transformation. Namely: #103=#101-40, Z coordinates value in the workpiece coordinate syste; #104=#5\*2+16-2\*#102,X coordinates value in the workpiece coordinate syste.

### 3.3 Cutting Parameters And The Coordinates Of The Key Points

T0101 is cylindrical roughing tool, roughing spindle speed of 800r/min, feed rate of 0.2mm/r, engagement of the cutting edge 1.5mm; T0202 is 35diamond finishing tool, finishing spindle speed of 1200r/min, feed rate of 0.1mm/r, X direction finishing allowance of 0.5 mm, Z direction finishing allowance of 0.2 mm.

A point of coordinates  $(2\sqrt{128}, -32)$ ; B Point of coordinates  $(2\sqrt{128}, -40)$ ; The coordinates of point C  $(6 + 2\sqrt{128}, -45)$ .

### 3.4 Program Flow Chart

For the case with parabolic and elliptic contour of programming, the macro program structure flow chart is the same, as shown in Figure 4.

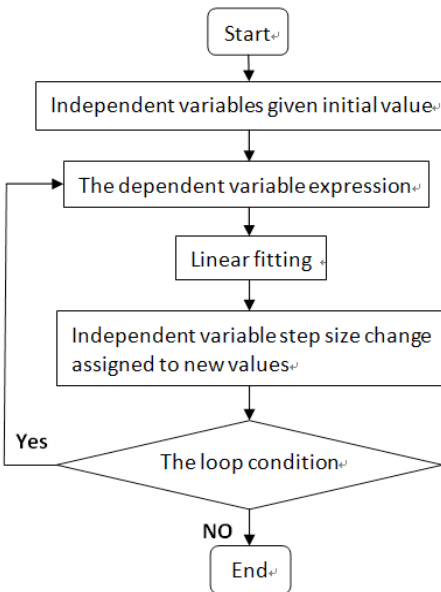


**Figure 4.. Non-circular Curve Contour Of Program Flow Chart.**

### 3.5 Write a macro program

#### 3.5.1 The Meaning of Independent Variables

- #1: Z coordinates value of the parabola.
- #2:single side values of X coordinates in a parabola.
- #3:bilateral values of X coordinates in a parabola.
- #4: step size.
- #101: Z coordinates valueof the ellipse.
- #102: X coordinates value of the ellipse.

#### 3.5.2 The Main Processing Procedures Are as Follows

- N010 G40 G97 G99, The program initialization
- N020 G54 X100 Z100,Set up the workpiece coordinate system
- N030 T0101, Calls on the 1st tool and the 1st tool compensation
- N040 M03 S800, Spindle rotation, the speed of 800 r/mm
- N050 G00 X42 Z5, Tool quickly move to the beginning roughing cutter point (42,5)
- N060 G71 U1.5 R1, Calls the G71 molding cycle roughing compound instruction rough parts of the surface
- N070 G71 P080 Q220 U0.5 W0.2 F0.2, Finishing line for the N080N220
- N080 G00 X0, Quickly move to the point (0,5)

N090 #1=0, Z coordinates value of the parabola is assigned to variables # 1  
 N100 #2=SQRT[-#1\*4], X coordinates value of the parabola is assigned to variables # 2  
 $\#3=\#2^2$ , X coordinates value in the workpiece coordinate system  
 $\#4=0.1$ , The step value is assigned to #4  
 N110 G41 G01 X#3 Z#1 S1200 F0.1, Set up the cutter of left cutter compensation, for linear interpolation approximation curve  
 N120 #1=#1-#4, Z coordinate values to average decline is assigned to a variable # 1  
 N130 IF[#1GE-32] GOTO100, If # 132, then the program jumps to the N100 execution  
 N140 #5=SQRT[128], Outer circle radius value assigned to # 5  
 N150 G01 X[#5\*2] Z-40, Turning cylindrical, linear interpolation to the workpiece coordinate point (#5\*2, -40)  
 N160 #101=0, Z coordinates value of the ellipse is assigned to variables #101  
 N170 #102=8\*SQRT[1-#101\*#101/25],  
 $\#103=\#101-40$ , Z coordinates value in the workpiece coordinate system  
 $\#104=\#5^2+16-2*\#102$ , X coordinates value in the workpiece coordinate system  
 N180 G01 X#104 Z#103, For linear interpolation approximation curve  
 N190 #101=#101-#4, Z coordinate values to average decline is assigned to a variable # 101  
 N200 IF[#101GE-5] GOTO170, If #101-5, then the program jumps to the N170 execution  
 N210 G01 Z-55, Turning cylindrical, linear interpolation to the workpiece coordinate point  
 N220 G40 G00 X42, Cancel tool compensation, tool quickly retracting from the workpiece  
 N230 G00 X100 Z100 M05, Tool quickly returned to the tool change point, main shaft stops  
 N240 T0202, Calls on the 2st tool and the 2st tool compensation  
 N250 M03 S1200, Spindle rotation, the speed of 1200 r/mm  
 N260 G70 P080 Q220 F0.1, Call G70 finish machining cycle, finishing line N080N220  
 N270 G00 X100 Z100, Tool quickly return to the tool change point  
 N280 M05, Spindle stop rotating  
 N290 M30, End of program and return to the beginning of the program

## 4 Simulation Verification

By the simulation software VERICUT, application of virtual simulation system of TK 36 CNC lathe to simulation machining of the non-circular curve parts model [7,8]. It not only can eliminate the phenomenon of the interference, over cutting and residual in the process of cutting, but also can optimization of cutting parameters and simplify NC code, thus eliminating the process of trial cut test is that can significantly improve the production efficiency and reduce the scrap rate of parts and the production cost in the actual machining process. The technology has wide application prospect.

Through the virtual machining simulation, the parameters are reasonable and achieved the expected goals, as shown in Figure 5, 6 and 7.

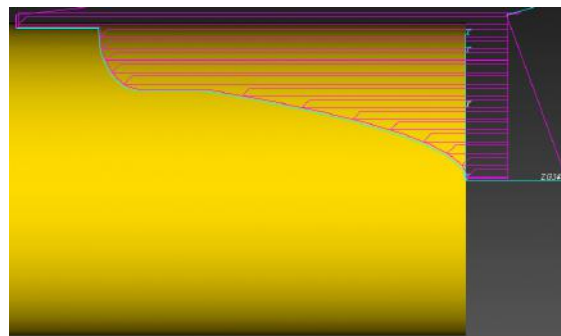


**Figure 5.** Schematic Of Tool Passes Track.

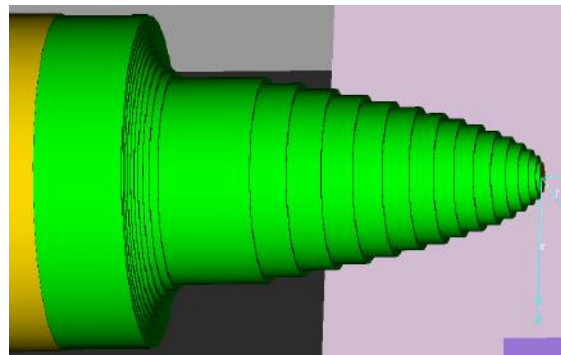


**Figure 6.** Rough Machining.

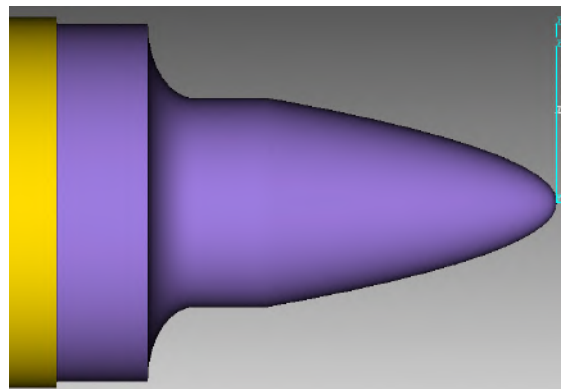


**Figure 7.** Simulation Result.

## 5 Conclusion

Macro programming combined with the mathematical formulas and related knowledge of differential equations to establish mathematical model, in addition combined with graphics size requirements for specific analysis. Macro program can effectively solve the system of traditional G code instructions can't turning the non-circular curve parts processing. The flexibility of the variable, and a significant increase in the scope of programming. For parts with similar structure is that only the value of the variable is changed, which is conducive to the general programming of numerical control program and greatly increases the efficiency of programming. Therefore, the macro program can give full play to the potential function of CNC machine tools, improve the processing efficiency and the economic efficiency of enterprises. It has a wide range of application value in the actual production.

**Acknowledgment:** This work supported by Scientific Research Program Funded by Shaanxi Provincial Education Department (Program name: The simulation system of NC machining for manufacturing industry; Program No:2010JC11) and Industrial Science and technology project of Shaanxi Province (project name: Research on data management and application technology of NC machining for manufacturing informatization, project number: 2016GY-019).

## References

- [1] ZhiGang Feng. FANUC system numerical control programming examples[M]. Beijing: mechanical industry press, 2013.
- [2] YanMin Pu. Typical parts processing 100 cases of FANUC nc system[M] .Beijing: chemical industry press, 2013.
- [3] Jun Du. Master FANUC macros - programming techniques and examples extract solution[M]. Beijing: chemical industry press, 2011.
- [4] YueFeng Zhu. Research on the macro program of FANUC Oi numerical control system[D] . Hefei: HeFei university of technology, 2008.
- [5] Ying Guan. Based on the FANUC system of parabolic macro programming and machining analysis[J]. Coal Mine Machinery, 2011, 32 (9): 112-114.
- [6] BinFeng Lin. Macro program in NC lathe machining method of elliptic [J]. Time Agricultural Machinery, 2015, 43 (32): 42-43.
- [7] QunYang Sheng. VERICUT nc machining simulation technology (second edition)[M] .Beijing: tsinghua university press, 2013.
- [8] YaFang Chen. Combination of macro program programming and VERICUT simulation technology[J]. Mechanical Engineering, 2013, 30(8): 963-966.
- [9] Qisen Cheng. Macro programming method for the application of non circular curve [J].Modern Manufacturing Engineering, 2010(3):46-48.
- [10] Yahui Su.Research on the NC parametric programming method based on macro-program[J]. Die and Mould Technology, 2014 (6):54-56.

Qiu-wei HE, Chao-peng ZHANG, Mei FENG\*, Xing-tian QU, Ji ZHAO

## Singular Configuration Analysis for the Structure of Hybrid Grinding and Polishing Machine

**Abstract:** Blade is a key component in the energy power equipment. Researchers have made a lot of research on precision machining equipment and process for blade. In this paper, based on the designed hybrid grinding and polishing machine tool for blade finishing, we analyzed the singular configuration and designed the reasonable dimension for it, which help us avoid or predict the singular configuration. Firstly, we analyzed the singular configuration of parallel mechanism by using the motion condition of the singular configuration. We established the utmost position of model of the parallel mechanism by using geometric method in Matlab. Secondly, the parallel mechanism of the series and parallel hybrid structure was replaced by the model of series structure, which can simplify the structure of machine to a model of series structure. Finally, the whole structure of machine was analyzed by spinor method. The analysis results show that the designed machine tool for blade finishing has avoided the singular configuration.

**Keywords:** singular configuration; 3-RPS parallel mechanism; limit position; hybrid grinding and polishing machine

### 1 Introduction

Blade is a key and major component in the energy power equipment of turbine, marine propeller, aircraft engines and so on. It is characterized by complex surface structure shape, difficult processing and high precision. As a result, the finishing process of blade is one of the most important and difficult problems in the field of aerospace. In recent years, researchers have made a lot of research on precision machining equipment and process for blade. Such as MTS1000-6CNC the six axis belt grinding machine of IBS company, HS-196GC six-axis grinding center of Huffman company, five axis linkage high precision vertical machining center of C.B. Ferrari company, copy grinding machine of Japan's Okamoto machinery [1-4]. Regardless of any form of mechanism, singular configurations are always unavoidable [5]. It can be summed up that when the mechanism during exercise extreme point, uncontrolled movements, or changes occur freedom, the mechanism will lost a smooth, mechanical or kinematic

---

\*Corresponding author: Mei FENG, College of Mechanical Science and Engineering, Jilin University, Changchun, China, E-mail:179776209@qq.com

Qiu-wei HE, Chao-peng ZHANG, Xing-tian QU, Ji ZHAO, College of Mechanical Science and Engineering, Jilin University, Changchun, China

properties of the phenomenon of instantaneous mutation. This makes the transfer mechanism motion and power capacity abnormal, in this case the structure in which the position of singularities. Singular configuration can't be avoided. The structure of machine early in the design should be calculated on the singular configurations and design a reasonable structure size, so we can avoid singular configurations or predict singular configurations and make compensation in control system [6]. One of the main concerns in the design of parallel mechanism is kinematic singularities. The notion of singularity in parallel mechanism kinematics refers to configurations in which a mechanism manipulator either loses or gains one or more degrees of freedom instantaneously. In other words, if a parallel mechanism is in a singular configuration, it will lose its designated motion and working capability. Hence, to design a parallel robot with a desired performance, e.g., high rigidity and manipulability, singularities must be excluded from its working area, if possible. As the singular configuration has an important influence on the performance of the mechanism, it has been paid more and more attention by researchers. Hunt apply the spinor theory to the singular configuration. Mer-let used Grassmann Geometry analyzed a special singular configuration of Stewart Platform. Kumar introduced a singular point because of drive joint selection. Gosselin and Angeles studied the singularity problem is generally parallel mechanism [7].

In this paper, the designed machine is series and parallel hybrid structure, which is shown in Figure 1 [8]. The machine is consisted by 3-RPS parallel mechanism and series structure. According to the processing requirement, the parallel mechanism just need rotate around the X axis and moving along the Z axis. Besides, the series structure include that moving along X axis, Y axis, rotating around Y axis. The parallel mechanism was analyzed by the motion condition of the singular configuration, which can reduce the calculation. When the parallel mechanism gets the result, we can convert the series and parallel hybrid structure to a model of series structure according to the result. Finally, the whole structure of machine can be analyzed by spinor method. The spinor method can carry out the results quickly. So the size of the machine can be designed according to the result of all the analysis and avoid the singular configuration.

## 2 Singular Configuration Analysis of Parallel Mechanism

3-RPS parallel mechanism is the most complex structure when we analyze serial hybrid grinding and polishing tool for singular configurations. There are many ways to analyze the singular configuration of parallel mechanisms such as Jacobi matrix, Grassmann law line geometry and kinematics condition [9], in which the kinematics condition is simple, so this paper we analyzes the singular configuration in kinematic condition [10]. The parallel mechanism model is shown in Figure 2.

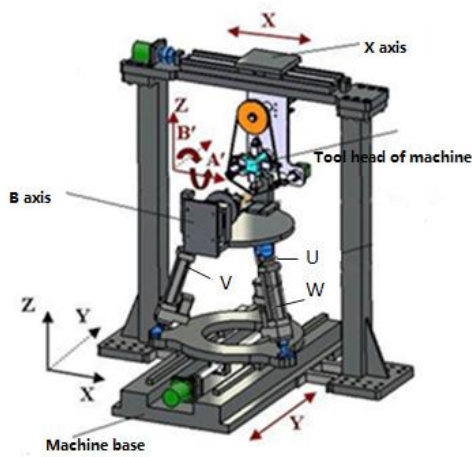


**Figure 1.** Structure of the machine.

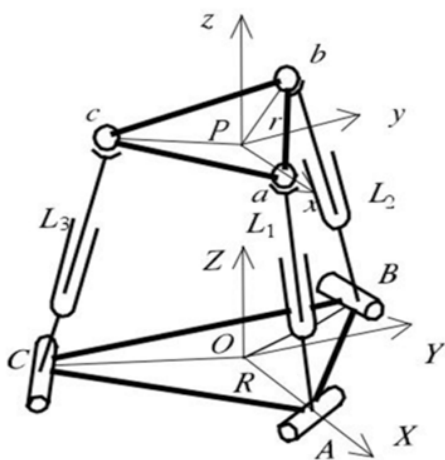


**Figure 2.** Parallel mechanism diagram.

According to the need of machining, the radius  $r$  of the moving platform is 250mm and the radius  $R$  of the static platform is 450mm. A, B, C of parallel mechanism is static platform triangle vertex respectively, in static platform coordinate system O-XYZ, the coordinates of three points are that:  $A = (R, 0, 0)$   $B = (-R/2, \sqrt{3}R/2, 0)$   $C = (-R/2, -\sqrt{3}R/2, 0)$ ; a, b, c of parallel mechanism is moving platform triangle vertex respectively, in the moving platform coordinate system P-xyz, the coordinates of three points are that:  $a = (r, 0, 0)$   $b = (-r/2, \sqrt{3}r/2, 0)$   $c = (-r/2, -\sqrt{3}r/2, 0)$ .

P-xyz moving platform coordinate system relative to the static platform coordinate system conversion O-xyz relations can be expressed as the homogeneous matrix  $T_0$ . P-xyz coordinate system of the three main unit vector with respect to the coordinate system O-XYZ direction cosine were presented by  $x_m, y_m, z_m$  ( $m=k,j,i$ ).  $X_p, Y_p, Z_p$  represent the position coordinates of the point P in the O-XYZ.

$$T_0 = \begin{bmatrix} x_i & y_i & z_i & X_p \\ x_j & y_j & z_j & Y_p \\ x_k & y_k & z_k & Z_p \\ 0 & 0 & 0 & 1 \end{bmatrix}. \quad (1)$$

Direction and position of the parallel mechanism described by Euler angles [5]. The moving platform will rotate around the z,x,y axis, which are angle for  $\alpha, \gamma, \beta$ . According to the requirement of movement of Serial hybrid grinding and polishing tool, 3 - RPS parallel mechanism of the rod  $L_1, L_2$  have the same state of motion. The moving platform only rotates around the Y axis, so  $\alpha=\gamma=0$ . Finally we get the value of T by (1).

In the coordinate system P-xyz,  $m_p$  is a point of the moving platform. In the coordinate system O-XYZ,  $m_p$  is converted to  $m_o$ .

$$T = \begin{bmatrix} \cos\beta & 0 & \sin\beta & X_p \\ 0 & 1 & 0 & Y_p \\ -\sin\beta & 0 & \cos\beta & Z_p \\ 0 & 0 & 0 & 1 \end{bmatrix}, \begin{bmatrix} m_o \\ 1 \end{bmatrix}_{XYZ} = T \begin{bmatrix} m_p \\ 1 \end{bmatrix}. \quad (2)$$

The three point a, b, c values into (2), so we can get the results.

$$\begin{cases} a_o = (r \times \cos\beta + X_p, Y_p, -r \times \sin\beta + Z_p) \\ b_o = (-r \times \cos\beta/2 + X_p, \sqrt{3}r/2 + Y_p, r \times \sin\beta/2 + Z_p) \\ c_o = (-r \times \cos\beta/2 + X_p, -\sqrt{3}r/2 + Y_p, r \times \sin\beta/2 + Z_p) \end{cases} \quad (3)$$

Because of the structure characteristics of 3-RPS parallel mechanism, a, b and c of the three ball hinge centers of the moving platform must be in the plane of the three perpendicular to the static platform. In the static platform coordinate system O-XYZ, the projection equation of three planes is obtained.

$$Y = 0, \quad Y = -\sqrt{3}X, \quad Y = \sqrt{3}X. \quad (4)$$

The (3) are put into the (4) corresponding to the projection plane, so we can get the values of  $X_p$  and  $Y_p$ . Beside the  $r$  is 250mm.

$$X_p = 125(\cos\beta - 1), \quad Y_p = 0. \quad (5)$$

The motion condition of the singular configuration has the following performance in the 3-RPS parallel mechanism [5]. When moving platform motion, three ball joint center points a, b, c of the instantaneous velocity is  $V_1, V_2, V_3$ , which corresponding

to the plane recorded as  $D_1$ ,  $D_2$ ,  $D_3$ . When these three planes hand in a point  $n$  and  $n$  is located in a plane which posed by points  $a$ ,  $b$ , and  $c$ , the mechanism is located in the singular configuration. According to these conditions, we can get the trajectory equation  $P$  of the center point of the moving platform when the singular configuration occurs.  $Z_p$  has three possible conditions when the singular configuration occurs.

$$\begin{cases} 1.Z_p = -125 \sin \beta \\ 2.Z_p = -(525 + 125 \cos \beta) \times \sin \beta / (1 + \cos \beta); \beta \in [-15^\circ, 15^\circ] \\ 3.Z_p = (325 - 125 \cos \beta) \times \tan \beta \end{cases} \quad (6)$$

According to (5) and (6), the trajectory of the  $P$  with a singular configuration is obtained as shown in Figure 3 by Matlab, when the moving platform is rotated in  $\beta \in [-15^\circ, 15^\circ]$ . In the end, the singular configuration may occur at the maximum position at  $Z_l=85\text{mm}$ .

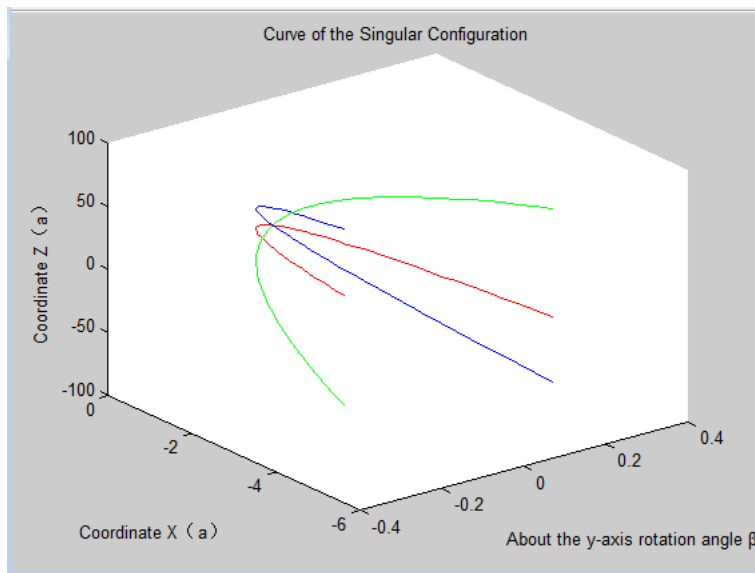


**Figure 3.** Singular configuration locus diagram.

### 3 Limit Position Analysis of Parallel Structure

According to the needs of machine tools, the initial length of the three electric cylinders  $L_1$ ,  $L_2$ ,  $L_3$  of the 3-RPS parallel mechanism is set to be 620 mm and maximum elongation of electric cylinder is  $\Delta L=160\text{mm}$ . In this dimension, the limit state of parallel mechanism is calculated. Because of electric cylinder  $L_2$ ,  $L_3$  running state is

consistent, according to Figure 1 shows, the electric cylinder  $L_2$ ,  $L_3$  and BC and bc constant form an isosceles trapezoid, as shown in Figure 4.

Because of the characteristics of the 3-RPS parallel motion, aA and vertical center line hH of isosceles trapezoid constant positioned in the same plane, which constitute the plane hHaA, as shown in Figure 5. The geometric center P of moving platform is located in ah and we can get the results is that  $2hP=aP$  by geometric properties of equilateral triangle. The spatial motion of the geometric center point P is converted to the model of plane motions.

The point H is coincident with the origin of the coordinate system O and Linear HA and Y axis coincidence. Suppose point h coordinates  $(x_1, y_1)$ ; point a coordinates  $(x_2, y_2)$ ; point P coordinates  $(x_3, y_3)$ . The turning angle of the line segment ha with respect to the line segment HA is  $\beta$ . We can establish the boundary condition of the point P motion through the plane motion model.

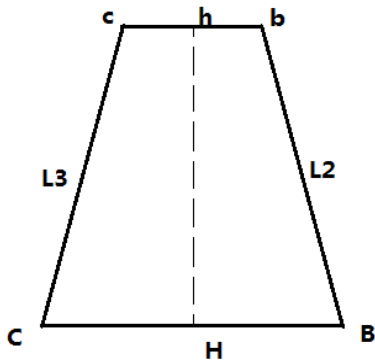


Figure 4. Isosceles trapezoid.

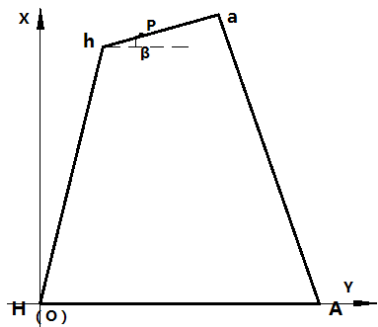


Figure 5. Point P motion plane model.

$$\left\{ \begin{array}{l} x_1^2 + y_1^2 = l_5^2 \\ (x_2 - 675)^2 + y_2^2 = l_1^2 \\ (x_1 - x_2)^2 + (y_1 - y_2)^2 = 375^2 \\ (y_1 - y_2)/(x_1 - x_2) = \tan\beta \\ 0 \leq x_1 \leq 675 \\ 0 \leq y_1 \leq 761 \\ 0 \leq x_2 \leq 675 \\ 0 \leq y_2 \leq 780 \end{array} \right. \quad \begin{array}{l} l_5 \in [595, 761] \\ l_1 \in [595, 761] \\ \beta \in [-15^\circ, 15^\circ] \end{array} \quad (7)$$

The point P vertical coordinate  $y_3$  is the movement range of the moving platform in the Z direction.

$$y_3 = (y_2 + 2y_1)/3. \quad (8)$$

In the MATLAB with the search method [5] to calculate the range of  $y_3$  value: 554mm~754mm. According to (7) and (8). Because the minimum value of the point P is 554mm, which is far greater than the maximum position 85mm of the singular configuration, so the design of the parallel mechanism is reasonable and has avoided the singular configuration.

#### 4 Analysis of the Singular Configuration of whole Machine Tool

The mixed structure should be split, before the analysis of the singular configuration of the series and parallel hybrid structure. More complex structure should be analyzed separately, then a simplified alternative model for finding complex structures. The simplified model into the hybrid structure, and then establish a hybrid structure model, finally on the overall analysis. The machine tool is a series and parallel hybrid structure. The parallel structure has been analyzed in the above and there is no singular configuration in the required range of motion [7]. It can be reduced to a mobile vice and a revolute pair, which are converted into the series and parallel hybrid structure, so we can get a simplified model as shown in Figure 6.

O-XYZ is the global inertial coordinate system;  $\theta_1$  is a mobile vice and moving along the X axis, beside its initial length is  $L_1$ ;  $\theta_2$  is a mobile vice and moving along the Y axis, beside its initial length is  $L_2$ ;  $\theta_3$  is a mobile vice and moving along the Z axis, beside its initial length is  $L_3$ ;  $\theta_4$  is a revolute pair and rotate around the X axis;  $\theta_5$  is a revolute pair and rotate around the Y axis;  $\theta_3$  and  $\theta_4$  are the equivalent substitution model of parallel mechanism.

The hybrid structure of the machine tool is simplified as a series structure. It is shown that the singular configuration of the Jacobi matrix is the occurrence of reduced rank, and the linear correlation between the various kinematic pairs. We calculate the Jacobi matrix by spinor method [11].

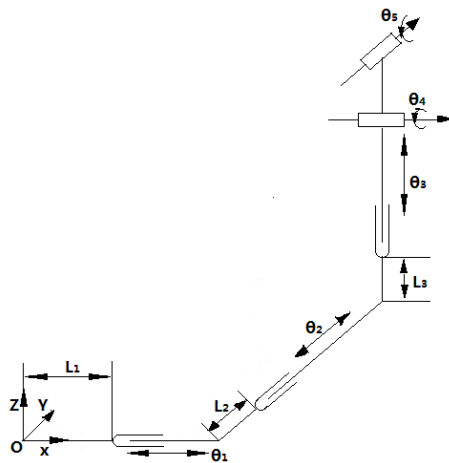


**Figure 6.** Schematic diagram of machine tool.

We can get the formula of the spinor method.

$$\$ = (s \ ; \ s^0) = (s \ ; \ r \times s + hs) \quad (9)$$

The  $s$  is the unit vector in the direction of the axis of spinor; the  $r$  is a point on the spinor axis; the  $s^0$  is dual of the spinor vector; the  $h$  is pitch. We can get Jacobi matrix.

$$J(\theta) = (\$, \$_2, \$_3, \dots, \$_i, \dots, \$_n) \quad (10)$$

$\theta_1, \theta_2, \theta_3, \theta_4, \theta_5$  are substituted into (9), so we can get  $\$, \$_2, \$_3, \$_4, \$_5$ . So the  $\$, \$_2, \$_3, \$_4, \$_5$  are substituted into (10).

$$J(\theta) = \begin{bmatrix} 0 & 0 & 0 & 1 & 0 \\ 0 & 0 & 0 & 0 & \cos\theta_4 \\ 0 & 0 & 0 & 0 & \sin\theta_4 \\ 1 & 0 & 0 & 0 & (L_2 + \theta_2)\sin\theta_4 - (L_3 + \theta_3)\cos\theta_4 - L \\ 0 & 1 & 0 & L_3 + \theta_3 & -(L_1 + \theta_1)\sin\theta_4 \\ 0 & 0 & 1 & -L_2 - \theta_2 & (L_1 + \theta_1)\cos\theta_4 \end{bmatrix} \quad (11)$$

Because the  $J(\theta)$  is the 6 row and 5 column type, the analysis of the rank need to be discussed. When the rank of the velocity Jacobi matrix is 5, it can ensure that the spinor of each pair of motion is linearly independent. At this time, the series mechanism has no singular configuration.

When  $\cos\theta_4 \cdot \sin\theta_4 \neq 0$ , Jacobi matrix can be simplified.

$$J(\theta) = [0, 0, 0, 1, 0; 0, 0, 0, 0, \sin\theta_4; 1, 0, 0, 0, 0; 0, 1, 0, 0, 0; 0, 0, 1, 0, 0].$$

Rank constant was 5, there was no reduction in rank; When  $\cos\theta_4 = 0$ , speed Jacobi matrix can be simplified as  $J(\theta) = [0, 0, 0, 1, 0; 0, 0, 0, 0, \sin\theta_4; 1, 0, 0, 0, 0; 0, 1, 0, 0, 0; 0, 0, 1, 0, 0]$ .

Rank constant was 5, there was no reduction in rank; When  $\sin\theta_4=0$ , speed Jacobi matrix can be simplified as  $J(\theta)=[0,0,0,1,0; 0,0,0,0,\sin\theta_4;1,0,0,0,0;0,1,0,0,0;0,0,1,0,0]$ . Rank constant was 5, there was no reduction in rank. So the series mechanism has no singular configuration.

## 5 Experiment

In order to test the analysis about singular configuration, We design these experiments. When moving and static platform of the 3-RPS parallel mechanism are coincident, the moving is stopped, which is a singular configuration [9]. When the length of the three electric cylinder is equal, the parallel mechanism is in the initial position. It shows in Figure 7a. It is non-singular configuration through the motion condition of the singular configuration. This position will be locked in the electric brake cylinder, the moving platform of the applied force, as shown in Figure 7b, which did not appear the phenomenon of structural instability. In the range of motion of the machine tool, the parallel mechanism rotates one angle around the X axis, and the phenomenon of instability of parallel mechanism is not appeared, as shown in Figure 7c. So the theoretical analysis is correct. In the same way, through the machine tool overall motion experiment, the structure is stable, does not appear the movement instability phenomenon.

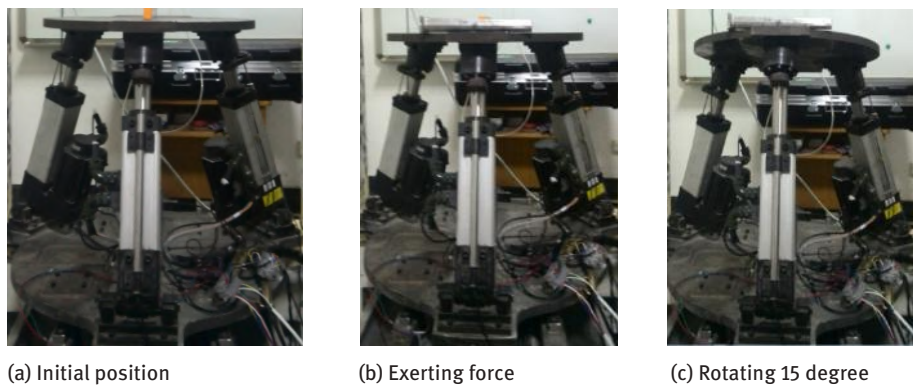


**Figure 7.** Non-singular configuration of experiment of parallel mechanism.

## 6 Conclusion

According to the experiment, the theory of singular configuration is correct. In the 3-RPS parallel mechanism minimum value of the point P is 554mm, which is far greater than the maximum position 85mm of the singular configuration, so the design

of the parallel mechanism has avoided the singular configuration. To sum up the overall speed of the machine tool the rank of Jacobi matrix is constant 5, so there is no singular configuration. The machine should be designed according to the processing requirements of machine tools. In the future we will analysis that if the mechanism has singular configurations, how to avoid the singular configurations by using the method of control.

**Acknowledgement:** In this paper, the research was sponsored by the National Nature Science Foundation of China (Grant No. 51135006).

## References

- [1] Y. Sun, D. J. Giblin, and K. Kazerounian, Accurate robotic belt grinding of workpieces with complex geometries using relative calibration techniques, *Robotics and Computer-Integrated Manufacturing*, vol. 25, pp. 204-210, 2009.
- [2] Z. Huang, *Study on Basic Applied Technology of CNC Abrasive Belt Grinding Blade Profile*, Chongqing: Chongqing University, 2010.
- [3] X. Ren, M. Cabaravdic, X. Zhang, and B. Kuhlenk, A local process model for simulation of robotic belt grinding, *International Journal of Machine Tools and Manufacture*, vol. 47, Issue 6, May 2007.
- [4] <http://www.willermin-macodel.com>.
- [5] Z. Huang, L. F. Kong, and Y. F. Fang, *Theory and Control of Parallel Robot Mechanism*, Beijing: Machinery Industry Press, 1997.
- [6] F. Wang, and X. Lin, Detection and Treatment of Singular Regions in Five Axis Machining, *Computer integrated manufacturing system*, vol. 17, 2011.
- [7] Z. Huang, *The theory of space mechanism*, Beijing: Higher Education Press, 2006
- [8] H. Chen, *The Research and Realization of Hybrid Polishing Machine Tool Control System for Vane*, Jilin University, 2015.
- [9] J. N. Xiang, Singularity analysis of a 3-RPS parallel manipulator using geometric algebra, *Zhejiang Sci-Tech University*, 2015.
- [10] Y. W. Li, *On Singularity of several kinds of Spacial Parallel Manipulators*, Yanshan University, 2005.
- [11] J. J. Yu, X. J. Liu, X. L. Ding, J. S. Dai, *Mathematics of robot mechanism*, Beijing: Machinery Industry Press, 2008.

Sha-na WANG\*

# Static Analysis and Size Optimization for the Bed of Gantry Milling Machine based on ANSYS Workbench

**Abstract:** Aiming at the phenomenon of heavy structure and high material consumption of the bed of gantry milling machine in machinery industry at present, this paper used the ANSYS Workbench simulation software, through the static analysis of the bed, and combined with its stress and strain contour, to judge whether it meets certain engineering constraints; made the size optimization under the condition of satisfying the condition of stiffness and strength, thus a lightweight design for the bed was realized, in order to achieve the goal of reducing the cost and enhancing the market competitiveness of enterprises.

**Keywords:** Bed; ANSYS Workbench; Size Optimization; Lightweight;

## 1 Introduction

At present, the milling machine is a very wide range of metal cutting machine tools, the gantry milling machine is one of the very common one kind of milling machine, its bed design is particularly important. This bed mainly supporting the working table and processing parts, it is connected with ground effect, and both sides of the bed connected to columns, is one of the components of the milling machine. However, there are different degrees of defects in the design phase of product structure, such as high cost, large supplies, low accuracy and so on, it has become a bottleneck restricting the development of modern manufacturing industry in our country [1]. In the design and manufacture of machine tool, the lightweight design of bed is one of key the design problems for designers at present.

## 2 The necessity of CAE in the design and application of bed

CAE Technology (Computer Aided Engineering) is a comprehensive process which including product design, engineering analysis, data management, testing, simulation and manufacturing; it is the basis of numerical analysis for all kinds of engineering analysis and calculation methods (such as finite element method, boundary element method, etc.) [2].CAE technology is the analysis of the function modules of the calculation analysis, simulation, optimization design and so on, it combining the

---

\*Corresponding author:Sha-na WANG, School of Art & Design Guilin University of Technology, Guangxi Univ, Guilin, China, E-mail: wangshana1987@126.com

computer technology with the modern engineering method. The technology is widely used in aerospace, automotive, machinery manufacturing and other industrial fields.

At present, in most design process of the machine rarely simulation analysis by CAE for the design of each module, generally, some design size only rely on the geometric parameters of the more mature the same type of products which rely on the experience of some old designer values, but most of them is not verified by the simulation analysis software, so it is very necessary to verify the performance by the CAE technology simulation. In recent years, designers had their own judgment and decision ability combined with the optimal design theory and method, which automatically find the optimal design scheme by using computer program on the basis of some optimization algorithms, to achieve the lightweight design for product, and to reduce production cost with low material consumption. At present, ANSYS is one of the most widely used CAE software for enterprise and scientific research in universities.

### 3 ANSYS Workbench Simulation analysis

The basic process of ANSYS Workbench simulation analysis can be divided into three parts, pre-processing, solution and post-processing [3]. Each process of the whole simulation analysis to deal with the corresponding functional requirements, the whole basic process of ANSYS Workbench simulation analysis as shown in Figure 1.

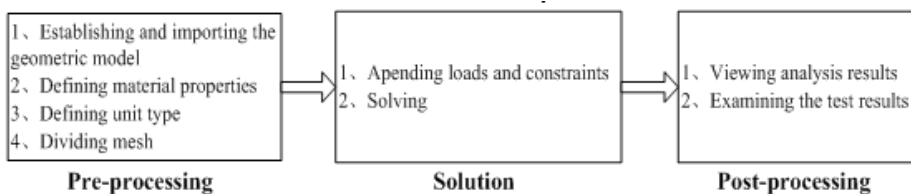


**Figure 1.** The basic process of ANSYS Workbench simulation analysis

#### 3.1 Pre-processing

The solid model of the bed is built by using 3D software, its length is 6700 mm and width is 1300 mm, the model is shown in Figure 2. Firstly, through the CAD and CAE data sharing transfer mode to achieve the geometric model sharing, the completion of the CAE in the process of geometric modeling in the pre-processing, and the geometric model of the processing is established. Secondly, according to the property of material of the bed of milling machine to set its properties parameters, the parts materials of machine used for gray cast iron HT300 (Elastic modulus:  $E = 1.45e11$  (N/m<sup>2</sup>),

Poisson ratio:  $\mu = 0.26$ , Density:  $\rho = 7400 \text{ (kg/m}^3\text{)}$ ), which Combined machine tool design handbook with enterprise design experience of engineers. Then the discrete model is realized by setting the cell size, and the mesh generation is generated for the next simulation analysis, and the part of the discrete model is shown in Figure 3.

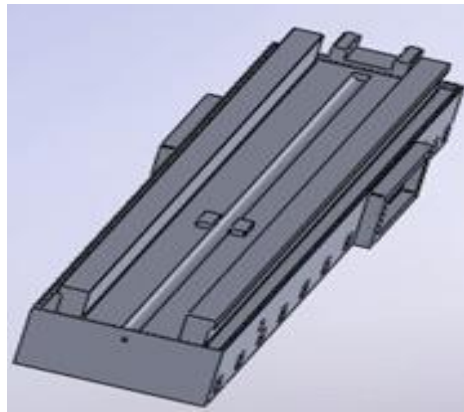


**Figure 2.** The 3D modeling model of the bed

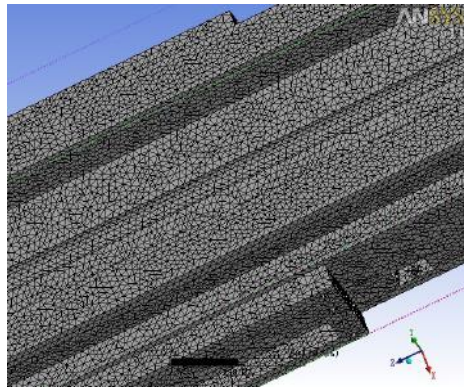


**Figure 3.** Partial screenshots of the discrete model

### 3.2 Solution

#### 3.2.1 Stress analysis of the bed

According to the actual processing conditions, the main force of the lathe bed are the gravity of work piece, cutting force, weight and gravity of the bed itself, its maximum stress condition is when the largest operating by Working table processing. When

the bed size is 6700mm\*1300mm, then working table size is 3000mm\*1250mm. and the weight is 3.2 tons, so that the cutting force is too small when it respects to the weight, it can be neglected. According to the designer's processing experience, per square area of the table can support the maximum load is 13600 kg for the work piece.

### **3.2.2 Constraint condition of bed**

Because the installation form of bed is directly connected with ground bolt, its anchor bolt can simply set up all constraint, both side of the bed contact with the column are also set up all constraints.

## **3.3 Post-processing**

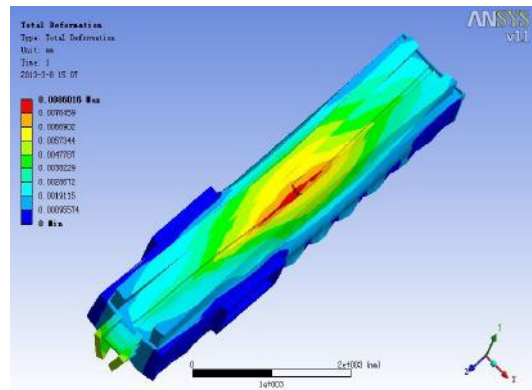
### **3.3.1 Static analysis**

It can solve the calculation after the completion of pre-processing, through the static analysis, it can obtain physical quantities which related to the engineering constraints, such as the total deformation, stress and strain, and so on. The results of static analysis are shown in the following Figure 4 (including the total deformation contour figures, strain contour figures and stress contour figures).

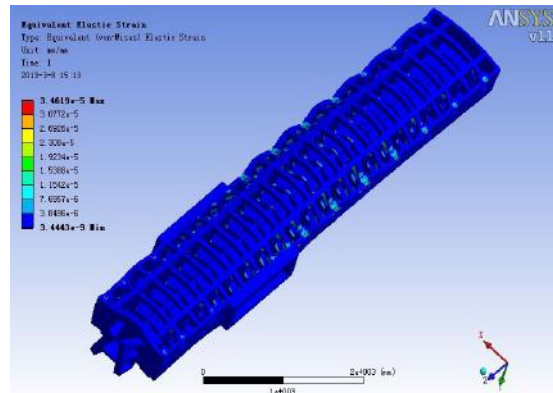
### **3.3.2 To determine whether to meet the strength of stiffness conditions**

Through analyzing the simulation results report file for data extraction, and comparing with material stress and strain limit values, it can determine the strength safety coefficient of the model is whether to consistent with the requirements of the enterprise by checking calculation. According to the above analysis of the stress contour figures and strain contour figures which can report the corresponding data, it is including some of the report data as shown in Figure 5.

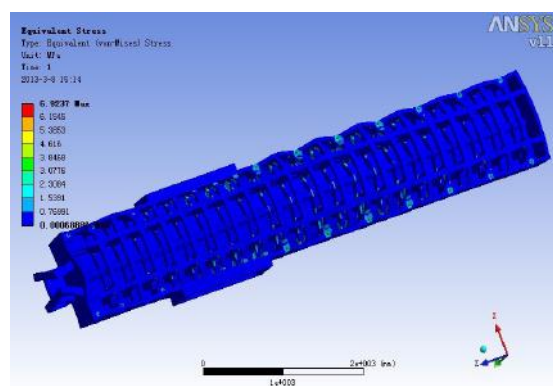
With the data of analysis report can be obtained: the maximum deformation is 8.6016E-3 mm, it is 0.86 silk, the maximum deformation is 8.6016E-3 mm, namely 0.86 silk, through combining machine design handbook with engineer experience, it obtains that per meter of machine parts length to allow the maximum deformation is 0.02 mm, the length of parts is 6.7 meters, allows the maximum amount of deformation for 0.134 mm, so it is to meet the requirement of stiffness; and the most stress value for 6.9237 MPa, according to the selected materials for HT300 which material yield limit is 250 Mpa. Then, the size of the bed design meets the stiffness strength condition of engineering constraints.



(a) Total deformation contour figures



(b) Strain contour figures



(c) Stress contour figures

**Figure 4.** Results of static analysis

TABLE Model > Static Structural > Solution > Results				
Object Name	Total Deformation	Directional Deformation	Equivalent Elastic Strain	Equivalent Stress
State	Solved			
Scope				
Geometry	All Bodies			
Definition				
Type	Total Deformation	Directional Deformation	Equivalent (von-Mises) Elastic Strain	Equivalent (von-Mises) Stress
Display Time	End Time			
Orientation	Y Axis			
Results				
Minimum	0. mm	-8.6013e-003 mm	3.4443e-009 mm/mm	6.8886e-004 MPa
Maximum	8.6016e-003 mm	2.1668e-005 mm	3.4619e-005 mm/mm	6.9237 MPa
Information				
Time	1. s			
Load Step	1			
Substep	1			
Iteration Number	1			

**Figure 5.** The data of analysis report

## 4 The size optimization of bed

Size optimization is a form of structure optimization, it refers to in the topology invariant which external shape and internal pore of structural elements, by optimizing to change unit properties for seeking the optimal size of structure element, and to find a kind of optimal method under the condition of meeting certain strength and stiffness requirements [4]. In carrying on structure displacement and stress are calculated by finite element method, the optimization process does not need re-meshing, it directly using sensitivity analysis and appropriate mathematical programming method to complete the optimization design of the specified size [5,6].

When the thickness of transverse stiffened plate as design variables (the primary design variables is 60 mm), maximum displacement, maximum stress values, the maximum strain value as the constraint condition, the bed total volume as the target variable. Then optimizing the design variables (60 mm), the optimal design results are obtained as shown in Figure 6. To meet the stiffness and strength, the volume is decreased (before the optimization model of volume for 8.430e \* 008 mm<sup>3</sup>), the lightweight design is achieved (it can reduce 108 kg after optimization), then the design optimal solution is achieved, so the thickness of transverse stiffened plate is 52 mm for obtaining lightweight design of product.

### Candidate Designs

Generate or update candidate designs based on the current goals					
Parameter	<input checked="" type="radio"/> Candidate A	<input type="radio"/> Candidate B	<input type="radio"/> Candidate C		
DS_1@sketch13@chaungshengj.Part	52.033	—	53.188	—	54.343
chaungshengj Volume	8.284e+008 mm <sup>3</sup>	★★★	8.29e+008 mm <sup>3</sup>	★★	8.2961e+008 mm <sup>3</sup>
Equivalent Elastic Strain Maximum	3.4198e-005 mm/mm	★★★	3.4311e-005 mm/mm	★★	3.4407e-005 mm/mm
Equivalent Stress Maximum	6.8396 MPa	★★★	6.8622 MPa	★★	6.8813 MPa
Total Deformation Maximum	8.6761e-003 mm	✗ ✗ ✗	8.6757e-003 mm	✗ ✗ ✗	8.6589e-003 mm

**Figure 6.** Optimization results

## 5 Conclusion

Through the analysis of the CAE technology, the static analysis of the Bed of Gantry Milling Machine in certain conditions, that with the aid of simulation analysis module and optimization module of this software, and to judge whether it meets certain engineering constraints, the size optimization of this bed was realized with to meet the prerequisite for the stiffness and strength. In this paper, through the simulation analysis, it is used to solve the problem of the estimation error of the product design and the reliability of the verification experience; and through the dimension optimization design, it is used to solve the problem of design level which is difficult to improve by the design level which is based on the individual visual judgment and experience accumulation by the designer, thus reducing the production cost and improving the market competitiveness of enterprises.

**Acknowledgment:** This work was financially supported by the project of improving the basic ability of young teachers in Colleges and universities in Guangxi (KY2016LX089); Guangxi district foundation funded project excellence program.

## Reference

- [1] Yang Qijiang. Study on Dynamic Modeling for Gantry Machining Center Beam Components Structure and Prediction of Chatter Stability [D].Guangzhou, Guangdong University of Technology.2011:10-26
- [2] Wang Shana, Liu Fuyun, Kuang Bing. Development of Parts Variant Design System Based on the Integration of CAD/CAE [J]. Journal of Machine Design and Research. 2013.29(4).64-66
- [3] Ling Gualong, Ding Jinbing, Wen Zheng. ANSYS Workbench 13.0 From Entry to Master [M]. Tsinghua University Press, 2012.P356-368
- [4] Wang Yingli. Structural topology and size optimization design of body-In-White in New Energy Vehicles [D].Dalian: Dalian University of Technology, 2012.11-13
- [5] Hu Qiuixiang. Application of structural topology, shape and size optimization method in design of stiffening girder of cable stayed bridge [D].Nanjing: Hohai University.2005.8-9
- [6] Wang Fei. Topology and Size Optimization Research Metro Vehicle Bogie Frame of Type B [D]. Beijing: Beijing Jiaotong University.2012. 15-17.

Da-xian HAO\*, Chao YUN, Hui JIN, Gang WANG

## Research and Optimization of Clip Type Passive Manipulator

**Abstract:** The Clip Type Passive Manipulator which can improve the refilling efficiency significantly to artificial recharge is designed for the Fast Medicine Dispensing System (FMDS) in Pharmacy. The Clip Type Passive Manipulator, which includes positioning unit, supporting unit, moving unit, is studied and applied for solving the problem of small capacity of the manipulator. The operating principle of the manipulator is powered by gravity. An optimal design of the key components in manipulator, dedicated ball screw, is improved in order to increase work efficiency of Clip Type Passive Manipulator. Based on the experiments and data analysis, results show the manipulator limit movement speed can be increased about 17% after the optimization. The refilling efficiency of manipulator met the demand of complementary medicines in a Fast Medicine Dispensing System and it makes the service life of ball screw in the manipulator longer.

**Keywords:** Clip Type Passive Manipulator; Fast Medicine Dispensing System (FMDS); Optimization Design; Ball Screw

### 1 Introduction

Manipulator is one kind simple and useful Robot, which is used for heavy and monotonous manual work because of the higher cost of labor. The research on application of started from the late 1940s, when Oak Ridge National Laboratory (ORNL) of America used it for transporting radioactive materials in experiment of atomic energy. The first manipulator has been developed in USA since 1958. Since the 1990s, with the rapid development of automatic, computer science, Web of things, operational research, and artificial intelligence have been merged together [1]. The direction of research on manipulator started to turn to standardization, modularization, networking and intelligentization. In the meantime, Manipulator technology in medical equipment is a new cross-over research field integrating medical science, biomechanics, robotics, mechanics of machinery, computer graphics and so on, and it has been a trend of research on manipulator in the world [2]. The main application of manipulator in medical industry is medical rehabilitation manipulator [3-5],

---

\*Corresponding author: Da-xian HAO, School of Mechanical Engineering & Automation, Beihang University, No37, XueYuan Road, Beijing, 100191, China, E-mail: haodaxian@buaa.edu.cn

Chao YUN, Hui JIN, Gang WANG, School of Mechanical Engineering & Automation, Beihang University, No37, XueYuan Road, Beijing, 100191, China

operation assistance manipulator [6-8] and medical logistics assistance manipulator [9-12]. In this paper, we mainly study the medical logistics assistance manipulator, and we develop a novel manipulator that aim at the low efficiency of refilling each time by manipulator. The Pallet Type manipulator, Scissors Type Manipulator and the Clip Type Passive Manipulator is developed to overcome low efficiency, and both of them are used in FMDS. The Scissors Type Manipulator is first type manipulator, and its shortcoming is also the problem of capacity. So the Clip Type Passive Manipulator is developed and applied in recent years.

## 2 The Clip Type Passive Manipulator

Rapid medicine refilling is the restrictive factor of FMDS. The medical logistics assistance manipulator is the key factor that influences the speed of the rapid medicine refilling. The shortcoming about the Manipulator of ROWA, Pallet Type manipulator and Scissors Type Manipulator is the capacity of supplementary medicine in one time, which structure is shown in the Figure 1a, 1b and 1c.

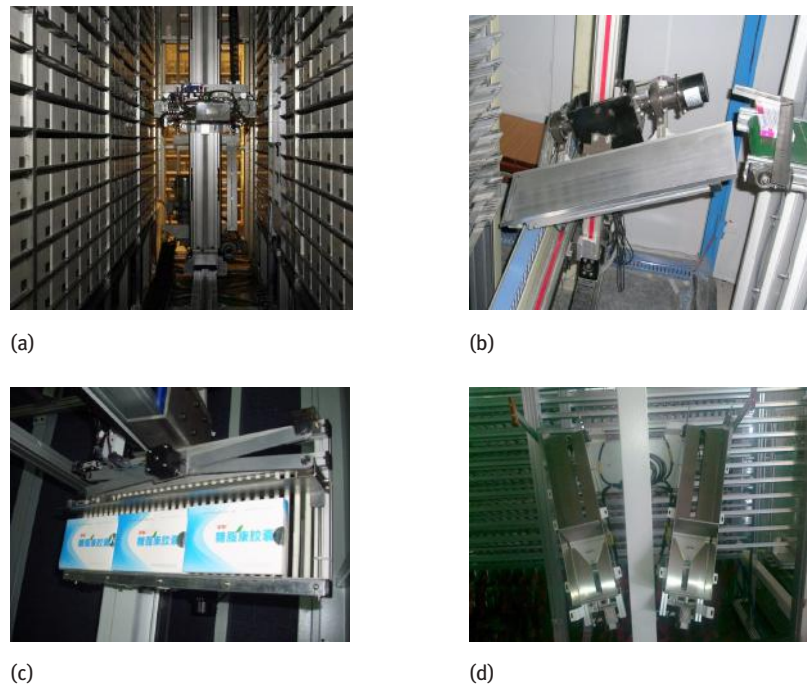


**Figure 1.** The Manipulator of ROWA (a), the Pallet Type Manipulator (b), the Scissors Type Manipulator (c), the Clip Type Passive Manipulator (d)

## 2.1 Cartesian coordinate robot

Through the widely research about the structure form, the movement performance, price performance ratio of the Cartesian coordinate robot, determine the drive and control method of plane positioning system. X, Y axis adopt servo motor driven synchronous belt transmission parts, through vertical and horizontal direction to complete the manipulator positioning, realize of the medicine refilling [13].

## 2.2 The key component of Clip Type Passive Manipulator module

In order to satisfy the multitudinous drug refilling, the system research and development the Clip Type Passive Manipulator module, which is shown in Figure 1(d). The core idea of this manipulator is to use the principle of gravity blanking, reduce the number of actuator, with a high performance price ratio.

Clip Type Passive Manipulator module including: positioning plate, limiting plate, supporting plate, chutes, lifting mechanism, stepper motor, etc.

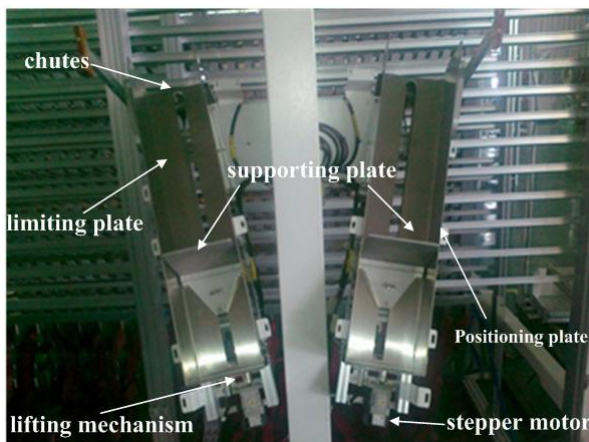


**Figure 2.** The Clip Type Passive Manipulator

The manipulator has two direction inclined angle, one ensure the medicine box location the in the direction of gravity, the other slide component force realize medicine decline. For positioning of different size kits is achieved by the tilt of the positioning plate. According to the types of drugs and the number of kits, stepper motor rotates to the right position, and the manipulator accepts a corresponding number of drugs. After the completion of the above steps, when the manipulator reach to the predetermined position, stepper motor rotated a certain angle according

to the kit height, synchronous belt drives the lifting plate rise a corresponding height. When the kit exceeds the front plate of the rack, it slides into the transition slot of the rack due to gravity, and then slide into the medicine storage groove of the storing cabinet. Stepper motor repeats the action until the lifting board finally finished out all of the medicine.

Clip Type Manipulator refilling the medicine is achieved by using a stepper motor driven the ball screw. Manipulator travel is short, starting and stopping frequently prone to vibration. The advantages of the ball screw are that the movement is stable, the precision of repeated positioning is high, and the inertia of starting is small, which is suitable for frequent start and stop. The ball screw of Clip Type Passive Manipulator is shown in Figure 3.

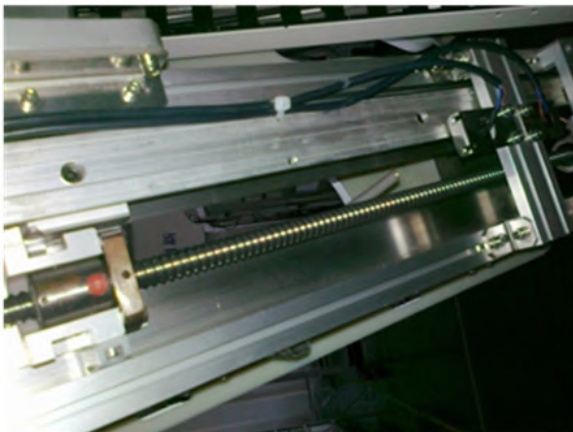


**Figure 3.** The ball screw of Clip Type Passive Manipulator

### 3 Research about the key components of Clip Type Manipulator

#### 3.1 Theoretical analysis of ball screw contact

Ball screw internal force can be applied to the Hertz contact theory analysis. On the basis of elastic mechanics, Hertz obtained the solution of the deformation and stress of two point contact cases in 1896, which is called Hertz contact stress. Hertz theory can be applied not only to the static elastic body, but also to the plastic deformation. Many of the collision parameters predicted by the Hertz theory were shown to be quite accurate in the later experiments [14].

Hertz theory is suitable for many kinds of shape of the contact bodies, surface coordinate formula is shown in (1), which contact point is original point.

$$\begin{aligned} Z_1 &= A_1 x_1^2 + B_1 y_1^2 + C_1 x_1 y_1 \\ Z_2 &= A_2 x_1^2 + B_2 y_1^2 + C_2 x_1 y_1 \end{aligned} \quad (1)$$

A suitable Cartesian coordinate system is shown in Figure 4. The  $Z$  axis is perpendicular to the tangent plane of the contact point and direction of the object is positive. The  $x_1y_1$  axis is in the tangent plane,  $x_1y_1$  can be removed by selecting the appropriate  $x_1y_1$  axis.

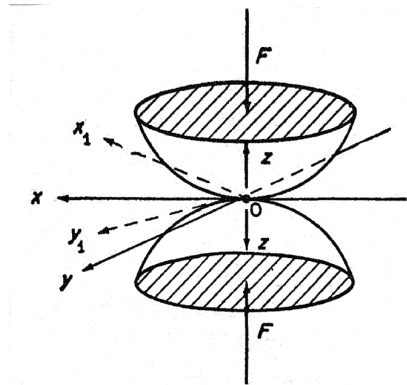


**Figure 4.** Contact state of two elastic bodies

The deformation of the two contact surfaces is parallel to the  $Z$  axis, and the formula is

$$\bar{d} = Z_1 + Z_2 = Ax_1^2 + By_1^2 \quad (2)$$

$A$  and  $B$  are the positive constant related to with contact body curvature radius,  $R_1$ ,  $R_1$  are the radius of curvature about contact body 1,  $R_2$  are the radius of curvature about contact body 2. The relationship between the radius of curvature of  $A$  and  $B$  is shown in the formula (3) and (4).

$$2(B + A) = \frac{1}{R_1} + \frac{1}{\bar{R}_1} + \frac{1}{R_2} + \frac{1}{\bar{R}_2}, \quad (3)$$

$$2(B - A) = \left[ \left( \frac{1}{R_1} - \frac{1}{\bar{R}_1} \right)^2 + \left( \frac{1}{R_2} - \frac{1}{\bar{R}_2} \right)^2 + 2 \left( \frac{1}{R_1} - \frac{1}{\bar{R}_1} \right) \left( \frac{1}{R_2} - \frac{1}{\bar{R}_2} \right) \cos 2\beta \right]^{\frac{1}{2}} \quad (4)$$

In the formula, the  $\beta$  angle is formed by two normal plane constrained by curvature  $1/R_1$  and  $1/R_2$ . Select the appropriate  $\theta$  angle can eliminate the  $\beta$  angle,  $\theta$  defined as

$$\cos \theta = \frac{B - A}{B + A} \quad (5)$$

$$2A \cos ec^2 \frac{1}{2} \theta = 2B \sec^2 \frac{1}{2} \theta = \frac{1}{R_1} + \frac{1}{\bar{R}_1} + \frac{1}{R_2} + \frac{1}{\bar{R}_2} \quad (6)$$

When the normal force F effects on the two objects along the Z axis, there will occur small deformation in the vicinity of the contact point and Form a small plane in the X-Y plane. The contact area and the separating surface can be distinguished by the formula (7) and (8).

$$w_1 + w_2 = \alpha - Ax^2 - By^2 \quad (7)$$

$$w_1 + w_2 > \alpha - Ax^2 - By^2 \quad (8)$$

$w_1$  and  $w_2$  express deformation of the two contact bodies in the Z axis,  $\alpha$  is the breakthrough volume, value is equal to  $w_1+w_2$  in the Z axis direction, also the max contact stress of part, all points of the two contact surfaces are deformed.

Comparing with contact area, the contact body can be regarded as semi-infinite, and the contact area is only a small part of the total area. The deformation w of the concentrated force acting on the semi-infinite body in the Z=0 plane is derived from the elastic deformation theory.

$$\begin{aligned} w|_{z=0} &= \frac{1-\mu^2}{\pi E} \iint \frac{pdx dy}{s} = \delta \iint \frac{pdx dy}{s} \\ \delta &= \frac{1-\mu^2}{\pi E} \end{aligned} \quad (9)$$

It only makes sense when the two objects in contact. Put the formula (9) into the formula (7) to get the formula.

$$\begin{aligned} w_1 + w_2 &= \alpha - Ax^2 - By^2 = \\ \left[ \frac{1-\mu_1^2}{\pi E_1} + \frac{1-\mu_2^2}{\pi E_2} \right] \iint \frac{pdx dy}{s} &= [\delta_1 + \delta_2] \iint \frac{pdx dy}{s} \end{aligned} \quad (10)$$

The two contact bodies can be calculated only if the following equilibrium conditions are satisfied, and the stress distribution and the stress distribution can be calculated:

- (1) The total force F is equal to the vertical reaction force provided by contact surface,  
 $F = \iint p dx dy$ .
- (2) The acceleration of deformation in each contact and contact area is 0.
- (3) Compared to the size of the contact surface, the deformation of the contact area can be very small.
- (4) Contact surface shear stress  $\tau_{xz}$ ,  $\tau_{yz}$  are 0, the normal force outside of contact area is 0.

The contact area and the contact stress can form an ellipsoid.

$$\frac{x^2}{a^2} + \frac{y^2}{b^2} + \frac{z^2}{c^2} = 1 \quad (11)$$

The total force acting on the two contact bodies is the mass of the ellipsoid.

$$F = \frac{4}{3}\pi abc\rho \quad (12)$$

$\rho$  is the density of the material ( $\text{kg}/\text{m}^3$ )

The formula for the stress distribution in the contact area is

$$p = \frac{3F}{2\pi ab} \sqrt{\left(1 - \frac{x^2}{a^2} - \frac{y^2}{b^2}\right)} \quad (13)$$

For the elliptic contact area, the stress of the geometric center is

$$p_m = \frac{3F}{2\pi ab} \quad (14)$$

The stress-strain formula of the two contact bodies is

$$F = k_h \alpha^{3/2} \quad (15)$$

In the formula,  $\alpha$  is the normal deformation,  $k_h$  is the Hertz contact stiffness, the value of which depends on the material properties and the geometry of the two contacts.

The formula for calculating the Hertz contact stiffness is

$$k_h = \frac{4}{3} \frac{q_k}{(\delta_1 + \delta_2) \sqrt{(A+B)}} \quad (16)$$

$$\delta_L = \sum \frac{1 - \mu_i}{\pi E_i} \quad i=1, 2 \quad (17)$$

The  $\mu$  is Poisson's ratio of two contact bodies,  $E$  is the elastic modulus of the contact bodies,  $\delta_L$  is equivalent elastic coefficient ( $\text{Mpa}\cdot\text{l}$ ) for two contact bodies of,  $A+B$  is half the sum principal curvature of two objects contact point.  $q_k$  is a function about  $A/B$  or  $\theta$ , including  $q_k$  and the  $A/B$  function can look-up table to obtain.

### 3.2 The optimization design of Special-purpose ball screw for Clip Type Passive Manipulator

Ball screw's main drawback is the limitation of speed, affecting the efficiency of manipulator. So it is necessary to optimize design the Clip Type Passive Manipulator module dedicated ball screw, in order to improve the speed of the linear motion of the ball screw, to adapt the manipulator medicine refilling speed.

The reverse curve is a key factor influence the properties of ball screw. Ball screw operates at high rotating speed, will causing the impact forces between the steel ball and return tube may generate high stresses and cause damage to the return tube after some significant service times [15]. Return tube quality directly affects the reverse curve

of ball screw that lead to low-frequency noise, vibration, temperature rise, the service life and the max feed rate. The end plug type return tube belongs to the fluid type, suitable for low noise, low temperature rise, high speed ball screw is shown in Figure 5.

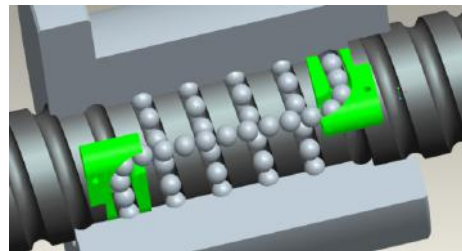


**Figure 5.** Ball screw internal structure

Ball in and out of the return tube is a process from loading to the unloading then loading again, during which the stress of the ball changes severe, so is the important to optimize the return tube. Due to the ball in the return tube is no preload, the ball forward movement is driven by the behind ball, lead to the collision between the balls, the friction and impact between the ball and the return tube and friction between the balls.

The force of the ball in the return tube is shown in Figure 6.  $F_a$  is the centripetal force,  $F_n$  is counterforce between return tube and ball,  $F_p$  is the driving force behind the ball,  $F_z$  is resistance in front of ball,  $F_u$  is ball friction,  $F_u$  is due to the centripetal force  $F_a$  and normal component of force before and after ball,  $F_{p1}$  is the driving force outside of the return tube,  $F_{z3}$  is the resistance outside of the return tube.  $R$  is the radius of the return tube curve,  $e$  is the offset distance between the ball and the return tube curve center line.

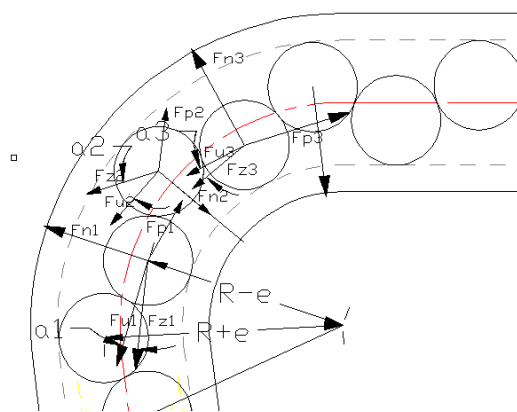


**Figure 6.** Force of the ball in the return tube

This paper innovative proposed the concept of driven resistance ratio, used to measure fluency that the ball through return tube [16]. The return tube ball screw is optimized by the optimization of the driven resistance ratio and the impact.

Definition of driven resistance ratio

$$\eta = \frac{F_{z3}}{F_{p1} \cos \alpha} \quad 0 \leq \eta \leq 1 \quad (18)$$

$F_{p1} \cos \alpha$  is the tangential force of Fp1, provides the driving force for the ball, greater than Fz3,  $\eta$  is driven resistance ratio.

$\eta$  is a variation function, and the driving efficiency can be optimized.

$$\max \{\eta\} \Rightarrow \max \left\{ \frac{F_{z3}}{F_{p1} \cos \alpha} \right\} \quad (19)$$

At the same time, the driven resistance ratio and radius of the return tube curve can be used as the objective function to be optimized.

$$\min \left[ \frac{1}{r'_1} + \frac{1}{r'_2} + \frac{1}{\eta} \right] \quad (20)$$

But it is difficult to determine the weighting factor of the driven resistance ratio and radius of the return tube curve in the function, so it is not distribution suitable weight factor in objective function. When the rotation speed of the screw is changed, the optimal value of the driven resistance ratio is also need to be recalculated.

The optimization objective can be simplified for reduce the impact force between a single ball and return tube, if a single ball can through the return tube fluency, it can be assumed all balls through the return tube will be smooth. To reduce the collision force between the ball and the return tube is need to increase the radius of the return tube curve. But this will also increase the length of the return tube curve, the number of balls in the return tube will increase, resulting in increased friction and resistance. In order to balance this contradiction, this paper uses the multi section arc transition curve, to optimize the design of the return tube.

The approximate shape of the return tube curve is shown in Figure 7. It consists of five segments, in keep return tube import and export position unchanged, by transforming the radius R1, R2, R3, arc angle  $\alpha_1, \alpha_2, \alpha_3$ , L1, L2 is the entry and exit at the two ends, and get optimal return tube curve.

The optimization objective is to choose the shortest length of the curve, and the design variables can be defined within a suitable range. Reducing the length of the curve can reduce the number of balls in the return tube, which can reduce the friction resistance, reduce the time of the ball that passes the return tube, reduces the collision and energy loss. It is need to increase the curve radius where the impact force is large, on the contrary decreasing curve radius.

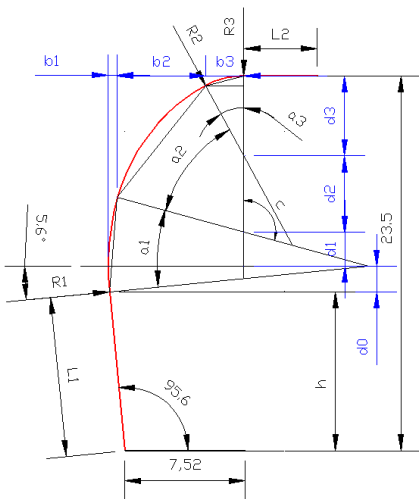


**Figure 7.** Return tube curve

### 3.3 Establishing optimization mathematical model

#### (1) Objective function

The optimization design criterion is limiting the arc radius and arc angle in reasonable range. The optimization objective is to achieve the optimization of the length of the return tube curve. The objective function of the optimization is,

$$\min L = L_1 + R_1\alpha_1 + R_2\alpha_2 + R_3\alpha_3 + L_2 \quad (21)$$

#### (2) Design variables

The design variables include the radius of the three arcs, which are expressed as  $R_1$ ,  $R_2$ ,  $R_3$ , the arc angles of three sections are expressed as  $\alpha_1$ ,  $\alpha_2$ ,  $\alpha_3$ .

#### (3) Constraint

The constraint conditions can be determined by the geometric relationships between the variables of the return tube curve, which guarantees that the ball enters the return tube with sufficient transition stage length, as shown in the formula.

$$\left\{ \begin{array}{l} h \geq 10 \\ R_1 > R_2 > R_3 \\ \alpha_1 + \alpha_2 + \alpha_3 = 95.6^\circ \\ d = d_0 + d_1 + d_2 + d_3 \leq 13.5 \\ L_1 \geq 0 \\ b = b_1 + b_2 + b_3 \\ L_1 = 23.5 - d \\ L_2 = 7.52 + L_1 \sin 5.6^\circ - b \geq 0 \end{array} \right. \quad (22)$$

Objective function and constraint conditions are both nonlinear functions, and the problem is summarized as a nonlinear programming problem with equality constraints and inequality constraints. According to the mathematical model established in the previous, the use nonlinear programming function 'fmincon' in the MATLAB optimization toolbox, programming the optimization procedure to run the optimization results.

### 3.4 Results and Analysis

Results after optimization as follow. The radius of the three section is  $R_1 = 16.2883$  mm,  $R_2 = 11.4018$  mm,  $R_3 = 5$  mm. The arc angles of the three sections arc are  $\alpha_1 = 0.3656$  rad,  $\alpha_2 = 0.8018$  rad,  $\alpha_3 = 0.5011$  rad. The total length of the curve was  $L = 27.6506$  mm. According to the obtained results we can draw the return tube curve Figure 8. The impact force before and after optimization are shown in Figure 9 and Figure 10.

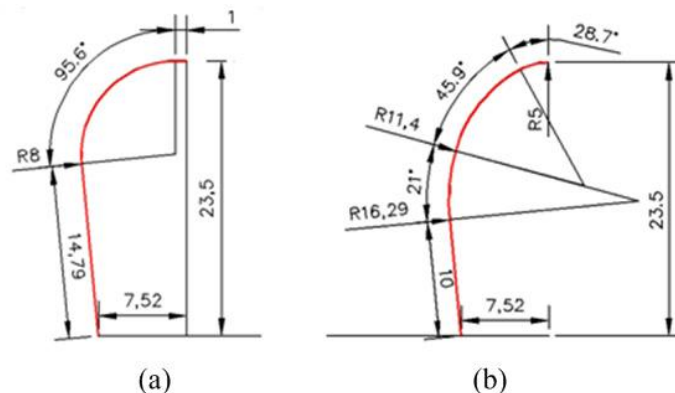


**Figure 8** Comparison of curves before and after optimization: (a) Curve before optimization; (b) Curve after optimization

**Table 1.** Performance comparison of the return tube

Return tube	Length of the curve	Pass time	Max impact force	Impact force range
Return tube before optimization	29.1383 mm	0.0065 s	378 N	120~215 N
Return tube after optimization	27.6506 mm	0.005 s	255 N	150~180 N
Performance improvement level	5%	23%	32.5%	64%

It can be known from the above table that the maximum impact force of the e return tube is reduced by 32.5%, and the limit movement speed can be increased about 17%. The Clip Type Passive Manipulator runs more fast, the medicine refilling velocity improved significantly, collision force fluctuations decreased, improve the service life of the ball screw in the manipulator.

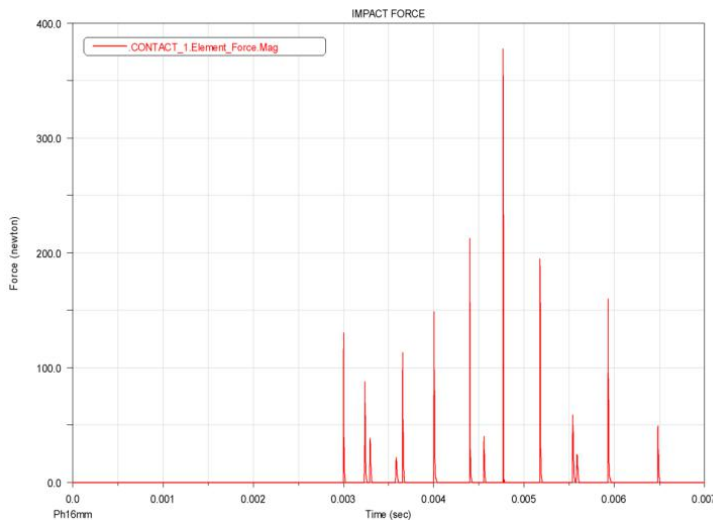


**Figure 9.** Impact force before optimization

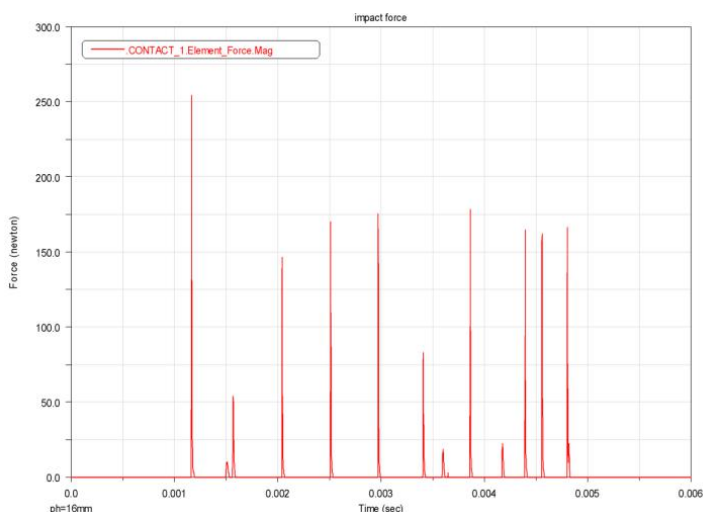


**Figure 10.** Impact force after optimization

### 3.5 Maintaining the Integrity of the Specifications

The template is used to format your paper and style the text. All margins, column widths, line spaces, and text fonts are prescribed; please do not alter them. You may note peculiarities. For example, the head margin in this template measures proportionately more than is customary. This measurement and others are deliberate, using specifications that anticipate your paper as one part of the entire proceedings, and not as an independent document. Please do not revise any of the current designations.

## 4 Conclusion

The Clip Type Passive Manipulator is a new type of modular manipulator which is used for Fast Medicine Dispensing System. It solves the problem of small capacity and low speed of the traditional manipulator, improves operating efficiency of manipulator. Manipulator limit movement speed can be increased about 17%. The position repeatability of the Manipulator meets requirements, refilling efficiency is high, system is stability and failure rate is low. The manipulator will be more useful to solve the key component shortcoming. The Clip Type Manipulator is suitable for using in the Fast Medicine Dispensing System.

## References

- [1] C.Q. Li, W. Wang, C. Yun, X. Zhu, J.B. Cao, and Y.H Zhang, The present situation and development of automatic pharmacy, *Robot Technique and Application*, 2007, pp. 27-32.
- [2] D.H. Huang, Y. Li, R.H. Chen, Research Report on application and development of medical service robot, *Development & Innovation of Machinery & Electrical Products*, vol. 27, no. 3, pp. 5-8, 2014.
- [3] B. H. Choi, H. R. Choi, A Semi-direct Drive Hand Exoskeleton Using Ultrasonic Motor international Workshop on Robot and Human Interaction Pisa, *Proceedings of the 2002 IEEE*, 1999, pp.52-66.
- [4] S. Hussain, S.Q. Xie, G.Y Liu, Robot assisted treadmill training: Mechanisms and training strategies, *Medical Engineering & Physics*, vol 33, pp.527-533, 2011.
- [5] W. Meng, Q. Liu, Z.D. Zhou, Q.S. Ai, B. Sheng, S.Q. Xie, Recent development of mechanisms and control strategies for robot-assisted lower limb rehabilitation, *Mechatronics*, April 2015.
- [6] P. Ballester, Y. Jain, K.R. Haylett, and R.F. Mccloy, Comparison of task performance of robotic camera holds EndoAssist and Aesop, *International Congress Series*, vol.2130, no. 1, pp.1100-1103, 2001.
- [7] T.C. Wei, H.J. Chung, A.T.L. Lin, K.K. Chen, Robot-assisted laparoscopic excision of a retroperitoneal paracaval tumor, *Journal of the Chinese Medical Association*, vol.76, no.12, pp.724-726, 2013.

- [8] L. Abramovici, C. Cartier, G. Rierre, R. Garrel, Robot-assisted transaxillary thyroidectomy: Surgical technique, European Annals of Otorhinolaryngology, *Head and Neck Diseases*, vol.32, no.3, pp. 153-156, 2015.
- [9] Y. Zhang, C.X. Sun, M. Li, Function design and implementation of medical service robot, *Application of Robot technology*, vol. 6, pp.36-39, 2011.
- [10] S.G. Tzafestas, 15 – Mobile Robots at Work, *Introduction to Mobile Robot Control*, pp.635-663, 2014.
- [11] H.L. Che, A simulation-based Genetic Algorithm approach for refilling process with Clip Type Passive Manipulator, *15th International Conference on Intelligent Systems Design and Applications (ISDA 2015)*, Morocco, 2015.
- [12] H. Jin, C. Yun, W. Wang, and D.J. Li, Application and research of the Clip Type Manipulator, *3rd IEEE/IFTOMM International Conference on Reconfigurable Mechanisms and Robots*, ReMAR 2015 Beijing, China.
- [13] H. Jin, C. Yun, and X.S. Gao, Application and research of the refilling path with Clip Type Manipulator, *2015 IEEE Conference on Robotics and Biomimetics*, 2015 Zhuhai, China.
- [14] W.Goldsmith, Imact: The Theory and Physical Behavior of Colliding Solids, 1964.
- [15] Hung J P, Shih-Shyn Wu J, Chiu J Y, Impact failure analysis of re-circulating mechanism in ball screw, *Engineering failure analysis*, vol. 11. no. 4, pp.561-573, 2004.
- [16] H.K. Jiang, X.C. Song, B.M. Li, W.C. Tang, J.S. Zhu, Optimal design of passage profile of a ball returner base on fluency of a ball screw mechanism, *Journal of vibration and shock*, vol. 31, no.2, 2012.

Qiu-wei HE\*, Xu YANG, Xiao-hui WU, Xing-tian QU, Ji ZHAO

## Research on Material Removal of Belt Polishing for Blade Complex Surface

**Abstract:** To improve the polishing precision of blade complex surface, the quantitative material removal method for belt polishing of blade complex is researched in this paper. The removal rate model for belt polishing of blade complex surface based on Preston equation is firstly established. Then, by analyzing the contact process between blade surface and contact wheel, the contact force model, relative velocity model as well as contact time model are established. The material removal depth is calculated by integrating the material removal rate within the contact time between the blade and the contact wheel. Relationships of material removal depth relative to contact force, feed rate, belt speed as well as workpiece curvature are acquired by simulation analysis. Finally, the material removal depth model is testified by experiments, and measurement error is analyzed. Theoretical analysis and experimental results show that the established model in this paper is correct, and we can design reasonably machining parameters and realize quantitative material removal of complex surface by applying it.

**Keywords:** material removal; modeling; simulation; belt polishing; blade complex surface

### 1 Introduction

As one of the important finishing processes of complex free-form surfaces, polishing has a crucial impact on surface quality and has been investigated for decades. In polishing of complex surfaces, such as turbine blade, there are strict dimensional accuracy requirements on the workpiece. Traditionally, the complex blade surfaces are polished manually. However, manual polishing is not only time and labor consuming but highly depends on labor's experience and technology. Recently, computer-controlled belt polishing has been introduced into precision manufacturing for its characteristics of flexibility, high-efficiency and labor liberation that make it very suitable for manufacturing workpiece with complex free-form surfaces [1-3]. However, the dimensional accuracy is prone hard to control as large amounts of factors contribute to the removal effect simultaneously, such as belt speed, in feed

---

\*Corresponding author: Qiu-wei HE, College of Mechanical Science and Engineering, Jilin University, Changchun, China, E-mail: heqw@jlu.edu.cn

Da-xian HAO, Chao YUN, Hui JIN, Gang WANG, School of Mechanical Engineering & Automation, Beihang University, No37, XueYuan Road, Beijing, 100191, China

rate, workpiece geometry, the belt material, the elasticity of contact wheel, grit size, grain distance and so on.

Over the years, many academics made a systematically theoretical study on computer-controlled belt polishing process. The calculation of contact force between the elastic contact wheel and the rigid complex surfaces is one of the key works to analyze this process. The signorini method, which focuses on the contact problem between an elastic body and a rigid body, has been used to solve the deformation of the elastic contact wheel. Blum and Suttmeier worked out a FEM model to solve this signorini contact problem and used an optimized mesh discretization strategy to enhance the efficiency and accuracy of the FEM model [4,5]. X. Ren proposed energy minimization principle to further help solving the signorini contact problem [6]. However, the modeling process is too computationally expensive since a small mesh size is required to ensure the calculating precision. Zhang developed a new model using support vector regression method as the learning machine to speed the calculation [7], but it is also time-consuming in the training phase and not suitable in real-time applications. S.H. Wu developed a super position force model based on Hertz method to approximately calculate pressure distribution in the workpiece-wheel contact area [8], it was proven not only time saving but also of high accuracy, for which the model will be used in this paper. Since the local removals are not homogeneously distributed in the whole contact area due to the complex geometry of workpiece [8], any changes of workpiece curvature would influence the material removal accuracy, so the influence of workpiece curvature on material removal is also studied in this paper.

In this paper, a quantitative material removal depth model is implemented. This model can be used to achieve the quantitative material removal with little calculation work. The rest of this paper is organized as follows. In Section II, the material removal rate model and the material removal deep model are established. In Section III, simulation and analysis to model are done. The experiments and error analysis are described in Section IV, followed by conclusions in Section V.

## 2 Material Removal Modeling

### 2.1 Material Removal Rate Model

Figure 1 is the schematic diagram of belt polishing process. For surfaces with non-uniform curvature, the contact state between the contact wheel and the blade surfaces varies according to the changes of surface curvature. The distribution of contact force and the relative velocity in different contact area are different. So it is meaningful to select appropriate process parameters based on the shape characteristics of blade surface to achieve quantitative removal. The traditional model of material removal rate is based on Preston equation [9,10].

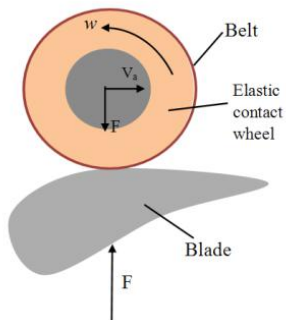


**Figure 1.** The diagram of belt polishing process.

$$d_h = K_p P_c V_s d_t \quad (1)$$

In the type:  $K_p$  is the comprehensive influence coefficient decided by experiments,  $P_c$  is the contact force,  $V_s$  is the relative velocity, and  $d_h$  is the material removal depth during contact time  $d_t$ .

Many factors influence the material removal rate simultaneously in belt polishing process. These factors include polishing parameters such as belt speed, feed rate and the contact force, and tool features such as the tension of the belt, grit size, grit density, belt wear rate and contact wheel hardness. In (1), the impact of all the factors, except the contact force and the relative velocity, attribute to an integrated constant  $K_p$ , which can be decided by experiments. Two most important factors on material removal rate, contact force and relative velocity, which are controllable, are modeled in next session based on the characteristics of blade surface and features of belt polishing tools.

## 2.2 Contact Force Model of Polishing Zone

According to (1), the force distribution in contact area is one of the most important factors for calculation of material removal rate. It can be calculated by FEA (finite element analysis) method precisely, but the method is time-consuming. Compared to FEA method, the Hertz method has been proven computationally easy and can effectively estimate the contact area and calculate the pressure distribution in contact area [8]. For the purpose of analyzing force distribution problem in the belt-polishing process of blade surfaces with Hertz method, the blade-wheel contact can be approximated by the contact between two cylinders based on the following facts [11]:

1. The polishing path is well planned so that when the workpiece-wheel contact occurs during the polishing process, the workpiece surface has minimum principal curvature along the axial direction of the contact wheel.

2. The deformation that occurs during the workpiece-wheel contact is much less than the radius of the contact wheel and the local radius of the workpiece.

The contact status between contact wheel and blade is shown in Figure 2. Assuming the blade is a rigid body that has no deformation while the contact wheel is of elasticity and deforms when the contact happens.

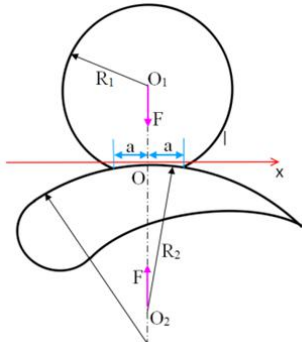


**Figure 2.** Contact status between contact wheel and workpiece.

For complex blade surfaces, it is also assumed that the contact area between the contact wheel and the blade surface is a line contact [12]. The contact force distribution between the contact wheel and workpiece can be calculated from (2) by applying Hertz method.

$$P_{Hertz}(x) = \begin{cases} \frac{2P}{\pi a^2} (a^2 - x^2)^{1/2}, & |x| < a \\ 0, & |x| \geq a \end{cases}. \quad (2)$$

$$\frac{1}{R_*} = \frac{1}{R_1} + \frac{1}{R_2}, \frac{1}{E_*} = \frac{1-v_1^2}{E_1} + \frac{1-v_2^2}{E_2}, a^2 = \frac{4PR_*}{\pi E_*}. \quad (3)$$

In the type:  $P$  is the contact pressure which can be further formulated as  $F/W$ , ( $F$  is the normal force;  $W$  is the thickness of contact wheel).  $R_1$  and  $R_2$  are the radiiuses of the contact wheel and the local radius of workpiece respectively,  $R_*$  is the equivalent radius.  $v_1$  and  $v_2$  are the Poisson's ratios of the contact wheel and the workpiece respectively.  $E_1$  and  $E_2$  are the Young's modulus of the contact wheel and the workpiece respectively,  $E_*$  is the equivalent Young's modulus.  $a$  is half of the width of the contact area.  $P_{Hertz}(x)$  is the pressure at the point with an  $x$  coordinate of  $x$ .

We can get the force distribution of the contact zone by using Hertz model when  $F$ ,  $R_1$ ,  $R_2$ ,  $E_1$ ,  $E_2$ ,  $v_1$ ,  $v_2$  and  $W$  are given. The given values are:  $F=5, 10, 15\text{N}$ ,  $R_1=50\text{mm}$ ,  $R_2=25.2, 35, 55\text{mm}$ ,  $E_1=2.18\text{Mpa}$ ,  $E_2=210\times 10^3\text{Mpa}$ . The  $H_{ertz}$  force distribution of polishing contact zone is shown in Figure 3.

Figure 3a shows that when the radius of workpiece is constant, the larger the normal force of contact wheel is, the greater the force distribution of contact zone is. Figure 3b shows that when the normal force of contact zone is constant, the greater the radius of workpiece is, the less the force distribution of contact zone in the middle is, while the greater the force distribution of contact zone in the edge is.

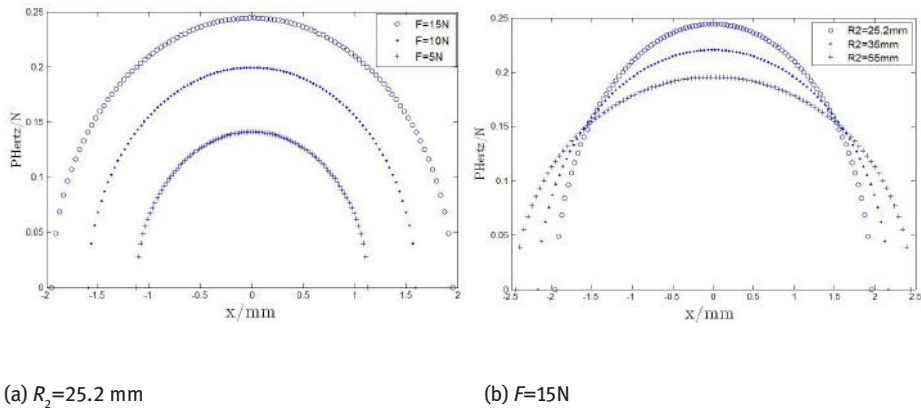


**Figure 3.** The diagram of Hertz force distribution of polishing contact zone.

### 2.3 Relative Velocity Model of Polishing Zone

The relative velocity which is along the tangential direction of contact point, is another important factor that affects the material removal rate greatly. As shown in Figure 4, the contact wheel moves along the polishing trajectory. The velocity of the contact wheel for its self-rotation on a point with coordinate of  $x$  is  $V_m$ , the feed rate of the contact wheel along the polishing trajectory is  $V_a$ , the rotational angular velocity of the contact wheel is  $w$ . So the relative velocity  $V_s$  along tangential direction between the contact wheel and the workpiece can be calculated with (4).

$$V_s = V_m \cos(\theta_1 + \theta_2) + V_a \cos \theta_2. \quad (4)$$

In Figure 4,  $\delta$  is the maximum deformation of the contact wheel [8], it can be calculated by (5).

$$\delta = P \frac{1 - v_1^2}{\pi \cdot E_1} [2 \ln(4R_1/a) - 1]. \quad (5)$$

According to (4) and Figure 4, we can get the (6).

$$V_s = w \cdot \frac{\left\{ R_1 + R_2 - \sqrt{R_2^2 - x^2} - P \frac{1 - v_1^2}{\pi \cdot E_1} [2 \ln(4R_1/a) - 1] \right\} \cdot \sqrt{R_2^2 - x^2} - x^2}{R_2} + \frac{V_a \sqrt{R_2^2 - x^2}}{R_2}. \quad (6)$$

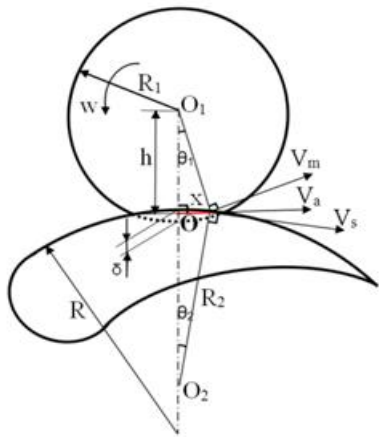
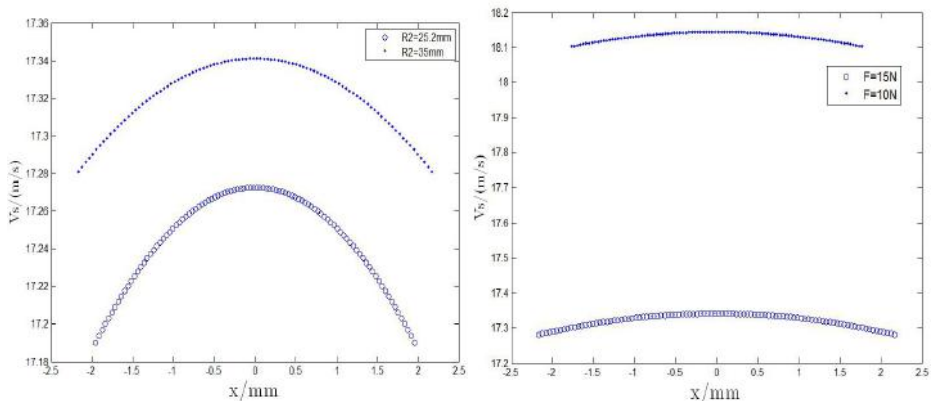


**Figure 4.** The distribution of relative velocity.

We can get the distribution of the relative velocity  $V_s$  by using (6) when polishing parameters  $w$  and  $V_a$  are given, while parameters mentioned above are constant. The given values are:  $w=400\text{rad/s}$ ,  $V_a=0.02\text{m/s}$ ,  $F=15, 10\text{N}$ ,  $R_2=25.2, 35\text{mm}$ . The distribution of the relative velocity of polishing contact zone is shown in Figure 5.



(a)  $F=15\text{N}$

(b)  $R_2=35\text{mm}$

**Figure 5.** The diagram of the distribution of relative velocity.

**Material Removal Depth Model** The material removal rate model is firstly built by integrating (2) and (6) into (1).

$$\frac{dh}{dt} = K_P \cdot \frac{2P}{\pi \cdot a^2} (a^2 - x^2)^{\frac{1}{2}} \cdot \left\{ w \frac{\left\{ R_1 + R_2 - \sqrt{R_2^2 - x^2} - P \frac{1-v_1^2}{\pi \cdot E_1} [2 \ln(4R_1/a) - 1] \right\} \sqrt{R_2^2 - x^2} - x^2}{R_2} \right\} + \frac{V_a \sqrt{R_2^2 - x^2}}{R_2}. \quad (7)$$

To obtain the contact time between the blade and the contact wheel, the polishing process should be analyzed. As is shown in Figure 6, in the process of polishing the blade surface, the contact between the contact wheel and blade is approximately linear. When the contact occurs in normal direction of the point  $i-m$  between the contact wheel and blade, the point  $i$  on the blade begin to contact with the contact wheel and its polishing begins too. The polishing of point  $i$  is over as the contact occurs in normal direction of the point  $i+m$ . Therefore, the material removal depth of point  $i$  is the integration of its material removal rate from the time of  $i-m$  ( $t_1$ ) to  $i+m$  ( $t_2$ ), as shown in (8).

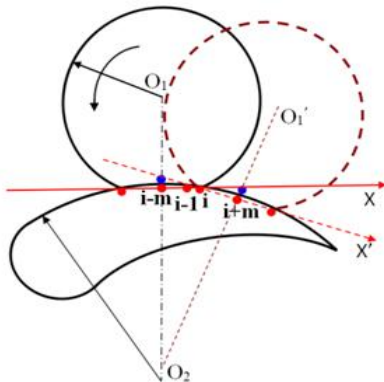


**Figure 6.** Polishing process of point  $i$ .

$$h(\rho) = \int_{t_1}^{t_2} K_P \frac{2P}{\pi \cdot a^2} (a^2 - x^2)^{\frac{1}{2}} \cdot \left\{ w \frac{\left\{ R_1 + R_2 - \sqrt{R_2^2 - x^2} - P \frac{1-v_1^2}{\pi \cdot E_1} [2 \ln(4R_1/a) - 1] \right\} \sqrt{R_2^2 - x^2} - x^2}{R_2} \right\} d_t. \quad (8)$$

It can be calculated that the arc from i-m to i+m is  $2R_2 \arcsin \frac{a}{R_2}$ , so the corresponding time is  $\frac{2R_2 \arcsin \frac{a}{R_2}}{V_a}$ . In addition, in the polishing process, the relationship between the coordinate of the point i and time can be presented with (9).

$$|x| = R_2 \sin(\arcsin \frac{a}{R_2} - \frac{V_a t}{R_2}). \quad (9)$$

Combining (9) to (8) and integrating (8) at  $(0, \frac{2R_2 \arcsin \frac{a}{R_2}}{V_a})$ , the material removal depth of point i can be calculated.

### 3 Simulation Analysis

The material removal depth model is simulated to forecast the quantitative relationship between the polishing parameters and the material removal depth. The workpiece material is Q235 steel with elastic modulus  $E_2$  of 210Gpa and poisson ratio  $\nu_2$  of 0.3 while the contact wheel is rubber wheel with elastic modulus  $E_1$  of 2.18N/mm<sup>2</sup> and poisson ratio  $\nu_1$  of 0.48.  $K_p$  is 0.09 that is introduced from X. Ren [6]. The true value of  $K_p$  can be defined by (10) to apply to the belt polishing of blade surface. The radiiuses of contact wheel and workpiece are  $R_1$  and  $R_2$  respectively.

$$\frac{h_{\text{experiment}}}{h_{\text{simulation}}} = \frac{K_{p\text{blade}}}{0.09}. \quad (10)$$

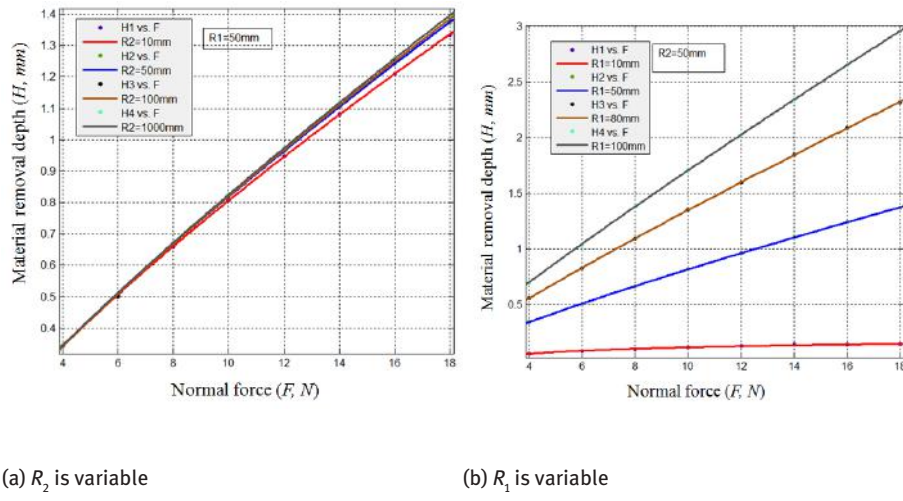
There are three unknown polishing parameters in the material removal model that can be controlled in actual polishing process, include the contact force, feed rate and belt speed. To clearly show their influence on material removal depth, simulations were developed to study the relationships between them.

Distribution of the contact force in contact area is a major factor that influences the removal depth, but it is hardly measured in real-time process. However, it can be expressed by the normal force  $F$  and their relationship has been discussed in section II. In Figure 7a, we chose  $R_1$  is 50mm and it is unchangeable,  $R_2$  changed from 10mm to 1000mm. It can be seen from Figure 7a that the material removal increase sharply with the increasing of normal force  $F$ , but it increases slightly with the increasing of  $R_2$ .

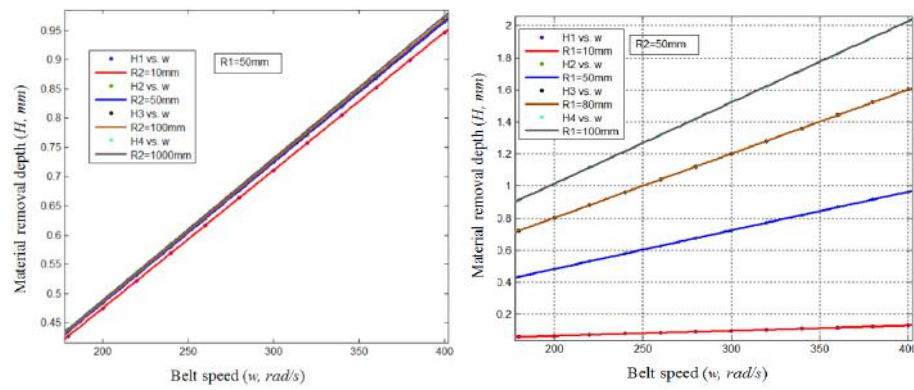
For the required removal depth, it is able to select proper  $F$  based on the curvature of blade to achieve quantitative removal. In Figure 7b, the blade curvature  $R_2$  is stable while  $R_1$  changes from 10mm to 100mm. It can be seen that the removal depth increase largely with the increasing of  $R_1$ . With this simulation, the appropriate contact wheel can be chosen according to the actual processing requirements.

The relative velocity  $V_s$  is another major factor which impacts the removal depth. It is composed of two parts: feed rate  $V_a$  and belt speed  $V_m$ .

Figure 7 and Figure 8 show that the material removal depth increases with the increasing of normal force  $F$  and belt speed  $V_m$ . This is because with the increasing of normal force  $F$ , the material removal rate increases. Similarly, with the increasing of belt speed  $V_m$ , the grinding grain number per unit time in polishing, so the removal rate increases.

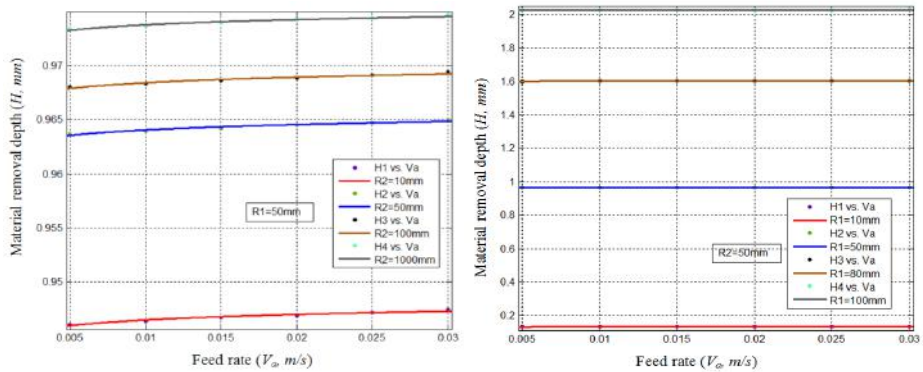


**Figure 7.** The relationship between normal force and the material removal depth.



**Figure 8.** The relationship between belt speed and the material removal depth.

Figure 9 shows that the feed rate  $V_a$  has little impact on the material removal depth. This is because in abrasive belt polishing, the workpiece feed rate is far less than the belt speed.

(a)  $R_2$  is variable(b)  $R_1$  is variable**Figure 9.** The relationship between feed rate and the material removal depth.

## 4 Experiments of Material Removal Depth

The material removal depth model of belt polishing is testified by experiments. The material removal depth is obtained by adjusting machining parameters which are the normal force  $F$ , the belt relative velocity  $V_s$  and the feed rate  $V_a$ . When a parameter is adjusted, other two parameters remain constant. When theoretical value is calculated by using (8), the comprehensive influence coefficient  $K_p$  is set as 1. Then  $K_p$  is revised by contrast and analysis between the measurement value and theoretical value. The revision equation is shown in (11).

$$\frac{H_{\text{measure}}}{H_{\text{theory}}} = \frac{K_p}{1}. \quad (11)$$

Error of revised theoretical value and measurement can be calculated as shown in (12).

$$e = \sum_n \left( \frac{|H_{\text{measure}} - H_{\text{theory}}|}{H_{\text{measure}}} \right) \times 100\% / n. \quad (12)$$

Where  $n$  is measurement times in each group. Here we set  $n$  as 30.

The machine tool used in the experiment is an adaptive grinding machine which is developed by the research group, as shown in Figure 10. We use disk force sensor as force measuring device. The force sensor is arranged on the lower part of the work piece, and is connected with the computer. When the tool head is pressed down, as the downward displacement increases, the force of the work piece increases, the force of the sensor increases, and the force of the sensor is displayed on the computer software. This force is the normal force of the workpiece during the machining process. The depth measuring device is Kean super depth VHK-900 optical microscope. The experiment selected medium-granular belt, which is P120 alumina. We use closed grinding patterns and lateral row cutting path.

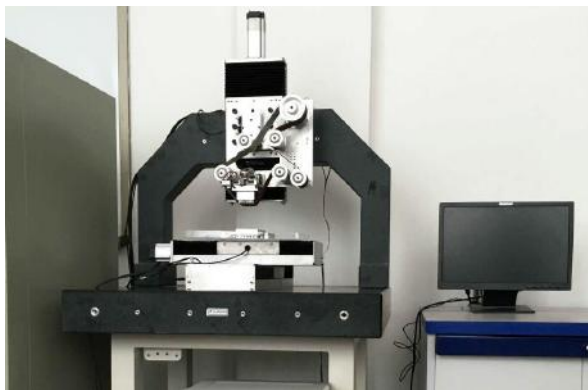


**Figure 10.** Adaptive grinding machine for complex surface.

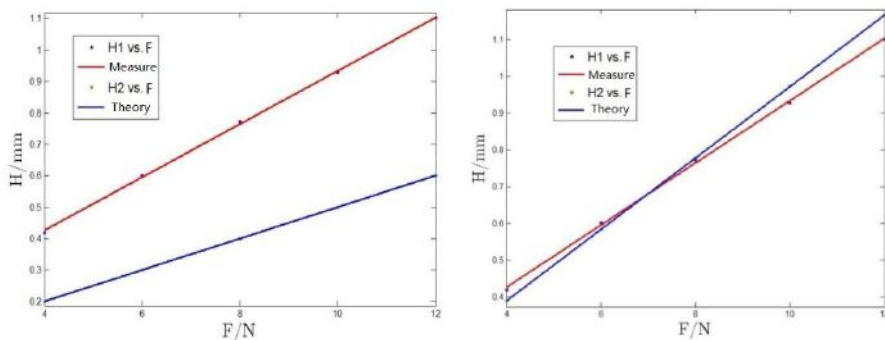
#### 4.1 Effect of Normal Force on Material Removal Depth

In the experiment, the workpiece is polished by increasing gradually the normal force  $F$  of the head of tool. Parameters are set as:  $V_s=0.25\text{m/s}$ ,  $V_a=0.1\text{mm/s}$ . Theoretical value and experimental value of material removal depth with different normal force is shown in Figure 11a.

According to (11),  $KP$  can be revised as 1.5290. Effect of the normal force  $F$  on the material removal depth which is calculated according to revised  $KP$  is shown in Figure 11b.

According to (12), we can get:  $e=4.172\%$ .

The error between the measured value and the theoretical value is 4.172%, which is got by (2).



(a)  $K_p=1$

(b)  $K_p=1.5290$

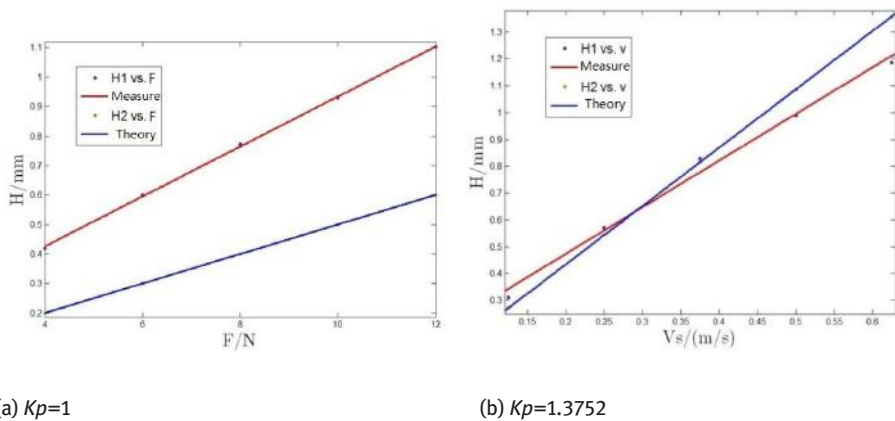
**Figure 11.** Theoretical value and experimental value of material removal depth with different normal force.

#### 4.2 Effect of Relative Velocity On Material Removal Depth

In the experiment, the relative velocity  $V_s$  is increased by increasing gradually the rotate speed of driving motor. Parameters are set as:  $F=8N$ ,  $V_a = 0.1mm/s$ . Theoretical value and experimental value of material removal depth  $H$  with different relative velocity  $V_s$  is shown in Figure 12a.

According to (11),  $K_P$  can be revised as 1.3572. Effect of the relative velocity  $V_s$  on the material removal depth which is calculated according to revised is shown in Figure 12b.

According to (12), we can get:  $e=8.72\%$ .



(a)  $K_p=1$

(b)  $K_p=1.3752$

**Figure 12.** Theoretical value and experimental value of material removal depth with different relative velocity.

#### 4.3 Effect of Feed Rate on Material Removal Depth

In the experiment, the workpiece is machined by increasing gradually the feed rate of the contact wheel along the polishing trajectory  $V_a$ . Parameters are set as:  $F=8N$ ,  $V_s=0.25m/s$ . Theoretical value and experimental value of material removal depth with different normal force is shown in Figure 13a.

According to (11),  $K_P$  can be revised as 1.3728. Effect of the feed rate  $V_a$  on the material removal depth which is calculated according to revised is shown in Figure 13b.

According to (12), we can get:  $e=2.32\%$ .

By comparing Figure 11, 12 and 13 to Figure 7, 8 and 9, we can see that the influence trend of main parameters to material removal depth  $H$  in experiments and simulation are accordance, which shows that established theoretical material removal depth model is correct.

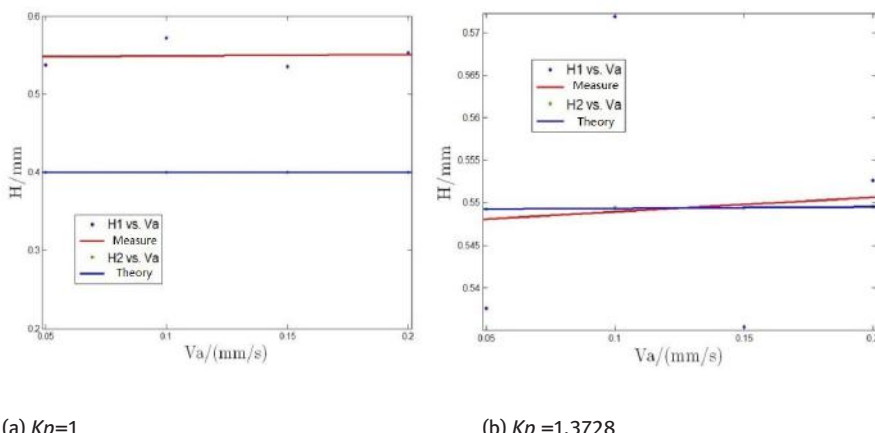


**Figure 13.** Theoretical value and experimental value of material removal depth with different feed rate.

And we find that  $KP$  is approximated in three experiments, so we can calculate average value of  $KP$  as comprehensive influence coefficient.

#### 4.4 Error Analysis

##### 1) Accuracy error of machine tool

There are some errors in the machine tool used in the experiment, which include the error of the machine tool slide guide and the transmission error of the machine tool. The flatness error of the slide guide has certain influence on the machining precision. The transmission errors that exist in the slide guide feed motion process lead to the change of machining parameters, thus the machining error is produced.

##### 2) Belt wear

In the experiment, abrasive grains increasing with time gradually fall off, which lead to the decline of grinding ability, reduce the removal amount with same conditions. It produces a certain error to the removal result.

##### 3) Machine tool fixture error

In the direction of workpiece longitudinal stress, workpiece fixture is located by bolts which are on the both sides of fixture, which lead to greater friction to fixture. When the tangential force increases, workpiece fixture will have tiny movement, which offsets parameters change trend, and has a certain impact on the final machining precision.

#### *4) Force sensor error*

The experiment depends on the force sensor installed at the bottom of the workpiece to realize the control of the normal force of the workpiece. Due to the operation of the staff and the vibration of the machine tool, the feedback value of the force sensor has a certain range of fluctuations, which has a certain impact on the final processing results.

#### *5) Measurement error*

After the workpiece is processed, the depth of the material is measured by optical microscope VHK-900. Measurement results are greatly affected by human factors. When the processing department 3D molding is made, operators will adjust the stage, the adjustment of the speed will result in a certain impact on the measurement results.

## 5 Conclusion

A quantitative material removal depth model that focuses on belt polishing of complex blade surfaces is established in this paper, and the relationship between the polishing parameters and material removal depth is established.

Through simulation to this model, it is testified that material removal with different curvature of blade complex surface is changeable when other machining parameters are invariable, and the contact force and belt speed have a great impact on removal while the feed rate of the wheel is of little influence, so that they can be combined properly to achieve precious polishing. It can also be deduced from the simulation that the smaller contact wheel can achieve a stable polishing, which is beneficial to realize precision manufacturing. Through experiments, it is testified that the model established is correct, and we can design reasonably machining parameters and realize quantitative material removal of complex surface by applying it.

**Acknowledgement:** This work was financially supported by the National Nature Science Foundation of China (Grant No. 51135006).

## References

- [1] X. Chen, Z. Gong, H. Huang, L. Zhou, S. S. Ge, and Q. Zhu, Smart robotic system for 3D profile turbine vane airfoil repair, *IntConflntAssocIndAutom*, vol. 21, pp. 275–283, 1999.
- [2] H. Huang, L. Zhou, X. Chen, and Z. Gong, Smart robotic system for 3D profile turbine vane airfoil repair, *Int J AdvManufTechnol*, vol. 21, pp. 275–283, 2003.
- [3] Y. Sun, Development of a unified flexible grinding process, Ph.D. Thesis, University of Connecticut, 2004.
- [4] H. Blum and F.-T. Suttmeier, An adaptive finite element discretization for a simplified signorini problem, *Calcolo*, vol. 37 pp. 65–77, 2000.

- [5] F.-T. Suttmeier, Error analysis for finite element solutions of variational inequalities, Ph.D. Thesis. Dortmund University, 2001.
- [6] X. Ren, M. Cabaravdic, X. Zhang, and B. Kuhlenkotter, A local process model for simulation of robotic belt grinding, *Int J Mach Tools Manuf*, vol. 47, pp.962–970, 2007.
- [7] X. Zhang, B. Kuhlenkotter, and K. Kneupner. An efficient method for solving the signorini problem in the simulation of free-form surfaces produced by belt grinding, *Int J MachTools Manuf*, vol. 45, pp. 641–648, 2005.
- [8] S. H. Wu, K. Kazerounian, Z. X. Gan, and Y. Q. Sun, A material removal model for robotic belt grinding process, *Machining Science and Technology*, vol. 18, pp.15–30, 2014.
- [9] F. W. Prestom, The theory and design of plate glass finishing machines, *Journal of the SOC. of Glass Technology*. Vol.11, pp. 214–256, 1927.
- [10] M. Y. Yang and H.C. Lee, Local material removal mechanism considering curvature effect in the polishing process of the small aspherical lens die, *Journal of Materials Processing Technology*, vol. 116, pp. 298–304, 2001.
- [11] S. H. Wu, K. Kazerounian, Z. X. Gan, and Y. Q. Sun, A simulation platform for optimal selection of robotic belt grinding system parameters, *Int J AdvManufTechnol*, vol. 64, pp. 447–458, 2013.
- [12] B. Wang, C. Q. Sun, J. T. Liu, The track research on NC belt grinding of turbine blade, *Journal of Shenyang Institute of Engineering (Natural Science)*, vol. 10, pp. 88–91, 2014.

Chao LI\*, Chu-qing CAO, Yun-feng GAO

## Visual Servoing based object pick and place manipulation system

**Abstract:** Object pick and place manipulation is essential both in the industrial and service robot field. In this work, we proposed a whole scheme utilizing eye-in-hand visual servoing for object pick and place manipulation system. The proposed paper makes the following three contributions over existing research, 1) a feasible scheme of object pick and place manipulation system is proposed in this work. 2) An efficient structured edge detector is used for contour extraction and object detection. 3) We use the feedback of force sensor to check whether the pick operation is successful.

**Keywords:** visual servoing; pick and place; structured edge detector; force feedback; eye-in-hand

### 1 Introduction

Robotic pick and place automation accelerates the procedure of picking workpieces up and placing them in new locations, which increasing production rates [1,2]. Traditional industrial manipulators that able to perform such operations often need to be programmed offline, and the workpieces are placed in the fixed location. Utilizing machine vision and computer vision to enhance the flexibility is critical to improve industrial profitability. Visual servoing is an approach to control the motion of a robot by visual feedback, involving many cutting-edge areas, such as computer vision, robotics, and control theory [3-5]. Integrating visual servo control system will enable better cooperation between humans and robots, which may enhance the man-machine collaboration. Numerous schemes have been proposed, which can be grouped into position-based methods and image-based methods. The image-based scheme is considered the most effective due to its simplicity of implementation [6-8].

To demonstrate the validity of the proposed unified dynamic control strategy, experiments were implemented by using a Baxter robot [9]. Baxter Research Robot is a humanoid robot platform with two 7-axis arms, integrated cameras, sonar, torque sensors, and direct programming access via a standard ROS interface [10]. Studies

---

\*Corresponding author: Chao LI, Forward-looking Technology R&D Center, HIT Wuhu Robot Technology Research Institute, Wuhu, China, E-mail: cynthia0217@163.com

Chu-qing CAO, Forward-looking Technology R&D Center, HIT Wuhu Robot Technology Research Institute, Wuhu, China

Yun-feng GAO, Department of Mechanical Engineering, School of Mechatronics Engineering, HIT, Harbin, China

on Baxter Research Robot cover human-robot interaction, collaborative robotics, planning, manipulation, control and perception in all applications.

This paper utilize the image-based visual servo system to assist the object pick and place manipulations. This work makes the following three contributions over existing research, 1) a feasible scheme of object pick and place manipulation system is proposed in this work. 2) An efficient structured edge detector is used for contour extraction and object detection, 3) we use the feedback of force sensor to check whether the pick operation is successful. The remainder of this paper is organized as follows. Section 2 detailed the whole object pick-and-place manipulation framework. In Section 3, edge detection results of two algorithms are illustrated. The conclusion of this work is drawn in Section 4.

## 2 The proposed pick and place manipulation system

Figure 1 describes the framework of visual servo system. Visual servo system usually consists of the visual system, control strategy and the robot system. Through image acquisition and visual processing, the visual system obtains appropriate visual feedback. Then the controller gains control input for robot. In specific applications, implementation of the visual servo system strategy needs to be designed according to practical task demand.

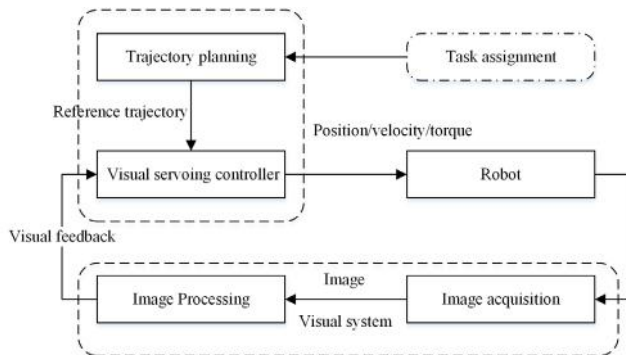


**Figure 1.** Framework of visual servo control system

The flowchart of object pick-and-place manipulation system is illustrated in Figure 2. To place scattered golf balls from the table into a box with separate compartments which we called ball tray. After image are obtained with eye-in-hand camera, image processing and detection algorithms are used for ball tray detection. Edge detection operator and Hough circle methods and visual servoing are employed to detect and locate balls on the table. And then basic planning is used to choose a ball and plan

a grip. Finally, an inverse kinematic solution of 7-DOF robot is made to conduct path planning, motion generation and control. Finally, force feedback is employed to check if the ball is successfully grabbed until there is no ball found outside the ball tray.

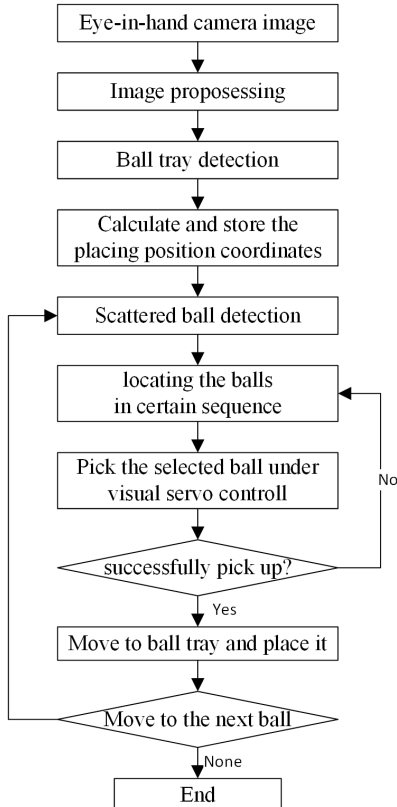


**Figure 2.** The flowchart of object pick-and-place manipulation system

### 3 Details of proposed system

#### 3.1 Camera Calibration

In the process of realizing the pick and place task, the positions of the balls and ball tray must be obtained with sufficient accuracy. With the range sensor integrated on Baxter arm, the distance of the arm to the table can be easily obtained. Combined with hand image acquired from hand camera, the object's position relative to robot can be determined. The calibration board was placed at varying distances from a camera and

images analyzed to find the camera calibration factor. The camera calibration factor is calculated as 2.5mm per pixel at 1 meter.

### 3.2 Coordinate frame transformation

The coordinate transformation of eye-in-hand visual system is achieved from the image plane to the robot reference coordinate frame [11]. We assume all arm movements are performed with Baxter's arm pointing vertically down at the table, which simplifies the coordinates transformation.

With robot's arm pose, the camera calibration factor and the height above the table pixel values can be converted to Baxter coordinates using the following formula:

$$B = (P_p - P_c) * cc * d + Pose_B + O_g \quad (1)$$

where  $B$  represents the Baxter coordinates,  $P_p$  is the pixel coordinates, and  $P_c$  are the center pixel coordinates,  $Pose_B$  represents the Baxter's pose, and  $O_g$  is the gripper offset,  $cc$  is the camera calibration factor, and  $d$  describes the distance from the table, which can be obtained with the infra-red range sensor on Baxter's wrist.

### 3.3 Locating the Segmented Tray in the workspace

The robot carries out pick and place task under unstructured environment, which is sensitive to illumination and shadow. Edge extraction of ball tray is the prerequisite for locating. Canny edge detector [12] is proved to be the optimal edge detector due to good localization and detection results, however it has some drawbacks. More false edges are detected caused by using Gaussian filtering and not adaptive in thresholding. Canny operator use two thresholds, and high and low threshold values need to be manually adjusted with many experiments. Recently Dollar and Zitnick [13] take advantages of the structure present in local image patches to learn both an accurate and computationally efficient edge detector. This novel structured edge (SE) detector achieves high-quality results while being orders of magnitude faster than most competing state-of-the-art methods. In the proposed scheme, we utilize SE detector to find the ball tray. As the tray is the largest bounded region if the bounded regions can be isolated and the largest area will be extracted. The gripper fingers obscure part of the tray. To find the bounded regions the outer region of the edge image is flood filled with white pixels and the areas of the remaining bounded regions calculated. All small areas and all but the largest bounded region are flooded with white pixels. If there is a large bounded area left it is assumed to represent the segmented tray. If there is no bounded area, the arm position is dithered and a new image evaluated. Upon finding a bounded area, the center of the area is found through averaging the pixel coordinates and the arm is moved towards the center of this area.

This is performed iteratively until the displacement is below a threshold value. This improves the accuracy of the calculated tray position. The camera gets a clear view of the tray so the gripper does not obscure part of the tray and the camera calibration is more accurate in the center of the image.

Once the ball tray is found in the image, the orientation of the tray and accurate locations of the ball to be dropped need to be determined. A good indication of the position of the bottom left corner of the ball tray is given by the left most pixel in the bounded area and the position of the bottom right corner is given by the lowest pixel in the bounded area. The coordinates of the two corners and the coordinates of the center of the tray can be used to calculate the position of the other two corners and the orientation of the tray.

Given two corners  $A_1$  and  $A_2$  and the center  $O$  of a rectangle the other two corners are given by the vector equations:

$$A_3 = 2M - A_1 \quad (2)$$

$$A_4 = 2M - A_2 \quad (3)$$

The segmented tray can contain 6 balls. The lengths of the sides of the tray will give the orientation of the tray:

$$\text{If } (A_1 - A_2)(A_1 - A_2) > (A_2 - A_3)(A_2 - A_3),$$

then  $A_1 \rightarrow A_2$  is the long side;

$$\text{If } (A_1 - A_2)(A_1 - A_2) < (A_2 - A_3)(A_2 - A_3),$$

then  $A_2 \rightarrow A_3$  is the long side.

Meantime, the accurate locations of each ball can be calculated.

### 3.4 Locating the balls

Shape detection in an image is highly important in practical industrial applications. Many algorithms have been proposed to detect circles. Among these algorithms, Circular Hough transform has been widely used for rapidity and robustness. In this paper, the circular Hough transform is employed to find circles of a given size in an image.

The transform is computed by taking the gradient of in gray scale images. The potential circles with approximately the right size are detected. The selecting strategy is always selecting the left most ball in the image with priority which is on the edge of the cluster. However, to avoid false detection of circles inside the tray due to tray structure, an exclusion area is considered during ball selection procedure. Baxter's arm is iteratively moved over the selected ball and the image analyzed until the arm is above the selected ball to within a given tolerance.

### 3.5 Pick the Balls

There are practical problems when perform the function of picking balls. When gripper pick the selected ball, the balls near the target ball may be touched and moved sideways. Thus Baxter's arm movements should be slowed down when close to the balls. Besides, analyze the neighborhood of the selected ball from the image and rotate the gripper to the best angle to minimize disruption of neighboring balls. Rotating the gripper and moving slowly results in minimal disturbance of neighboring balls. The robot grip a ball and lift it vertically, and then transfer to a position a little height above the free space in the tray and dropped it.

## 4 Experiments

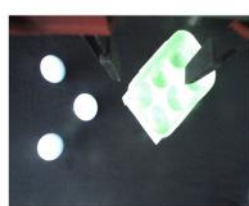
We tested our proposed whole system on Baxter research robot. For pick and place operation, we use the stock two fingered parallel gripper with a maximum width (open state) of 75mm and a minimum width (close state) of 37mm. Figure 3 illustrates some intermediate results of eye-in-hand visual servoing. Figure 3a displays the experimental Baxter research robot platform. Figure 3b shows one frame image obtained from eye-in-hand camera. Figure 3c shows the edge detection result using Canny operator, while Figure 3d illustrates edge detection result using SE detector. Figure 3e shows ball tray detection results. Therefore by comparing the edge detection results of two algorithms, we conclude that SE detector is more robust to noises and no need of tuning the parameters. In addition, with the processing speed up to 60 fps, SE detector adequately meets the real-time requirement.

## 5 Conclusion

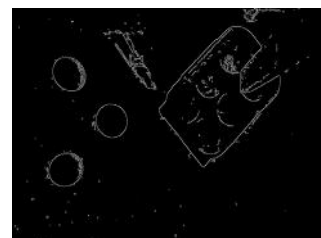
In this paper, a visual servoing based object pick-and-place manipulation system is designed and tested. The structured forest based edge detector achieves accurate results in real-time. Effectiveness of the eye-in-hand visual servoing system has been evaluated through Baxter research robot. However, there are several aspects will be discussed in our further studies: first, employing machine learning algorithms to classify various shapes of workpieces; second, adopting advanced methods to solve the inverse kinematics problem; third, improve the image-based visual servo control scheme.



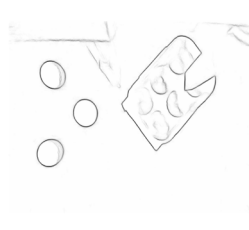
(a)



(b)



(c)



(d)



(e)

**Figure 3.** Eye-in-hand camera based visual servoing. a) the experimental Baxter research robot platform; b) one frame image obtained with eye-in-hand camera; c) the edge detection result using Canny operator ; d) edge detection result using SE detector; e) ball tray detection results

## References

- [1] Huang T, Mei J, Li Z. A Method for Estimating Servomotor Parameters of a Parallel Robot for Rapid Pick-and-Place Operations [J]. Journal of Mechanical Design, 2005.
- [2] Felker A. Design and Implementation of an Automated Pick and Place System for Johanson Technology, Inc.[J]., 2011.
- [3] Francois Chaumette, Seth Hutchinson, Visual Servo Control Part I: Basic Approaches, IEEE Robotics & Automation Magazine, 2016
- [4] H. Yang, J. Zhang, Y. Ji, Y. He, and Y. Lee, Experimental demonstration of multi-dimensional resources integration for service provisioning in cloud radio over fiber network, Scientific Reports, vol. 6, 30678, Jul. 2016.
- [5] H. Yang, J. Zhang, Y. Zhao, Y. Ji, J. Han, Y. Lin, and Y. Lee, CSO: Cross Stratum Optimization for Optical as a Service, IEEE Communications Magazine, vol. 53, no. 8, pp. 130-139, Aug. 2015.
- [6] Omar Tahri, Helder Araujo, Francois Chaumette, Youcef Mezouar, Robust image-based visual servoing using invariant visual information, PP. 1588–1600, 2013
- [7] Xavi Gratal, Javier Romero, Jeannette Bohg, Danica Kragic, Visual servoing on unknown objects, Mechatronics, 22 PP.423–435, 2012
- [8] Yun-Hui Liu, Hesheng Wang, Weidong Chen, Dongxiang Zhou. Adaptive visual servoing using common image features with unknown geometric parameters, Automatica, 49, PP. 2453–2460, 2013
- [9] Parida S, Wachs J, Cabrera M. Dynamic Surgical Tool Tracking and Delivery System using Baxter Robot [J]. 2014.
- [10] Morgan Quigley, Ken Conley, Brian Gerkey, Josh Faust, Tully Foote, Jeremy Leibs, Rob Wheeler, and Andrew Y Ng. Ros: an open-source robot operating system. In ICRA, volume 3, PP 5, 2009.
- [11] Heller J, Henrion D, Pajdla T. Hand-Eye and Robot-World Calibration by Global Polynomial Optimization. [J]. Clinical Orthopaedics and Related Research, 2014.
- [12] Canny J. A Computational Approach to Edge Detection. IEEE Transactions on Pattern Analysis and Machine Intelligence, 1986: 679-698.
- [13] Piotr Dollar, C, Lawrence Zitnick. Structured Forests for Fast Edge Detection, IEEE International Conference on Computer Vision, ICCV, 2013

Hai-Sheng XIONG, De-Xing ZHANG\*

## Research on Wind Loads of Container Ship based on CFD

**Abstract:** The maximization trend of the transport ship makes wind loads play an important role in ship manoeuvring and energy saving. Having a large windage area makes container ship especially large container ship more sensitive to wind loads. Traditional research methods of ship wind loads are not only time and money consuming but also cannot completely reflect on the wind loads. Bearing this in mind in this paper a three-dimensional numerical simulation of airflow around a full scale Post-Panamax container ship based on CFD is presented. Several cases of numerical simulation of airflow around the container ship are carried out to investigate the wind forces acting on it and flow pattern around it. Wind loads coefficients are obtained, which are compared with the ones obtained by Isherwood empirical formula and wind-tunnel experiment to examine the accuracy. A good agreement is obtained among these three methods which prove the reliability of CFD simulation.

**Keywords:** CFD; wind loads; container ship

### 1 Introduction

The fuel efficiency and performance of container ship is of great concern for ship owners due to the economic and environmental considerations [1]. All ships experience wind resistance while underway, they may experience adverse effects of wind while manoeuvring in harbors and confined waterways. Unlike the majority of other type of ships, container ship has a large windage area especially those big scale container ships causing the wind influence more severe. It is necessary to study the wind forces acting on the container ships.

The traditional research methods of ship wind loads mainly include two kinds: wind-tunnel experiment and empirical formula. Wind-tunnel experiment is a method using corresponding technology and measurement equipment to measure the forces acting on ship model and the relevant information of the flow field by putting the scale model in a specific laboratory which can simulate the wind environment [2]. This method is an accurate and reliable method to obtain the wind loads of ships which also plays an important role in the research of the wind field and the wind loads. Because of the deflating scaling experiment the wind-tunnel experiment cannot completely

---

\*Corresponding author: De-Xing ZHANG, Navigation College, Dalian Maritime University, Dalian, China,  
E-mail: 1209286642@qq.com

Hai-Sheng XIONG, Dept. of Maritime College, Tianjin Maritime College, Tianjin, China

reflect on the wind loads acting on ships, besides it is time and money consuming and cannot simulate complicated wind conditions. Empirical formula method is derived from the regression calculation of large amount of ship wind-tunnel experiments of different types of ships [3]. However, the empirical formula method has a narrow application range and can only meet with high accuracy standard in full loaded and ballast conditions. With the advent of booting calculating ability of the computer, the numerical simulation method based on CFD (Computational Fluid Dynamic) has drawn the attention of many researchers. Comparing with traditional methods, the CFD method has many advantages like short numerical simulation period, low implementation cost, easy tuning process [4]. Additionally, the drawbacks of detecting points limitations in wind-tunnel experiment can be overcome by utilizing the CFD method and CFD method can display the simulated data by vivid diagrams. CFD technology has been employed in many fields including architecture wind engineering, ship, and aerospace field.

In this paper, the wind load of a Post-Panamax container ship is investigated by utilizing numerical simulation. Wind load coefficients and wind flow characteristics around the ship in wind angles of 0-180 degrees with steps of 10 degrees are obtained. The comparison of experiment data among these three methods show grate agreement.

## 2 Ship wind load coefficients

The wind loads acting on a ship in a horizontal motion is described in figure1, which including  $F_x$  in bow direction,  $F_y$  in transverse direction and yawing moment  $N$ . The wind angle is the angle between the wind direction and ship heading direction.

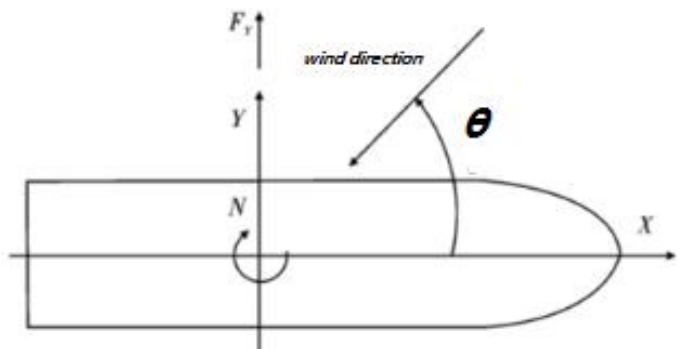


**Figure 1.** Coordinates definitions and forces

For the sake of independence of the results, non-dimensional process is needed, so wind load coefficients are calculated with the formulas:

$$C_x = \frac{F_x}{0.5\rho v_r^2 A_T} \quad (1)$$

$$C_y = \frac{F_y}{0.5\rho v_r^2 A_L} \quad (2)$$

$$C_N = \frac{N}{0.5\rho v_r^2 A_L L_{OA}} \quad (3)$$

Where  $F_x$  refers to longitudinal wind force, unit N;  $F_y$  refers to the transverse wind force, unit N;  $\rho$  refers to air density ( $1.255 \text{ kg/m}^3$ );  $v_r$  refers to the relative wind velocity, unit m/s;  $L_{OA}$  refers to the overall length of the ship, unit m;  $A_T$  refers to the front project area of the ship structure above water line, unit  $\text{m}^2$ ;  $A_L$  refers to the side projection area of the ship construction above water line, unit  $\text{m}^2$ .

### 3 Isherwood wind load calculation method

Isherwood proposed the empirical formula of wind loads through a regression of the wind tunnel experiment data of large quantities of merchant ships [3]. The formulas are shown as below:

$$C_x(\theta) = a_0 + a_1 \frac{2A_L}{L_{OA}^2} + a_2 \frac{2A_T}{B^2} + a_3 \frac{L_{OA}}{B} + a_4 \frac{C}{L_{OA}} + a_4 \frac{d}{L_{OA}} + a_6 m \quad (4)$$

$$C_y(\theta) = b_0 + b_1 \frac{2A_L}{L_{OA}^2} + b_2 \frac{2A_T}{B^2} + b_3 \frac{L_{OA}}{B} + b_4 \frac{C}{L_{OA}} + b_4 \frac{d}{L_{OA}} + b_6 \frac{A_{ss}}{A_F} \quad (5)$$

$$C_N(\theta) = c_0 + c_1 \frac{2A_L}{L_{OA}^2} + c_2 \frac{2A_T}{B^2} + c_3 \frac{L_{OA}}{B} + c_4 \frac{S}{L_{OA}} + c_5 \frac{C}{L_{OA}} \quad (6)$$

Where  $C_x(\theta)$ ,  $C_y(\theta)$  refers to the wind load coefficients in longitudinal and transverse direction when wind angle equals to  $\theta$ , respectively. The definition of  $A_T$ ,  $A_L$  are in line with above mentioned.  $A_{ss}$  is the side projection area of the super structure;  $L_{OA}$  is the overall length of ship;  $B$  refers to the ship width;  $S$  refers to circumference of the side projection area above water line;  $d$  is the distance from centroid of the side projection area above water line to bow;  $m$  refers to the number of mast and pillar in central longitudinal plane.

### 4 Numerical simulation

#### 4.1 Ship parameters

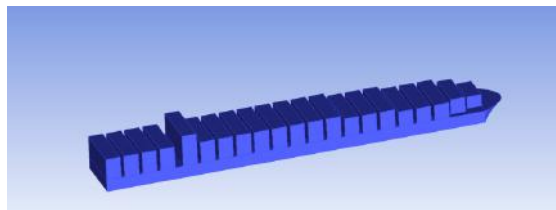
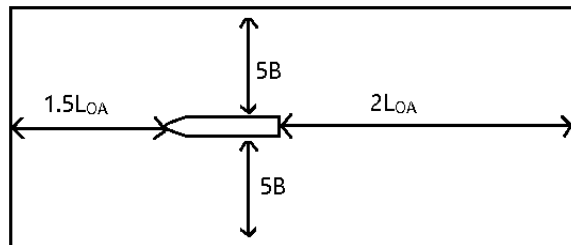
In this paper, a Post-Panamax ship is investigated, with a capacity of 9,000 containers. In full loaded condition, 40 bays container can be stacked on the deck, with a highest of 7 tiers. Main parameters can be described as follows.

**Table 1.** Main parameters of the ship

Length over all	Length between perpendiculars	molded breadth	Moulded depth	Laden draught
340m	320m	45m	23m	13m

#### 4.2 Pre-process of numerical simulations

The geometry model of the ship above water line was formulated by pre-process software ICEM CFD. It mainly includes part of ship hull and the containers stowed on the deck. Ship geometry is appropriately simplified in the pre-process which is shown in Figure 2. A proper computational domain is very important to the numerical simulation. Blockage ratio of the domain should less than 3% in wind field simulation [4]. The Rectangle shape computational domain which is shown in Figure 3 was employed with dimensions:  $4 L_{OA} \times 10B \times 5H$ , where  $L_{OA}$  refers to overall length of ship,  $B$  refers to ship width,  $H$  refers to vertical height from waterline to the highest level of the ship. The wind angle from 0 to 180 degree with one step of 10 degrees is realized by rotating the computational domain, which contributes to the simulation of wind flow around container ship with different wind angle. Structural meshes are applied for the discretization of the computational domain and the surfaces of container ship, which can accelerate the convergence and reduce truncation errors [5].

**Figure 2.** Ship geometry**Figure 3.** The ratio relationship between the computational domain and ship

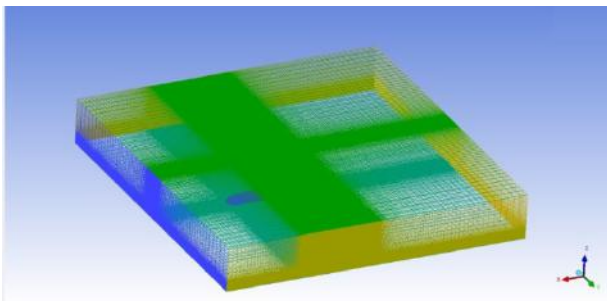


**Figure 4.** Structural meshes of computational domain

### 4.3 Numerical simulation settings

#### 4.3.1 Governing equations

This simulation is based on Reynolds-averaged Navier-Stokes equations, and RNG k- $\varepsilon$  turbulent model. Therefore, the governing equations are shown as below:

The continuity equation:

$$\frac{\partial u_i}{\partial x_i} = 0, (i=1,2,3) \quad (7)$$

The momentum equation:

$$\frac{\partial}{\partial t}(\rho u_i) + \frac{\partial}{\partial x_j}(\rho u_i u_j) = -\frac{\partial p}{\partial x_i} + \frac{\partial \tau_{ij}}{\partial x_j} + \rho g_i \quad (8)$$

And two turbulence closure equations:

$$\frac{\partial}{\partial t}(\rho k) + \frac{\partial}{\partial x_i}(\rho k u_i) = \frac{\partial}{\partial x_j} \left[ \left( \mu + \frac{\mu_t}{\sigma_k} \right) \frac{\partial k}{\partial x_j} \right] + G_k - \rho \varepsilon \quad (9)$$

$$\frac{\partial}{\partial t}(\rho \varepsilon) + \frac{\partial}{\partial x_i}(\rho \varepsilon u_i) = \frac{\partial}{\partial x_j} \left[ \left( \mu + \frac{\mu_t}{\sigma_\varepsilon} \right) \frac{\partial \varepsilon}{\partial x_j} \right] + C_{1\varepsilon} \frac{\varepsilon}{k} - C_{2\varepsilon} \rho \frac{\varepsilon^2}{k} \quad (10)$$

Where  $G_k$  is turbulent kinetic production;  $G_b$  is turbulent kinetic energy caused by buoyancy force.  $C_{1\varepsilon}$  and  $C_{2\varepsilon}$  are model constants 1.48, 1.68;  $\sigma_k$  (= 1.0) and  $\sigma_\varepsilon$  (= 1.3) are turbulent Prandtl number;  $\mu_t$  is the turbulent viscosity expressed as:

$$\mu_t = \rho C_\mu \frac{k^2}{\varepsilon} \quad (11)$$

The governing equations are solved by means of a collocated grid system using the finite volume method. Segregated method is used to solve the discretized equations. Second-order centred difference scheme is adopted for all spatial derivatives. SIMPLEC algorithm is used to correct the velocities with smaller relaxation factor and to improve the initially assumed pressure fields.

#### 4.3.2 Boundary conditions

The boundary conditions represent the surroundings of the object being researched [6], appropriate boundary condition can accelerate convergence. Velocity inlet boundary condition simulation is imposed to the inlet of computational domain. For the sake of approaching the real wind flow at sea an exponential wind profile is applied which is described as:

$$u(z) = u_0 \left( \frac{z}{z_0} \right)^\alpha \quad (12)$$

Where  $u_0$  refers to a reference height which traditionally is 10 meters.  $\alpha$  is the exponent representing the velocity profile which we choose 0.16. The turbulence intensity  $I$  and Turbulence Kinetic Energy  $k$  in velocity inlet were obtained through formulas below:

$$\begin{cases} 0.31 & Z \leq 5 \\ 0.1 \left( \frac{Z}{450} \right)^{-0.25} & 5 < Z \leq 450 \end{cases} \quad (13)$$

$$k=1.5 \quad (14)$$

$$\xi = \bar{u}\bar{u}^{-\frac{3}{4}} k \frac{3}{2} l \quad (15)$$

The velocity inlet boundary condition mentioned above is achieved by UDF. No slip wall condition is imposed along the bottom of the domain and the surfaces of the container ship. Symmetry boundary condition can enforce a parallel flow [7], so the two sides of the domain are applied to symmetry boundary condition, which can reduce the influence of domain to the simulation.

## 5 Results and discussion

### 5.1 Wind load coefficients

Wind forces of the container ship in X direction and Y direction and yaw moment in Z direction are obtained by numerical simulation. Wind loads coefficients are obtained according to formulas (1)-(3). Another set of coefficients are calculated according to the Isherwood empirical formula. The coefficients acquired by CFD and empirical formulas are compared with coefficients obtained through wind-tunnel experiment conducted by Andersen [8]. Companions are shown in Figure 5, 6 and 7.

These three figures present graphical comparison of longitudinal force coefficients  $C_x$ , lateral force coefficients  $C_y$  and yaw moment Coefficients  $C_n$ . The shapes of coefficients curves among these three methods are approximate which make the numerical method reliable.

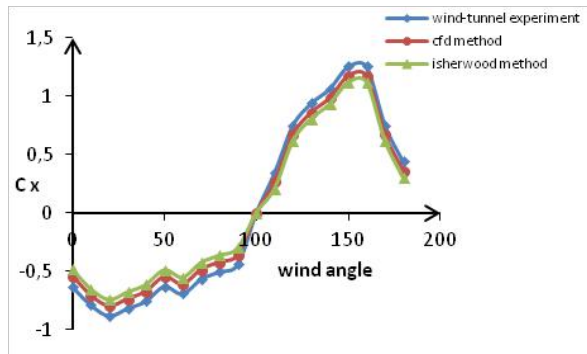
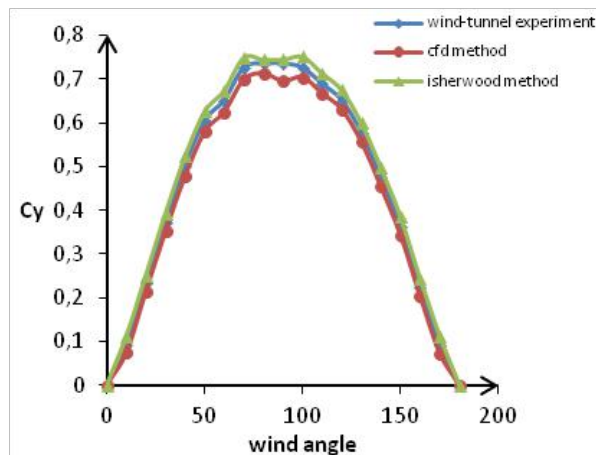
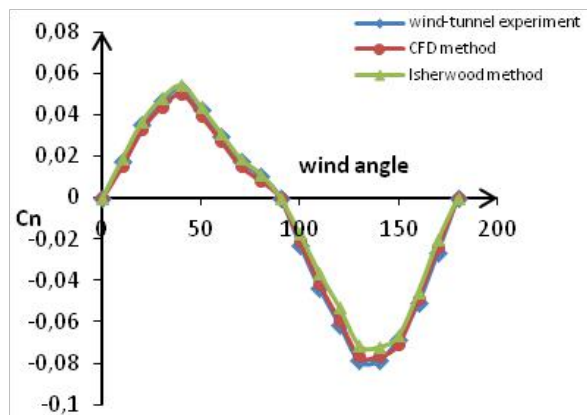
Figure 5.  $C_x$  curve obtained from three methodsFigure 6.  $C_y$  curve obtained from three methodsFigure 7.  $C_n$  curve obtained from three methods

Figure1 shows the wind pressure coefficients increase with the wind angle increases when wind angle is between 0 to 30 degrees, coefficient reach the first climax when wind angle is 30 degree. When wind angle is between 30 to 100 degrees, the coefficients reduce with the wind angle increase and a fluctuation occurs when wind angle 50 and 60 degrees. The coefficients present a trend which is increase first and then decrease with the growth of the wind angle when wind angle exceed 100 degrees. And it reaches another climax when wind angle is 150 degree. It can be conclude from Figure2 that lateral force coefficients increase first and then decrease with the increase of the wind angle, and climax occur when wind angle is 70 degrees and 100 degrees. Figure 3 shows that the yaw moment Coefficients reach its extreme positive value when wind angle is 40 degrees and negative extreme value when wind angle is 135 degrees. By comparing the wind load coefficients obtained by these three methods, it can be seen that the value of coefficients obtained by Isherwood empirical formula is the greatest among these three methods, and value of coefficients acquired by numerical method is the smallest. The reason of this phenomenon is that numerical method can effectively simulate the atmospheric boundary layer, in which the wind load acting on the ship is dramatically weakened, making the numerical simulation data smaller. Wind tunnel experiment, however, cannot stimulate atmosphere boundary layer well, making the result bigger. Isherwood formula is based on the wind tunnel experiment data, and for the sake of safety It is more conservative, which makes the wind load coefficients the biggest among the above mentioned methods.

## 5.2 Wind field traits around ship

In order to make a thorough investigation on the surrounding wind field traits of the ship, horizontal section where  $z=10$  is being chosen to be researched in this paper. There are two reasons: on one hand, it is where the stacking recording begins, which makes it more special; on the other hand, by choosing several different planes in different Z value, it is found that more wind flow field information can be extracted abound from  $z=10$  than others. In this paper we choose some typical results of the simulation which are when the wind angle equals to 0 degree, 30 degrees, 90 degrees, 120 degrees and 180 degrees.

The wind flow field information can be effectively obtained from the velocity contour and streamline. Based on the horizontal section at  $z=10$ , it can be concluded that the surrounding wind field is almost symmetrically distributed where the wind angle is 0, 90, and 180 degree. The backflow area increases first then decreases with the wind angle changing from 0 to 180 degree.

### **5.2.1 Wind angle is 0 degree**

When the air flow reaches the bow area, some of it will separate on the up edge of deck, while the other parts flow to left and right sides of the hull and then separate. The separation points on left and right sides are on the crossline where the bow fender meets the broadside on both sides. The separation points above the deck locate on sharp edges of containers. The air flow reattached onto ship, and the reattached point is  $1/3 L_{OA}$  away from ship bow. The reattached wind flow will separate again in ship astern. Two vortexes symmetrically distributed along the central line with a diameter of one  $1/5 L_{OA}$  will be formed in ship astern.

### **5.2.2 Wind angle is 30 degree**

The backflow in the windward side will almost disappear, in the meanwhile backflow in leeward area increase. Reattachment points located in leeward is about one third of  $L_{OA}$  from ship astern.

### **5.2.3 Wind angle is 90 degree**

A large backflow area is formulated leeward side and no separations occur in windward side. Because of the squeezed streamline astern, the biggest flow velocity lies in the astern area, where the velocity is bigger than that of the bow area. The vortexes formed leeward are basically symmetrically distributed in transverse direction with width of half ship width.

### **5.2.4 Wind angle is 120 degree**

Vortexes are mainly distributed leeward and on the bow area. There are two vortexes in leeward side, one is formed by the separated flow in ship astern, the other is formed by the separated flow in bow area. The two vortexes intermingle with each other, the width of the total vortex area is about  $1L_{OA}$ . The maximum velocity occurs in ship astern.

### **5.2.5 Wind angle is 180 degree**

Wind flow separated in the right and left sharp edge of the ship astern forming two vortexes which are along with the two sides of the ship hull. Reattachment points are about  $1/5 L_{OA}$  from the ship astern, no separation occurs until to the ship bow where another small-scale vortex occurs.

### 5.3 Pressure contour analysis

Pressure distribution around the ship can be of great use to analyse the characteristics of wind flow [9]. The negative pressure zones in the pressure contour can reflect location and scale of vortices. It can be concluded that the intensity and scale of the negative pressure zone change with the change of wind angle from Figure 8. When wind angle is 0 degree the pressure around the ship distributes symmetrically, in which condition the wind drag and yaw moment will be relatively small. When wind angle reaches to 30 degrees, the positive wind pressure center is close to ship bow and the negative pressure center is close to astern, which cause a big yaw moment. When wind angle is 90 degrees, there is a big positive pressure zone in the windward and a big negative pressure zone in the leeward causing a huge wind force in transverse direction. The huge transverse wind force will make the ship lateral move which is dangerous for ship navigation. When the wind angle reaches 120 degrees, there generates a big yaw moment in opposite direction to the direction of yaw moment occurs when wind angle is 30 degrees. In the case of wind angle is 180 degrees negative pressure zones and positive pressure zones are all located at ship astern which leads small ship drag and yaw moment.

## 6 Conclusion

This paper has investigated the wind loads and flow pattern of a Post-Panamax container ship by using CFD numerical simulation. Wind loads coefficients are obtained by CFD and Isherwood empirical formula, and both results are compared with wind-tunnel experiment. The comparison shows good agreement, which indicates that the numerical simulation method is reliable.

It also can conclude from the comparison that the value of coefficients obtained by Isherwood empirical formula is the greatest among these three methods, and value of coefficients acquired by numerical method is the smallest.

The wind field around ship is almost symmetrically distributed when wind angle is 0, 90, and 180 degree. The backflow area increases first then decreases with the wind angle changing from 0 to 180 degree.

The position and scale of the negative pressure zone in leeward have great relationship with the wind angle.

**Acknowledgment:** This study was financially supported by the Ministry of transportation science and technology funds (2012-329-225-090).

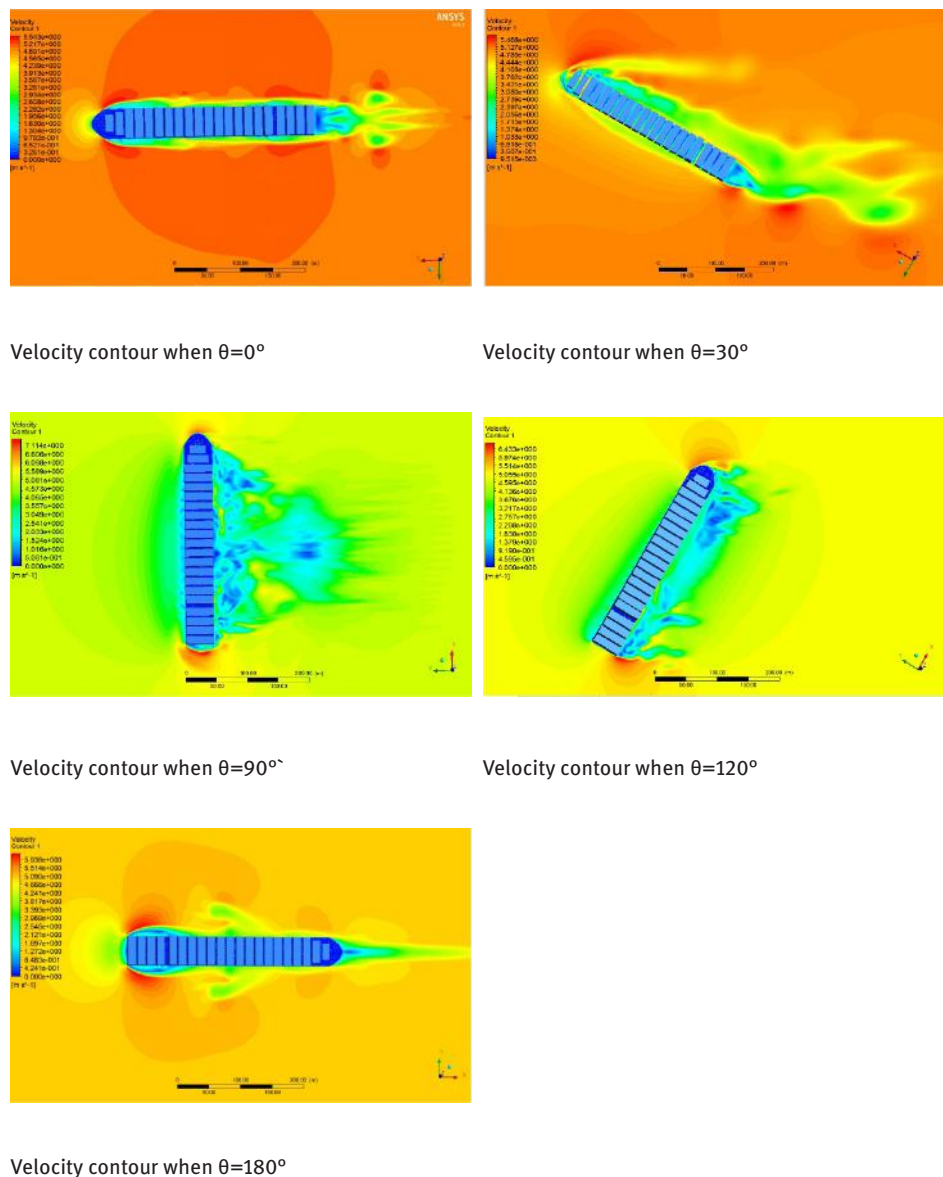
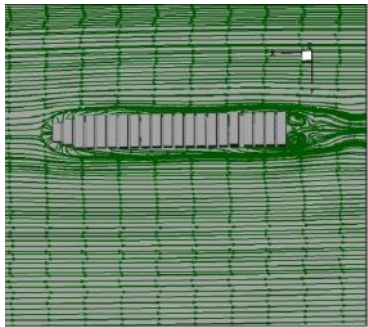
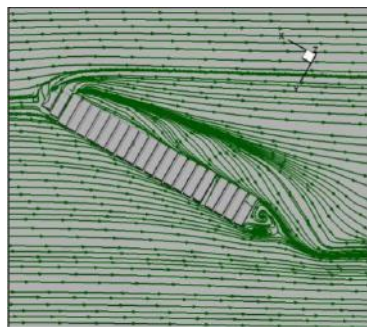


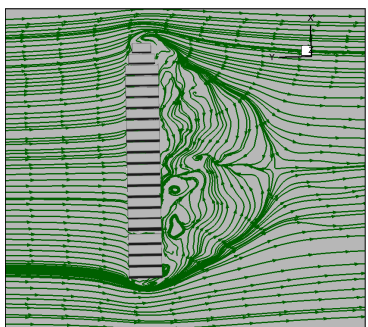
**Figure 8.** Velocity pressure contour in plane  $Z=10m$



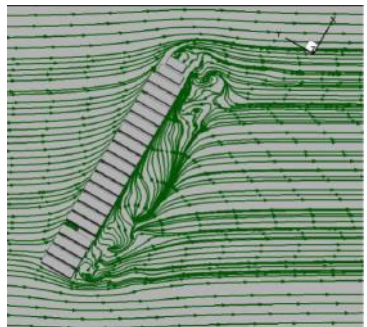
streamlines when  $\theta=0^\circ$



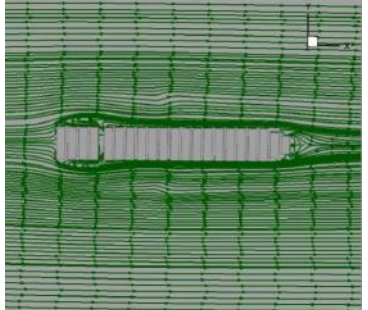
streamlines when  $\theta=30^\circ$



streamlines when  $\theta=90^\circ$



streamlines when  $\theta=120^\circ$



streamlines when  $\theta=180^\circ$

**Figure 9.** Streamlines in plane Z=10m

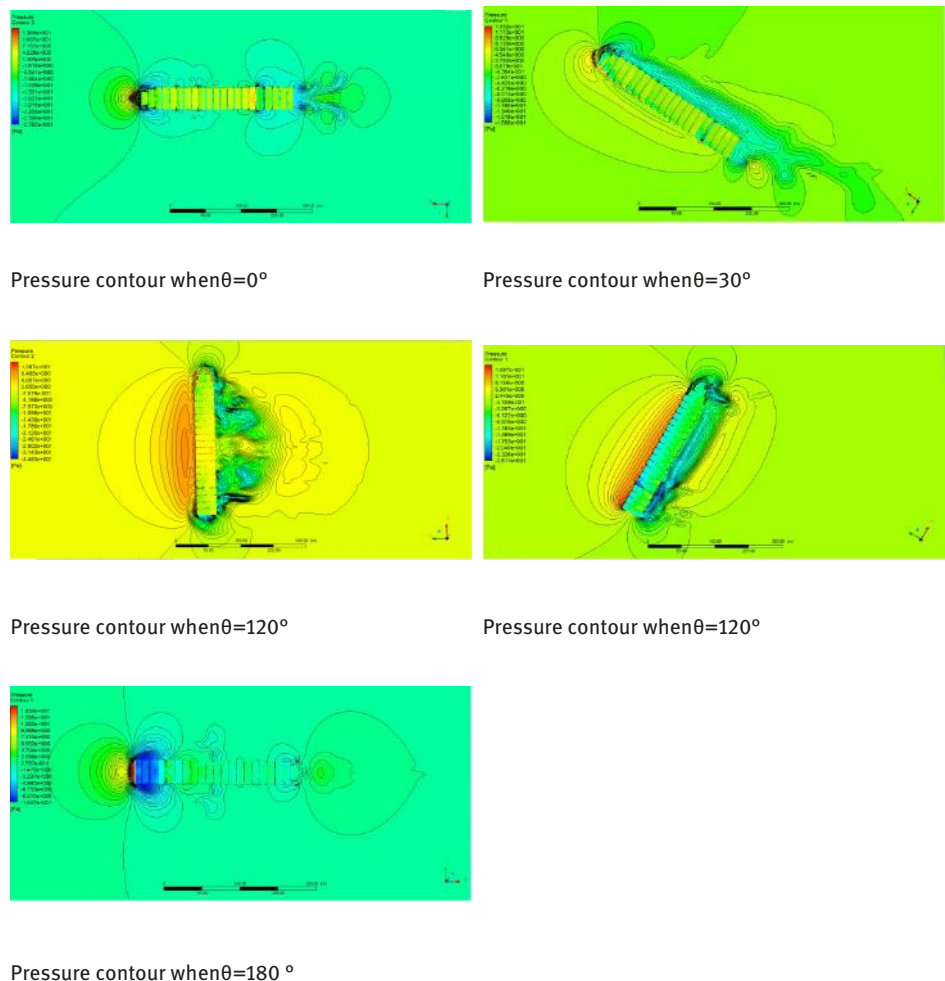


**Figure 10.** Pressure contour in plane  $Z=10\text{m}$

## References

- [1] Wnęk A D, Soares C G. CFD assessment of the wind loads on an LNG carrier and floating platform models[J]. Ocean Engineering, 2015, 97: 30-36.
- [2] W. Blendermann, Wind Loading of Ships – Collected Data from Wind Tunnel Tests in Uniform Flow, Institut für Schiffbau der Universität Hamburg, Bericht No 574, pp. 53 (1996).
- [3] R.M. Isherwood, Wind resistance of merchant ships, Trans. of Roy. Inst. Naval Architects 114, pp. 327-338 (1972).
- [4] Viola I M. Downwind sail aerodynamics: A CFD investigation with high grid resolution[J]. Ocean Engineering, 2009, 36(12):974–984..

- [5] Ferziger, J.H and perc, M, Computational Methods for Fluid Dynamics, Springer Verlag, Berlin Heidelberg New York, 3<sup>rd</sup> edition, 2002.
- [6] FRNTER FJ, etal. Recommendations on the use of CFD in predicting pedestrian wind environment[J]. Journal of wind engineering and Industrial Aerodynamics, Submitted, 2005.
- [7] Linjia Yang, Pengfei Zhu, Numerical Analysis of Wind Pressure Characteristics around Two Combinatorial Hemispheres. Proceedings of Asia Navigation Conference 2014.485-495.
- [8] Anderson IMV. Wind loads on post-panamax container ship[J]. Ocean Engineering. 2013;58(2):115-134.
- [9] A.D. Wnek, A. Paco, A.D. Wnęk, A. Paço, X-Q. Zhou, C. Guedes Soares, Numerical and experimental analysis of the wind forces acting on a floating LNG platform, In proceedings of the 13th International Congress, IMAM2009, pp. 697–702 (2009).

Qiang LUO\*, Ping ZHOU, Wen GAI, Fei LIAO

## Design and Research of Model Sting Support Control System of Icing Wind Tunnel

**Abstract:** The sting support device of icing wind tunnel is a four-axis position closed-loop servo system consisting of a variable angle mechanism and a Y-direction mechanism. Due to motion coupling among the four axes, synchronous control is required. To ensure that the support device rotates uniformly at the specified angular velocity while accurately positioning the attack angle  $\alpha$  and the sideslip angle  $\beta$ , and that the model center will not deviate from the axis of the wind tunnel during the rotation, this paper provides a detailed solution of complicated motion based on comprehensive mathematical analysis of the kinematic relationship between velocity and positions of the attack angle  $\alpha$ , sideslip angle  $\beta$  and Y-direction lifting mechanism. In addition, the method used for controlling the multi-axis motion velocity and position is further discussed. At last, this paper sets forth the unique method for controlling virtual principal axis and  $\alpha$ ,  $\beta$  and y mechanisms position following. By use of this method, the velocity and positions of attack angle  $\alpha$  mechanism sideslip angle  $\beta$  mechanism and Y-direction mechanism can be controlled in a highly-accurate manner.

**Keywords:** Tunnel; Sting Support; Motion Control; Kinematic Relation; Multi-axis Motion

### 1 Introduction

Control precision of wind tunnel model attitude angle is critical to acquisition of excellent model test data. Shown by relevant documents [1], most model test errors may be traced to model attitude error. The elevation angle  $\alpha$  and yaw angle  $\beta$  are the most important model attitude angles. Research fellows have designed different types of mechanical structures and design approaches to control  $\alpha$  and  $\beta$  angles of the model; however, only single-degree-of-freedom of  $\alpha$  and  $\beta$  angles is controlled respectively by use of the conventional control method. It is difficult to implement synchronous control due to arduous arithmetical operation and unsatisfactory angle positioning precision; furthermore, the most important model security issue has not considered duly [2].

---

\*Corresponding author: Qiang LUO, China Aerodynamics Research and Development Center, Mianyang City, Sichuan Province, China, E-mail: qluo2006@163.com

Ping ZHOU, Wen GAI, Fei LIAO, China Aerodynamics Research and Development Center, Mianyang City, Sichuan Province, China

The new sting control system, specially developed for the icing wind tunnel, provides a unique multi-degree of freedom model support mechanism synchronous motion control approach, through which the elevation angle and yaw angle of the model can be controlled in a precise, safe and highly-effective manner.

## 2 Basic requirements for sting control system

The sting support system is composed of the angle of attack and sideslip angle of mechanism and Y mechanism, which lies in high speed test section. The overall structure is shown in Figure 1.

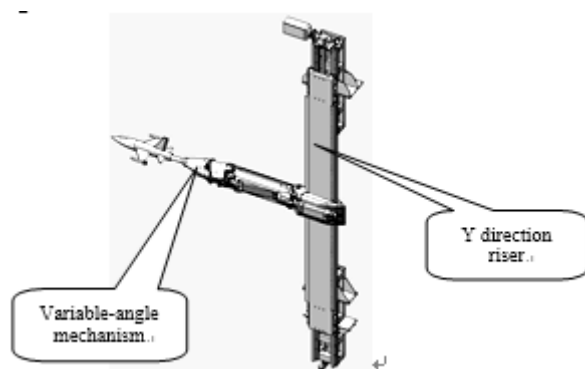


**Figure 1.** Schematic diagram of support device

The System is a four-axis closed loop servo system. Due to motion coupling among the four axes, synchronous control is required. See Table 1 for the design technical specifications.

**Table 1.** Main technical specifications

Control range	Attack angle	Yaw angle	Roll angle
	-15°-35°	-30°-30°	0°-360°
<b>Mechanical precision</b>	±0.02°	±0.05° (forward β) ±0.025 (backward β)	-
<b>Control precision</b>		±0.02°	
<b>Control velocity</b>	<b>Test velocity</b>	1°/s	Manual

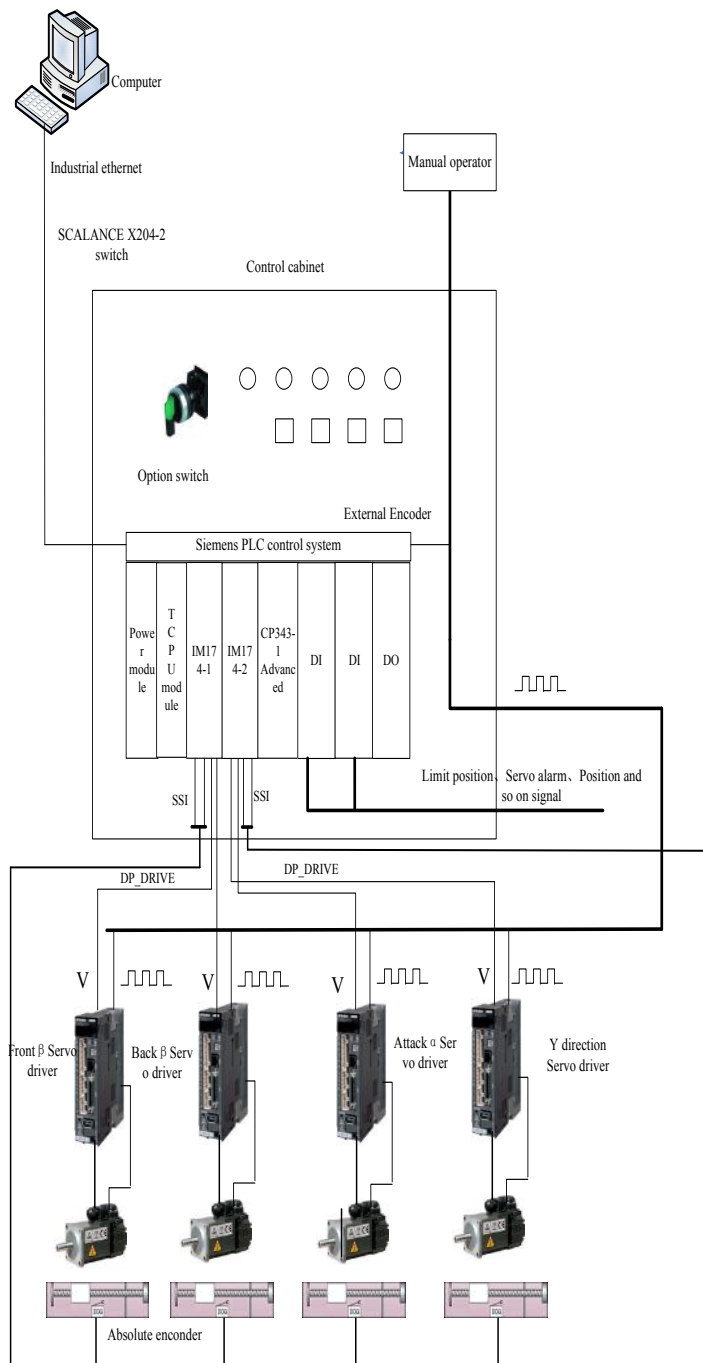


Figure 2. Composition block diagram of control system

### 3 Composition of control system and analysis of kinematic relationship

#### 3.1 System composition

As shown in Figure 2, the sting support control system is composed of a control cabinet (containing PLC, HMI, motion control unit, etc.), 4 sets of AC servo amplifiers, servo motor, etc. An upper control computer, as the user's operation interface, is used to implement remote control upon the attack angle, sideslip angle and lifting mechanism, and to display the motion status of these mechanisms and operating situation of servo drive in real time. PLC is used to transmit the data (like the motion status of these mechanisms, operating situation of servo drive) to the upper computer via industrial Ethernet, and the upper computer forwards control commands to PLC via the industrial Ethernet. Upon receipt of the control commands, PLC will implement velocity control or position control through motion control unit as per corresponding control strategy [3,4].

#### 3.2 Analysis of kinematic relationship between mechanisms

##### 3.2.1 Analysis of kinematic relationship between attack angle $\alpha$ mechanism and Y-direction mechanism

See the Figure below for the geometrical relationship after simplification of attack angle mechanism.

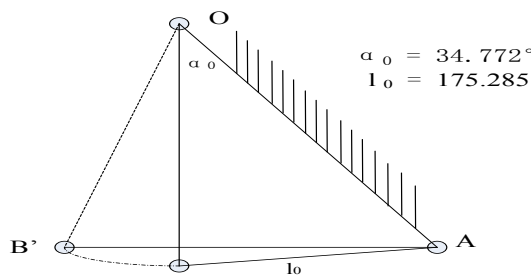


**Figure 3.** Theoretical dimensions of attack angle mechanism

Given that the clockwise moving direction of the screw is positive and  $\alpha$  augmentation positive, then the relational expression of  $\alpha$  and  $l$  is as shown in Figure 4:

$$l = \sqrt{304.138^2 + 224.555^2 - 2 \times 304.138 \times 224.555 \times \cos(34.772^\circ + \alpha)} - 175.285 \quad (1)$$

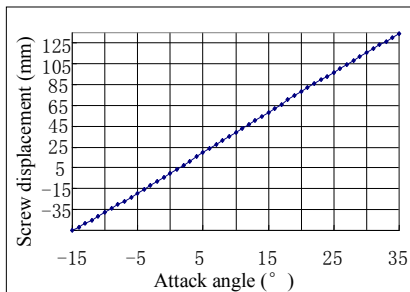


**Figure 4.** Displacement relationship between attack angle and screw

By taking derivative with respect to the two sides of the Expression (1), the relational expression (2) between the screw moving velocity and attack angle velocity is solved, as shown in Figure 5:

$$\frac{dl}{dt} = \frac{304.138 \times 224.555 \times \sin(34.772^\circ + \alpha)}{\sqrt{304.138^2 + 224.555^2 - 2 \times 304.138 \times 224.555 \times \cos(34.772^\circ + \alpha)}} \frac{d\alpha}{dt} \quad (2)$$

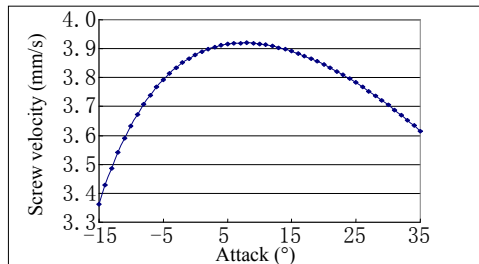


**Figure 5.** Velocity relationship between attack angle and screw

### 3.2.2 Analysis of kinematic relationship between forward/backward sideslip angle mechanisms

During the changing process of forward sideslip angle  $\beta_1$  from  $-60^\circ$  to  $60^\circ$ , the backward sideslip angle  $\beta_2$  changes from  $-30^\circ$  to  $30^\circ$ . The  $\beta_1$  is dependent upon the screw displacement  $l_1$ , the displacement relationship between the forward sideslip angle and screw is as shown in Figure 6:

$$\beta_1 = \arccos \left( \frac{160.078^2 + 950.842^2 - (962.521 + l_1)^2}{2 \times 160.078 \times 950.842} \right) - 89.379^\circ$$

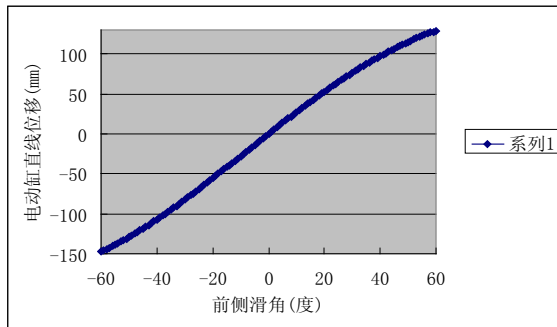


Figure 6. Displacement relationship between  $\beta_1$  and screw

By taking derivative respectively, the velocity relationship between forward sideslip angle and screw is obtained, as shown in Figure 7:

$$\frac{dl_1}{dt} = \frac{160.078 \times 950.842 \times \sin(\beta_1 + 89.379^\circ)}{\sqrt{160.078^2 + 950.842^2 - 2 \times 160.078 \times 950.842 \cos(89.379^\circ + \beta_1)}} \frac{d\beta_1}{dt}$$

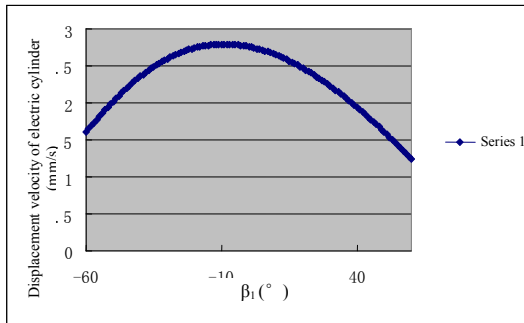


Figure 7. Velocity relationship between  $\beta_1$  and screw

Displacement relationship between the backward sideslip angle and screw is as shown in Figure 8. The  $\beta_2$  is dependent upon the screw displacement  $l_2$ , the displacement relationship between the backward sideslip angle and screw is as shown below:

$$\beta_2 = \arccos\left(\frac{185^2 + 747.329^2 - (730.428 + l_2)^2}{2 \times 185 \times 747.329}\right) - 77.641^\circ$$

By taking derivative respectively, the velocity relationship between the backward sideslip angle and screw is obtained, as shown in Figure 9:

$$\frac{dl_2}{dt} = \frac{\sin(\beta_2 + 77.641^\circ)}{\sqrt{185^2 + 747.329^2 - 2 \times 185 \times 747.329 \times \cos(\beta_2 + 77.641^\circ)}} \frac{d\beta_2}{dt}$$

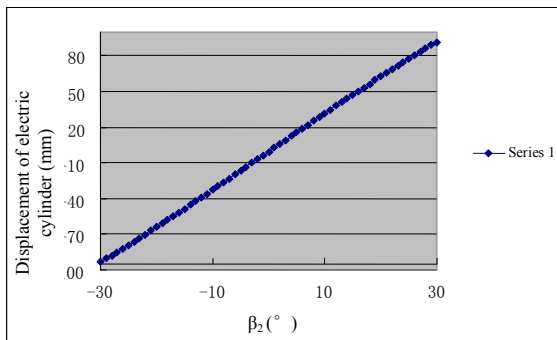


**Figure 8.** Displacement relationship between  $\beta_2$  and screw

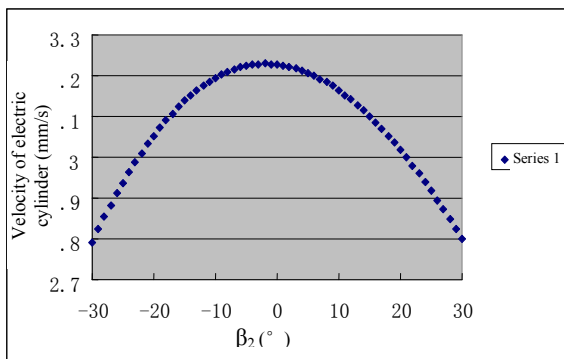


**Figure 9.** Velocity relationship between  $\beta_2$  and screw

The relationship between the sideslip angle and forward/backward sideslip angles:

$$\beta = \beta_1 - \beta_2$$

When  $d\beta_1=0.02^{\circ}$ ,  $\alpha=0$ , to satisfy the precision requirement that the sideslip angle shall be  $0.05^{\circ}$ , the positioning precision of forward sideslip electric cylinder must be up to 0.055mm under limiting case. According to  $d\beta_2=0.02^{\circ}$ , the positioning precision of backward sideslip electric cylinder can be solved; i.e., about 0.065mm.

#### 4 Control approach and control strategy

According to the analysis above, a mountain of arithmetical operation is required for conversion between straight line displacement at different degrees of freedom and

the target angle if control is made based on the aforesaid kinematic relationship; in addition, mechanism machining error, installation error and calculation error may be enlarged inevitably and control precision decreased accordingly. Furthermore, it is difficult to implement synchronous control due to improper synchronicity. However, the synchronous motion control approach of the sting support mechanism developed by us presents a sound resolution. This approach involves establishing a mapping relationship between the target position and the velocity of elevation angle/yaw angle of support device model and the motion parameters of actual mechanism at different DOF; simplifying mathematical derivation process and optimizing the motion control precision of the mechanism at different DOF by way of data fitting with the measured value; implementing positioning control of the mechanism support model by use of synchronous coordinated motion of DOF axis of the mechanisms; implementing motion protection of support model by use of the parameters concerning the DOF axis of the mechanisms, thus achieving synchronous coordinated control upon the elevation angle and yaw angle of the model, and improving control precision, operating efficiency and reliability.

#### **4.1 Constant-speed variable attack angle control approach with virtual axis as principal axis (sideslip angle $\beta=0^\circ$ )**

During the multi-axis motion process, the relationship between the position and motion velocity of the attack angle  $\alpha$  screw and Y-direction lifting mechanism varies with the attack angle  $\alpha$ . The attack angle  $\alpha$  is the control core and control principal axis in the entire support system and the primary control mission is to achieve constant-speed variation and precise positioning of attack angle  $\alpha$ . However, positioning of the attack angle  $\alpha$  cannot be achieved by driving rotation axis with electric motor but by screw driving. Since non-linear relationship exists between the attack angle  $\alpha$  and screw velocity & position, so the precise positioning and constant-speed variation of attack angle  $\alpha$  can be implemented only by controlling the screw as per Expression (1) and function (2) above. It is difficult to implement such non-linear velocity control. By deep analysis, this paper provides an approach of building virtual  $\alpha$  rotation axis. In using control algorithm, a virtual  $\alpha$  rotation axis is built. Meanwhile, camshaft curve relationship is also built between  $\alpha$  screw mechanism and  $\alpha$  angle, and Y-direction mechanism and  $\alpha$  angle. By controlling the virtual axis to rotate at the  $\alpha$  target angular velocity,  $\alpha$  screw mechanism and Y-direction mechanism will implement position follow-up in strict accordance with the camshaft relationship, thus achieving non-linear velocity and position linkage during the multi-axis motion process. In this way, non-linear velocity control becomes position follow-up control while the operation process is simplified greatly and control precision improved remarkably.

During the test, the distance of multi-axis motion test model center deviating from the wind tunnel axis when the attach angle  $\alpha$  motions from  $-15^\circ$  to  $+35^\circ$  is as shown in Figure 10.

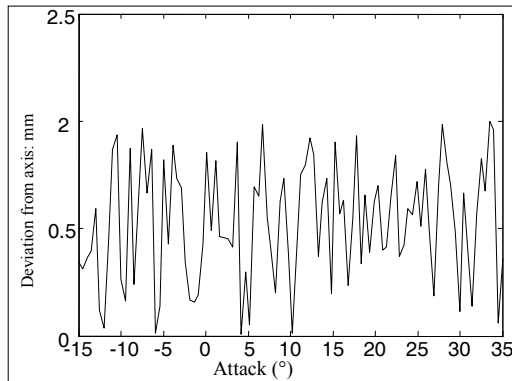


**Figure 10.** Distance away from axis of wind tunnel

#### 4.2 Multi-axis follow-up control approach with virtual $\alpha$ rotation axis as principal axis (sideslip angle $\beta \neq 0^\circ$ , working condition of constant $\beta$ and variable $\alpha$ )

To keep  $\beta$  be a constant angle other than  $0^\circ$ , the forward/backward  $\beta$  shall made follow-up compensatory motion and the four axes make combined motion in addition to variation of  $\alpha$  angle by way of linkage of  $\alpha$  mechanism and Y-direction mechanism. Firstly, the virtual  $\alpha$  rotation axis rotates at the ideal angular velocity required by the attack angle and is located precisely at the target position. During the rotation of the virtual axis, the dynamic target position of all mechanisms can be worked out according to the position and motion velocity relationship among the attack angle  $\alpha$  screw mechanism, Y-direction lifting mechanism and forward/backward  $\beta$  mechanism; in this way, the position follow-up of attack angle  $\alpha$ , Y-direction lifting mechanism and forward/backward  $\beta$  mechanism can be implemented by control the axes. See Figure 11 for the calculation block diagram of multi-axis position follow-up.

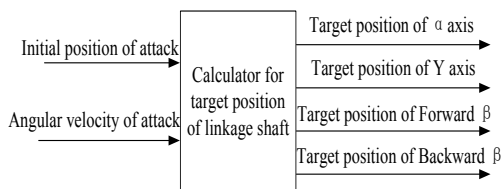


**Figure 11.** Calculation block diagram of multi-axis motion follow-up

## 5 Test result and analysis

As shown in Figure 12, the precision error of attach angle of sting support is less than  $0.01^\circ$ , superior to the design requirements.

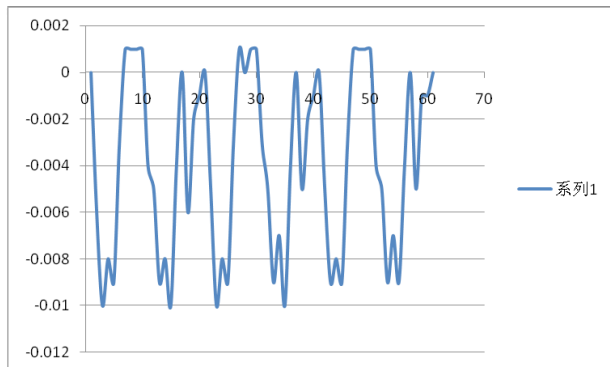


**Figure 12.** Test data of attack precision

As shown in Figure 13, the precision error of the forward sideslip angle is less than  $0.015^\circ$ , satisfying the design requirements.

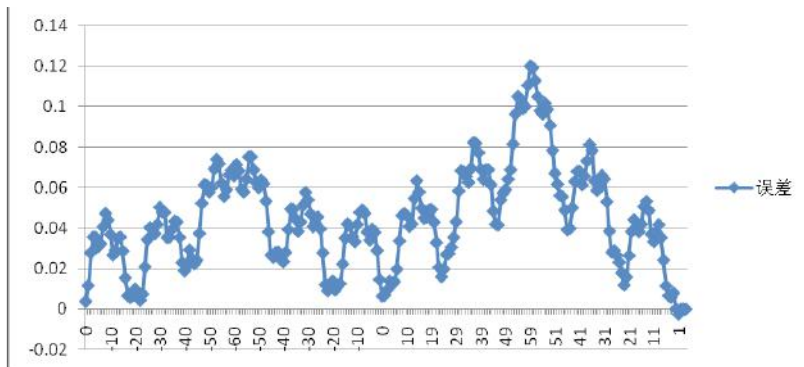


**Figure 13.** Test data of  $\beta_1$  precision

As shown in Figure 14, the precision error of the backward sideslip angle is less than  $0.01^\circ$ , superior to the design requirements.

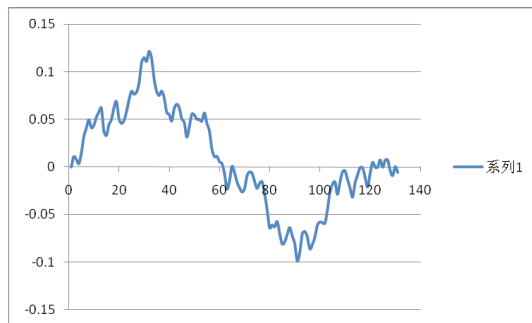


Figure 14. Test data of  $\beta_2$  precision

As shown in Figure 15, most of linkage test data of the sideslip angle is better than  $0.02^\circ$ ; most of linkage test data of the sideslip angle is better than  $0.02^\circ$ .

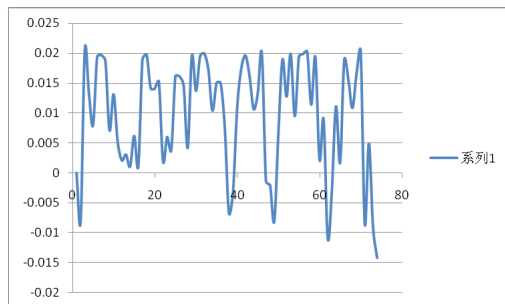


Figure 15. Test data of  $\beta_1$  and  $\beta_2$  precision

Y-direction precision is as shown in Figure 16. Considering that the measured absolute zero may be changed to  $-0.05$ , the precision is up to the design requirement.

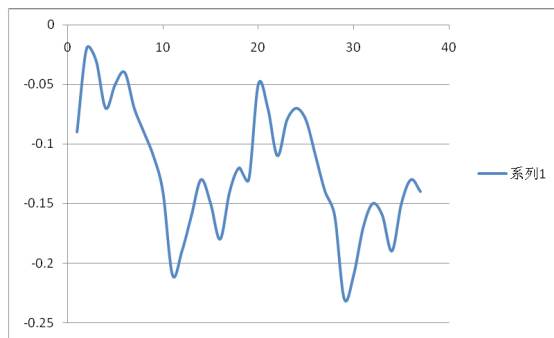


Figure 16. Test data of Y axis precision

## 6 Conclusion

For a sting support control system, a mountain of mathematical operation as required by conversion between straight-line motion displacement at different DOF and target angles is omitted by way of building a virtual axis and data fitting with measured data, and the operation process is simplified greatly. By measuring with highly-precise test apparatus, a mapping relationship is built between the actual straight line displacement value at different DOF and the attitude angle variable of the actual model, and corresponding function relationship is obtained by interpolation and data fitting; in this way, the mechanism machining error, installation error and calculation error may be reduced greatly and control precision improved. Introduction of new control approaches (including virtual axis, electronic camshaft) may facilitate implementation of synchronous control and bring about proper synchronicity. During the operation of mechanisms, the occurrence of accidents such as uneven stress, undue vibration and tunnel wall touching of mechanism will be minimized by monitoring the parameters and specifications in real time, like operation synchronicity of the axes, angle variation uniformity, and deviation of model center from the wind tunnel axis. According to the test results of function, safety and technical specifications of sting support system, the System is proved to be comprehensive, safe and reliable, and most of its specifications are up to even superior to the design requirements.

## References

- [1] Liu Yanpeng, Motion Control New Technology and its Application [J]. Equipment Manufacturing Technology, 2009(8).
- [2] Wu Lin, Tan Ying, Motion Control Technology Development and Prospective [J]. Machine Tool & Hydraulics, 2011, 35(7):231-233.
- [3] Tian Yu, Servo and Motion Control System Design [M]. Beijing: Posts & Telecom Press, 2010.05.
- [4] Wu Jun, Design and Application of Multi-axis Motion Control System [D]. Shanghai: master degree thesis of Shanghai Jiaotong University 2011.02.
- [5] Fan Liuqun, Real-time Ethernet and Motion Control Bus Technology [M]. Shanghai: Tongji University Press, 2009:194.
- [6] Yuan Jiping, Liu Hailiang, Research of Digital PID Control Algorithm [J]. Aerospace Control, Oct.2010, 28 (5):9-11.
- [7] Siemens. Siemens S7-300 System Reference Manual [M]. Beijing: Siemens Automation & Drives Group, 2012:10-200.
- [8] Xiao Liangliang, Design of Multi-axis Synchronous Motion Control System Based on Virtual Axis Approach [D]. Zhejiang: Master degree thesis of Zhejiang Sci-Tech University, 2009.12.
- [9] Zhao Haibo, Zhou Xianghong, Smart PID Control of Dual-Motor Synchronous Linkage Servo System [J]. Journal of Tongling University, 2009, (1):89-91.
- [10] Chen Yonghong, Zhu Congqiao, Li Jing, et al. Analysis and Research Concerning Variable Parameters PID Controller [J]. Micro-computer Information, 2005, (10): 47-48.
- [11] Islam S, Liu X P. Robust Sliding Mode Control for Robot Manipulators [J]. IEEE Transactions on Industrial Electronics, 2011, 58(6): 2444-2453. [107]

- [12] Yun S, Cho HS. Application of Adaptive Model Following Control Technique to a Hydraulic Servo System Subjected to Unknown Disturbances [J]. *J Dyn Syst Meas Contr*, 1991, 113:479-486.
- [13] PHELAN R M. Automatic Control System [M]. New York: Cornel University Press, 1997.
- [14] Kolhe J P, Shaheed M, Chandar T S, et al. Robust control of robot manipulators based on uncertainty and disturbance estimation[J]. *International Journal of Robust and Nonlinear Control*, 2013, 23(1): 104-122. [106].
- [15] Bascetta L, Rocco P. Revising the Robust-Control Design for Rigid Robot Manipulators [J]. *IEEE Transactions on Robotics*, 2010, 26(1): 180-187.

Ping ZHOU\*, Qiang LUO, Wei-kai HUANG, Zheng-hua GU

## Development of Control System of Icing Wind Tunnel

**Abstract:** A 3m×2m Icing Wind Tunnel is a continuous transonic wind tunnel where icing test and conventional aerodynamic test can be conducted. In the wind tunnel, several systems are arranged and control system is complicated, and the total pressure, air speed and temperature control systems are featured by long-time delay, non-linearity and strong coupling properties. To meet the performance requirements of control system, controlled system of wind tunnel are analyzed. According to the analysis results, PROFINET industrial real-time network technology is applied toward wind tunnel control system and corresponding design scheme is worked out, and the characteristics are analyzed. In addition, appropriate control strategy is put forward for flow field parameters multi-variable control system. According to the commissioning process and effects, it is proved that the wind tunnel control system can satisfy the performance and specification design requirements of the wind tunnel.

**Keywords:** icing wind tunnel; control system; PROFINET; industrial real-time network; Control Strategy

### 1 Introduction

Icing Wind Tunnel is important test equipment via which aircraft icing mechanism and relevant theoretical research can be conducted, influence of different icing patterns and ice accumulation process upon the aerodynamic characteristics of aircrafts is researched, so as to ensure flight safety of the aircrafts under icing weather condition. Meanwhile, in the Icing Wind Tunnel, aircraft low Reynolds number test can be conducted. Therefore, it can meet the subsonic aerodynamic test requirements for the high-altitude aircrafts (airfoil, semi-scale model and full-scale model )[1-3].

Compared with conventional wind tunnels, the Icing Wind Tunnel is equipped with several and large-scale systems (some of them have thousands of control I/O nodes) and internal control of subsystems is complicated. There exists coupling between the flow field pressure, wind speed and temperature control system in the Icing Wind Tunnel, therefore, such System is deemed as a typical MIMO system with non-linearity, large time delay and strong coupling property. A spraying system may exert strong interference upon the total pressure, temperature and wind speed

---

\*Corresponding author: Ping ZHOU, China Aerodynamics Research and Development Center, Mianyang city Sichuan Province, China, E-mail: cardczp@163.com

Qiang LUO, Wei-kai HUANG, Zheng-hua GU, China Aerodynamics Research and Development Center, Mianyang city Sichuan Province, China

control system. Furthermore, according to the requirements, the Icing Wind Tunnel can be used to conduct low-temperature high Reynolds number test by corresponding operation control modes, in addition to icing test.

Through development of the Icing Wind Tunnel Control System, the following key technologies are addressed:

- Due to large quantity and large size of systems arranged in the Icing Wind Tunnel, a distributed control scheme is used for it. However, concentrated real-time control function shall be provided to meet the requirements of flow field multi-variable control to hardware platform.
- The "concentrated control + distributed control" scheme is used to achieve remote closed-loop control of network. The network system shall be of real-time, punctuality and reliability, so as to facilitate implementation of flow field multi-variable control strategy.
- The control strategy for Non-linearity, large time delay, and strong coupling MIMO system.

This Paper, in light of the features and requirements of the control system of the Icing Wind Tunnel, provides the overall design scheme applying PROFINET technology toward the control system, and introduces the design idea concerning the wind tunnel flow field parameter control strategy. In addition, this Paper sets forth the actual effect which verifies the feasibility of design scheme of control system.

## 2 Controlled Systems and Requirements of Icing Wind Tunnel

The layout of Icing Wind Tunnel is as shown in Figure 1 [1,2]. It is mainly composed of fan system, altitude simulation system, cooling system, spraying system, anti/de-icing system, humidification system, model support system, etc.

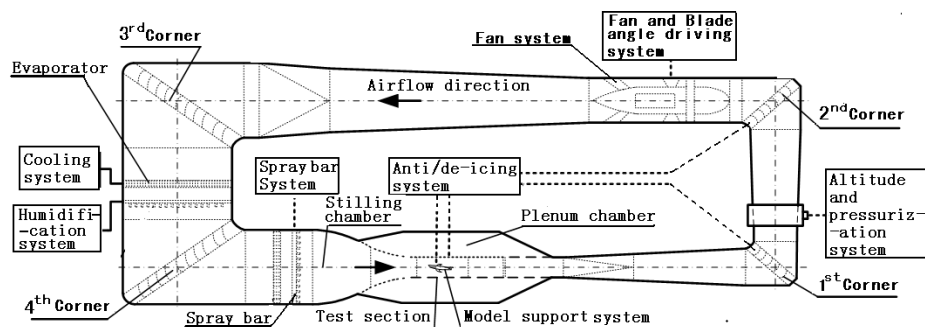


Figure 1. The layout of Icing Wind Tunnel

## 2.1 The technical specifications and requirements

The technical specifications and the requirements of wind tunnel are as follows:

- Max. wind speed: main test section: 210m/s, second test section: 78m/s; high-speed test section: 256m/s. Wind speed control accuracy: better than 0.3%.
- Altitude simulation: maximum altitude: 20000m. Altitude control precision: control accuracy better than  $\pm 100\text{Pa}$ , in the range between local elevation to 7000 meters. Accuracy better than  $\pm 50\text{Pa}$ , in the range between 7000 meters to 20000 meters.
- Temperature range: ambient temperature  $\sim -40^\circ\text{C}$ . Temperature control accuracy: better than  $\pm 0.5^\circ\text{C}$ .
- Liquid water content: 0.2~3g/m<sup>3</sup>. Median Volumetric Diameter(MVD): 10~300μm.
- Humidity control range: 70%~100%, in the range between  $-15^\circ\text{C}$  to  $-20^\circ\text{C}$ , and 100% in the range between  $-20^\circ\text{C}$  to  $-40^\circ\text{C}$ . Humidity control accuracy:  $\pm 5\%$ .
- Control precision of attitude angle of test model: better than  $0.02^\circ$ . The maximum move speed:  $2^\circ/\text{s}$ .
- Hot air deicing system, mass flow rate control precision: 2g/s; pressure control accuracy:  $\pm 0.005\text{MPa}$ ; temperature control accuracy:  $\pm 5^\circ\text{C}$ .

## 2.2 Controlled systems description

Wind tunnel operation control refers to control upon the following systems [2,3]:

### 2.2.1 Fan system

The Fan system is composed of fan and its drive system, with the power of motor output axis being 6000kW, rated rotation speed of motor being 475rpm, maximum rotation speed 600rpm. The fan blade pitch angle is adjustable when it is in shutdown, with adjustment range between  $-20^\circ$  to  $+20^\circ$ , adjustment positioning accuracy better than  $\pm 6'$ .

The Fan system is used to control air speed. The system objects include: inverter system, variable blade pitch angle mechanism, cooling fan of electric motor, motor stator internal anti-dew electrical heater and automatic grease-filling system. The system can monitor the axis temperature, vibration, motor temperature and other status. Siemens-ROBINCON perfect harmonic-free series of HV frequency converters are used. Control of air speed is implemented via adjustment of fan speed. Both altitude simulation system and spraying system can impose influence upon the air speed control system.

### 2.2.2 Altitude simulation system

Altitude simulation system is mainly used to control pressure of air in the Icing Wind Tunnel, thus simulating different altitudes. The System is composed of vacuum pump set (water ring pump + roots pump), piping, valves and relevant control units. The water ring pump set adopts inverter speed control and coordinates with the air make-up regulating valves on the main inlet piping. It is mainly used to simulate vacuum pressure control when the altitude < 7000 meters (39kPa). The vacuum pump set, consisting of roots pumps and water ring pumps, is used to vacuum pressure control when the altitude is between 7000 meters to 20000 meters < 7000m (39kPa~5kPa).

Two 2BEC72A and one 2BEA203 are used as water ring vacuum pump and four LQ2500 and one LQ600 air-cooling roots pump are used as roots pump.

To match up various working conditions in the system, air make-up regulating valves with different nominal diameters are arranged on the air inlet main pipes of the vacuum pump set and are used to control the vacuum pressure in the wind tunnel by coordination with the vacuum pump set.

The controlled objects mainly cover: variable-frequency speed regulating control of vacuum pump set, flow rate control of air make-up regulating valves, cooling of vacuum pump set and monitoring of softened water. The spraying system, cooling system and fan system will impose influence upon the altitude control system.

### 2.2.3 Cooling system

The cooling system is mainly used to control total temperature at stable stage in the wind tunnel. This system involves startup, operation energy level control of refrigerating compressor unit; control of lubricating oil station (used to lubricating the refrigerating compressor unit) and of auxiliary systems like cooling water circulation system; control of ammonia liquor circulation pump set; control of liquid supply electromagnetic valves, return-gas electromagnetic valves; electric regulating valve system subject to low-pressure circulation air suction pressure closed-loop control; in the way, operation safety interlocking of the system is implemented.

The maximum refrigerating capacity of the cooling system is 11000kW (temperature at the evaporator outlet: -30°C), the minimum refrigerating capacity: 330kW. Such system is composed of 12 compressor drives and auxiliary systems. The temperature in the wind tunnel is regulated by controlling the compressor units and low-pressure circulation cylinder air suction pressure. Fine control of temperture is implemented by controlling the low-pressure circulation cylinder suction pressure (to adjust the energy levels of compressor units).

### 2.2.4 Spraying bar system

The Spraying Bar System (SBS) is used to simulate the cloud and mist environment aircrafts pass through under which the cloud layer contains super-cooled water

drops. The SBS is able to generate water droplets with diameters (MVD) and Liquid Water Content (LWC). Furthermore, the system is capable to generate Super-Cooled Large droplets (SLD),with the range of freezing drizzle conditions.

The SBS consists of spraying bars, water supply subsystem, air supply subsystem and control subsystem. The SBS has 20 bars. Each bar is equipped with 50 spraying nozzles, totaling 1000 nozzles. Each nozzle water supply line is equipped with a solenoid valve that can be remotely switched on and off. Nozzles can be controlled independently, and by controlling the proportion of air supply pressure to the water supply pressure,can meet requirements for any combination and implement different cloud & mist parameters.

Two types of nozzles can be replaced mutually to form MVD covering 10~300 $\mu\text{m}$ . The system's controlled objects include: water and gas heater system, more than 50 valves of water and gas lines, 1000 solenoid valves.

### **2.2.5 Anti/de-icing system**

Anti/de-icing system falls into: hot air de-icing system and electrical deicing system. The former is used to Anti/de-icing the wind tunnel parts and aircraft, so as to ensure test is conducted successful. The later is used to conduct aircraft anti/de-icing test.

The aircraft anti/de-icing system currently provided mainly includes: hot gas anti-icing system, aerodynamic de-icing boot system and aerodynamic pulse de-icing boot system. Different systems put forward different requirements for mass flow, pressure and temperature of output hot gas, and all require precise control. The system is typical multi-variable control system.

### **2.2.6 Humidification system**

The system controls the humidity in the wind tunnel through controlling the temperature of water and gas heaters and regulating the flow rate and pressure. Humidity control range: 70%~100% (-15°C~20°C), 100% (-20°C~40°C).

### **2.2.7 Model support mechanism system**

The model support mechanism has been designed in order to support the model weight and the aerodynamic loads generated by model aircraft. It includes upper and lower turntable mechanism, yaw angle mechanism and pitch angle mechanism equipped for primary test section. Lower turntable mechanism, yaw angle mechanism and pitch angle mechanism equipped for secondary test section. Left/right turntable mechanism and sting support mechanism for high-speed test section.

The controlled mechanisms vary from the test sections. Motion controllers will be used to achieve the synchronous control strictly of the related angle mechanisms.

### 2.2.8 Wind tunnel auxiliary system

Readiness of wind tunnel auxiliary system is the essential interlocking condition precedent for startup of wind tunnel. This system is composed of variable diffuser widened angle system, plenum chamber lifting platform and its hydraulic system, aerated sealing gas control system (gate and wicket of plenum chamber, gate of stilling chamber, variable diffuser front/rear flange and variable diffuser sealing ring) and gas distribution system.

## 3 Overall Design of Control System of Icing Wind Tunnel

For the coupling between the flow field control system, such scheme integrating the characteristics of distributed control system and centralized control system shall be applied toward the control system architecture.

In light of the features, the control system employs the overall architecture scheme of PROFINET-based control system. By this scheme, the control system can combine the advantages of the distributed control system and centralized control system in terms of performance.

### 3.1 PROFINET performance [4-12]

PROFINET (Process Field Net) is updated automatic bus criteria based on industrial Ethernet technology put forward by PROFIBUS International (PI). Such technology, by combining the automation technology and Ethernet network technology, can integrate other profibus system on a seamless basis. It is a complete network resolution available in the automation field, and covers real-time Ethernet, motion control, distributed automation, fault safety and cyber safety technologies, and can be completely compatible with the industrial Ethernet and existing profibus technology as cross-vendor technology.

PROFINET supports three communication modes: TCP/IP protocol communication, real-time (RT) communication; IRT communication.

#### *a) TCP/IP communication*

TCP/IP and IT protocol is applied based on Ethernet technology. It can meet wind tunnel management-level (such as wind tunnel operation management level or wind tunnel information-based system) communication requirements, with response time about 100ms.

#### *b) RT communication*

PROFINET provides an optimized real-time communication channel based on Ethernet Layer 2, as shown in Figure 2. By using such real time channel, data processing time in communication stack is shortened greatly, thus improving the automated data

refresh rate. The typical response time of real-time communication is between 5 ~10ms, satisfying the requirements for data exchange among sensors, executors and controllers.

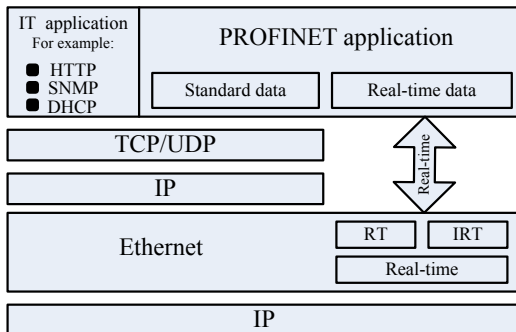


**Figure 2.** Operating mechanism of PROFINET

### c) IRT communication

IRT function of PROFINET is provided by embedded ERTECT synchronous RT exchange chip on Layer 2. This hardware-based IRT communication resolution can ensure sufficient time accuracy while a large quantity of data is transmitted; meanwhile, the communication task of the processor on PROFINET equipment can be eased. In case of 100 nodes, the response time is less than 1ms, jitter error less than 1μs, in this way, punctual and defined response can be supported.

## 3.2 Overall design of control system

Trunk network of the control system of Icing Wind Tunnel is of distributed control system network structure built with PROFINET industrial Ethernet. The trunk network is of optical fiber transmission media and ring-network structure, as shown in Figure 3 [13]. The entire control system architecture is divided into three layers: wind tunnel operation management layer, network layer and subsystem execution layer. The wind tunnel core control PLC and local controllers of subsystems are connected to the trunk network of the control system via switch with synchronous real-time communication function. The subsystem controllers are used to implement operation control and safety interlocking of local subsystems according to the instructions from the wind tunnel core control PLC.

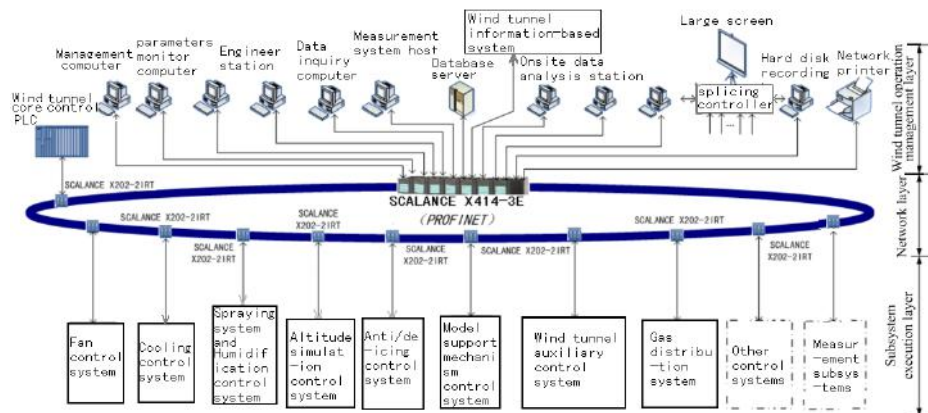


**Figure 3.** Block diagram of control system network of icing wind tunnel

Configuration and function design of the system is set forth below [13].

### 3.2.1 Design of wind tunnel operation management layer

Design contents include: wind tunnel core control PLC, wind tunnel test run supervisory computer, engineer station, operation monitor, database server, data analysis station, measurement system host, projection & display system, etc.

Wind tunnel test run supervisory computer is mainly used to prepare and publish wind tunnel control missions and monitor important wind tunnel parameters and status. Such supervisory computer publishes the test missions (working conditions) to the “wind tunnel core control PLC” which implements dispatching control of subsystems (as shown in Figure 3). In addition, it forwards the wind tunnel operation data from the wind tunnel “core control PLC” to the database server for storing (as shown in Figure 4). Both the supervisory computer and operation monitor acquire wind tunnel operation data from the wind tunnel “core control PLC” via TCP/IP communication.

S7-400PLC is used as wind tunnel core control PLC. It, as the Controller of the PROFINET I/O Device/Controller communication mode, communicates with subsystems in RT communication, thus implementing operation control and safety interlocking of the wind tunnel.

The engineer station is used for programming of subsystem, program debugging, maintenance or monitoring upon several systems during the test via PROFINET network.

Database server is used to enable network server and database functions; namely, storing and inquiring of test control data, parameters, measured data and parameters, status information parameters and fault information. In addition, the

database server can output various data curve, time sequence and reports as per specified requirements.

Data analysis station provides the aerodynamic staff or user with test data for analysis and processing.

### **3.2.2 Design of network layer**

Network layer is composed of main switch and sub-switches via which subsystems are connected to the trunk network.

Main switch is provided with IRT webmaster function, and supports PROFINET, integrate with redundancy management function and supports layer 3 exchange technology, VLAN technology, SNMP, web-based management and PROFINET diagnosis functions. Thanks to supporting VLAN technology, the main switch can define different VLANs to prevent data network broadcast storm and improve cyber reliability. The sub-switch is equipped with IRT switch module, with two 10/100Mbit/s RJ45 ports, two 100Mbit/s multi-modulus BFOC interfaces, and it is provided with fault signal indicating function, connection setting buttons, redundant power supply input, PROFINET IO design and network management function. Therefore, ring network functions can be provided.

Also, such network supports TCP/IP, RT and IRT communication, satisfying the system requirements for different communication modes.

### **3.2.3 Design of execution layer of subsystems**

Internal network of subsystems can be configured independently based upon actual requirements, and is controlled on a concentrated basis by local controller of subsystems. Local controller communicates with the wind tunnel core control PLC via RT communication (PROFINET I/O Device/Controller communication mode) for concentrated control and management.

Internal expansion of subsystems mainly includes: Ethernet network, Profibus, Profibus-DP Drive and Modbus. Profibus-DP Drive bus is used to support motion control system (TCPU controller is used).

See Figure 4 and Figure 5 for schematic diagram of instruction and data transmission among systems and composition diagram of measurement & control software.

According to above, the design scheme is provided with the following characteristics:

- To support several communication protocols and satisfy the different requirements at different layers.
- Be of ring network structure, optical fiber communication, to improve reliability of network control.

- To combine the advantages of concentrated control & management and distribute control, with functions superior to conventional distributed control system.

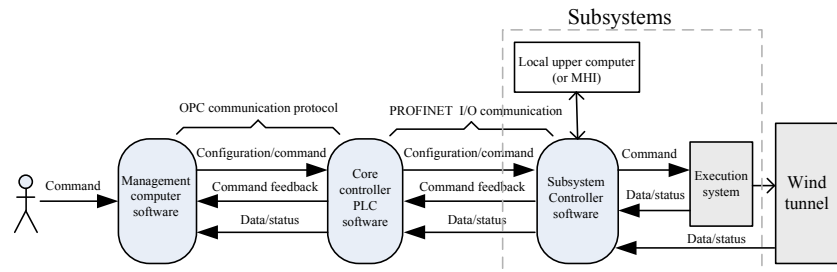


**Figure 4.** Schematic diagram of data flow direction among systems

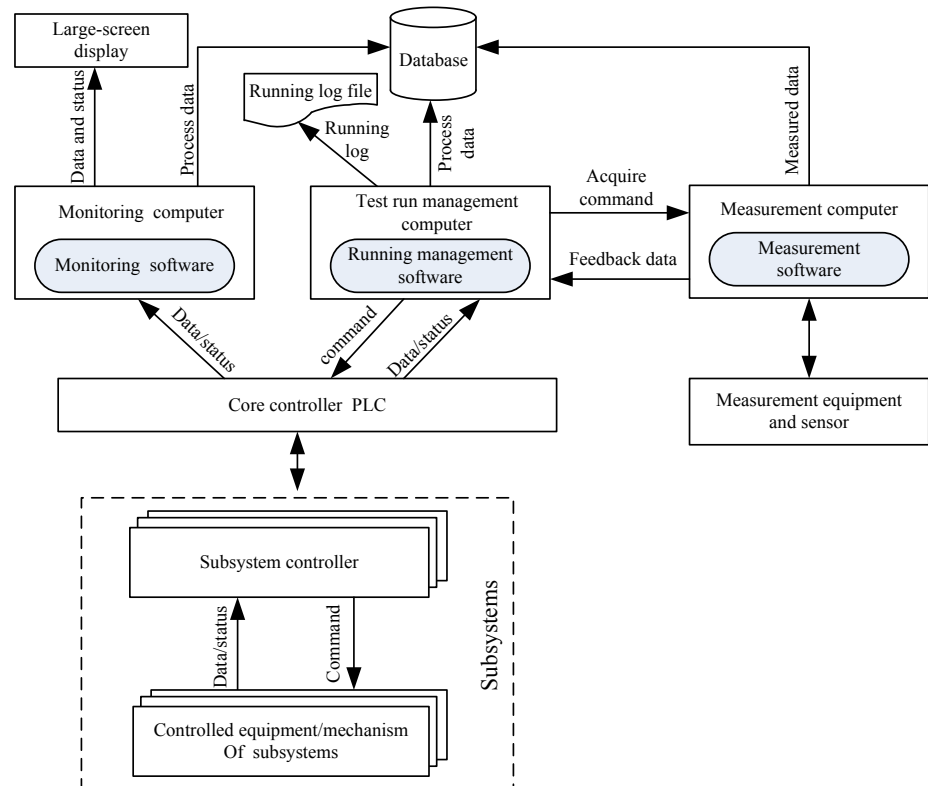


**Figure 5.** Composition of measurement & control system software

## 4 Control Strategies of Wind Tunnel Flow Field Parameters

Wind tunnel test run control is currently divided into three operating models: icing (anti/de-icing) test run, ambient temperature test run; high-altitude low Reynolds number test run.

Under icing (or anti/de-icing) test run operating model, control system is made to control the wind speed, altitude (total pressure) and total temperature(at stilling chamber); cloud & mist parameters are controlled by combination of large-size and small-size nozzles and regulating of water and gas pressure and temperature. If model anti/de-icing test is conducted, the model anti/de-icing control system needs to be put into tuning. Both the altitude control system and temperature control system are featured by long-time delay, the wind speed, altitude and temperature control system is a MIMO coupling system. In addition, when the spraying system starts to work, it may impose different influence upon the wind speed, altitude simulation and temperature control system. However, flow field parameters as required by tests shall be get stable rapidly.

Ambient temperature test run and high-altitude low Reynolds number test run operating model are mainly used to conduct force test. For offset heat generated by fan system, the cooling system shall work. High-altitude low Reynolds number test requires the altitude simulation system to participate into pressure control, and the following working conditions shall be implemented: constant pressure (constant altitude), stepped variable wind speed for force test; constant pressure (constant altitude), constant wind speed and continuous or stepped variable model attitude for force test, etc. For coupling between wind speed control and pressure control, speediness and stability of wind speed and pressure shall be addressed during the stepped variable control of wind speed. During the regulation of wind speed and total pressure, temperature control shall meet specified control precision requirements, so as to ensure the repeatability of the test.

In relation to control strategy, the control algorithm of conventional control theory for the long-time delay system and multi-variable system generally relies upon transfer function [15]. However, transfer functions focus on the objects described by linear ordinary differential equations. For the controlled system with severe non-linearity and time-varying properties, it can be expected that sound control effect can not obtained. According to the characteristics of the Icing Wind Tunnel, we, based on references [14,16-26], utilizes the “open-loop stability” feature of the flow field for the design of control strategy, and divide the flow field control process into “startup establishment process” and “fine tuning process”. In this way, the complicated multi-variable decoupling algorithm is decomposed into single-variable control algorithm, and the coupling is deemed as disturbance, so as to improve the system’s robustness and resolve the coupling issues, thus implementing precise control upon flow field parameters.

For control on “start establishment process” of flow field, the required target value obtained through test is corresponding to “preset” control target value of relevant systems. System coupling will not be considered for control at this stage. In light of establishment time of system corresponding parameters and through time sequence scheduling, the systems can be controlled according to the “preset” control target value, then switched to the “fine tuning process” after establishment of the flow field.

Intelligent PID or self-adaptive control algorithm that is of increment cascade control structure is used for the “fine tuning process”, so as to improve the system’s robustness and implement precise control upon flow field parameters.

With further commissioning, if the required target value obtained through test is corresponding to the “preset” control target value of relevant systems, expert knowledge-based can be built, thus building a intelligent control system based on expert knowledge.

Control block diagrams of total pressure (simulation altitude), wind speed and temperature are as shown in Figure 6, 7 and 8. The intelligent controller as shown in the figures below is used to enable the “knowledge-based” to calculate the “preset” control target value of relevant systems based on the given target value, and automatically complete switch between “start establishment process” and “fine tuning process” and intelligent PID algorithm according the parameters change. Its software functions are implemented jointly by relevant subsystem controllers and “wind tunnel core control PLC”, therefore, the cyber communication will be subject to the higher requirements of punctuality and reliability.

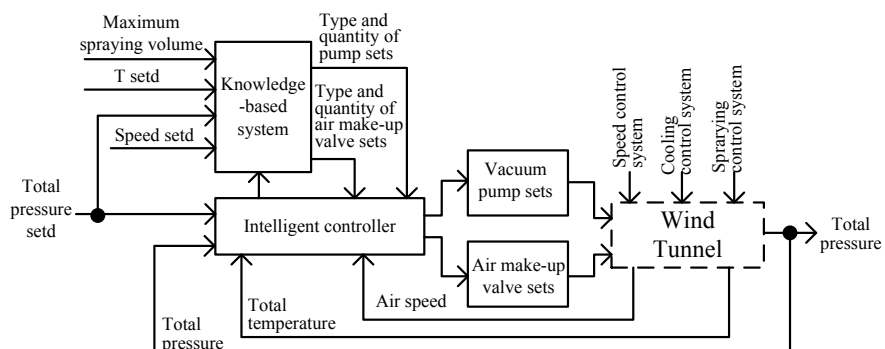


**Figure 6.** Block diagram of total pressure (altitude) control system

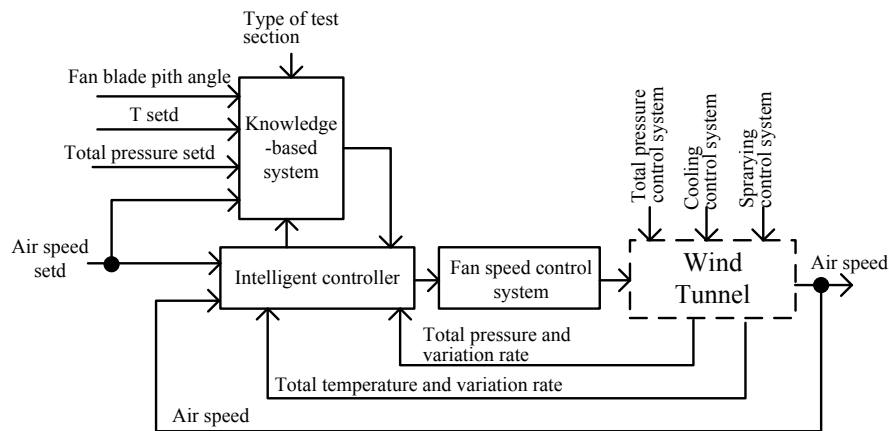


**Figure 7.** Block diagram of wind speed control system

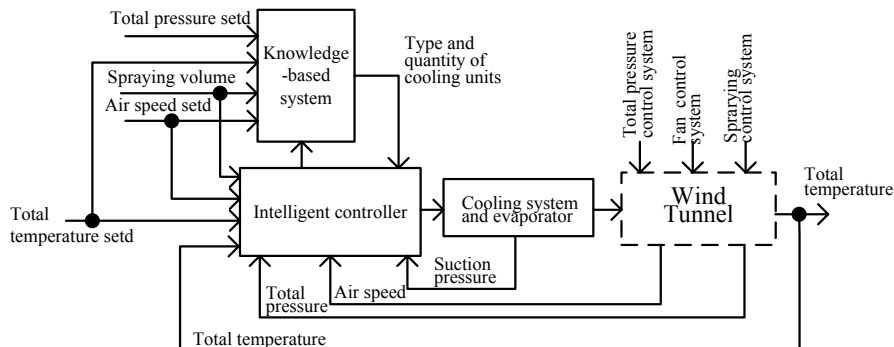


**Figure 8.** Block diagram of total temperature control system

## 5 Control Commissioning

Ventilation test for the Icing Wind Tunnel was deemed successful in July 2013, and the first icing test was conducted in October of same year. From July 2013 to date, we have been conducted commissioning of control system. During the commissioning, the control network system has been operated stably and reliably, without any fault. Control software is developed in convenient and rapid manner. Control strategy of flow field control can meet all specification requirements. Icing test effect of aerofoil front-edge is as shown in Figure 9, and the flow field parameter control response curve (wind speed: 35m/s; total pressure: 39kPa, total temperature: -20°C) during

control commissioning is as shown in Figure 10 [13]. After the air speed, total pressure and the total temperature stability, the air speed changed, the flow field parameter response curves is as shown in Figure 11. The Control commissioning results shows the precision of total pressure, wind speed and total temperature is superior to design requirements.



Figure 9. Airfoil icing test

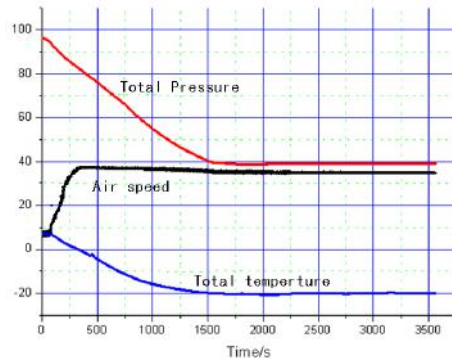


Figure 10. The process parameter response curves

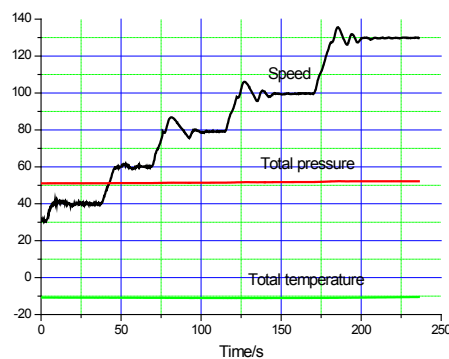


Figure 11. The flow field parameter response curves when speed changed

At present, we have completed the primary commission of wind tunnel and are conducting further and optimization commissioning.

## 6 Conclusion

Based on the actual conditions and effect of commissioning of icing tunnel control system, it can be concluded that:

- Distributed control system based on IRT network is superior to conventional distributed control system and can integrate distributed control and concentrated control. Thanks to application of ring network structure and optical fiber transmission, the cyber reliability is improved, thus satisfying the requirements of large-size systems and correlative multi-variable control systems.
- PROFINET, by supporting various communication protocols, can achieve consistent communication from management layer to equipment layer. It has advantages including succinct, reliable structure and sound openness.
- Control process is divided into “star establishment process” and “fine tuning process”. By using smart control strategy based on expert knowledge, the multi-variable coupling control of flow field parameter can be implemented successfully. With further commissioning, the “knowledge-based” can be improved and optimized continuously, thus optimizing the flow field parameters control performance specifications.

## References

- [1] Qiang PENG, Cheng FU, Technical Specifications for 3m×2m Icing Wind Tunnel Design [R], EJ-4-2011043, 2008.
- [2] Xiao Bin, Lai Huan, Technical Conditions for 3m×2m Icing Wind Tunnel Control System Design [R], EJ-4-2011044, 2010.
- [3] Ping ZHOU, Preliminary Proposal for 3m×2m Icing Wind Tunnel Control System Design [R], EJ-4-2013163, 2010.
- [4] Ferrari. P, Flammini. A, Vilturi. S., Performance analysis of PROFINet networks[J], Computer Standards & Interfaces, 2006, 28(4), 369-385.
- [5] Robertinit, A. PROFINET: the Future of the Ethernet 2 Based Automation[D], IPLnet Workshop, 2003.
- [6] Popp M., PROFINET 2 linking words[A], 2011 8th IEEE International Conference on[C], 2001, 519-522.
- [7] Liu Guohai, Li Kangji, Xue Wenping, et, al., Field Bus PROFINET[M], Beijing: Electronic Industry Press, 2007, pp. 15-17.
- [8] Cui Jian, Siemens Industrial Ethernet Communication Guideline (Volume Two) [M], Beijing: China Machine Press, 2007, pp. 200-204.
- [9] Profibus International. PROFINET IO Part 5: Application Layer Service Definition[S]. Version 1.0: 2004.

- [10] Profibus International. PROFINET-Connect all Fields[J]. Instrument Standardization and Metrology, 2001(2):24-27.
- [11] CHEN Hai-dong, PROFINET-Ethernet Fieldbus Solutions to the Future-oriented Automation[J], Maschinen Markt, 2004(12), pp. 34-361.
- [12] Sun Rong, Su Li, Lv Shuping, et.al. Design and Research of PROFINET Control System [J], Research and Exploration in Laboratory, 2014, 33(4), pp. 103-107.
- [13] Ping ZHOU, Summary of 3m×2m Icing Wind Tunnel Control System R&D Technologies [R], EJ-4-2013199, 2013.
- [14] Ping ZHOU, Dong Yixin, et.al. Research of Control Strategy of 2.4m Wind Tunnel M Number and Total Pressure at Stable Section [J], Fluid Mechanics Test and Measurement, 2001, 15(1), pp. 75-81.
- [15] Wang Yongchu, Decoupling Control System [M], Chengdu: Sichuan Press, 1985:10-80.
- [16] Arustrong E., Tripp J. S., An Application of Multivariable Design Techniques to The Control of The National Transonic Facility[R], NASA TP 1887, pp. 212-220, 1983.
- [17] Charles S. Bryant, The National Transonic Facility Data System Complex[R], NASA CP-2122, Part II, 1980, pp. 287-297.
- [18] James A. Osborn, A Description of The National Transonic Facility Process Control System[R], NASA CP-2122, Part II, pp. 249-258, 1980.
- [19] Joseph F. Guarina, Instrumentation Systems for The National Transonic Facility[R], NASA CP-2122, pp. 281-286, 1980.
- [20] Bruce, Walter E. Jr., Blair B. Gloss., The U.S. National Transonic Facility, NTF[R], N90- 15942, pp. 231-350, 1990.
- [21] Mckinney, Linwood W., Operation Experience With The National Transonic Facility[R], AGARD CP-348, pp. 320-330, 1980.
- [22] Bruce, Walter E. Jr., National Transonic Facility Shakedown Test Result and Calibration Plans[R], AIAA Paper, pp. 84-584, 1984.
- [23] Kern, Frederick A., Knight, Charles W., National Transonic Facility Mach Number System[R], IS Paper, pp. 85-174, 1985.
- [24] Fuller, D. E., Testing Experience With The Nation Transonic Facility[R], AIAA, Paper, pp. 86-748, 1986.
- [25] A. F. Pels, Closed-Loop Mach Number Control in A Transonic Wind Tunnel[J], Journal A. 30(4), 1989, pp. 25-32.
- [26] Li Shiyong., Fuzzy Control: Neural Control and Smart Control Theory [M], Harbin: Harbin Industry Press, 1996, pp. 241-248.

Chen LU, Hai-min YU, Zhen-wei YU, Kun-jie CHEN\*

## Railway Track Collapse Monitoring System in Mining Area based on KALMAN Filter

**Abstract:** Facing on the phenomenon of railway track collapse in mining areas, Basing on KALMAN filter, a kind of railway track collapse monitor system was proposed in this study. Firstly, the basic design principle of the system was analyzed. Secondly, MEMS gyroscope and GPS module were used as attitude measurement components, adopting PLC to collecting real-timing sampling of gyroscope and GPS information, customizing Windows CE operating system of ARM to control the whole system. What is more, the data of gyroscope and GPS were fusion by using KALMAN filter method on MATLAB software. The test results showed that the system has accurate readings in the flat and bumpy road, Besides, the system can feedback the results effectively when the angle error is more than 0.4 degrees. The system conformed to the index of railroad track dynamic detection in China, which can be widely used in railway track subsidence monitoring.

**Keywords:** track collapse; gyroscope; KALMAN filter; MATLAB; angle error

### 1 Introduction

Railway track transportation has an irreplaceable role in our daily life. Track collapse may cause the train run unstably and create serious accidents [1]. In remote areas, ordinary artificial static test was low efficiency and the period of calling large track inspection vehicle was too long, which could not meet the requirement of the safety production. What is more, multiple sensor components and complex algorithm in most detection system cannot apply for the track collapse test [2,3]. This article designed a low cost portable track collapse monitoring system and related algorithms. In the end, the system experiment was proposed to verify the effect.

---

\*Corresponding author: Kun-jie CHEN, College of Engineering, Nanjing Agricultural University, Nanjing 210031, China, E-mail: kunjiechen@njau.edu.cn

Chen LU, Hai-min YU, Zhen-wei YU, College of Engineering, Nanjing Agricultural University, Nanjing 210031, China

## 2 The hardware and software design of the system

### 2.1 The Overall Structure of the System

Track collapse monitoring system consists of three parts, acquisition unit, storage unit and data process unit. Firstly, system collected angles and corresponding location information through MEMS gyroscope and GPS module by means of PLC. Secondly, PLC sent the test data to the Win CE system ARM through serial port. What is more, KALMAN algorithm was used to make the data fusion and remove noise [4, 5] on personal computers. Finally, the analysis data of track collapse situation were shown on screen. Figure 1 is the overall structure of the system.

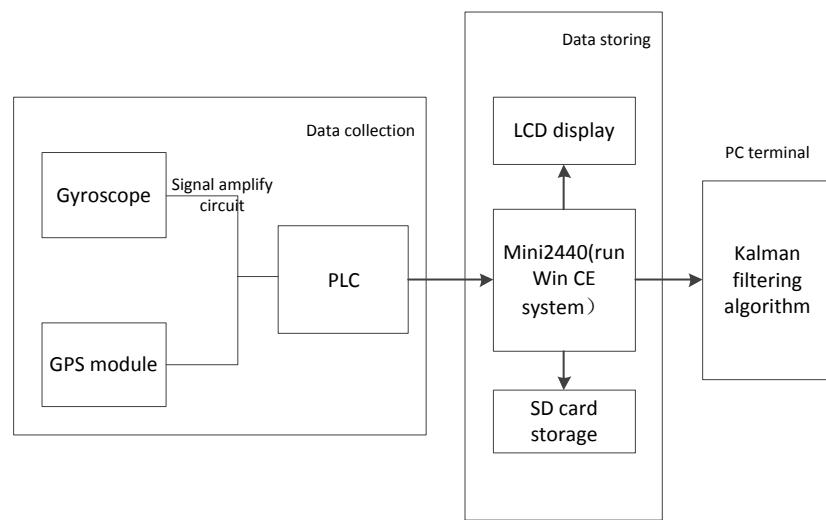


**Figure 1.** The overall structure of the system

### 2.2 Hardware design

The accuracy of system depends on the performance of gyroscope sensor and GPS module [6]. System chose LPMS-CU gyroscope and TIANBAO BD970 GPS module after thinking of comprehensive factors. Latitude and longitude information that GPS transfer back can be directly collected by PLC [7]. It is no need to have signal amplification, which only need to demodulation for location information in the PLC program. But the gyroscope signal is relatively weak. So it is important to design signal amplification circuit [8] on gyroscope. Circuit diagram designed was shown in Figure 2.

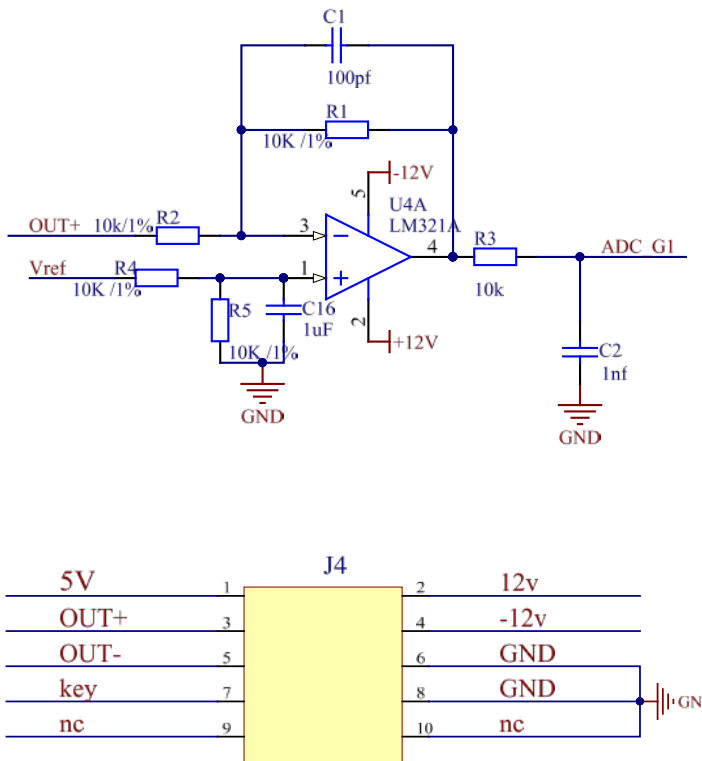


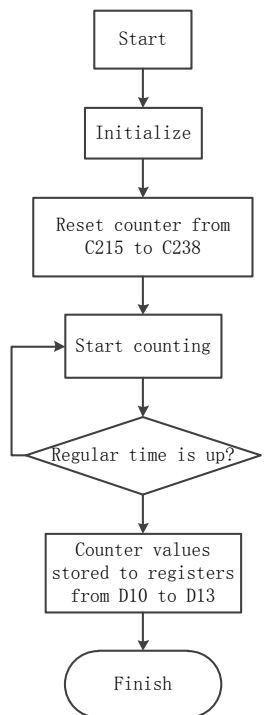
Figure 2. Signal amplification circuit diagram

### 2.3 Software design

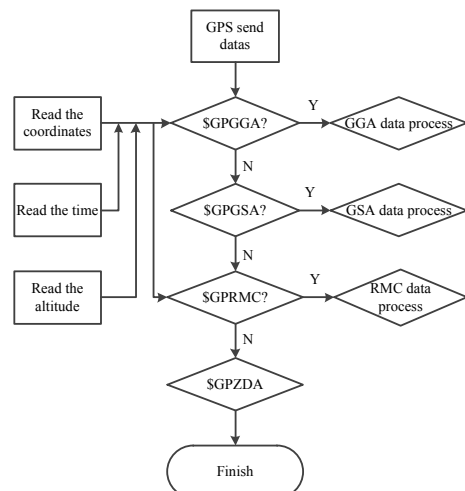
Software design includes three parts: Custom Windows CE operating system, PLC data acquisition program, KALMAN filtering algorithm.

Firstly, system board completed custom Windows CE operating system by a series of processes, which includes installing drivers and system components.

PLC data acquisition program was written through a software named GX Developer. The program accomplished the acquisition of gyroscope and GPS information. Two signal information was required to be collected at period of 0.2 seconds. Internal registers range from D10 to D13 were used to store data signals. The flow chart of PLC data acquisition was shown on Figure 3a. The data communication between PLC and GPS is another important part. Data communication must obey NMEA 0183 protocol [9]. GPS receiving data was transformed to PLC through serial port according to the NMEA 0183 protocol. Coordinates, time and altitude were output regularly by means of sequential control method. Figure 3b told us the details.



(a) PLC data acquisition



(b) GPS communication

**Figure 3.** The flow chart of signal management

KALMAN filter algorithm (optimization regression data processing algorithm) obtained optimal value angle by fusing the measured value of GPS and gyroscope. If we want to estimate the actual angle values of k time, we need to predict the angle of k time according to the angle value of k-1 time [10,11]. And then system calculated the Gaussian noise according to the predicted angle of k time [12]. Finally, the KALMAN filtering algorithm continually did recursive variance to the end. The formulas were derived according to the method above.

$$X(k|k-1) = AX(k-1|k-1) + BU(k) \quad (1)$$

$$P(k|k-1) = AP(k-1|k-1)A^T + Q \quad (2)$$

$$K(k) = P(k|k-1)H^T / (HP(k|k-1)H^T + R) \quad (3)$$

$$X(k|k) = X(k|k-1) + K(k)(Z(k) - HX(k|k-1)) \quad (4)$$

The formulas above were updated equation of KALMAN filter. A and B were state transition matrix. K was KALMAN gain. Z(k) was the observation matrix and H was parameter matrix. We performed the KALMAN filtering algorithm through MATLAB software on PC terminal System, which can eliminate the gyroscope drift and noise reduce noise, so as to optimize angle value through KALMAN filtering algorithm.

### 3 System experiment

#### 3.1 Experimental method

Experiment Chose flat and bump roads instead of the railway track and equipped sensors on the car. Car speed ranges from 1m/s to 1.5 m/s, Both running distance were ten meters and sampling period were 0.2 seconds. Three experiments were carried out in respectively three days. Each test was able to detect both direction Angle and location information. Finally, drawing the conclusion by using KALMAN filter algorithm on the computer.

#### 3.2 Experimental result

1. Firstly, dedicated level protractor was used to measured the static values of sampling points before the system test. Three measurements made the average to determine the scope of the system angle adjustment.
2. Afterwards, setting sample frequency of 5 Hz after the system run smoothly. Three experiments were carried out in respectively three days to get the measuring values of corresponding position coordinates.

3. Finally, data was uploaded to the computer and system obtained the absolute error values of corresponding position coordinates(the difference between readings after filtering and static values) and covariance value of the system by means of KALMAN algorithm. Covariance value determines the system precision. The smaller covariance value is, the higher system precision will be. The absolute errors value determines whether the collapse is out of limits. In case of the measured horizontal Angles, the typical experimental data of horizontal Angle in flat and bumpy roads were showed in the Table 1 and Table 2.

**Table 1.** Horizontal angle measured changes in the flat road test

Coordinates (E 118°57')/ "	44.32	44.33	44.34	44.35	44.36	44.37
Static values/°	3.28	5.15	2.82	3.96	4.46	2.60
Absolute angle/°	0.12	0.19	0.05	0.42	0.21	0.09

**Table 2.** Horizontal angle measured changes in the bumpy road test

Coordinates (E 118°57')/ "	44.41	44.42	44.43	44.44	44.45	44.46
Static values/°	5.77	-17.05	-10.92	26.49	12.18	9.85
Absolute angle/°	0.15	0.45	0.37	0.63	0.22	0.25

Note: covariance value is 0.0048 in the flat road and 0.0036 in the bumpy road.

## 4 Conclusion

This paper designed a set of railway track subsidence monitoring system based on MEMS gyroscope. System design, hardware selection circuit and software algorithm were accomplished in the study. Through the actual system test and the analysis of relevant data, the conclusion is made as follows:

- 1) System mainly obtained gyroscope Angle and GPS location signals by PLC. GPS and gyroscope data were fusion by KALMAN filtering algorithm, which have a good dynamic response in the experiment.
- 2) The system test results showed that the system has accurate readings in the flat and bumpy road. Besides, the system can feedback the results effectively when the angle error is more than 0.4 degrees, The system conforms to the index of railroad track dynamic detection in China, which can be widely used in railway track subsidence monitoring.

**Acknowledgment:** First of all, I would like to thank to my tutor professor Kun-jie CHEN for his care and train in two years. From the topic selection, learning to use a new instrument and design to the final paper writing, professor Chen devoted a

great deal of effort and energy to give me a lot of advice and guidance. Afterwards, Thanks to my family, thanks to my lab partner that gave me help in the process of the experiment. It is because of your help and support, I can overcome all difficulties and doubt until the smooth completion of this paper. Finally, I would like to thank to the science and technology support plan funded project of Jiang Su province.

## References

- [1] Liu Xiaowu. 3D posture sensor design based on MEMS gyroscope [D]. Xi an University of technology, 2014.
- [2] Yong-jun zheng, for tan, etc. The two axis attitude control system based on MEMS sensor design and test [J]. Journal of agricultural engineering, 2015, S1:28 to 37.
- [3] Fang Luping Gao Kun, Pan Qing, Cao Ping, etc. Puncture surgery navigation system design based on gyroscope [J]. Journal of Zhe Jiang University of technology, 2016, 02:129-133.
- [4] King Zhu Jingfu. Custom Windows CE system and USB camera driver design [J]. Journal of heilong jiang August first land reclamation university, 2014, 06, 97-100.
- [5] Wang Xinguo. Portable rail check-out car [D]. Nanjing university of science and technology, 2008.
- [6] Ren Yi south. Based on the modern testing technology of high speed railway curve state evaluation and whole is method [D]. Southwest jiaotong university, 2014.
- [7] Li xiang, Jiang Zhaohui, Liu Yuanzhou, wei, etc. Based on the micro sensor array hive temperature monitoring and analyzing system [J]. Journal of sensors and micro systems, 2015, 11:63-65 + 68.
- [8] Joe, Du Puxuan Li Hu, etc. Based on the attitude of the MEMS accelerometer and gyroscope test system [J]. Journal of railway computer applications, 2012, 03:15-18.
- [9] Qiao, jiang li jie, Yale, etc. Based on single chip microcomputer of GPS/MEMS gyroscope heading Angle in real time measurement system [J]. Journal of sensing technology, 2011, 06, 919-922.
- [10] Lou Gang, Li Wei, Deng Xuebo. Small signal amplifier circuit design [J]. Journal of Zhe Jiang university of technology, 2007, 6:661-664.
- [11] Wang Juan, Ren Bowang, Wei Xing. Embedded wireless video transmission system based on Windows CE design [J]. Journal of hunan agricultural machinery, 2012, 01, 63-64.
- [12] Zhang Fung, Chen Xinlin.GPS receiver and the realization of serial communication between PC computer [J]. Journal of technology and innovation management, 2009, 01, 99-101.
- [13] Tension, king. Labview with mitsubishi PLC implementation of serial communication [J]. Micro computer and application, 2013, 12:51-53.
- [14] Cao Hui Liang, Hong Shengli, Shou Rongwang, et al. MEMS gyroscope structure model and system simulation [J]. Journal of Chinese inertial technology, 2013, 2013:524-529.
- [15] Li Jie, Wen Dongzhang, Ya Lei. Kalman filtering method based on time series analysis in the application of MEMS gyroscope random drift error compensation study [J]. Journal of sensing technology, 2006, 5:2215-221

Xiao-ming LI, Jia-yue YIN\*, He-zuo QU, Cheng-qiong BI, Hao-jun XU,  
Li ZHU

## The Method of Harmonic Source Identification in Power Supply System

**Abstract:** With the continuous expansion of the scale of the grid, more and more new electrical equipment and precision equipment access to electricity power system, and they have inject a large amount of harmonic power grid, the problem is very prominent. Since the system harmonic source numerous and dispersed, this make accurate measurement become a difficult problem, and in order to make a fair price in electricity charges, This is closely related to the harmonic source identification. In order to solve this problem, This paper proposes the method based on harmonic source identification, and through calculation and analysis of the fundamental and harmonic by separation. Analyzing the harmonic power flow in measurement point, and it can provide a basis for reasonable electricity charges in measure harmonics bilateral energy. This paper has create a digital simulation to show its correctness and feasibility.

**Keywords:** Harmonic Source; Harmonic Source Identification; Power Flow; Digital Simulation.

### 1 Introduction

Power system harmonics are periodic functions by Fourier series decomposition, those components' angular frequency are  $n$  times to the fundamental angular frequency [1]. Under the presence of harmonics in the power system, the linear load electricity metering points, and the power metering is the fundamental power plus the harmonic power. While in the non-linear load energy metering point, the power metering is the fundamental power minus the harmonics power. According to the different harmonic currents flowing judge this load branch harmonic power of positive and negative, and then judge the true harmonic power generation side and consumption side [2,3]. In this paper, the relevant research lack of harmonic interference on electric energy metering, research on harmonic source identification, and propose the method based on harmonic source identification, and it can be able to solve complex power system

---

\*Corresponding author: Jia-yue YIN, Power System and Automation, School of Electrical Engineering, Wuhan University, Wuhan, China, E-mail: 1162484454@qq.com

Xiao-ming LI, He-zuo QU, Cheng-qiong BI, Hao-jun XU, Li ZHU, Power System and Automation, School of Electrical Engineering, Wuhan University, Wuhan, China

energy metering which have large errors. And effectively identify sources of harmonic power in grid load branch, accurate identification of harmonic source. This method is feasible and effective.

## 2 The method of harmonic source's harmonic power identification

In order to analysis the nonlinear network of the distribution of power relations, using the harmonic power flow to distinguish harmonic source. Established linear load and nonlinear load equivalent network, as it shown in Figure 1.

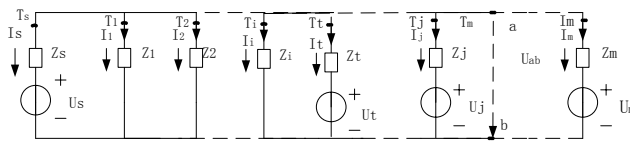


Figure 1. The equivalent model network of linear load and nonlinear load

The network that only harmonic source work is shown in Figure 2.

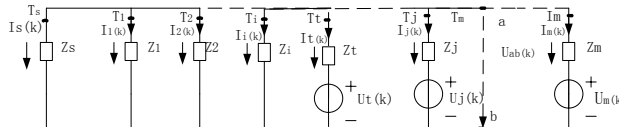


Figure 2. The network that only harmonic source work

There is a total of  $m$  branches in Figure 2, among them, the power supply system branch is  $T_S$  branch and linear branch is  $T_i$  ( $i = 1, 2, 3, \dots, t$ ) branch. And  $Z_i = R_i + jX_i$ , nonlinear branch is  $T_j$  ( $j = t+1, \dots, m$ ) branch. And  $T_j$  branch where nonlinear equivalent harmonic source  $U_{j(k)}$  and equivalent impedance  $Z_{jk}$  ( $Z_j = R_j + jX_j$ ),  $k$  represents the number of harmonics, and  $k=2,3,\dots,n$ .  $U_{ab(k)}$  representatives the voltage between two points a and b in  $k$  harmonic.

According to circuit theorems.

$$U_{ab(k)} = \frac{\sum_{j=t}^m \frac{U_{j(k)}}{Z_{j(k)}}}{\sum_{j=t}^m \frac{1}{Z_{j(k)}} + \sum_{i=1}^{t-1} \frac{1}{Z_{i(k)}} + \frac{1}{Z_{s(k)}}} \quad (1)$$

Branch current in power system:

$$I_{s(k)} = \frac{U_{ab(k)}}{Z_{s(k)}} \quad (2)$$

Its system power active power consumption:

$$P_{s(k)} = I_{s(k)}^2 R_s \quad (3)$$

The current of linear branch  $T_i (i = 1, 2, 3, \dots, t)$ :

$$I_{i(k)} = \frac{U_{ab(k)}}{Z_{i(k)}} \quad (4)$$

The linear branch active power consumption of each branch:

$$P_{i(k)} = I_{i(k)}^2 R_i \quad (5)$$

The current of non-linear branch  $T_j (j = t+1, \dots, m)$ :

$$I_{j(k)} = \frac{U_{ab(k)} - U_{j(k)}}{Z_{i(k)}} \quad (6)$$

The nonlinear branch active power consumption of each branch:

$$P_{j(k)} = U_{ab(k)} I_{j(k)} \cos(\theta_{u_{ab(k)}} - \theta_{I_{j(k)}}) \quad (7)$$

The system power working alone is shown in Figure 3.

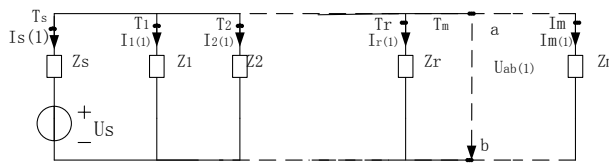


**Figure 3.** The circuit diagram of power system working alone

Among them,  $U_s$  is system power,  $r$  represents branch,  $r=1,2,3,\dots,m$ . According to circuit theorems,

$$U_{ab(1)} = \frac{\frac{U_s}{Z_{s(1)}}}{\frac{1}{Z_{s(1)}} + \sum_{r=1}^m \frac{1}{Z_{r(1)}}} \quad (8)$$

Active power consumption in power system  $U_s$  branch:

$$P_{U_s} = U_{ab(1)} I_{s(1)} \cos(\theta_{U_{ab(1)}} - \theta_{I_{s(1)}}) \quad (9)$$

The current in other branch  $T_r (r = 1, 2, \dots, m)$ :

$$I_{r(k)} = \frac{U_{ab(k)}}{Z_{r(k)}} \quad (10)$$

Active power consumption in other branch:

$$P_{r(k)} = I_{r(k)}^2 R_r \quad (11)$$

In expression of active power consumption in linear load,  $P_{i(k)}$  and  $P_{r(k)}$  are positive. Description linear user consume fundamental power from the power system. And

also absorb harmonic power; In linear load branch, harmonic power from the grid side to the user side. Active power consumption in nonlinear loads,  $P_{r(k)}$  is positive, it means that nonlinear user consume fundamental power from the power system;  $P_{j(k)}$  is negative, it means that nonlinear user feedback harmonic to the grid, thus, the branch  $T_j$  have harmonic source.

By analyzing these results, it can get further harmonic source identification method by harmonic power flow: Judging by the direction of harmonic power flow in measurement point, if the harmonic power flows from the power system to the load branch, the load branch is not have harmonic source. Conversely, if harmonic power from the load side to the power system, it is determined that the load branch have harmonic source [4,5].

### 3 The digital simulation of harmonic power identification

For ease of calculation, set the number of branches to four, the simplified model shown in Figure 4.

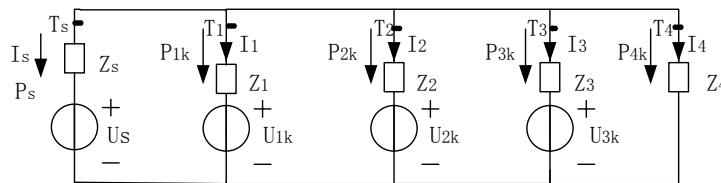


**Figure 4.** The circuit diagram of harmonic power flow identification

Among them,  $Z_s = R_s + jX_s$  is equivalent impedance of system source,  $Z_i = R_i + jX_i$  is equivalent impedance of load branch 1,  $Z_2 = R_2 + jX_2$  is equivalent impedance of load branch 2,  $Z_3 = R_3 + jX_3$  is equivalent impedance of load branch 3;  $U_{1k}$ ,  $U_{2k}$  and  $U_{3k}$  respective for the three branches of the load harmonic voltage;  $T_1$ ,  $T_2$  and  $T_3$  are power metering points;  $U_s$  is system source, only produce the fundamental voltage [6,7]. Each module parameters in Figure 4 are as follows:

$$\begin{aligned} f_0 &= 50\text{Hz} ; \omega_0 = 2\pi f_0 = 100\pi ; \omega_3 = 3\omega_0 = 300\pi ; \\ \omega_5 &= 5\omega_0 = 500\pi ; U_s = 220\sqrt{2}\sin(100\pi t) ; \\ U_{1k} &= 100\sqrt{2}\sin(300\pi t + \frac{\pi}{3}) ; U_{2k} = 20\sqrt{2}\sin(500\pi t + \frac{\pi}{5}) ; \\ U_{3k} &= 100\sqrt{2}\sin(300\pi t + \frac{\pi}{3}) + 20\sqrt{2}\sin(500\pi t + \frac{\pi}{5}) ; R_s = 6\Omega ; \\ R_1 &= 2\Omega ; R_2 = 1\Omega ; R_3 = 1\Omega ; R_4 = 1\Omega . \end{aligned}$$

Modeling results of fundamental and harmonic current in each branches [8,9], are as it is shown in Table 1; And each of branches of power consumed by the fundamental and harmonic power [10,11], as it is shown in Table 2.

**Table 1.** The fundamental and each harmonic currents in Measuring point

Load branch	Fundamental wave	3rd harmonic	5th harmonic
s(A)	-35	6.82	1.82
1(A)	5	-29.55	5.45
2(A)	10	40.91	-9.09
3(A)	10	-59.09	-9.09
4(A)	10	40.91	10.91

**Table 2.** Active power consumption of fundamental and each harmonic in Measuring point

Load branch	Fundamental wave	3rd harmonic	5th harmonic
s(W)	-350	278.93	19.83
1(W)	50	-1208.68	59.50
2(W)	100	1673.55	-99.17
3(W)	100	-2417.35	-99.17
4(W)	100	1673.55	119.01

According to Table 1 and Table 2, in the fundamental wave, the measuring point are  $T_s, T_1, T_2, T_3, T_4$ . Only fundamental power in  $T_s$  is negative, while fundamental power in  $T_1, T_2, T_3, T_4$  are positive. Explanation only the branch  $T_s$  have the fundamental source, other branch doesn't have the fundamental source. The sum of active power consumed by branches  $T_1, T_2, T_3, T_4$  is equal to active power issued by  $T_s$ . In the fundamental source of the active power consumption in branches  $T_s, T_1, T_2, T_3, T_4$ , algebraic is the 0. In the 3rd harmonic, 3rd harmonic power in  $T_1, T_3$  are negative, while 3rd harmonic power in  $T_s, T_2, T_4$  are positive. Explanation the branches  $T_1, T_3$  have 3rd harmonic source,  $T_s, T_2, T_4$  doesn't have the 3rd harmonic source. And in the 3rd harmonic source of the active power consumption in branches  $T_s, T_1, T_2, T_3, T_4$  algebraic is the 0. In the 5th harmonic, 5th harmonic power in  $T_2, T_3$  are negative, while 5th harmonic power in  $T_s, T_1, T_4$  are positive. Explanation the branches  $T_2, T_3$  have 5th harmonic source,  $T_s, T_1, T_4$  doesn't have the 5th harmonic source. And in the 5th harmonic source of the active power consumption in branches  $T_s, T_1, T_2, T_3, T_4$  algebraic is the 0. Then, the comprehensive analysis, the  $T_s$  branch only have the fundamental source, the branch  $T_1$  only have the 3rd harmonic source, the branch  $T_2$  only have the 5th harmonic source, the branch  $T_3$  have both the 3rd harmonic source and the 5th harmonic source, the branch  $T_4$  doesn't have any harmonic source or fundamental source. This is consistent with the parameters that have set, thus verifying the correctness of MATLAB simulation.

## 4 Conclusion

Conclude the analysis results of this paper, we can get the conclusions as follows:

1. Abandon the existing measurement methods based on the total distortion of the waveform to calculate active power consumed by the user, and separate the fundamental wave and harmonic. Refinement analysis of each harmonic power load, and identification system harmonic source.
2. Analyzing the flow of harmonic power measurement point, if the harmonic power from the power grid to the load, the load branch doesn't have harmonic source. On the contrary, if the harmonic power from the load to the power grid, the load branch have harmonic source.
3. In the linear load energy metering point, energy metering power is the fundamental power plus harmonic power. In the non-linear load energy metering point, energy metering power is the fundamental power minus harmonic power.

**Acknowledgment:** This research is financially supported by Scientific and Technological Project of State Grid Hubei Electric Power Company in Xiangyang power company, the coding of State Grid ERP (5215D01502QM).

## References

- [1] Zhao Zhentao, Zhang Dahai, Li Yongsheng, Liu Yang, Sun Deda. The method based on generalized least squares regression inter harmonic source identification. *Power System Protection and Control*, 2013, 15: 36-40.
- [2] Shi Guochao. Research and Implementation of the harmonic source identification. North China Electric Power University (Hebei), 2007.
- [3] Zhao Yong, Shen Hong. Harmonic source identification and its relationship with non-harmonic source separation methods. *Chinese Society for Electrical Engineering*, 200222 (5): 84-87.
- [4] Wang Jianxun, Liu HuiJin, Liu Chunyang. Inter-harmonic source recognition based on harmonic complex criterion. *Electric Power Automation Equipment*, 2013, 07: 63-69+80.
- [5] Feng Lihong. Analysis of harmonic error on the power meter. North China Electric Power University (Beijing), 2008.
- [6] Li Jing, Yang Yihan, Yu Wenbin, Zhang Guoqing, Ning Weihong. Summary of energy measurement system development. *Power System Protection and Control*, 2009, 11: 130-134.
- [7] Wang Yue zhi. Energy measurement technology. Beijing: China, Electric Power Press, 2007.
- [8] Pang Hao, Lidong Xia, Zu Yunxiao. Improved algorithm by application FFT analysis harmonic of power system. *Chinese Society for Electrical Engineering*, 200323 (6): 50-54.
- [9] Sun Hongwei, Li Mei, Yuan Jianhua. Interpolated FFT algorithm for power system harmonic analysis. *High Voltage Engineering*, 200430 (8): 52-55.
- [10] Cui Wei, Li Jianhua, Zhao Juan. Power Supply Network Harmonic flow calculation. *Electric Power Automation Equipment*, 2003, 23(2):11-14.
- [11] Xu Min, Zhang Hongbo. FFT interpolation based on Blankman-harris correction algorithm. *Zhengzhou University learned journal (Engineering Science)*, 2005, 26 (4): 99-101.

Chun-yu WEI\*, Shuai LIU, Wen-da YU, Zhan WANG

## Optimization for the Balancing Cylinder of a 3-DOF Planar Manipulator

**Abstract:** 3-DOF planar manipulator is used for loading and unloading materials and as a accessory for machine tool. A new approach is presented for design and optimization for the balancing cylinder. The working environment of the manipulator is introduced and according to the loading and unloading working processes, path planning is designed and expressed by piecewise function. In a period of motion of the manipulator, every component generates the torque caused by gravity. The static total torque is calculated by the theoretical analysis and kinematics simulation used ADAMS. Then the balancing cylinder is designed and the relevant parameters are optimized. The results show that the method of the optimization is right and effective.

**Keywords:** manipulator; design and optimization; balancing cylinder; static total torque

### 1 Introduction

3-DOF planar manipulator is a special mechanism as a accessory for machine tool to load and unload materials. It is different from general industrial robot because of being installed in the machine, obviously more compact and cheaper. Especially, a numerical control machine mainly processes a class of part, this manipulator will be very suitable for this occasion.

The manipulator consists of big arm, small arm and gripper. The motor and reducer that drive the big arm rotate relative to the base must output big torque because of the gravity of load and every component. So balancing cylinder is very important to neutralize the total torque caused by the gravity of them.

About balancing cylinder, many experts and scholars have conducted a lot of research, and some results have been achieved. These results are very helpful for this research. Jakob Weström presented an automated approach in optimal design of the spring balancing cylinder of an industrial robot using multi-disciplinary and multi-objective design optimization, and the developed methodology was robust and efficient enough for use in the engineering practice [1]. Simon Lessard designed a new medical parallel robot and analyzed its static balancing to enhance the safety

---

\*Corresponding author: Chun-yu WEI, School of Mechanical Engineering, Shenyang Jianzhu University, Shenyang, China, E-mail: weiyu001@163.com

Shuai LIU, Wen-da YU, Zhan WANG, School of Mechanical Engineering, Shenyang Jianzhu University, Shenyang, China

of the proposed robot [2]. In this article, five-bar assembly with torsion springs were presented and its main objective of static balancing is the safety enhancement of the proposed robot structure. Because the static balancing can reduce motor torque, it is very useful for increasing safety in operating mode and the mobility of the robot (by decreasing the motor weight). Professor W.J. Zhang researched on force balancing in robot mechanism design and a force balancing method called adjusting kinematic parameters (AKP) for robotic mechanisms or real time controllable (RTC) mechanisms is proposed [3]. The key idea in the AKP method is that when a system is not in a force balancing status, change of the kinematic parameters can make the system balanced. V. Arakelian proposed a new approach for balancing of spatial parallel manipulators that involves connecting a secondary mechanical system to the initial robot, which generates a vertical force applied to the platform of the manipulator [4]. The suggested balancing mechanism was designed on the base of the multi-loop pantograph linkage introduced between the robot base and the platform. The minimization of the input torques was carried out by constant and variable forces for static and dynamic modes of operation. The study conducted by Alberto Martini dealt with the compensation of gravity loads in closed-loop mechanisms as a possible strategy for enhancing their working performance [5]. Dan Zhang designed dynamic balanced legs that were combined to synthesize parallel mechanisms [6]. These researchers are very enlightening and in this article a 3-DOF manipulator is designed and related parameters are optimized. So the motor and reducer can become much lighter and smaller and the safety can be enhanced.

## 2 3-DOF manipulator and its path planning

The numerical control machines VTC3240 have configured 3-DOF manipulator according to the characteristics of the processed object, as shown in Figure 1. The manipulator designed is 3-DOF planar series mechanism. Panasonic servo motors and reducers are used in three joints. The pneumatic gripper is Schunk imported from Germany. The working process of the manipulator is shown in Figure 2, and can be described as: workpiece conveyor belt moves along vertical paper direction, left side is the placing area for processing parts and right side is the placing area for processed parts, the gripper firstly grab the workpiece to be processed, then moves to the triangle chuck of machine and put it on the right position, at last the manipulator returns to the initial position waiting for processing the workpiece. When the process is over, the manipulator moves to grab the part and put it on the right side of the conveyor belt, and then moves to grab another new workpiece again along the same track.

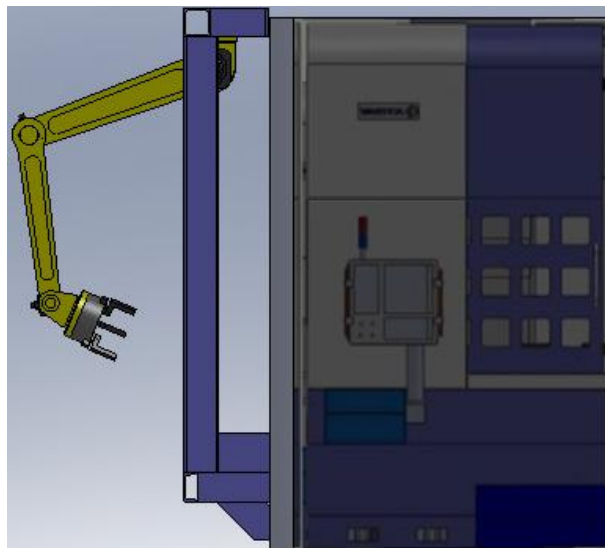


**Figure 1.** VTC3240 and its 3DOF manipulator.

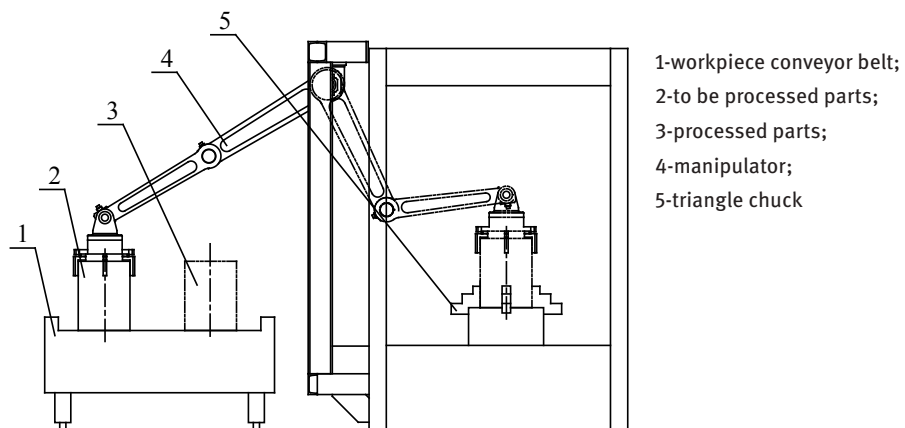


**Figure 2.** Loading and unloading working process.

The manipulator moves to grab the workpiece from original position, then put it on the triangle chuck and then returns back to the original position. This process is a working period. In this period, the trajectory of the gripper palm is “A→B→C→B→A→D→E→D→A”, as shown in Figure 3. The running time of AB, AD, DE are all 3 s, and BC is 4 s, so the full working period is 26 s.

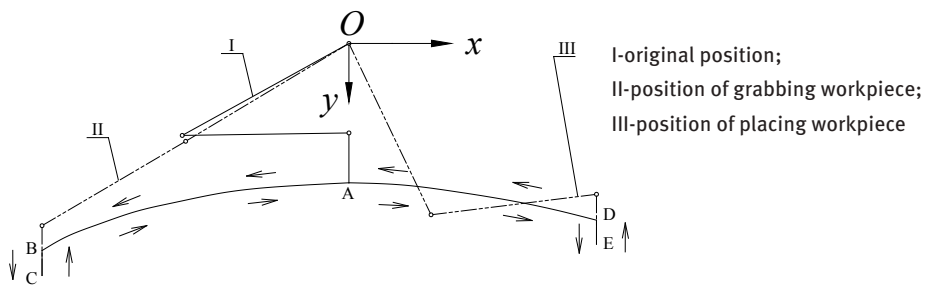


**Figure 3.** Path planning of the manipulator.

According to the characteristics of movement and function of the manipulator, we can make the workpiece always kept upright posture during the movement process of loading and unloading. So if the trajectory coordinates of palm point  $M(x_M, y_M)$  are given, the pose of workpiece during the whole movement process can be obtained. The coordinate system is established according to Figure 3, the motion trajectory equation of point M can be expressed as the form of piecewise function: (unit:m)

$$\left. \begin{array}{l} AB : y_M = 0.1682x_M^2 + 0.6094; \quad x_M \in [-1.255, 0] \\ BC : x_M = -1.255; \quad y_M \in [0.8744, 0.9794] \\ AD : y_M = 0.1459x_M^2 + 0.6094; \quad x_M \in (0, 1.040] \\ DE : x_M = 1.040; \quad y_M \in [0.7670, 0.8679] \end{array} \right\} \quad (1)$$

### 3 Static torque of shaft I

The Figure 3 shows that the manipulator is a three-bar mechanism, upper arm, lower arm and gripper from top to bottom, and the axes of rotation are I, II and III. During the process of loading and unloading, the motion is slow and steady, so although the acceleration at the start of the moment is a little high and should be considered seriously, the servo motor can bear a lot of instantaneous overload and static torque is more important if we want to design and optimize balancing cylinder. According to the related parameters, the instantaneous acceleration can be get by experiment, and the maximum instantaneous dynamic torque can be calculated. If this value is lower than the times of instantaneous overload of servo motor, it is reasonable not to consider this factor. We can calculate static torques of the 3 axes. Among them, the static torque of axis I is maximum, and it is due to the gravity of workpiece, gripper, lower arm, upper arm and all of the motors and reducers.

At any time, the total static torque is formed by every component's gravity acting on the axis I, as shown in Figure 4. Assuming that clockwise is positive and anti-clockwise is negative, equation (2) is obtained:

$$\left. \begin{aligned} M_z &= G_b \cdot x_{cb} + G_{sm} \cdot x_A + G_s \cdot x_{cs} + (G_{hm} + G_h + G_w) \cdot x_B \\ x_B &= x_M \end{aligned} \right\}, \quad (2)$$

where  $M_z$  is the total static torque on axis I,  $G_b$  is the gravity of upper arm,  $x_{cb}$  is the horizontal coordinate of the centre of gravity of upper arm  $C_b$ ,  $G_{sm}$  is the gravity of motor and reducer of axis II,  $x_A$  is the horizontal coordinate of A,  $G_s$  is the gravity of lower arm,  $x_{cs}$  is the horizontal coordinate of the centre of gravity of lower arm  $C_s$ ,  $G_{hm}$  is the gravity of motor and reducer of axis III,  $x_B$  is the horizontal coordinate of B.

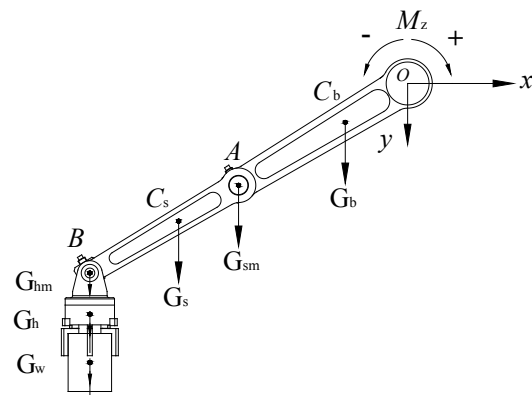


**Figure 4.** Composition of total static torque.

Measure the parameters of each part of the manipulator, as shown in Table 1.  $m_i$  is the mass of every component,  $l_i$  is the length of upper arm and lower arm,  $l_{ci}$  is the distance to O and A from upper arm gravity center and lower arm gravity center.

**Table 1.** Parameters of manipulator model

Every component	$m_i(\text{kg})$	$l_i(\text{m})$	$l_{ci}(\text{m})$
upper arm	32.2	0.80	0.35
lower arm	18.3	0.7	0.32
motor II	10.0	-	-
motor III	6.0	-	-
gripper	30.0	-	-
workpiece	50.5	-	-

The horizontal coordinates of  $B$ ,  $C_s$ ,  $A$  and  $C_b$  are obtained by kinematics simulation according to the target track of the workpiece, in a period, as shown in Figure 5.

And then according to the formula (2), the total static torque around axis I,  $M_z$ , can be obtained, in a period, as shown in Figure 6.

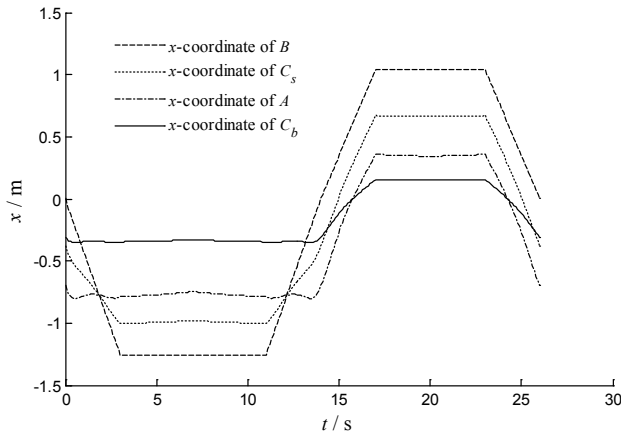


**Figure 5.** x-coordinate of every point during a period.

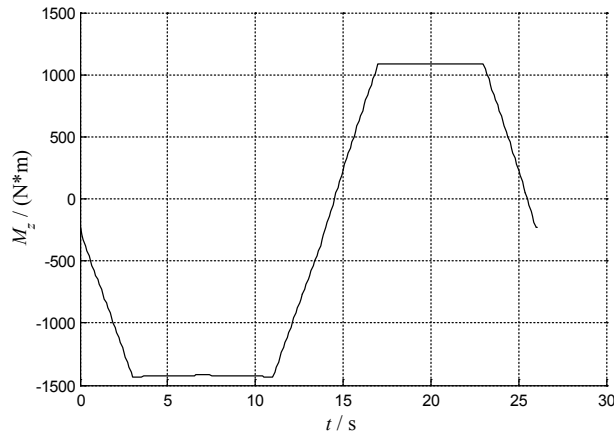


**Figure 6.**  $M_z$  around I axis during a period.

## 4 Parameter design and optimization

According to the installation space of actual device, a balanced cylinder system, as shown in Figure 7, is used. One end of the balancing cylinder is hinged at the  $S$  point, and the other end is hinged at the  $C_b$  point. Theoretically  $S$  point can be change on the whole plane, but considering the actual structure and the symmetry about Y

axis of movement, S point should be located on the Y axis, and its coordinate can be optimized.  $C_b$  point can't be changed and is a constraint condition.

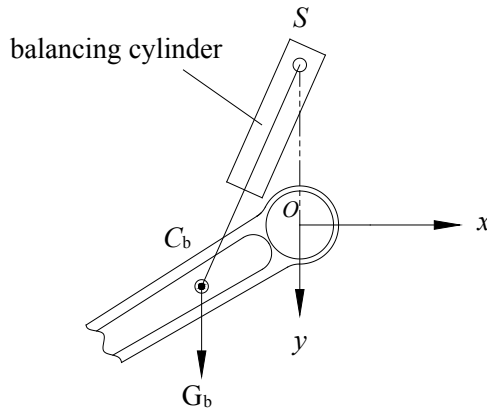


**Figure 7.** The adopted balancing cylinder.

The spring stiffness of the balance cylinder system is determined according to the empirical formula (3) given by the author which is proved to be effective:

$$k \cdot |l_1 - l_2| = |M_{z\max}| - |M_{z\min}| \quad (3)$$

where  $k$  is the spring stiffness;  $l_1$  and  $l_2$  are respectively the distances between point S and  $C_b$  when  $M_z$  reaches the maximum value  $M_{z\max}$  and minimum value  $M_{z\min}$ . Further, establish the objective function to optimize the coordinates of S point:

$$f = \sum_{i=1}^n [k \cdot (\sqrt{x_{cbi}^2 + (y_s - y_{cbi})^2} - l_0) - M_{zi}]^2, \quad (4)$$

where  $n$  represents the number of discrete points in Figure 5 and 6;  $(x_{cbi}, y_{cbi})$  are the coordinates of point  $C_b$  at the  $i$  position in the trajectory, and  $y_s$  is the vertical coordinate of the point S;  $l_0$  is the original length of the balancing cylinder spring;  $M_{zi}$  is the total static torque at the  $i$  position in the trajectory.

The optimization goal is  $f = f_{\min}$ , and then calculate the parameters  $k$  and  $y_s$ . According to the empirical value and actual position of assemble, there are another constraint conditions:  $y_s \in [0.1, 0.5]$  (unit: m).

The program is established and optimized with MATLAB software according to the formula (3) and (4). The result is that  $y_s = 0.312$  m. So we can further get the change curve of balancing cylinder output force  $F_c$ , as shown in Figure 8. The torque  $M_{bc}$  produced by the balancing cylinder on the I axis can be calculated according to the formula (5):

$$M_{bc} = -|F| \cdot \frac{|y_s| \cdot x_{cb}}{\sqrt{x_{cb}^2 + (y_s - y_{cb})^2}} \quad (5)$$

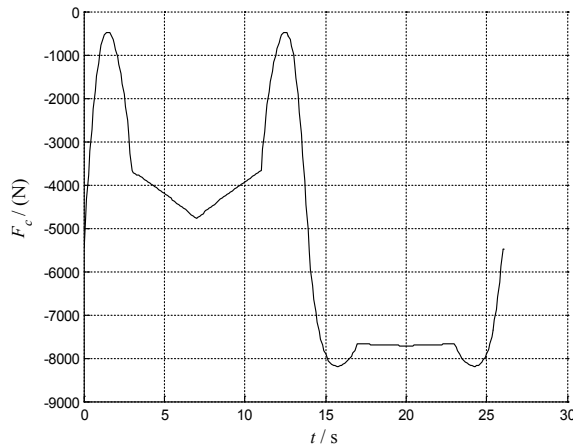


**Figure 8.** Curve of output force of balancing cylinder.

Further, the synthetic moment  $M_{zz}$  on the I axis after adding balancing cylinder can be calculated according to the formula (6):

$$M_{zz} = M_z + M_{bc} \quad (6)$$

The change curve of  $M_{zz}$  in a movement cycle is shown as in Figure 9. Before and after adding the balancing cylinder system the total static torques on the I axis are shown as in Figure 10. We use  $\Delta M$  to express the level of reducing torques needed by balancing cylinder, and the curve of  $\Delta M$  is shown as in Figure 11.

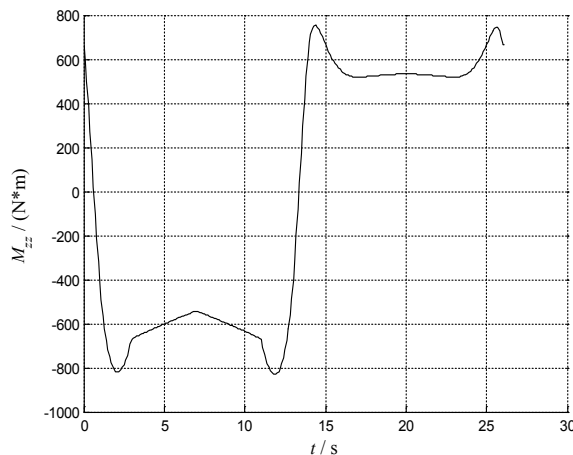


**Figure 9.** Curve of the synthetic moment.

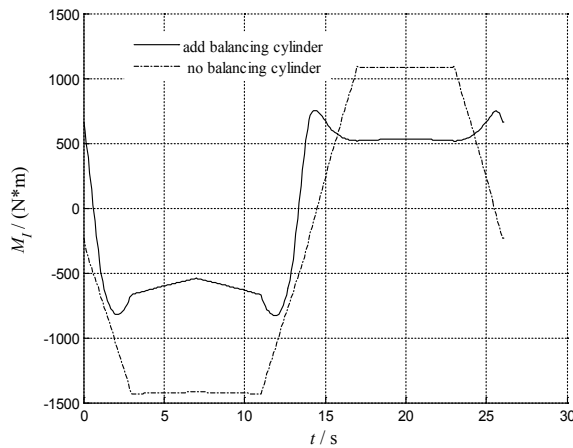


**Figure 10.** Effect of after adding balancing cylinder.

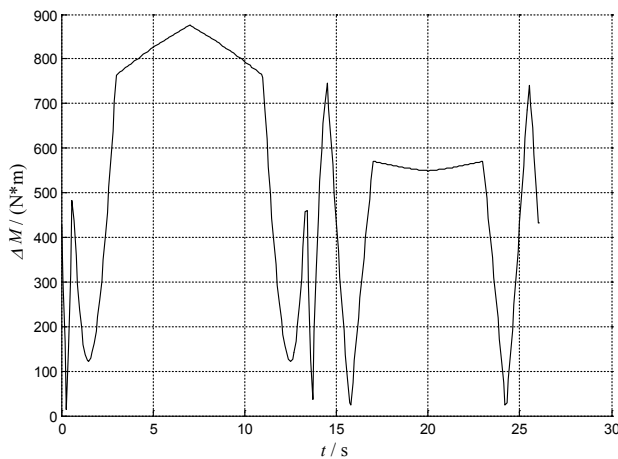


**Figure 11.** Curve of the level of reducing torques.

## 5 Conclusion

In conclusion, aiming at a 3-DOF planar manipulator used for loading and unloading for machine, a method of parameters optimization has been proposed. The simulation results show that the balancing cylinder can effectively reduce total static torque on axis I, so the manipulator can be much lighter and safer. The method of balancing cylinder design and parameters optimization for a 3-DOF manipulator is right and

effective, the whole process of analyzing is complete and can play an important role in development of manipulator for numerical control machine.

**Acknowledgment:** The authors acknowledge the financial support from the scientific research general project of Liaoning Provincial Department of Education of China (L2014236) and Discipline Content Education Project XKHY2-34.

## References

- [1] Jakob Weström, Hans Andersson, Xiaolong Feng, et al, Optimal Spring Balancing Cylinder Design of an Industrial Robot Using Multi-Disciplinary and Multi-Objective Optimization, *Proceedings of the ASME 2012 11th Biennial Conference on Engineering Systems Design and Analysis*, Nantes, France, (2012).
- [2] Simon Lessard, Pascal Bigras and Ilian A. Bonev, A New Medical Parallel Robot and Its Static Balancing Optimization, *Journal of Medical Devices*, 1 (1) (2007) 272-278.
- [3] P. R. Ouyang and W. J. Zhang, Force Balancing of Robotic Mechanisms Based on Adjustment of Kinematic Parameters, *Journal of Mechanical Design*, 127 (5) (2005) 433-440.
- [4] C. Baradat, V. Arakelian, S. Briot, et al, Design and Prototyping of a New Balancing Mechanism for Spatial Parallel Manipulators, *Journal of Mechanical Design*, 130 (5) (2008) 072305:1-13.
- [5] Alberto Martini, Marco Troncossi, Marco Carricato, et al, *Static Balancing of a Parallel Kinematics Machine With Linear-Delta Architecture. Proceedings of the ASME 2014 12th Biennial Conference on Engineering Systems Design and Analysis*, Copenhagen, Denmark(2014).
- [6] Dan Zhang and Bin Wei, Dynamic Balancing of Parallel Manipulators Through Re-configuration, *Proceedings of the ASME 2015 Dynamic Systems and Control Conference*, Columbus, Ohio, USA(2015).

En-de ZHOU, Xi-shun WANG, Hai-tao FANG\*, Kai HE, Ru-xu DU

# **Finite Element Modal Analysis of an Eight-axis Industrial Robot Painting System Applied to Boarding Bridge Painting**

**Abstract:** An eight-axis industrial robot painting system (EIRPS) for painting the boarding bridge is presented. In order to understand the dynamic performance of this robot system, the finite element analysis software Workbench is used to make the modal simulation in this paper. Firstly, the overall mechanical structure of the EIRPS is described. And then, the finite element model is built and the modal analysis procedures are set out detailedly. In a configuration which conforms to the actual situation, the natural frequencies and corresponding vibration modes of the first six orders of the robot system are obtained. On the basis of the calculation results, relative weak parts of the robot system are shown and the optimum proposals are put forward. The analysis results indicate that the modal analysis of the mechanical structure of the EIRPS is reasonable.

**Keywords:** Finite element analysis; Modal analysis; Eight-axis; Modeling; Industrial robot; Painting System; Boarding bridge.

## **1 Introduction**

Nowadays, movable terminal-to-aircraft structures such as boarding bridge finished with primer and topcoat could last over 10 years even while suffering extreme weather conditions and constant use. Jetway systems coat the interior of its passenger boarding bridges with a rust-inhibitive, water-reducible white primer. The exterior is finished with epoxy primer and a polyurethane topcoat. The combination provides adhesion and resistance to impact, abrasion and corrosion. Therefore, flexible painting robot system for large boarding bridges has become the hot topic of the current research [1].

At present in domestic, spray painting operation mainly relies on manpower to complete in most manufacturing factories, especially during the surface coating

---

\*Corresponding author: **Hai-tao FANG**, Shenzhen Institutes of Advanced Technology, Chinese Academy of Sciences, Shenzhen, China, E-mail: ht.fang@siat.ac.cn

**En-de ZHOU, Xi-shun WANG**, College of Mechanical and Automotive Engineering, South China University of Technology, Guangzhou, China

**Kai HE**, Shenzhen Institutes of Advanced Technology, Chinese Academy of Sciences, Shenzhen, China

**Ru-xu DU**, Institute of Precision Engineering, The Chinese University of Hong Kong, Hong Kong SAR, China

process of boarding bridge [2], as shown in Figure 1. The quality consistency of products obviously depends on the proficiency of the spray painters, while the respray ratio is high and the productivity is low. Moreover, the cost of labor is high and the environment of spray painting room is terrible, which is harmful to the workers' health [3]. Therefore, it is necessary for the enterprises to use automation equipment to replace manual operation.



**Figure 1.** The current painting process for the boarding bridge.

Vibration is an inevitable old problems for mechanical structures. Because the working stability, reliability and accuracy of the robot system could be directly influenced by the vibration characteristics. Moreover, it can cause the mechanism fatiguing or resonating, and even make the structure destroyed. Modal analysis is an effective method to demonstrate the dynamic performances of the mechanical structures [4,5], such as damping factors, natural frequencies and vibration modes and so on. Through the modal analysis, we can intuitively see the strength and weakness of the existing mechanical structures and the corresponding vibration modes. And it is helpful to improve the dynamic rigidity and vibration resistance of the structure at working state.

What the mostly used methods in modal analysis are the vibration experimental method and the finite element analysis method. Therefore, a lot of researchers focus on the hot spot of modal analysis. For example, T. Nagarajan [6] and his mates made a survey of the finite element methods applied to the dynamic analysis of the robot manipulators. J. Tlusty [7] and Q.K. Han [8] studied the modal parameters by using the dynamic structural identification task methods and vibration experimental method respectively. C. Yun [9] and X.P. Liu [10] researched the dynamic performance of the spot welding robots with experimental modal analysis method too. Evidently, experimental method helps to obtain the vibration parameters of the robots more accurately, but its cost of both time and expenditure are usually high. Luckily, the

finite element modal analysis provides a convenient and feasible pathway to evaluate the structure performance and make the further optimization for the structure, especially during the structure design stage of the robot system [11-13].

This paper introduces a new kind of EIRPS for painting the boarding bridge. The optimized robot system can paint the boarding bridges efficiently on the basis of the conclusions of the finite element analysis in section III.

## 2 Structural DESCRIPTION of the EIRPS

This automatic painting robot system adopts the structure of a mobile lifting platform carrying a wall-mounted six-joint manipulator. The integral mechanical structure model of the robot system mainly includes Y-axis guide rails, Z-axis guide rails, lift, support plate, six-axis manipulator, as shown in Figure 2. The six-axis manipulator mainly includes body and external devices. Its body includes base, shoulder, large arm, elbow, small arm, wrist and flange which is used to installed the end-effector, as shown in Figure 3. These parts constitute six motion-coupled joints such as S, L, U, R, B, T axis. And the external devices mainly includes electric control cabinet, operation panel, centralized paint-feeding system, spraying gun and the fixture module of the spraying gun.

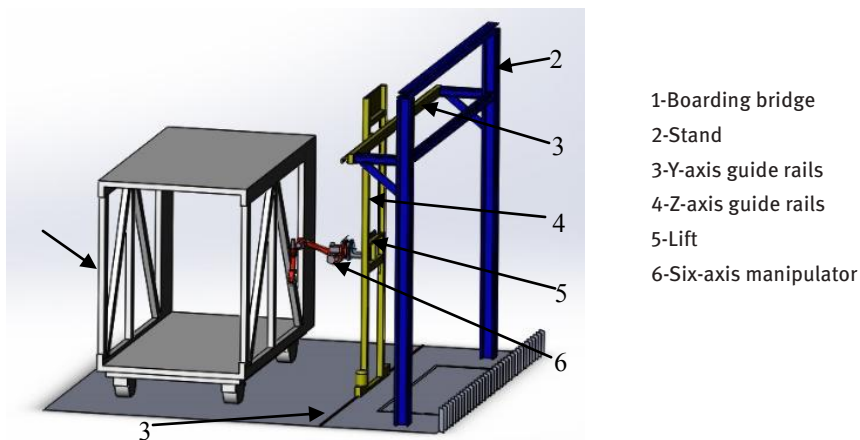


**Figure 2.** The integral structure model of the robot system.

As shown in Figure 2, the Y/Z two-external-axis linear coordinate motion system adopts the type of gantry layout and the six-axis manipulator is installed on the lifting platform. The boarding bridge is very large and its two sides are truss structure. The spray painting task includes not only the outside surface of the boarding bridge, but also the inside surface. So the six-axis manipulator should be flexible enough to stretch into the inside of the boarding bridge through the hole of the truss.

Additionally, the paint is inflammable and explosive goods, the painting location should prohibit fire and select explosion-proof electrical equipment. Such conditions require that the driving motors of the manipulator should not be exposed to the outside and manipulator's size should not be too large. Therefore, a manipulator of small and explosion-proof type is preferred and the two external translation axes are added to expand the workspace.

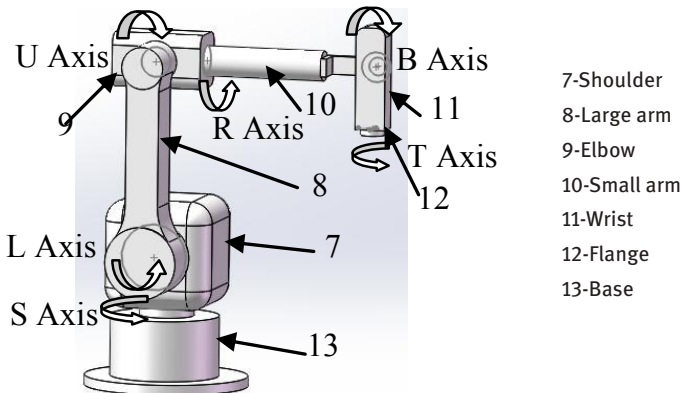


Figure 3. The simplified model of manipulator.

### 3 Modal analysis of the eirPs

#### 3.1 Theoretical basis of the modal analysis

Modal analysis is the study of the natural frequency and main modes of mechanical system. The natural frequency and vibration displacements are two important parameters on the dynamic performance of the mechanical structure, which are helpful for optimizing the structural system with eliminating noise and vibration. Both of them are only related to the rigidity characteristics and mass distribution of the structure, and have nothing to do with external factors. So modal analysis can be studied through the free vibration of the system. The motion equation of the typical undamped free vibration system can be represented as:

$$[M]\{\ddot{x}\} + [K]\{x\} = \{0\} \quad (1)$$

Where,  $[M]$  is mass matrix;  $[K]$  is stiffness matrix;  $\{\ddot{x}\}$  is acceleration vector;  $\{x\}$  is displacement vector. Then the general form of the solution of the above equation can be expressed as:

$$\{x\} = \{\mu\} \sin(\omega t + \varphi) \quad (2)$$

Where,  $\{\mu\}$  is real constant vector,  $\omega$  is the frequency of simple harmonic motion,  $\varphi$  is an arbitrary constant. From (1) and (2), the characteristic equation of structural free vibration can be obtained:

$$([K] - \omega^2[M])\{\mu\} = \{0\} \quad (3)$$

It can be seen that (3) is a linear homogeneous algebraic equation, which is the problem of the classical characteristic value. The characteristic root of the frequency equation is  $\omega_i^2$  and  $\omega_i$  is called the natural vibration circular frequency,  $\omega_i/2\pi$  is the inherent frequency [3]. Put  $\omega_i^2$  into the characteristic equation (3), the eigenvector  $\{\mu_i\}$  corresponding to the characteristic value can be solved. The eigenvector  $\{\mu_i\}$  is known as modal vector, which embodies the vibration mode of the structure. These two parameters of the inherent frequency  $\omega_i/2\pi$  and the modal vector  $\{\mu_i\}$  are the specific nature of the structure itself, and they have nothing to do with the applied load, so they reflect the dynamic characteristic of structure.

### 3.2 Finite Element Modeling of the EIRPS

The whole system structure contains a lot of small features such as small screw holes, small convex platform, corners and fillets and so on. The existence of small features may lead to mesh generation too dense, even mesh failed. So the model should be properly simplified for improving the quality of mesh [4]. The finite element model of the simplified robot system and six-axis manipulator are respectively shown in Figure 4 and Figure 5.

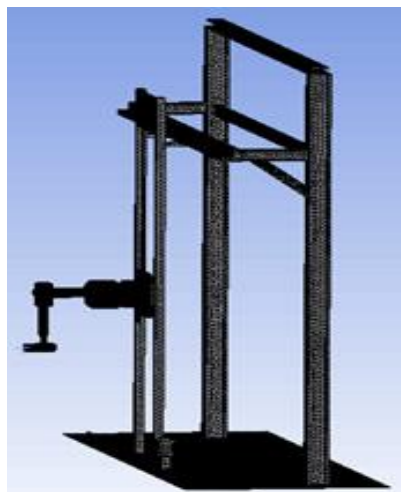


**Figure 4.** The FEM of the EIRPS.

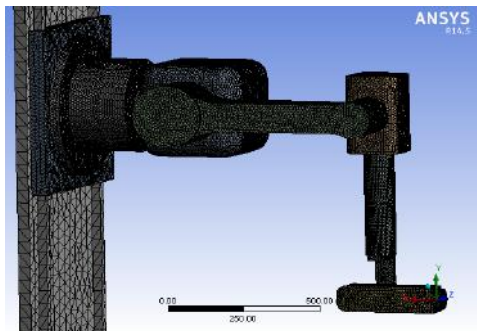


**Figure 5.** The FEM of the simplified six-axis manipulator.

We use ANSYS Workbench as the integrated simulation platform to make modal analysis of the EIRPS [5]. Then, the following demonstrates the detailed procedures for the modal analysis.

- 1) *The definition of material property of each part.* According to the operating condition, the materials of the main components such as the Y-axis guide rails, Z-axis guide rails, elevating platform, and foundation support adopt the structural steel while the six-axis manipulator adopts the cast aluminium.
- 2) *The application of the constraints.* In modal analysis, in order to simulate the actual installation condition of the robot system, the bottoms of the Y-axis guide rails and stand are fixed on ground.
- 3) *The settings of the connecting relation.* Binding contact processing method is used for the connected component interface of the spraying robot through fasteners. And the bottoms of the stand and ground rail are handled as fixed support.
- 4) *The meshing of the model.* Meshing is one of the most fatal steps in the modal analysis. Its quality will directly determine the precision of the result and the calculation time. In view of both the accuracy and the computer arithmetic ability, the tetrahedrons dominant meshing method is used to get the distribution of the mesh. Its total number of nodes is 1613135 and the total number of elements is 992729. The size of the element is 40mm. The execution part of the robot system can be simplified as 11 bodies and the element sizes are divided according to the different sizes of the parts, as shown in Table 1.

**Table 1.** The scope and element size of mesh

Object Name	Body Sizing1	Body Sizing 2	Body Sizing 3	Body Sizing 4	Body Sizing 5
Geometry	Stand	Y-axis guide rails, Lift Z-axis guide rails	Base	Shoulder elbow Large-arm	Small-arm Wrist Flange
Element Size (mm)	50	30	20	10	8

### 3.3 The results and analysis of the EIRPS modal simulation

In the practical engineering application, it is often just required to solve the first six orders natural frequencies and vibration modes of the robot system. Because in the general case, only the natural frequencies and vibration modes of the first few orders may cause structure to generate the risk of resonance.

Through calculating of the workstation, the inherent frequencies and corresponding vibration modes of the first six orders are obtained, as shown in Table 2.

**Table 2.** The total deformations and frequencies of the bodies

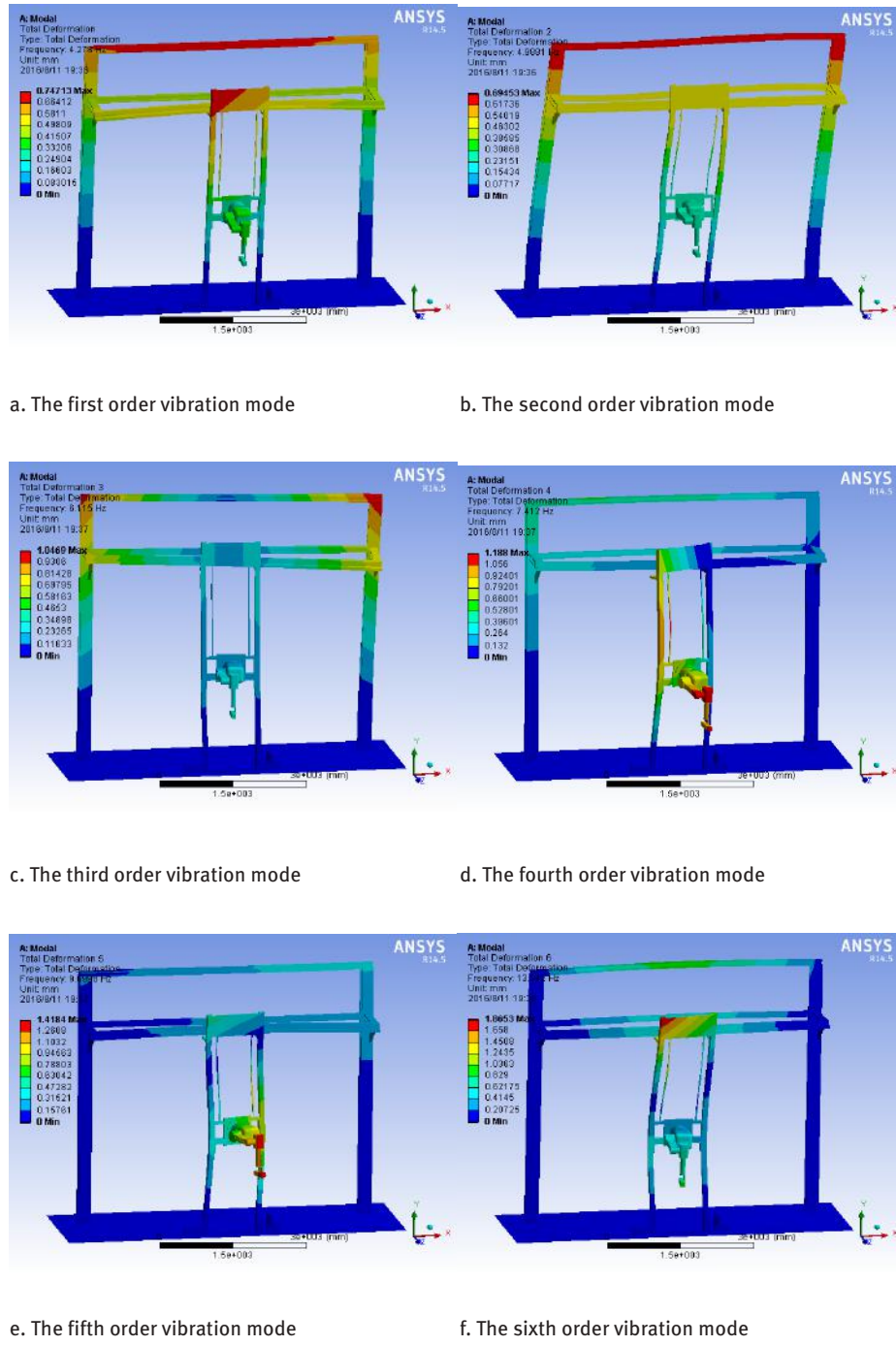
Mode	1.	2.	3.	4.	5.	6.
Minimum deformation(mm)	0					
Maximum deformation(mm)	0.7471	0.6945	1.0469	1.188	1.4184	1.8653
Minimum occurs on	Guide rails					
Maximum occurs on	Stand	Stand	Stand	Large arm	Flange	Lift
Frequency(Hz)	4.278	4.9881	6.115	7.412	9.6998	13.342

As the color cloud pictures of the total deformations shown in Figure 6, the natural frequencies of the robot system are relatively low and their maximum deformations are gradually increasing by orders. The maximum deformations of the first three orders all occur on the top of stand. The maximum deformations of the latter three orders separately occur on the large arm, flange and lift. The Y-axis guide rails almost have no vibration, which indicates that the dynamic rigidity of these supporting parts is enough to cope with the low frequency vibration. The stiffness of the large arm, flange and lift should be reinforced to improve the dynamic rigidity and vibration resistance.

According to the data, the mechanical properties of the optimized system can be evaluated, resonance could be avoided and the structural stability could be ensured.

## 4 Conclusion

The mechanical structure of the eight-axis industrial robot painting system for boarding bridge is introduced in this paper. The system consists of a S/L/U/R/B/T six-joint manipulator, Y/Z two external translational axes, electric control cabinet, operation panel, centralized paint-feeding system, spraying gun and the fixture module of the spraying gun.

**Figure 6.** The vibration modes of the EIRPS.

The modal simulation analysis is demonstrated by finite element analysis software Workbench. The first six orders natural frequencies and the corresponding mode shapes of the robot are obtained. The conclusions drawn from simulation are as follows:

The natural frequencies of the robot system are relatively low and their maximum deformations are gradually increasing as order increasing. They should eliminate the negative effects brought by low order modes vibration at working state.

The stand is the most possible part to vibrate. It should use stronger and lighter material. Large arm and flange of the 6-joint manipulator and the lift also are the weak parts during vibration. Its stiffness should be increased for the better dynamic performance.

Because the stiffness of the joints will affect the accuracy of the modal analysis result of the manipulator, the joints should be focused on when simplifying the model. The stronger and stiffer the robot model is, the preciser analysis result will be.

In the future work, the disturbance frequency of the work environment will be studied in order to find out the resonant source and avoid the resonant frequency.

**Acknowledgment:** This research was accomplished by relying on the project fund provided by Science and Technology Planning Project of Guangdong Province (2013A090100018), Shenzhen technology development project (CXZZ 20140904104336050) and the cooperation project of Foshan and Chinese Academy of Sciences (2014HT100103). Thanks should also be given to Shenzhen CIMC-TianDa Airport facilities CO.LTD for their support.

## References

- [1] Anon, Epoxy/polyurethane paint system protects passenger boarding bridges, *Modern Metals*, vol. 50, n.7, August. 1994, pp. 67-68.
- [2] W. Chen, Dynamic modeling of eight-link flexible robotic manipulators, *Computers and Structures*, vol. 79, 2001, pp. 183-195.

### Article in a conference proceedings:

- [3] X. P. Liao, C. L. Gong and Y. Z. Lin, The finite element modal analysis of the base of welding robot, 3rd Advanced Computer Theory and Engineering (ICACTE), IEEE Press, vol. 2, Mar. 2010, pp. 123-126
- [4] L. Cheng and H. G. Wang, Finite element modal analysis of the FPD glass substrates handling robot, Proc. IEEE International Conference on Mechatronics and Automation(ICMA 2012), IEEE Press, August. 2012, pp. 1341-1346.

### Article in a journal:

- [5] G. P. Zhang, Y. W. Fang, Z. Q. Tian, Dynamic evaluation of a whole structure of an industrial robot, *Journal of Xi'an University of Technology*, no. 1, 2004, pp. 5-9.
- [6] T. Nagarajan, N. Sivaprasad, S. Ramachandran, Survey of finite element methods application for the dynamic analysis of robot manipulators, *Modelling, simulation & control. B*, vol.27, n1, 1990, pp. 23-34.

- [7] J. Tlusty and F. Ismail, Dynamic structural identification task methods, Annals CIRP Tlusty, J., and F. Ismail. Dynamic Structural Identification Tasks and Methods. Annals CIRP-Manufacturing Technology, vol. 29, 1980, pp. 251-255.
- [8] Q. K. Han, T. Yu, W. Du, Experimental modal measurement and dynamical analysis for 6 link parallel robot, Journal of Vibration Engineering, vol. 16, no. 3, September 2003.
- [9] C. Yun, L. L. Song, R. Li, Experimental modal analysis of 120Kg spot welding robots, Chinese Journal of Mechanical Engineering, vol. 37, no. 6, June 2001, pp. 38-42.
- [10] X. P. Liu, J. Y. Li, C. Yun, Dynamic characteristic analysis of 120Kg spot welding robots under movement, China Mechanical Engineering, vol. 13, no. 13, July 2002.
- [11] X. Dong, Z. J. Li and J. M. Xv, Based on ANSYS Workbench dynamic characteristics analysis of six DOF industrial robot, Precision manufacturing and automation, vol. 3, 2014, pp. 10-13, doi:10.16371/j.cnki.issn1009-962x.2014.03.014.
- [12] D. S. Tian, M. Hu and P. Zou, Modal analysis of 6-DOF industrial robot system based on ANSYS, Mechanical and electronic, vol. 2, 2009, pp. 59-62.
- [13] M. Bratland, B. Haugen, T. Rølvåg, Modal analysis of active flexible multibody systems, Computers & Structures, vol. 89, no.9-10, May 2011, pp. 750-761.

Ming YU\*, Meng-xin LI, Hai WANG, Cang-hua JIANG, Hao XIA, Si CHEN

## **Bayesian based Fault Identification for Nonlinear Mechatronic System with Backlash**

**Abstract:** This article attempts to solve the problem of fault identification of nonlinear mechatronic system with backlash. The fault detection and isolation are carried out by evaluating the residuals and the fault signature matrix derived from the bond graph model of the system. In order to refine the fault candidates set after fault isolation, a Bayesian method is adopted where the potential faults in the fault candidates set are treated as the special states to facilitate the unknown parameters estimation. According to the estimation results, the true faults can be obtained which are useful for further maintenance purpose. Simulation studies are conducted to validate the proposed method.

**Keywords:** fault identification; mechatronic system; backlash; fault signature matrix

### **1 Introduction**

With the increase of complexity of modern industrial system, fault diagnosis becomes more and more important. It is critical to carry out fault diagnosis in a timely manner to avoid serious consequence happening in the monitored system, thus the reliability and operation safety will be enhanced. In general, there are three major steps in fault diagnosis: fault detection, fault isolation and fault identification. Fault detection attempts to indicate the occurrence of the fault by comparing the model outputs with the actual system outputs. Fault isolation tries to locate the fault after it is detected. Fault identification involves the estimation of the size and the nature of the fault. For model based fault diagnosis, the algorithm performance mainly depends on the model accuracy. Bond graph (BG) provides a systematic way to model complex system with multiple energy domains, such as mechanical, electrical, hydraulic and so on. The major advantage of BG is the causality which links the variables in BG model in a systematic manner and in turn provides an efficient tool for fault detectability and isolability analysis.

Fault diagnosis of mechatronic system has received substantial attentions in recent decades. General speaking, the method used for fault diagnosis of mechanic system can be divided into two categories: signal based method and model based

---

\*Corresponding author: Ming YU, School of Electrical Engineering and Automation, Hefei University of Technology, Hefei, China, E-mail: mltrym@163.com

Meng-xin LI, Hai WANG, Cang-hua JIANG, Hao XIA, Si CHEN, School of Electrical Engineering and Automation, Hefei University of Technology, Hefei, China

method [1]. Signal based method utilizes the signal processing techniques to extract the fault feature for diagnosis purpose [2-5]. The advantage of this method is that no deep understanding of the monitored system is required. As a result, it is relatively easy to apply this method to industrial system. In [6], a signal analysis approach for machine health monitoring using the Hilbert-Huang Transform (HHT) is proposed. It extracts instantaneous frequency components from the intrinsic-mode functions of the signal. The HHT method is not constrained by the uncertain limitations with respect to the time and frequency resolutions suffered by some time-frequency techniques, which has shown quite promising performance in terms of fault severity evaluation.

On the other hand, model based fault diagnosis usually models the system under monitoring based on physical law [7]. This method is able to provide physical insights which link the fault to the component parameter variations [8]. Thus, the diagnosis accuracy is better than signal based method. However, this method demands good knowledge about the concerned system which may limit its application scope, especially for complex systems. In [9], a robust fault-detection and isolation (FDI) method is developed for an electric vehicle traction system in the presence of structured and unstructured uncertainties. The BG is adopted to model the traction system with multiple energy domains. The adaptive thresholds considering uncertainties are derived based on the causality of the BG. Uncertainties raised from the parameters and structured are identified by a least-square algorithm. A quantitative hybrid bond graph (HBG) based fault diagnosis method is proposed in [10]. In this method, the concept of controlled junction is utilized to capture the discrete event in hybrid dynamic systems. A set of global analytical redundancy relations (AGARRs) are established to represent the dynamic evolution of the monitored hybrid systems in a unified manner. Based on the AGARRs, fault detectability and isolability under different operating modes can be considered.

This paper proposes a BG model based fault diagnosis of nonlinear mechatronic system using Bayesian method. The mechatronic system under monitoring includes DC motor, reducer and load. Nonlinear phenomena such as backlash and friction are considered and modeled in the BG framework. After the fault is detected based on the numerical evaluations of analytical redundancy relations (ARRs), fault identification is carried out in which a Bayesian method is adopted. The nonlinear model of the mechatronic system is put in discrete time form for identification purpose. Based on the identification results, true fault can be obtained. Simulation studies are conducted to validate the proposed fault diagnosis method.

## 2 Modeling and fault diagnosis of nonlinear mechatronic system via BG

The BG is a pictorial representation of systems which is based on energy conservation law. The bond in BG refers to the half arrow line with effort and flow as energy variables [11]. The causality of BG links model variables in a clear and systematic way which paves the way for efficient FDI analysis. Based on the BG model of the system, a set of dynamic constraints, called ARR, are derived from the causal path of the graphic model. Numerical evaluations of ARR lead to residuals which indicate the consistency of the ARR. A residual will exceed the threshold if it is sensitive to the occurred fault.

The mechatronic system consists of a DC motor, reducer and a load. The motor is modeled by friction  $R_m$  and inertia  $J_m$  with input torque  $T$ . The friction  $R_m$  is a nonlinear function which includes both Coulomb friction  $F_{mc}$  and viscous friction  $f_m$ . The  $C$  element represents the stiffness  $K_0$  of the transmission shaft. The motor reducer is modeled by the TF element in BG with parameter  $N$ . The load part is represented by friction  $R_s$  with parameters  $F_{sc}$  and  $f_s$  and load inertia  $J_s$ . There are two incremental encoders representing sensors to measure the positions whose derivations are modeled by BG flow sensors  $D_f : \dot{\theta}_m$  and  $D_f : \dot{\theta}_s$ . The modulated effort sources  $d_m$  and  $d_s$  model the disturbance torques caused by the backlash at the input and output reducer shafts [12]. Thus,

$$d_m = -4K_0 j_0 \frac{1-e^{-\gamma z}}{1+e^{-\gamma z}}, \quad d_s = N d_m \quad (1)$$

where  $z = \theta_m - N\theta_s$ ,  $j_0$  and  $\gamma$  are constants.

The diagnostic bond graph (DBG) of the mechatronic system is shown in Figure 1, where all storage elements are put in derivative causality to avoid the initial condition, except the  $C$  element still remains in integral causality since the initial condition is known. To determine the ARR, two sensor attached junctions  $1_1$  and  $1_2$  are considered.

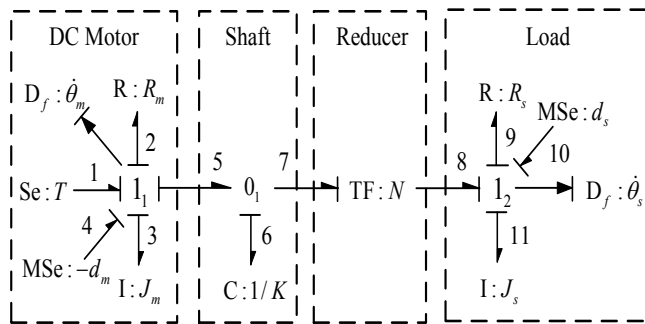


**Figure 1.** Diagnostic bond graph model of the mechatronic system.

From junction 1, the first ARR can be obtained as

$$ARR_1 : e_1 + e_4 - e_2 - e_3 - e_5 = 0 \quad (2)$$

The second ARR can be derived from junction 1 as

$$ARR_2 : e_8 + e_{10} - e_9 - e_{11} = 0 \quad (3)$$

The unknown variables in (2) and (3) can be eliminated by covering the causal paths from sensors to unknown variables. Thus

$$\begin{aligned} e_2 &= F_{mc} \cdot \text{sign}(\dot{\theta}_m) + f_m \cdot \dot{\theta}_m \\ e_3 &= J_m \cdot \ddot{\theta}_m \\ e_5 &= K_0(\theta_m - N\theta_s) \\ e_8 &= N \cdot K_0(\theta_m - N\theta_s) \\ e_9 &= F_{sc} \cdot \text{sign}(\dot{\theta}_s) + f_s \cdot \dot{\theta}_s \\ e_{11} &= J_s \cdot \ddot{\theta}_s \end{aligned} \quad (4)$$

Combine (2) ~ (4), two structurally independent ARRs can be expressed as

$$\begin{aligned} ARR_1 : T + 4K_0 j_0 \frac{1-e^{-\gamma z}}{1+e^{-\gamma z}} - F_{mc} \cdot \text{sign}(\dot{\theta}_m) \\ + f_m \cdot \dot{\theta}_m - J_m \cdot \ddot{\theta}_m - K_0(\theta_m - N\theta_s) = 0 \end{aligned} \quad (5)$$

$$\begin{aligned} ARR_2 : N \cdot K_0(\theta_m - N\theta_s) - 4K_0 N j_0 \frac{1-e^{-\gamma z}}{1+e^{-\gamma z}} \\ - F_{sc} \cdot \text{sign}(\dot{\theta}_s) f_s \cdot \dot{\theta}_s - J_s \cdot \ddot{\theta}_s = 0 \end{aligned} \quad (6)$$

Based on the two ARRs, the fault signature matrix which represents the cause and effect relation between faults and residuals can be established in Table 1.

**Table 1.** Fault Signature Matrix

	$r_1$	$r_2$	$D_b$	$I_b$
$R_m$	1	0	1	0
$J_m$	1	0	1	0
$K_0$	1	1	1	0
$R_s$	0	1	1	0
$J_s$	0	1	1	0
$j_0$	1	1	1	0
$N$	1	1	1	0

Fault detection is carried out by evaluating the consistency of residuals of the ARRs in (5) and (6) in an online manner. A coherence vector (CV) is used to indicate the health condition of the mechatronic system. In other words, if the CV is a nonzero vector, the

system is faulty, and the system is fault free when CV is zero. After a fault is detected, the obtained CV is compared with the row of the FSM in Table 1 to find the set of fault candidates which can account for the fault symptom. Since no fault in the FSM is isolable which indicates more than one fault can lead to the observed CV, fault identification is required to refine the set of fault candidates to determine the true fault.

### 3 Fault identification using bayesian method

The BG model of the mechatronic system is nonlinear and linear parameter estimation methods might not be used.

In this article, a Bayesian estimation method called particle filter (PF) is adopted to identify the unknown fault parameters. PF is a sequential Monte Carlo method which is based on probability theory [13]. This method aims to approximate the posterior probability density function (PDF) of the state using a set of samples (or particles) with associated weights. The main advantage of PF is that it can be applied to nonlinear systems with non-Gaussian noises.

Since the PF operates in discrete time domain, the mechatronic system model needs to be put in discrete form as follows

$$\begin{aligned}
 x_{1,k} &= x_{1,k-1} + x_{2,k-1} \cdot T_s + \omega_{1,k-1} \\
 x_{2,k} &= (t_1 \cdot T_s + 1) \cdot x_{2,k-1} + t_2 \cdot T_s \cdot (x_{1,k-1} - N \cdot x_{3,k-1}) \\
 &\quad + t_3 \cdot T_s \cdot \text{sign}(x_{2,k-1}) - t_4 \cdot T_s \cdot \frac{1 - \exp[-\gamma(x_{1,k-1} - N \cdot x_{3,k-1})]}{1 + \exp[-\gamma(x_{1,k-1} - N \cdot x_{3,k-1})]} \\
 &\quad + t_5 \cdot T_s \cdot u_{k-1} + \omega_{2,k-1} \\
 x_{3,k} &= x_{3,k-1} + x_{4,k-1} \cdot T_s + \omega_{3,k-1} \\
 x_{4,k} &= t_6 \cdot T_s \cdot (x_{1,k-1} - N \cdot x_{3,k-1}) + (t_7 \cdot T_s + 1) \cdot x_{4,k-1} \\
 &\quad + t_8 \cdot T_s \cdot \frac{1 - \exp[-\gamma(x_{1,k-1} - N \cdot x_{3,k-1})]}{1 + \exp[-\gamma(x_{1,k-1} - N \cdot x_{3,k-1})]} \\
 &\quad + t_9 \cdot T_s \cdot \text{sign}(x_{4,k-1}) + \omega_{4,k-1}
 \end{aligned} \tag{7}$$

$$\begin{aligned}
 y_{1,k} &= x_{2,k} + \varepsilon_{1,k} \\
 y_{2,k} &= x_{4,k} + \varepsilon_{2,k}
 \end{aligned} \tag{8}$$

where  $t_1 = -f_m/J_m$ ,  $t_2 = -K_0/J_m$ ,  $t_3 = -F_{mc}/J_m$ ,  $t_4 = -4 \cdot K_0 \cdot j_0/J_m$ ,  $t_5 = 1/J_m$ ,  $t_6 = K_0 \cdot N/J_s$ ,  $t_7 = -f_s/J_s$ ,  $t_8 = -4 \cdot K_0 \cdot j_0/J_s$ ,  $t_9 = -F_{sc}/J_s$ .

Let  $x = [x_{1,k} \ x_{2,k} \ x_{3,k} \ x_{4,k}] = [\theta_m \ \dot{\theta}_m \ \theta_s \ \dot{\theta}_s]$  to be the state vector,  $y = [y_{1,k} \ y_{2,k}] = [\theta_m \ \dot{\theta}_s]$  to be the output vector.  $T_s$  is the sampling rate,  $\omega_{1,k-1}$ ,  $\omega_{2,k-1}$ ,  $\omega_{3,k-1}$  and  $\omega_{4,k-1}$  are process noises,  $\varepsilon_{1,k}$  and  $\varepsilon_{2,k}$  are measurement noises.

After fault isolation, the set of fault candidates, denoted as vector  $\theta$ , can be obtained. In order to realize parameters estimation under the PF framework, the state of the system is augmented as  $z = [x \ \theta]$ . As a result, the PF can be used for joint state and unknown parameters estimation [14]. The main purpose of PF is to represent the posterior PDF of the augmented state  $z$  as

$$p(z_k | y_{1:k}) = \sum_{i=1}^{N_0} w_k^i \delta(z_k - z_k^i) \quad (9)$$

where  $z_k^i$ ,  $i = 1, 2, \dots, N_0$  is a set of random particles,  $N_0$  is the number of particles,  $w_k^i$  is the particle weight, and  $\delta$  is the Dirac delta function.

The particle weights are put in a recursive form as [15]

$$w_k^i \propto w_{k-1}^i \frac{p(y_k | z_k^i) p(z_k^i | z_{k-1}^i)}{q(z_k^i | z_{k-1}^i, y_k)} ; \quad w_k^i = \frac{w_k^i}{\sum_{i=1}^{N_0} w_k^i} \quad (10)$$

If the importance density function is chosen as the transitional prior  $q(z_k^i | z_{k-1}^i, y_k) = p(z_k^i | z_{k-1}^i)$ , the weights update process can be rewritten as

$$w_k^i = w_{k-1}^i p(y_k | z_k^i) \quad (11)$$

The posterior distribution  $p(z_k | y_{1:k})$  can be represented by resampled particles from the systematic resampling method

$$p(z_k | y_{1:k}) \approx \frac{1}{N_0} \sum_{i=1}^{N_0} \delta(z_k - \hat{z}_k^i) \quad (12)$$

where  $\hat{z}_k^i$  is the particle after resampling.

## 4 Simulation study

To investigate the effectiveness of the proposed fault identification method, simulation experiment is conducted. The physical parameter values of the mechatronic system in simulation are set as:  $J_m = 0.8 \text{Nm}^2$ ,  $K_0 = 1 \text{Nm/rad}$ ,  $f_m = 0.1 \text{Nms/rad}$ ,  $F_{mc} = 0.01 \text{N m}$ ,  $J_s = 10 \text{Nm}^2$ ,  $f_s = 8 \text{Nms/rad}$ ,  $F_{sc} = 0.1 \text{N m}$ ,  $N = 5$ . Sampling time is  $T_s = 0.02 \text{s}$ . A friction fault in motor mechanical part is introduced at time step  $k = 2500$  (i.e.,  $t = 50 \text{s}$ ) in which the parameter  $f_m$  is changed abruptly from its nominal value to faulty one  $0.5 \text{Nms/rad}$ . The residual responses are illustrated in Figure 2, where the dot lines are thresholds with value 0.2. It is observed that the CV = [1 0] after 50s due to the friction fault. After comparing the observed CV with the FSM, a set of fault candidates can be obtained  $\theta = [f_m \ J_m \ F_{mc}]$ . This set of fault candidates is used for the state augmentation of PF for the purpose of joint state and unknown parameters estimation. In PF, the particle number is  $N_0 = 1000$ . The estimation is carried out during the time interval [2500, 2700]. Figure 3 shows the estimation states versus the sensor measurements. It is not hard to find that the PF can track the system states in a smooth way based on the available observations.

Figure 4, 5 and 6 demonstrate the PF estimates of unknown parameters in  $\theta$  where the dashed lines are 95% confidence interval. It is found that the mean estimates  $\bar{J}_m = 0.8045 \text{Nm}^2$  and  $\bar{F}_{mc} = 0.0108 \text{N m}$  are close to their nominal values which indicates no fault in these parameters. However, the mean estimate of  $f_m$  shows significant deviation from its nominal

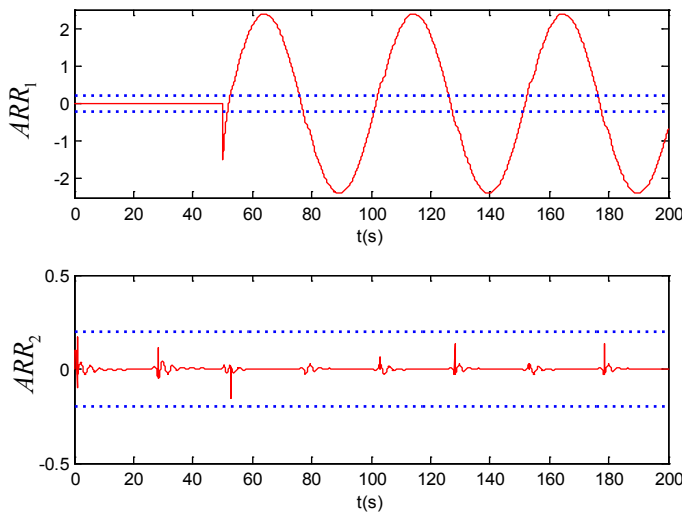


**Figure 2.** Residual responses under the friction fault.

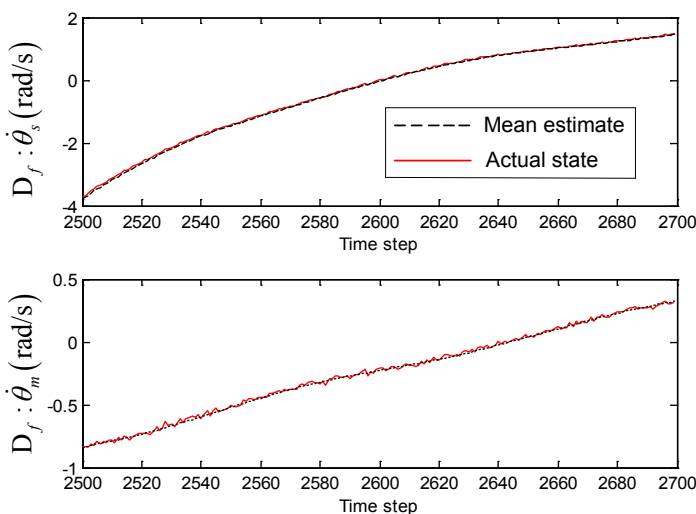


**Figure 3.** Sensor measurements versus PF estimated states.

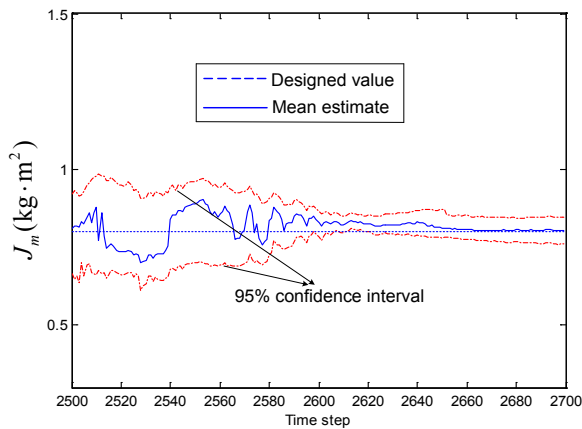


Figure 4. PF esitmate of  $J_m$ .

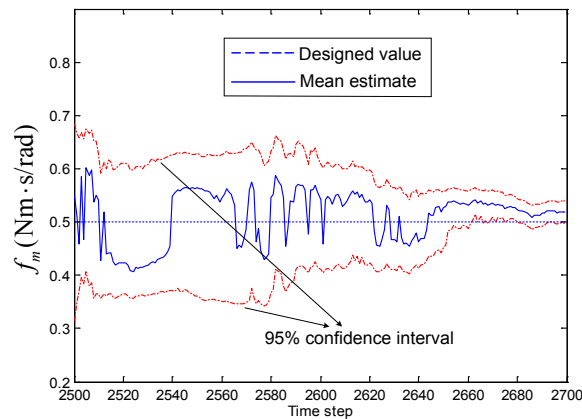


Figure 5. PF esitmate of  $f_m$ .

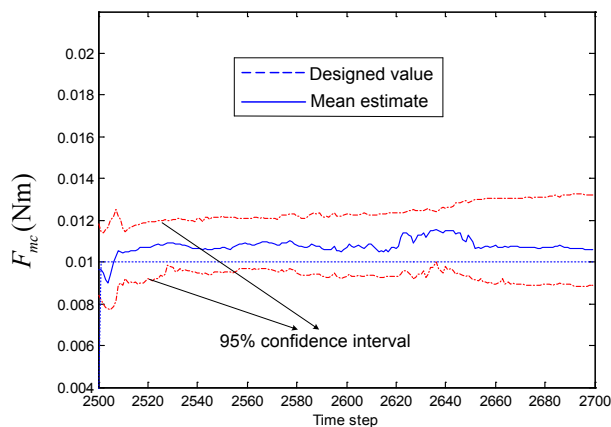
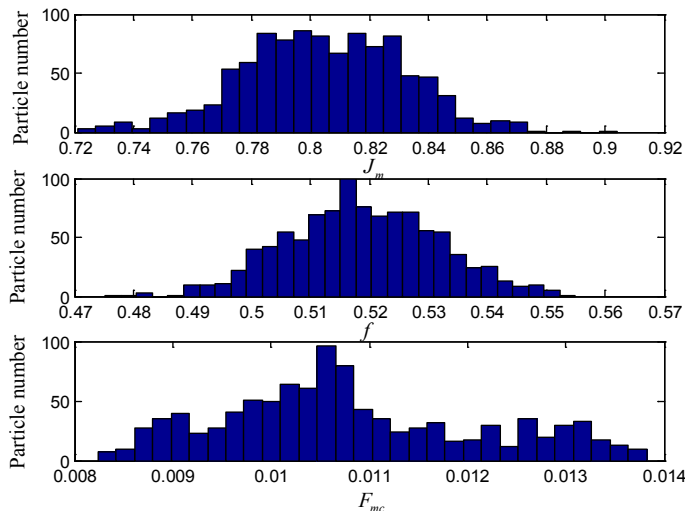


Figure 6. PF esitmate of  $F_{mc}$ .



**Figure 7.** PF estimated parameters distribution.

value which means a fault condition. The mean estimate  $\bar{f}_m = 0.5187 \text{ Nms/rad}$  which matches the designed one. As a result, the true fault in  $f_m$  is found and estimated by the PF algorithm. Figure 7 shows the distribution of the estimated parameters where the central part with more particle number represents the approximated values of PF estimation. From the simulation results, it is concluded that the fault estimation method can accurately find the true fault which leads to the observed CV.

## 5 Conclusion

In this work, a PF based fault identification method is developed for nonlinear mechatronic system with backlash. The fault detection is realized by online evaluation of ARRs. After a nonzero CV is detected, the set of fault candidates can be established based on the FSM. In order to further refine the set of fault candidates, a Bayesian based fault estimation method is developed where the PF is adopted for joint state and unknown parameters estimation. Simulation results validate the proposed methodology. Future works will be devoted to the implementations of the proposed fault identification method in the real test bed including nonlinear friction and backlash.

**Acknowledgment:** This work is supported by the project of National Natural Science Fund of China (Grant No.61673154), and supported by the startup project of Hefei University of Technology (Grant No. 407037159).

## References

- [1] Z. Gao, C. Cecati, and S. X. Ding, A survey of fault diagnosis and fault-tolerant techniques-part I: fault diagnosis with model-based and signal-based approach, *IEEE Transactions on Industrial Electronics*, vol. 62, no. 6, 2015, pp. 3757-3767.
- [2] W. Caesarendra, A. Widodo, and B. S. Yang, Application of relevance vector machine and logistic regression for machine degradation assessment, *Mechanical Systems and Signal Processing*, vol. 24, no. 4, 2010, pp. 1161-1171.
- [3] B. Zhang, T. Taimoor, R. Patrick, G. Vachtsevanos, M. Orchard, and A. Saxena, Application of blind deconvolution de-noising in failure prognosis, *IEEE Transactions on Instrumentation and Measurement*, vol. 58, no. 2, 2009, pp. 303-310.
- [4] N. Freire, J. Estima, and A. Cardoso, Open-circuit fault diagnosis in PMSG drives for wind turbine applications, *IEEE Transactions on Industrial Electronics*, vol. 60, no. 9, Sep. 2013, pp. 3957-3967.
- [5] C. De Angelo, G. Bossio, S. Giaccone, G. O. Garcia, J. Solsona, and M. I. Valla, Model based stator fault detection in induction motors, *Proc. 32nd Annu. Conf. IEEE Ind. Electron. Soc. IECON*, París, France, Nov. 7-10, 2006, pp. 1095-1100.
- [6] R. Yan and R. Gao, Hilbert–Huang transform-based vibration signal analysis for machine health monitoring, *IEEE Transactions on Instrumentation and Measurements*, vol. 55, no. 6, Dec. 2006, pp. 2320-2329.
- [7] S. Arogeti, D. Wang, C. B. Low, and M. Yu, Fault detection isolation and estimation in a vehicle steering system, *IEEE Transactions on Industrial Electronics*, vol. 59, no. 12, 2012, pp. 4810-4820.
- [8] C. B. Low, D. Wang, S. Arogeti, and J. B. Zhang, Causality assignment and model approximation for hybrid bond graph: fault diagnosis perspectives, *IEEE Transactions on Automation Science and Engineering*, vol. 7, no. 3, 2010, pp. 570-580.
- [9] M. Djeziri, R. Merzouki, and B. Ould-Bouamama, Robust monitoring of electric vehicle with structured and unstructured uncertainties, *IEEE Transactions on Vehicle Technology*, vol. 58, no. 9, Nov. 2009, pp. 4710-4719.
- [10] C. B. Low, D. Wang, S. Arogeti and M. Luo, Quantitative hybrid bond graph-based fault detection and isolation, *IEEE Transactions on Automation Science and Engineering*, vol. 7, no. 3, 2010, pp. 558-569.
- [11] D. Karnopp, D. Margolis and R. Rosenberg, *System dynamics: A unified approach*. New York: John Wiley, 1990.
- [12] C. Kam and G. Dauphin-Tanguy, Bond graph models of structured parameter uncertainties, *Journal of The Franklin Institute*, vol. 342, 2005, pp. 379-399.
- [13] S. Arulampalam, S. Maskell, N. J. Gordon, and T. Clapp, A tutorial on particle filters for online nonlinear/non-Gaussian Bayesian tracking, *IEEE Transactions on Signal Processing*, vol. 50, no. 2, Feb. 2002, pp. 174-188.
- [14] M. Daigle and K. Goebel, A model-based prognostics approach applied to pneumatic valves, *International Journal of Prognostics and Health Management*, vol. 2, no. 1, 2011.
- [15] B. Ristic, S. Arulampalam, and N. J. Gordon, *Beyond the Kalman Filter: Particle Filters for Tracking Applications*. Boston, MA: Artech House, 2004.

Chi ZHOU, Li-hua FANG\*, Jun-jie DENG, Wen-tao ZHANG

## A CAD/CAE Integrated Optimization of Hot Runner System

**Abstract:** Hot runner technology has been widely applied in the plastic injection mold industry. However, overheating of plastic melt inside the manifold plate will cause various defects in plastic parts. Nowadays, the design of hot runner systems is still mainly depended on the designers' experiences and a time-consuming trial and error process is inevitable. An automatic optimization framework of hot runner systems is proposed in this paper. It integrates CAD/CAE/Optimization software to find an optimum design of manifolds. A skeleton model, which is a parameter repository that contains geometry and analysis parameter, is the core of this framework. It can effectively interoperate and propagate change between CAD model and FEA model. The ISIGHT platform adopted in this framework provides an efficient way to find the optimum layout of heaters.

**Keywords:** CAD/ CAE Integration; optimum design; Hot-runner

### 1 Introduction

A Hot-runner system is used in plastic injection molds to transfer and inject molten plastic into the cavities of the mold. It is usually composed of a heated manifold plate and several heated nozzles. The plastic melt runs in the runner inside the manifold plate at a high temperature, around 240°C. Compared with traditional cold runner systems, hot runners can reduce plastic waste and shorten the cycle time because the plastic melt in the runner is not ejected with the plastic part when the mold is opened and therefore it is not necessary to wait until the runner freezes. Furthermore, hot runners make the design more flexible because they can carry the plastic melt to many places without worrying about that the plastic melt will be cooled down in the runners and cause the problems of under-filling.

Although hot-runner molds offer so many advantages as mentioned above, they also bring various defects such as dark spots, flow marks and gate marks if the temperature of the plastic melt is not well controlled [1]. In engineering practice, manifold plates are usually heated by coiled tubular heaters to keep the plastic melt in the runners at a stable temperature. Hence, an optimum layout of heaters is required to achieve thermal homogeneity, which means uniform temperatures

---

\*Corresponding author: Li-hua FANG, South China University of Technology, E-mail: flh@mail.scut.edu.cn  
Chi ZHOU, Jun-jie DENG, Wen-tao ZHANG, South China University of Technology

throughout the entire manifold plate. With the help of CAE, designers are now able to catch the potential issues on their designs and revise their designs before manufacturing. But a tedious loop of model-evaluate-remodel is still needed to find a satisfactory solution.

Efforts have been devoted to the automation and optimization of the injection mold design for the past two decades. Dimla et al. [2] have constructed a virtual model using I-DEAS and Moldflow to optimize cooling channels positioning. In his method, the candidate cooling channels layout plans were manually set and the modification of CAE and CAD model were also done by manual. Li et al. [3] used a graph traversal algorithm to generate possible candidate cooling circuits and a heuristic search algorithm was employed to find a satisfactory design. Ivan et al. [4,5] used genetic algorithms to optimize the family mold layout design, which is generally considered a demanding and experience-dependent task. The above-mentioned works showed that the two most important issues in design optimizations are the optimization algorithms and the efficiency of interoperations between CAD and CAE.

The optimization of the injection mold design has no extra constrains on the selection of optimization algorithms. Besides heuristic search algorithm [3] and genetic algorithm [4-6] used in the previous systems, other algorithms such as Taguchi method, back-propagation neural networks [7] and sequential approximation optimization algorithm [8] can also be used. Several reported design optimization systems [8,9] were developed based on the commercial optimization platform ISIGHT. Because ISIGHT embeds a comprehensive selection of the most popular optimizers, it can be applied to a variety of design optimization problems and greatly shorten the development cycle.

The efficiency of interoperations between CAD and CAE model is another important issue to be considered in design optimization because the CAD and CAE need to transfer data in every iteration. In order to improve efficiency, various intermediate models are designed to integrate CAD and CAE data. Gujarathi et al. [10] proposed a CAD/CAE integration method using a common data model (CDM), which serves to record the driving design parameters and key constraints. Zhiyi Pan et al. [11] proposed a modeling mechanism named as CADWE (Computer-Aided Design-While-Engineering), which merges the two application models into a single pattern and can be manipulated synchronously. Byoung-Keon Park et al. [12] presented a sharable format, Practical post-Analysis Model(PAM), which allows the efficient sharing of FEA data in a collaborative design process. Other scholars [13-16] proposed different intermediate models.

A CAD/CAE integrated optimal framework for a hot runner system design is proposed in this paper. The framework is based on the ISIGHT optimization platform and a skeleton model for CAD/CAE integration.

## 2 Overview of the framework

Conventionally, CAD models only contain geometric information and do not consider the information for analysis, such as load conditions, boundary conditions, key constraints et al. Therefore, it cannot meet the needs of interoperations and change propagation between CAD model and FEA. Furthermore, although the CAD and analysis models represent the same object, it is time-consuming to prepare a qualified CAE model from the CAD geometry. To meet the requirements on the efficiency of CAD/CAE data exchange in optimization computation, a CAD/CAE integrated optimization framework is proposed.

As shown in Figure 1, the framework includes the following components:

- The skeleton model is a collection of design semantic parameters required to build geometry model, finite element model and to conduct engineering analysis.
- A CAD model can be generated based on the geometric information of the skeleton model. It has more details than the skeleton model and is a complete 3D model.
- Analysis process description (APD) file is automatically generated by a user-developed routine, which transforms the geometry and analysis information in the skeleton model to an ASCII text file according with the specification of ANSYS parametric design language (APDL).
- A CAE support environment is used to parse the APD file, construct geometry, mesh, create boundary conditions and then solve the problem.
- An optimization tool will evaluate the simulation results. If the results meet the requirements, the whole process will be completed. Otherwise, it will adjust the parameters in the skeleton model and another cycle begins until the goal is achieved.

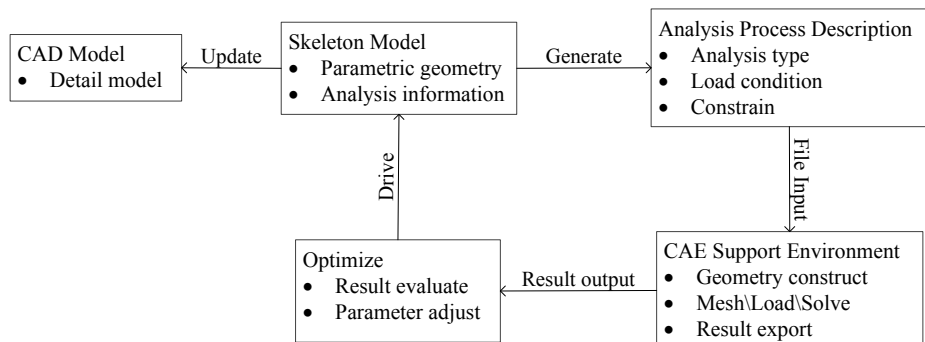


**Figure 1.** CAD-CAE integration framework

### 3 Proposed design process for hot runner design

A typical hot runner manifold is composed of a plate and several coiled tubular heater are embedded into it. The heaters will heat up the plate and keep the plastic melted inside the manifold at a stable temperature. The optimization of hot runner system is to find a suitable layout of heaters that makes the temperature distribution through the manifold plate as uniform as possible.

The skeleton model of a hot runner contains parametric geometry information and FEA information. The parametric geometry information includes the sketch of the plate outline, the thickness of the plate, the section dimensions, size and position of the heaters. As show in Figure 2, the size of a heater is expressed by the length L and the width W. The position point of a heater is the center of the rectangle.

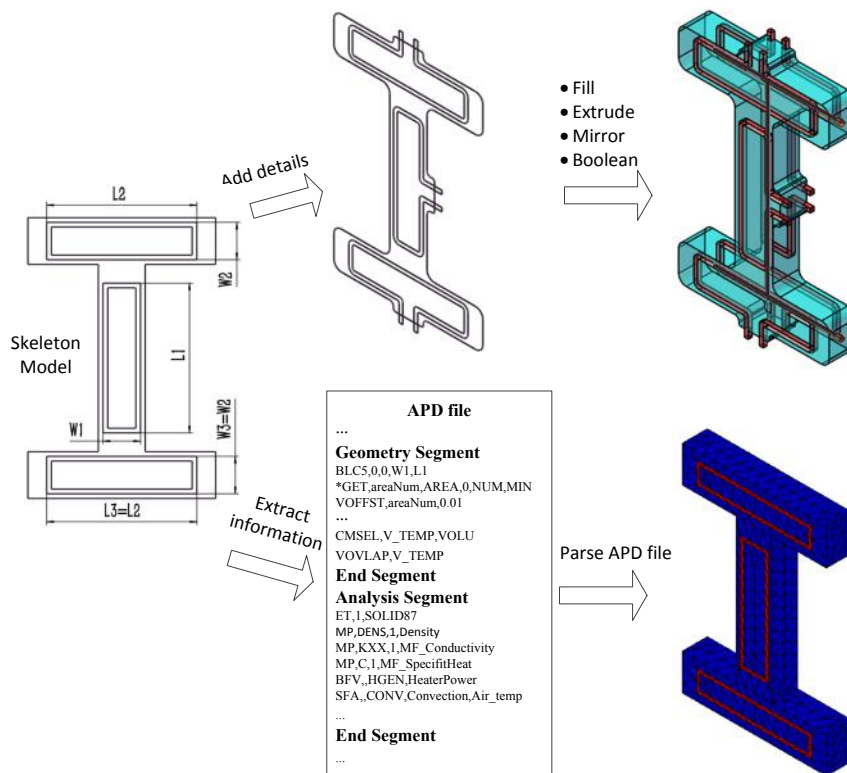


**Figure 2.** Design process with skeleton model

Analysis information in a skeleton model includes material properties, meshing information, and boundary conditions. For example, the material properties of the plate are: the material density ( $7800 \text{ kg/m}^3$ ), the coefficient of thermal conductivity

(70 W/m·°C) and the specific heat (448 J/kg·°C). Meshing information includes element type, meshing method and so on. The boundary conditions for thermal equilibrium analysis include the heat transfer coefficient, the heat generation rate and the air temperature.

A detailed sketch for a manifold can be constructed from the skeleton model by adding some extra features, such as the fillets and bulges. Then by using the preset parameters including the thickness of the manifold and the section dimension of heater, a 3D manifold part can be generated as shown in Figure 2. This 3D CAD model is same with traditional feature-based CAD model.

The APD file is automatically created from the skeleton model by a user-developed routine. An APD file mainly includes a geometry section and a analysis section. All of the geometries for analysis are represented in the geometry section. For this case, the outline sketch of the manifold is expressed as curves and the heaters are expressed as parametric blocks. Take the middle heater as an example, the APD description is as follows:

```

!heater block length
L1=0.32
!heater block width
W1=0.06
!heater section width
C=0.01
!heater section thickness
D=0.01
!Outer rectangle
BLC5, 0, 0, W1, L1
CM,ABASE,AREA
!inner rectangle
BLC5,0,0,W1-2*C,L1-2*C
CM,ASUB,AREA
!heater block= Outer rectangle -inner rectangle
ASBA,ABASE,ASUB
CM,AOFF,AREA
!extrude the block with a thickness D
VOFFST,AOFF,D

```

The analysis information in the skeleton model is also transferred to the analysis section of APD file as follows:

```

! as foll information:
!element type: SOLID87
ET,1,SOLID87
!element size

```

```

ESIZE,MS,0
/ element shape
MSHAPE,1,3D
/ meshing method
MSHKEY,0
/ Material properties:
/ define mass density,Density=7800 kg/m³
MP,DENS,1,Density
/ define thermal conductivities,
/MF_Conductivity=70 W/(m·°C)
MP,KXX,1,MF_Conductivity
/define specific heat,MF_SpecificHeat=448 J/(kg·°C)
MP,C,1,MF_SpecificHeat
/ Boundary condition:
/ define a body force load on heater,
/ HeatPower=4.6×106 W/m³
BFV,,HGEN,HeatPower
/define surface loads,
/ Convection=12 W/(m²·°C)Air_temp=40°C
SFA,,CONV,Convection,Air_temp

```

As shown in Figure 1, ANSYS will then import the generated APD file and run simulation. Guided by ISIGHT, an optimum solution will be found after a large number of iteration. In each iteration, the size, position and heating rate of the heaters in the APD file is within the searching space. Then these optimized parameters are used to drive the skeleton model and the CAD models.

The above optimization process is governed by ISIGHT. ISIGHT supports many optimization algorithms, including Evol (Evolutionary Optimization), MIGA (Multi-Island Genetic Algorithm), ASA (Adaptive Simulated Annealing). The Optimization interface, as shown in Figure 3, allows the user to specify design variables, constraints, and objectives in ISIGHT. In this paper, Evol algorithm was selected because it is suitable for non-linear and discontinuous problems.

The Optimization model is defined as following:

$$\begin{aligned}
 & \min f(X) \\
 \text{s.t } & \left\{ \begin{array}{l} 0.05 \leq W1 \leq 0.10 \\ 0.05 \leq W2 \leq 0.10 \\ 0.25 \leq L1 \leq 0.40 \\ 0.25 \leq L2 \leq 0.40 \\ 3 \leq P \leq 5 \\ 240 \leq \text{Avg} \leq 250 \end{array} \right.
 \end{aligned}$$

The design variables of this problem are the heater size parameters (L1,L2,W1,W2) and the heat generation (P), which control heat flow rate per unit volume. The Object function:  $f(X)$  is the temperature variance calculated from some selected nodes along the runners. During the optimization process, the design variables are adjusted to obtain a minimum temperature variance.

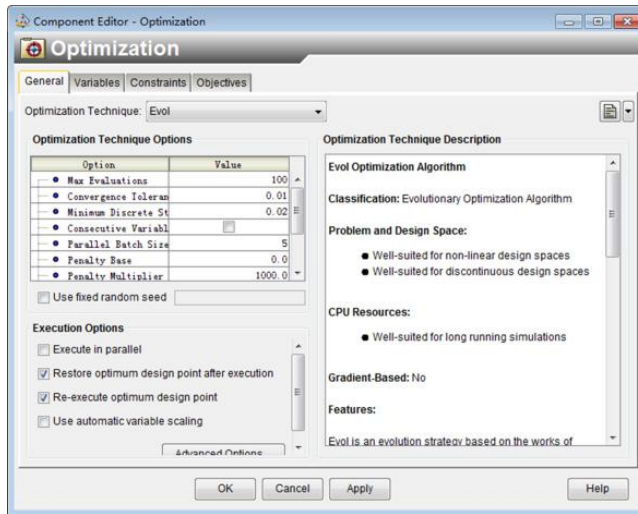


**Figure 3.** Optimization tab

#### 4 An example of optimization

Take the manifold plate in Figure 2 as an example. The initial and optimized values of design variables are listed in Table 1. These initial values are decided according to experience. An initial APD file is created from user skeleton model. Then the design variables, constraints, objective function and the APD file are input into ISGHIT.

**Table 1.** Optimization results

	Initial	Optimized
W1 (m)	0.060	0.069
W2 (m)	0.060	0.069
L1 (m)	0.320	0.300
L2 (m)	0.320	0.380
P ( $\times 10^6 \text{ W/m}^3$ )	4.60	3.92
Avg (average temperature $^\circ\text{C}$ )	255.35	243.91
Sigma (temperature variance)	2.54	0.16

Figure 4 shows the temperature distribution in the manifold before and after optimization. The temperature range before optimization is from 249 to 264°C, while this range is narrowed to from 242 to 244. Finally, the optimized parameters can be used to drive the skeleton model. The 3D detailed design of Manifold can also be updated.

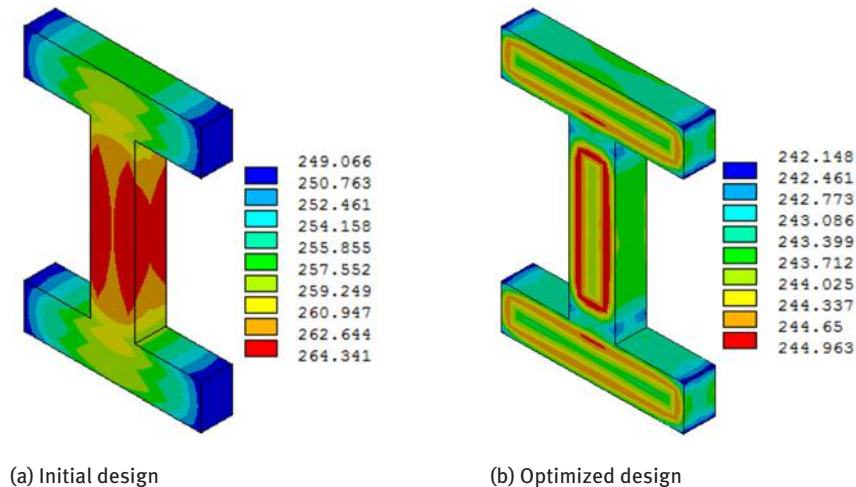


**Figure 4.** The temperature distribution in the manifold before and after optimization

## 5 Conclusion

In this paper, a framework of optimum design and its application for hot runner system are proposed. In this framework, a skeleton model acts as bridge connecting CAD, CAE and Optimization software. The design cycle can be considerably shortened because the parametric skeleton model has much higher efficiency in exchange data with CAE model than the traditional CAD model. The automatic optimization process is helpful for hot runner mold designers to quickly find a satisfactory layout of heaters.

**Acknowledgment:** The authors would like to thank Natural Science Foundation of Guangdong (Grant No: 2016A030313519) for financial support of this work.

## References

- [1] Hidetoshi Yokoi, Yoshinori Kanetoh, Ryohei Takamatsu, Takumi Endo, Hao Chang, and Toru Chayamichi, ‘Visualization Analysis of Injection Molding Phenomena in Hot-Runner System’, 1713 (2016), 040008.

- [2] D. E. Dimla, M. Camilotto, and F. Miani, 'Design and Optimisation of Conformal Cooling Channels in Injection Moulding Tools', *Journal of Materials Processing Technology*, 164-165 (2005), 1294-300.
- [3] C. L. Li, C. G. Li, and A. C. K. Mok, 'Automatic Layout Design of Plastic Injection Mould Cooling System', *Computer-Aided Design*, 37 (2005), 645-62.
- [4] Ivan W. M. Chan, Martyn Pinfold, C. K. Kwong, and W. H. Szeto, 'Automation and Optimisation of Family Mould Cavity and Runner Layout Design (Fmcrl) Using Genetic Algorithms and Mould Layout Design Grammars', *Computer-Aided Design*, 47 (2014), 118-33.
- [5] Ivan W. M. Chan, Martyn Pinfold, C. K. Kwong, and W. H. Szeto, 'A Review of Research, Commercial Software Packages and Patents on Family Mould Layout Design Automation and Optimisation', *International Journal of Advanced Manufacturing Technology*, 57 (2011), 23-47.
- [6] Chun-Yin Wu, Chih-Chiang Ku, and Hsin-Yi Pai, 'Injection Molding Optimization with Weld Line Design Constraint Using Distributed Multi-Population Genetic Algorithm', *The International Journal of Advanced Manufacturing Technology*, 52 (2010), 131-41.
- [7] Wen-Chin Chen, Min-Wen Wang, Chen-Tai Chen, and Gong-Loung Fu, 'An Integrated Parameter Optimization System for Miso Plastic Injection Molding', *The International Journal of Advanced Manufacturing Technology*, 44 (2008), 501-11.
- [8] Xuan-Phuong Dang, 'General Frameworks for Optimization of Plastic Injection Molding Process Parameters', *Simulation Modelling Practice and Theory*, 41 (2014), 15-27.
- [9] Irene Ferreira, Olivier de Weck, Pedro Saraiva, and José Cabral, 'Multidisciplinary Optimization of Injection Molding Systems', *Structural and Multidisciplinary Optimization*, 41 (2009), 621-35.
- [10] G. P. Gujarathi, and Y. S. Ma, 'Parametric Cad/Cae Integration Using a Common Data Model', *Journal of Manufacturing Systems*, 30 (2011), 118-32.
- [11] Zhiyi Pan, Xin Wang, Rumin Teng, and Xuyang Cao, 'Computer-Aided Design-While-Engineering Technology in Top-Down Modeling of Mechanical Product', *Computers in Industry*, 75 (2016), 151-61.
- [12] Byoung-Keon Park, and Jay J. Kim, 'A Sharable Format for Multidisciplinary Finite Element Analysis Data', *Computer-Aided Design*, 44 (2012), 626-36.
- [13] Okba Hamri, J. Claude Léon, Franca Giannini, and Bianca Falcidieno, 'Software Environment for Cad/Cae Integration', *Advances in Engineering Software*, 41 (2010), 1211-22.
- [14] Seong Wook Cho, Seung Wook Kim, Jin-Pyo Park, Sang Wook Yang, and Young Choi, 'Engineering Collaboration Framework with Cae Analysis Data', *International Journal of Precision Engineering and Manufacturing*, 12 (2011), 635-41.
- [15] Ivan Matin, Miodrag Hadzistevic, Janko Hodolic, Djordje Vukelic, and Dejan Lukic, 'A Cad/Cae-Integrated Injection Mold Design System for Plastic Products', *The International Journal of Advanced Manufacturing Technology*, 63 (2012), 595-607.
- [16] Yanli Shao, Yusheng Liu, and Chunguang Li, 'Intermediate Model Based Efficient and Integrated Multidisciplinary Simulation Data Visualization for Simulation Information Reuse', *Advances in Engineering Software*, 90 (2015), 138-51.

Wei LI, Zhi-gang SUN\*, Kai HE, Qi-yang ZUO, Qing-yin LIU, Ru-xu DU

## **Study On Tool Path Design for a Novel Incremental Sheet Metal Bending Process**

**Abstract:** A novel incremental sheet metal bending process for manufacture of hull plates has been proposed based on the concept of flexible forming technology, and comprehensive experimental studies for deepening the understanding of forming mechanism are being continued towards its practical application in the shipbuilding industry. This process utilizes a punch set to incrementally punch the sheet metal supported by a flexible supporting system consisting of multiple supporting pillars to form it into a desired shape. The tool path that controls the movements of the tools in the complete forming process is the key to realize the high-quality production required from real industry. Therefore, design of a reasonable tool path is essential to this new process. In this paper, algorithms for calculating the forming parameters relating to the tool path design such as the punch feeds, the positions of supporting pillars are presented. A method of springback compensation, which also falls into the category of tool path design, is also presented. A forming experiment performed by applying the tool path designed with the aid of them is given at the end of this paper to demonstrate their effectiveness.

**Keywords:** sheet metal forming; incremental bending; hull plate; tool path design; springback compensation

### **1 Introduction**

With the rapid development of modern industry, there is more and more a demand for sheet metal forming parts in multi-variety and small-batch production, especially in the shipbuilding field. Up to now, traditional line heating formed by

---

\*Corresponding author: Zhi-gang SUN, Shenzhen Institutes of Advanced Technology, Chinese Academy of Sciences, Shenzhen Key Laboratory of Precision Engineering, Shenzhen, China,  
E-mail: zg.sun@siat.ac.cn

Wei LI, Shenzhen Institutes of Advanced Technology, Chinese Academy of Sciences, Shenzhen Key Laboratory of Precision Engineering, Shenzhen, China, China University of Petroleum (Beijing), Beijing, China

Kai HE, Shenzhen Institutes of Advanced Technology, Chinese Academy of Sciences, Shenzhen Key Laboratory of Precision Engineering, Shenzhen, China

Qi-yang ZUO, Shenzhen Institutes of Advanced Technology, Chinese Academy of Sciences, Shenzhen Key Laboratory of Precision Engineering, Shenzhen, China

Qing-yin LIU, Taian Hualu Metal-forming Machine Tool Co. Ltd, Taian, China

Ru-xu DU, The Chinese University of Hong Kong, Institute of Precision Engineering, Hong Kong SAR, China

manual operation [1] has been the main method for manufacturing complicated curved thick hull plates in shipyards. However, this kind of method is gradually becoming difficult to meet the growing demand for high-quality and high-efficiency production in modern shipbuilding industry due to the fact that the forming quality and efficiency relies completely on the experience of highly-skilled workers, usually leading to long processing time and unsatisfactory forming quality. In light of this background, a novel automated incremental bending process different from general incremental sheet forming [ISF] for thin sheet metal parts [2], in which the sheet metal is incrementally formed into a desired shape layer by layer using a punch and a flexible supporting system consisting of multiple height-adjustable supporting pillars with rotating heads, has been proposed based on the concept of “Dieless” flexible forming technology [3]. For thick sheet metal parts, two major “Dieless” flexible forming technologies have been proposed: cyclic multi-point incremental forming (CMPIF) [4] and multi-point forming (MPF) [5] that employ a number of die units to form the sheet metal. Compared to the MPF and CMPIF, the novel process has the advantage of smaller investment on forming equipment, contributing to low-cost production. The feasibility of this process has been confirmed by comprehensive experimental studies, however, there are still many problems remaining to be solved by further studies. The tool path, which controls the movements of the tools in the complete forming process, plays a critical role in forming quality and efficiency, hence needs to be designed reasonably. Therefore, studies concerning tool path design are of great significance for this new process. The first step in designing the tool path is the planning of the number of forming layers as well as the pressing positions and sequence on each layer. The next step is the numerical determination of the relevant forming parameters, i.e. the determination of the punch feeds and the positions of supporting pillars. In this paper, numerical algorithms to calculate these forming parameters are presented. Springback is the most significant factor to cause poor forming quality in this new process, in which the sheet metal undergoes bending-dominant deformation, and needs to be correctly compensated in order to achieve the required target shape. A method of springback compensation analogous to the displacement adjustment method [6] for general stamping process, including the calculation of springback amount, the generation of trial target shape and the modifications of punch feeds and supporting pillar positions, is also presented. A forming experiment has been carried out by applying the tool path designed with the aid of those presented here, and their effectiveness was validated. The experiment is given at the end of this paper.

## 2 Novel incremental bending process

The new incremental bending process utilizes the principle of layered forming technology. As shown in Figure 1, the total deformation of the sheet metal is resolved

into a series of forming layers, each layer being formed by applying a punch to press the sheet metal fitted either by electromagnets or bolts on the rotating heads of specified outer supporting pillars, stroke by stroke, following the given pressing positions and sequence. The supporting pillars in the supporting system are height-adjustable so that they can be adjusted to the heights where the positions of their heads form the required target shape. In the process, firstly, the punch presses the sheet metal to form the first layer, then moves to form the next one and so on until the last layer is finished.

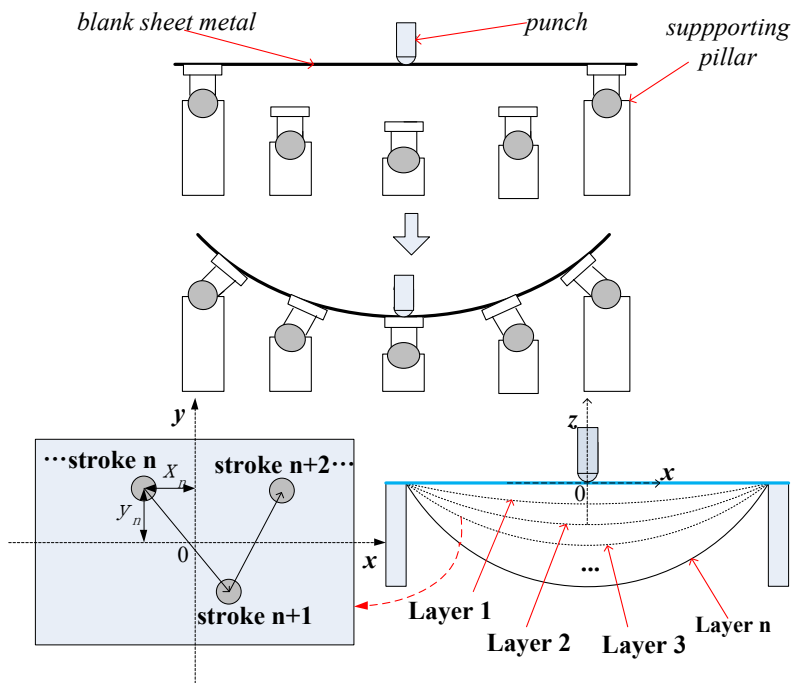


**Figure 1.** Novel incremental bending process

A prototype machine has been manufactured based on a CNC milling machine as shown in Figure 2. It is mainly composed of a 1-DOF[vertical(z-axisial) direction] punch controlled by a step motor, a supporting system setting on a 2-DOF[horizontal(x and y-axisial) directions] working table controlled by servo motors and a 3D surface scanning system. The supporting system is composed of a 4(x-axisial direction) 3(y-axisial direction) matrix of supporting pillars that can be adjusted up and down along z-axisial direction by step motors according to the target shape of the sheet metal.

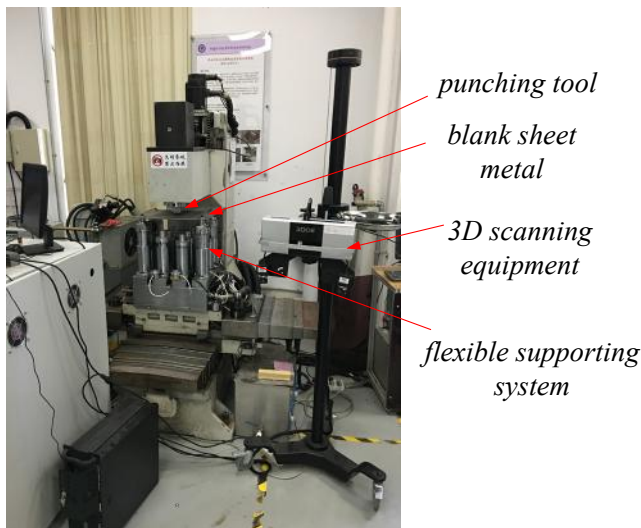


**Figure 2.** Prototype machine of novel incremental bending process

### 3 Algorithms for calculating punch feed and supporting pillar position

Once the target shape of sheet metal part and the information of the designed forming layers along with pressing positions are given, the punch feed at each pressing position of forming layers as well as the height of each supporting pillar needs to be calculated.

The 3D CAD model of the target shape is designed first. Then, it is converted into a triangular mesh model in STL format. All the calculations are based on the STL model.

#### 3.1 Punch Feed

First, based on the target shape, the total punch feed at a given pressing position is calculated as follows.

As illustrated in Figure 3, a triangular facet onto which the point at the pressing position is projected along the z-axis direction can be identified by the condition:

$$-1 \leq r, s \leq 1, \quad (1)$$

$$r = \frac{[(y-y_1) \cdot (x_3-x_1) - (x-x_1) \cdot (y_3-y_1)]}{[(x_1-x_2) \cdot (y_3-y_1) - (y_1-y_2) \cdot (x_3-x_1)]}, \quad (2)$$

$$s = \frac{[(y-y_1)\cdot(x_2-x_1)-(x-x_1)\cdot(y_2-y_1)]}{[(x_1-x_3)\cdot(y_2-y_1)-(y_1-y_3)\cdot(x_2-x_1)]}. \quad (3)$$

Where, and are the natural coordinates of the projection of the point on the facet;  $x$ ,  $y$  and  $z$  are the global Cartesian coordinates of the point.  $x_i$ ,  $y_i$  and  $z_i$  ( $i=1,2,3$ ) are the global Cartesian coordinates of the three vertexes of the facet.

The total punch feed at the pressing position is calculated as:

$$h = (1 - r - s) \cdot z_1 + r \cdot z_2 + s \cdot z_3. \quad (4)$$

Thus, the punch feed increment of each forming layer is calculated by dividing the above-calculated total feed equally into the given number of forming layers and the punch feed is obtained as:

$$h_i = h \cdot i/n. \quad (5)$$

Where,  $i$  is the number of  $i$ th layer,  $n$  is the total number of layers.

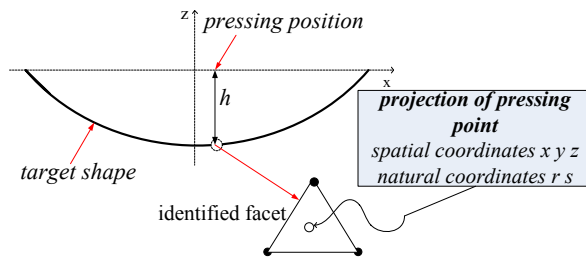


**Figure 3.** Target shape and total punch feed at pressing position

Finally, performing the same calculation procedure shown above, the punch feeds at all the pressing positions of every forming layer can be obtained.

### 3.2 Supporting Pillar Height

As mentioned above, the supporting pillars in the supporting system are adjusted to the heights where their rotating heads form the required target shape. This is important for this new forming process to constrain the deformed shape to the target one at the final forming stage in order to acquire accurate geometric shape, especially in the case when a complicated curved shape is to be formed. The height of each supporting pillar is indicated by the z-axial position of the rotating center of its head, i.e. the z-axial position of the ball-joint center. It is calculated as follows.

The rotating head of each supporting pillar fits the target shape in the manner as shown in Figure 4.

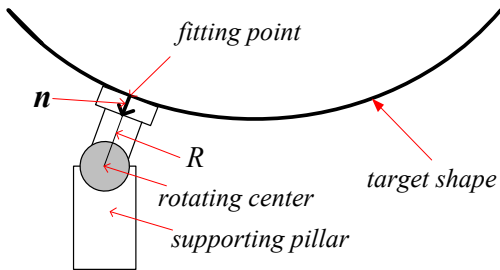


**Figure 4.** Supporting pillar and target shape

In this configuration, the position of rotating center of the head satisfies the condition:

$$\begin{aligned} \mathbf{x}_c - \mathbf{x}_{fp} &= R \cdot \mathbf{n} \\ \mathbf{x}_c &= (x_c, y_c, z_c) \\ \mathbf{x}_{fp} &= (x_{fp}, y_{fp}, z_{fp}) \\ \mathbf{n} &= (n_x, n_y, n_z). \end{aligned} \quad (6)$$

Where,  $\mathbf{x}_c$  is the vector of the coordinates of rotating center,  $\mathbf{x}_{fp}$  is the vector of the coordinates of fitting point,  $\mathbf{n}$  is the normal vector at fitting point,  $R$  is the rotating radius of the head of supporting pillar.

From equation (6), the z coordinate (z-axial position) of the rotating center can be obtained as:

$$z_c = (1 - r - s) \cdot z_1 + r \cdot z_2 + s \cdot z_3 + R \cdot n_z. \quad (7)$$

Where,  $r$  and  $s$  are the natural coordinates of the fitting point in the fitting facet identified by the condition:

$$-1 \leq r, s \leq 1, \quad (8)$$

$$r = \frac{\{(y_c - R \cdot n_y) - y_1\} \cdot (x_3 - x_1) - [(x_c - R \cdot n_x) - x_1] \cdot (y_3 - y_1)}{[(x_1 - x_2) \cdot (y_3 - y_1) - (y_1 - y_2) \cdot (x_3 - x_1)}, \quad (9)$$

$$s = \frac{\{(y_c - R \cdot n_y) - y_1\} \cdot (x_2 - x_1) - [(x_c - R \cdot n_x) - x_1] \cdot (y_2 - y_1)}{[(x_1 - x_3) \cdot (y_2 - y_1) - (y_1 - y_3) \cdot (x_2 - x_1)} . \quad (10)$$

Where,  $x_i$ ,  $y_i$  and  $z_i$  ( $i=1,2,3$ ) are the coordinates of the three vertexes of the fitting facet.

## 4 Springback compensation method

A method similar to the displacement adjustment method proposed for the general stamping process, which iteratively modifies the die surface shape with the springback magnitude in the opposite direction, is adopted here.

The iteration procedure of this approach is shown in Figure 5. First, the blank sheet is formed into a trial target shape following the designed tool path, the first trial target shape coinciding with the designed target shape. Then, the deformed shape after

springback is measured by the 3D surface scanning system and its triangular mesh model is generated using the point cloud data collected. This model is subsequently used to determine the z-axial springback magnitudes of the nodal points of trial target shape (denoted by  $\Delta z$ ) using the same algorithm as presented in section III.

$$\begin{cases} \Delta z = (\Delta z_1, \dots, \Delta z_n) \\ \Delta z_i = z_i - z_i^p \end{cases} \quad (11)$$

Where, n is the total number of the nodal points of the trial target shape.  $z_i$  and  $z_i^p$  are the z coordinates of the i<sup>th</sup> nodal point and its projection on the deformed shape after springback, respectively. Thus, a new trial target shape for the next iteration is obtained by adding the  $\Delta z$  to the current trial target shape. The next iteration is performed using the new tool path with the punch feeds and supporting pillar positions updated based on the new trial target shape. The iterations will be continued until the  $\Delta z$  lies within a specified tolerance.

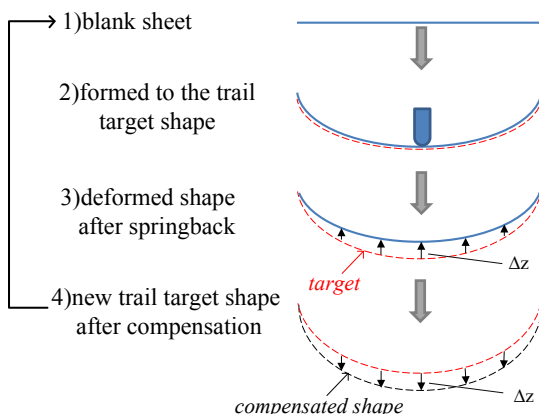


**Figure 5.** Iteration procedure for springback compensation

## 5 Forming experiment

A forming experiment has been carried out to validate those presented above. As the first experimental study, only a single punch and four supporting pillars were used. The pillars were located in the corners of sheet metal, and the distances between their axes were 360mm and 240mm in x and y directions, respectively. The dimension of the sheet blank was 450mm(x) 330mm(y) 3mm(z), and the material was Q235 steel(china steel) which is commonly used for hull plates. A target sheet metal part with a singly curved surface was chosen for this study as shown in Figure 6.

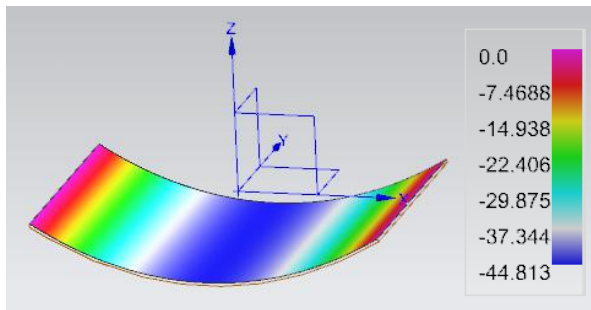


**Figure 6.** Target sheet metal part

In the experiment, the blank sheet metal was fitted on the rotating heads (rotating radius of 40mm) of the four supporting pillars by bolts, and was formed in 4 forming layers. The same punching positions and sequence were applied on all layers as shown in Figure 7.

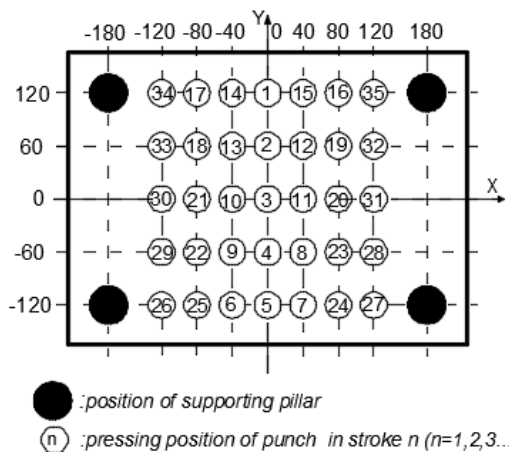


**Figure 7.** Pressing positions and sequence

Figure 8 and Table 1 show, respectively, the initial experiment configuration and total punch feeds at pressing positions determined by the algorithms in section III.

The experiment results are summarized in Figure 9.

It can be seen that after just one iteration for springback compensation the deformed shape after springback approached the target. The geometric accuracy in the effective forming region of 240mm x 240mm is within error of 1.5mm (discrepancy in z direction between the shape after springback and the target). The result is acceptable.

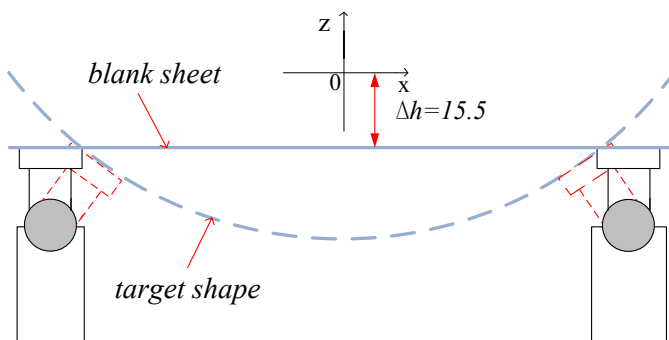
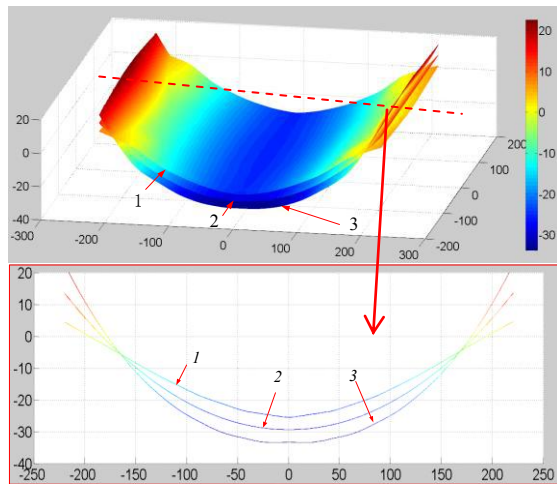


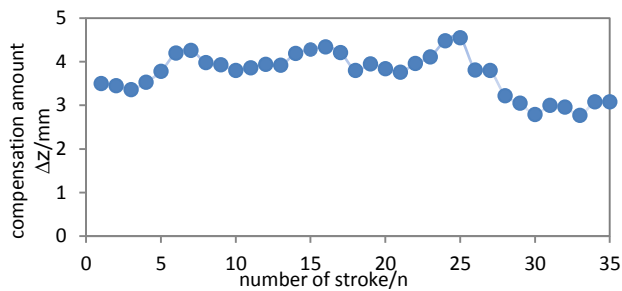
**Figure 8.** Initial configuration of experiment

**Table 1.** Initial total punch feeds at pressing positions

stroke n	total feed	stroke n	total feed
1	-29.32	19	-23.84
2	-29.32	20	-23.84
3	-29.32	21	-23.84
4	-29.32	22	-23.84
5	-29.32	23	-23.84
6	-27.95	24	-23.84
7	-27.95	25	-23.84
8	-27.95	26	-16.92
9	-27.95	27	-16.92
10	-27.95	28	-16.92
11	-27.95	29	-16.92
12	-27.95	30	-16.92
13	-27.95	31	-16.92
14	-27.95	32	-16.92
15	-27.95	33	-16.92
16	-23.84	34	-16.92
17	-23.84	35	-16.92
18	-23.84		



a) Comparison of shapes: 1- springback shape for 1st trial target shape; 2- 1st trial target shape (designed shape); 3 - 2nd trial target shape after 1st springback compensation

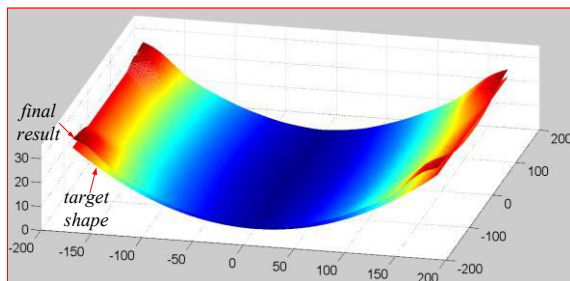


b) Total feed compensation amount for 1st springback compensation



c)Real deformed sheet metal part after 1st springback compensation

**Figure 9.** Results of the experiment



d) Comparison between springback shape after 1st springback compensation and designed target shape

**Figure 9.** Results of the experiment

## 6 Conclusion

In this paper, numerical algorithms for calculating the punch feeds and the heights of supporting pillars as well as a springback compensation method which are essential to the design of the tool path for a novel incremental sheet metal bending process were presented. A validation experiment was also given. The maximum geometric error of the final deformed shape by the experiment was within 1.5mm in the effective forming region. The result demonstrates that the presented numerical algorithms and springback compensation method are feasible and applicable to practical use.

**Acknowledgment:** This research is supported by Shenzhen Basic Research Project(JCYJ20150521094519483), Taishan Scholar of Leading Talent in Ocean Engineering – A Special Project of Numerical Control Ship Building Machines, key cooperative program of the Bureau of International Cooperation (172644KYSB20160024), Chinese Academy of Science and the cooperation project of Foshan and Chinese Academy of Sciences (2014HT100103).

## References

- [1] C.D. Jang and S.C. Moon, An algorithm to determine heating lines for plate forming by line heating method, *Journal of Ship Production*, 14(4), 1998, pp.238-245.
- [2] W. C. Emmens, G. Sebastiani, and A. H. van den Boogaard, The technology of Incremental Sheet Forming—A brief review of the history, *Journal of Materials Processing Technology*, 210, 2010, pp. 981-997.
- [3] J.M. Allwood, H. Utsunomiya, A survey of flexible forming processes in Japan, *International Journal of Machine Tools & Manufacture*, 46, 2006, pp. 1939-1960.

- [4] Luo, yuanxin, Wanmian Yang, Zhifang Liu, Yongqin Wang, and Ruxu Du. Numerical simulation and experimental study on cyclic multi-point incremental forming process, *The International Journal of Advanced Manufacturing Technology*, 85, 2016, pp 1249-1259.
- [5] Zhong-Yi Cai, Ming-Zhe Li, Multi-point forming of three-dimensional sheet metal and the control of the forming process, *International Journal of Pressure Vessels and Piping*, 79(4), 2002, pp. 289-296.
- [6] Wei Gan, R. H. Wagoner, Die design method for sheet springback, *Internatiaj Journal of Machanical Science*, 46, 2004, pp. 1097-1113.

Fan-yi MENG\*, Xiao-feng GONG, Xu KANG

## **Research on Tribological Characteristics of 316L Stainless Steel against PEEKHPV under Water Lubrication**

**Abstract:** Compared with traditional oil hydraulic elements, water makes the key friction and wear of water hydraulic pump/motor more serious for its low viscosity and lubricant. To find the appropriate paired friction materials of water hydraulic pump/motor, 316L Stainless Steel and PEEKHPV were studied as research subject. The contact surface friction coefficient, temperature of friction pairs in water were investigated by using a MMW-1 vertical universal friction and wear tester at different speed and load. After the friction test the worn surface morphologies and wear extent were observed by a laser scanning confocal microscope. The result turns out that when the rotational speed is 100 r/min and load is 100 N, friction coefficient of 316L Stainless Steel and PEEKHPV is lower with more excellent friction wear performance which makes it the suitable key friction pairs materials of water hydraulic pump/motor.

**Keywords:** water lubrication; friction pairs; PEEKHPV; friction-wear test

### **1 Introduction**

Water hydraulic system is a new type of green hydraulic technology that uses filtered fresh water or seawater to instead of mineral oil as working medium [1]. Water medium has advantage of no pollution, good security, etc that makes the water hydraulic system widely used in water treatment, water mist fire extinguishing, nuclear reactor, ships, underwater operation, food processing and other industries [2-4]. Water hydraulic pump/motor is the power of the water hydraulic system and actuators. It is also a key element of water hydraulic system. Compared with oil pump/motor, water medium's difference of physical and chemical properties makes it more serious in leakage, corrosion, cavitation, friction and wear. The key friction pair of relative speed is high, the contact stress is big, the condition working environment of lubrication is poor that greatly limits the service life of water hydraulic pump/motor. Therefore it becomes the bottleneck of water hydraulic systems technology's application. Viscosity of water is low and it is 1/30-1/50 of hydraulic in the same temperature. Fitting clearance of

---

\*Corresponding author: Fan-yi MENG, Transportation Equipment and Ocean Engineering College, Dalian Maritime University, Dalian China, 116026, E-mail: mengfy713@163.com

Xiao-feng GONG, Xu KANG, Transportation Equipment and Ocean Engineering College, Dalian Maritime University, Dalian China, 116026

friction pair is very small of design. The above two points make hydraulic component occurs on the surface of the direct contact of the friction pair so easily and the surface wear not work. Therefore, the developed water hydraulic components must be with good characteristics of wear, corrosion, fatigue and cavitation resistances.

In order to make the water hydraulic piston pump/motor can operate normally in the water (sea water) environment, research on materials of high hardness, corrosion resistance and wear resistance has become an indispensable link in study of water hydraulic components. In water environment (especially sea water), metal can form a corrosive cell that result in a galvanic corrosion. Therefore the friction pair is impossible single metal material of water hydraulic components. In recent years, with the development of new materials, such as engineering ceramics and polymer materials, water hydraulic transmission technology has made considerable progress and development. Compared with metals, engineering plastics have many advantages, which include better self-lubricating and friction wear capability, lower friction coefficient, and more outstanding wear resistance. These characteristics make engineering plastics a new option of key friction pair material of water hydraulic pump/motor. Jiao Sujuan from Zhe Jiang University proves the tribological behavior of modified poly (ether ether ketone) and plasma ceramic coating is better than stainless steel by test machine of M-200 friction and wear [5-6]. Shen Fengmei from Beijing University of Technology studies friction-wear character of CFRPEEK against 316L, 17-4PH, Silicon nitride ceramic by MCF-10 friction wear testing machine. The conclusion is that Ceramic silicon oxynitride's friction character is the best [7]. Wang Zhiqiang from Yanshan university studies 10 kinds of engineering plastics such as 316L, 9Cr18Mo against PTFE, Hard ABS resin, PEEK450CA30 with the help of MMU-5G friction wear testing machine. It proves that 316L-PEEK450CA30 is the best option for paired friction of torque seawater hydraulic motor. The conclusion also comes to that the friction coefficient increases with the increase of rotate speed and loading. In the mean time, it is also found that the influence of rotate speed to friction coefficient is bigger than the loading to friction coefficient. researched tribological behavior of the resulting filled PEEK composites and plasma-sprayed ceramic coating sliding against stainless steel under water lubrication was investigated on an MM-200 friction and wear tester, in a ring-on-block contact configuration and found that PEEK composites have better performance. Shen investigated the tribological behavior of and found that the CFRPEEK-Silicon nitride ceramic has low friction coefficient Wang studied friction and wear between stainless steel and 10 kinds of engineering plastics such as PTFE, CFR-PAI, CFRPEEK, PEEK450CA30, and showed that 316L stainless steel and CFRPEEK are more suitable for torque seawater hydraulic motor [8-10].

Through the analysis of the documents above, tribology performance of engineering plastic against metal are mainly studied by scholars, while tribology performances of Stainless steel and PEEK under water lubrication are less focused on. The research group that author belongs to comes to conclusion that the friction pair of 316L-PEEKHPV between the tribology performance is the best, suitable for water hydraulic piston

pump/motor friction pair material through the friction and wear experiment of 316L stainless steel with four common kinds of polyether ether ketone (PEEK). This thesis based on 316L stainless steel against PEEKHPV as experiment subject and design of the water hydraulic pump/motor by simulating the actual works of friction pair to further study the tribology performance. It studies the friction and wear performance at load of 100 ~ 300 N (0.8 ~ 2.4 MPa) and speed at 100 ~ 300 r/min (1.4 ~ 4.2 m/s) in water.

## 2 Experiment Materials and Methods

Friction and wear experiment are conducted on MMW-1 vertical universal friction and wear tester. Ring-plate sliding contact forms are adopted to simulate the contact form of water hydraulic pump/motor friction pair in experiment. The upper specimen ring was made of 316L stainless steel with dimension of 25 mm (outer diameter) 27 mm (inner diameter) and friction diameter of 26.5 mm on average, thickness of 5 mm, surface roughness Ra of 0.4 microns. whereas the bottom specimen disc was made of PEEKHPV with dimension of 16 mm (outer diameter) 31.7 mm (inner diameter) a thickness is 10 mm, surface roughness Ra of 0.4 microns. Figure 1 shows the theory of friction wear testing machine. The upper specimen is driven by principal axis to rotate in clockwise. The bottom specimen is fixed and provide loading force of axial direction through loading axis. Both the upper and bottom specimen are in water box which is full of water. Thereby friction pair realizes to slide continuously on contact surface under the condition of water lubrication.

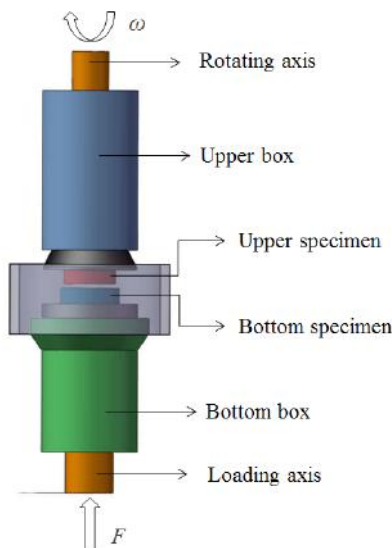


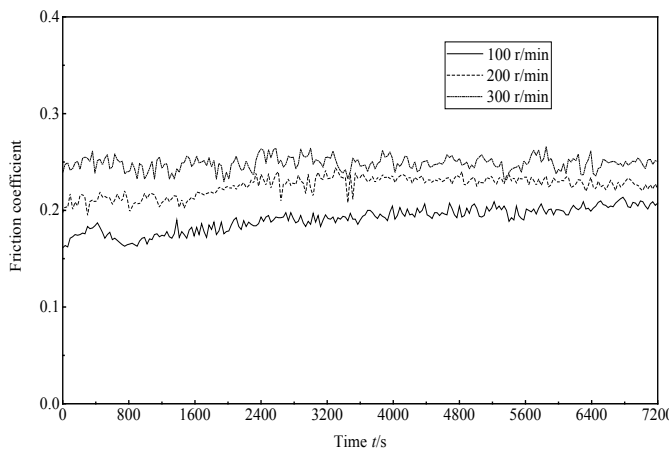
**Figure 1.** MMW-1 vertical universal friction and wear tester

In order to simulate real working condition of water hydraulic pump/motor, experiment were respectively performed wear condition between the friction pair when 100 N load is at different speed and when speed 100 r/min is at different load. Experiment lubricant is filtered tap water with filtration precision in 3-20  $\mu\text{m}$ , 2 h test time and room temperature to make record of friction coefficient and water temperature. After experiment, use a laser confocal microscope to observe sample surface morphology before and after wear.

### 3 Results and Analysis

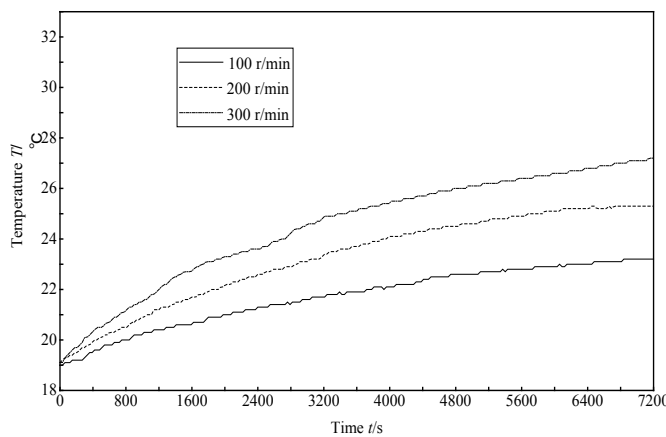
#### 3.1 The influence of rotating speed on the friction performance

Figure 2 shows when the load is 100 N, curve of friction coefficient that dual friction pair at different rotate speed with test time changed. It can be found that when the load (100N) is certain, friction coefficient of 316L-PEEKHPV friction pair increases with the increase of rotate speed, while the increase amplitude is small. When the rotate speed is at 100r/min, friction coefficient increase stabilizes around 0.19 with small fluctuation amplitude. When the rotate speed is at 200r/min, 3300 s internal friction coefficient of volatile is big within 3300 s. Then it is tending to stabilize and maintain between 0.22 and 0.27. When the rotate speed is at 300r/min, compared with the former two volatilities, friction coefficient in whole process is bigger and vibrates between 0.22 and 0.27.



**Figure 2.** The variation of the friction coefficient of 316L-PEEKHPV with test time at different rotate speed.

Interior environment temperature in experiment is 18.1°C. Figure 3 demonstrates curve that friction coefficient of dual friction pair leads to the change of water temperature in water box. It can be found from the graph curve, water temperature is increased with time passing and rotate speed is in proportion to speed. Two hours later, when speed is at 100r/min, seawater temperature stabilizes at 23.2°C. When speed is at 200r/min, seawater temperature stabilizes at 25.3°C. When speed is at 300r/min, seawater temperature stabilizes at 27.3°C. The change of water temperature reflects friction power consumption. The higher the speed is, the bigger coefficient of friction between the friction pair is and more friction works. Therefore power consumption is more.



**Figure 3.** The variation of the temperature of 316L-PEEKHPV with test time at different rotate speed.

### 3.2 The influence of load on the friction performance

Figure 4 shows curve of friction coefficient that dual friction pair at different load with time changed when the speed is at 100r/min. As you can see, when the speed (100r/min) is certain, 316 L - PEEKHPV duality between vice friction coefficient increases with the increase of load. Compared with Figure 2, amplification and vibration of friction coefficient increase is much more obvious. When the load is 100 N, the friction coefficient stabilizes around 0.19 and the fluctuation amplitude is small with time passing; when the load is 200 N, the friction coefficient is between 0.21 and 0.26; when the load is 300 N, the fluctuations and vibration are biggest with friction coefficient about 0.35 after 2 hours. It can be found that compared with Figure 2, change of friction coefficient at different rotate speed, when load increases, friction coefficient between dual vice oscillation increases sharply. While rotation speed

increases, vibration change of dual pair of friction coefficient is not particularly obvious. Thus load makes bigger effect on friction coefficient.

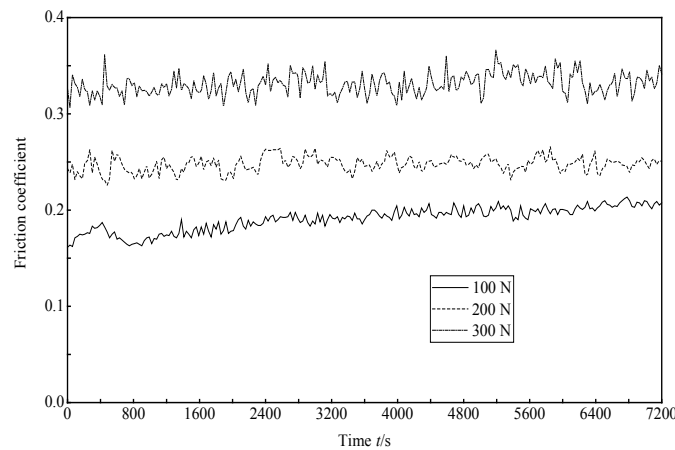


Figure 4. The variation of the friction coefficient of 316L-PEEKHPV with test time at different load.

Figure 5 demonstrates curve that friction coefficient of dual friction pair leads to the change of water temperature in water box. It can be seen from the curve that the temperature of water is increased with time passing. Temperature is in proportion to load. After 2 hours, when rotate speed is at 200N, seawater temperature stabilizes at 26.6°C. When rotate speed is at 300 N, seawater temperature stabilized at 30.2°C. Compared with effect that rotate speed makes on water temperature, load makes temperature rise. It is because load makes bigger effect on friction coefficient. The bigger friction coefficient is, the more friction works. Therefore, temperature may rise more.

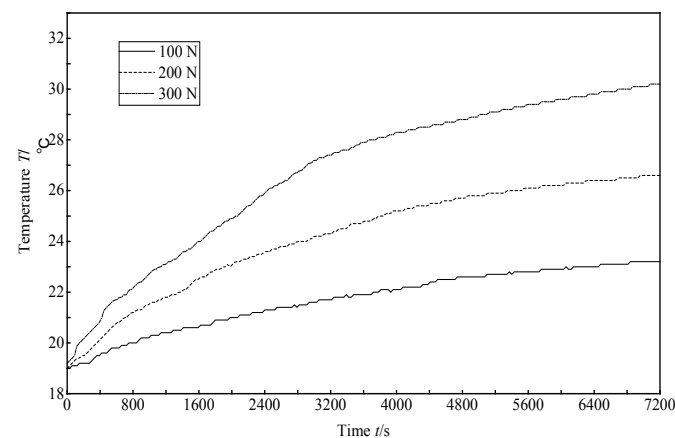
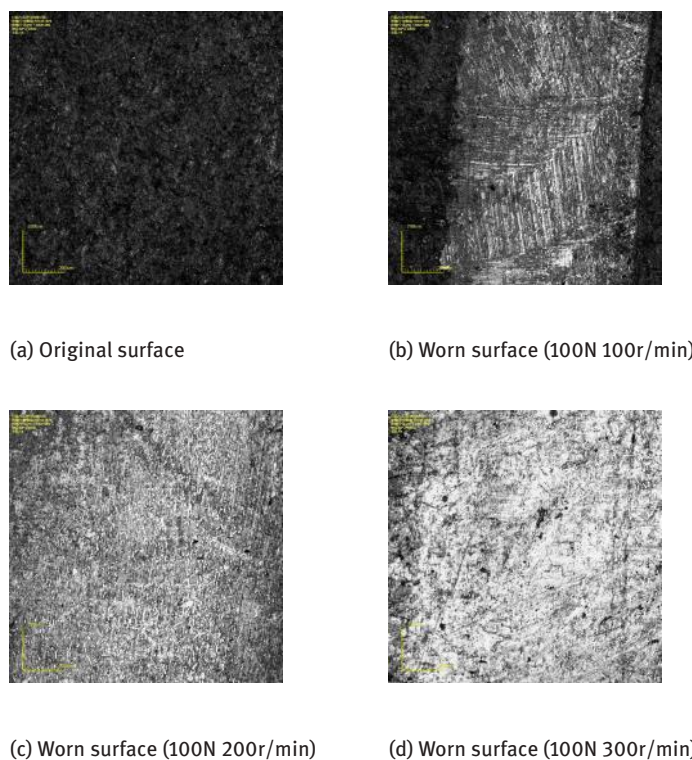


Figure 5. The variation of the temperature of 316L-PEEKHPV with test time at different load

### 3.3 Analysis of friction and wear mechanism

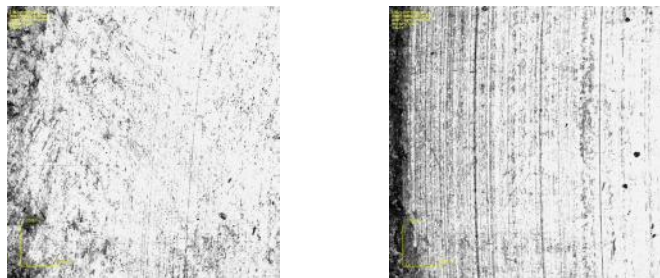
Through analysis of friction coefficient at different rotate speed and load above, when rotate speed at 100 r/min, and load at 100 N, 316L-PEEKHPV dual friction pair of friction coefficient is smaller. It is because relatively low speed and load avail to form effective lubrication on contact surface so as to reduce friction. In the meantime, relatively low speed and load will not result in temperature on friction surface rises instantly so that impacts hardness and strength of PEEKHPV then avoid more serious adhesive wear happening.

In order to study PEEK HPV's mechanism of friction and wear, wear surface morphology were analyzed through Olympus confocal laser microscope.. Figure 6 shows the topography at different speeds and loads before and after friction. It is seen from Figure 6b, when load is 100N and speed is 100r/min, surface PEEKHPV's surface wear is relatively even with fine scratches. Wear area is smallest and wear mechanism is mainly scratches; As rotate speed increases to 200r/min, it can be seen from Figure 6c that the wear area expands with increased scratch. When the speed reaches at 300r/min, It can be seen from Figure 6d that surface wear is very serious and a large number of irregular scratches in varying thickness are emerged.



(c) Worn surface (100N 200r/min) (d) Worn surface (100N 300r/min)

**Figure 6.**



(e) Worn surface (200N 100r/min)

(f) Worn surface (300N 100r/min)

**Figure 6.**

Seen from Figure 6b, when the speed is at 100r/min and load is 200N, scratches increase with phenomenon of a slight furrow emerging; When speed is at 100r/min and load is 200N, furrows phenomenon continues to grow. A quantity of 316L shedding particles is also found on the surface of wear. It indicates that at this speed, a slight adhesion wear of friction dual deputy happens.

Through the above on different speeds and under different load coefficient of friction, the analysis shows that, when the speed is too load, friction coefficient is small. This is because the relatively low speed and load contact surface facilitates the formation of effective lubrication, thereby reducing friction. Meanwhile, the lower speed and load will not cause a transient increase hardness and strength of the friction surface temperature and impact, and thus avoid more serious adhesive wear.

## 4 Conclusion

- Under water lubrication, the dual friction pair 316 l - PEEKHPV friction coefficient increases with the increase of rotational speed and load, and at the same time also found that the load on the influence of friction is greater than the influence of the rotational speed on the friction coefficient.
- By contrast morphology at different speeds and loads PEEKHPV wear before and after shows that the wear mechanism is scratched, the rotational speed of 100r/min, the case load of 300N, the dual friction 316L-PEEKHPV occur slight adhesive wear.
- Comprehensive analysis of the friction and wear properties even friction 316L-PEEKHPV various aspects shows that, when the rotational speed of 100r/min, a load of 100N, the friction coefficient of friction between the smallest and lowest temperature rise caused by the water, the degree of wear-resistant it is good.

**Acknowledgment:** This work was financially supported by the Fundamental Research Funds for the Central Universities.

## References

- [1] YANG Hua-yong, ZHOU Hua, New Achievements in Water Hydraulics, Chinese Hydraulics & Pneumatics, 2013(2): 1-6.
- [2] LIU Yinshui, WU Defa and LI Donglin, Applications of Seawater Hydraulics in Deep-sea Equipment, Journal of Mechanical Engineering, 2014, 02: 28-35.
- [3] Finn Conrad. Trends in design of water hydraulics-motion control and open-ended solutions, Proceedings of the 6th JFP-S International Symposium on Fluid Power [C]. Tsukuba, 2005: 420-431.
- [4] Mikko Siuko, PitkaahoM and RanedaA, et al. Water hydraulic actuators for ITER maintenance devices, Fusion Engineering and Design, 2003, 69 (1-4): 141-145.
- [5] JIAO Su-juan, ZHOU Hua, YANG Hua-yong, et al. Tribological Behavior of Filled Polyetheretherketone Composites in Sliding against Stainless Steel under Water Lubrication, Tribology, 2003, 05:385-389.
- [6] Jiao Sujuan. The Tribological Properties of Key Friction Pairs in Water Hydraulic Piston Pump and Water Hydraulic Relief Valves, Zhejiang University, 2004.
- [7] Shen Fengmei. Material Matching Property and Reliability Rearch of Key Friction Pairs in the Sea Water Hydraulic Piston Pump, Beijing University of Technology, 2014.
- [8] Zhiqiang Wang, Dianrong Gao. Comparative investigation on the tribological behavior of reinforced plastic composite under natural seawater lubrication, Materials and design, 2013
- [9] Zhiqiang Wang, Dianrong Gao. Friction and wear properties of stainless steel sliding against polyetheretherketone and carbon-fiber-reinforced polyetheretherketone under natural seawater lubrication, Materials and design, 2014.
- [10] WANG ZQ, NI J ang GAO D R. Friction and Wear Properties of Stainless Steel Sliding Agaisnt GFRPEEK and CFRPEEK Under Seawater Lubrication, China Surface Engineering, 2016, 02:49-57.

Ning-shan WANG\*, Yong-sheng YANG

## Turbofan Engine Controller Optimal Design based on Grey Wolf Optimizer

**Abstract:** This paper describes a controller parameter optimization algorithm for a high-bypass turbofan engine controller. The turbofan engine is a nonlinear system working under extreme environment. Under such circumstances the engine system should ensure high reliability, stability and transient response performance. The contribution of the research lies in providing a new off-line optimization algorithm—the Grey Wolf Optimizer (GWO) to optimize the parameters of turbofan engine's Proportional Integral controller to provide the engine a better transient performance under certain working condition. The simulation results shows that compared with the original controller, the new controller provides better transient performance.

**Keywords:** PI controller, Grey Wolf Optimizer, Turbofan Engine, Transient Performance

### 1 Introduction

Gas turbine engines (GTE), especially high bypass turbofan engine have played a significant role in the expansion of the flight capabilities of modern aircraft [1]. The high bypass turbofan engine installed in commercial aircraft must be operated by means of feedback control. The objective of the controller is to achieve nice thrust response performance while maintaining the engine output inside safety intervals [2]. To improve the transient performance of the turbofan engine, many advanced methods have been applied to the turbofan its control system.

Generally speaking, the turbofan engine is a complex system with strong nonlinearity. The performance of certain turbofan engine will change considerably with working condition, aging and maintenance. So, designing its controller to fulfill the requirements is a very difficult task. Classical linear compensation has been widely applied on the turbofan engine control to govern the engine close to a certain operating point [2]. Since the thrust of the turbofan engine installed on the aircraft cannot be measured in real time, Low Pressure Turbine (LPT) rotation speed or Engine Pressure Ratio (EPR) measured is usually designed to be the controlled variable. And, although many advanced control methods appear [2].

---

\*Corresponding author: Ning-shan WANG, School of Mechanical Engineering, Shanghai Jiao Tong University, Shanghai, China, E-mail: zgmf@sjtu.edu.cn

Yong-sheng YANG, School of Aeronautics and Astronautics, Shanghai Jiao Tong University  
Shanghai, China

Since the thrust of the turbofan engine installed on the aircraft cannot be measured in real time, Low Pressure Turbine (LPT) rotation speed or Engine Pressure Ratio (EPR) measured is usually designed to be the controlled variable. And, although many advanced control methods appear [2], the classical Proportional Integral (PI) controller is still used in Turbofan engine control because of its robustness and adaption. Optimizing the PI controller design is still a valuable method to improve the turbofan engine performance.

If the controlled variable of the turbofan engine is the LPT rotation speed, the control problem is similar to the Load Frequency Control (LFC) problem in stationary steam thermal power system. In Guha and Sharma's researches, an evolutionary algorithm (EA) known as grey wolf optimization (GWO) has been applied for optimal design of PI/PID controller to solve LFC problem [3,4]. The simulated result shows that the optimized controller design shows pretty good performance.

In view of the above discussion, the main aim of the present research is to use the GWO algorithm to optimize the PI controller design of a high bypass turbofan engine. A dynamic model of P&W JT9D established in previous research is applied here [5]. Based on the given model, the turbofan engine working under changing working condition is simulated. The parameter of the PI controller is optimized by the GWO under certain working condition. The simulated transient response of the optimal controller is evaluated.

The following part of the paper is organized as follows. Section 2 the system scheme of the certain turbofan engine. The GWO algorithm is briefly described in Section 3. Section 4 presents detailed information about the controller. Section 5 is about the result and the comparison. Section 6 shows the conclusion and future work.

## 2 Model Description

The components structure and the close-loop scheme of the certain turbofan engine is shown in Figure 1 [5,6]. The whole dynamic model of the turbofan engine is built based on the example provided by NASA [6]. The steady state nonlinear maps of the turbo machinery, including the Fan, Low Pressure Compressor (LPC), High Pressure Compressor (HPT), Low Pressure Turbine (LPT) are achieved from real data collected. The Dynamic Iterative Solver (DIS) inside the scheme can simulate the transient state performance of the engine under dynamic state condition. According to the previous research, the JT9D modeled shows nice accuracy compared with real data [5-7]. The component system scheme of the turbofan engine is presented in Figure 1. The dynamic system scheme is presented in Figure 2.

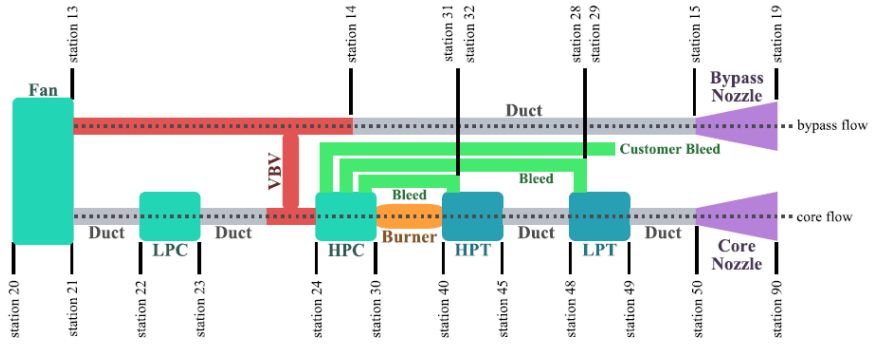


**Figure 1.** P&W JT9D Turbofan Engine Components Scheme[5]

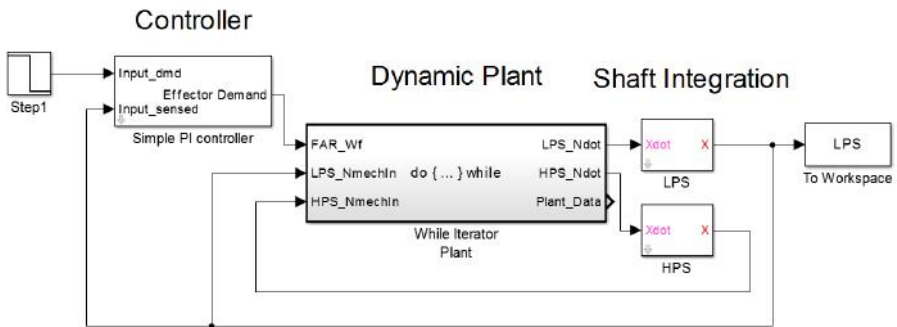


**Figure 2.** High bypass Turbofan Engine Dynamic Scheme [8]

### 3 Optimizazation method

#### 3.1 Grey Wolf Optimizer

GWO, as a heuristic optimization technique, can find the candidate solution from very large solution space with no specific input parameters required. Such characteristics are very suitable to deal with the nonlinear problems like controller parameter tuning. The algorithm is designed to achieve its target through mimicking the social hierarchy and hunting mechanism of the wolf society.

The social hierarchy of the wolf society is a special one. The wolves at the top of the wolf pack are called alphas. They are responsible for making important decisions about hunting, sleeping place, wake time, etc. However, some kind of democratic behavior is also observed in which they follow other wolves in the wolf pack. In

gatherings, the entire wolf pack acknowledges the alpha by holding their tails down. The alpha wolves are also called the dominant wolves.

In the second level of the hierarchy, the grey wolves are named as beta category wolves and they are subordinate of alpha category wolves. They help alphas in the decision-making process and/or other pack activities. They are probably the best candidate and may transform into the alpha category wolves in case one of the alpha wolves passes away or become very old.

The lowest stage of the hierarchy is occupied by the omega types of wolves. They are basically used as a scapegoat and always follow the decision made by other dominant wolves. They are the worst category of wolves those are all owed to eat.

The wolves which do not come under alpha, beta and omega categories are grouped under delta or subordinate category. Delta types of wolves always follow the alphas and betas but dominate omegas [3,9].

During hunting, the main steps are listed as follows and shown in Figure 3.

- (i) Tracking, chasing and approaching the prey.
- (ii) Pursuing, encircling and harassing the prey until it stops moving.
- (iii) Attack towards the prey.



**Figure 3.** Hunting behavior of grey wolves: (A) chasing, approaching, and tracking prey (BCD) pursuing, harassing, and encircling (E) stationary situation and attack [9], [10]

In the following sections, the hunting process is rewritten into three stages: encircling prey, hunting and attacking [9]. The characteristics of the social hierarchy, and hunting are represented mathematically in the following section to show how the algorithm works.

### 3.2 Social Hierarchy

For modeling of the social hierarchy of the grey wolf, alpha is considered to be the fittest solution followed by beta and delta, respectively, and the rest of the solutions are group edunder omega. In GWO, the hunting (optimization) process is guided by alpha, beta and delta, whereas omega always follows these three wolves [3]. The society structure of the wolf pack is presented in Figure 4.

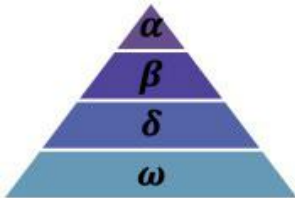


**Figure 4.** Hierarchy of grey wolf [9]

### 3.3 Encircling Prey

In order to mathematically model encircling behavior the following equations are presented as:

$$\vec{D} = |\vec{C} \cdot \vec{X}_p(t) - \vec{X}(t)| \quad (1)$$

$$\vec{X}(t+1) = \left| \vec{X}_p(t) - \vec{A} \cdot \vec{D} \right| \quad (2)$$

Where  $t$  indicates the current iteration,  $\vec{A}$  and  $\vec{C}$  are coefficient vectors,  $\vec{X}_p$  is the position vector of the prey, and  $\vec{X}$  indicates the position vector of a grey wolf.  $\vec{A}$  and  $\vec{C}$  are defined as follows:

$$\vec{A} = 2\vec{a} \cdot \vec{r}_1 - \vec{d} \quad (3)$$

$$\vec{C} = 2 \cdot \vec{r}_2 \quad (4)$$

Where components of  $\vec{d}$  are linearly decreased from 2 to 0 over the course of iterations and  $\vec{r}_1$ ,  $\vec{r}_2$  are random vectors in  $[0, 1]$  [3,9].

### 3.4 Hunting

In order to mathematically simulate the hunting behavior of grey wolves, we suppose that the alpha (best candidate solution) beta, and delta have better knowledge about the potential location of prey. Therefore, we save the first three best solutions obtained so far and oblige the other search agents (including the omegas) to update their positions according to the position of the best search agents [9].

$$\vec{D}_\alpha = \left| \vec{C}_1 \cdot \vec{X}_\alpha - \vec{X} \right| \quad (5)$$

$$\vec{D}_\beta = \left| \vec{C}_2 \cdot \vec{X}_\beta - \vec{X} \right| \quad (6)$$

$$\vec{D}_\gamma = \left| \vec{C}_3 \cdot \vec{X}_\gamma - \vec{X} \right| \quad (7)$$

$$\vec{X}_1 = \vec{X}_\alpha - \vec{A}_1 \cdot \left( \frac{\vec{D}_\alpha}{\vec{D}_\alpha} \right) \quad (8)$$

$$\vec{X}_2 = \vec{X}_\beta - \vec{A}_2 \cdot \left( \frac{\vec{D}_\beta}{\vec{D}_\beta} \right) \quad (9)$$

$$\vec{X}_3 = \vec{X}_\gamma - \vec{A}_3 \cdot \left( \frac{\vec{D}_\gamma}{\vec{D}_\gamma} \right) \quad (10)$$

$$\vec{X}(t+1) = \frac{\vec{X}_1 + \vec{X}_2 + \vec{X}_3}{3} \quad (11)$$

### 3.5 Attack

As the cost function converges to the neighborhood of a certain point, the cost function has reached the optimal value. The wolves begin to attack the prey.

### 3.6 Whole Optimization Process Overview

The whole optimization pseudocode is shown Figure 5.

```

Initialize the grey wolf population  $X_i$  ( $i = 1, 2, \dots, n$ )
Initialize  $a$ ,  $A$ , and  $C$ 
Calculate the fitness of each search agent
 $X_a$ =the best search agent
 $X_\beta$ =the second best search agent
 $X_\delta$ =the third best search agent
while ( $t < \text{Max number of iterations}$ )
    for each search agent
        Update the position of the current search agent by equation (3.7)
    end for
    Update  $a$ ,  $A$ , and  $C$ 
    Calculate the fitness of all search agents
    Update  $X_a$ ,  $X_\beta$ , and  $X_\delta$ 
     $t=t+1$ 
end while
return  $X_a$ 
```

Figure 5. Pseudo code of the GWO algorithm [9]

## 4 Controller and Problem Formation

### 4.1 Controller Description

According to the dynamic scheme shown in Figure 1. This PI controller is used to govern the LPT rotation Speed (LPS). The parameters required to be optimized are proportional gain  $K_p \cdot M$  and integral gain  $K_i \cdot M$ .

The PI controller output/plant input can be described as following equations:

$$FAR\_W_f = K_p \cdot M e(t) + K_i \cdot M \int e(t) dt \quad (12)$$

$$e(t) = LPS_d - LPS \quad (13)$$

Here  $FAR\_W_f$  stands for the input control signal, which is the fuel signal.  $e(t)$  stands for the error signal, which is the difference between  $LPS_d$ , the  $LPS$  demanded, and the  $LPS$  measured.

### 4.2 Objective Function

There exist many objective functions which are used to evaluate the performance of a controller. In this research, Integral Time Absolute Error (ITAE) is applied to evaluate the controller's performance.

$$ITAE = \int_0^{t_0} |e(t)| dt \quad (14)$$

## 5 Implementation of GWO

In this paper, GWO algorithm is applied to solve turbofan engine control problem. The algorithm sequences of the proposed method are listed as below [3].

**Step 1.** Initialize input parameters of GWO algorithm such as search agents no, number of control variables according to the controller structure, upper and lower bounds of the search space, number of elitism parameters and total number of generations.

**Step 2.** In the initialization process, search agents or grey wolves (a two row vector  $[K_p \cdot M, K_i \cdot M]$ ) are randomly generated between upper and lower bounds in the search space.

**Step 3.** Evaluate the fitness function using (14) and assign alpha, beta, delta wolves in the search space.

**Step 4.** Update the positions of alpha, beta and delta using pseudo code shown in Figure 6.

**Step 5.** Update the positions of alpha, beta and delta using pseudo code shown in Figure 6.

```

for i = 1 : searchagents_no

    if fitness < alpha
        alpha ← update fitness
    end

    if fitness > alpha & & fitness < beta
        beta ← update fitness
    end

    if fitness > alpha & & fitness > beta & & fitness < delta
        delta ← update fitness
    end

end

```

**Figure 6.** Positions Update Pseudo Code [6]

**Step 6.** Defining two random numbers  $r_1$  and  $r_2$  source between  $[0, 1]$  and  $\vec{\alpha}$  linearly decreasing from 2 to 0.

**Step 7.** Check whether any search agent goes beyond the search space or not and infeasible solutions are replaced by the randomly generated feasible solution set.

**Step 8.** Sort the positions of search agents obtained in step 6 from the best value to worst value and use for next generation.

**Step 9.** Go to **Step 4.** until the termination criterion is fulfilled.

## 6 Simulation Result and Discussion

To test the effectiveness and superiority of proposed algorithm, the whole process is simulated under MATLAB condition and GWO is written in the.m file. ITAE criterion based objective function is minimized using GWO algorithm to find optimum gains of controller parameters.

### 6.1 Simulated Turbofan Working Condition

The turbofan engine is simulated working under certain outer condition, which is listed in the Table 1. In the 30s simulation, the  $LPS_d$  is a step change signal from 3667r/min to 3467r/min at 15s.

**Table 1.** Initial condition

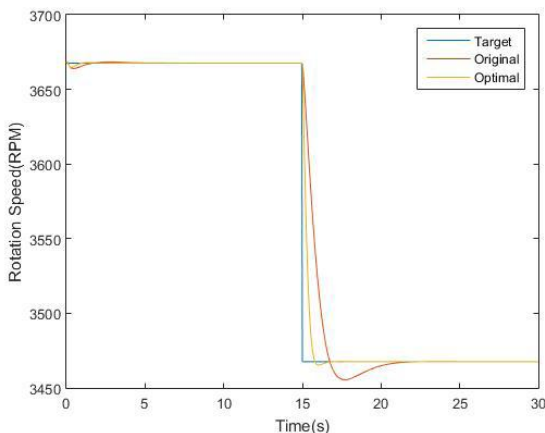
<b>Gas path flow (pps)</b>	<b>674.22</b>
Enthalpy (BTU/lbm)	130
Total Temperature (degR)	448.46
Pt - Total Pressure (psia)	5.528

## 6.2 Algorithm Setting

Search agents (the capacity of the wolf pack), Iteration time and the boundary of searching are required to be set initially. In this research, the number of search agents is 30, and the max iteration time is 50. The original control parameters provided by the given model in previous research are  $K_p \cdot M = 8e - 6$ ,  $K_i \cdot M = 1e - 5$  [6]. To search for the optimal control parameters, specific searching boundary is selected. The boundary of the searching area is built around the original control parameters. The lower boundary of the searching area is  $8e - 7$ . The higher boundary of the searching area is  $3e - 5$ . For simplicity, searching of the controller parameter  $K_p \cdot M$  and  $K_i \cdot M$  shares the same boundary in this research.

## 6.3 Result and Comparison

The simulation results can be seen in Table 2 and Figure 7. It can be seen that the performance of the controllers are well optimized. All of the optimized controllers show pretty good performance compared with the original controller.

**Figure 7.** Simulation result

**Table 2.** Simulation result

Group	$K_p \cdot M$	$K_i \cdot M$	ITAE ( $r \cdot s/min$ )
Optimal	3e-5	1.453e-5	58.34
Original	8e-6	1e-5	175.68

## 7 Conclusion

From the research carried out, the PI controller parameters for LPS control of JT9D turbofan engine are optimized through GWO. The simulation work has been done to verify the effectiveness of the proposed method. The simulation result shows that compared with the controller parameters given in previous research, the optimized parameters show better performance under certain working condition.

## References

- [1] S. Jafari and M. Montazeri-Gh, Evolutionary optimization for gain tuning of jet engine min-max fuel controller, *Journal of Propulsion and Power*, vol. 27, no. 5, pp. 1015–1023, 2011.
- [2] H. Richter, *Advanced control of turbofan engines*. Springer Science & Business Media, 2011.
- [3] D. Guha, P. K. Roy, and S. Banerjee, Load frequency control of interconnected power system using grey wolf optimization, *Swarm and Evolutionary Computation*, vol. 27, pp. 97–115, 2016.
- [4] Y. Sharma and L. C. Saikia, Automatic generation control of a multi-area st-thermal power system using grey wolf optimizer algorithmbased classical controllers, *International Journal of Electrical Power & Energy Systems*, vol. 73, pp. 853–862, 2015.
- [5] A. M. Zinnecker, J. W. Chapman, T. M. Lavelle, and J. S. Litt, Development of a twin-spool turbofan engine simulation using the toolbox for the modeling and analysis of thermodynamic systems (t-mats), in 2014 AIAA Joint Propulsion Conference, Cleveland, OH, 2014.
- [6] J. W. Chapman, T. M. Lavelle, R. D. May, J. S. Litt, and T.-H. Guo, Toolbox for the modeling and analysis of thermodynamic systems (t-mats) user's guide, 2014.
- [7] J. W. Chapman, T. M. Lavelle, J. S. Litt, and T.-H. Guo, A processfor the creation of t-mats propulsion system models from npss data, in 2014 AIAA Joint Propulsion Conference, Cleveland, OH, 2014.
- [8] J. S. Litt, Toolbox for the modeling and analysis of thermodynamicsystems workshop, 2015. Article in a conference proceedings:
- [9] S. Mirjalili, S. M. Mirjalili, and A. Lewis, Grey wolf optimizer, *Advances in Engineering Software*, vol. 69, pp. 46–61, 2014.
- [10] C. Muro, R. Escobedo, L. Spector, and R. Coppinger, Wolf-pack (*canislupus*) hunting strategies emerge from simple rules in computationalsimulations, *Behavioural processes*, vol. 88, no. 3, pp. 192–197, 2011.



---

## **Part VI: Mechatronics and Electrical Engineering II**



Jian-Hua LI\*, Ting-Ting RAO, Wei-Hua WANG, Wei-Bo ZHU

## Research of the EMI Suppression Circuit in the ASM Power

**Abstract:** As to the EMI in ASM, a power system is the main interference source and receiver. The EMI rejecting ability of power system determines the electromagnetic compatibility of ASM, so, it plays a very important role in the progress of ASM design. In this paper, we first summarize the program of switching power EMI suppression; focus on analyzing the form of switching power EMI filter. Then the ADS software was used to simulate the circuit performance of the EMI filter we designed. Through iterative simulation and optimization, an EMI filter with excellent performance which applied to ASM secondary power source is finally achieved.

**Keywords:** ASM; the secondary power source; EMI filter.

### 1 Introduction

A stable and reliable power system is the prerequisite for the safe operation of an electronic system. The purpose of secondary power sources to convert the 28V DC power that supplied by the aircraft, to various lower voltages which could be used by the missile. Besides the radiated EMI produced by other applications in the ambient environment, the power system inside the missile could also be interfered by the high frequency switching noise and rectifier diode noise in the secondary power source, which will result in output containing some severe harmonic waves both highly in amplitude and frequency. The switching noise and higher harmonic wave have severe negative effects on the EMC performance and power source stabilization, it will cause a potential threat to the system is existed without proper measurements. So an effective EMI suppression circuit must be designed in a power supply lines to keep the system work in a stable state.

### 2 Secondary power system EMI suppression tactics

Currently, the secondary power source in ASM, mostly use the  $\pm 28V$  provided by the aircraft as the input voltage, whose output voltages lie on the actual demands of the system, as  $\pm 15V$ ,  $\pm 5V$ . Figure 1 shows a EMI filter diagram, used with the

---

\*Corresponding author: Jian-Hua LI, Hongdu AVIC, Nanchang, China, E-mail: Jianhua703@163.com  
Ting-Ting RAO, Wei-Hua WANG, Wei-Bo ZHU, Hongdu AVIC, Nanchang, China

secondary power source in ASM, which consists of six blocks: voltage or current spike suppression, surge suppression circuits, input filter circuit, short-break energy storage circuit, and output filter [1]. Transient voltage suppression (TVS) diodes are usually used in the spike suppression circuit to weakening the highly transient voltage between the power lines, clamping the input voltage in a preset-value, so that others electronic elements could work normally under a safety voltage [2-4]. The function of surge suppression circuit is to deal with the overvoltage and under voltage problems when the aircraft system is in a short-break condition or high current switching [5-7]. The short-break energy storage circuit which generally made up by the current limiting resistor, high-capacity tantalum capacitors and diodes, is aimed at providing power continuously when power system is in high current switching.

The input filter is working as a frequency filter, dealing with the power signal which had processed by the spike suppression circuit and the surge suppression circuit to meet the requirements of DC-DC module, while the output filter is adjusting the DC-DC output quality to satisfy the application circuit's requirements [8].

### 3 Secondary power ripple suppressing method

Spike suppressing and surge suppressing can be treated as the preliminary process for the aircraft power source, providing a relatively stable environment for the secondary power source input. Standardized design has been implemented on the circuit system of ASM, causing the same kind of EMI problems, so universal EMI filters could be used in the input power lines. Considering some restrict factors, such as weight, size, function, and cost, the choice of a DC-DC converter is complicated, thus special output ripple attenuation circuit should be designed accordingly.

#### 3.1 The sources of secondary power output noise

Figure 1 shows the secondary side circuit of the DC-DC converter. Figure 2 illustrates the output EMI noise, consisted of two parts, one is the ripple caused by the switching frequency. It's a triangular wave, whose cycle is determined by the switching frequency; the other noise is the fast transient spike voltage caused by the PCB distributed parameter at the time the DC-DC converter's working state change into ON/OFF, this spike voltage is superimposed on the peak of the triangular wave. The switching frequency is relatively low, while the frequency of transient voltage spikes is relatively high, thus the spectrum of EMI is very wide. Therefore a wide-band output filter network is supposed to increase to the DC-DC terminal to filter out high frequency noise and ripple noise.

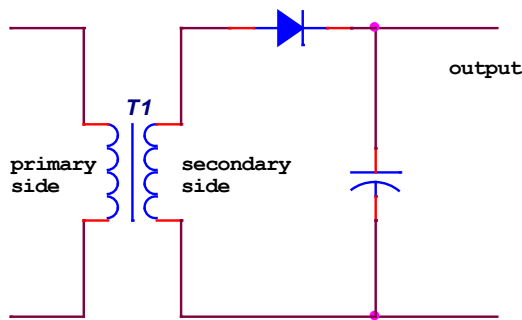


**Figure 1.** Diagram of the secondary circuit of switching power

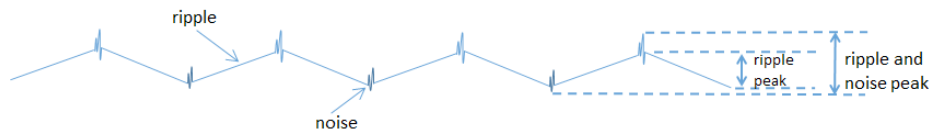


**Figure 2.** DC-DC switching power output noise

### 3.2 Filter structure

The interference signal on Secondary side power lines can be represented as differential-mode noise and common-mode noise. Differential-mode noise is the interference signal between power line L and N, common-mode noise interference is the interference signal between power line L and the ground. Thus, the suppressing to ripple noise of DC-DC converter output filter can be understood as the suppressing to common-mode and differential-mode noise. The output filter can be divided into common filter and differential filter according to the function structure.

#### 3.2.1 General performance EMI filter

The general performance EMI filter circuit contains a common-mode choke (common-mode inductance) L, differential-mode and common-mode capacitor C<sub>x</sub>, C<sub>y</sub>. Common-mode choke is made up of two coils which were wounded on a magnetic ring (closed magnetic circuit)'s upper and lower half-rings with same number of turns but wounded opposite. The magnetic flux direction of the two coils is the same, and when the common-mode interference appears, the total inductance increases rapidly to a large value which can suppress common-mode interference effectively. EMI filter

circuit in Figure 3 can be seen as the combination of the common-mode equivalent circuit and differential-mode equivalent circuit shown in Figure 4a and 4b and  $L_{dm}$  is the leakage inductance of common-mode choke.

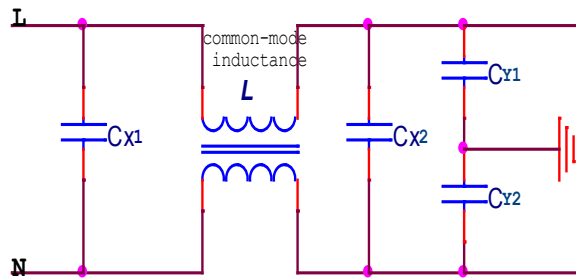


**Figure 3.** General performance EMI filter

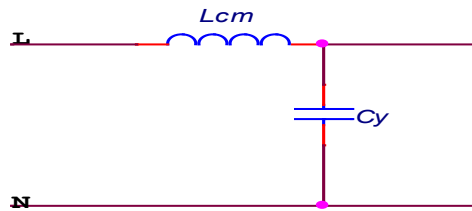


**Figure 4 .(a)** Common-mode equivalent circuit

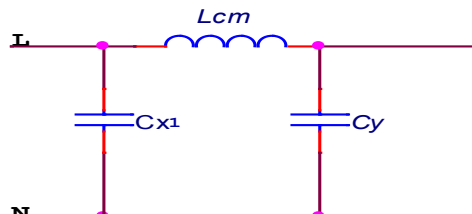


**Figure 4. (b)** Differential-mode equivalent circuit

Common-mode equivalent circuit A parameter matrix:

$$A = \begin{bmatrix} 1 - \omega^2 L_{cm} C_y & j\omega L_{cm} \\ j\omega C_y & 1 \end{bmatrix} \quad (1)$$

Differential-mode equivalent circuit A parameter matrix:

$$A = \begin{bmatrix} 1 - \omega^2 L_{cm} C_y & j\omega L_{cm} \\ j\omega(C_{x1} + C_x - \omega^2 C_{x1} C_x L_{dm}) & 1 - \omega^2 L_{dm} C_{x1} \end{bmatrix} \quad (2)$$

Take A parameter matrix value into insertion loss calculation and get the formula of common-mode equivalent circuit insertion loss:

$$\text{I.L} = 10 \lg \left[ (Z_L - \omega^2 L_{cm} C_y Z_L + Z_S)^2 + (\omega C_y Z_S Z_L)^2 \right] - 20 \lg (Z_S + Z_L) \quad (3)$$

The formula of differential-mode equivalent circuit insertion loss:

$$\text{I.L} = 10 \lg \left[ (Z_L - Z_L \omega^2 L_{dm} C_x + Z_S - Z_S \omega^2 L_{dm} C_{x1})^2 + (\omega L_{dm} + \omega Z_S Z_L C_{x1} + \omega Z_S Z_L C_x - \omega^3 Z_S Z_L C_{x1} C_x L_{dm})^2 \right] - 20 \lg (Z_S + Z_L) \quad (4)$$

The formula above gives the relationship between insertion loss and circuit parameters. In practice, the filters typically work in impedance mismatch situation because the switching power resistance value changes with frequency. a special equipment could be used to measure the equivalent impedance of interference source and load, the spectrum whether the filter is used or not. After all these steps, a simulation design can be start based on EMI filter common-mode and differential-mode model.

### 3.2.2 Differential-mode suppressing performance enhanced filter

To strengthen the differential-mode suppression effect, one or more differential-mode inductance may be added into the general structure circuit. Enhanced differential-mode suppressing filter circuit is shown in Figure 5.

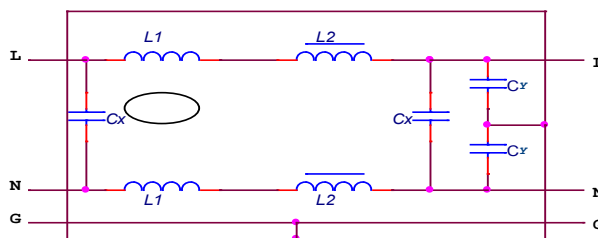
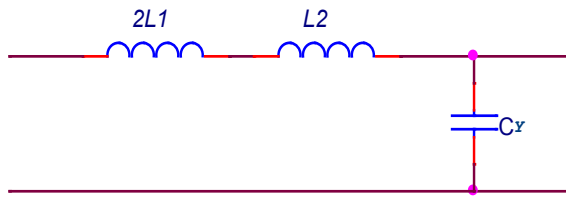


Figure 5. Differential-mode suppressing performance enhanced filter

C<sub>x</sub>, C<sub>y</sub> are differential-mode and common-mode capacitor, L<sub>1</sub> is common-mode choke, L<sub>2</sub> is differential-mode inductance, the equivalent circuit of the differential-mode suppressing performance enhanced filter is shown in Figure 6a and 6b.

In an EMI filter, common-mode circuit and differential-common circuit have a certain contribution to mutual noise. As a differential-mode inductance, L<sub>2</sub> also exists in the L-type circuit composed of common-mode inductance L<sub>1</sub> and

capacitance  $C_y$ , and it is contributed to suppressing common-mode noise; Similarly, the leakage inductance  $L_e$  of common-mode choke  $L$ , and common-mode capacity  $C_y$ , also existing in the  $\pi$ -type circuit target for differential-mode suppressing, will suppress differential-mode noise as differential-mode filter circuit do. Therefore, doing parameter values selecting should take the mutual contribution effect between common-mode and differential-mode circuit into account during the filter design.



**Figure 6. (a)** Common-mode equivalent circuit

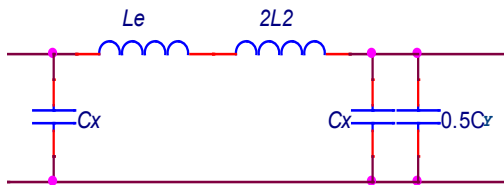


**Figure 6. (b)** Differential-mode equivalent circuit

## 4 EMI filter design and simulation analysis of ASM secondary power

### 4.1 Filter schematic design suppressing DC-DC output ripples, including one level common-mode filter and three level cascade differential-mode filters.

To suppress common-mode noise more effectively, the common-mode choke with high permeability, good high-frequency performance core should be given priority. Common-mode choke inductance values are related with current ratings. Differential capacitor  $C_x$  usually select metal film capacitors, in the range of  $0.1 \sim 1\mu F$ .  $C_y$  is used for suppressing high frequency common-mode interference signals, often select ceramic capacitor with high self-resonance frequency. Since connect to ground,  $C_y$  will produce the common-mode leakage current  $I_{ld}$ , and the leakage current will cause harm to human security, so the leakage current should be as small as possible,

typically <1.0mA. Common-mode capacitance varies with the size of the leakage current, it should not be too large, generally in the range of 2000~4700pF.

#### 4.2 Simulation optimization

The simulation of Circuit system is divided into pre-simulation and post-simulation. Pre-simulation does not need to consider the PCB layout information and directly do a simulation of the circuit schematic by connecting the discrete devices. While post-simulation take the distribution parameters of PCB layout and routing into consideration. Take Figure 8 as the input excitation signal and post-simulating the Figure 7 EMI filter network, each node's waveforms of the filter shows in Figure 9.

In Figure 9, the waveform with glitch is the output voltage of the first stage differential-mode inductance. The waveform marked by blue line is the output voltage of the second stage differential-mode inductance. The waveform marked by symbol  is the output voltage of filter terminal. Compared with the input signal of 300mV ripple fluctuations, output ripple amplitude of every differential inductance is very small, less than 15mV, and the signal spikes are completely filtered out in final output port. In ADS pre-simulation, it looks like the trend of waveform in each node is reasonable, but the suppression is too ideal. The reason is that the signal path is not taken into consideration, while the layout situation and the discrete devices parameters should be combined when doing a simulation.

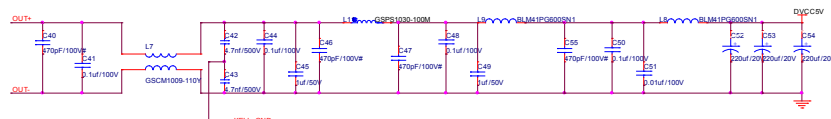


**Figure 7.** Power EMI filter circuit

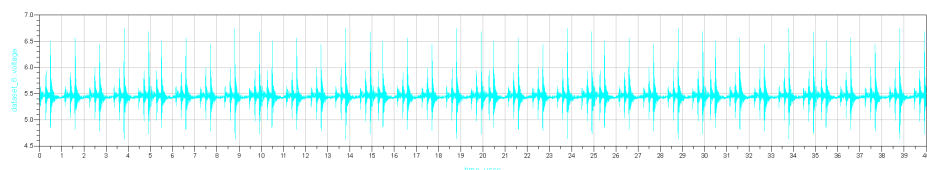


**Figure 8.** Input power signal with different frequency

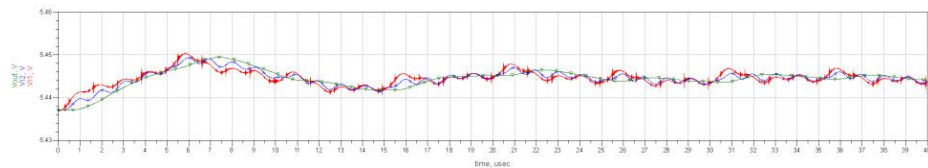


**Figure 9.** Output voltage at input frequency(the unit “usec” means “microsecond”)

Figure 10 shows the connecting information after importing Allegro PCB layout with discrete devices, Figure 11 shows a simulation result for the system layout optimization.

Draw a comparison between Figure 11a and 11b, we can get that the EMI filter circuit can suppress most of the interference signal. Meanwhile, the spike can be suppressed, but not completely be eliminated.

Figure 12 is the actual test waveform of Figure 11, from the comparison of Figure 11 and 12; it is highly similar both in ripple value (80mV and 100mV respectively) and fluctuation of waveform.

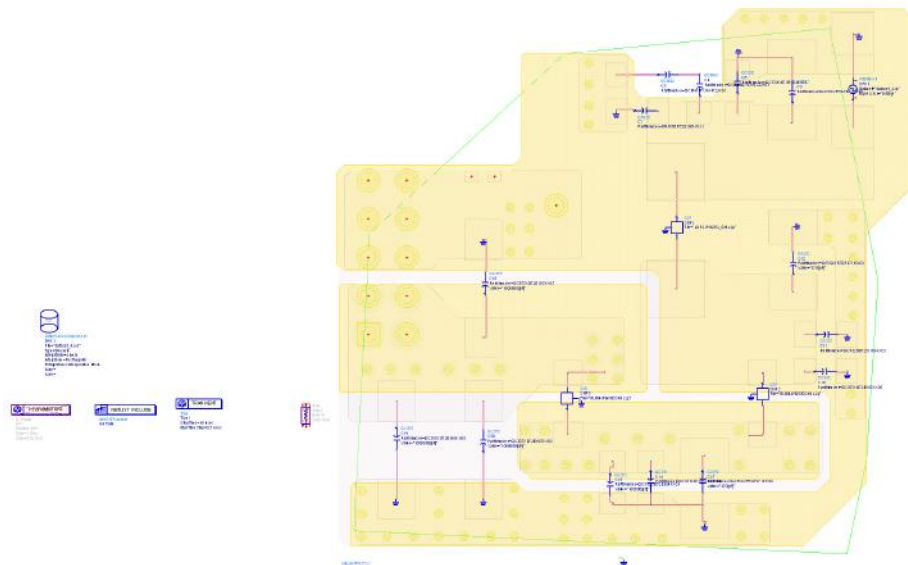


**Figure 10.** EMI co-simulation circuit

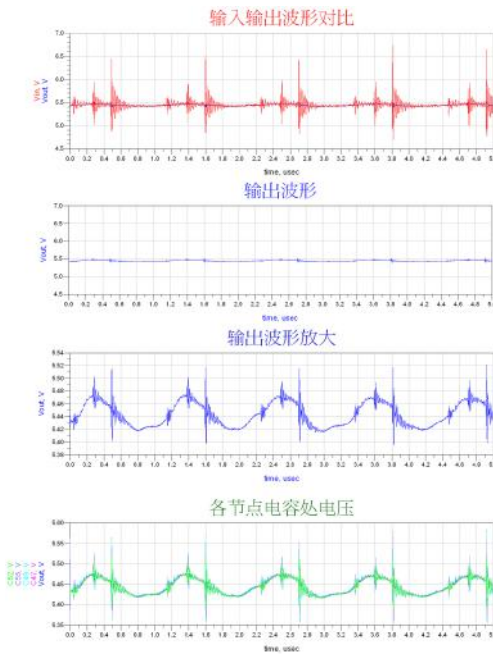


Figure 11. (a) The input and output voltage comparation of co-simulation

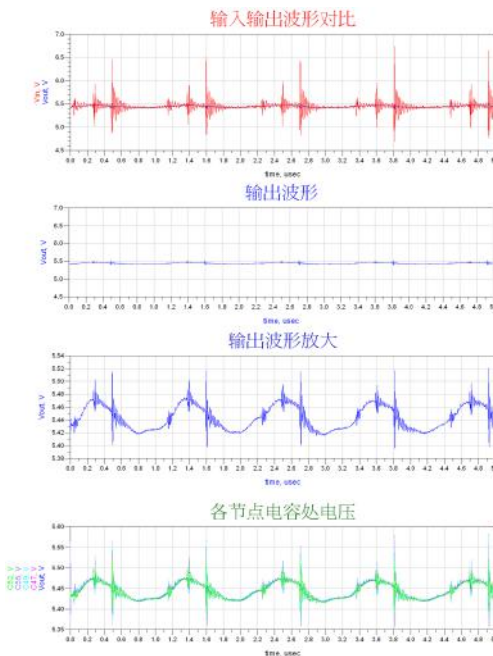
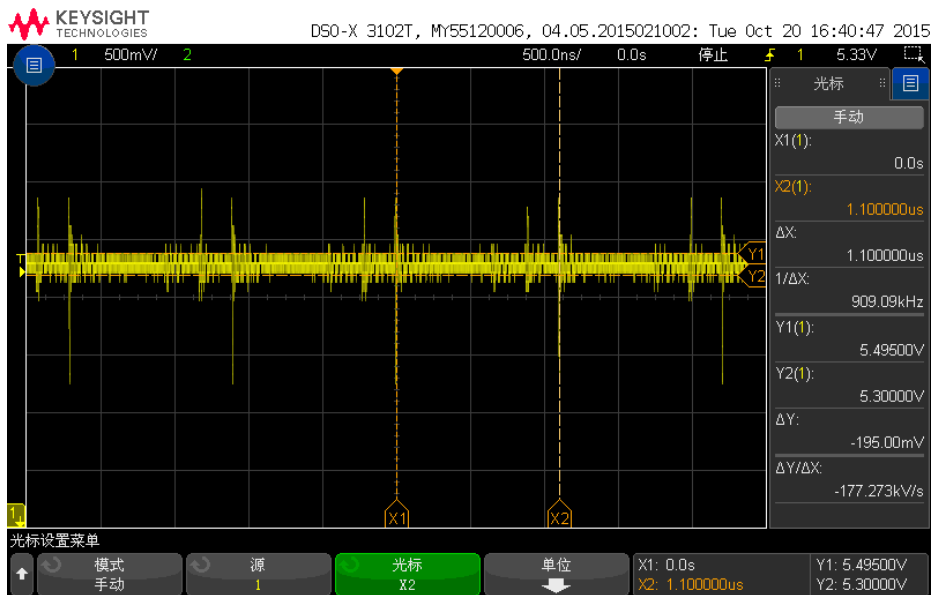


Figure 11. (b) The output voltage of co-simulation



**Figure 12.** Waveform of measured output

## 5 Conclusion

In this paper, an EMI filter circuit is designed specified for the switching power which ranges widely in switching frequency and has high-frequency harmonics. By simulating and optimizing the circuit, the output waveform of the simulation results is familiar with the actual test results, which not only prove the reasonability of filter structure selection, the setting of device parameters, and the circuit layout, but also show that making use of the post-simulation can better predict the performance of the power design and provide optimization support for the EMI filter circuit of ASM secondary power.

## References

- [1] Wang Shumin, Zhang Dong, Lvming Hai. A practical design method of switching power EMI filter. *Power Electronics*, 2007.Vol.41, No.6, 16-18.
- [2] Zhou Lifu, Lin Mingyao. Design and simulation analysis of EMI filter. *Electrical Engineering*, Southeast University, low-voltage electrical 2004.04
- [3] Liu Xiang, anti-electromagnetic interference design of mini switching power, Hefei Technology University, Ministry of Education photovoltaic systems engineering research vol.21 No.5 bus Electronic Design Engineering

- [4] Lin Jinjie, Gensheng, Li Wei ripple suppression measures and Method of Guangxi Light Industry, 2008, September 9 (Total 118)
- [5] Liao Jianjun Huang Bo Li Wenhao Airborne DC surge suppressors designed China Electronics Technology Group Corporation Institute for the twenty-fourth Microelectronics Vol. 43 Fourth August 2013
- [6] Yung Yan Wang Gang its high reliability DC-DC switching power supply inrush current suppression circuit design, Lanzhou Institute of Space Physics Power Technology 2011 7 vol.14 No.7
- [7] Cao Liping Zhang Xun Chen Chen Liu Tao switching power supply input EMI filter design and simulation of Xi'an University of Electronic Science and Technology Institute of Electronic Engineering, vol. 23, 2010 fourth
- [8] Taosheng GuiLiucheng Yong Hu Bing DC Switching Power Supply Ripple Urban Rail Transit 2003

Yun-na WU, Ge-di JI, Ji WANG\*

## **Research on the Relationship Identification and Governance Countermeasures of Stakeholder in Two Phases of Thermoelectric Projects**

**Abstract:** In previous studies, the researchers found that the project stakeholder relationship governance research often focused on the various stakeholders of the construction period but lacked research on stakeholders within the operation period and two stage stakeholders correlation. This paper uses scientific and reasonable methods to identify the stakeholders according to the construction period and operation period of the project, measure the importance degree, influence scope and the intensity of the relationship among the various stakeholders, and then determine the interests relationship network in the project, core stakeholders and key stakeholder groups. On this basis, it is of great theoretical and practical value to formulate the strategy of relational governance and to coordinate the relationship among stakeholders of thermoelectric projects.

**Keywords:** thermoelectric project; stakeholders; relationship governance; social network analysis

### **1 Introduction**

In recent years, the domestic scholars have carried out research on relationship governance and project organization construction [1-3], and using the social network analysis method (SNA) which developed in the last century 60's carries out the related research [4-6] has obtained pretty good research results, however, in previous studies, stakeholder research often focused on construction period of the project, but lacked research on the stakeholders relationship governance of operation period and the two stage stakeholder relationship, in view of this, the article selects the thermoelectric project in the core position of the industrial chain of circular economy as the research carrier [7], tries to use the social network analysis method to identify the stakeholders of the two phase of the thermoelectric project construction-operation period, and then determine the interest relations network in the project, the core stakeholder group. Based on this formulation of relational governance countermeasures and

---

\*Corresponding author: Ji WANG, School of Management, Inner Mongolia University of Technology, Huhhot, China, E-mail: nmgwangji2016@163.com

Yun-na WU, School of Business and Administration, North China Electric Power University, Beijing, China

Ge-di JI, School of Business and Administration, School of Management, North China Electric Power University and Inner Mongolia University of Technology, Beijing, China; Huhhot, China

coordination thermoelectric projects at various stages of the interests of stakeholders, the research can provide reference for the identification of stakeholder relationship and the development of countermeasures in each stage of the construction project.

## 2 Construction of the social network model of the stakeholders in the thermoelectric project

The data were obtained by triangulation method, and the snowball method was used to identify the stakeholders from the three dimensions of the task, purpose and role of thermoelectric project. Build the adjacency matrix of stakeholders, using Ucinet 6.0 for qualitative model quantitative analysis, and the use of software NetDraw can get the relationship network structure of the project stakeholders.

### 2.1 Identification of Stakeholders in Thermoelectric Project

First, identify all stakeholders involved in the thermoelectric project; Secondly, Quantify the relationship between the related parties. In this paper, the stakeholders of thermoelectric project are defined as the organizations and individuals involved in the construction or operation period of the thermoelectric project, as well as their own interests affected by the thermoelectric project.

### 2.2 Definition of Stakeholder Relationship in Thermoelectric Project

The definition of stakeholder relationship in construction period. In the thermoelectric projects construction period, each stakeholder is mainly around the thermoelectric project construction, build activities. During the construction period of the thermoelectric project, the relationship types of stakeholders can be expressed as the coordination relationship, the contract relationship, the information exchange relationship, the performance incentive relationship, the order relationship between the five types of relationships.

The definition of the relationship between the stakeholders in operation period. The circular economy industrial chain, which is the core of the thermoelectric enterprises and is constructed in the operation period of the project. During the operation period of the project, the relationship of stakeholders is mainly embodied in the business aspects between upstream and downstream enterprises in the industrial chain, and the thermoelectric enterprises in the industrial chain give full play to the role of radiation and link.

During the operation period of thermoelectric project, the relationship between the stakeholders can be expressed as heat energy transmission, power transmission, material metabolism, water cycle and the use of steam.

### 2.3 Construction of Relation Matrix

After defining the relationship between the stakeholders of the thermoelectric project, the relationship between the stakeholders is expressed, and the intensity of the relationship between the stakeholders is formed. Thermoelectric projects include the construction period of the project without the adjacency matrix, as shown in Table 1, and the thermoelectric project operating period of the undirected adjacency matrix is shown in Table 2.

**Table 1.** Thermoelectric projects construction period interest related parties adjacency matrix

**Table 2.** Thermoelectric projects operation period interest related parties adjacency matrix

	Thermoelectric enterprises	Cement plant	Brick factory	Gypsum factory	Sewage treatment plant	Local government department	Coal plant	Mechanical equipment manufacturing enterprises	Bio- pharmaceutical enterprises	Garment processing enterprises	Food processing enterprises	Feed mills	Residents
Thermoelectric enterprises	0	2	2	2	2	2	2	3	2	3	3	2	2
Cement plant	2	0	0	1	1	1	0	0	0	0	0	0	0
Brick factory	2	0	0	1	1	1	0	0	0	0	0	0	0
Gypsum factory	2	1	1	0	1	1	0	1	0	0	0	0	0
Sewage treatment plant	2	1	1	1	0	1	1	1	1	1	1	1	1
Local government department	2	1	1	1	1	0	1	1	1	1	1	1	1
Coal plant	2	0	0	0	1	1	0	0	0	0	0	0	0
Mechanical equipment manufacturing enterprises	3	0	0	1	1	1	0	0	0	0	0	0	0
Bio-pharmaceutical enterprises	2	0	0	0	1	1	0	0	0	0	2	2	0
Garment processing enterprises	3	0	0	0	1	1	0	0	0	0	0	0	0
Food processing enterprises	3	0	0	0	1	1	0	0	2	0	0	1	0
Feed mills	2	0	0	0	1	1	0	0	2	0	1	0	1
Residents	2	0	0	0	1	1	0	0	0	0	0	1	0

## 2.4 The Formation and Distribution of the Social Network Model of Stakeholders

From the Table 1 and Table 2, it can be found that the thermoelectric enterprises, government departments and residents participate in the construction period and operation period at the same time, so as to construct the social network model of the thermoelectric project stakeholders.

## 3 Analysis of stakeholder social network model

### 3.1 Analysis of Network Density of Stakeholders

After the two value of the stakeholder relationship data in the thermoelectric projects is transformed, the overall network density analysis of the stakeholders is carried out. The results are shown in Table 3:

**Table 3.** Thermoelectric projects stakeholder social network density

	Density	No. of Ties
Network density of thermoelectric projects	0.3467	389.0000

As can be seen from table 3, the total amount of the 34 stakeholders of the thermoelectric projects is 389, that is, the average number of stakeholders is 11.44 and the network density is 0.3467. Network density is low but the total relationship amount is higher, shows that the thermoelectric projects among stakeholders in the general information exchange capacity is higher, but the interaction frequency is low, the thermoelectric project network agglomeration level is not high, the relationship between the stakeholders could be relatively concentrated in a certain number of related parties. Therefore, thermoelectric enterprises, as the owner of the project and the main unit, should take positive measures to promote the interaction between the stakeholders, and to avoid excessive concentration of resources and information between a few stakeholders.

### 3.2 Analysis of Stakeholder Centrality

Through the calculation, it is concluded that the thermoelectric projects stakeholders social network three centrality index, and then do a comparative analysis, the results shown in the Table 4. The score in the centrality measure of thermoelectric enterprises and local government departments are maximum. The central degree of thermoelectric enterprises is 91.000 and the central degree of the local government department is 87.000, namely indicates that the two are the most influential individuals in this project. In thermoelectric project construction, the local government department needs to manage the construction safety, construction progress and construction quality and worker organization of the project. In the project operation period government department needs to manage the construction and optimization of the industrial chain of the whole industrial park, it also has considerable information control ability.

In addition, local residents in the project also has a high centrality (30.000), due to the project in the construction period of land acquisition, construction and other acts will have a direct impact on the local residents groups, the relevant departments to do a good job of placement and appease. In the period of production and operation of the thermoelectric project, and the operation of the enterprises needs the input of the local labor, and can solve the local employment problem, thermoelectric enterprises in the production of heat, electricity and other resources can provide protection for the lives of the residents.

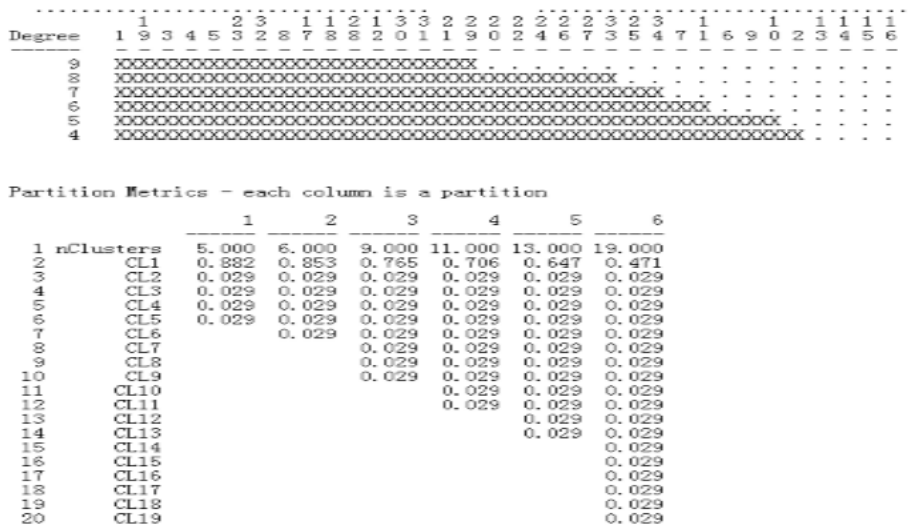
**Table 4.** The thermoelectric projects stakeholders network center

	1 Degree	2 NrmDegree	3 Share
1 Thermoelectric enterprises	91.000	55.152	0.123
12 Local government department	87.000	52.727	0.118
3 Construction unit	62.000	37.576	0.084
4 Development organization	62.000	37.576	0.084
5 Design unit	31.000	18.788	0.042
8 Local residents	30.000	18.182	0.041
21 Sewage treatment plant	27.000	16.364	0.036
29 Feed mills	18.000	10.909	0.024
11 Management consulting company	17.000	10.303	0.023
17 Cement plant	16.000	9.697	0.002
30 Farms	16.000	9.697	0.002
19 Brick factory	15.000	9.091	0.020
23 Mechanical equipment manufacturing enterprises	15.000	9.091	0.020
31 Dairy enterprise	15.000	9.091	0.020
28 Beer enterprises	15.000	9.091	0.020
32 Food processing enterprises	15.000	9.091	0.020
10 Equipment suppliers	14.000	8.485	0.019
18 Bricks and tiles plant	14.000	8.485	0.019
27 Garment processing enterprises	14.000	8.485	0.019
33 Beverage enterprises	14.000	8.485	0.019
9 Material suppliers	14.000	8.485	0.019
26 Textile enterprises	14.000	8.485	0.019
24 Bio enterprise	13.000	7.879	0.018
20 Gypsum factory	13.000	7.879	0.018
22 Coal plant	13.000	7.879	0.018
34 Building materials enterprises	13.000	7.879	0.018
6 Bidding Proxy Companies	12.000	7.273	0.016
14 The investor	12.000	7.273	0.016
25 Pharmaceutical enterprises	12.000	7.273	0.016
7 Survey party	11.000	6.667	0.015
2 Supervision party	11.000	6.667	0.015
13 National examination and approval department	8.000	4.848	0.011
16 The insurance company	3.000	1.818	0.004
15 Bank	3.000	1.818	0.004

### 3.3 Analysis of Agglomeration Subgroups of Stakeholders

The analysis of the k-core and cliques. We can get the core degree of various stakeholders in the thermoelectric projects by k-core analysis, the distribution of the members of the faction can be obtained through the Cliques analysis.

The analysis results of stakeholder's k-core and thermoelectric projects stakeholder's social network k-core are shown in Figure 1 below.

**Figure 1.** K-core running results

It can be found from the analysis results of Figure 1 that in the thermoelectric project stakeholders k-core analysis, can distinguish the six core degree, the degree respectively 4, 5, 6, 7, 8, 9. Degree of 9 of the core (ie, 9- core) contains 16 stakeholders, which represents the core group of the project. There are more thermoelectric project stakeholders with high core degree, and form a longer relationship chain. During the construction period, the core degree of construction unit and design unit are higher, there are more related stakeholders who are in the important position of information transmission, they are not only affect the stakeholders of the construction period, but also their behavior and decisions will have an impact on the stakeholders in the operating period. During the operating period, the core degree of the enterprises which participated in a number of industries is generally higher, and the enterprises have contact with stakeholders in a number of different industrial chain.

The social network Cliques analysis of the stakeholders in thermoelectric project. Through the Cliques analysis, it can be known that the minimum number of members is set to 10, this moment the thermoelectric project is divided into 3 factions, and the classification is more reasonable. Table 5 below shows the distribution of the stakeholders in the 3 factions when the minimum number of members of the thermoelectric project is 10.

It can be learned from the members of the thermoelectric project faction classification list, the 3 factions have a very high degree of overlap, which shows that the relationship between stakeholders is very close. Through the analysis, we can get to know that the stakeholder who are repeated emergence in the three factions are exactly the same, they are all thermoelectric enterprises, construction units,

construction units, design units, local residents and local government departments, sewage treatment plant, feed plants and plant breeding, and the 9 stakeholders have a greater impact on other stakeholders in the project. In the thermoelectric project, the key subgroups of the project are mainly related to the stakeholders in the construction period, during the operating period, the enterprises that participate in multiple industry chain are often in the core area of the thermoelectric project, which is the key stakeholder groups of the thermoelectric project.

**Table 5.** List of stakeholder faction member in thermoelectric projects

Cliques1:	Thermoelectric enterprises	Development organization	Construction unit	Design unit
	Local residents	Local government departments	Sewage treatment plant	Beer enterprises
	Feed mills	Breeding plant		
Cliques2:	Thermoelectric enterprises	Construction unit	Design unit	Development organization
	Local residents	Local government departments	Sewage treatment plant	Feed mills
	Breeding plant	Dairy enterprises		
Cliques3:	Thermoelectric enterprises	Construction unit		
	Development organization	Design unit	Local residents	Local government departments
	Sewage treatment plant	Feed mills	Breeding plant	Food processing enterprises

### 3.4 The Thermoelectric Project Stakeholders' social Network Core - edge Structure analysis

The core degree average value of the 34 stakeholders involved in the thermoelectric project is 0.144, using the core degree average value of thermoelectric project stakeholders to divide the core stakeholders of the thermoelectric project, half edge stakeholders and edge stakeholders. The results are shown in Table 6.

**Table 6.** The division of thermoelectric projects stakeholder core - edge area

Starting fitness: 0.000	Final fitness: 0.692
Core/Periphery Class Memberships:	
1: Thermoelectric enterprises Supervision party Construction unit build unit Survey party Design unit Local residents Management consulting company Local government departments Sewage treatment plant	
2: Bidding agent company Equipment suppliers Material supplier National examination and approval department Investment side Bank The insurance company Cement plant Bricks and tiles plant Brick factory Gypsum plant pharmaceutical enterprises Textile enterprises Machinery and equipment manufacturing enterprises Garment processing enterprises Breeding plant Coal plant Bio enterprise Beer enterprise Feed mills Dairy enterprise Food processing enterprise Building materials enterprises Drinks companies	

The original goodness of fit of thermoelectric project core - edge structure analysis is 0, the final goodness of fit is 0.692. Thermoelectric project's final fitting goodness is relatively large, and the numerical well illustrates that the thermoelectric project stakeholder relational data and the ideal model of similarity is higher, and the core - edge structure model of the data collected by the thermoelectric project stakeholders is significant.

## **4 Thermoelectric project stakeholder relationship governance countermeasures**

Based on the study, we find that the center degree of thermoelectric enterprises in the social network of the whole project is higher, therefore, the relational governance of thermoelectric projects stakeholder is also from the perspective of thermoelectric enterprises, which puts forward the governance countermeasures of the relationship between the stakeholders of the thermoelectric project.

### **4.1 Strengthen the management of thermoelectric project constraints system**

Due to the stakeholders in the thermoelectric projects construction period and operation period involved in the project are different, the personnel are complex, the social network is huge, the network relationship is complex, so we should comprehensively consider the factors such as the compatibility of interests, the level of trust, the intensity of cooperation, establish and improve the corresponding rules and regulations and the mechanism of conflict warning and coordination. To prevent the situation of management chaos caused by section's stakeholders breaking rules and regulations from happening.

### **4.2 Overall planning of thermoelectric projects industry chain layout**

Thermoelectric project stakeholders are numerous, project cycle is long, during the thermoelectric projects construction period, stakeholders' plans, behavior and decisions affect the thermoelectric projects stakeholders of operating period. At the beginning of the thermoelectric projects, it needs a comprehensive investigation, system design, scientific layout, reasonable distribution of manpower, material resources, financial resources, and comprehensive optimization of thermoelectric projects design, to ensure that the implementation of thermoelectric projects is carried out smoothly.

#### 4.3 Pay close attention to the change of internal and external environment of thermoelectric projects

The thermoelectric project's life cycle is long, stakeholders involved in every stage is different and are faced with different internal and external environment. In the implementation process of thermoelectric project should pay close attention to the change of internal and external environment of the project, according to the analysis results to build information sharing platform, capture the factors of change accurately, make adjustments according to the changes in the environment timely, and respond to thermoelectric project risk actively, to ensure the smooth implementation of thermoelectric project.

### 5 Conclusion

Through the social network analysis of the stakeholder of the two phases in the project construction and operating period, it is found that the decisions of the stakeholders in the construction period will have an impact on the behavior of the stakeholders in the operating period. During the operating period, companies that involved in multiple industrial chain are often in the core area of the thermoelectric projects, and they are the key stakeholder groups of the thermoelectric projects which are greatly influenced by the stakeholders in the construction period. In the thermoelectric projects, the key subgroups are mainly related to the stakeholders in the construction period. The amount of the relationship between stakeholders throughout the thermoelectric projects is higher, but the relationship is relatively concentrated on the stakeholders who have higher center degree, at the same time to participate in the construction and operating periods, the center degree of stakeholders is higher, the center degree of the stakeholders in constructing period is generally higher than the center degree of the stakeholders in operating period. The local government departments have a higher center degree, and they are the key stakeholders which play an important role in the stability of the network. Local residents in the social network of thermoelectric projects also have higher center degree and the influence is relatively large, it should pay attention to the influences of local residents on the social network of stakeholders in thermoelectric project.

In future studies, it needs to further consider the difference between different types of relationships, to set weights according to different types of relationship, to strengthen the research on the relationship governance countermeasures between the different stakeholders and to improve the scientific and enforceable of the relationship governance countermeasures between the stakeholders of the thermoelectric projects.

**Acknowledgment:** This work is supported by the Inner Mongolia Natural Science Foundation (2014MS0705) and The National Natural Science Foundation of China (71661026)

## References

- [1] Chong Dan, Li Yongkui, Le Yun. Study on the relationship governance of urban infrastructure construction project group organization network: A Perspective of network organization [J]. Soft science, 2012, 02:13-19
- [2] Li Yongkui, Le Yun, Lu Yujie. General control mechanism and demonstration of large scale construction project organization based on SNA [J]. Journal of Tongji University (NATURAL SCIENCE EDITION), 2011, 11:1715-1719
- [3] Le Yun, Chong Dan, Cao Dongping. Research on construction project organization based on social network analysis method [J]. Building economy, 2010, 08:34-38.
- [4] Guo Jin. Research on the carbon emission reduction measures of industrial sector based on network analysis [J]. Technology and economy, 2014, 07:90-95.
- [5] Liu Xingzhi, Yan Wei Wang, Wei Wei. Based on SNA project governance relationship network analysis and response strategy research [J]. East China economic management, 2011, 06:124-129
- [6] Ding Ronggui. Project stakeholders and their needs to identify [J]. Projects management technology, 2008, 01:73-76
- [7] Gigedi, Du Hongrun. To thermoelectric enterprises as the core of the circular economy industrial chain construction [J]. Renewable resources and circular economy, 2013, 06:5-9.
- [8] Liu Junzhu. Introduction to social network analysis [M]. Social science literature press, 2004
- [9] J Turner. Towards a theory of the project management: The functions of project management [J], International Journal of Project Management, 2006(2).

Zhong-hua ZHANG\*, Yan-hai XU, Dao-jie JU, Xu-qiang QIAO

## **Study on the Fluctuating Pressure and Aerodynamic Noise at Car Rearview Mirror Zone**

**Abstract:** In order to study on the flow characteristics and the formation of aerodynamic noise quantitatively at car rearview mirror zone, the numerical simulation method is applied in the paper. Firstly, a wind tunnel computational model that includes review mirror, body characteristics and detailed wheel structures based on an actual car is established. The effects of rotating wheels and moving ground on air flow are also taken into account in the model. Then, a large eddy simulation (LES) technology and transient numerical method are used to solve the computational domain and study the flow field characteristics and pulsating pressure at mirror and side window zone. Finally, the FW-H method is applied to calculate the aerodynamic noise at rearview mirror zone. The results show that a strong swirling motion in the wake of the A-pillar and rearview mirror is the reason caused fluctuating pressure that is the main dipole sound sources at side window zone. Additionally, it also shows that reducing flow separation movement at rearview mirror zone will ameliorate the drag eddy scale in the wake area which is the key to control aerodynamic noise source at side window zone.

**Keywords:** rearview mirror zone; fluctuating pressure; aerodynamic noise; LES

### **1 Introduction**

Recently, with the gradual improvement of road infrastructure, vehicle speed becomes faster and faster. Car aerodynamic noise is proportional to sextic vehicle speed and it will increase about 18 dB when vehicle speed is double [1,2]. So car aerodynamic noise has become a dominant factor affecting the ride comfort and the life quality for people living near roads. The theoretical analysis, numerical simulation, wind tunnel test and vehicle road test are major research methods on car aerodynamic noise. With the rapid development of CFD software and computer technology, the numerical simulation has become an important research tool for automotive flow field aerodynamic noise, which is a convenient and reliable method to reveal the car flow field characteristics. Numerical simulation is not only with low cost, but also it can explore the complex flow phenomena

---

\*Corresponding author: Zhong-hua ZHANG, School of Automotive and Transportation, Xi Hua University, Chengdu 610039, China, E-mail: zzh923878949@163.com

Yan-hai XU, Dao-jie JU, Xu-qiang QIAO, School of Automotive and Transportation, Xi Hua University, Chengdu 610039, China

Yan-hai XU, Sichuan Key Laboratory of Automotive Engineering, Chengdu 610039, China

of car flow field. It has become one of the important ways on car aerodynamic analysis in the automotive development process. Because car shape has a lot of surface corner, sectional change and some protruding objects, airflow will lose adhesion and induce complex unsteady vortex motion in these areas. So a strong pressure fluctuation will be produced in car surface layer and thus generate aerodynamic noise and radiation to the surrounding [3,4]. In addition, improving the accuracy of numerical model for analyzing car external flow field is also important. By using a large eddy simulation of transient and the FW-H method to study the mechanism and characteristics of car aerodynamic noise at the side window zone, it has great significance to predict and control car aerodynamic noise in car design stage.

## 2 Geometric model

A 3D geometric model based on a real car was established in this paper, the model contains the main features of a real car such as body, mirrors, complex wheel structure, A-pillar and body waist. A numerical model for automotive flow field to simulate wind tunnel experiments is also established in software platform. The geometric size of the car is 4500 mm in length ( $L$ ), 2200 mm in width ( $w$ ) and 1350 mm in height ( $h$ ). The front computational domain ( $L_1$ ) is three times of car length. The rear ( $L_2$ ) is seven times of car length. The height ( $C$ ) is five times of car height and each side width is two times of car width. It is shown in Figure 1 and Figure 2.

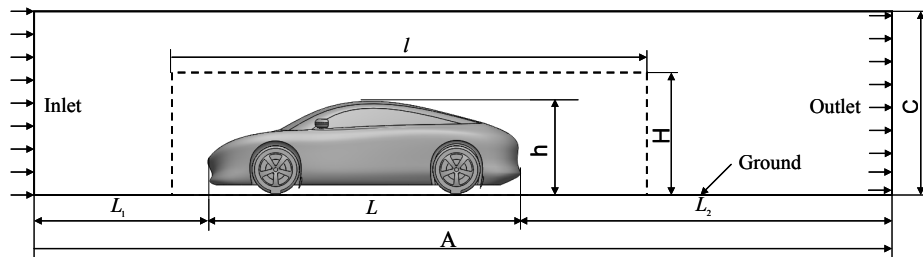


**Figure 1.** Side view of computational domain

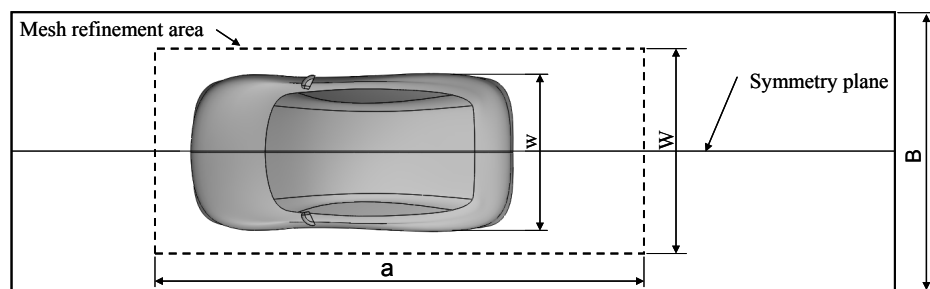


**Figure 2.** Top view of the computational domain

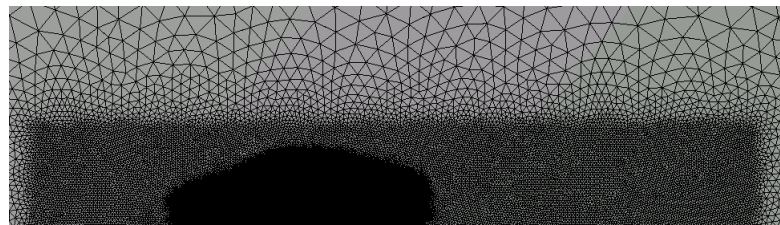
### 3 Mesh generation

Considering the complexity of car body surface and the fully expressed body shape features, this paper applies a hybrid grid scheme, which can take advantages of tetrahedral grid has good adaptability and hexahedral grid has high accuracy [5]. The method of mesh control to set the mesh size of the computational domain is about 3mm-8mm. The grid surrounding car body wall is refined as marked in dotted line shown in Figure 2. The element length is controlled about 5mm.

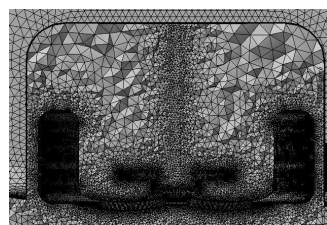
The domain near the wall of body, tires, review mirror and wheel cover is meshed with an inflation grid to improve the accuracy. The mesh settings are presented in Table 1. The total number of grid is about 12 million and the result of mesh generation is shown in Figure 3.

**Table 1.** Mesh settings

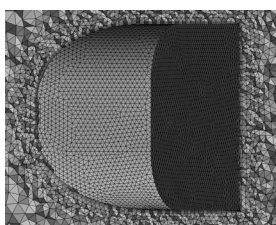
	Mesh Size				Inflation			
Relevance	10	Curvature Normal Angle	18deg	Definition	Body	Rim	tire	
Min Size	3mm	Proximity Accuracy	0.5	First Layer Height	0.8	1	0.4	
Max Size	40mm	Num Cells Across Gap	3	Maximum layers	5	3	3	
Max Face Size	60mm	Proximity Min Size	6mm	Growth Rate	1.15	1.05	1.15	
Growth Rate	1.2	Minimum Edge Length	0.9mm	Inflation Option	First Layer Thickness			



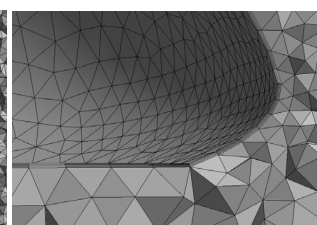
(a) The whole mesh for numerical simulation



(b) Inflation at wheel



(c) Inflation at body



(d) Inflation at review mirror

**Figure 3.** Mesh of computational domain

## 4 Boundary conditions

In order to match the actual situation and ensure the accuracy of calculation result, the effect of wheel rotation on flow field must be considered [6]. So rotating wall is used to simulate rotating wheels and moving wall is applied to simulate the relative movement between vehicle and ground. To avoid solving the whole computational domain and reduce the computational cost, the amount of calculation is reduced by using a symmetric boundary condition. Wall function is applied with standard wall function. The parameter settings of boundary conditions can be found in Table 2.

In addition, six signal points are set to monitor the fluctuating pressure in the longitudinal of symmetry within the rearview mirror zone and another eight signal points are set to monitor the aerodynamic noise at the side windows zone. These monitoring points are shown in Figure 4.

**Table 2.** Settings of boundary conditions

Inlet	Velocity Magnitude: V=28 m/s; Gauge Pressure: 0 Pa	
Outlet	Gauge Pressure: 0 Pa	
Symmetry	Symmetry Wall	
Car Body	Stationary Wall, Shear Condition: No Slip	
Ground	Moving Wall; Speed: U=28 m/s	
Wheel	Moving Wall, Speed: 100 rad/s	
Acoustics Model	Ffowcs-williams & Hawkings	
Viscous Model	Large Eddy Simulation(LES)	
Solution Settings	Time Step Size: 0.0001s	Number of Time Steps: 1500

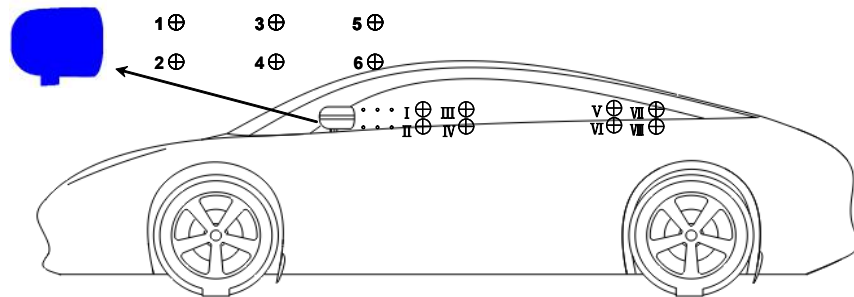


**Figure 4.** Monitoring points of fluctuating pressure and aerodynamic noise

## 5 Simulation and analysis

The flow field at the side windows zone of the vehicle combined with the effect of A-pillar and rearview mirror are calculated by numerical simulation. The total equivalent pressure contour of the flow field at side window zone at  $t = 0.15s$  is shown in Figure 5. There is a large pressure gradient at the surface of A-pillar, rearview mirrors and side windows as well as the longitudinal center plane of the rearview mirror and several independent vacuum central regions appears in those areas. There is high pressure around the wake zone of the rearview mirror and low pressure zone in the center, which demonstrates that the pressure is very unstable and there is a strong complex vortex motion in the rearview mirror wake region, thus making the car aerodynamic drag and the pressure pulsation increased.

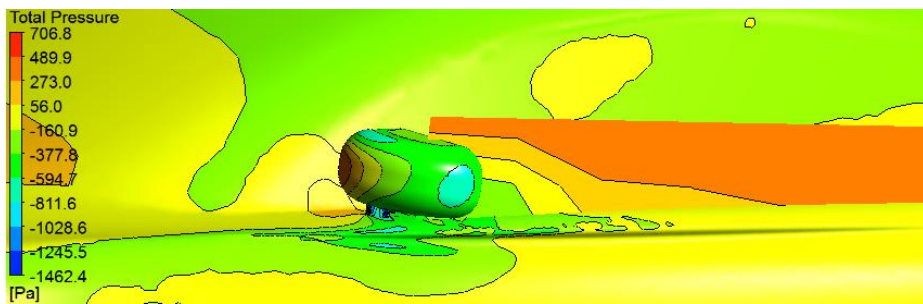


**Figure 5.** The total equivalent pressure contour at the side windows zone

The velocity vector within the longitudinal center plane of rearview mirror wake at different times is shown in Figure 6. When the front airflow reaches the windward surface of the rearview mirror, the speed of airflow is greatly reduced since the flow is blocked. The dynamic pressure becomes static pressure and forms a positive pressure zone in front of rearview mirror. This part of airflow generates flow separation at the surface of rearview mirror. The velocity of upper airflow is accelerated significantly, but due to the impact of the body surface, the lower airflow separation is weaker. The small airflow through the gap between A-pillar and rearview mirror to the side window and it falls off in the edge of the A-pillar.

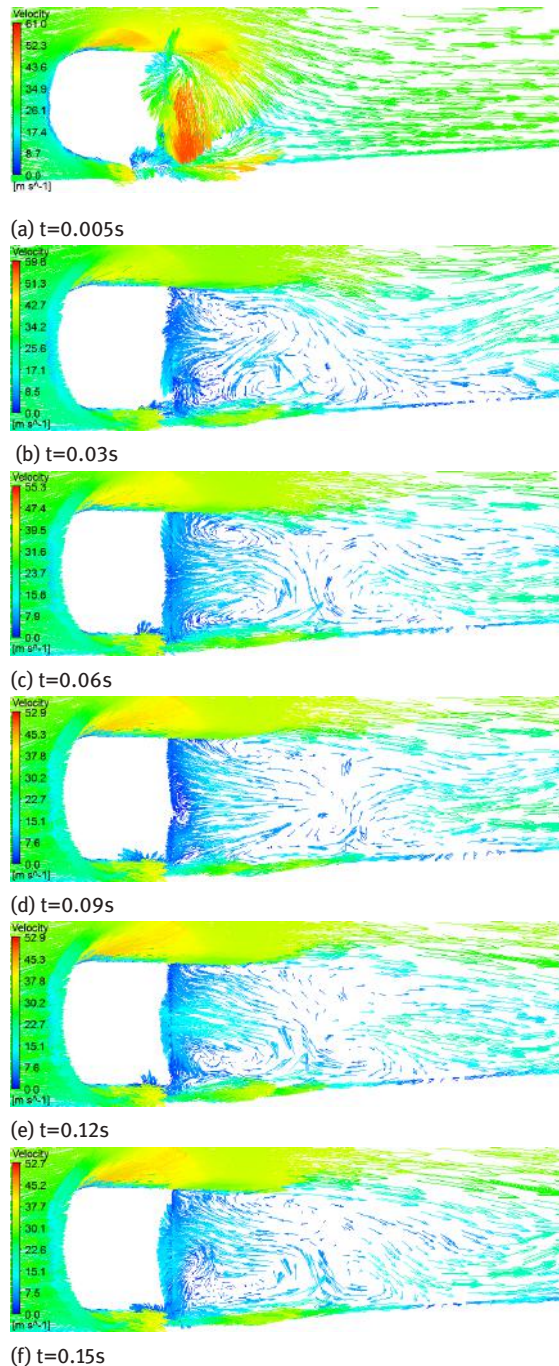


Figure 6. Velocity vector at different times

In the early flow field, when the flowing time is 0.005s, the airflow is slightly twisted in the rearview mirror rear zone, but it is still mainly laminar flow. Due to the impact of air flow separation at the edge of rearview mirror, the rear airflow is outward flow gradually and causes the central pressure dropped in the wake zone. The core of the vortex is forming gradually when the flowing time is 0.03s. The vortex motion in wake region is completely developed when the flowing time is 0.06s, a clockwise drag vortex is formed in the upper region and the location of a counterclockwise drag vortex is lower. The swirling motion is gradually developed to downstream until crushing, dissipated and it is accompanied by energy dissipation. The drag vortex is disappearing when the flowing time is 0.09s and a larger negative pressure region appears. The surrounded airflow is sucked into the wake region because pressure difference and the swirling motion are developing again when the flowing time is 0.12s. It is given in Figure 6e and 6f. The swirling motion is a reciprocating process contains formation, development and shedding in rearview mirror wake vortex motion region. The Hussain and Zaman pointed out that the vortex motion and fragmentation is the main reason for the development of aerodynamic noise on subsonic jet terms. Thus mirror wake has significant unsteady transient characteristics and will induce fluctuating pressure at side window zone.

The total pressure curves of each monitoring points in the wake area of rearview mirror are shown in Figure 7. The values of monitoring point 1 and 2 remains negative. The pressure value of point1 is fluctuating within a certain range and the pressure value of point 2 is relatively stable which stays at about -500 Pa. The reason is that there are two symmetrical vortex cores located near the measuring point 1 and 2 and the strength and instability at the top vortex is greater than the downward vortex. Similarly, the fluctuating pressure strength of monitoring point 3 to 6 is significantly enhanced and presents a periodic fluctuation. It is also found that the pressure values at top pressure monitoring points are always greater than the below pressure monitoring points resulting in that visible swirling motion causes pressure fluctuation directly.

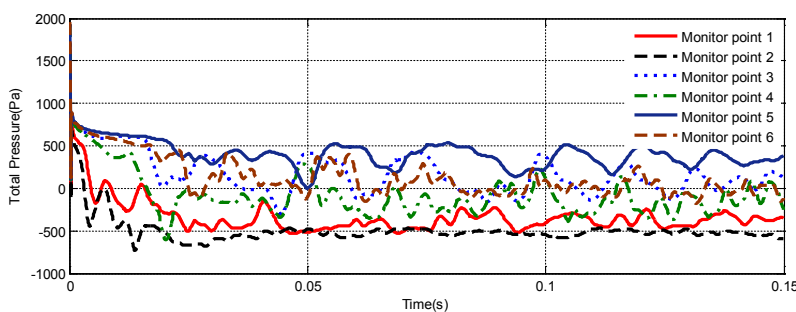
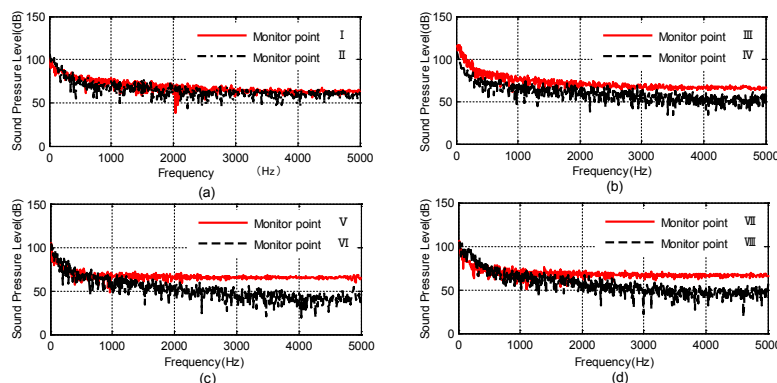


Figure 7. The total pressure curve of different monitoring points

The Sound Pressure Level (SPL) is a key evaluative indicator of car aerodynamic noise performance. Therefore, there are eight aerodynamic noise monitoring points set in the vicinity of the front and rear side window corresponding to the positions of car occupants' ears. By using FW-H method and fast Fourier transform, the spectrum SPL of each monitoring point is obtained as shown in Figure 7. It is shown from the results that car aerodynamic noise belongs to a wide spectrum of noise. In the low frequency band of 0 to 600 Hz, the magnitude of the sound pressure level is the maximum. The SPL peak reaches about 100dB and it presents a sharply declining. In the medium frequency band of 600 to 3000 Hz, the SPL values present a slow downward trend. In the high frequency band of 3000 to 5000 Hz, the SPL amplitude keeps stable.

In addition, located in the upper part of the mirror monitoring points I, III, V, VII, the amplitudes of sound pressure level are significantly greater than the lower part of the measuring point II, IV, VI, VIII. The spectrum curve trends of the SPL monitoring point I and II as well as point III and IV are in consistence as shown in Figure 8a and 8b. It results in that the front of side windows near the rearview mirror is mainly impacted by the symmetrical drag vortex motion and it presents the same spectral characteristics. Because the upper vortex motion is intense, the SPL amplitude of upper location is bigger than the lower location. There is a difference for the SPL amplitude in the high frequency of the monitoring point V and VI as well as point VII and VIII. The SPL magnitudes of upper measuring point V and VII are higher than the lower measuring point 20dB, respectively. Moreover, the SPL amplitude of medium frequency range has smaller change than the monitoring point I and III. After the airflow separation occurs at the edge of A pillar and rearview mirror, the airflow is attached again in the lower region of rear side window and it causes that the SPL presents some weakening. But the upper airflow near the side windows is separated again at the edge of C pillar and the airflow motion is very unstable.



**Figure 8.** The SPL spectrum of monitoring points at side window zone

## 6 Conclusion

The following conclusion can be drawn from the study by numerical simulation:

- (1) The investigation illustrates the mechanism of fluctuating pressure that there is a strong swirling motion in the wake of A-pillar and rearview mirror and the causes that the main dipole sound sources is at side windows zone.
- (2) Aerodynamic noise belongs to a wide spectrum of noise. In low frequency band, it is with high amplitude and declined sharply. In high frequency band, it is with low amplitude and stabilized. From the height difference of monitoring points, it is shown that its impact on the amount of the high frequency aerodynamic noise is also very obvious.
- (3) Reducing flow separation movement at rearview mirror edges and the drag eddy scale in wake zone is the key to control car aerodynamic noise source at side window. The shape design optimization of rearview mirror will be able to ameliorate aerodynamic noise effectively.

**Acknowledgment:** The authors are grateful for the support from the Ministry of Education of PRC through Chui Hui project (z2012024) and the funding from Science & Technology Department of Sichuan Province through a key project (2011J00043) is also appreciated.

## References

- [1] Sofie. Koitrand, Sven. Rehnberg. A Computational Investigation of Wheel and Underbody Flow.2013
- [2] Liang Jianyong, Liang Jun and Fan Shijie. Comparison Among Turbulence Models in CFD Analysis on Flow Field Around a Car. Automotive Engineering. China. 2008.
- [3] Johan. Cederlund, Jacob. Vikstrom. The Aerodynamic Influence of Rim Design on a Sports Car and its Interaction with the Wing and Diffuser Flow. 2010.
- [4] Wu Dejiu, Hu Xingjun and Yang Bo. A Simulation Study on the Wake Field of a Notchback Car Model. Automotive Engineering. China.7.2014.
- [5] HU Jie-hua, CU Zheng-qi, HE Yi-in. Numerical Simulation and Experimental Research on Turbulent Wake of Vehicle. Journal of System Simulation, 2.2010.
- [6] Zhang Zhonghua, Xu Yanhai. Numerical Simulation of Car External Flow Field with Rotating Wheels. National Conference on Information Technology and Computer Science, March 21-22, 2015: Session 1 Information Technology Part 2, page400-40.

Hongyan Yu\*, Jianjiang Chen, Zhengwei Dong, Guitang Liu

## **Model and Simulation of Vehicle Based on Modelica Language**

**Abstract:** Multi-field unified model based on Modelica language is the most important developing direction of multi-field model and co-simulation today. Firstly the aim of this paper is virtual flight simulation, and the universality of model need to be considered with the blocking methods. Then model of aerospace vehicle is divided, and the relationship between parameters of model is got, and model simulative bank of aerospace vehicle is based on Modelica language. At last, flight simulative model of aerospace vehicle is build on the model bank, however guidance and control of aerospace vehicle is carried out, which is used for availability of model bank.

**Keywords:** Modelica; Simulation X; Model Simulation.

### **1 Introduction**

Co-simulation and unified model need to be solved for multi-field physical system, Modelica language is brought out, which is relate to the equation statement model, and is base on method of induction and summary for prior multi-language of model. Modelica language is adapt to the cumulative, repeatability and rebuild of acknowledge, and physical laws of different field subsystem are described with mathematics language of Modelica. According to topology relation of physical system, with model construct and integration of multi-field based on the mechanism of connected components of language ingrown, system simulation can be run through solving the differential-algebraic equation. So model method of Modelica language being adopted in this paper, model and simulation of aerospace vehicles are researched, and model bank is construct, and flight simulation of aerospace vehicles is realized.

### **2 Flight simulation model**

#### **2.1 Layered structure of flight simulative model**

In order to finish flight simulation, according to model method and blocking method of Modelica language, model parameters should be divided from main parameters

---

\*Corresponding author: Hongyan Yu, Beijing Institute of Electrical and Mechanical Engineering, Case 230, P.O.Box 7293, Beijing, China, E-mail: yuswangoose@163.com

Jianjiang Chen, Zhengwei Dong, Guitang Liu, Beijing Institute of Electrical and Mechanical Engineering, Case 230, P.O.Box 7293, Beijing, China

of system, and universality and materiality of model should be considered. Then model parameters are regarded as initial input data, which is no relation to imulation. Layered structure of flight simulative models can be divided and showed in Figure 1.

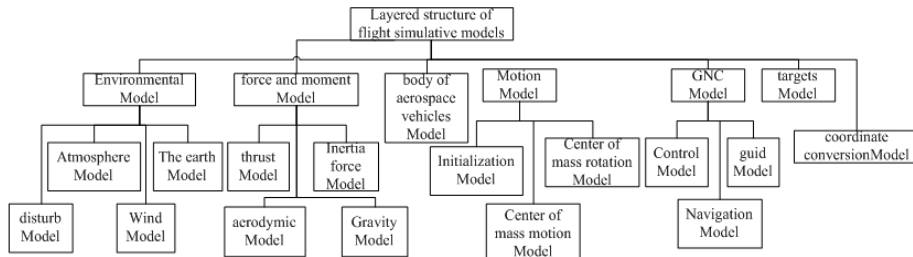


**Figure 1.** Layered structure of flight simulative model.

Model about environmental, force and moment, body of aerospace vehicles, motion, GNC, targets, and coordinate conversion should be built for finishing the flight simulation. The meaning of above words is explained as following:

- Model of environmental: different factors of model which influences aerospace vehicles;
- Model of force and moment: the total force and moment of aerospace vehicle;
- Model of body of aerospace vehicles: the moment of inertia, mass, reference area, reference length end mote of the boost phase, and end note of cruising phase;
- Model of motion: level motion and turning motion of aerospace vehicles;
- Model of GNC: real position of aerospace vehicles, the relation between vehicles and targets, commands which is used to guide vehicles to targets;
- Model of targets: position, velocity and attitude of aerospace vehicles;
- Model of coordinate: different coordinate of different models, questions for the coordinate conversion.

## 2.2 The relation between parameters of flight simulative model

In order to finish flight simulation, according to output relation of parameters of different models, divided submodels should be assembled under the condition of multi-field model and co-simulation, and flight simulative system is completed. The relation between different models is showed as following Figure 2. Within Figure 2, initial model is the entrance of simulation, after simulation running, three dash line related with initial condition should be canceled.

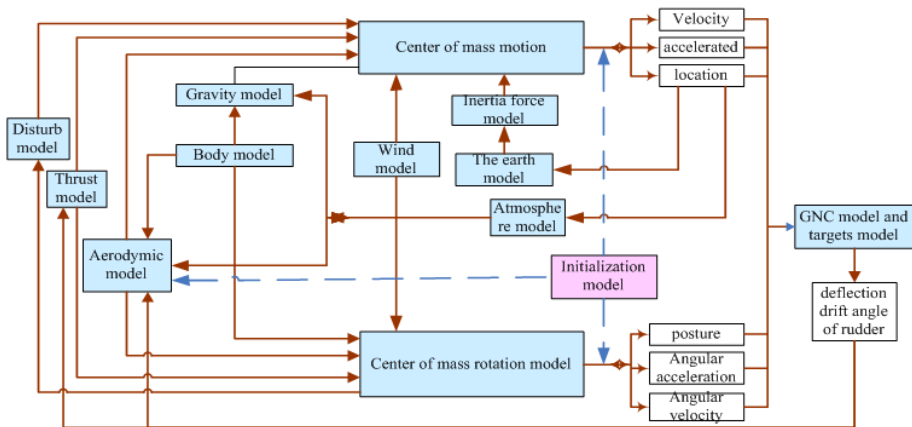


Figure 2. The relation between different models

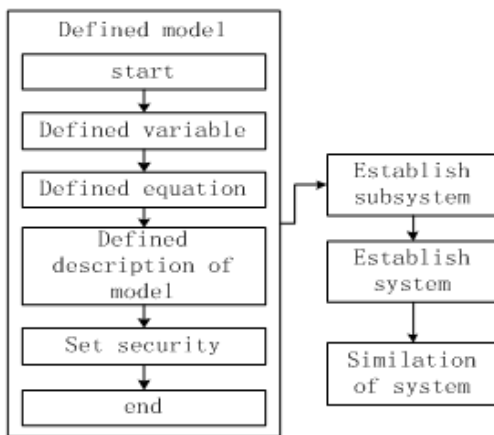
### 3 Model and simulation of vehicles

#### 3.1 Building the simulative bank of aerospace vehicles

Based on layered structure of flight simulative models, model simulative bank can be built with modelica language. For example, aerodynamic moment can be divided into three components according to body coordinate of aerospace vehicles, that is roll moment  $M_x^A$ , yaw moment  $M_y^A$ , and pitch moment  $M_z^A$ , and this mathematical model is described as equation(1), Within equation (1),  $m_x$ ,  $m_y$ ,  $m_z$  is respectively coefficient of roll moment, coefficient of yaw moment, and coefficient of pitch moment, (however, they should be got by interpolating slide angle, angle of attack, and Mach number) ; L is span of wing,  $b_A$  is mean dynamic chord.

$$\begin{cases} M_x^A = m_x q S L \\ M_y^A = m_y q S b_A \\ M_z^A = m_z q S L \end{cases} \quad (1)$$

From mathematical model, the process of modeling is showed as following Figure 3 with Modelica language, and the definition of equations with Modelica language is noted as Figure 4. From two figures, model can be built by initial equations, which possesses stronger readability and higher efficiency than other models.

**Figure 3.** The process of model

```

//enter your equations here
//aerodynamic model
Mx=mx_Curve(beta, alpha, Ma) ;
My=my_Curve(beta, alpha, Ma) ;
Mz=mz_Curve(beta, alpha, Ma) ;
//moment of pitch. yaw. roll
Mx=mx*q*S*L
My=my*q*S*L
Mz=mz*q*S*L
  
```

**Figure 4.** Description of mathematical model

### 3.2 Building the simulative system of aerospace vehicles

The simulative system of aerospace vehicles include many subsystem, and the relationship between different subsystem need be hold together by data transferring. Subsystems catch their required data to simulate, and send out required data for other subsystems. According to management of layered structure of flight simulative model, simulative system of aerospace vehicles is showed as following Figure 5.

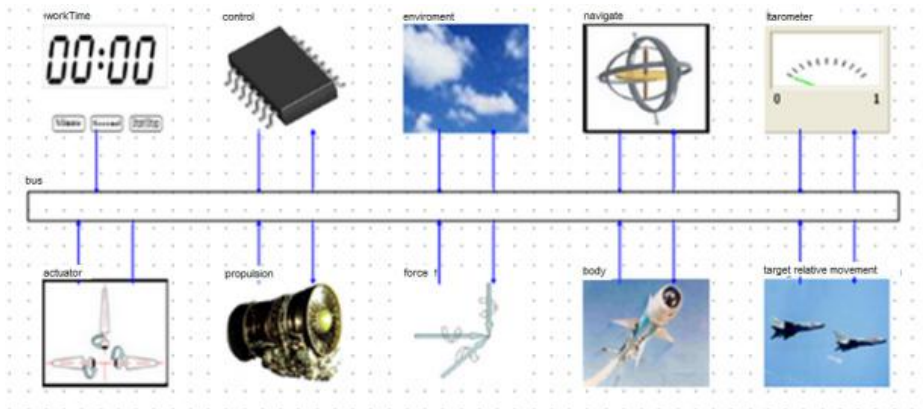


**Figure 5.** Simulative system of aerospace vehicles

### 3.3 Simulative analysis

The whole trajectory of aerospace vehicles can be simulated with simulative system of aerospace vehicles. Initial conditions can be set as Figure 6, and results about angle of pitch, Ma, flight height, and deflections of effectors according to three directions are noted as Figure 7 to Figure 12, which is the same as curves got form traditional methods of model and simulation.

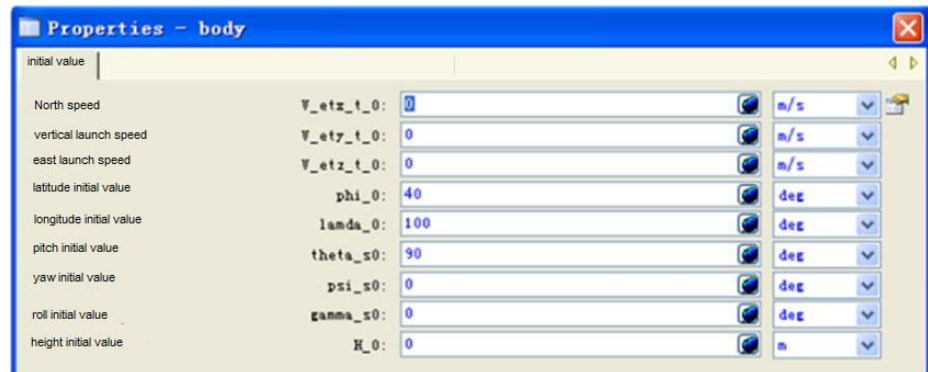


**Figure 6.** Set initial conditions of simulation

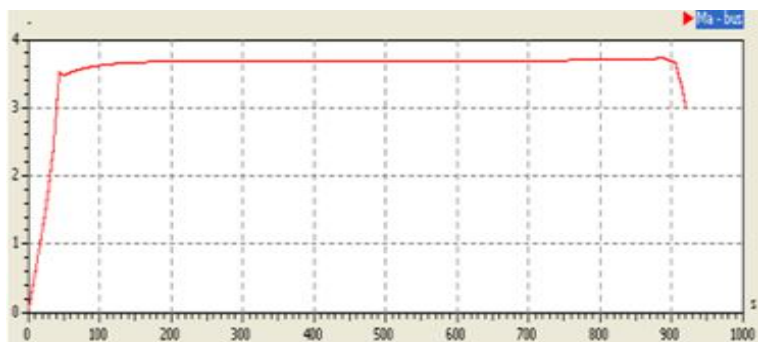


Figure 7. Pitch angle curve

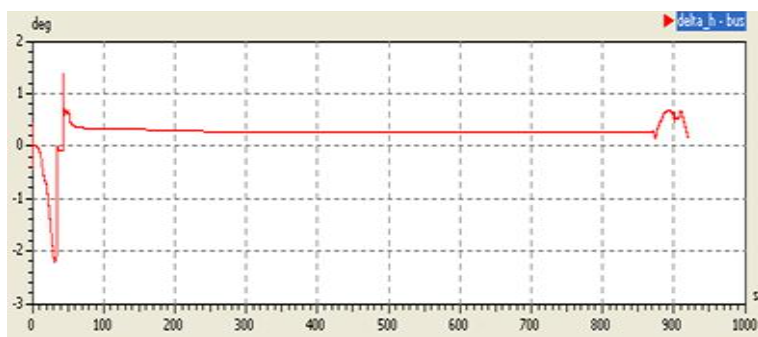


Figure 8. Ma curve

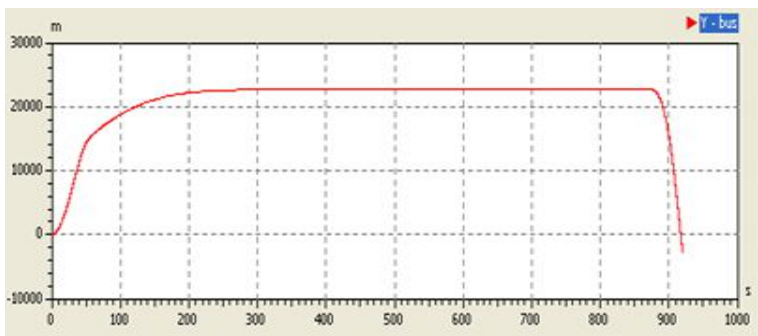


Figure 9. Flight height curve

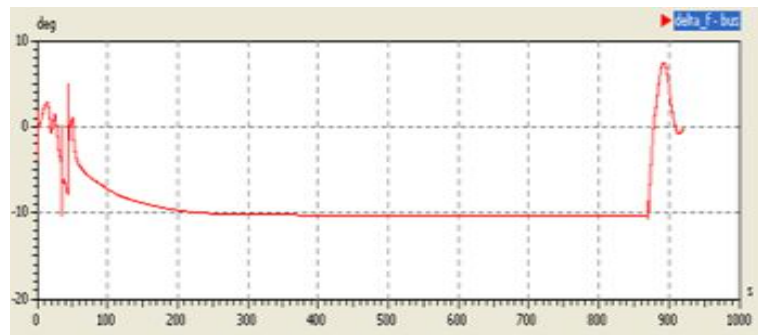


Figure 10. Deflection curve of elevator

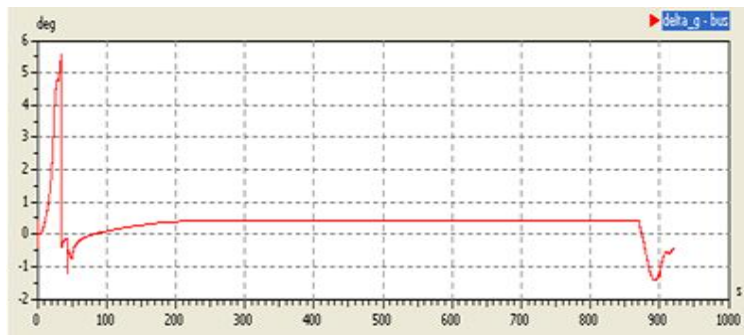


Figure 11. Deflection curve of aileron

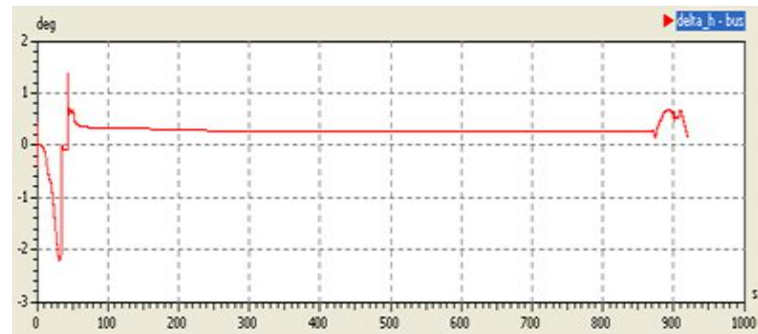


Figure 12. Deflection curve of rudder

## 4 Conclusion

Base on mathematical model of aerospace vehicles, flight simulative bank is built with Modelica language, and simulative system of aerospace vehicles is built, the simulation of the whole trajectory of aerospace vehicles is realized.

**Acknowledgment:** This work was financially supported by the Twelfth Five-year Plan of National Defense Basic Research under Grant No.A0420131501.

## References

- [1] Shiyi Guan, Development and prospect of simulation technology for tactical missile, J. system and simulation. 1992, 4(1):55-62.
- [2] Mingliang Tang, Design of general-purpose software for flight vehicle trajectory simulation, master's thesis, Northwestern Polytechnical University, 2006.
- [3] Seigler T M.Dynamics and control of morphing aircraft. Blacksburg: Virginia Polytechnic Institute and State University, 2005.
- [4] Pierre Apkarian, Richard J Adams.Advanced Gain-Scheduling Techniques for Uncertain Systems. IEEE Trans on Control Systems Technology, 1998, 1 ( 6 ) : 21-32
- [5] Chun-Hsiung Fang, Yung-Sheng Liu, Lin Hong, et al. A new LMI-based approach to relaxed quadratic stabilization of T-S fuzzy control systems[J]. IEEE Trans. on Fuzzy systems, 2006, 14(3): 386-397.
- [6] C.Barbu, R.Reginatto, A.R.teel Luca, Zaccurian. Anti-windup for exponentially unstable linear systems with inputs limited in magnitude and rate. Proceedings of the American control conference.2000, 1230-1234.

Le HE\*, Xiaoming LI, Xianyong MU, Ying LIU, Kunjie WANG

## **Research on Asynchronous Starting Characteristics of Synchronous Motors Based on TSC Reactive Power Compensator**

**Abstract:** The asynchronous starting current of synchronous motor is very large, which will cause a sharp decline of power grid voltage. Therefore, TSC reactive power compensator was used to provide the reactive components of the starting current to maintain grid voltage stability. TSC reactive power compensator provides is in accordance with 8:4:2:1 unequal capacity grouping mode and the reactive power control mode, using thermistor switches to put in or cut out respective capacitors in real time based on reactive power of the synchronous motor needed to asynchronous starting. The asynchronous starting process were simulated with using MATLAB/Simulink. The feasibility of reducing system voltage drop with using reactive power compensation in asynchronous starting process was verified by the simulation. On the other hand, Simulation results showed that reactive power compensation can effectively improve the starting speed and reduce starting time. To ensure the quality of the grid voltage, the asynchronous starting with using reactive power compensation should be used for synchronous motor, compared with the direct asynchronous starting mode.

**Keywords:** synchronous motor; asynchronous starting; voltage drop; TSC reactive power compensator

### **1 Introduction**

Synchronous motors have the advantages of high overload capacity and operational stability, its rotor speed completely depends on the power frequency, does not change with the load in steady state operation. It has become the main power of industrial and mining enterprises. The disadvantage is that the synchronous motor cannot

---

\*Corresponding author:Le HE, Power System and Automation, School of Electrical Engineering Wuhan University, Wuhan, China, E-mail: hele@whu.edu.cn

Xiaoming LI, Institute of electric power information and control, School of Electrical Engineering Wuhan University, Wuhan, China

Xianyong MU, Kunjie WANG, Operation and maintenance department, Hubei Bailianhe Pumped Storage Co., Ltd, Huanggang, China

Ying LIU, Company leadership department, Hubei Bailianhe Pumped Storage Co., Ltd Huanggang, China

directly start by its own. Therefore, it's important to research on the start-up mode of synchronous motors.

When using auto transformer to reduce voltage to start large synchronous motors [1], although the starting current is reduced [2], but starting torque decreases with the square of the voltage [3], leading to start time increased more. Literature [4] studied soft start technology principle and control system of frequency conversion starting. However, due to the long starting time, the technical defects of harmonic interference and the high cost of soft start equipment, the use of frequency conversion starting still subject to certain restrictions. Literature [5] considered the line impedance, the mathematical model of asynchronous full-voltage starting were established, but the measures to stabilize the voltage of the network were not presented.

In order to solve the starting problem of synchronous motor, this paper proposes an asynchronous start mode based on TSC reactive power compensator. In this start mode, according to the monitored reactive power required to start the motor, the TSC reactive power compensator send a switching signal, then the corresponding capacitors are connected to the grid to provide reactive power and compensate starting current, so as to maintain grid voltage stability. Finally, the feasibility of this start mode was verified by the simulation example.

## 2 Asynchronous starting based on reactive power compensation

### 2.1 Asynchronous starting principle based on reactive power compensation

Asynchronous starting principle of synchronous motor based on reactive power compensation is shown in Figure 1.

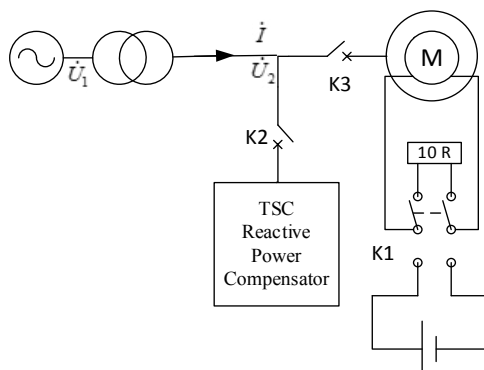


**Figure 1.** Asynchronous starting principle of synchronous motor based on reactive power compensator

Before starting the motor, all switches are open. To start the motor, firstly, the bidirectional switch K1 of the rotor winding access the additional resistance, whose value is 10 times of the value of the field winding resistance. Then switch K2 is closed, that is synchronous motor stator via the transformer is put into power grid. Synchronous motors rely on asynchronous starting torque to accelerate rotation of the rotor until its speed is close to synchronous speed. When the rotor speed reaches 90% of synchronous speed, throw the bidirectional switch K1 to the excitation power, then the rotor will be pulled in synchronization relying on the synchronizing torque. Be noted that the switch K3 should be closed ahead of the switch K2. Put some capacitors in advance to ensure that the system voltage does not exceed 5% of rated voltage. By doing that, avoid pulling voltage down and resulting in low reactive power compensation value in initial period of starting. Then the dynamic reactive power compensation device by analyzing the detected reactive power put in the appropriate number of capacitor groups to compensate the inductive current whose value is several times of the rated current during the motor startup process.

Thus synchronous motors use the start mode without obtaining excessive reactive power from the system, this can improve the power grid voltage, reduce line losses, improve the transmission capacity of the power system, and improve utilization of other devices in power system.

## 2.2 Effect of reactive power compensation on voltage drop

When the circuit is calculated, generally use per unit form, take each bus rated voltage as the reference voltage. The equivalent reactance of the infinite system is  $X_s = S_b / S_c$ ,  $S_c$  is short-circuit capacity at the exit of the infinite grid system;  $S_b$  is reference capacity.

The equivalent impedance of the motor access system is  $Z_{net} = X_s + X_T + Z_L$ ,  $X_T$  is the equivalent reactance of transformer;  $Z_L$  is equivalent impedance of transmission lines.  $Z_{net}$  is a complex number, which can be decomposed into real and imaginary parts.  $R_{net}$ , the real part, is the equivalent resistance of the motor access system, generally is small;  $X_{net}$ , the imaginary part, is the equivalent reactance of the motor access system. The voltage drop from the outlet side of the motor to the grid side is shown in (1).

$$\Delta \dot{U} = \dot{U}_1 - \dot{U}_2 = \dot{I} \cdot Z_{net} \quad (1)$$

When the synchronous motor is directly started, if the reactive power compensation device is not set up, that is the switch K2 in Figure 1 is not closed, the voltage drop of the motor outlet to the power network side is shown in (2).

$$\Delta \dot{U} = \dot{I}_{start} \cdot Z_{net} = \dot{I}_{start} \cdot R_{net} + \dot{I}_{start} \cdot jX_{net} \quad (2)$$

$\dot{I}_{start}$  in (2) is the starting current, its value is usually several times the rated current, can be divided into resistive components and inductive components, that is  $\dot{I}_{start} = \dot{I}_R + \dot{I}_X$ .

When synchronous motors is started asynchronously based on reactive power compensation, the dynamic reactive power compensation device put in the appropriate number of capacitor groups to compensate reactive power generated by synchronous motor. Thus capacitive current generated by capacitor groups and inductive components of starting current of synchronous motor offset each other, that is  $\dot{I}_C = -\dot{I}_X$ . At this time the current at the motor outlet is  $\dot{I}' = \dot{I}_{start} + \dot{I}_C = \dot{I}_R$ . Therefore, the current at the motor outlet is purely resistive component, the voltage drop of the motor outlet to the power network side is shown in (3).

$$\Delta\dot{U}' = \dot{U}_1 - \dot{U}'_2 = \dot{I}_R \cdot R_{net} + \dot{I}_R \cdot jX_{net} \quad (3)$$

The relationship between the above voltage and current is shown in Figure 2.

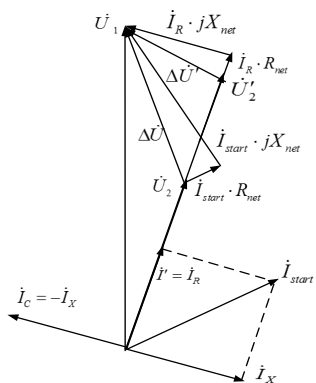


Figure 2. Phasor diagram of Voltage and current before and after reactive power compensation

Figure 2 shows that, the gap of voltage drop before and after reactive power compensation is obvious. With the line impedance increasing, especially in long distance power supply of large synchronous motors, voltage drop caused by the direct asynchronously starting also increased, causing severe voltage fluctuations of other electrical equipment in the power line. besides with the grid voltage reducing, motor starting process will be extended [5]. Therefore, it is necessary to set reactive power compensation according to the network parameters during starting asynchronously in order to stable grid voltage and reduce power loss.

### 3 Grouping and switching control of TSC reactive power compensator

Thyristor switched capacitor (TSC) cannot continuously adjust reactive power, but TSC does not produce harmonics, and generate a smaller loss and noise [6,7], therefore TSC has been more widely used in the power system. TSC has the function of phase separation. Each phase chooses different input time, to ensure that each phase does not generate impulse current, reducing interference on the power grid, increasing the life of the compensating device [8]. In addition, TSC device uses star wiring, the phases were separately sampled. TSC reactive power compensator compensates by putting different capacitors separately based on each phase reactive power, without causing overcompensation and making three-phase voltage is more stable.

TSC is a kind of reactive power compensation device which can export intermittent adjustable reactive power. If the number of the capacitor is sufficiently refined, the continuous adjustment can be achieved basically. There are isochoric capacity grouping and unequal capacity grouping. In this paper, according to the capacity ranging grouping and the principle of 8:4:2:1, setting four capacitors, 16 kinds of different combinations can be achieved. The four capacitors are connected in parallel, the capacity of which respectively were  $8Q_{C_0}$ ,  $4Q_{C_0}$ ,  $2Q_{C_0}$ ,  $Q_{C_0}$ , the total capacity of compensation is  $15Q_{C_0}$ ,  $Q_{C_0}$  is the single stage compensation capacity, whose theoretical value is about one-fifteenth of the maximum reactive power demand during asynchronous start of synchronous motor. The actual setting can be further adjusted to avoid excessive compensation. Each capacitor in series with bidirectional thyristor is connected to the grid, where the thyristor acts as a switch.

Its single phase compensation principle is shown in Figure 3. In Figure 3,  $Q_{C_0}$  is setting to avoid switching frequently the thyristors in the steady running state with small disturbance, whose value is the reactive power demand of the motor in the steady running state.

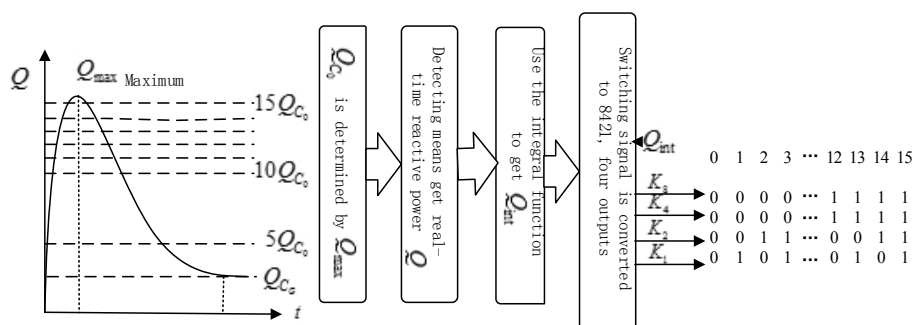


Figure 3. Switching schematic diagram of Single-phase capacitors

In Figure 3, the waveform is the assumption of the single phase reactive power demand of the synchronous motor asynchronously starting in the absence of reactive power compensator. The single stage compensation capacity  $Q_{C_0}$  is determined by (4). The level of reactive power demand  $Q_{\text{int}}$  is determined by (5), the function  $\text{INT}$  can make a numeric rounded down to the nearest integer. Four signals  $K_8, K_4, K_2, K_1$  correspond to the switching signal of four sets of capacitors in Figure 3, using 1 and 0 to indicate input and removal of the corresponding capacitor,  $K_8, K_4, K_2, K_1$  are determined by (6).

$$Q_{C_0} = Q_{\max}/15 \quad (4)$$

$$Q_{\text{int}} = \text{INT}\{Q/Q_{C_0}\} \quad (5)$$

$$\begin{cases} K_8 = \text{INT}\{Q_{\text{int}}/8\} \\ K_4 = \text{INT}\{(Q_{\text{int}} - K_8 * 8)/4\} \\ K_2 = \text{INT}\{(Q_{\text{int}} - K_8 * 8 - K_4 * 4)/2\} \\ K_1 = \text{INT}\{Q_{\text{int}} - K_8 * 8 - K_4 * 4 - K_2 * 2\} \end{cases} \quad (6)$$

When the thyristor receives switching signals, in order to make the impact of current is zero, the control strategy of thyristor is triggered by zero voltage moment. The trigger pulse corresponding to the reactive power demand are obtained by Switching signal and zero-voltage pulse signal through the logic AND gate. The trigger pulse control putting corresponding capacitors into system to compensate reactive power. When  $K_n (n = 8, 4, 2, 1)$  is 0, the trigger pulse of the reactive power demand is always 0, so the corresponding capacitors are removed from the system. When  $K_n (n = 8, 4, 2, 1)$  is 1, the zero-voltage pulses work, the corresponding capacitors are access to the system.

#### 4 The analysis of simulation

In the MATLAB/Simulink environment, the power frequency 50Hz system is established. The simulation parameters are shown in Table 1. Infinite system power grid through the 3km long line supply power to the 100kW load and synchronous motor. In order to improve the load terminal voltage, TSC reactive power compensator is added between the load and the synchronous motor.

**Table 1.** Simulation Parameters Table

item	value	item	value
Grid voltage	440 V	Load power	100 kW
Internal resistance	0.058 Ω	Line resistance	0.01273 Ω/km
Internal inductance	1.85e-3 H	Line inductance	9.337e-5 H/km
stator resistance	0.266 Ω	Line capacitance	1.274e-8 F/km
Stator reactance	1.883 e-3 H		

Without TSC reactive power compensator, motor at the time of 4.2s or so ended the asynchronous starting process, at the time of 5s, motor was gradually pulled into synchronization. With TSC reactive power compensator, motor at the time of 3.3s or so ended the asynchronous starting process, at the time of 4.2s, motor was gradually pulled into synchronization. So the start speed can be improved significantly by TSC compensation. In the course of starting process and steady state process, the voltage effective value and voltage offset of the motor outlet are shown in Table 2. As shown in Table 2, without reactive power compensator, the voltage offset during the startup process is too large to meet the requirement of power system. However, with reactive power compensator, the voltage offsets during the startup process and steady state process are in line with the requirements. Therefore, reactive power compensation can improve and stabilize the voltage of the motor outlet. Through the analysis, we can draw: when synchronous motor is started asynchronously, TSC reactive power compensator can improve and stabilize terminal voltage, and can increase the startup speed.

**Table 2.** Simulation Results Table

item	Without reactive power compensator		With reactive power compensator	
	Starting process	Steady state process	Starting process	Steady state process
RMS voltage (V)	370	430	420	433
Voltage excursion	15.9%	2.27%	4.55%	1.59%

## 5 Conclusion

This paper puts forward a kind of asynchronous starting mode of synchronous motors based on TSC reactive power compensator. Simulation results show that the asynchronous starting of synchronous motor when using TSC reactive power compensator with the advantages in two aspects: compensating the start current can effectively improve and stabilize the system voltage; due to the stability of the voltage of the motor outlet, the startup speed of the synchronous motor can be significantly improved.

**Acknowledgment:** This research is financially supported by Scientific and Technological Project of State Grid Xinyuan Company Ltd (5257001400S9).

## References

- [1] Herman S. Industrial motor control [M]. Cengage Learning, 2013.
- [2] Si Xiaoqing, Wang Xuyan, Ye Ting, et al. Influence of Large Capacity Motor Starting Modes on Power Grid [J]. Electric Power Construction, 2014, 35(7): 121-125.
- [3] Zhang Yong qin, Lei Likun, Wu Yin. Dynamic Model Experimental Study on 10kV bulk impact on the grid voltage motor starting [J]. Gansu Science and Technology, 2009, 25(1): 45-48.
- [4] Pei Jia. Research on Start-up Control System of the Synchronous Generator/motor in Pumped-Storage Power Station [D]. North China Electric Power University, 2003.
- [5] Wang Xiaoyuan, Li Zhiguang. The Study of Asynchronous Direct on Line Starting of the Synchronous Motor [J]. Micro-motor, 1999, 32(6): 7-11.
- [6] Wang Geng Liang. Reactive power compensation technologies and economical efficiency studies for 10kV distribution Power System [D].North China Electric Power University, 2014.
- [7] Niu Yinan, FENG Ting, Wang Yang, LI Cheng-bo, et al. Review on the reactive power compensation of power system[J]. Information and communications, 2011 (1): 48-51.
- [8] Gao Jingjing. Studies on the Low-Voltage Dynamic Reactive Power Compensation Device [D]. Northeast Agricultural University, 2004.

Yun-de SHEN\*, Jing-yi ZHANG, Su-jie ZHOU, Lei WANG, Dong-ji XUAN

## **Motorcycle Engine Controller Design and Matlab/Simulink Simulation**

**Abstract:** In order to meet the requirements of environmental protection, energy-saving when people using motorcycle, the main propose of this article is to design a motorcycle engine controller based on the comprehensive control method of fuzzy control and PID control to control output speed and current air-fuel ratio(AFR) of motorcycle engine precisely under transient conditions. Then establishing the mathematical model of the motorcycle engine assembly based on Matlab/Simulink according to building fuel evaporation and dynamic oil film sub model, intake dynamic characteristic sub model, power output sub model and idle speed throttle control sub model. Finally combined with the control method of this paper, the simulation analysis is carried out to verify the feasibility of the scheme.

**Keywords:** Air-fuel ratio; control; Matlab/ Simulink; Motorcycle engine modeling; PID control.

### **1 Introduction**

In recent years, environmental pollution and energy crisis is still generally concerned of all sectors of the community. Therefore, the future development trends of motorcycles also focus on low pollution emissions, energy-saving and more advanced technology. Accurate air-fuel ratio control is the key control technology for modern motorcycle engine and air-fuel ratio control technique based on model which is researched hotspot at home and abroad currently [1,2]. Air-fuel ratio has a very direct influence on the dynamic performance, fuel economy performance and emission performance of the engine, especially for the emission of tail gas [3].

This paper is organized as follows. Firstly, establishing four mathematical sub models of the motorcycle engine, then according to the correlation between them, the model assembly of the engine is obtained. Secondly, proposing an air-fuel ratio control strategy based on the comprehensive control method of fuzzy control and PID control under transient conditions. Concrete, Fuzzy control is adopted when there is big

---

\*Corresponding author: Yun-de SHEN, College of Mechanical and Electrical Engineering, Wenzhou University, Wenzhou China, 325035, E-mail: shenyunde63@163.com

Su-jie ZHOU, Dong-ji XUAN, College of Mechanical and Electrical Engineering, Wenzhou University, Wenzhou China, 325035

Jing-yi ZHANG, ETAS(Shanghai) Co., Ltd, Shanghai China, 200335

Lei WANG, Department of Mechanical Technical Application, Wenzhou Technician Institute, Wenzhou China, 325035

difference between the measurement result and the target quantity; on the contrary, classical PID control is priority. Making the fluctuation of the air fuel ratio is within the scope of design by using a precise control of the throttle opening and the input volume of cylinder fuel. Consequently, ensuring the engine speed and reducing the pollutant emission. Finally, it is combined with the control method of fuzzy control - PID control. The simulation analysis of motorcycle engine which obtains air-fuel ratio changes in the three cases include non-controller, PID controller and fuzzy control and PID control is carried out. And verifying the feasibility of the scheme through compare and analyses the simulation result of the three cases mentioned above.

## 2 The establishment of engine model

It's important to establish the mathematical model of the motorcycle engine, so as to simulate and control the input and the output quantity changes, such as air intake and air output, fuel injection mass and power output speed, etc. Laying the foundations for air/fuel ratio of motorcycle engine. Firstly, establishing four mathematical sub models of the motorcycle engine, including fuel evaporation and dynamic oil film sub model, intake dynamic characteristic sub model, dynamic output sub model and idle throttle control sub model. Then the four models are connected by the parameter association between them to generate the model assembly of the engine.

### 2.1 Fuel evaporation and dynamic oil film sub model

The fuel sprayed from the injector enters the cylinder in two ways: one part is to adhere to the inlet or the inlet valve wall, so a portion of the oil film is formed. This layer of oil film continues to evaporate and enters the cylinder with the air. While the other part of the fuel is directly gasified into fuel vapor to enters the cylinder. The differential equation of the sub model can be expressed as:

$$\dot{m}_{fv} = (1 - X)\dot{m}_f \quad (1)$$

$$\ddot{m}_{ff} = (1/\tau)(-\dot{m}_{ff}) + X\dot{m}_f \quad (2)$$

$$\dot{m}_f = \dot{m}_{fv} + \dot{m}_{ff} \quad (3)$$

Where  $x$  is the distribution coefficient of fuel,  $\tau$  is the time constant of oil film,  $\dot{m}_f$  is fuel mass flow sprayed from the injector,  $\dot{m}_f$  is the fuel mass flow in the cylinder,  $\dot{m}_{ff}$  is the evaporation capacity of deposited oil film and  $\ddot{m}_{ff}$  is the mass change rate of oil film.

There is a dynamic balance in the formation and evaporation of oil film: if the fuel injection quantity, the engine speed or the cylinder temperature changes, it will interfere with the balance of fuel oil film to affect the quality of the fuel in the cylinder.

And when the engine is under acceleration and deceleration transient condition, the balance of oil film will be broken. The volume of fuel injected into the cylinder and the volume of oil emitted by the fuel injectors are no longer equal. So air-fuel ratio (AFR) of motorcycle engine will be impacted by the dynamic characteristics of oil film.

Although the fuel evaporation and dynamic oil film sub model is presented in the form of linearity on the surface, the fuel evaporation and dynamic oil film sub model is a nonlinear dynamic model actually because of the two nonlinear parameters and X it contains. Hendricks Elbert, a professor at the Technical University of Denmark proposed that in the case of fully preheating of the engine, the two parameter model  $\tau$  and X can be expressed as [4-6]:

$$\tau(p_i, n) = 1.35 (0.672n + 1.68)(p_i - 0.825)^2 + (0.06n + 0.15) + 0.56 \quad (4)$$

$$X = -0.277p_i - 0.055n + 0.68 \quad (5)$$

Where  $p_i$  is absolute pressure of intake manifold and  $n$  is the speed of engine.

According to the equations mentioned above, fuel evaporation and dynamic oil film sub model showed in Figure 1 can be established based on MATLAB/Simulink.

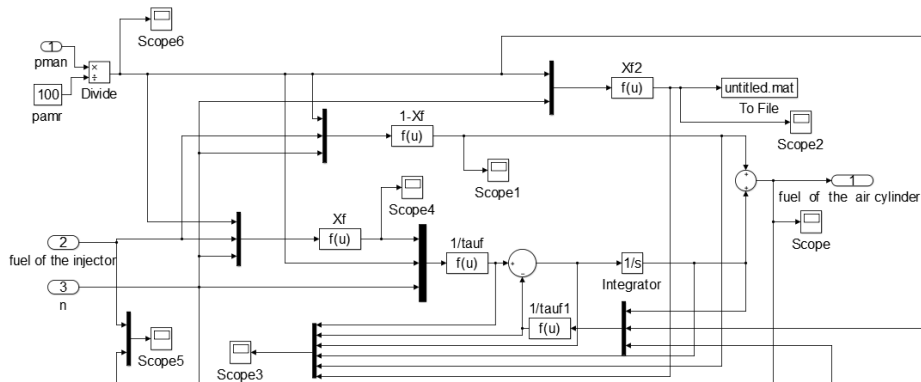


**Figure 1.** Fuel evaporation and dynamic oil film sub model

## 2.2 Intake dynamic characteristic sub model

The intake dynamic characteristic sub model is derived from the mass conservation equation. The following equations can be obtained according to the structure of the engine:

$$\dot{m}_a = \dot{m}_{at} - \dot{m}_{ap} \quad (6)$$

Where  $\dot{m}_a$  is the air quality change rate of air intake pipe,  $\dot{m}_{ap}$  is air mass flow at the intake valve and  $\dot{m}_a$  is air mass flow at the throttle.

The air mass flow at the intake valve can be written as:

$$\dot{m}_{ap} = \frac{nV_d \eta_{vol}^{man}}{120RT_{man}} P_{man} \quad (7)$$

Where  $\eta_{vol}^{man}$  is referred to as volumetric efficiency based on manifold conditions respectively. It mainly depend on engine speed  $n$ , intake pressure  $P_{man}$  and intake temperature  $T_{man}$ .  $V_d$  is the displacement volume of the engine and  $R$  is the specific gas constant. And according to the ideal gas state equation, the air quality change rate of air intake pipe can be derived as:

$$\dot{m}_a = \frac{\dot{P}_{man} V}{RT_{man}} \quad (8)$$

$$\dot{P}_{man} = -\frac{nV_d \eta_{vol}}{120V} P_{man} + \frac{RT_{man}}{V} \dot{m}_{at}(\alpha, p_{man}) \quad (9)$$

The air mass flow at the throttle can be calculated in accordance with the compressible flow of the nozzle:

$$\dot{m}_{at} = C_1 \frac{\pi}{4} D^2 \frac{P_{man} \sqrt{2K/(K-1)}}{\sqrt{RT_{amb}}} \beta_1(\alpha) \beta_2(P_{man}) + \dot{m}_{at0} \quad (10)$$

$$\beta_1(\alpha) = \begin{cases} 0 & 0 \leq \alpha \leq \alpha_0 \\ 1 - \cos(\alpha) & \alpha_0 \leq \alpha \leq 90^\circ \end{cases} \quad (11)$$

$$\beta_2(P_{man}) = \begin{cases} \sqrt{P_{r,x}^{2/x} - p_r^{K+1/x}} & P_r \geq (\frac{2}{K+1})^{\frac{K}{K-1}} \\ \sqrt{(\frac{x-1}{2x} - \frac{2}{x+1})^{\frac{K+1}{K-1}}} & P_r < (\frac{2}{K+1})^{\frac{K}{K-1}} \end{cases} \quad (12)$$

Where  $\dot{m}_{at0}$  is the minimum air flow at throttle,  $D$  is throttle plate diameter and  $\dot{m}_a$  is air mass flow at the throttle,  $T_{amb}$  is the atmospheric temperature,  $K$  is the specific heat of air,  $R$  is the specific gas constant,  $C_1$  is the gas flow coefficient of throttle,  $P_{amb}$  is the barometric pressure,  $\alpha$  is the opening of throttle and where

$$P_r = \frac{P_{man}}{P_{amb}} \quad (13)$$

According to the equations mentioned above, fuel evaporation and dynamic oil film sub model showed in Figure 2 can be established based on MATLAB/Simulink.

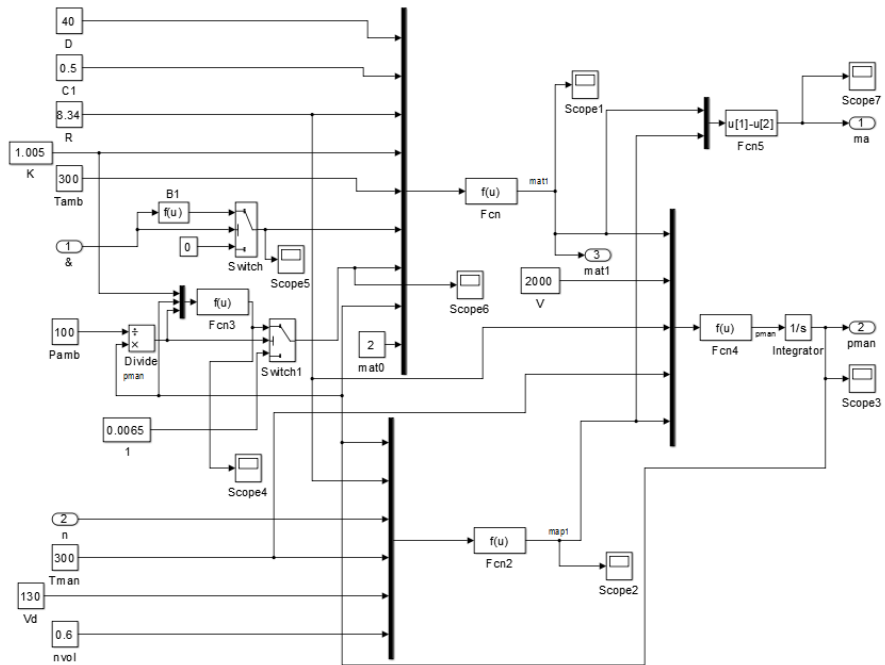


**Figure 2.** Intake dynamic characteristic sub model

### 2.3 Power output sub model

The main parameters associated with the engine power output sub model are the fuel mass flow in the cylinder of fuel evaporation, dynamic oil film sub model and air mass flow in the cylinder of intake dynamic characteristic sub model and there are some other parameters of the engine such as: ignition timing, engine speed and so on, in order to calculate the change rate of the output power and speed of the engine.

When air and fuel vapor enter the cylinder, they will be ignited by a spark plug, then burn severely and release energy driving the piston motion to rotate the crankshaft to produce the torque. Basing on the law of conservation of energy, external output torque of the engine is equal to the value that the running torque of crankshaft minus the friction resistance moment, pumping resistance moment and load torque, it's equation is given as follows [7-11]:

$$\dot{n} = -(P_f + P_p + P_h)/(I \cdot n) + H_u \eta_i \dot{m}_f(t - \tau_d)/(I \cdot n) \quad (14)$$

$$P_f + P_h + P_p = n(a_0 + a_1 n + a_2 n^2) + n(a_3 + a_4 n)P_{man} \quad (15)$$

$$\eta_i = \eta_m(n)\eta_p(P_{man})\eta_{i\lambda}(\lambda)\eta_{i\theta}(\theta, n, P_{man}) \quad (16)$$

Where  $a_i$  is the parameters of engine state.  $\eta_m(n)$ ,  $\eta_p(P_{man})$ ,  $\eta_{i\lambda}(\lambda)$ ,  $\eta_{i\theta}(\theta, n, P_{man})$  are the combustion efficiency coefficients related to the usage status of the engine.  $P_f$  is friction power and  $P_h$  is output power.  $H_u$  is the calorific value of fuel.  $\theta$  is the ignition timing.  $\tau_d$  is total time delay.  $P_p$  is pumping power.  $I$  is the moment of inertia of engine moving parts.  $\eta_i$  is the heat efficiency obtained of the engine and  $\lambda$  is excess air ratio.

According to the equations mentioned above, fuel evaporation and dynamic oil film sub model showed in Figure 3 can be established based on MATLAB/Simulink.

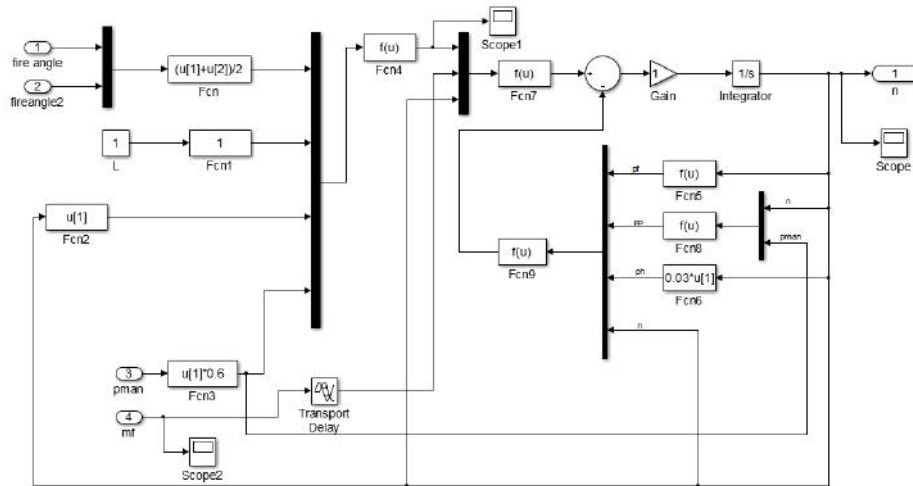


**Figure 3.** Power output sub model

## 2.4 D. Idle speed throttle control sub model

The size of the throttle opening is realized by controlling the rotation angle of permanent magnet brushless DC wheel motor and the error value of the target and the current opening can be obtained by using the encoder-error detector. At the same time, an error signal is produced and be converted to a load power

by using an encoder gain and a power amplifier to control the rotation angle of permanent magnet brushless DC wheel motor. The equation is as follows:

$$\theta_e(t) = \theta_i(t) - \theta_o(t) \quad (17)$$

$$e(t) = K_s \theta_e(t) \quad (18)$$

$$e_a(t) = K_A e(t) \quad (19)$$

$$L_a \frac{di_a(t)}{dt} + R_a i_a(t) = e_a(t) - e_b(t) \quad (20)$$

$$e_b(t) = K_b \omega_M(t) \quad (21)$$

$$T_M(t) = K_T i_a(t) \quad (22)$$

$$J \frac{d\omega_M(t)}{dt} + B \omega_M(t) = T_M(t) \quad (23)$$

According to the equations mentioned above, fuel evaporation and dynamic oil film sub model showed in Figure 4 can be established based on MATLAB/Simulink.

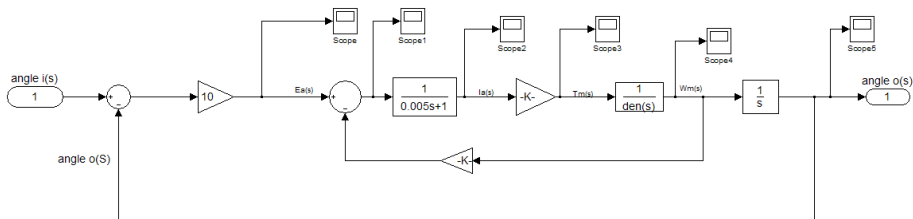


**Figure 4.** Idle speed throttle control sub model

## 2.5 The model of the motorcycle engine assembly

The most important characteristic of this mean value engine model is that the fuel evaporation and dynamic oil film sub model and the inlet dynamic characteristic sub model are studied separately and their effects can be analyzed accurately. Meanwhile, the effects of dynamic characteristics are showed in the power output sub model.

The model of the motorcycle engine assembly is illustrated in Figure 5, it is established by connecting the four sub models according to the correlation of their parameters.

## 3 The design of air-fuel ratio controller for motorcycle engine

In this article, a motorcycle engine controller based on the comprehensive control method of fuzzy control and PID control is designed. When air enters the cylinder, the fuel injection has a time delay and there are a process of the formation and evaporation of oil film to make the value of air-fuel ratio larger during the prophase. If using PID control at this time, it may cause an phenomena of integral saturat and it can even cause system instability. While fuzzy control can be a better solution to the problem that air-fuel ratio may be too large during the prophase. Using the classic PID control during the anaphase to control air -fuel ratio more precisely, stably.

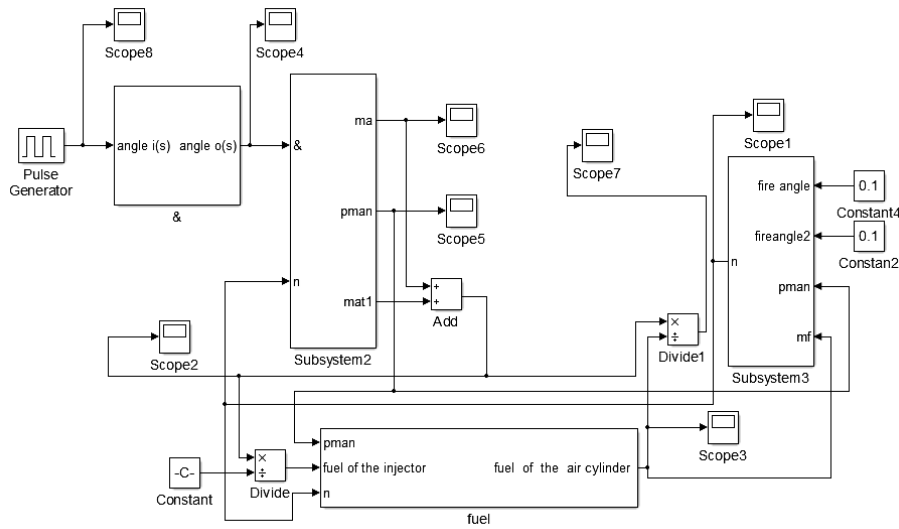


**Figure 5.** The model of the motorcycle engine assembly

### 3.1 Fuzzy control for air fuel ratio

#### 3.1.1 Overview

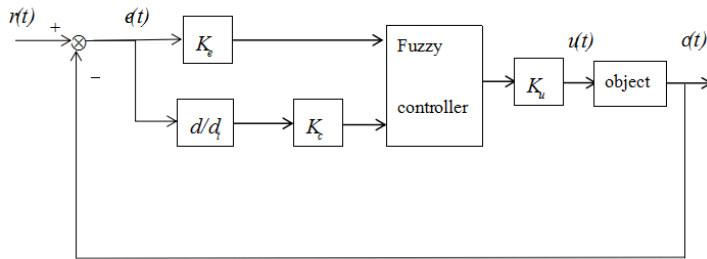
Up to now, there is no clear definition of fuzzy control. It is universally acknowledged that fuzzy control is a kind of computer digital control technique, which is based on fuzzy set theory, fuzzy language variable and fuzzy logic reasoning. Compared with the traditional control method, the fuzzy control has the following prominent features:

1. It has strong robustness, when the parameters of the controlled objects are changed, it can still control the object smoothly.
2. It is applicable for all kinds of nonlinear, time-varying and delay system.
3. The control effect to the system is well without strict requirement of equipment, moreover it pay well in economy.

When we design the fuzzy controller, we don't have to set up the exact mathematical model of the controlled object. This feature makes fuzzy control very special compared to the general control.

#### 3.1.1.1 Basic principle of fuzzy control

The basic structure of the fuzzy control system is shown in Figure 6.

**Figure 6.** Block diagram of fuzzy control

### 3.1.1.2 Design of fuzzy controller

Fuzzy sets and domain must be defined according to the basic principle of fuzzy control [1]. In this paper, E and EC are respectively error and error rate. U is regarded as the control variable. For the output variables seven fuzzy subsets have been used (PB,PM,PS,ZE,NS,NM,NB), in order to smooth the control action. And set corresponding to the domain between [-6,6]. Choosing trigonometric function which is the most common and of a high resolution as a membership function of input variables. For control variable, simple Gauss function is used. The specific parameters of membership functions are shown in Figure 7 and 8. Besides, basing on the principle of Fuzzy-PID parameter setting, the fuzzy control rule table is established in Table 1.

By doing the work mentioned above, the establishment of the fuzzy inference system is completed. Finally, based on Matlab/simulink, establishing the fuzzy control system for air-fuel ratio of motorcycle engine shown in Figure 9 is established. Because the domain is [-6,6] and the actual amount is between [-0.5,0.5], so it is easily to determine the magnification  $K_E$ ,  $K_{EC}=2$ ,  $K_U=0.2$  ( $K_E=12$ ,  $K_{EC}=2$ ,  $K_U=0.2$ ).

**Table 1.** Rule table for Fuzzy control

	U	NB	NM	NS	ZO	PS	PM	PB
EC \ E	PB	PB	PB	PB	PM	ZO	ZO	ZO
NB	PB	PB	PB	PB	PM	ZO	ZO	ZO
NM	PB	PB	PB	PB	PM	ZO	ZO	ZO
NS	PM	PM	PM	PM	ZO	NS	NS	NS
ZO	PM	PM	PS	ZO	NS	NM	NM	NM
PS	PS	PS	ZO	NM	NS	NM	NM	NM
PM	ZO	ZO	NM	NB	NB	NB	NB	NB
PB	ZO	ZO	NM	NB	NB	NB	NB	NB

NB: Negative Big ; NM: Negative Medium; NS: Negative small; ZE: Zero; PB: Positive Big ; PM: Positive Medium ; PS: Positive Small

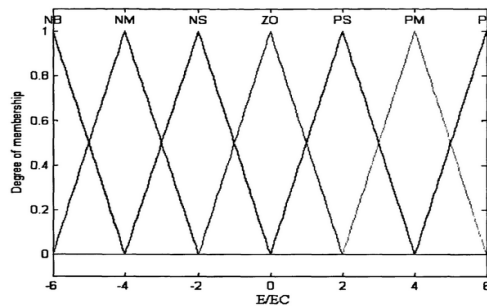


**Figure 7.** Membership functions of E and EC

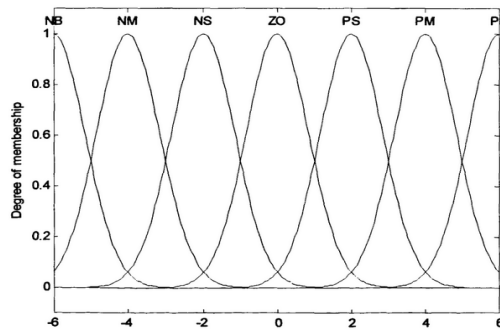


**Figure 8.** Membership functions of control variables

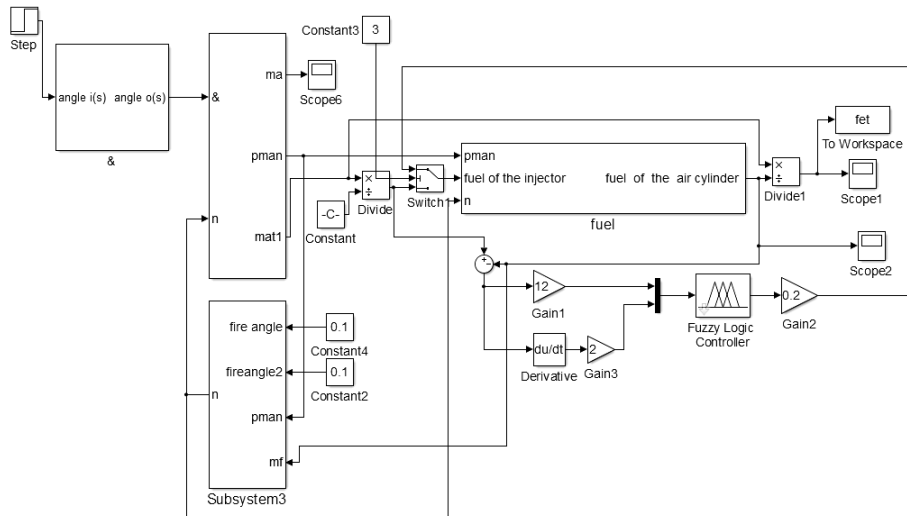


**Figure 9.** Fuzzy control system for air-fuel ratio of motorcycle engine

## 3.2 Classic PID control for air fuel ratio

### 3.2.1 A method of PID control design

The basic principle of PID control is relatively simple, it mainly consists of three elements, including proportional element P, integral element I and differential element D. The controlling rule can be described as  $G(s) = K_p + \frac{K_i}{s} + K_d s$ . The method of PID control design is usually divided into the following steps:

#### 3.2.1.1 Determine the proportional gain

In order to avoid the influence on the KP parameters due to integral terms and differential terms, it's better to remove the integral terms and differential terms in PID controller first to make the controller become a pure proportional control system. Then set the input value to 60% of the maximum value which is allowed of the system and increase the proportion gain gradually until there is an obvious oscillation of the system. And then reduce the proportional gain gradually until the system oscillation completely disappeared. Record the proportion of gain at this time, while setting the proportion gain of PID to 60% of the current value.

#### 3.2.1.2 Determine the integral time constant

After determining the proportion gain, it's better to give a initial value of first, then to reduce this value gradually until there is an obvious oscillation of the system. And then reduce the proportional gain gradually until the system oscillation completely disappeared. Record the integral time constant at this time, while setting the integral time constant of PID to 150% of the current value.

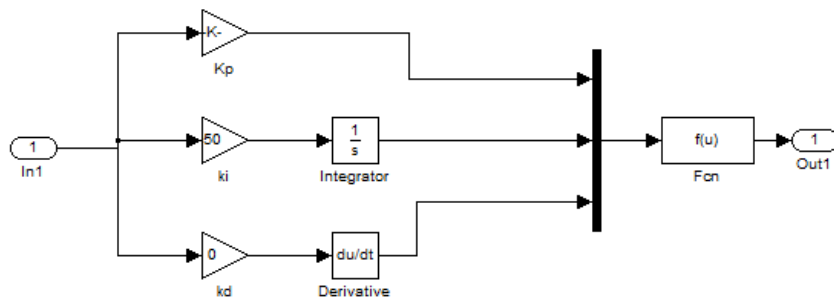
#### 3.2.1.3 Determine the integral time constant

The method to Determine the integral time constant is the same as the method of determining  $T_i$ , and set the integral time constant to 30% of the current value, which is recorded when there is no oscillation in system.

Finally, fine tune the data based on the simulation curve.

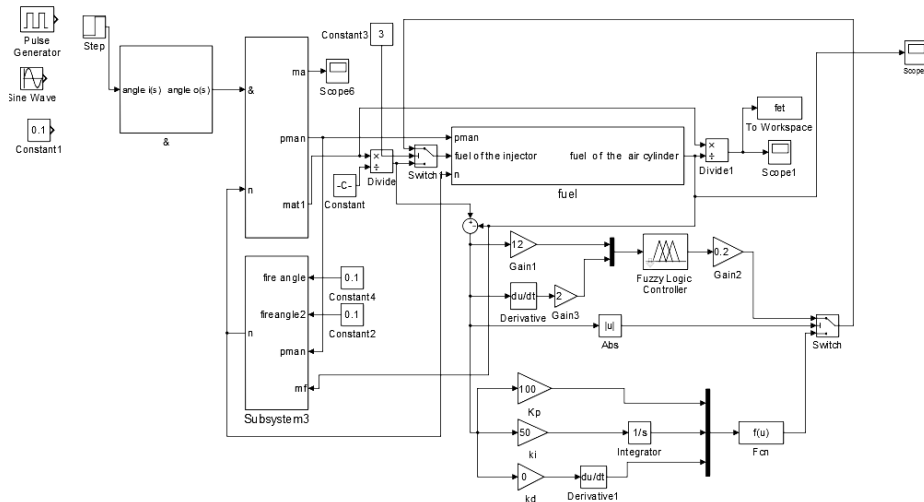
### 3.2.2 The establishment of PID controller

PID controller is shown in Figure 10. In this paper, step signal is selected as input signal to ensure that the state of the entire system is stable, and set the time of initial value is within a high range.

**Figure 10.** PID controller

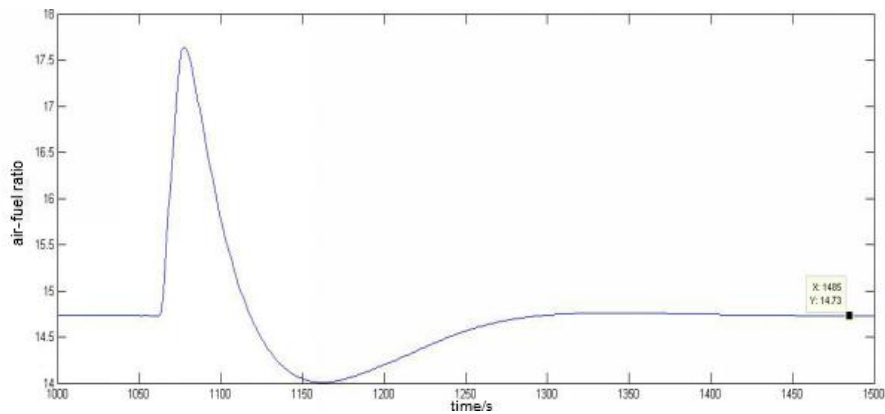
### 3.3 A design of fuzzy -PID controller

The value of air-fuel ratio is large during the prophase, while in anaphase it becomes smaller. So as mentioned above it's reasonable to use the method combining fuzzy control and PID control, as shown in Figure 11. In this paper, a difference comparison between the target air-fuel ratio and the actual air-fuel ratio is carried out. And a threshold is set to make a judgement to choose fuzzy control or PID control.

**Figure 11.** Fuzzy-PID controller

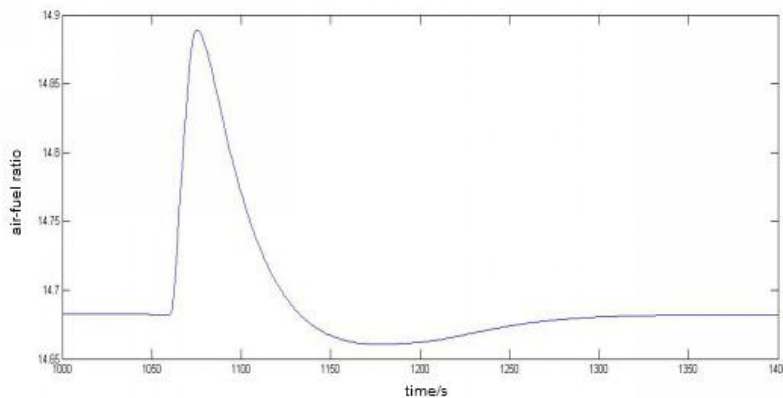
## 4 The results and analysis of simulation

Figure 12 shows a change curve of the air fuel-ratio without control, we can see the fluctuant of the curve ranges between 14-17.5, so it's far beyond the scope of what we want to control and it has a long transition time.



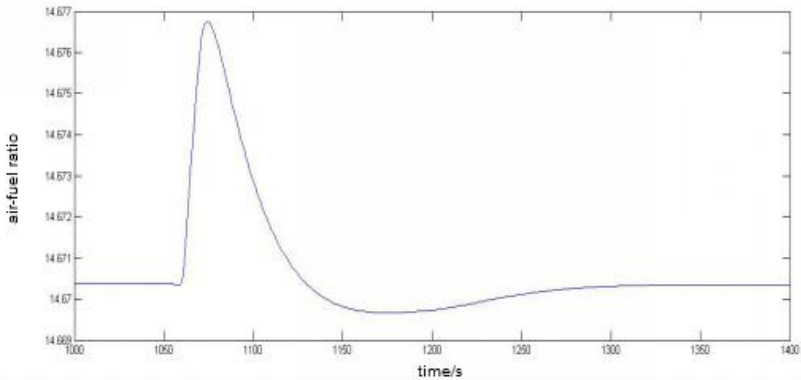
**Figure 12.** Change curve of the air fuel-ratio without control

Figure 13 shows a change curve of the air-fuel ratio under the control of PID controller. As shown in Figure 13, the fluctuant of the curve ranges between 14.8888-14.6605, besides, the maximum overshoot and the final steady-state value were 0.2188 and 14.673 respectively. There a difference of 0.03 between the target air-fuel ratio 14.67 and the current air-fuel ratio in case of the control of a PID controller. This means the steady state error is relatively small under this condition.



**Figure 13.** Change curve of the air fuel-ratio under the control of PID controller

Figure 14 shows the change curve of the air-fuel ratio with the control of Fuzzy-PID controller, and the maximum overshoot and the final steady-state value were 14.677 and 14.669 respectively. It can be seen that this kind of control method has the best control effect of air-fuel ratio.



**Figure 14.** Change curve of the air fuel-ratio with the control of Fuzzy-PID controller

## 5 Conclusion

Air-fuel ratio has a very direct influence on the dynamic performance, fuel economy performance and emission performance of the engine, especially for the emission of tail gas. This paper propose an control strategy of air-fuel ratio for motorcycle engine based on the comprehensive method of fuzzy control and PID control.

In this paper, we establish four mathematical sub models and the model assembly of the motorcycle engine. Using Fuzzy-PID comprehensive controller under transient conditions and making the fluctuation of the air fuel ratio is within the scope of design by using a precise control of the throttle opening and the input volume of cylinder fuel. The simulation analysis of motorcycle engine which obtains air-fuel ratio changes in the three cases include non-controller, PID controller and fuzzy control and PID control is carried out. And verifying the feasibility of the scheme through compare and analyze the simulation result of the three cases mentioned above.

**Acknowledgement:** This work was financially supported by Zhejiang International Science and Technology Cooperation Project (2013C14015).

## References

- [1] Yu Jichao, Liu Dexin, Wang Tianyou, Wang Jian, Feng Hongqing, Liu Shuliang.A Review on Combustion, Fuel Consumption and Emission Control of Motorcycle Engines[J].Small Internal Combustion Engine, 2003.
- [2] Gu Weidong.Research on Air/Fuel Ratio Control of EFI Motorcycle Engine[D].China, Tianjin University, 2006.
- [3] ZHANG Fu-jun, DUAN Xiao-bo, HAN Kai, WANG Yu-ming.Method of Realization for a Motorcycle Engine Having Fuel-Film Model Based Transient Air -Fuel Ratio Control[J].Transactions of Beijing Institute of Technology, 2005, 25(7).
- [4] Li Bi.Study on Simulation of Transient Air-fuel Ratio Control Strategy for Gasoline Engine[D]. Changsha University of Science and Technology, 2010.
- [5] Hendricks E, Sorenson S.C.Mean Value Engine Modeling of Spark Ignition[J]. SAE PaPer900616, 1990.
- [6] Elbert Handicks, Donn Engler, Marco Fam.A Generic Mean for Spark ignition[J].SAE PaPer, 1999.
- [7] Pan Shengjun.Research on the idle speed control of CG125 motorcycle engine[D].Zhejiang University, 2002.
- [8] A Chevalier, M Müller, E Hendricks. On the Validity of Mean Value Engine Models During Transient Operation[J]. Sae Technical Papers, 2000, 34(27):2947–2951.
- [9] P Mattavelli, L Rossetto, G Spiazzo, P Tenti[J].General-purpose fuzzy controller for DC/DC converters[J].Applied Power Electronics Conference & Exposition, 1995, 12(1):79-86
- [10] M Massaro, R Lot, V Cossalter.On Engine-to-Slip Modelling for Motorcycle Traction Control Design.Proceedings of the Institution of Mechanical Engineers Part D Journal of Automobile Engineering, 2011, 225(1):15-27.
- [11] Tu Xinyang. Research on EFI control strategy for single-cylinderengine of motorcyle, Hunan University, 2014.

Wenyu HU\*, Zhao WANG, Xiaosong YANG, Jian J. ZHANG

## An Efficient Bilinear Factorization based Method For Motion Capture Data Refinement

**Abstract:** As a preprocessing step, motion capture (mocap) data refinement is to predict missing data and remove noises and outliers. In recent years, low-rank matrix completion has been successfully applied to mocap data refinement by considering the low-rank property of motion data, wherein a representative approach is called TSMC proposed by Feng et al. However, this approach heavily depends on singular value decomposition (SVD) and requires to calculate the inversion of a smoothing related matrix at each iteration whose size is equal to the frame number of motion sequence. Thus, it is very slow for long motion sequences. In this paper, we aim to present an efficient method, in which the matrix bilinear factorization and the variational definition of matrix nuclear norm are employed to avoid SVD. Besides, after analyzing the eigendecomposition of the smoothing related matrix, we convert matrix inversion into discrete cosine transform (DCT) and inverse DCT. The augmented Lagrange multiplier algorithm is adopted to solve the refinement optimization model. Experimental results show the proposed approach is much more accurate and efficient than TSMC.

**Keywords:** Motion capture data; Matrix factorization; Low rank matrix completion; Augmented Lagrange function

### 1 Introduction

Optical motion capture (mocap) is a prevalent technology used to record the 3d position and orientation information of a moving subject from multiple cameras. Such information has various applications. For example, in the entertainment industry, virtual characters can be animated by using the motion data captured from actors; In sports, athletes can boost their training performance by analyzing the mocap data from their motion [1,2]. However, even with the most expensive commercial mocap systems, e.g. Vicon and Motion Analysis, there still exist instances where noises and missing data are inevitable. To make sure high-quality performance in each application, the corrupted mocap data should be refined. Therefore, it becomes an important research branch of motion processing to handle the following two sub-

---

\*Corresponding author: Wenyu HU, College of Mathematics and Computer Science, Gannan Normal University, Ganzhou, China, E-mail: wenyu.huu@gmail.com

Zhao WANG, Xiaosong YANG, Jian J. ZHANG, National Centre for Computer Animation, Bournemouth University, Poole, United Kingdom

problems: to predict the missing values and to remove both the noises and outliers. These two sub-problems are collectively referred to as mocap data refinement [3].

Mocap data refinement is a challenging problem because human motion consists of highly coordinated movements. During processing, well exploiting the structural relationship among different human joints and the spatio-temporal patterns embedded in human motion would bring better refining results [3-9]. Due to the high articulation and correlation of human motion, when representing a human motion sequence as a matrix, it will be an approximately low-rank matrix. The low-rank property thus was used as a prior, and then the mocap data refinement problem was correspondingly formulated as the low-rank matrix completion in [7]. Based on that work, Feng *et al.* [3] proposed a noise robust and temporal stable matrix completion (TSMC) model which takes the temporal stability and low-rank structure properties of motion data into account, and consequently performs better than the method [7] and three other commonly used methods, i.e. linear interpolation, spline interpolation and Dynammo [5]. While the work [3] is effective, it is slow, especially for long motion sequences, because its implementation is based on singular value thresholding (SVT) [8] which requires the computation of a full or partial SVD at each iteration that becomes increasingly costly as matrix dimensions grow.

This paper addresses the computational efficiency of the TSMC algorithm. Inspired by the bilinear factorization [9], we use the variational definition of nuclear norm that is defined as the average of two squared Frobenius norms, instead of the sum of singular values. Besides, as the dimension of the smoothing related matrix is equal to the frame number of mocap data that is very large for long motion sequences, it's too expensive to directly calculate its inverse matrix at each iteration. We so take into consideration the transposition problem of TSMC and then simplify the inverse calculation of the smooth matrix into the discrete cosine transform (DCT) and inverse DCT (IDCT). Compared to TSMC, the proposed approach is able to not only produce comparable and even better refining results, but also perform much faster (about 7 times faster than TSMC for a motion sequence consisting of about 5000 frames).

The remainder of this paper is organized as follows. Section II briefly reviews the TSMC algorithm. Section III introduces the proposed approach in details. Section IV gives various experimental results. Finally, we conclude this paper in Section V.

## 2 The TSMC algorithm

In this paper, we denote a motion sequence consisting of  $n$  frames as a matrix  $X = [x_1, x_2, \dots, x_n] \in \mathbb{R}^{3J \times n}$ , where  $J$  is the number of all joints in a human skeleton, and  $x_i \in \mathbb{R}^{3J}$  represents a frame. Mocap data are captured as a sequence of frames, but some frames contain missing data and some contains noises and outliers.

Before introducing our approach, we briefly describe the TSMC algorithm in [3]. Assume that the noise is sparse in the observed part, the TSMC refines the corrupted mocap data via the following model:

$$\begin{aligned} \min_{Y,E} \quad & \text{rank}(Y) + \alpha \|\Omega \circ E\|_0 + \frac{\beta}{2} \|YO\|_F^2, \\ \text{s.t.} \quad & X = Y + E, \end{aligned} \tag{1}$$

where  $\Omega \in \{0,1\}^{3J \times n}$  is a mask matrix, namely  $\Omega_{ij} = 1$  for the observable entry and  $\Omega_{ij} = 0$  for the missing entry.  $X$  denotes the corrupted motion data,  $Y$  denotes the clean motion data, and  $E$  denotes the sparse noises and outliers.  $A \circ B$  is the entry-wise product called Hadamard product.  $O \in \mathbb{R}^{n \times n}$  is a tridiagonal, symmetrical square matrix which is to ensure  $C^2$  continuity on every marker's trajectory:

$$O = \begin{bmatrix} -1 & 1 & & & & \\ 1 & -2 & 1 & & & \\ & \ddots & \ddots & \ddots & & \\ & & 1 & -2 & 1 & \\ & & & 1 & -1 & \end{bmatrix}. \tag{2}$$

Unfortunately, Eq. (1) is NP-hard due to the discontinuous and nonconvex nature of the rank function and  $l_0$  norm. Therefore, a widely used strategy is to replace the rank function and  $l_0$  norm with the nuclear norm (the sum of all the singular values of a matrix) and  $l_1$  norm (the sum of the absolute values of all the entries), respectively [12]. More specifically, it yields the following optimization model:

$$\begin{aligned} \min_{Y,E} \quad & \|Y\|_* + \alpha \|\Omega \circ E\|_1 + \frac{\beta}{2} \|YO\|_F^2, \\ \text{s.t.} \quad & X = Y + E. \end{aligned} \tag{3}$$

Then, the augmented Lagrange multipliers (ALM) method [13] was employed to solve (3), which is partitioned into several sub-problems and solves them alternatively. These sub-problems are based on the thresholdings:

$$\begin{cases} US_\tau(\Sigma)V^T = \arg \min_A \tau \|A\|_* + \frac{1}{2} \|A - W\|_F^2, \\ S_\tau(W) = \arg \min_A \tau \|A\|_1 + \frac{1}{2} \|A - W\|_F^2, \end{cases} \tag{4}$$

where  $U\Sigma V^T$  is the singular value decomposition (SVD) of  $W$  and  $S_\tau(w) = \text{sgn}(w) \max(|w| - \tau, 0)$  is the soft shrinkage operator. In summary, the TSMC method is described in Algorithm 1 (for details see [3]).

**Algorithm 1** The TSMC method [3]

---

**Input:**  $X, \Omega, O$ , parameters  $\alpha, \beta, \gamma, \lambda_{\max}$  ;  
**Output:**  $Y$  and  $E$  ;

1: **Initialize:**

$$i = 0, Y_1^{(0)} = Y_2^{(0)} = X / \max(\|X\|_2, \|X\|_\infty) ;$$

$$Y^{(0)} = E^{(0)} = M^{(0)} = 0 ; \lambda_1 > 0, \lambda_2 > 0 ;$$

2: **While not converged do**

$$3: Z_Y \leftarrow \frac{Y_1^{(i)} + Y_2^{(i)} + \lambda_1^{(i)}(X - E^{(i)}) + \lambda_2^{(i)}M^{(i)}}{\lambda_1^{(i)} + \lambda_2^{(i)}} ;$$

4: Compute the SVD of  $Z_Y$ , i.e.  $Z_Y := U \Sigma V^T$  ;

$$5: Y^{(i+1)} \leftarrow US_{1/\lambda_1^{(i)} + \lambda_2^{(i)}}(\Sigma)V^T ;$$

$$6: Z_e \leftarrow \frac{1}{\lambda_1^{(i)}}Y_1^{(i)} + X - Y^{(i+1)} ;$$

$$7: E^{(i+1)} \leftarrow \Omega \circ S_{1/\lambda_1^{(i)}}(Z_e) + (1 - \Omega) \circ Z_e ;$$

$$8: M^{(i+1)} \leftarrow (\lambda_2^{(i)}Y^{(i+1)} - Y_2^{(i)})\left(\lambda_2^{(i)}I + \beta O^2\right)^{-1} ;$$

$$9: Y_1^{(i+1)} \leftarrow Y_1^{(i)} + \lambda_1^{(i)}(X - Y^{(i+1)} - E^{(i+1)}) ;$$

$$10: Y_2^{(i+1)} \leftarrow Y_2^{(i)} + \lambda_2^{(i)}(M^{(i+1)} - Y^{(i+1)}) ;$$

$$11: \lambda_1^{(i+1)} \leftarrow \min(\gamma\lambda_1^{(i)}, \lambda_{\max}), \lambda_2^{(i+1)} \leftarrow \min(\gamma\lambda_2^{(i)}, \lambda_{\max}) ,$$

12:  $i \leftarrow i + 1$  ;

13: **end while.**

---

### 3 The proposed scheme

As shown in Algorithm 1, Step 4 requires computing the SVD of a matrix of size  $3J \times n$ . It is evident that computing a full SVD at every iteration is too costly to be practical for solving truly large-scale problems [14-15]. Even for the partial SVD strategy which only computes a proper subset of dominant singular pairs (values and vectors) instead of the full set, its computation cost can still be quite high on a wide range of large matrices. Meanwhile, Step 8 requires calculating the inverse of a matrix of size  $n \times n$ . It's still too expensive to calculate it when  $n$  is large. Therefore, it's desirable to exploit an alternative approach that avoids SVD computation and inversion calculation, by replacing them with some less expensive ones. The target of this paper is to investigate such a non-SVD approach meanwhile without calculating

the inversion of any big matrix in order to more efficiently solve the mocap data refinement problem.

### 3.1 Bilinear factorization model

For a low-rank matrix  $A \in \mathbb{R}^{n \times m}$ , bilinear factorization aims to find two smaller low-rank matrices  $U \in \mathbb{R}^{n \times d}$  and  $V \in \mathbb{R}^{m \times d}$  such that  $A = UV^T$ , where  $d$  is an upper bound on the rank of  $A$ , i.e.  $d \geq r = \text{rank}(A)$ . First, to avoid computing SVD like Step 4 in Algorithm 1, we adopt the variational definition of nuclear norm, that is

$$\|A\|_* = \min_{A=UV^T} \frac{1}{2} (\|U\|_F^2 + \|V\|_F^2), \quad (5)$$

where  $\|\cdot\|_F$  stands for the Frobenius norm of a matrix. Second, to avoid calculating the matrix inversion like Step 8 in Algorithm 1, we study the transposition version of (3), i.e.

$$\begin{aligned} \min_{Y, E} \quad & \|Y^T\|_* + \alpha \|\Omega^T \circ E^T\|_1 + \frac{\beta}{2} \|OY^T\|_F^2, \\ \text{s.t. } & X^T = Y^T + E^T \end{aligned} \quad (6)$$

Note that the following norm properties are used in (6):

$$B_* = \|B^T\|_* \text{ and } \|B\|_1 = \|B^T\|_1.$$

Emerging (5) into (6) finally yields

$$\begin{aligned} \min_{U, V, E} \quad & \frac{1}{2} (\|U\|_F^2 + \|V\|_F^2) + \alpha \|\Omega^T \circ E\|_1 + \frac{\beta}{2} \|OUV\|_F^2, \\ \text{s.t. } & X^T = UV + E \end{aligned} \quad (7)$$

where  $U \in \mathbb{R}^{n \times d}$ ,  $V \in \mathbb{R}^{3J \times d}$  and  $E \in \mathbb{R}^{n \times 3J}$ .

### 3.2 Optimizaiton

To solve (7), we present an inexact augmented Lagrange multiplier method, called IALM [13]. We first consider an equivalent form of (7):

$$\begin{aligned} \min_{U, V, E, M} \quad & \frac{1}{2} (\|U\|_F^2 + \|V\|_F^2) + \alpha \|\Omega^T \circ E\|_1 + \frac{\beta}{2} \|OM\|_F^2, \\ \text{s.t. } & M = UV, \\ & X^T = UV + E. \end{aligned} \quad (8)$$

Then, the augmented Lagrangian function of (8) is:

$$\begin{aligned} L(U, V, E, M, Y_1, Y_2) = & \frac{1}{2} (\|U\|_F^2 + \|V\|_F^2) + \alpha \|\Omega^T \circ E\|_1 \\ & + \frac{\beta}{2} \|OM\|_F^2 + \langle Y_1, M - UV \rangle + \frac{\lambda_1}{2} \|M - UV\|_F^2 \\ & + \langle Y_2, X^T - UV - E \rangle + \frac{\lambda_2}{2} \|X^T - UV - E\|_F^2, \end{aligned} \quad (9)$$

where  $Y_1, Y_2 \in \mathbb{C}^{n \times 3J}$  are Lagrangian multipliers,  $\lambda_1, \lambda_2$  are penalty parameters. According to IALM, we solve (9) by minimizing each variable alternatively while fixing the other variables, so that the optimization problem can be divided into four sub-problems and two multipliers updating:

$$\begin{aligned} U^{(k+1)} &= \underset{U \in \mathbb{C}^{n \times d}}{\operatorname{argmin}} L(U, V^{(k)}, E^{(k)}, M^{(k)}, Y_1^{(k)}, Y_2^{(k)}), \\ V^{(k+1)} &= \underset{V \in \mathbb{C}^{3J \times d}}{\operatorname{argmin}} L(U^{(k+1)}, V, E^{(k)}, M^{(k)}, Y_1^{(k)}, Y_2^{(k)}) \\ E^{(k+1)} &= \underset{E \in \mathbb{C}^{n \times 3J}}{\operatorname{argmin}} L(U^{(k+1)}, V^{(k+1)}, E, M^{(k)}, Y_1^{(k)}, Y_2^{(k)}) \\ M^{(k+1)} &= \underset{M \in \mathbb{C}^{n \times 3J}}{\operatorname{argmin}} L(U^{(k+1)}, V^{(k+1)}, E^{(k+1)}, M, Y_1^{(k)}, Y_2^{(k)}), \\ Y_1^{(k+1)} &= Y_1^{(k)} + \lambda_1 \left( M^{(k+1)} - U^{(k+1)} V^{(k+1)} \right), \\ Y_2^{(k+1)} &= Y_2^{(k)} + \lambda_2 \left( X^T - U^{(k+1)} V^{(k+1)} - E^{(k+1)} \right). \end{aligned}$$

More specially, to solve the variable  $U$ , we fix the other variables and solve the following least-square problem:

$$\begin{aligned} U^{(k+1)} &= \underset{U}{\operatorname{argmin}} \frac{1}{2} \|U\|_F^2 + \frac{\lambda_1}{2} \left\| M^{(k)} - U \left( V^{(k)} \right)^T + \frac{Y_1^{(k)}}{\lambda_1} \right\|_F^2 \\ &\quad + \frac{\lambda_2}{2} \left\| X^T - U \left( V^{(k)} \right)^T - E^{(k)} + \frac{Y_2^{(k)}}{\lambda_2} \right\|_F^2 \\ &= Z_u V^{(k)} \left[ I_d + (\lambda_1 + \lambda_2) \left( V^{(k)} \right)^T V^{(k)} \right]^{-1}, \end{aligned} \tag{10}$$

where  $Z_u := Y_1^{(k)} + Y_2^{(k)} + \lambda_1 M^{(k)} + \lambda_2 \left( X^T - E^{(k)} \right)$ .

Similarly, we update the variable  $V$  as follows:

$$V^{(k+1)} = Z_u^T U^{(k+1)} \left[ I_d + (\lambda_1 + \lambda_2) \left( U^{(k+1)} \right)^T U^{(k+1)} \right]^{-1} \tag{11}$$

For fixed  $U, V, M$ , we get the following optimization problem for finding  $E$ :

$$\begin{aligned} E^{(k+1)} &= \underset{E}{\operatorname{argmin}} \alpha \left\| \Omega^T \circ E \right\|_1 + \frac{\lambda_2}{2} \left\| X^T - U^{(k+1)} \left( V^{(k+1)} \right)^T - E + \frac{Y_2^{(k)}}{\lambda_2} \right\|_F^2 \\ &= \Omega^T \circ S_{\frac{\alpha}{\lambda_2}} (Z_e) + (1 - \Omega^T) \circ (Z_e), \end{aligned} \tag{12}$$

where  $Z_e := X^T - U^{(k+1)} \left( V^{(k+1)} \right)^T + Y_2^{(k)} / \lambda_2$ .

Finally, we update  $M$  as follows:

$$\begin{aligned} M^{(k+1)} &= \arg \min_M \frac{\beta}{2} \|OM\|_F^2 + \frac{\lambda_1}{2} \left\| M - U^{(k+1)} \left( V^{(k+1)} \right)^T + \frac{Y_1^{(k)}}{\lambda_1} \right\|_F^2 \\ &= (\lambda_1 I_n + \beta O^2)^{-1} \left( \lambda_1 U^{(k+1)} \left( V^{(k+1)} \right)^T - Y_1^{(k)} \right). \end{aligned} \quad (13)$$

Note that in (13), we require to calculate the inversion of matrix  $\lambda_1 I_n + \beta O^2$  whose size is  $n \times n$ . When we process a long motion sequence which means  $n$  is very large, it thus might be too expensive to carry out the inverse operation. Fortunately, we can transform such an inversion calculation into DCT and IDCT by analyzing the eigen-decomposition of  $O$  which is defined as (2). As discussed in [16], an eigendecomposition of  $O$  yields  $O = W \Lambda W^{-1}$ , where  $\Lambda$  is the diagonal matrix containing its eigenvalues defined by  $\Lambda = \text{diag}(t_1, \dots, t_n)$ ,  $t_i = -2 + 2 \cos((i-1)\pi/n)$  and  $W$  is a unitary matrix (i.e.  $W^T = W^{-1}$ ) containing the eigenvectors. Also it is worth noting that  $W^T$  and  $W$  are actually the n-by-n type-2 DCT and IDCT matrices. Therefore, we have

$$\begin{aligned} (\lambda_1 I_n + \beta O^2)^{-1} &= W \left( \text{diag} \left( \frac{1}{\lambda_1 + \beta t_1^2}, \dots, \frac{1}{\lambda_1 + \beta t_n^2} \right) \right) W^T \\ &= \text{IDCT} \left[ \left( \text{diag} \left( \frac{1}{\lambda_1 + \beta t_1^2}, \dots, \frac{1}{\lambda_1 + \beta t_n^2} \right) \right) \text{DCT} \right]. \end{aligned} \quad (14)$$

### 3.3 Rank estimation

Since a proper estimation to the rank of mocap data is essential for the bilinear factorization in (5), we make use of the concept of last significant jump (LSJ) rule proposed in [17-18] to adaptively estimate the rank. Indeed, the basic principle of LSJ is to detect the support of a sparse vector consisting of eigenvalues whose cardinality is the rank of a low-rank matrix.

Due to that the given mocap data  $X$  is incomplete, we first given an initial guess for the missing markers by apply linear interpolation method and thus obtain  $\tilde{X}$ . Next, we apply the LSJ rule based on thresholding to estimate the rank of  $\tilde{X}$ . In details, let  $\Lambda = (\lambda_1, \lambda_2, \dots, \lambda_k)$ , with  $k = \min(3J, n)$  be the singular values of  $\tilde{X}$  satisfying  $\lambda_1 \geq \lambda_2 \geq \dots \geq \lambda_k \geq 0$ .

The LSJ rule is to look for the largest index  $k_0$  such that  $|\lambda_{k_0} - \lambda_{k_0+1}| > \varepsilon$ , and then define  $r = \text{rank}(Y) \approx k_0$ , where  $\varepsilon$  is a threshold value (in this paper  $\varepsilon = 0.1$ ). Finally, considering that  $X$  also contains noises and outliers, the rank estimated above may be a little conservative, and thus we specify the parameter  $d$  satisfying  $d \geq r$  as

$$d = \min(\lfloor 1.1 \times r \rfloor, 3J, n). \quad (15)$$

### 3.4 Algorithm

Based on the previous analysis, we can derive a bilinear factorization based method for refining mocap data which is summarized in Algorithm 2.

We remark that the main complexity of Steps 3 and 4 in Algorithm 2 is  $O((n+d)(3J+d)d)$ , where  $d$  by (15) is very small ( $d \leq \min(3J, n)$ ), while the complexity of Step 4 in Algorithm 1 is  $O(3Jn^2)$ . It is also much faster to take (14) to compute  $(\lambda_1 I_n + \beta O^2)^{-1}$ , because the DCT merely has a complexity of  $O(n \log(n))$ , whereas directly computing the inversion has a complexity of  $O(n^3)$ . Therefore, as the other steps are similar, Algorithm 2 has much less complexity than Algorithm 1.

---

#### Algorithm 2 Algorithm for the proposed method

---

**Input:**  $X, \Omega, O$ , parameters  $\alpha, \beta, \gamma, \varepsilon, \lambda_{\max}$ ;

**Output:**  $Y$  and  $E$ ;

**1: Initialize:**

Estimate the rank  $r$  and compute  $d$ ;

$$k = 0, Y_1^{(0)} = Y_2^{(0)} = X^T / \max(\|X^T\|_2, \|X^T\|_\infty);$$

$$V^{(0)} = \text{randn}(3J, d), V^{(0)} = V^{(0)} / \|V^{(0)}\|_F;$$

$$E^{(0)} = M^{(0)} = 0; \lambda_1 > 0, \lambda_2 > 0;$$

**2: While not converged do**

3: Update  $U^{(k+1)}$  using (10);

4: Update  $V^{(k+1)}$  using (11);

5: Update  $E^{(k+1)}$  using (12);

6: Update  $M^{(k+1)}$ :

$$M^{(k+1)} = IDCT \left[ \left[ \text{diag} \left( \frac{1}{\lambda_1 + \beta t_1^2}, \dots, \frac{1}{\lambda_1 + \beta t_n^2} \right) \right] DCT \left( \lambda_1 U^{(k+1)} (V^{(k+1)})^T - Y_1^{(k)} \right) \right];$$

7: Update the multipliers:

$$Y_1^{(k+1)} \leftarrow Y_1^{(k)} + \lambda_1 \left( X - U^{(k+1)} (V^{(k+1)})^T - E^{(k+1)} \right);$$

$$Y_2^{(k+1)} \leftarrow Y_2^{(k)} + \lambda_2 \left( M^{(k+1)} - U^{(k+1)} (V^{(k+1)})^T \right);$$

8: Update the penalty parameters:

$$\lambda_1 \leftarrow \min(\gamma \lambda_1, \lambda_{\max}), \lambda_2 \leftarrow \min(\gamma \lambda_2, \lambda_{\max});$$

9:  $k \leftarrow k + 1$ ;

10: **end while**

$$11: Y \leftarrow V^{(k)} (U^{(k)})^T, E \leftarrow (E^{(k)})^T.$$


---

## 4 Experimental results

In this section, we compare the proposed method only with TSMC, since TSMC performs more effectively than many existing approaches, such as linear interpolation, spline interpolation, Dynammo and SVT. To evaluate the performance, we selected six motion sequences (walk, gymnastics, dance, acrobatics, basketball and boxing) from the CMU mocap dataset (<http://mocap.cs.cmu.edu/>), where the number of joints in a human skeleton is  $J = 31$ . Like the work [3], we simulate four classical situations to synthesize four different kinds of corrupted data, which are briefly listed as follows: Randomly corrupt data (rdrupt), Randomly lose data (rdlose), Mixed corrupt data (mxrupt) and Regularly lose data (rglose). All the experiments were implemented in Matlab (version R2010a) on an Intel Core i5-4210U CPU@1.70GHz PC with 4GB memory.

The parameters in our method were set as follows for all experiments:  $\alpha = 1.0$ ,  $\beta = 100$ ,  $\lambda_1 = \lambda_2 = 10^{-5}$ ,  $\gamma = 1.4$ , and  $\lambda_{\max} = 10^{10}$ . To verify the refining accuracy, we adopt the root mean squared error (RMSE) measurement:

$$RMSE(x_i, \tilde{x}_i) = \sqrt{\frac{1}{n_p} \|x_i - \tilde{x}_i\|^2},$$

where  $x_i$  and  $\tilde{x}_i$  correspond to the imperfect and refined poses, respectively, and  $n_p$  is the total number of imperfect entries, i.e. the missing and noise entries.

For the four cases (rdrupt, rdlose, mxrupt and rglose), the RMSEs of TSMC (in red color) and the proposed method (in blue color) were shown in Figure 1 to 4, where we can easily see that our approach outperforms TSMC for most of the refined results in each case. The reason lies in that our approach exploits the true low-rank property of mocap data by using bilinear factorization, while TSMC depends on partial SVD (pSVD) to solve model (3) which causes the information corresponding to the singular values under the pSVD specified threshold dropped. Besides, Table 1 lists the elapsed cpu time, in which we can find the elapsed time by our method is significantly reduced. As the frame number increases, the time gap between TSMC and our method grows rapidly. For example, our method is about 1 second faster than TSMC for “Walk” whose frame number is 343, but our method becomes about 7 times faster than TSMC for “Boxing” and “Basketball” whose frame numbers are around 5000. These statistical data demonstrate that the proposed bilinear factorization and DCT-based inverse matrix calculation indeed accelerate our method.

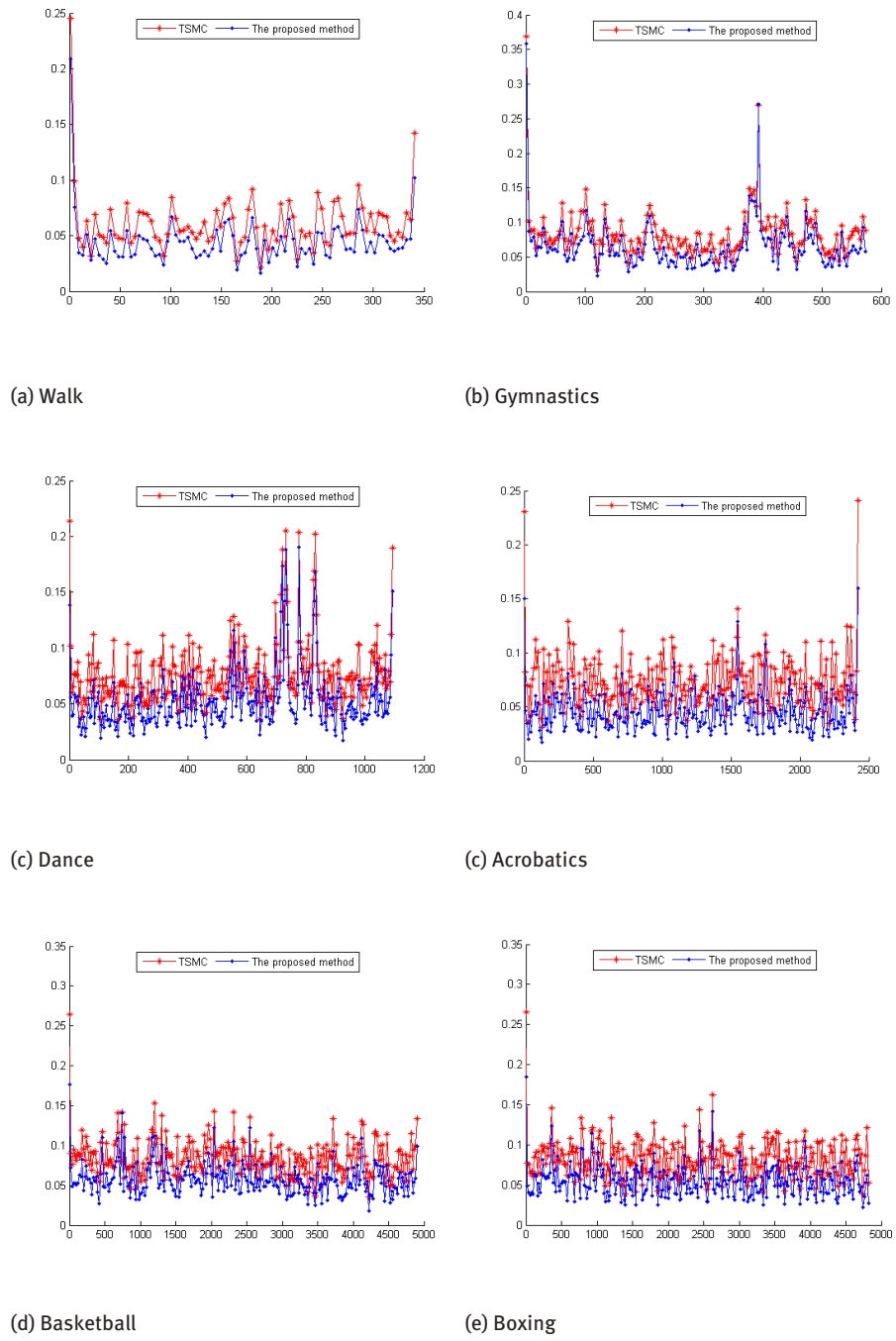


**Figure 1.** Comparisons of refined results for the case of randomly corrupt data (rdcrupt): Gaussian noises ( $\sigma = 2$ ) were randomly added on 30% data for each motion sequences, wherein x-label denotes the frame index and y-label the RMSE of each frame (cm/frame).

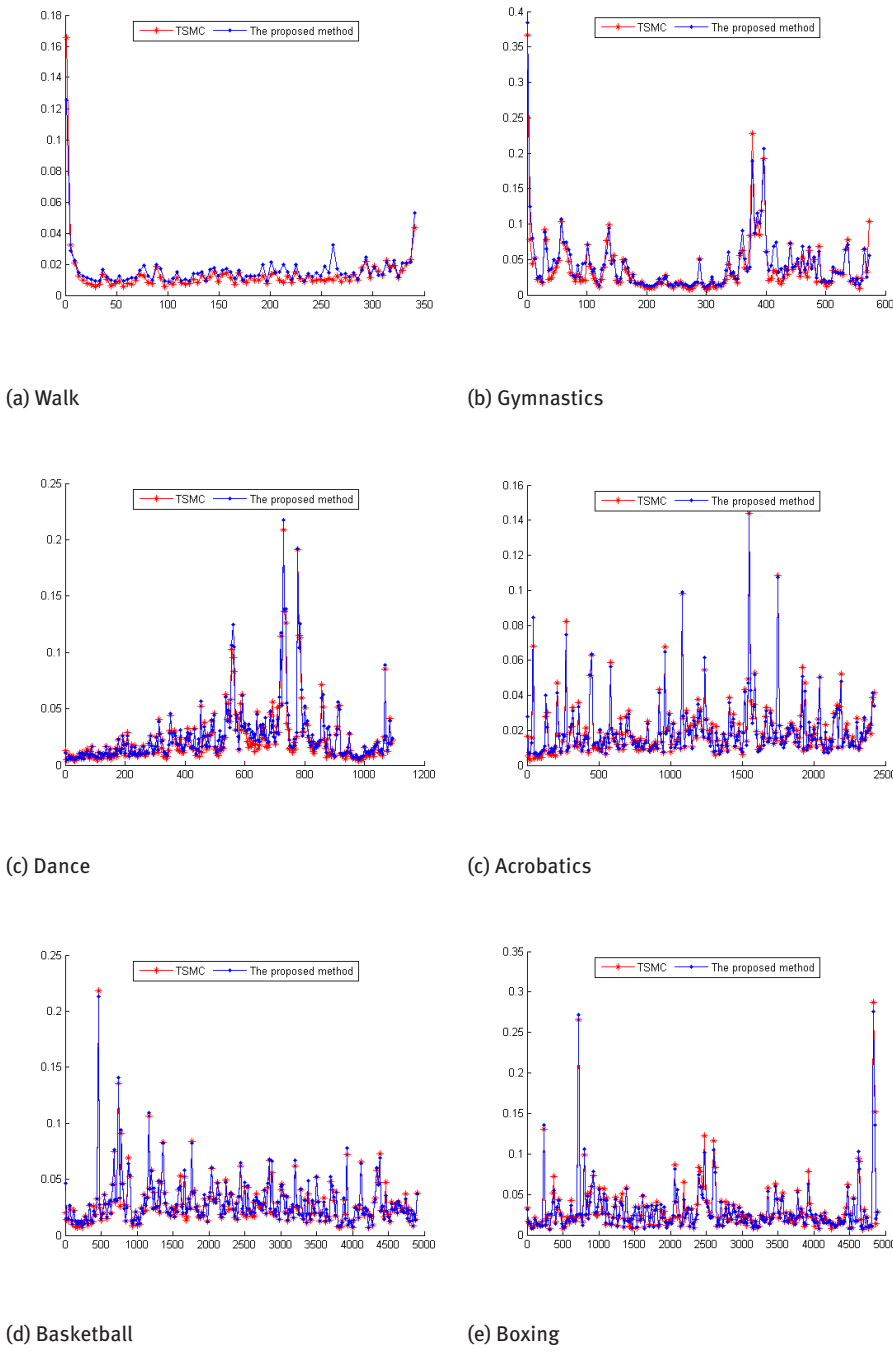


**Figure 2.** Comparisons of refined results for the case of randomly lose data (rdloss): 40% data of each motion sequence were randomly missing, wherein x-label denotes the frame index and y-label the RMSE of each frame (cm/frame).

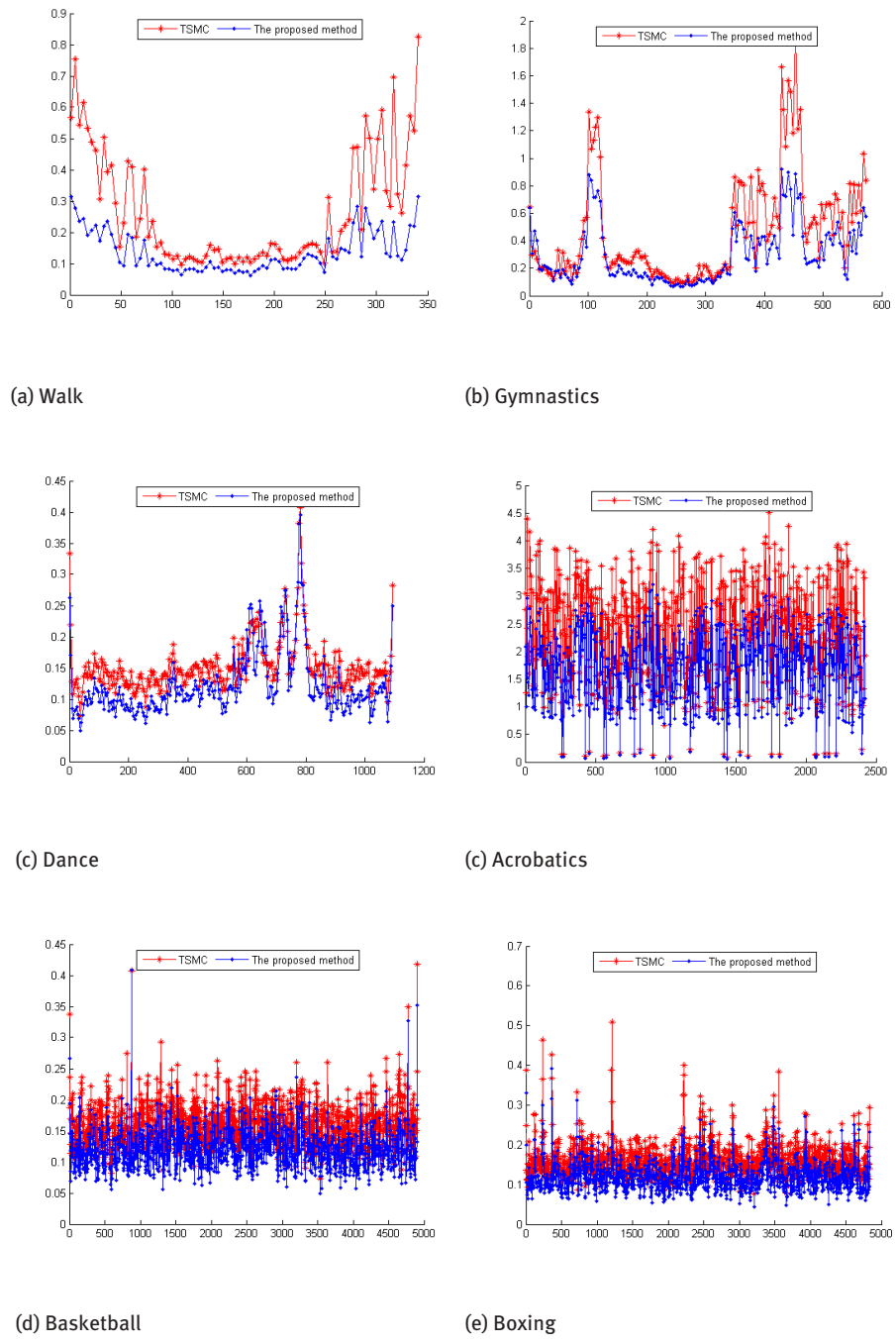


**Figure 3.** Comparisons of refined results for the case of mixed corrupt data (mxcrupt): 30% data were randomly missing and then 30% of the remaining data were corrupted by Gaussian noise ( $\sigma = 2$ ), wherein x-label denotes the frame index and y-label the RMSE of each frame (cm/frame).

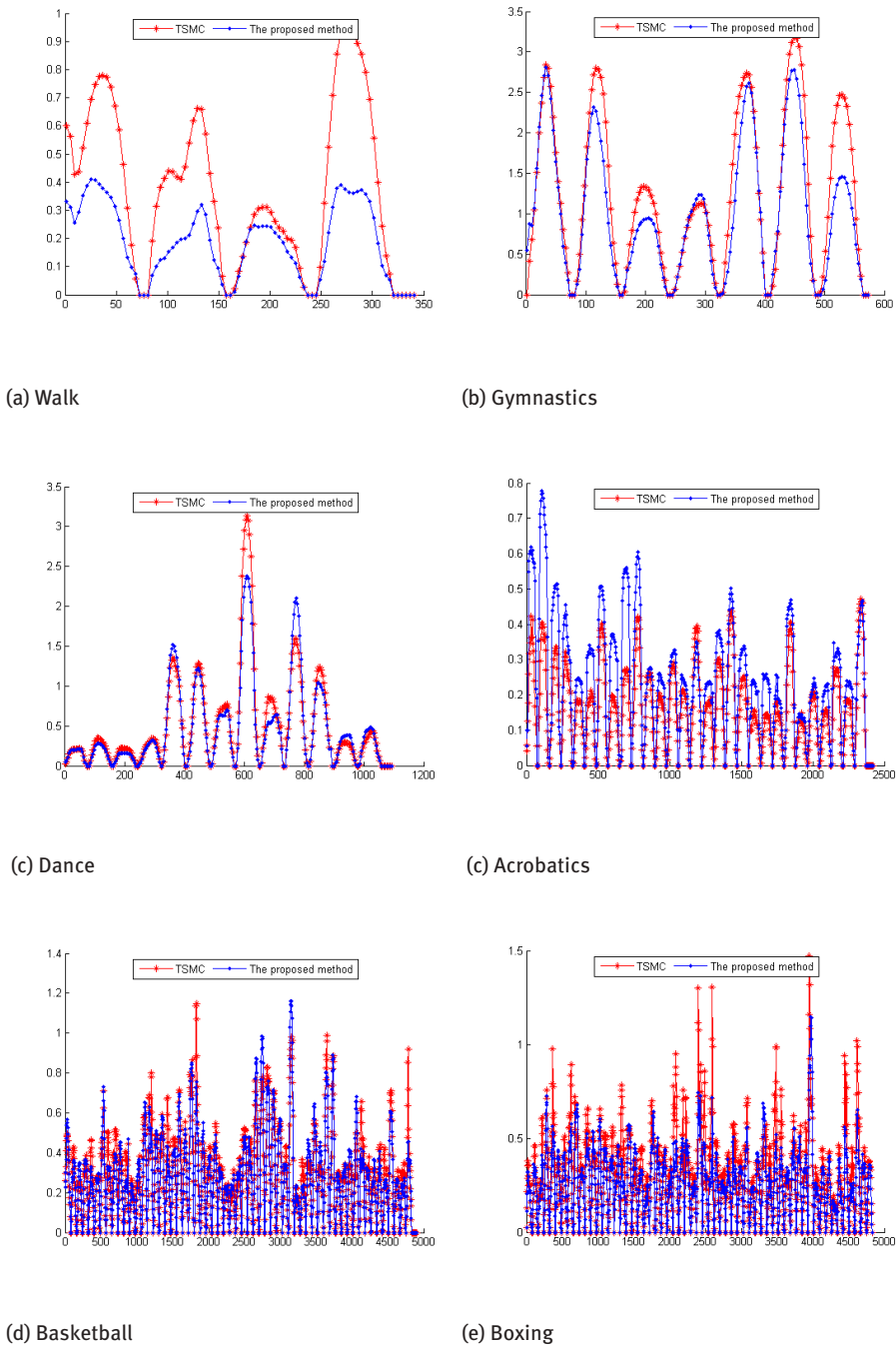


**Figure 4.** Comparisons of refined results for the case of regularly lose data (rgloss): 30% data were randomly removed wherein the number of selected missing markers is fixed to be 10 and each missed 60 frames, wherein x-label denotes the frame index and y-label the RMSE of each frame (cm/frame).

**Table 1.** The elasped Cpu time comparison between TSMC and the proposed method (in second), where the number in the parentheses is frame number.

Sequences		rdcrupt	rdclose	mxcrupt	rgclose
Walk (343)	TSMC	4.5327	4.5778	4.1895	4.2034
	Ours	3.6799	3.2344	3.4169	3.1651
Gymnastics (575)	TSMC	8.4847	8.5558	8.3841	8.3981
	Ours	6.6387	5.9020	6.4214	5.9558
Dance (1095)	TSMC	39.7993	40.7735	40.5113	40.7787
	Ours	13.8910	13.7368	14.3889	12.9879
Acrobatics (2422)	TSMC	184.4452	208.5139	207.9337	184.2060
	Ours	31.975	33.665	35.7294	32.0166
Boxing (4840)	TSMC	502.1291	500.2536	487.2015	466.1518
	Ours	56.611	70.3079	58.9476	55.0996
Basketball (4905)	TSMC	585.8815	589.1388	622.4648	571.7665
	Ours	84.2322	86.1375	92.7852	80.0888

## 5 Conclusion

In this paper, we have presented an efficient mocap data refinement method based on the matrix bilinear factorization and (inverse) discrete cosine transform. Experimental results show the proposed method outperforms TSMC and also performs more and more fast as the frame number of motion sequence grows. However, from the results in Figure 4, we find both of the methods have a sharp decline in performance for the case of regularly and continuous lose data, which needs to be explored further.

**Acknowledgment:** This work was supported by funding from the National Science Foundation of China (61502107, 11361005), the Sino-UK Higher Education Research Partnership for Ph.D. Studies project, the National Science Foundation of Jiangxi Province (20151BAB211014, 20161BAB202069), research programme of Gannan Normal University (14zb21), Science and technology programme of Jiangxi Education Committee (LDJH12088), Santander PGR, the “Qinggu” project of China Scholarship Council (CSC) and Development for Local Colleges and Universities Foundation of China-Applied Mathematics Innovative Team Building.

## References

- [1] J. Hou, L. Chau, Y. He and N. Magnenat-Thalmann, Low rank based compact representation of motion capture data, Proc. IEEE International Conference on Image Processing (ICIP), IEEE, 2014, pp. 1480-1484.
- [2] H. Yang, J. Zhang, Y. Ji, Y. He, and Y. Lee, Experimental demonstration of multi-dimensional resources integration for service provisioning in cloud radio over fiber network, Scientific Reports, vol. 6, 30678, Jul. 2016.
- [3] Y. Feng, J. Xiao, Y. Zhuang, X. Yang, J.J. Zhang and R. Song, Exploiting temporal stability and low-rank structure for motion capture data refinement, Inform. Sci. 2014, 227(2): 777-793.
- [4] H. Lou and J. Cai, Example-based human motion denoising, IEEE Trans. Visual. Comput. Graph. 2010, 16(5): 870-879.
- [5] L. Li, J. McCann, N. Pollard and C. Faloutsos, Dynammo: mining and summarization of coevolving sequences with missing values, Proc. 15th ACM SIGKDD International Conference on Knowledge Discovery and Data Mining, ACM, 2009, pp. 507-516.
- [6] Y. Feng, M. Ji, J.Xiao, X. Yang, J.J. Zhang, Y.Zhuang and X. Li, Mining spatial-temporal patterns and structural sparsity for human motion data denoising, IEEE Trans. Cybern. 2015, 45(12): 2693-2706.
- [7] R. Lai, P. Yuen and K. Lee, Motion capture data completion and denoising by singular value thresholding, Proc. Eurographics, Eurographics Association, 2011, pp. 45-48.
- [8] C. Tan, J. Hou and L. Chau, Human motion capture data recovery using trajectory-based matrix completion, Electron. Lett. 2013, 49(12): 752-754.
- [9] X. Liu, Y. Cheung, S. Peng, Z. Cui, B. Zhong and J. Du, Automatic motion capture data denoising via filtered subspace clustering and low rank matrix approximation, Signal Process. 2014, 105: 350-362.
- [10] J. Cai, E. Candes and Z. Shen, A singular value thresholding algorithm for matrix completion, SIAM J. Optim. 2010, 20(4), 1956-1982.
- [11] R. Cabral, F. De la Torre, J. Costeira and A. Bernardino, Unifying nuclear norm and bilinear factorization approaches for low-rank matrix decompositon, Proc. IEEE International Conference on Computer Vision (ICCV), 2013, pp. 2488-2495.
- [12] J. Wright, A. Ganesh, S. Rao, Y. Peng and Y. Ma, Robust principal component analysis: Exact recovery of corrupted low-rank matrices via convex optimizaiton, In Advances in Neural Information Processing Systems (NIPS), 2009.
- [13] Z. Lin, M. Chen and L. Wu, The augmented lagrange multiplier method for exact recovery of corrupted low-rank matrices, Technical Report UILU-ENG-09-2215, Univ. Illinois. Urbana-Champaign, 2009.
- [14] H. Yang, J. Zhang, Y. Zhao, Y. Ji, J. Han, Y. Lin, and Y. Lee, CSO: Cross Stratum Optimization for Optical as a Service, IEEE Communications Magazine, 2015, 53(8): 130-139.
- [15] Z. Wen, W. Yin and Y. Zhang, Solving a low-rank factorization model for matrix completion by a nonlinear successive over-relaxation algorithm, Math. Prog. Comp. 2012, 4: 333-361.
- [16] G. Damien, Robust smoothing of gridded data in one and higher dimensions with missing values, Comput. Stat. Data Anal. 2010, 54: 1167-1178.
- [17] Y. Wang and W. Yin, Sparse signal reconstruction via iterative support detection, SIAM J. Imaging Sciences 2010, 3(3): 462-491.
- [18] Y. Wang and X. Su, Truncated nuclear norm minimizaiton for image restoration based on iterative support dection, Math. Probl. Eng. 2014, 1-17.

Zheng RAN\*, Hua YAN, Yun LI

## Reliability Evaluation of Embedded Real-time System based on Error Scenario

**Abstract:** The embedded electronic devices may run in an uncertain environment. The electromagnetic interference, voltage fluctuation and high or low temperature may easily generate intermittent or permanent failures in the semiconductor devices, which can potentially result in running errors in real-time system. In order to cope with such a situation, real-time systems generally have the fault-tolerant mechanism. Although the existing fault-tolerant mechanism can tolerate some kinds of errors, it has limitations. It cannot deal with some fatal errors or situations with huge number of errors. In this paper, under the assumption that the reach of fault is Poisson process approximately, a fault-tolerant model for embedded system is proposed. With the analysis of the fault-tolerant scheduling, the breadth-first traversal methods are used to build the error scenarios of real-time system. In addition, a key novel algorithm is designed to calculating of the system reliability. The experimental results show the feasibility of proposed evaluation method.

**Keywords:** embedded; real-time system; fault-tolerant scheduling; reliability evaluation

### 1 Introduction

Nowadays, embedded software running in safety-critical system, such as avionics mission computing and automotive vehicle controls, is mainly used to collect information from external stimuli and respond timely under various interference environments. To meet the requirements on its critical properties, especially reliability, it is necessary to evaluate the ability of fault-tolerance for real-time system precisely, otherwise missing time requirements may lead to system failures, and that may result in catastrophic consequences. Reliability [1] is the ability of a system or component to perform its required functions under stated conditions for a specified period of time. For example, IEC61508 [2] proposed a set of risk evaluating method.

Reliability analysis has been a hot research topic since the early 1960s. However, most of the methods were applied in software implementation phase. Evaluating the reliability in the early system design phase is a faster formal method. It builds up the

---

\*Corresponding author:Zheng RAN, School of Computer Science and Engineering, University of Electronic Science and Technology of China, Sichuan, China, E-mail: ranzheng517@sina.com

Hua YAN, Yun LI, School of Computer Science and Engineering, University of Electronic Science and Technology of China, Sichuan, China

probabilistic model of real-time system and analyzes the temporal property based on schedulability analysis. It identifies potential security threats in early time, so that less costly changes are made in system design phase. A lot of existing literatures mainly considered the relationship between task priority and worst-case response time under fault-tolerant condition. However, those approaches often led to pessimistic results.

In this paper, we present an approach to evaluate the reliability of embedded real-time system under fault-tolerant condition. This approach analyzes the schedulability of preemptive task set and traverses the error scenario to compute the reliability accurately by the method of reduction.

The rest of this paper is organized as follows. Section II introduces the probabilistic fault-tolerant model of task and formulates the problem about reliability evaluating. Section III describes the method of reliability analysis approach in detail. Then, the experiments and evaluation are given in Section IV. Section V gives an overview of related work. Finally, we conclude our work in Section VI.

## 2 Related work

With the growing requirements of safety in embedded software, a lot of research emerged in the area of fault-tolerance and reliability evaluation. The traditional approach mainly relies on the testing failure data to predict the future failure behaviors of software. The method based on statistics, such as Monte-Carlo simulation [3] was used to deal with the transient faults depended on simulation experiment with large number of samples.

Due to lots time computation in statistics-based approach, formal analysis of fault-tolerance scheduling and reliability analysis has been addressed by some previous research activities. The Framework for Software Fault Tolerance in Real-Time Systems [4] and the method of check-point and time redundancy [5] give the basic software reliability prediction models. A. Burns et al. [6] introduced a probabilistic model in schedulability analysis within probabilistic guarantee that all tasks always complete by their deadlines. I. Broster et al. [7] extended this method in CAN network to compute accurate predictions of failure probability by probability distribution of response times. However, those approaches [6,7] have certain limitations and lead to extremely pessimistic results.

Safety-critical applications have to function correctly and meet their timing constraints even in the presence of faults. G. Lima et al. [8] proposed worst-case response time schedulability analysis for fault-tolerant hard real-time systems in considering the recovery of tasks running with higher priorities, and then, introduced a priority assignment algorithm [9] to improve system fault resilience. They discussed the relationship between the processor utilization and fault tolerance performance. Li Jun et al. [10] propose a new fault-tolerant priority assignment algorithm based on worst-case response time schedulability analysis for fault-tolerant hard real-time tasks

with limited priority levels [11] and arbitrary large deadlines [12]. Zhaojun Wu et al. [13] discussed the worst-case response time for tasks under the group-based preemptive scheduling and verified the temporal property in the early system design step. However, those methods mainly focused on the relationship between schedulability and priority assignment of tasks, and no probabilistic model to evaluate reliability of system was included into consideration.

M. Sebastian et.al introduced a reliability estimation method [14] that computed reliability of system during a period of time. Comparing with the statistical fault simulation, the method of numerical analysis was fast and accurate, but it was used in CAN network with non-preemptive scheduling strategy. S. Gui et al. [15] presented a reliability model to analyze the schedulability with faults occurring and compute the probability of tasks still being schedulable in the worst-case execution scenario, but the factor of time in reliability was not taken into consideration. V. Izosimov [16] and Petru Eles et al. [17] proposed several optimization algorithms for mapping real-time safety-critical applications on distributed embedded systems by processing re-execution and replication for tolerating transient faults.

The method of reliability above concentrated on the transient faults, such as temperature variation and electromagnetic interference, and not deal with the permanent faults. Xiao Qin et al. [18] introduced a scheduling algorithm in which non-preemptive tasks with two copies scheduled on different processors can tolerate one processor's permanent failure in a heterogeneous system with fully connected network.

### 3 Task model

Considering the fault-tolerant feature of real-time system, the task can be divided into two parts: primary task and the recovery. When no fault occurs, the primary task is scheduled. However, when the fault has occurred, the primary task is suspended and the recovering process is triggered to deal with the fault and recover the primary task from the fault. The task set is defined as:  $\Gamma = \{\tau_1, \dots, \tau_n\}$   $\tau_i = (C_i, P_i, D_i, C'_i)$  where,  $C_i$  is task execution time,  $P_i$  is the period,  $D_i$  is the deadline and  $C'_i$  is the processing time of recovery. In this paper, we assume that recovering time is equal to task execution time ( $C_i = C'_i$ ) and  $P_i = D_i$ .

#### 3.1 Error model

In embedded system, the external interference may result in hardware faults or software errors. In this paper, we assume that the error (including hardware faults) arrival process follows Poisson process with rate  $\lambda$ . Then, the probability that task executes successfully in one of its period is defined as  $P_s(i)$ .

$$P_S(i) = e^{-\lambda C_i} \quad (1)$$

Similarly, the probability that task  $\tau_i$  fails in one of its period is defined as  $P_F(i)$ .

$$P_F(i) = 1 - e^{-\lambda C_i} \quad (2)$$

If error occurs during the execution of task, the recovering process is triggered to deal with the error. If the recovery is also failed, we say, there is another error occurs, and then the recovering process retries.

According to the formula (1), (2), the probability that task  $\tau_i$  fail  $j$  times and finally has been recovered successfully during one of its period is defined as  $P_i(j)$ .

$$P_i(j) = [P_F(i)]^j \times P_S(i) = (1 - e^{-\lambda C_i})^j \times e^{-\lambda C_i} \quad (3)$$

### 3.2 Metric of the reliability

Although recovery can retry many times, this process needs extra time that may make the task non-schedulable. Hence, when evaluating the reliability of real-time system, the schedulability of task set needs to take into account.

**Definition 1:** if the instance of every task in the task set  $\Gamma$  is finished within its deadline, we called the task set  $\Gamma$  is schedulable.

**Definition 2:** the reliability is the probability that the task set  $\Gamma$  is schedulable in one period of time. The reliability of task set  $\Gamma$  in the period of time  $(0, T)$  is denoted by  $R(T)$ .

**Definition 3:** the hyperperiod [15] of task set  $\Gamma$  is the Least Common Multiple of the period of all the tasks, denoted by  $LCM(\Gamma)$ .

The approach proposed in this paper tries to evaluate the reliability of real-time system in a specific time interval  $(0, T)$ . Generally, the hyperperiod is selected for analysis interval, because  $T$  can be represented as  $N$  times of  $LCM(\Gamma)$  then plus  $t$  ( $0 \leq t \leq LCM(\Gamma)$ ). Hence, the reliability in time interval  $(0, T)$  can be defined as:

$$R(A * LCM(\Gamma) + t) = R(LCM(\Gamma))^A * R(t), 0 \leq t \leq LCM(\Gamma) \quad (4)$$

## 4 Reliability analysis

In this section, we present a new analytical method to evaluate the reliability of real-time system. Firstly, the model of error vector is introduced. Then, fault-tolerant schedulability analysis is made to build up the error scenario. Finally, an algorithm used to compute the probability is designed

#### 4.1 Error vector

Let the total number of tasks is  $n$ . We defined error vector of dimension  $n$ , in which the  $i^{\text{th}}$  element presents the number of errors which may occur on task  $\tau_i$ . Error vector is denoted by  $\omega$ ,  $\omega = (e_1, \dots, e_n)$ . That is to say, there are  $e_i$  errors occurring on task  $\tau_i$ , and then the recovery may retry  $e_i$  times in the execution of task  $\tau_i$ .

#### 4.2 Fault-tolerant schedulability analysis

For the fault-tolerant real-time systems, the tasks need to be finished within its deadline even if fault occurs. If the fault occurs  $e_i$  times in task  $\tau_i$ , and all the task in task set  $\Gamma$  is also schedulable, we say, the task  $\tau_i$  can tolerate  $e_i$  errors. If the task set is  $\Gamma$  schedulable under the error vector  $\omega$ , we say, the task set can tolerate the error vector. The number of errors that task  $\tau_i$  can tolerate, not only depend on the task itself, but also is related to execution of other tasks. Therefore, schedulability analysis should be used to compute how many errors tasks set can tolerate.

In this paper, we assume that the system adopt rate-monotonic scheduling (RMS) strategy [19]. Let the tasks be ordered by their period. The cumulative demand on the processor of tasks  $\tau_1, \dots, \tau_i$  until time  $t$  (when 0 is supposed to be a critical instant) is given by

$$W_i(t) = \sum_{j=1}^i \left( C_j * \left\lceil \frac{t}{P_j} \right\rceil \right) + \sum_{j=1}^i \left( e_j * C'_j * \left\lceil \frac{t}{P_j} \right\rceil \right) \quad (5)$$

We defined the notations.

$$L_i(t) = \frac{W_i(t)}{t}; L_i = \min_{t \in [0, P_i]} L_i(t); L = \max_{1 \leq i \leq n} L_i \quad (6)$$

Task  $\tau_i$  can be scheduled for any task phasings using RMS if and only if  $L_i \leq 1$ . The entire tasks set can be scheduled for all task phasings using RMS if and only if  $L_i \leq 1$  [20]. A sketch of the pseudo code for schedulable judging procedure is given in Algorithm 1. The time complexity of algorithm 1 is  $O(n^2)$ .

---

#### Algorithm 1: SCH( $\omega$ ) - Schedulability analysis

---

Input: error-vector  $\omega = (e_1, \dots, e_n)$ .  
Output: weather the task set  $\Gamma$  is schedulable

```

1      for i ← 1 to n do
2          W ← 0
3          for j ← 1 to i do
4              W ← W + Cj *
5              if W > Pi then
6                  return FALSE
7      return TRUE

```

---

### 4.3 Error scenario

Let the error scenario, denoted by  $\Omega$ , be defined as a set of error vectors under which the task set can be schedulable. If the task set  $\Gamma$  is schedulable under the error vector  $\omega = (e_1, \dots, e_n)$ , we say,  $\omega \in \Omega$ .

Example 1: we build up a task set within two tasks,  $\Gamma = \{\tau_1, \tau_2\}$ ;  $\tau_1 = (P_1=4, C_1=1)$ ;  $\tau_2 = (P_2=10, C_2=2)$ . In Figure 1, the dimension of error vector is two, because of two tasks. The error vector (0, 2) present there might be no error in the task  $\tau_1$  and 2 errors in task  $\tau_2$ .

The white rectangular is error vector under which the task set  $\Gamma$  is schedulable, while under error vector of gray rectangular the task set  $\Gamma$  is non-schedulable. Therefore, the error scenario of task set  $\Gamma$  has six error vectors and under the other vectors the task set is non-schedulable. Hence,  $\Omega = ((0,0), (0,1), (0,2), (1,0), (1,1), (2,0))$ .

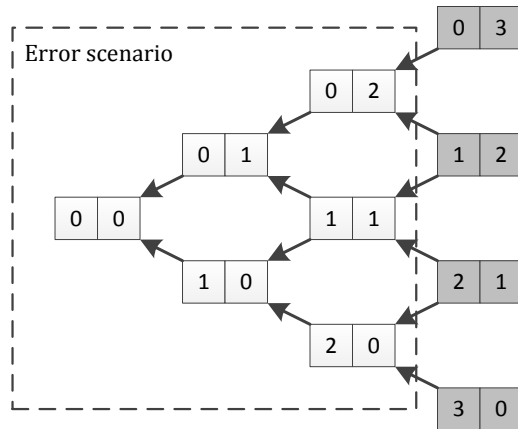


**Figure 1.** Error scenario

In this section, we design an algorithm based on breadth first search to collect all the error vectors under which the task set  $\Gamma$  is schedulable, and then build up the error scenario.

There are some variables used in this algorithm.  $\Psi$  and  $\omega$  is vector of dimension  $n$ . number of  $e_i$  errors in the  $i^{\text{th}}$  task.  $E_i$  is times of recovery retrying in task  $\tau_i$ . The structure of error scenario is like a tree in Figure 1. In this structure,  $Q$  is the queue for save all the error vectors in searching process,  $\pi(\omega)$  is parent node of  $\omega$  and  $b(\omega)$  is the searching breadth of  $\omega$ .  $b(\omega)$  is crucial for reliability computing in next section.

A sketch of the pseudo code is given in Algorithm 2. Combining with the schedulable analysis function  $SCH(\omega)$  in algorithm 1, the total time complexity of algorithm 2 is  $O(|\Omega|^*n^2)$ , where  $|\Omega|$  is total number of error vectors in error scenario.

**Algorithm 2:** ESS - error scenario search

Input: task set  $\Gamma$  and  $E_1, \dots, E_n$ .  
 Output: error-scenario  $Q$ , searching breadth  $b(\omega)$

ESS

```

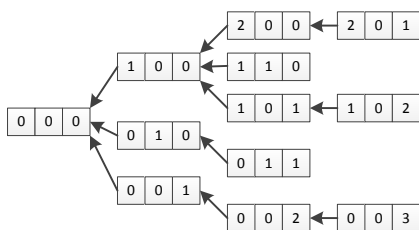
1      allocate  $\Psi$ 
2       $b(\Psi) \leftarrow 0$ 
3      for  $i \leftarrow 0$  to  $n$  do
4           $e_i \leftarrow 0$ 
5           $\Psi \leftarrow (e_1, \dots, e_i, \dots, e_n)$ 
6          ENQUEUE ( $Q, \Psi$ )
7      for  $\omega \in Q$  do
8          ESS-VISIT ( $\omega$ )
ESS -VISIT ( $\Psi$ )
1      for  $i \leftarrow b(\Psi)$  to  $n$  do
2          allocate  $\omega$ 
3           $\omega \leftarrow \Psi$ 
4           $\omega = (e_1, \dots, e_i \leftarrow e_i + 1, \dots, e_n)$ 
5          if SCH( $\omega$ ) = OK then
6               $\pi(\omega) \leftarrow \Psi$ 
7               $b(\Psi) \leftarrow i$ 
8              ENQUEUE ( $Q, \omega$ )
9          else free  $\omega$ 

```

**4.4 Reliability computing**

Before computing the reliability, we must firstly work out how many instances of each task are loaded in one hyperperiod. Let the task executes times in one hyperperiod. That is to say, there are instances of task in one hyperperiod.

Example 2: we build up a task set within three tasks:  $\Gamma = \{\tau_1, \tau_2, \tau_3\}$ ;  $\tau_1 = (P_1=6, C_1=1)$ ;  $\tau_2 = (P_2=10, C_2=2)$ ;  $\tau_3 = (P_3=24, C_3=3)$ . After algorithm 2 ESS, the error scenario has been built up in Figure 2. For the task set  $\Gamma$ , the hyperperiod is 120 ( $LCM(P_1, P_2, P_3)=120$ ), so we focus on the reliability in the time interval (0,120). For task set  $\Gamma$ ,  $x_1=20$ ;  $x_2=12$ ;  $x_3=5$ .

**Figure 2.** Error scenario after ESS

Firstly, we define the probability that there are at most  $e_i$  errors occurring in at least one instance of task  $\tau_i$ .

$$P_{i,x_i}(e_i) = \left( \sum_{j=0}^{e_i} P_i(j) \right)^{x_i} - \left( \sum_{j=0}^{e_i-1} P_i(j) \right)^{x_i} \quad (7)$$

For the tree-like structure of error scenario, the reliability can be computed by the method of dimension reduction. For the task set  $\Gamma$  (in example 2), there are three tasks, so the dimension of error vector is 3. The  $i^{\text{th}}$  element in  $e_i$  error vectors presents the number of error in task  $\tau_i$ .

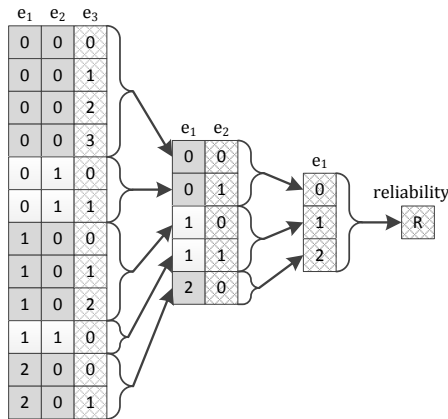


**Figure 3.** Reliability computing in method of reduction

In the process of computing, the error vectors is reduced into the vectors  $\omega(e_1, e_2, e_3)$  of dimension 2,  $\omega(e_1, e_2)$ . This step only focuses on the probability on. The error vectors with the same value in its first two elements are reduced into one vector of dimension 2 on first step. At the same time, the probability of  $e_3$  is calculated. Similarly, on the next step, compute he probability on, and so on. Finally, the reliability in time interval (0,120) is calculated. The process of reduction is shown in Figure 3 and the detailed computing process is shown as follows by formulization.

We compute the reliability by dimension reduction, so we first define the probability of error vectors in every dimension. Let  $P(\omega(e_1, e_i))$  be the probability of in dimension i.  $P(\omega(e_1, e_i))$  is accumulated from the probability of  $\omega_1$  to that of  $\omega_n$ . In first step,  $P(\omega(e_1, e_n))$  is the probability of  $e_n$ .

$$P(\omega(e_1, e_n)) = P_{n,x_n}(e_n) \quad (8)$$

Then, the dimension of vector  $\omega(e_1, e_i, e_{i+1})$  reduces from  $i+1$  to  $i$ , so  $P(\omega(e_1, e_i, e_j))$  ( $0 < i < n$ ) is computed by accumulating from  $P(\omega(e_1, e_i, e_{i+1}))$  to the probability of  $e_i$ .

$$P(\omega(e_1, e_i, e_j)) = P_{i,x_i}(e_i) * \sum_{j=0}^{e_{i+1}} P(\omega(e_1, e_i, e_j)) \quad (9)$$

After reducing layer by layer, the reliability is finally the sum of  $P(\omega(e_i))$ .

$$P_r = \sum_{i=0}^{e_1} P(\omega(i)) \quad (10)$$

A sketch of the pseudo code is given in Algorithm 3 where  $Q$  and  $\omega$  is the queue of error vector and the searching breadth of  $\omega$  respectively in Algorithm 2. In this section, there are three new variables.  $P(\omega)$  is used to save the probability of error vector  $\omega$ .  $x_i$  is the times of task executing and  $pro$  is a temporary variable for saving probability. In the process of reducing, Algorithm 3 need to traverse all the error vectors in error scenario, so the time complexity is  $O(|\Omega| \times (N + D(\Omega)))$ , where  $D(\Omega)$  is depth of breadth first search.

---

**Algorithm 3:** PRO\_CAL( $Q$ ) - reliability computing

---

Input: error-scenario set, searching breadth  
Output: reliability of task set

```

1      for  $\omega \leftarrow$  head ( $Q$ ) to tail( $Q$ ) do
2           $P(\omega) \leftarrow 0$ 
3          for  $i \leftarrow n - 1$  to 0 do
4              for  $\omega \leftarrow$  head ( $Q$ ) to tail( $Q$ ) do
5                  if  $b(\omega) \leq i$  then
6                       $pro \leftarrow 0$ 
7                      for  $j \leftarrow 0$  to  $\omega(e_i)$  do
8                           $pro \leftarrow pro + (1 - e^{-\lambda c_i})^j \times e^{-\lambda c_i}$ 
9                       $pro \leftarrow pro^{x_i}$ 
10                      $\psi \leftarrow \omega$ 
11                     while  $\pi(\Psi) \neq \emptyset$  &&  $b(\Psi) = i$  do
12                          $pro \leftarrow pro - P(\Psi)$ 
13                          $\Psi \leftarrow \pi(\Psi)$ 
14                      $P(\omega) \leftarrow P(\omega) \times pro$ 
15                     for  $\omega \leftarrow$  head ( $Q$ ) to tail( $Q$ ) do
16                         if  $b(\omega) = i$  then
17                              $\Psi \leftarrow \pi(\Psi)$ 
18                             while  $\Psi \neq \emptyset$  &&  $b(\Psi) = i$  do
19                                  $\Psi \leftarrow \pi(\Psi)$ 
20                              $P(\omega) = P(\omega) + P(\Psi)$ 
21                     return  $P(\text{head}(Q))$ 
```

---

## 5 Experiments

We perform a series of experiments to evaluate the reliability of fault-tolerant real-time system. All the programs are implemented under environment Microsoft Visual C++ 2010 and run on Windows7 64-bit with Intel(R) Core(TM) i5-4460 CPU @3.2GHz and 8 GB memory.

### 5.1 Case study

This section shows the results obtained by applying our approach on a use case. Firstly, a task set is built up within three tasks:  $\Gamma_1 = \{\tau_1, \tau_2, \tau_3\}$ ;  $\tau_1 = (P_1=6, C_1=1)$ ;  $\tau_2 = (P_2=10, C_2=2)$ ;  $\tau_3 = (P_3=24, C_3=3)$ . The utilization of processor in task set is 0.4917. The fault rate ranges from 0 to 0.2. Next, generate n task sets ( $\Gamma_1 \sim \Gamma_n$ ) by separating each task in  $\Gamma_1$  into n tasks and each task has the same period and  $1/n$  execution time of its original task. The utilization of CPU for  $\Gamma_1 \sim \Gamma_n$  is the same as that for  $\Gamma_1$  (0.4917). Finally, we evaluate the reliability of  $\Gamma_1 \sim \Gamma_5$  in the period of 480 $\mu$ s under the fault rates of [0, 0.2] was shown in Figure 4.

In Figure 4, two conclusions emerge from the comparison in fault rate and granularity of task. Firstly, taking  $\Gamma_4$  as example, when the fault rate is less than 0.08, the reliability does not decrease significantly. However, when the fault rate is greater than 0.08, the reliability drops rapidly and when the fault rate is greater than 0.12 the reliability is close to zero. Secondly, under the same fault rate, the reliability of  $\Gamma_i$  ( $i > 1$ ) is obviously higher than that of  $\Gamma_{i+1}$ . For example, under the fault rate of 0.06, the reliability  $\Gamma_4$  is close to 1, and the reliability  $\Gamma_1$  is close to zero. That is to say, the reliability can be improved by dividing the task into some small sub-tasks.

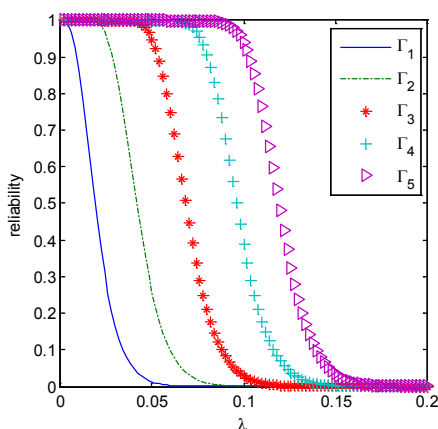


**Figure 4.** The effects on reliability from fault rate

## 5.2 Simulation

In this section, we set up two experiments with synthetic tasks to show the effects on reliability from fault rate of faults. The periodic task sets used in all experiments are generated randomly by the following ways: (1) Set the task count of each task set as  $N = 10$ ; (2) The CPU utilization of each task set is 50 %; (3) The fault rate of faults ranges from 0 to 0.2; (4) Evaluate the reliability in the time of 1000. (5) The scheduling strategy is Rate-Monotonic Scheduling (RMS); (6) The execution time of tasks is equal to their recovering time,  $C_i = C'_i$ .

In the first experiment, we generate period of ten task sets randomly, and set their execution time that  $C_i = P_i \times (1/2N)$ , shown in Figure 5a. For the second experiment, the period of all the tasks is also set randomly, while all the tasks have the same execution time, shown in Figure 5b. In the two figures, it is seen that although the CPU utilization of each task set are the same, the reliability among the task sets has a huge difference. For example,  $\Gamma_1$  and  $\Gamma_6$  can tolerate the fault rate 0.008 with the reliability close to 100%, while the reliability of  $\Gamma_2$  and  $\Gamma_9$  is close to zero.

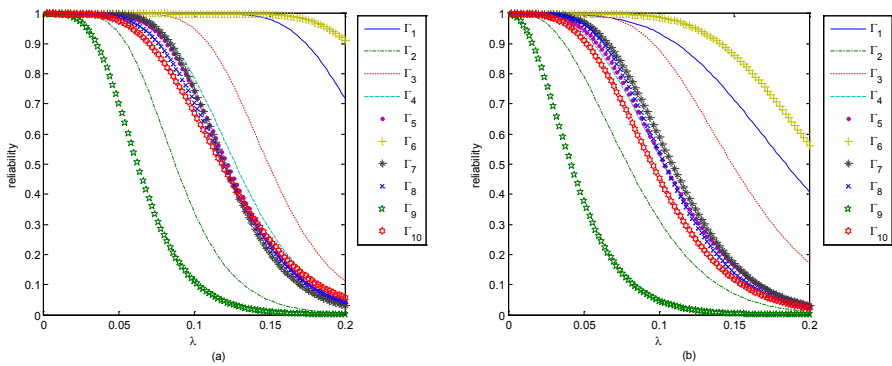


**Figure 5.** Simulation results of synthetic tasks

Therefore, there are two ways to enhance reliability. The first is to try to reduce the arrival rate of faults in each task. If we can guarantee that the fault rate is small enough for all tasks to be schedulable, then the reliability of the system can be close to 100 %. The second way is optimize the construction of task set to enhance the reliability.

## 6 Conclusion

In this paper, we present a novel reliability model, which apply the method of schedulability analysis based on worst-case response time to evaluate the reliability

of system in the design phase of real-time software. In our approach, the breadth-first traversal algorithm was applied to search all the error vectors, and then, we present the method of reduction which was used to accelerate the computing of reliability. From the case study, we found that the reliability of real-time system can be improved by dividing the task into some small sub-tasks and simulation result gives another way to enhance the reliability by optimizing the construction of task set.

## References

- [1] IEEE (1990) 610.12-1990 - IEEE Standard Glossary of Software Engineering Terminology, pp 1-84
- [2] International Electrotechnical Commission (2010) Functional safety of electrical/electronic/programmable electronic safety-related systems.
- [3] M. Sebastian, R. Ernst (2008) Modelling and Designing Reliable On-Chip-Communication Devices in MPSoCs with Real-Time Requirements. In: 13th IEEE International Conference on Emerging Technologies and Factory Automation, pp.1465-1472.
- [4] T. Anderson, J.C. Knight (1983) A Framework for Software Fault Tolerance in Real-Time Systems. IEEE Transactions on Software Engineering, SE-9(3): 355-364.
- [5] C. M. Krishna, A. D. Singh (1993) Reliability of Checkpointed real-time systems using time redundancy. IEEE Transactions on Reliability, 42(3): 427-435
- [6] A. Burns, S. Punnekkat, L. Strigini, D.R. Wright (1999) Probabilistic scheduling guarantees for fault-tolerant real-time systems. In: Dependable Computing for Critical Applications, pp 361-378
- [7] I. Broster, A. Burns, G. Rodriguez-Navas (2002) Probabilistic analysis of CAN with faults. In: 23rd IEEE Real-Time Systems Symposium, pp 269-278
- [8] G. M. de A. Lima, A. Burns (2001) An Effective Schedulability Analysis for Fault-Tolerant Hard Real-Time Systems. In: 3th Euromicro Conference on Real-Time Systems, pp 209-216.
- [9] G. M. de A. Lima, A. Burns (2003) An Optimal Fixed-Priority Assignment Algorithm for Supporting Fault-Tolerant Hard Real-Time Systems. IEEE Transactions on Computers, 52(10): 1332-1346.
- [10] Li Jun, Yang Fumin, Lu Yansheng (2005) A Feasible Schedulability Analysis for Fault-Tolerant Hard Real-Time Systems. In: Proceeding of the 10th IEEE International Conference on Engineering of Complex Computer Systems, pp 176-183
- [11] Li Jun, Yang Fumin, Tu Gang, Cao wanhua and Lu Yansheng (2007) Schedulability Analysis for Fault-Tolerant Hard Real-Time Tasks with Limited Priority Levels. In: The 4th International Conference on Autonomic and Trusted Computing, pp 529-538
- [12] Li Jun, Yang Fumin and Lu Yansheng. (2007) Schedulability Analysis for Fault-Tolerant Hard Real-Time Tasks with Arbitrary Large Deadlines. In: the 6th International Symposium on Parallel and Distributed Computing, pp 149 – 156
- [13] Z. Wu, L. Wang, G. Yang, Z. Zheng (2005) Schedulability Analysis For Fault-Tolerant Group-Based Preemptive Scheduling. Journal of Pervasive Computing and Communications, 1(3): 71-76.
- [14] M. Sebastian, R. Ernst (2009) Reliability Analysis of Single Bus Communication with Real-Time Requirements. In: 15th IEEE Pacific Rim International Symposium on Dependable Computing, Shanghai, pp.3-10.
- [15] S. Gui, L. Luo (2013) Reliability analysis of real-time fault-tolerant task models. Design Automation for Embedded Systems, 17(1): 87-107

- [16] V. Izosimov, P. Pop, P. Eles, Zebo Peng (2005) Design optimization of time- and cost-constrained fault-tolerant distributed embedded systems. In: Proceedings of Design, Automation and Test in Europe, pp 864 – 869.
- [17] P. Eles, V. Izosimov, P. Pop, Zebo Peng (2008) Synthesis of Fault-Tolerant Embedded Systems. In: Proceedings of the conference on design, automation and test in Europe, pp 1117–1122.
- [18] X. Qin, H. Jiang (2006) A novel fault-tolerant scheduling algorithm for precedence constrained tasks in real-time heterogeneous systems. *Journal of Parallel Computing*, 32(56): 331-356.
- [19] C. L. Liu J. W. Layland (1973) Scheduling Algorithms for Multiprogramming in a Hard-Real-Time Environment. *Journal of the Association for Computing Machinery* 20(1): 46-61
- [20] C. M. Krishna, Kang G. shin (2001) Real-time Systems. Tsinghua University Press, 48-72.

Chun-xiang XU\*, Wei SHI, Dong-mei CHEN, Xiang-wei WU

## Coordinate Transformation on CNC Machining of Quasi-Hypoid-Gear

**Abstract:** The structure model of mechanical shaking table machine tools and CNC gear milling machine was analyzed and the corresponding machine coordinate system was established in this paper. Under the condition of ensuring constant relative motion and relative position between the work piece and the tool of the shaking type machine tool. Using the principle of coordinate transformation, the function of instantaneous moving position was deduced as NC milling machine processing to program of CNC machining.

**Keywords:** coordinate transformation; quasi-hypoid-gear; CNC machining model

### 1 Introduction

Now the production of the gears, especially the helical bevel gears occupied the important position in modern manufacturing industry, particularly a considerable proportion in automobiles, tractors and machine tools. Quasi-hypoid-gear is more complex in the form of the helical bevel gear and the overlapped coefficient is greater than the bevel gear with the intersecting shafts. So it is more stable in motion. Just because of this, it is almost universally used in cars [1].

The extensive use of multi-axis machine tools has brought about great advances in manufacturing technology of helical bevel gear, changing the tedious adjustment situation in machine producing of traditional shaking table machines.

Using the principle of the special coordinate transformation, the mechanical shaking desktop machine tool for quasi-hypoid gears can be equivalently switched to the environment of CNC machine tool.

### 2 CNC transformation model

Figure 1 is a conception model of traditional shaking desktop machine tool [2], as can be seen, the number of the shaft is up to ten in traditional shaking desktop machine tool, and most of them were used for machine adjustment before working [4]. In the

---

\*Corresponding author: Chun-xiang XU, Zhengzhou Institute of Technology, Zhengzhou, China, E-mail: xchx\_2002@126.com

Wei SHI, Dong-mei CHEN, Xiang-wei WU, Zhengzhou Institute of Technology, Zhengzhou, China

process of working, only the cradle shaft and the piece spindle are in linkage to form generating motion which achieved by gear train [3]. Various adjustment and different change gears are used for manufacturing different gears, so the transmission chain is complex. While 5shafts linkage can be realized at Phoenix Free-form machine as working by NC system [5]. The result is shorter transmission chain, more exact motion and wider manufacturing range.

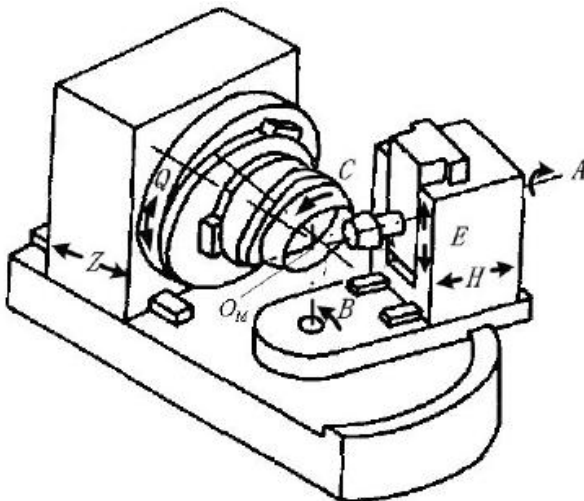


**Figure 1.** Traditional Mechanical Shaking Table Machine Tool

The essence of transformation from the traditional shaking desktop machine to free machining machine tool is to reproduce the processing principle of traditional machine tool on new machine tool. This needs to ensure any position while processing, the relative position of the cutter and the work piece is the same with traditional machine tool.

To reappear motion relationship between the tool coordinate system  $S_t$  and the work piece coordinate system  $S_p$  of the machine, the transition matrix of  $S_t$  and  $S_p$  is firstly studied.

- 1) Suppose that there is a  $4 \times 4$  coordinate transformation matrix of  $M_{pt}(k)$  ( $k=C, G$ ), where the superscript C and G respectively represent CNC gear milling machine and mechanical gear milling machine.
- 2) If there is the equation (1) of  $M_p^{(C)} = M_p^{(G)}$ , there can guarantee the tool and the work piece are in the same relative motion direction and position when generating the tooth surface of two kinds of the machine tools.

## 2.1 The traditional mechanical shaking table machine coordinate system

Set machine tool machining coordinate system according to the model of structure of traditional mechanical shaking table machine. The following is to take manufacturing a pinion on a hobbing machine for example to establish the machine tool coordinate system.

The following coordinate system is set: the fixed coordinate system Sm1 and Sq which rigidly consolidated with the gear cutting machine is shown in Figure 2 and Figure 3; respectively correspond to the moving coordinate system Sc and S1 of the cutting machine cradle and the pinion rigid consolidation [6]. During working, the cradle and Sc rotate around the axis Zm1 at the angular velocity of  $\vec{\omega}^{(c)}$ , while the pinion and S1 rotate around the axis Xq at the angular velocity of  $\vec{\omega}^{(1)}$ .

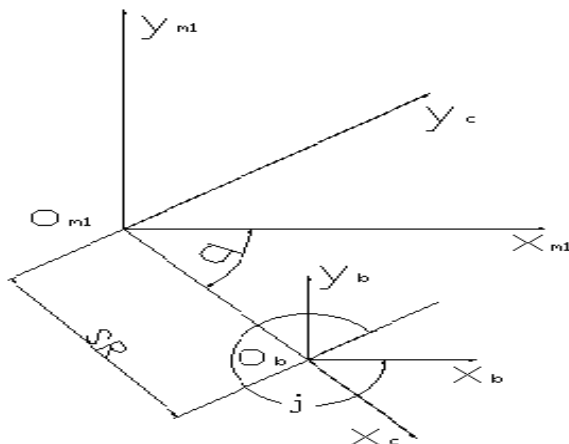


**Figure 2.** Sm1, Sc and S b Coordinate System

The cutter disc mounted on the shaking table rotates with it. Coordinate system St1 rigidly consolidated to the shaking table. In order to describe the tool relative to the direction of the shaking table, use the coordinate system of Sb to achieve the following steps: Firstly consolidate coordinate system Sb to St1, then turn them as one rigid body around the axis of Zc to a rotation angle j; secondly, incline the tool disc and St1 system to an angle of i around Yb axis. The tool disc can rotate around its axis of Zt1.

The parameters of installation and adjustment of the pinion follows.

Em: Offset of the wheel blank on the machine tool,  $\Gamma_m$ : installation angle of the wheel blank,  $\Delta B$ : moving distance of slider,  $\Delta A$ : Distance from the machine center to supporting surface of the blank.

The parameter of installation and adjustment of the tool disc follows.

SR: Radial installation adjustment value, j: swivel angle, i: Cutter tilt

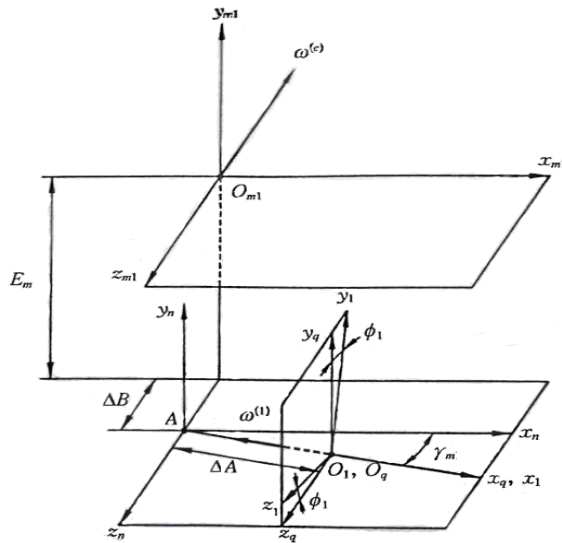


**Figure 3.** Machine Coordinate System as Manufacturing Pinion

According to Figure 3, the following number sentence can be gotten through coordinate transformation of matrix [1].

$$M_p^{(G)} = M_{1q} M_q M_{m1} M_{m1c} M_b M_{b1} = \begin{bmatrix} a_1 & a_2 & a_3 & a_4 \\ a_1 & a_2 & a_3 & a_4 \\ a_3 & a_2 & a_3 & a_4 \\ a_4 & a_2 & a_3 & a_4 \end{bmatrix}$$

Among them:

$$\begin{aligned} a_{11} &= \cos i \cos \gamma_m \sin(q - j) - \sin i \sin \gamma_m \\ a_{12} &= -\cos(q - j) \cos \gamma_m \\ a_{13} &= \sin i \cos \gamma_m \sin(q - j) + \cos i \sin \gamma_m \\ a_{14} &= S_R \cos q \cos \gamma_m - \Delta B \sin \gamma_m - \Delta A \\ a_{21} &= \cos i \sin \gamma_m \sin \varphi_1 \sin(q - j) + \cos i \cos(q - j) \cos \varphi_1 \\ &\quad + \sin i \cos \gamma_m \sin \varphi_1 \\ a_{22} &= -\cos(q - j) \sin \gamma_m \sin \varphi_1 + \sin(q - j) \cos \varphi_1 \\ a_{23} &= \sin i \sin \gamma_m \sin \varphi_1 \sin(q - j) + \sin i \cos(q - j) \cos \varphi_1 \\ &\quad - \cos i \cos \gamma_m \sin \varphi_1 \\ a_{24} &= -S_R (\sin q \cos \varphi_1 - \cos q \sin \gamma_m \sin \varphi_1) + E_m \cos \varphi_1 \\ &\quad + \Delta B \cos \gamma_m \sin \varphi_1 \\ a_{31} &= -\cos i \sin \gamma_m \cos \varphi_1 \sin(q - j) + \cos i \cos(q - j) \sin \varphi_1 \\ &\quad - \sin i \cos \gamma_m \cos \varphi_1 \end{aligned}$$

$$\begin{aligned}
 a_{32} &= \sin \gamma_m \cos \varphi_1 \cos(q-j) + \sin(q-j) \sin \varphi_1 \\
 a_{33} &= -\sin i \sin \gamma_m \sin(q-j) \cos \varphi_1 + \sin i \cos(q-j) \sin \varphi_1 \\
 &\quad + \cos i \cos \gamma_m \cos \varphi_1 \\
 a_{34} &= -S_R (\sin q \sin \varphi_1 + \cos q \sin \gamma_m \cos \varphi_1) + E_m \sin \varphi_1 \\
 &\quad - \Delta B \cos \gamma_m \cos \varphi_1 \\
 a_{41} = a_{42} = a_{43} &= 0, a_{44} = 1
 \end{aligned}$$

## 2.2 CNC Machine Tool Coordinate System

The coordinate system of the Phoenix Free-form machine is shown in Figure 4.

As seen in Figure 4, coordinate system St and Sp is respectively consolidated to the tool and the work piece, Sh and Sm is respectively consolidated to the cutter base and the sliding base. Coordinate axis Sh is parallel to coordinate axis Sm. (x,y,z) is used to represent the position of Sh relative to the position of Sm. Coordinate St rotates around the axis of zh relative to Sh. Coordinate system Se and Sd is used to describe coordinate transformation from Sm to Sp.

Coordinate system Se achieves rotation around the axis of ym. The coordinate axis of coordinate system Sd parallels to coordinate axis of Se;  $\Delta X = C$  is used to confirm the original point position of Od relative to Oe. Coordinate system Sp achieves rotation around the axis of xd relative to Sd.

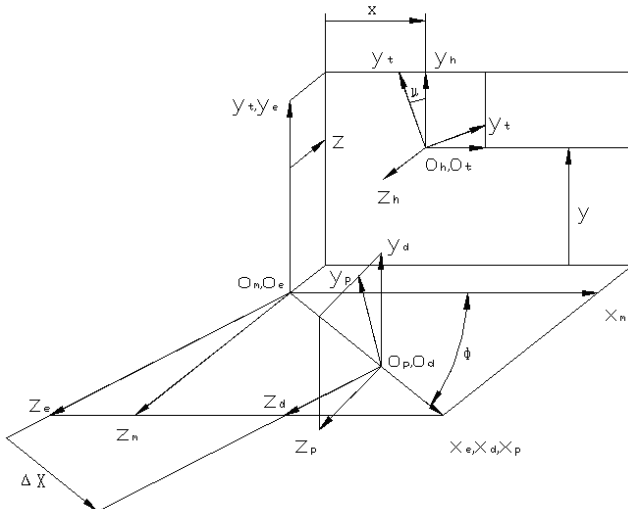


**Figure 4.** The Coordinate System of Phoenix Free-form

According to Figure 4, the following number sentence can be gotten through coordinate transformation of matrix as the following formula (3).

$$M_{pt}^{(c)} = M_{pd} M_{de} M_{em} M_{mh} M_{ht} = \begin{bmatrix} b_{11} b_{12} b_{13} b_{14} \\ b_{21} b_{22} b_{23} b_{24} \\ b_{31} b_{32} b_{33} b_{34} \\ b_{41} b_{42} b_{43} b_{44} \end{bmatrix}$$

$$\begin{aligned} b_{11} &= \cos \mu \cos \varphi; b_{12} = -\sin \mu \cos \varphi; b_{13} = \sin \varphi; \\ b_{14} &= \Delta X - x \cos \varphi - z \sin \varphi \\ b_{21} &= -\cos \mu \sin \varphi \sin \psi + \sin \mu \cos \psi; \\ b_{22} &= \sin \mu \sin \varphi \sin \psi + \cos \mu \cos \psi; b_{23} = \cos \varphi \sin \psi; \\ b_{24} &= x \sin \varphi \sin \psi - y \cos \psi - z \cos \varphi \sin \psi; \\ b_{31} &= -\cos \mu \sin \varphi \cos \psi - \sin \mu \sin \psi; \\ b_{32} &= \sin \mu \sin \varphi \cos \psi - \cos \mu \sin \psi; b_{33} = \cos \varphi \cos \psi; \\ b_{34} &= x \sin \varphi \cos \psi + y \sin \psi - z \cos \varphi \cos \psi; \\ b_{41} &= b_{42} = b_{43} = 0, b_{44} = 1 \end{aligned}$$

According to formula (2) and (3), solving the equation (1) can be used to determine the NC model of Phoenix Free-form machine tool by adjusting parameter of traditional shaking table milling machine.

### 3 Parameter Determination

- 1) Determine the installation angle  $\varphi$  of the pinion of the work piece,  $\sin \varphi = a_3$ ;
- 2) Determine the work piece spindle rotation angle  $\psi$ ,  $\cos \varphi \cos \psi = a_3$ ;
- 3) Determine the cutter spindle rotation angle  $\mu$ ,  $\cos \mu \cos \phi = a_1$ ,  $-\sin \mu \cos \phi = a_2$ ;
- 4) Determine the displacement of the three axes of X, Y, Z, and solve the system of linear equation contained three unknown numbers of x, y, z

$$\begin{cases} a_1 = b_1 \\ a_2 = b_2 \\ a_3 = b_3 \end{cases}$$

In summary, the six-axis linkage instantaneous movement position can be obtained when machining hypoid pinion by the face hobbing method on CN milling machine, instantaneous movement position of each axis can be expressed by a function to realize the machine tool programming and machining. It also provides the reference for setting the parameters of the Quasi-Hypoid-Gear CNC machining.

## 4 Conclusion

The machine model of the mechanical shaking table milling machine and CN milling machine was analyzed when processing the quasi-hypoid-gear and the machining coordinate system was established in the paper. According to the working principle, coordinate transformation was completed as machining of CN milling machine. The instantaneous movement position of each axis was got when CN milling gear by coordinate transformation. It can be applied in simulation study on CN milling machine tool of making quasi-hypoid-gear and the parameter transformation between the mechanical machine tool and the CN machine tool and has theoretical and practical value. The method provides the practical and theoretical value in the coordinate transformation and calculation of the multi-axial linkage machine, the working simulation of CNC machining of Quasi-Hypoid-Gear and the parameter settings of multi-axial CNC machines.

## Reference

- [1] F.L. Li Tewen Gear Geometry and Applied Theory, Shang Hai, Shanghai Science and Technology Press 2008, pp. 658-659.
- [2] Su Zhijian, Wu Xutang Manufacture of Quasi-Hypoid-Gear on Sprial Bevel Gear Machine Tool Based on CNC, Chinese Journal Of Mechanical Engineering, 2007, vol. 43 (5), pp. 57-63.
- [3] Ceng Tao Design and Manufacture of Spiral Bevel Gear, Harbin, Harbin Institute of Technology Press, 1989, pp. 382.
- [4] Zhang Wei, Hypoid-Gear NC Machining Theory and Simulation Research, Tianjin, Tianjin University, 2007, pp. 28-42
- [5] Liu Ganhua, Yan Hongzhi, Xie Yaodong Phoenix II NC Machining Model of Face Hobbing Method with Dry Cutting on NC Milling Machine, Manufacturing Technology and Machine Tool, 2011, pp. 87-92
- [6] Dong Xuezhu, Design and Manufacture of Cycloid Tooth Bevel Gear and Quasi-Hypoid-Gear, Beijing, Machinery Industry Press, 2003, pp. 352
- [7] Cheng Xiaofeng, Wang Qiang, Cutter Location Analysis of Generating Machining for Spiral Bevel Gears on NC Machine Tool, Journal of Xihua University, 2009 Vol.3, pp. 10-13
- [8] Tang Dafang, Wang Hewen, The Calculation of Cutting and Setting and the Design of Program Module for the Hypoid Gears, Manufacturing Technology & Machine Tool, 2009 Vol.12, pp. 107-109
- [9] Wu Xuncheng, Xu Hongshan, Function-oriented Design of Point-contact Tooth Surfaces of Hypoid Gears with the Generated Gear, 2011 Vol.3, pp. 16-18
- [10] Wang Lihuai, Wei Bingyang, The New Method of Designing Parameters of Quasi-Hypoid-Gear, Journal of Henan University of Science & Technology, 2008 Vol.4, pp. 25-27

Yan-wei TAN\*, Sheng-ya LI, Yan-hai XU, Ke-qj LI

## Study on the Influence of Rolling Wheels on Car External Flow Field and Aerodynamic Noise

**Abstract:** In order to illustrate the external flow field and aerodynamic noise of cars with the influence of rolling wheels, the investigation is conducted through numerical simulation in this paper. Wheel rolling is modeled by using a rotating wall. Combined with Realizable  $k - \epsilon$  and LES, the flow field and aerodynamic noise of the rolling wheels and the stationary wheels are simulated, respectively. Then the related monitoring points are set to provide the basis for further evaluation. The transient calculation is carried out with two typical cases. Furthermore, air fluctuating pressure and sound pressure level spectrum of the monitoring points in wheel cavity is obtained. The results show that rolling wheels have distinctive influence on vortex formation and car aerodynamic characteristics.

**Keywords:** Rolling wheel; Aerodynamic noise; Fluctuating pressure.

### 1 Introduction

Aerodynamic noise caused by the automobile is one of the focuses in automotive engineering. With the increasing of vehicle speed and car ownership, car noise problem becomes important sharply [1]. Vehicle external flow field is a kind of complex disturbed flow motion, the rolling of wheels makes car external flow field more complex and it results car aerodynamic noise. Previous study on automobile wheels is simplified and does not consider the effect of rolling wheels. Although the results have certain significance, there are still large gaps compared with real cars. The latest studies involve the rolling wheels, but they do not conduct a detailed analysis and discussion of car flow field and aerodynamic noise near the rolling wheel. Literature [2] shows that wheels noise was relatively loud through the study of aerodynamic noise contribution quantity of car body parts.

In this paper, the simulation research of flow field characteristics and aerodynamic noise distribution of the wheel in both rolling and static conditions are conducted through numerical simulation.

---

\*Corresponding author: Yan-wei TAN, School of Automotive and Transportation, School of Automotive and Transportation, Xi Hua, University, Chengdu, China, E-mail: 373302311@qq.com

Sheng-ya LI, Yan-hai XU, Ke-qj LI, School of Automotive and Transportation, School of Automotive and Transportation, Xi Hua University, Chengdu, China

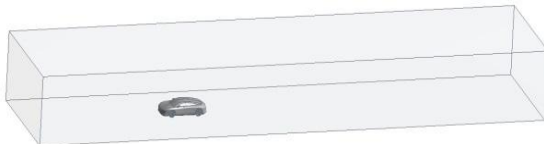
## 2 Numerical model for vehicle external flow field

### 2.1 Description of Vehicle Model

In this paper, a vehicle model including the key features of vehicle body such as rear view mirror, wheel and side window is established. Due to wheel spokes and wheel brake disc disturb the airflow motion when rolling, which will change the flow fields, car wheel is no longer depicted by a simple cylinder, but a wheel model including spokes, tread grooves and brake disc, as shown in Figure 1. The front of the computational domain is 3 times of car length, the rear for 7 times of car length, one side is 3 times of car width, height is 5 times of car height [3], as shown in Figure 2.



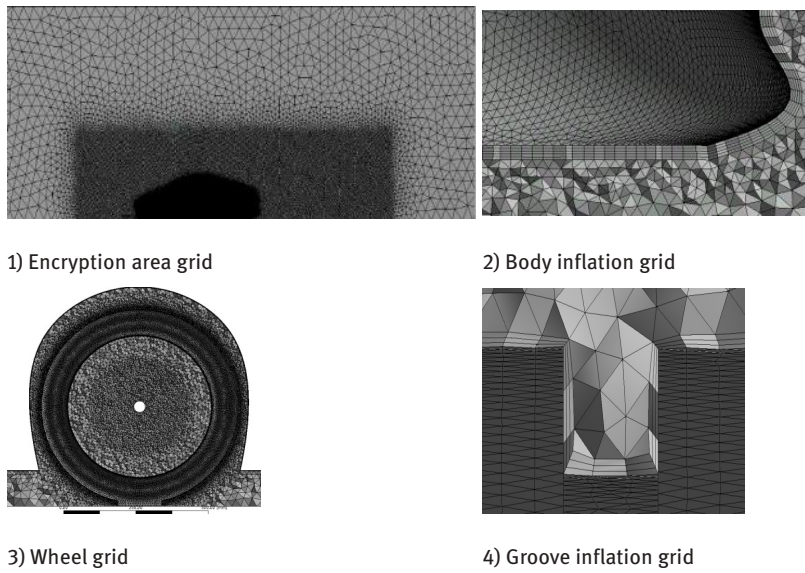
**Figure 1.** Three dimensional model



**Figure 2.** Computational domain

### 2.2 Mesh for Vehicle Model

This paper uses tetrahedral and triangular prism grid to mesh the computational domain. The mesh size of the computational domain is controlled between 3mm and 40mm by integral control method. In the vicinity of the surface of car body, in order to capture the turbulent situation around the body as far as possible, a region surrounding car body is established and the grid is encrypted. The unit length of encryption area is set to 10mm. Additional, to improve the accuracy of the calculation, the inflation grid is adopted in near wall of the body, tires and wheel cover, the inflation layer of the body is 5 and the wheel is 3 [4]. The total number of meshes is 12 million. The mesh is shown in Figure 3.

**Figure 3.** Mesh generation

### 2.3 Boundary Conditions and Solving Settings

Vehicle motion belongs to the incompressible flow in low speed and the solution of this study is based on pressure based solver [6]. First, the steady state calculation is carried out by the Realizable  $k - \varepsilon$  model, and then the transient calculation is carried out by the large eddy simulation method.

(1) Inlet boundary: a velocity inlet boundary is set. The vehicle speed is 27.8m/s.

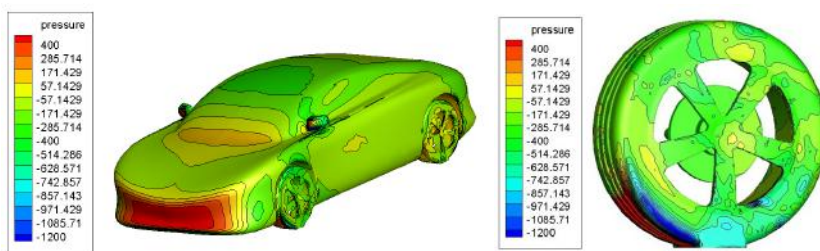
(2) Outlet boundary: outlet boundary is set as pressure boundary.

(3) Wheel and the ground: For rolling wheel, rotating wall is used to simulate wheel rolling with a radius of 0.315m and an angular velocity of 88.2rad/s. The mobile wall is applied to simulate the movement of the ground and the speed of the movement is the same as that of the inlet velocity. For static wheel, car wheels are set to the static wall and the ground is still moving wall.

The frequency domain is generally determined by the time step. In the study, the maximum frequency is 5000Hz. Due to the maximum frequency of fast Fourier transform (FFT) of a time series is  $1/(2\Delta t)$ , the calculation time step is set to 0.0001s. The time steps are set to 2000, 20 iterations per time step [5]. So the total computation time is 0.2 seconds.

### 3 Simulation results and analysis

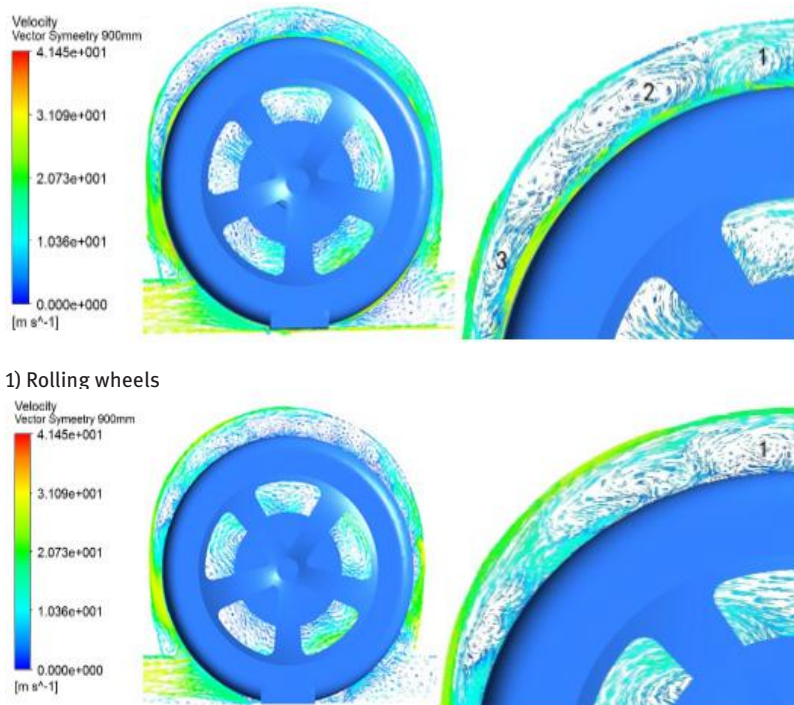
The pressure distribution around car will affect the aerodynamic noise around car surface directly. To analyze car aerodynamic noise, this paper analyzes the pressure on the surface of car body firstly. Figure 4 presents the static pressure contours of car body surface and wheel. It can be seen that the contour of the wheel is denser, the pressure gradient is larger, which indicates that the pressure fluctuation of the wheel is intense. This paper will focus on the analysis of the characteristics of the aerodynamic noise of the wheel cavity and the far field.



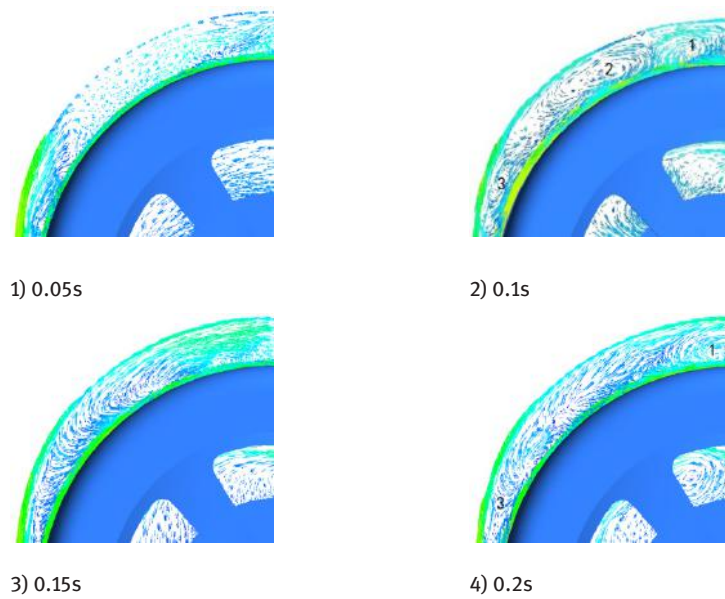
**Figure 4.** Air Pressure distribution of body and wheel surface

Figure 5 and 6 give the velocity vector diagram of longitudinal symmetric cross section of rolling wheel and static wheel. Due to wheel rolling motion driving airflow attached to tread counterclockwise, the two phase flow between tire tread and the wheel cover are encountered mutually. This causes many vortices with different sizes and different directions formed between tire tread and wheel cover. When wheels are rolling, there are three obvious vortices at the top left of the front wheel as shown in Figure 5 (1) marked with 1,2,3. Compared with the rolling wheel, there is only one vortex in the stationary front wheel as shown in Figure 5 (2) marked with 1.

Figure 6 gives the velocity vector diagram of wheel cavity of the front rolling wheel at different times. It can be seen that vortex is in a constantly changing process. In 0.05 seconds, vortex is not obvious. In 0.1 second, three obvious vortices can be seen. After which, vortices are broken away. Then they are reformed. The formation of vortex in the whole time is in the process of formation, development, disappearance and reformation, with the dissipation of energy. It cause the change of the pneumatic pressure around car wheel and then lead to the increasing of drag and lift force of the whole vehicle in rolling condition. Because the airflow movement of the rear wheel is affected by the front wheel, the rear wheels of the two working conditions have no obvious vortex.



**Figure 5.** Velocity vector of front wheel cavity



**Figure 6.** Velocity vector at different time

Rolling wheel not only has an influence on the flow field characteristics of the cavity but also affects car aerodynamic noise. The monitoring points are set to analyze the noise in wheel cavity. The monitoring point is arranged along the circumference of the tire in the longitudinal center of tire and the distance between the monitoring point and the tire is 2cm. The monitoring points are distributed with 30 degrees. Because the location of the ground can't be set, there are 11 monitoring points.

From simulation results, it is found that the fluctuating pressure of each monitoring point is changed with time in 0-0.2 seconds. The distribution of sound pressure level spectrum is similar to the change. In the low frequency region sound pressure level drops, and later, with the increase of frequency, the sound pressure level keep stable in a certain range. Figure 7 presents the fluctuating pressure of vehicle front wheel monitoring point 1 in the rolling situation. The sound pressure level spectrum of the rolling front wheel monitoring point 1 is shown in Figure 8.

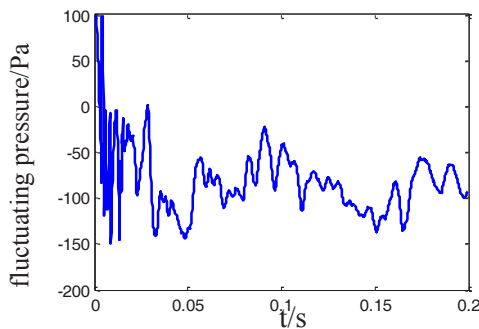


**Figure 7.** Fluctuating pressure in time domain

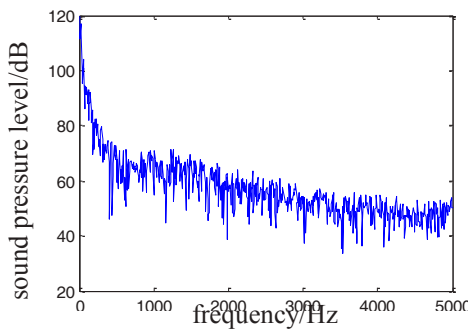


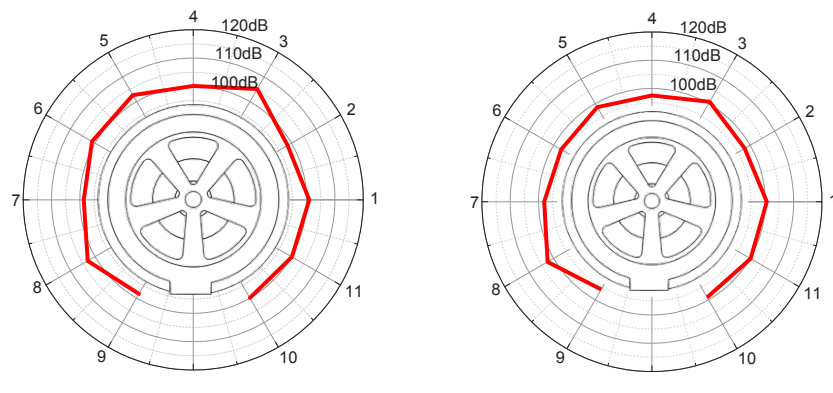
**Figure 8.** Acoustic spectrum

To superimpose the sound pressure level at each frequency, the total sound pressure level of each monitoring point is obtained [7]. The total sound pressure level of the front and rear wheel of the rolling wheel and the static wheels are shown in Figure 9 and 10. The results show that the value of most monitoring points is 100 dB or so. From points 4, 5, 6, 7 corresponding to the velocity vector map, it is shown that these places have a large number of vortices, due to the vortex's constantly formation, constantly shedding, make air pressure fluctuating. These lead to the increasing of sound pressure level. In addition, it can be seen that the value of sound pressure level at monitoring point 9 is all the monitoring point of minimum. This is because the special position of the point, when the airflow flowed through the bottom of body and met the wheel, the airflow is obstructed, and most of the airflow gathered here, led to the accumulation of a large amount of air, the airflow velocity get slower, and therefore smaller sound pressure level numerical. The numerical value of the front wheel of the stationary case is not the same as the rolling wheel, because the vortex generated by the static condition is less, the sound pressure level of the upper part of the wheel cavity is smaller than the rolling condition. Similarly, monitoring 9 in static situation, sound pressure level is smaller.

In analyzing the sound pressure level of the various monitoring points of rear wheel cavity, it is shown that the distribution is not the same as front wheel, the rear wheel cavity is not as the same as front wheel to produce more obvious vortices. The sound pressure level of the upper part of the rear wheel cavity is lower than that of the front wheel due to the absence of intense vortex motion.



**Figure 9.** Sound pressure level distribution of front wheel



1) Rolling wheels 2 ) Static wheels  
**Figure 10.** Sound pressure level distribution of rear wheel

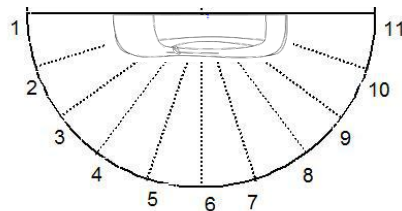


**Figure 11.** Layout of monitoring points

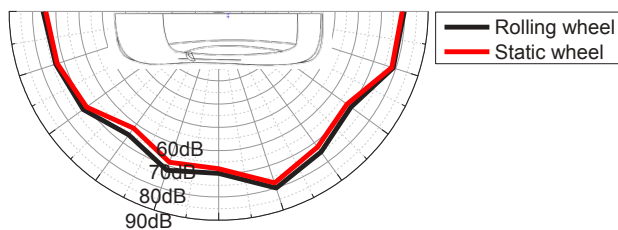


**Figure 12.** Sound pressure level distribution of car far field

By using the center of car to establish a half arc with a radius of 5 meters and an interval of 18 degrees, 11 receiving points with a height of 1.2 m above ground are set to study the impact of wheel rolling on the outside car noise. The layout of the monitoring points is shown in Figure 11.

It is shown in Figure 12 that the sound pressure level of rolling wheel at each monitoring point in the far field is higher than static wheel. It is shown in the left that

the amount of change is small and the sound pressure level at monitoring points 1, 2, 3 changes are less than 1 dB, which indicates that the wheel rolling has little noise impact on the front of the car. But the change of sound pressure level is relatively large in the middle body central and the rear car body. It indicates that when the wheel in the rolling, it disturbs air flow motion in the middle and rear which led to the change of the aerodynamic noise around the body. The sound propagates outward and outside and car noise increases in far field.

## 4 Conclusion

This paper takes into account wheel rolling on the influence of car aerodynamic noise. The influence on flow field characteristics and the far field noise is studied through numerical simulation system under the condition of rolling and static wheels. From the simulation results, the following conclusions can be drawn:

1. The effect of rolling wheels on car aerodynamic noise is illustrated through the present research. It not only qualitatively explains the significance of rolling wheel, but also gives the quantitative effect at the cavity and the far field of car aerodynamic noise.
2. The results also illustrate the flow field characteristics of wheel cavity quantitatively. It gives the causes producing the change of car noise. The generating process of vortices is investigated in detail in the paper. The generating process of vortices accompanies with air pressure fluctuating. It is useful for further research on ameliorate car aerodynamic noise.

**Acknowledgement:** The research is supported by the Ministry of Education (Z2012024) and spring plan key project supported by the science and Technology Department of Sichuan province (2011J00043).

## Reference

- [1] Ji Yurong. The influence of traffic noise on the environment and the harm to the environment[J]. China Science and technology, 2010, vol.17:128
- [2] Liu Longgui, Zhang Yong et al. Automobile body parts air dynamic noise contribution in the amount of numerical simulation[J]. Science technology and engineering, 2014, 14 (10): 89-94.
- [3] Marco Lanfrat. Best practice guidelines for handing Automotive External Aerodynamics with fluent[a]. Frankfurt.FLUENT 's second by consumer associations worldwide European automotive CFD conference [C].Germany, 2005, 29 ~ 30.
- [4] Kuo-Huey C, Jim J, Urs D. Wind noise measurements for automotive mirrors[C]. SAE Paper, 2009-01-0184.
- [5] GU Zhengqi, HE Yibin. Numerical Simulation Analysis of External Flow Field of Wagon-Shaped Car at the Moment of Passing[J]. Journal of Mechanical Engineering, 2008, 21(4):76-80.

- [6] Lars Davidson. Flow and Dipole Source Evaluation of a Generic SUV[J].Journal of Fluids Engineering. MAY 2010, Vol. 51111 132
- [7] F Felten, Y Fautrelle, Y Du Terrail, et al.Numerical modeling of electro gnetically-riven turbulent flows using LES methods [J].Applied Math ematical Modeling, 2004, 28(1):15-27.

Jian-xian ZHANG\*, Duan ZHOU, Xue-hong QIU, Rui LAI

## **Hardware/Software Partitioning Algorithm under Multi-Constraints for the Optimization of Power Consumption**

**Abstract:** An improved particle swarm algorithm with multiple neighborhood optimizations was proposed for hardware/software partitioning of system on chip under multiple constraints. A method for fitness calculation was designed with the unity of multiple constraint conditions and objective function. The particle position was updated by the average of the best position for all particles, the individual optimal location and the global optimal position. The effect of the average of position on particle position was adjusted adaptively according to the number of iterations. The multiple neighborhood of the optimal solution was searched for a better solution. The variation information of the optimal position was randomly produced by the Gaussian function. An arbitrary particle in population would be replaced by the variation particle whose fitness was better than the optimal fitness. The experimental results show that the proposed algorithm achieves hardware/software partitioning with lower power in a shorter searching time under the same constraints.

**Keywords:** Hardware/Software Partitioning; System on Chip; Particle Swarm Optimization; Multi-neighborhood Optimization

### **1 Introduction**

The complexity of system functions is increased by the diverse application requirements, while the operation efficiency of the reconfigurable system on chip (SoC) is improved by the combination of the processor on chip and reconfigurable FPGA resources. Hardware/software partitioning of system has a significant impact on system performance. How to obtain an optimal performance of the hardware/software partitioning solution under system constraints has become a research hotspot [1,2].

A variety of hardware and software partitioning algorithms have been proposed, such as dynamic programming, integer programming, the genetic algorithm, simulated annealing, tabu search, and the particle swarm optimization algorithm.

---

\*Corresponding author: Jian-xian ZHANG, School of Computer Science and Technology, Xidian University, Xian, 710071, China, E-mail: jianxianzhang@mail.xidian.edu.cn

Duan ZHOU, Xue-hong QIU, School of Computer Science and Technology, Xidian University, Xian, 710071, China

Rui LAI, School of Microelectronics, Xidian University, Xian, 710071, China

A hardware/software partitioning algorithm based on genetic algorithm (GA) is presented for partial dynamic reconfiguration of system-on-chip in [3]. A partitioning algorithm of embedded system based on genetic particle swarm optimization is proposed in [4], which introduces crossover and mutation of the genetic algorithm into the particle velocity updating and improves the global search ability of the algorithm. However, the execution time of the proposed algorithm becomes longer because of the complexity of the particle update operation. In [5] a greedy algorithm is introduced into the simulated annealing to accelerate the convergence of the algorithm, reducing the search time for partitioning. An adaptive partitioning algorithm based on chaos genetic annealing (ACGSA) is presented in [6] under multi-performance index constraints. An objective function is designed with different proportions of punishment based on the multiple constraints to reduce the system power effectively. A hardware/software partitioning based on mixed integer linear programming is proposed for the region-based partial dynamic reconfigurable FPGA in [7]. A graph reduction technique is proposed to reduce the design space for HW/SW partitioning without sacrificing the partition quality [8].

Some scholars resolve the partitioning problem by transforming it into other issues. A heuristic approach which treats the HW/SW partitioning problem as an extended 0–1 knapsack problem is presented in [9] to minimize the hardware cost under software and communication constraints, and tabu search is used to further improve the solution obtained by the proposed heuristic algorithm. In [10], three algorithms for the multiple-choice hardware-software partitioning with the objectives of minimizing execution time and power consumption under the area constraint are discussed: the heuristic and tabu search algorithms for proximate solutions as well as the dynamic programming algorithm for exact solutions.

The algorithms mentioned above have achieved some optimization effect, but some of them require a long time to search for optimization [3,4, ], some do not consider the performance constraints [8], while others only consider one constraint [5,9,10], thus a poor efficiency and quality of partitioning. We present a hardware/software partitioning algorithm for power optimization of hardware/software partitioning under multiple constraints, design the fitness calculation with the unity of objective function and multiple constraints, and introduce an improved particle swarm optimization into partitioning algorithm to save the system power and reduce the searching time effectively under multiple constraints.

## 2 Hardware/Software Partitioning System Models

For reconfigurable SoC system hardware and software partitioning, the software functions are realized by a processor (soft or hard core) on a chip, and the processor area is a certain fixed value. The hardware part is implemented by the field programmable gate array (FPGA) logic modules, whose area is represented by the

number of logical units for the module occupied. For FPGA-based SoC systems, the system function modules which are implemented in hardware or software result in corresponding power consumption, occupied area, development cost and execution time.

In this paper, the system model is described with the task data flow graph (TDFG), and the communication overhead between tasks is combined into the execution time of the task node, which simplifies the system model. There are four function parameters: the system power, the system area, the development cost and the execution time for each task node. For a system with  $n$  functional modules, it is assumed that  $(b_1, b_2, \dots, b_n)$ ,  $b_i \in S$  represents a feasible solution to hardware/software partitioning.  $b_i = 0$  and  $b_i = 1$  represent the task is implemented in hardware and software, respectively. The power optimization problem of hardware/software partitioning can be described as

$$\left\{ \begin{array}{l} \text{min(Power)} \\ \text{s.t. } \sum_{i=1}^n (\text{cs}_i b_i + (1-b_i) \text{ch}_i) \leq \text{Cost}_{\text{limit}} \\ \quad \sum_{i=1}^n (1-b_i) \text{ah}_i \leq \text{Area}_{\text{limit}} \\ \quad \sum_{i=1}^n (\text{ts}_i b_i + (1-b_i) \text{th}_i) \leq \text{Time}_{\text{limit}} \\ \quad b_i \in S \end{array} \right. \quad (1)$$

For the  $i_{\text{th}}$  functional module,  $\text{cs}_i$  and  $\text{ch}_i$  represent the development cost implemented with software and hardware, respectively.  $\text{ah}_i$  stands for the hardware area, and the software area is the processor area, which is constant in the process and thus is set to zero in the area calculation.  $\text{ts}_i$  and  $\text{th}_i$  represent the execution time of software and hardware, respectively.  $\text{Cost}_{\text{limit}}$ ,  $\text{Area}_{\text{limit}}$  and  $\text{Time}_{\text{limit}}$  represent the constraint values of the development cost, the system area and the execution time, respectively.

### 3 Particle Swarm Partitioning Algorithm With Multiple Neighborhood Optimization

#### 3.1 Particle Position Update

The base particle swarm optimization (PSO) is a global optimization algorithm analogous to the food-searching behavior of birds, but it easily falls into local optimum. A quantum-behaved particle swarm optimization algorithm is introduced to achieve a better result in [11]. To accelerate the particle status update, the particle position is updated by removing the particle flight speed parameter and directly calculating the mean best position of all particles, the global and local best positions.

In this paper, the particle position update formula is improved for hardware/software partitioning. With the increment of the number of iterations, the impact of the mean best position of all particles on the particle is reduced, so that all particles tend to be close to the best location. The particle position is updated by

$$\left\{ \begin{array}{l} p_{id}(k+1) = (\phi \times pbest_{id} + (1-\phi)gbest_d) \\ \quad \pm \beta \times |mbest - p_{id}(k)| \\ \text{s.t. } \phi = rand(); \\ \beta = 1 - 0.5 \times \frac{k}{N}; \\ mbest = \frac{1}{M} \sum_{i=1}^M p_i \\ = \left( \frac{1}{M} \sum_{i=1}^M p_{i1}, \frac{1}{M} \sum_{i=1}^M p_{i2}, \dots, \frac{1}{M} \sum_{i=1}^M p_{id} \right) \end{array} \right., \quad (2)$$

where  $k$  and  $N$  are the current number and the maximum number of iterations, respectively.  $\phi$  is a random value of uniformly distributed in  $[0,1]$ .  $\beta$  is a coefficient of expansion and contraction, which is decreased adaptively from 1 to 0.5 according to the number of iterations.  $M$  stands for the size of the particle population, and  $mbest$  represents the mean best position of all particles.  $p_{id}$ ,  $pbest_{id}$  and  $gbest_d$  represent the current position, the individual and the global best position for the  $d_{th}$  dimension of the  $i_{th}$  particle, respectively.

### 3.2 Fitness Function Calculation

The system constraints are included in the objective function, which simplifies the decision process for constraints. The optimization under system constraints can be obtained by optimizing the objective function value directly in [6]. In this paper, the method is improved to reduce some custom parameters, thus less impact of human factors on the partitioning results. The optimal power for hardware/software partitioning problem under multiple constraints in (1) can be converted into a specific objective function

$$\min(\text{Power}) = A \times (f(x_A) + f(x_T) + f(x_C)) + B \times g(x_P) \quad (3)$$

There are two parts of the objective function: the system constraint information and the system optimization performance information.

In the function,  $f(x)$  and  $g(x)$  denote the system constraint penalty function and the objective performance function, which are specifically defined in (4) and (5), respectively.  $x_A$ ,  $x_T$ ,  $x_C$  and  $x_P$  represent the area consumed, the execution time, the development costs and the power consumption for all the system modules.  $A$

and  $B$  determine the ratio of the two parts of the objective function. The feasibility of the design is determined by the system performance demand, so  $A$  should be greater than  $B$ .

$$\left\{ \begin{array}{l} f(x) = \exp \left( \alpha \times \frac{x - x_L}{x_{\max} - x_{\min}} \right) \\ \text{s.t. } \alpha = \begin{cases} 1 & \text{if } x \leq x_L \\ K & \text{otherwise} \end{cases} \\ x_L = x_{\min} + \mu(x_{\max} - x_{\min}) \\ 0 < \mu < 1 \end{array} \right. \quad (4)$$

$$g(x) = \frac{x - x_{\min}}{x_{\max} - x_{\min}} \quad (5)$$

where  $x$ ,  $x_L$ ,  $x_{\max}$  and  $x_{\min}$  represent the performance parameters of system functions implemented (power, area, cost and time) corresponding to the current value, constraints, maximum and minimum values, respectively.  $x_L$  is a value between the minimum and maximum values, which can be regulated by the constraint factor  $\mu$ . The different performance indexes may not be bound by the same factor.  $\alpha$  is a penalty factor.  $K$  is a constant greater than 1, which is set to be 100 in the experiment. All parameters should be normalized because of different performance parameters at different magnitudes. The exponential function based on  $e$  and the penalty factors are used to make a larger penalty to the solution which does not meet the constraints, while the feasible solution is spared.

Among solutions that meet the constraints, the constraint value is much smaller than the value of default constraints, but the power consumption is not optimal. For example, with the same area, shorter running time comes along with higher power consumption. In addition, the module performance of the hardware modules implemented with FPGA is primarily improved through the parallel structure, which means that the parallelism is improved by increasing the system area and reducing the running time to reduce the power consumption. So the optimal partitioning is the one that exactly meets the system constraints, when the value of the objective function is the minimum.

According to the calculation value of the objective function, the calculation result that does not satisfy the constraints will be greater than the one that satisfies the constraints. The smaller the function value, the lower power the solution obtained consumes. Therefore, this paper takes the objective function as the fitness function of the particle to search for a particle with the smallest fitness, which is hardware and software partitioning solution with the lowest power.

### 3.3 Multi Neighborhood Optimization For Optimal Value

For better accuracy and convergence rate of the optimal solution, multiple neighborhoods of optimal value are searched for a better solution. One of the neighborhood positions is changed by the Gaussian random function each time, so a neighborhood particle of optimal value is obtained. The specific procedures are as follows.

- Step 1: A randomly-generated mutated position  $i$  is changed by using the Gaussian distribution function to obtain a new particle  $px_k$  ( $k=1,2,\dots,R$ ).
- Step 2: The fitness  $x_{fit_k}$  of the particle  $px_k$  is calculated using (3). If  $x_{fit_k}$  is smaller than the best fitness  $g_{fit}$ , one particle of the population will be replaced by  $px_k$  randomly to increase the population diversity.
- Step 3: The operations above are executed iteratively, until  $k = R$ .
- Step 4: Assume  $x_{fit}^* = \min\{x_{fit_1}, x_{fit_2}, \dots, x_{fit_S}\}$ , for  $x_{fit}^* < g_{fit}$ ,  $g_{fit} = x_{fit}^*$ ,  $g_{best}$  will be updated as the particle position.

### 3.4 Algorithm Process

The proposed multi-neighborhood particle swarm optimization (MNPSO) partitioning algorithm is improved based on the quantum-behaved particle swarm optimization algorithm, searching multi-neighborhood of optimal solution to improve the local searching ability of the algorithm. The specific steps of algorithm are as follows,

- Step 1: Population initialization. Each particle is composed randomly of 0 and 1, which are produced by the random function  $rand()$  for 2 modulo arithmetic.
- Step 2: The performance parameter information of system task is read from the task file. Each particle is combined with every task to obtain the performance parameters.
- Step 3: The fitness of each particle is computed by (3), and the individual best position  $p_{best}$  and the global best position  $g_{best}$  are selected.
- Step 4: If the end conditions (the maximum number of iterations or the number of the optimal value which hasn't changed) are met, go to Step 8. Otherwise, go to Step 5.
- Step 5: The mean position of all the particles  $m_{best}$  is calculated.
- Step 6: The global best solution  $g_{best}$  is searched for multi-neighborhood by multi-neighborhood optimization algorithm.
- Step 7: The particle position is updated using (2), and the fitness of each particle is computed by (3).  $g_{best}$  is updated. Return to Step 4.
- Step 8: The hardware/software partitioning result with optimal power is obtained, and the position information of  $g_{best}$  is output.

## 4 Experimental Analysis

In this section, the experimental results of the proposed approach are presented. The MNPSO algorithm is implemented in C language to evaluate the algorithm performance. Our approach is compared with the approaches GA, PSO and ACGSA by several experiments. There are 8 randomly generated TDFGs (using the TGFF tool) in which the number of nodes varies from 60 to 2000. For each graph, there are 4 different values which represent the power, area, cost and time for each task node. The parameters of objective functions A and B are set to be 0.6 and 0.4, respectively. The experiments are conducted on a PC with an Intel i7-2640 2.8GHz CPU and 4GB RAM main memory. Our simulator is developed in Microsoft VS2010 on the Windows 7 32bit operating system.

Random tasks of 200 nodes are tested by the MNPSO algorithm for 100 times to show the effect of different constraints on the partitioning results. The constraint factor of the development cost is set to be 0.8. The constraint factor of the system area grows from 0.125 to 1.0, and the constraint factor of the execution time increases from 0.2 to 0.8. The experimental results are shown in TABLE I. The symbol “v” indicates that the solution that satisfies constraints can be found each time, and the symbol “x” indicates that there is no solution that meets the constraints. The numerals in the table represent the number of found solutions that satisfy the constraints among 100 searches, as shown in Table 1.

**Table 1.** Effect of different constraints on the partitioning results

Constraints	$\mu_T(1/5)$	$\mu_T(2/5)$	$\mu_T(3/5)$	$\mu_T(4/5)$
$\mu_A(1/8)$	x	x	x	x
$\mu_A(2/8)$	x	x	x	x
$\mu_A(3/8)$	x	x	1	59
$\mu_A(4/8)$	x	x	v	v
$\mu_A(5/8)$	x	v	v	v
$\mu_A(6/8)$	x	v	v	v
$\mu_A(7/8)$	v	v	v	v
$\mu_A(1)$	v	v	v	v

The more stringent the constraints, the lower probability for solutions that can meet constraint conditions to be found. For the same time constraint factor  $\mu_T(4/5)$ , there is a probability of 59% to obtain a solution under the area constraint factor  $\mu_A(3/8)$ , but there is no solution that satisfies the constraints under some smaller area

constraints (indicated by "x"), and under a larger area constraints, the probability is 100% to find a solution that meets the constraints (indicated by "v").

The GA, PSO, ACGSA and MNPSO algorithms are implemented with several tests for the power optimization of hardware/software partitioning under the time constraint factor  $\mu_T(4/5)$  and the cost constraints factor  $\mu_C(4/5)$ . Each test runs 100 times to calculate the average power consumption of optimal partitioning solution, as shown in Table 2.

**Table 2.** Table Type Styles

Nodes	Max Power	Area constraint factor $\mu_A(1/2)$				Area constraint factor $\mu_A(3/4)$			
		GA	PSO	ACGSA	MNPSO	GA	PSO	ACGSA	MNPSO
60	23.4	21.99	21.99	21.85	21.85	21.33	21.23	21.08	21.08
120	44.5	41.68	41.63	41.33	41.33	40.46	40.32	39.93	39.93
200	82.67	74.85	74.35	73.12	72.80	71.51	69.66	68.23	68.12
300	141.34	123.32	122.14	119.34	118.57	115.92	112.00	108.26	107.81
500	255.68	213.45	212.43	207.15	205.33	198.63	191.88	182.61	181.37
800	452.68	368.49	365.85	354.29	351.08	335.84	326.68	305.21	302.73
1000	610.37	485.35	481.43	462.60	458.54	437.33	423.94	388.45	385.42
2000	1516.68	1123.42	1118.96	1072.56	1062.65	1022.81	988.81	853.45	846.55

When the task system is small-scale (less than 300 nodes), the power of partitioning results are obtained by the four algorithms are close. With the increasing size of the system, the difference between the algorithms is gradually displayed. When the area constraint factor is stringent ( $\mu_A(1/2)$ ), the GA falls into the local optimal value more easily than the other three algorithms. When the area constraint factor is loose ( $\mu_A(3/4)$ ), the GA algorithm is converged prematurely due to the lack of local searching ability, while the PSO algorithm obtains a solution with lower power consumption due to the larger flying space of the particle. The local search ability of ACGSA is enhanced by introducing the chaos, annealing, and other optimization strategies, thus better results by the ACGSA. But the proposed MNPSO algorithm achieves a even better solution with lower power consumption than the other three algorithms under different sizes and different constraints of system, for searching multi neighborhood of the optimal solution. With the increase of the system size, more power consumption is reduced. Further, since the power consumption of FPGA is reduced by increasing the system area, a smaller area constraint leads to a higher power consumption, a fact verified by the results shown in Table 2.

In order to analyze power consumption saving, the power consumptions in Table 2 are compared with the maximum power of the same system size under the

area constraints factor  $\mu_A$  ( $3 / 4$ ) , as shown in Figure 1. With the increase of the system size, the power consumption of hardware /software partitioning solution obtained by each algorithm is continuously decreased. For the task system with 60 task nodes, the GA and PA achieve power reductions of 8.8% and 9.2%, respectively, and the other two algorithms reduce power consumption by 9.9%. For the task system with 500 task nodes, compared with the maximum power, the power obtained by the GA, PSO, ACGSA and MNPSO algorithm are much lower, saving 22.3%, 24.9%, 28.6%, and 29.1% power, respectively. For the task system with 1000 task nodes, the power by all the four algorithms is reduced more than 28%, with the MNPSO achieves the greatest reduction of power (36.9%). When the task nodes are increased to 2000, the power by the four algorithms is reduced more than 32%, with the MNPSO algorithm reducing by up to 44.2%. Compared with the ACGSA, GA and PA, the MNPSO achieves power reduction increases of 0.5%, 9.4% and 11.7%, respectively.

According to the algorithm time complexity analysis, the computational complexity of the GA, PSO, ACGSA and MNPSO are  $O(N \times n \times m)$  , where  $N$  is the number of loop iterations,  $n$  is the population size, and  $m$  represents the number of task nodes. Since the crossover and mutation operation of genetic algorithm are executed for the entire population, the searching time of the GA is approximately twice the time of the PSO. The chaos and the annealing optimization algorithms are introduced into the ACGSA based on the genetic algorithm which takes the longest time for searching. A better partitioning solution is obtained at the expense of the search time. Although the multi-neighborhood searching of the optimal solution is introduced into the MNPSO algorithm in this paper, its computational complexity is much smaller than the population size, so that the searching for the optimal solution is significantly accelerated. The searching time of the proposed algorithm is less than the time of the other three algorithms.

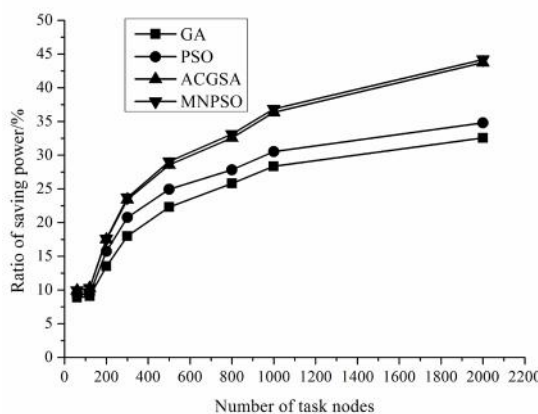


**Figure 1.** Ratio of saving power consumption for the partitioning algorithm results.

This paper compares the searching time of four algorithms under the area constraint factor  $\mu_A (3 / 4)$ , as shown in Figure 2. With the growth of the system size, the algorithm searching time increases, where the searching time of the ACGSA grows the fastest, and that of the MNPSO grows the slowest.

When the task system is small-scale (less than 300 nodes), except the ACGSA, the time of the other three algorithms is very closer, i.e., less than 1s. For 300 task nodes, the searching time of the ACGSA is the longest, i.e., more than 1.7s, while those of the PSO and the MNPSO are less than 0.5s and 0.3s, respectively. Although the ACGSA has better optimum performance, it takes a long time to search. Less searching time is needed by the proposed MNPSO algorithm due to the strong astringent properties, with a longest searching time of less than 2s.

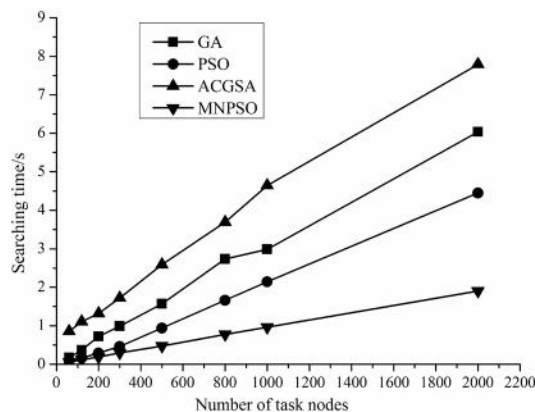


**Figure 2.** Comparison of algorithm searching time.

According to the obtained experimental results, the MNPSO achieves the optimal partitioning solution most quickly. For the system with 2000 task nodes, when the factors of the time constraints and the cost constraints are 0.8, and the area constraint factor is  $\mu_A (3 / 4)$ , the MNPSO achieves a 44.2% power reduction in 1.9s, while by GA it takes three times as long to achieve a 32.5% power reduction, by PSO it takes 2.3 times as long to achieve a 34.8% power reduction, and by ACGSA it takes 4.1 times as long to achieve a similar power reduction, which is still 0.5% lower than that obtained by the MNPSO. Therefore, in terms of the optimal power for hardware/software partitioning search algorithms, the MNPSO algorithm is a time-saving partitioning algorithm.

## 5 Conclusion

This paper proposes a multi neighborhood particle swarm optimization algorithm for the optimal power of hardware/software partitioning under multiple constraints. The mean best position of all particles is introduced into the particle position status updating, and the optimal solution is searched for better solution in multi-neighborhood to expand the local search capacity. The Gaussian distribution is used to generate mutated position information and increase the population diversity. A multi-constraint penalty function is integrated into the calculation of the objective function, speeding up the searching of partitioning solution under the system constraints. Experimental results show that the algorithm effectively achieves hardware and software partitioning for power optimization. Compared with the GA, PA and ACGSA, the proposed algorithm achieves a better partitioning solution with lower power consumption in shorter time under multiple constraints.

**Acknowledgment:** This work is supported in part by the national natural science foundation of China under Grant No. 61474087, and the Fundamental Research Funds for the Central Universities under Grant No. JB150315.

## References

- [1] E. Azari and H. Koc, Improving Performance through Path-Based Hardware/Software Partitioning, Proc. of the 2015 Fifth International Conference on Digital Information Processing and Communications (ICDIPC), IEEE Press, Oct. 2015, pp.54-59, doi:10.1109/ICDIPC.2015.7323005.
- [2] Y. Hou, R. Wang, Y. Jiang, Y. Guan, X. Li and Z. Shi, et al. Embedded System Design with Reliability-Centric Optimization, Proc. of the 2015 IEEE 39th Annual International Computers, Software & Applications Conference, IEEE Press, July 2015, pp.33-38, doi: 10.1109/COMPSAC.2015.40.
- [3] N. Janakiraman and P. N. Kumar, A Novel Hardware/Software Partitioning Technique for System-on-Chip in Dynamic Partial Reconfiguration Using Genetic Algorithm, Proc. of the Second International Conference on Soft Computing for Problem Solving (SocProS 2012), Springer Press, Feb. 2014, pp.83-91, doi: 10.1007/978-81-322-1602-5\_10.
- [4] A. Liu, J. Feng, X. Liang and X. Yang, Algorithm of hardware/software partitioning based on genetic particle swarm optimization, Journal of Computer-Aided Design & Computer Graphics, vol.22, June 2010, pp. 927-933+942, doi: 10.3724/SP.J.1089.2010.10834.
- [5] Y. Jing, J. Kuang, J. Du and B. Hu, Application of Improved Simulated Annealing Optimization Algorithms in Hardware/Software Partitioning of the Reconfigurable System-on-Chip, Proc. of the 25th International Conference on Parallel Computational Fluid Dynamics (ParCFD 2013), Springer Press, May 2014, pp.532-540, doi: 10.1007/978-3-642-53962-6\_48.
- [6] Y. Cui, X. Qiu, J. Zhang and D. Zhou, SoC hardware/software partitioning algorithm for multi-performance index constraints, Journal of Xidian University(Natural Science), vol.40, Oct.2013, pp.92-98, doi:10.3969/j.issn.1001-2400.2013.05.015.

- [7] Y. Ma, J. Liu, C. Zhang and W. Luk, HW/SW Partitioning For Region-based Dynamic Partial Reconfigurable FPGAs, Proc. of the 2014 32nd IEEE International Conference on Computer Design (ICCD), IEEE Press, Oct.2014, pp.470-476, doi:10.1109/ICCD.2014.6974721.
- [8] G. Jiang, J. Wu, S. K.Lam, T. Srikanthan and J. Sun, Algorithmic aspects of graph reduction for hardware/software partitioning, Journal of supercomputing, vol.71, June 2015, pp.2251-2274, doi: 10.1007/s11227-015-1381-4.
- [9] J. Wu, P. Wang, S. K.Lam and T. Srikanthan, Efficient heuristic and tabu search for hardware/software partitioning, Journal of supercomputing, vol.66, Oct. 2013, pp.118-134, doi: 10.1007/s11227-013-0888-9.
- [10] W. Shi, J. Wu, S. K.Lam and T. Srikanthan, Algorithms for bi-objective multiple-choice hardware/software partitioning, Computers and Electrical Engineering, vol.50, Feb. 2016, pp.1-16, doi: 10.1016/j.compeleceng.2016.01.006.
- [11] J. Zhang, D. Zhou, and Y. Yang, System Reliability-Aware Energy Optimization for Network-on-Chip with Voltage-Frequency Islands, Proc. of the 2013 International Conference on Information Science and Cloud Computing Companion (ISCC-C), IEEE Press, Dec. 2013, pp.117-122, doi: 10.1109/ISCC-C.2013.133.

Zhi XIE\*, Jia-ju WANG, Chen LIU, Wei-min CHEN

## Research of Metering Arithmetic for Distortion Power

**Abstract:** Under the condition of voltage and current waveform distortion, in order to make the metering fair and rational, this paper proposed measurement model of fundamental wave plus harmonics wave and the distortion power algorithm. Studied and compared two measurement models, namely fundamental wave and full wave, a mixed measurement model of fundamental wave plus harmonic wave is proposed. Then, the distortion power calculation formula and algorithm are proposed based on the definitions recommended in IEEE Std 1459-2010, and analyzed the feasibility of the proposed method in combination with the existing smart meter technology. By field measuring data validated that, the proposed distortion power metering is necessary and the algorithm is practical.

**Keywords:** distortion power; metering algorithm; smart meter; field recorded data validation

### 1 Introduction

The electrical energy metering, as the main evidence of economic accounting in power grid, its accuracy and rationality is related to the economic benefits of power supply and demand [1,2]. With the development of power electronics technology, more and more nonlinear load were connected to power grid and produced a large number of harmonic, that has an passive affect on the rationality of smart meter which is designed for using in the traditional sinusoidal fundamental frequency [3-5]. Therefore, it is necessary to study the power measurement algorithm of nonlinear load, and the key point is the distortion power metering algorithm.

At present, a lot of researches have been carried out on the definition and metering of distortion power, but still have some controversy. IEEE Std 519-2014 [6] specifies maximum limits for the harmonic current and harmonic voltage magnitudes, but can not meter distortion power accurately just by these values. Budeanu described distortion power as the remaining quantity of apparent power, active power and reactive power [7], the definition of distortion power meet power conservation relationship, but do not possess the attributes which can be related to the power phenomena in circuits with nonsinusoidal waveforms [8]. Fryze proposed a definition

---

\*Corresponding author: Zhi XIE, State Grid Sichuan Electric Power Corporation Metering Center, Chengdu, China, E-mail: sy\_uanea@163.com

Jia-ju WANG, Chen LIU, Wei-min CHEN, State Grid Sichuan Electric Power Corporation Metering Center, Chengdu, China

of current component [9], which is clear and correct in physical and mathematical, but not revealing all the details of the instantaneous power and not representing the true mechanism of energy transfer to the load. Depenbrock improved on Fryze's method, creating a more detailed current component [10], he defined distortion current equal difference between wattles current and fundamental reactive current, but not gave complete physical explanation. Czarnecki's model is more complete, can explain the power flow in detail [11], but the complexity of the decomposition method also make it difficult to implement in practical project.

Based on the recommended definitions of distortion power in IEEE Std 1459-2010 [12], which meet the electromagnetic distortion energy flow physics laws when voltage and current occur distortion, this paper proposed the distortion power metering algorithm, and analyzed the feasibility in combination with the existing smart meter technology. As a case study, field recorded data in one iron and steel plant is used to validate the proposed distortion power metering algorithm.

## 2 Measurement model

Established a single-phase circuit with nonlinear load and linear load, as shown in Figure 1. AC represent a sine alternating current source, which amplitude is 100 V. The ideal rectifier diode D series resistance  $R_3$  is used to represent the nonlinear load. The value of  $R_1$ ,  $R_2$  and  $R_3$  equal  $2\Omega$ ,  $10\Omega$  and  $10\Omega$ , respectively.

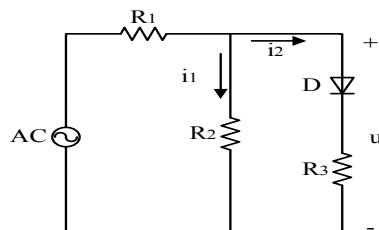


**Figure 1.** Single phase circuit model including linear and nonlinear loads

Perform Fast Fourier Transform (FFT) on the voltage and current data of linear and nonlinear loads as follows

$$X(k) = \sum_{n=0}^{N-1} x(n) e^{-j \frac{2\pi}{N} n} \quad (1)$$

The results are showed in Table 1. Using the data of Table 1, calculated power value of linear and nonlinear load in the measurement model of fundamental wave and full wave, respectively. The results are showed in Table 2.

**Table 1.** Current and voltage data

U	Current of linear load I1		Current of nonlinear load I2	
	Amplitude(V)	Phase angle	Amplitude(A)	Phase angle
0th	3.79	270	0.379	270
1th	77.38	0	7.738	0
2th	2.5225	90	0.2523	90
4th	0.0164	90	0.00164	90
6th	4.5911 E-05	90	4.5911 E-06	90
8th	7.3458 E-08	90	7.3458 E-09	90
RMS	77.514	—	7.751	—

**Table 2.** Power values

		Linear load	Nonlinear load
Fundamental wave	P <sub>1</sub>	598.76	276.32
	Q <sub>1</sub>	0	0
Full wave	P	600.84	267.71
	Q	0	3.83
	S	600.84	349.54

Where

$$P_1 = V_1 I_1 \cos \theta_1 \quad (2)$$

$$P = \sum_{h=0}^N P_h = \sum_{h=0}^N V_h I_h \cos \theta_h \quad (3)$$

As it can be seen from Table. 2, under the measurement model of full wave, linear load absorb fundamental and harmonic power and they are in the same direction, thus metering result is greater than fundamental power; nonlinear load absorb fundamental power and inject harmonic power, the metering is lesser than fundamental power. In other words, nonlinear load inject harmonic that pollute power grid, at the same time, the metering result is lesser. Therefore, the measurement model is unfair.

Under the measurement model of fundamental wave, linear and nonlinear load both only be metered fundamental wave. It is fair for linear load, but neglect the harmonic pollution that nonlinear load produced.

In conclusion, the rationality of the measurement model of full wave and fundamental wave both exist shortcoming, cannot satisfy requirement of metering. Thus, the measurement model of fundamental wave plus harmonic wave is another choice, but still need study distortion power definition and metering algorithm.

### 3 Distortion power metering algorithm

#### 3.1 The recommended definitions in IEEE Std 1459-2010

Under stationary conditions, voltage and current that occur distortion can be decomposed into power frequency component and the rest of the component, be represented by  $v_1$ ,  $i_1$ ,  $v_h$  and  $i_h$ , respectively. Power frequency voltage components as reference, then

$$\begin{aligned} v &= v_1 + v_h \\ i &= i_1 + i_h \end{aligned} \quad (4)$$

Where:

$$v_1 = \sqrt{2}V_1 \sin wt \quad (5)$$

$$v_h = V_0 + \sqrt{2} \sum_{h \neq 1} V_h \sin(hwt + \alpha_h) \quad (6)$$

$$i_1 = \sqrt{2}I_1 \sin(wt - \theta_1) \quad (7)$$

$$i_h = I_0 + \sqrt{2} \sum_{h \neq 1} I_h \sin(hwt + \beta_h) \quad (8)$$

With the root mean square (RMS) value can be represented as:

$$V^2 = V_1^2 + V_H^2; \quad V_H^2 = \sum_{h \neq 1} V_h^2 \quad (9)$$

$$I^2 = I_1^2 + I_H^2; \quad I_H^2 = \sum_{h \neq 1} I_h^2 \quad (10)$$

According to type (9) and (10), apparent power can be decompose as follows

$$\begin{aligned} S^2 &= V^2 I^2 = (V_1^2 + V_H^2)(I_1^2 + I_H^2) \\ &= (V_1 I_1)^2 + (V_1 I_H)^2 + (V_H I_1)^2 + (V_H I_H)^2 \\ &= S_1^2 + D_I^2 + D_V^2 + S_H^2 \end{aligned} \quad (11)$$

Where  $DI$ ,  $DV$  and  $SH$  are defined as current distortion power, voltage distortion power and harmonic apparent power, respectively.

In the type (11), harmonic apparent power can be decomposed into two component, namely active harmonic power  $PH$  and distortion power  $DH$ , respectively.

$$S_H = \sqrt{P_H^2 + D_H^2} \quad (12)$$

Where

$$P_H = \sum_{h \neq 1} V_h I_h \cos \theta_h \quad (13)$$

Total harmonic voltage and current distortion is defined as:

$$\begin{aligned} THD_V &= \frac{V_H}{V_1} = \sqrt{\sum_{h \neq 1} \frac{V_h^2}{V_1^2}} \\ THD_I &= \frac{I_H}{I_1} = \sqrt{\sum_{h \neq 1} \frac{I_h^2}{I_1^2}} \end{aligned} \quad (14)$$

According to type (12) to (14), distortion power can be calculated as follows

$$D_H = \sqrt{S_1^2 (THD_V)^2 (THD_I)^2 - P_H^2} \quad (15)$$

Based on the definition of IEEE Std 1459-2010, apparent power decomposition as shown in Figure. 2.

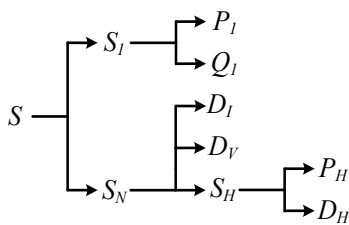


**Figure 2.** Apparent power decomposition based on IEEE Std 1459-2010

### 3.2 Distortion power metering in smart meter

The common smart meter is composed of measurement, data processing, communication and other units. The electric energy metering chip can measure and store the real-time voltage and current data. In the case of RN 83208 metering chip, can chose sample frequency 6.4 kHz, and it will meet the needs of harmonic analysis in the scope of 64 harmonic frequency spectrum, according to the Nyquist sampling theorem. The chip can store data of voltage, current, fundamental apparent power and apparent power.

According to type (13), calculate distortion power  $D_H$  need known the value of fundamental apparent power  $S_1$ , total harmonic voltage distortion  $THD_V$ , and total harmonic current distortion  $THD_I$ . Therefore, smart meter only need to perform FFT on the voltage and current data, and then acquisition amplitude and phase of voltage and current in each frequency spectrum. After calculate  $THD_V$ ,  $THD_I$  and  $P_H$ , get further calculate distortion power  $D_H$  according to type (15). The distortion power algorithm flow as shown in Figure 3.

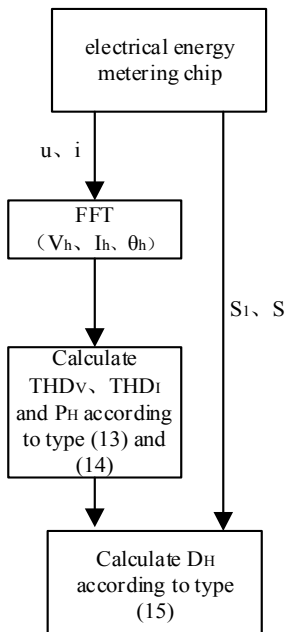


**Figure 3.** The algorithm flow chart of distortion power

#### 4 Field test verification

In this section, the practical of the proposed distortion power algorithm is evaluated by using the actual field recorded data. The field measurement was carried out at a refining furnace in one iron and steel plant in 2 hours, the sample frequency is 1000 Hz. Considering the recommended in IEC Std 61000-4-30 [13], data processing per 200 ms, calculate and record the full wave and fundamental wave apparent power. According to Figure 3, the FFT is applied to acquisition amplitude and phase of voltage and current in each frequency spectrum, total 36,000 groups of data. The value of THD<sub>v</sub> and THD<sub>i</sub> as shown in Figure 4. Refining furnace is arc load and is the main harmonic source in iron and steel plant. The result show that the maximum of THD<sub>v</sub> and THD<sub>i</sub> is 4.09% and 92%, respectively.

Using the calculated data of THD<sub>v</sub> and THD<sub>i</sub>, included the measurement data of the full wave and fundamental wave apparent power, calculated distortion power D<sub>H</sub> according to type(15). The Result of full wave and fundamental wave apparent power and distortion power are showed in Table. 3.

As it can be seen from Table 3, the maximum of distortion power D<sub>H</sub> is 38.41 kW in the test period, and the average value is 11.35 kW. Assumed the refining furnace work 5000 hours in a year, calculate by the average value in the test period, then the

distortion energy of the refining furnace is 56772 J. Illustrates that it will cause unfair metering and economic loss if neglect distortion energy.

From Figure 3, this paper proposed the distortion power algorithm based on IEEE Std 1459-2010 is clear and easy to implement just need to improve exist smart meter.

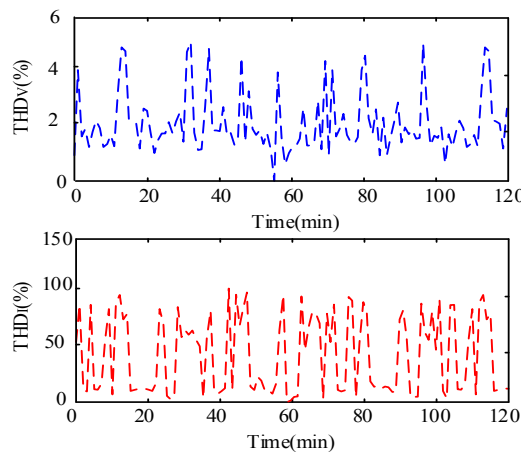


**Figure 4.** The trend chart of THD<sub>v</sub> and THD<sub>l</sub>

**Table 3.** POWER VALUES FOR FURNACE

	Maximum (kW)	Minimum (kW)	Average (kW)
S	10584.63	636.07	3455.36
S <sub>1</sub>	9377.49	553.01	3584.67
D <sub>H</sub>	38.41	1.42	11.35

## 5 Conclusion

- (1) By simulation a simple system model with linear and nonlinear load, proved that the irrationality of the measurement model of fundamental wave and full wave, and then proposed a measurement model named “fundamental wave plus harmonic wave”, and the distortion power metering is the key;
- (2) According to the recommended definitions of distortion power in IEEE Std 1459-2010, considered the existing smart meter technology, this paper proposed the distortion power metering algorithm.
- (3) Through field test validated that, the proposed distortion power metering algorithm is reasonable and feasible.

**Acknowledgement:** This work was supported by project: Research of Electric Energy Measurement and Power Consumption Information Collection for Grid-Integration of Distributed Resources, in part by Grid Sichuan Electric Power Corporation Metering Center, and in part by State Grid Tianfu Electric Power Company, and in part by State Grid Panzhihua Electric Power Company.

## References

- [1] Yu Xiu-na. Effect of Harmonics on Electric Energy Measurement [J]. Statistics and Management, 2014, 10:159-160
- [2] Ju Han-ji, ZHENG Li-ping. Electricity Metering Equipment Radiated Emission Test System Design and Analysis Electrical[J] Measurement & Instrumentation, 2013, 50(11):16-21
- [3] LI Bin-qin, CHEN Wei-gen. Analysis on Affects of Harmonics on Active Energy Metering Devices [J]. Power System Technology, 2010, 34(6):154-159
- [4] Yang Jin-tao, LE Jian. Analysis of Measurement Error for Electric Energy Metering System under Harmonic Conditions [J]. Automation of Electric Power Systems, 2015, 39(13):144-150
- [5] Wang Ni, LE Jian. Quantitative Analysis on Measuring Errors of Time Division Multiple under Harmonic Conditions [J]. Automation of Electric Power Systems, 2014, 38(23):71-76
- [6] IEEE 519-2004. IEEE Recommended Practices and Requirements for Harmonic Control in Electric Power Systems [S]. New York: IEEE Press, 2004
- [7] Budeanu C I. Puissance Reactive et de Fictive [M]. Institut National Roumain pour l'Etude de l'Amenagement et de l'Utilisation des Sources d'Energie, Bucarest, 1927
- [8] Czarnecki L S. What is Wrong with the Budeanu Concept of Reactive and Distortion Power and why it should be Abandoned [J]. IEEE Trans on Instrumentation and Measurement, 1987, 36(3):834-837
- [9] Fryze S. Effective, Wattles and Apparent Power in Circuits with Nonsinusoidal Waveforms of Current and Voltage [J]. Elektrotechnische Zeitschrift, 1931, 25:596-599, 625-627
- [10] Depenbrock M. The FBD-Method, A Generally Applicable Tool for Analyzing Power Relations [J]. IEEE Trans On Power Systems, 1993, 8(2):381-387
- [11] Czarnecki L S. Considerations on the Reactive Power in Nonsinusoidal Situations [J]. IEEE Trans on Instrumentation and Measurement, 1985, 34(3):399-404
- [12] IEEE 1459—2010 IEEE Standard Definitions for the Measurement of Electric Power Quantities under Sinusoidal, Non-Sinusoidal, Balanced, or under Balanced Conditions[S]
- [13] IEC 64000-4-30, Power Quality Measurement Method[S]

Gui-tian GONG\*, Hai-feng CHEN

## Study of the Influence of the Diode Ideality Factor on the Si Solar Cell

**Abstract:** This paper studies the influence of the Diode Ideality Factor  $n$  values on the characteristics of a Si solar cell. It focuses on the influence of different  $n$  values on the output result respectively in a standard and different environments. Based on the I-V and P-V curves obtained from the simulation using MATLAB software, a mathematical model of solar cells is obtained. It is found that  $n$  value is linearly related to the maximum output power and the influence of difference  $n$  value on maximum output power is significant under the different illumination and temperature.

**Keywords:** component; diode ideality factor; model; power

### 1 Introduction

The solar cell has been greatly developed as a clean and renewable energy technology in recent years. Due to the effect of temperature and light intensity on power generation, its curves of I-V and P-V both present nonlinear variations. Under the condition without considering the environment, the factors influencing the output characteristic curve also include solar cell materials, equivalent series-parallel resistance and diode ideality factor and etc. In the literature [1-3], all of the simulations of solar cells ignore the influence of solar cells' characteristics on the output power and just focus on the influence of external temperature and illumination on the I-V and P-V curves. In the literature [6], the photo-generated electromotive force in solar cells is mentioned to cause the forward bias for a PN junction and then generate a leakage current flowing through the diode. It also found that the size of the diode-ideality-factor  $n$  depends on the size of the leakage current. However, the value of  $n$  is often an artificially fixed value in the above literatures. Because  $n$  influences the simulation process and its different value should lead to the different simulation results. So it is necessary to study the influence of  $n$  on the output results of the simulation.

This paper investigates the influence of  $n$  on the simulation for solar cells in MATLAB/Simulink environment. Under different  $n$  values, the simulation of I-V and P-V output curves of solar cells are simulated. More details are shown in the following sections.

---

\*Corresponding author: Gui-tian GONG, Xi'an University of Posts and Telecommunications, School of Electronic Engineering, Xi'an, China, E-mail: 328335060@qq.com

Hai-feng CHEN, Xi'an University of Posts and Telecommunications, School of Electronic Engineering, Xi'an, China

## 2 Classical I-V model of solar cells and ideal factor n

The I-V equation of solar cell can be given according to the equivalent circuit[3].

$$I = I_L - I_s \left[ \exp\left(\frac{V + R_s}{nkT N_s / q}\right) - 1 \right] - \frac{V + R_s}{R_p} \quad (1)$$

Where,  $R_s$  means the equivalent series resistance and  $R_p$  is the equivalent parallel resistance.  $n$  is the diode ideality factor and  $k$  is the Boltzmann constant.  $q$  is the charge constant.  $N_s$  and  $T$  are the number of series unit and the battery temperature( $^{\circ}$ F), respectively.

From the I-V equation, it can be concluded that the values of  $I_L$ ,  $I_s$ ,  $R_s$ ,  $R_p$ ,  $N_s$  must be obtained at first in order to get the I-V curve. However, those values are all sensitive to specific environment, battery temperature and illumination intensity. Generally speaking, their values under the specific circumstances can be calculated via the equations in the [1,2,7].

The simulation model built in the MATLAB/SIMULINK can be obtained under the condition of corresponding solar cells I-V, P-V curves.

It can be concluded from (1) that the diode ideality factor  $n$  is another reference which can influence the I-V characteristic. However, in most cases the value of  $n$  given in the simulation does not regard to its influence on the simulation result. And this thesis will give analysis to the different values of diode ideality factor.

There is a leak current in the real solar cell due to the forward bias of PN junction caused by photo-induced voltage, which flows in the opposite direction of the light-generated current, offsetting part of light-generated current. At the time of I-V curve fitting, superposition is conducted to two diodes to simulate the dark features of solar cell.  $I_{s1}$  is used to denote the recombination saturation current flowing through the body area or the surface trap level, and the corresponding  $n=1$ ;  $I_{s2}$  is made to denote recombination saturation current flowing through PN junction or crystal boundary depletion region, and the corresponding  $n=2$ . Thus the I-V curve can be interpreted as[6]:

$$\begin{aligned} I &= I_L - I_{s1} \left\{ \exp\left[\frac{q(V + R_s)}{kTN_s}\right] - 1 \right\} \\ &\quad - I_{s2} \left\{ \exp\left[\frac{q(V + R_s)}{2kTN_s}\right] - 1 \right\} - \frac{V + R_s}{R_p} \end{aligned} \quad (2)$$

It can be seen from (2) that different  $n$  values lead to different maximum power output. Thus it is important to choose a reasonable value of  $n$  for carrying out simulation to solar cell.

## 3 Simulation and analysis of ideality factor n

According to the aforementioned mathematical modeling, the simulation modeling on solar cell can be carried out in the MATLAB/Simulink environment. This thesis

hereby simulates the solar panel. Detailed references of the panel are available in table (1) below:

**Table 1.** Detailed references of solarex msx60 solar panel

TYPE	solarex	MSX60
Max-power	$P_m(W)$	60
Max-power Voltage	$V_m(V)$	17.1
Max-power Current	$I_m(A)$	3.5
Open-Circuit Voltage	$V_{oc}(V)$	21.0
Short-Circuit Current	$I_{sc}(A)$	3.74
Isc Temperature Coefficient	(%/°C)	0.24
Voc Temperature Coefficient	(%/°C)	-0.22

Through the simulation, the I-V and P-V output characteristic curves under the different n values are all in standard environment ( $T = 25^\circ\text{C}$ , illumination intensity  $S = 1000\text{W/m}^2$ ). The results are shown in the Figure 1 and Figure 2.

From the Figure 1 and Figure 2, it can be seen that in a standard environment, the curvature degree of I-V curve decreases with the increase of n value. The smaller the n value is, the more similar the curve is to a rectangle. And the greater the n value is, the more similar the curve is to a triangle. It can see from Figure 1, the P-V curve approaches its maximum power point when  $n=1$ , and the maximum output power decreases linearly with increasing n. Figure 3 abstracts the total maximum powers under the different n from Figure 1 through integration, as shown in Figure 3.

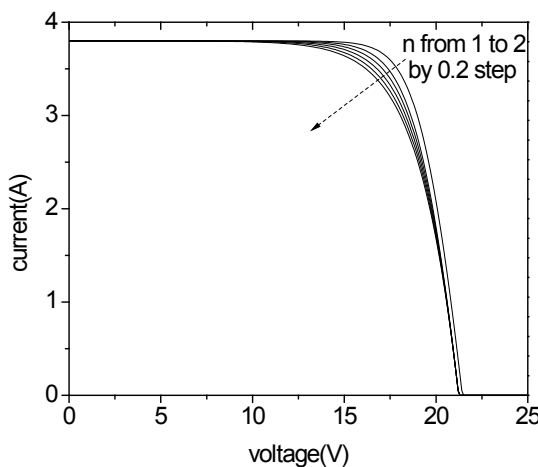


**Figure 1.** Simulated I-V curves at different n

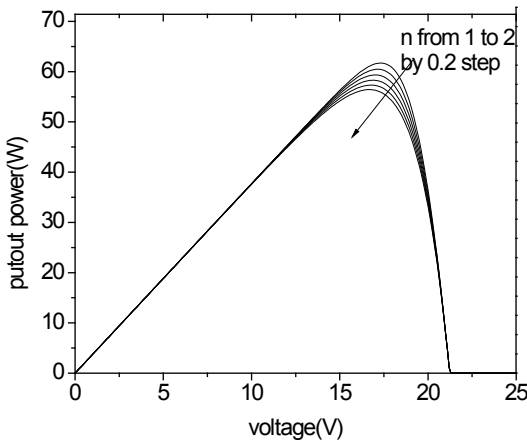


**Figure 2.** Simulated P-V curves at the different n

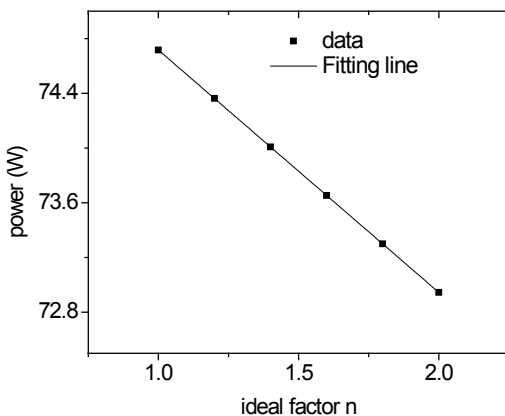


**Figure 3.** The output total power curve of different n value

From Figure 3, the solar cells total output power decreases with increasing n. It is found that the total maximum powers has the linear relationship with the n. The linear relationship is as following:

$$P = a \times n + b \quad (3)$$

Where a and b are the coefficients. a is the slope of the line and is -1.77 in this paper. b is the intercept of the fitting line and the different solar cells with different b values.

Under the standard environment, the n value should influence the I-V and P-V curves of solar cells. But the temperature and illumination intensity are changing all the time in an actual environment. So the maximum output power of different n value at 25°C under the different illumination intensity is as shown in Figure 4.

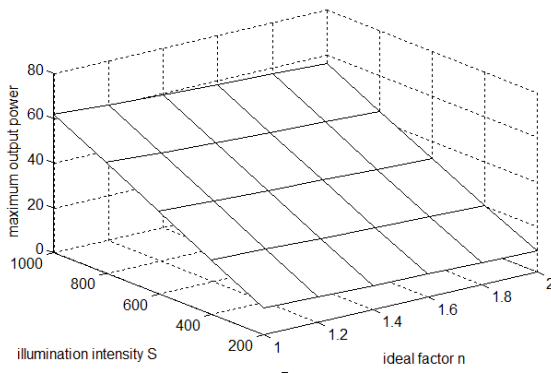


**Figure 4.** Maximum power of different n value at 25 °C under the different illumination intensity

It can be seen from Figure 4 that the illumination intensity influences the output power much more than n. But to maximize the conversion efficiency of solar cells, the selection of n value is very important. From Figure 4, it can be also seen that the growth rate of maximum output power corresponding to the illumination intensity in the case of n between 1 and 1.3 is maximum.

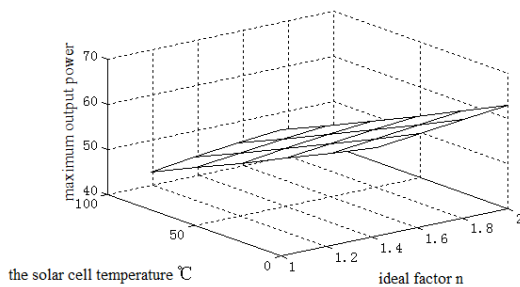


**Figure 5.** The maximum output power of different n value under the illumination intensity of  $S=1000\text{W}/\text{m}^2$  at different temperature

Figure 5 shows the maximum output power of different n value under the illumination intensity of  $S=1000\text{W}/\text{m}^2$  at the different temperature. From Figure 5, it can be seen

that when the temperature and n value influence the maximum output power under certain illumination intensity, the temperature plays the leading role. The lower the temperature is, the larger the maximum output power will be. However, it can also be seen that the growth rate of maximum output power corresponding to the temperature under the n between 1 and 1.3 should be the maximum.

Combined with the results of Figure 4 and Figure 5, an important conclusion about the influence on the output characteristics of solar cells is given as following:

$$\text{Illumination-intensity} > \text{temperature} > n$$

On the basis of the analysis of actual situation and simulation results, it can be seen that the diode ideality factor n cannot be 1 when the recombination saturation current flowing through the body area or the surface trap level and recombination saturation current flowing through PN junction or crystal boundary depletion region exist together. Therefore, in the actual situation, it is necessary to improve the illumination intensity and make the n value between 1.1 and 1.3 in order to achieve the maximum conversion efficiency of PV cells.

## 4 Conclusion

This paper discusses the influence of different n on the output characteristics. It set up a model and do the simulation under the MATLAB/SIMULINK environment. The simulation results shows that n values influence the I-V and P-V output characteristics of solar cells. Further, it is found that n value is linearly related to the maximum output power and the slope is -1.77, and the influence of difference n value on maximum output power is significant under different illumination and temperature.

The results of this paper should be helpful for the studies of characteristics of a Si solar cell.

**Acknowledgments:** This work is Supported by the National Natural Science Foundation of China (Grant No.61306131).

## References

- [1] YANG Yongheng and ZHOU Keliang, Photovoltaic Cell Modeling and MPPT Control Strategy, Transactions of China Electrotechnical Society, vol. 26, 2011, p. 230.
- [2] Villalva M G, Gazoli J R, Filho E R. Comprehensive approach to modeling and simulation of photo voltaic arrays, IEEE Transaction on Power Electronics, 2009, p. 1200.
- [3] CAI Xichen. Based on the constant voltage and impedance matching method of MPPT algorithm research, Hubei Wuhan University, 2012, p. 7.

- [4] LIU Enke, ZHU Bingsheng, LUO Jinsheng. Semiconductor Physics, Electronic Industry Press, 2011, p. 296.
- [5] ZHANG Xing, HUANG Ru, LIU Xiaoyan. Introduction to Microelectronics, Peking University Press, 2010, p. 270.
- [6] Martin A.Green. PV cells Operating Principles(Australia), Technology and System Application, Duxiu Database, 2011, p. 60.
- [7] CUI Yan, CAI Binghuang, LI Dayong and so on. Acta Energiae Solaris Sinica, 2006, p. 532.

Wei SONG\*, Huai-yuan LIU, Bin XIANG, Hong HU, Cheng-jiang WANG, Ling-yun WAN

## Application of the Haar Classifier in Obstacle Target Detection

**Abstract:** Aimed at obstacles on 500kV high voltage transmission lines, such as shockproof hammers, spacers and suspension clamps, a strong classifier with high recognition accuracy and fast speed is proposed in this paper by using a collection of video files, extracting Haar-like features of the target object, and combining the optimal weak classifier through a filter cascade. In the process of feature extraction, extended Haar-like features and the integral graph method with high efficiency are applied. The experimental results show that the Haar classifier can achieve high accuracy and fast speed in the detection of obstacles on high voltage transmission lines.

**Keywords:** Haar classifier; Adaboost algorithm; Object detection

### 1 Introduction

In today's rapidly developing societies, the need for electricity has penetrated all aspects of life such that a high quality and reliable power supply is essential. High voltage transmission lines are the main long-distance power transmission mechanism and one of its basic requirements is security and stability. However, power lines and tower annexes are completely exposed, causing many security risks. Due to the long duration of mechanical tension, wind and sun, aging of materials, broken stock, wear, corrosion and other phenomena often arise that will cause huge losses if they are not attended to in time. That is the reason why there is a focus on research into power system disaster management in most countries around the world [1]. In order to be able to identify potential problems in a timely manner, it is necessary to regularly inspect transmission lines. At present, in addition to the traditional high voltage line inspection methods, such as the artificial visual method and the helicopter aerial survey method, a most popular way is the inspection robot [2]. The principle [3] is the

---

\*Corresponding author: Wei SONG, State Grid Chongqing Electric Power CO. Electric Power Research Institute, Chongqing, China, E-mail: 42274316@qq.com

Ling-yun WAN, State Grid Chongqing Electric Power CO. Electric Power Research Institute, Chongqing, China

Huai-yuan LIU, Hong HU, Harbin Institute of Technology Shenzhen Graduate School, Shenzhen, China

Bin XIANG, State Grid Chongqing Electric Power Company, Chongqing, China

Cheng-jiang WANG, Shenzhen Institute of Advanced Smart Technology, Shenzhen, China

use of a camera that is mounted on the inspection robot, shooting the pictures needed, passing them to a computer for analysis and processing, and then making them available for judgment. However, the inspection robot will inevitably encounter some attachments in the process of walking, such as shockproof hammers, spacers, and suspension clamps. It is therefore necessary to recognize these types of attachments in time to perform the relevant operation to safely cross them.

Haar-like features combined with the Adaboost classification are very successful for face detection [4-6]. The Haar feature is a simple rectangle feature in the face detection system introduced by Viola [4] and Jones [5] and is so named because it is very similar to the Haar wavelet. A Haar-like wavelet feature and integral graph method based on the Adaboost algorithm is used to perform object detection. Viola and Jones were not the first to use the proposed wavelet feature, but they designed a more effective feature for face detection and did a cascade for the strong classifiers trained by Adaboost. A vehicle identification algorithm based on the class Haar feature and improved Adaboost classifier was designed by Xuezhi Wen et al. [7], which got good results both in training time and recognition performance. Learning from the success of the Haar classifier in the above fields and considering the specific conditions of the high voltage transmission lines, the class Haar feature and the Adaboost classification algorithm are applied to the identification and detection of shockproof hammers, spacers, and suspension clamps. The experimental results show that this method can achieve a good detection of specific objects and a satisfactory result is obtained in terms of speed and accuracy.

The whole algorithm includes two aspects: the training process and the recognition process. The training process mainly has two aspects: one is to extract the feature that plays a key role in classification detection from video images, while the other one is to prepare the Adaboost classifier for the recognition process. The recognition process firstly extracts Haar-like features from the test samples, and inputs them to the Adaboost classifier to detect the existence of the target. The algorithm structure is shown in Figure 1.

## 2 Obstacle target image training

As shown in Figure 1, the target training process mainly involves four aspects: preliminary processing of the image, integral graph calculation, Haar-like feature extraction, and Adaboost classifier training. A trained classifier detector provides Haar-like feature information and the classifier for the identification process.

Main points of the Haar classifier algorithm are as follows:

1. Using Haar-like features to perform the testing.
2. Using Integral Image to accelerate the evaluation of Haar-like features.
3. Using the Adaboost algorithm to train a strong classifier to distinguish between a target and non-target.
4. Using filtered cascade to combine the strong classifiers to improve accuracy.

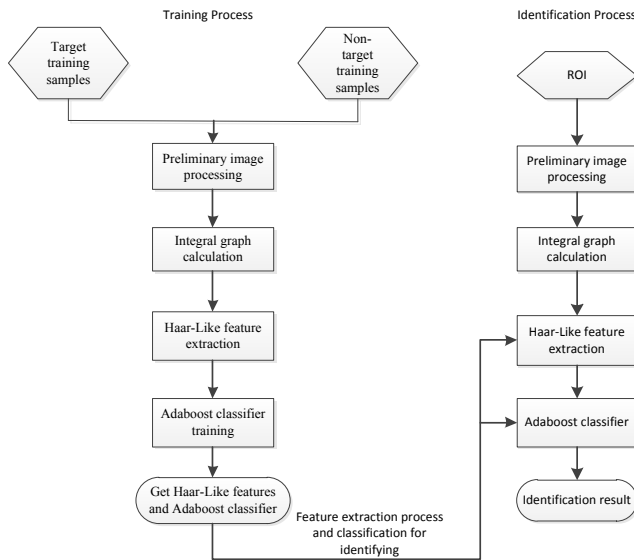


**Figure 1.** Algorithm chart

## 2.1 Preliminary Processing of Images and Calculation of Integral Image

Three target objects are extracted from the captured video images, with gray scale operation, and normalized to 30x30. Three kinds of target object image are shown in Figure 2.



**Figure 2.** Three kinds of obstacle image

Integral graph plays a very important role in the process of this algorithm as it is the real-time assurance of Haar classifier in the detection of targets. Encountered with each sample images or each sub-window image, the key problem is how to calculate the eigenvalue of the current sub-image in both Haar classifier training and target detection. Before training, there is no way of knowing how to arrange Haar-like

features in one window to better reflect the characteristics of the target. These entire features can only be obtained through the permutation and combination exhaustive method. However, taking the most basic four features put forward by Viola as an example, any arrangement in a window size 30 x 30 can produce at least thousands of features, and evaluation of these features requires a very large amount of calculation. However, integral graph is a fast algorithm for calculating pixels in all areas of the image based on scanning the image one time, and it can greatly improve the efficiency of image eigenvalue calculation.

Integral graph is a matrix representation method to describe global information. Integral graph is that the value  $ii(i,j)$  of the location  $(i,j)$  is constructed from the sum of the pixels in the top left corner of the original image  $(i,j)$ .

$$ii(i,j) = \sum_{m \leq i, n \leq j} f(m,n) \quad (1)$$

Integral Figure construction algorithm [6]:

1. Let  $s(i,j)$  represent the cumulative sum of the row direction, and initialize  $s(i,-1)=0$
2. Let  $ii(i,j)$  represents the integral image, and initialize  $ii(-1,i)=0$
3. Scan the image line by line; calculate  $s(i,j)$  of each pixel  $(i,j)$  and the values of integral image  $ii(i,j)$

$$s(i,j) = s(i,j-1) + s(i,j) \quad (2)$$

$$ii(i,j) = ii(i-1,j) + s(i,j) \quad (3)$$

4. Scan the image one time and when reaching the right bottom corner of the image pixels, the integral image  $ii(i,j)$  construction is done.

After constructing the integral graph, the cumulative pixel sum in any image matrix region can be obtained by a simple operation, as shown in Figure 3.

A	B	
C	D	

**Figure 3.** Calculating the cumulative pixel sum in any image matrix region

Let  $\alpha, \beta, \gamma, \delta$  respectively represent D's four vertices, and the pixel sum of D can be expressed as:

$$D_{sum} = ii(\alpha) + ii(\beta) - [ii(\gamma) + ii(\delta)] \quad (4)$$

Haar-like feature value is the difference between the pixels sum of two matrices, and can be done in constant time.

## 2.2 Haar-Like Feature Extraction

Haar-like feature is defined as the difference of the summation of image pixel value in the adjacent area. It reflects the gray change of local characteristics in the image to be detected [7]. We can find it from equation (4) that by introducing the concept of integral image, the extraction rate of haar-like features is greatly improved.

Viola et al. [4,5] proposed four basic rectangle features, as shown in Figure 3. Lienhart et al. [6] introduced a set of extended haar-like features, which are based on Viola's basic simple haar-like features as shown in Figure 4. This algorithm not only uses the characteristics of the horizontal and vertical direction in a rectangular area, but also rotates the rectangle area to get  $45^\circ$  rotated features; they also proposed a fast calculation method for the  $45^\circ$  rotated features. It was shown that Recognition performance of the system could be improved, while the speed of feature evaluation was not affected seriously.

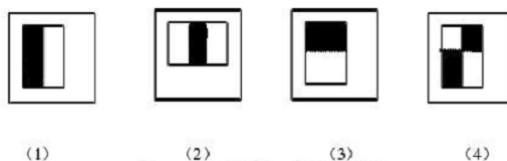


**Figure 3.** Four basic rectangle features

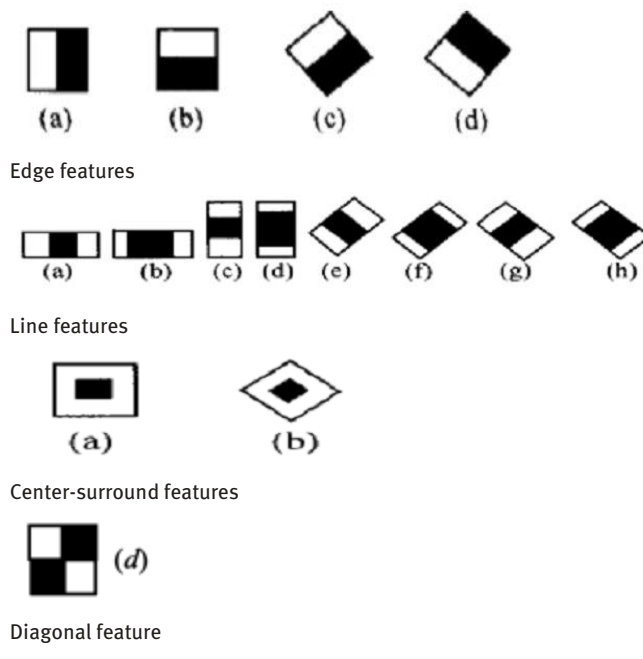


**Figure 4.** Extend Haar-like Features Proposed by Lienhart et al. [6]

In order to better represent the features of three obstacles, this study introduced a set of extended Haar-like features to describe the structure of the targets. The 15 feature prototypes of four kinds are shown in Figure 4, while Figure 5 is part of the diagram used to describe the target features.

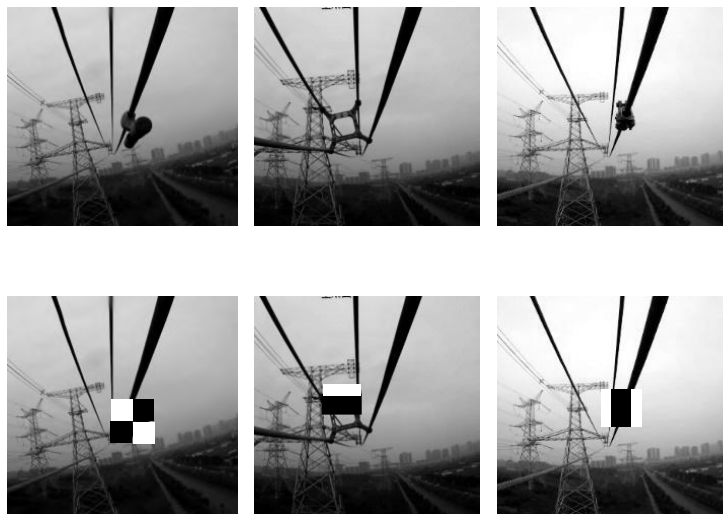


**Figure 5.** Examples of Haar-like features

### 2.3 Feature Selection Based on the Adaboost Classifier

The quantity of characteristic values of the object obtained by the above method is so huge that it is not possible to calculate all the features. Therefore, it is necessary to select only those features that play key roles in the classification; an effective means of doing this is to use the Adaboost algorithm.

Based on a theoretical analysis of the PAC learning model, Valiant [8] proposed the Boosting algorithm with the two important concepts of weak learning and strong learning, which laid the theoretical foundation for the subsequent adaptive Boosting algorithm named Adaboost. Weak learning is a learning algorithm whose recognition rate for a set of concepts is only a little better than random identification, whereas strong learning is a learning algorithm with a high recognition rate. To address the several drawbacks of Boosting, Freund and Schapire proposed an available and practical adaptive Boosting algorithm named Adaboost [9], whose main principle is that all samples be given an equal initial classification weighting, This is done by firstly identifying a number of weak classifiers and then, according to certain combinations, get a high recognition accuracy for strong classifiers.

### 2.3.1 Weak classifier

The original weak classifier may only include a basic Haar-like feature. By calculating the input image Haar-like characteristic value and then comparing it with the initial weak classifiers characteristic value, it can determine whether the input image is a target or not.

Each Haar-like feature can generate a classifier in the following form:

$$f_i = \begin{cases} 1, & p_i h_i(x) < p_i \theta_i \\ 0, & \text{otherwise} \end{cases} \quad (5)$$

Where  $x$  represents the sample,  $h_i(x)$  represents the value of  $i$ -th Haar-like feature  $h_i$  on  $x$  in the sample,  $p_i$  ( $p_i \in \{-1, +1\}$ ) is the classification direction symbol to control the direction of inequality,  $f_i$  is the classifier characterized by feature  $h_i$ , and  $\theta_i$  is the threshold for classification  $f_i$ .

This kind of initial weak classifier may not be better than random judgment in terms of identification accuracy, so it is necessary to train this kind of weak classifier to obtain a relatively lower-error weak classifier known as an optimal weak classifier. The training process for an optimal weak classifier involves looking for the right classification thresholds, so that the classifier has the lowest identification error for all samples.

The specific operations are as follows.

- 1) For each feature  $f$ , the first job is to calculate eigenvalues for all training samples and sort them. Scan sorted eigenvalues again and calculate the following four values for each element according to the list:

All target samples weight sum  $t_1$ ;

All non-target samples weight sum  $t_0$ ;

Target samples before this element weight sum  $s_1$ ;

Non-target samples before this element weight sum  $s_0$ .

- 2) The classification error for each element  $r$  is:

$$r = \min((s_1 + (t_0 - s_0)), (s_0 + (t_1 - s_1))) \quad (6)$$

Find the smallest value of  $r$  in the table and the corresponding element as the optimal threshold.

### 2.3.2 Strong classifier

A strong classifier is an effective combination of a number of optimal weak classifiers and its birth needs to be iterated  $T$  times. The specific operations are as follows.

1. For the training sample set  $S$ , including  $N$  samples, where  $X$  and  $Y$  respectively represent the positive samples and negative samples,  $T$  is the largest training cycles.
2. Initialize the samples weight as  $1 / N$ .
3. The first iteration, training the  $N$  samples to obtain the first optimal weak classifier (see Section 2.3.1).
4. Increase the weight for samples that were wrongly identified.

5. Place the new samples and the last turn correct identified samples together and start a new round of training.
6. Execute steps 4 and 5 cyclically after the T round iterations to obtain T optimal weak classifiers.
7. Combine the optimal T weak classifiers to get the strong classifiers using the following formula:

$$\alpha(x) = \begin{cases} 1, & \sum_{t=1}^T \alpha_t h_t(x) \geq \frac{1}{2} \sum_{t=1}^T \alpha_t \\ 0, & \text{otherwise} \end{cases}$$

$$\alpha_t = \log \frac{1}{\beta_t} \quad (7)$$

The weighted sum of the weak classifiers vote is then calculated according to the weak classifiers error rate. The sum is compared with the average voting result to find which one is better, while at the same time a strong classifier for the recognition process is formed.

### 3 The detection of target obstacle object

Recognition process is used to detect the ROI for target obstacle existence, and it includes image preprocessing, computing integral graph, extracting Haar-like features and classifying based on the Adaboost classifier. The image processing and computing integral image are similar to the training process, which extract Haar-like feature that is using Haar-like feature selected by training process which including the position, structure and type of information to calculate the corresponding Haar-like feature values and feature vector, forming the feature vectors. The Adaboost classifier uses the feature vectors to detect obstacle target existence for under identifiable ROI, and then output the final classification test results.

### 4 Result and analysis of the detection

According to the images of the same obstacle acquired by the moving robot at different distances and from different perspectives, we chose the more representative images as the input samples. As an example, for shockproof hammers we choose 1500 positive sample images and selected 100 images as the test sample, while randomly selecting 3500 negative sample images that had been removed from the target. Some of the negative sample images are shown in Figure 6.

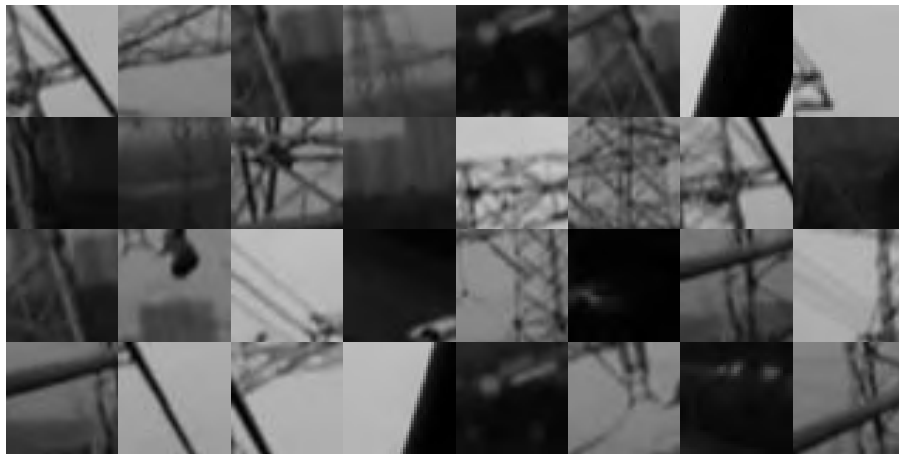


**Figure 6.** Example of negative sample

We use a similar method to select samples for spacers and suspension clamps.

For each of the target obstacles we trained a respective classifier and then used the test sample to test the trained classifier. The recognition accuracy and speed is shown in Table 1 while the examples of identification results are shown in Figure 7.

**Table 1.** Experimental result

The type of obstacle	accuracy rate/%	Time /ms
Shockproof hammers	91	11
Spacers	92	13
Suspension clamps	90	11



**Figure 7.** Examples of identification results

As can be seen from the experimental results, the classifier trained by using Haar-like feature and the Adaboost algorithm can detect the predetermined object effectively: shockproof hammer, spacer, suspension clamp. The accuracy and speed of detection are within the desired range and generally good results have been obtained.

## 5 Conclusion

Drawing on the successful application of the Haar classifier for face detection, this paper proposes an obstacle recognition method based on Haar-like features and the Adaboost algorithm for 500kv high voltage transmission line shockproof hammers, spacers, and suspension clamps. We first calculated the Haar-like features of the image using the integral graph method, and then trained the extracted feature set by applying the Adaboost algorithm, and finally obtained a classifier with high recognition accuracy and fast speed. The experimental results show that this method can achieve very good results in obstacle detection on high voltage transmission lines.

## References

- [1] Qun Yu. Meta-synthesis of complex power system disaster prevention [J]. Chinese power, 2006, 39(1):27-30.
- [2] Qi Zuo. Development and application of inspection robot [J]. Robotics and Applications, 2007.10(2):37-42.
- [3] Caishi Hu, Gongping Wu. Study on high voltage transmission line inspection robot vision obstacle detection and identification [J]. Sensing Technology, 2008, 21(12):2092-2096.
- [4] Viola P, Jones M. Rapid object detection using a boosted cascade of simple features [A]. In Proceeding of International Conference on Computer Vision and Pattern Recognition [C]. Kauai, HI, USA 2001, 1:511-518.
- [5] Viola P, Jones M. Robust real-time face detection [J]. International Journal of Computer Vision, Published by Springer, 2004, 57(2):137-154.
- [6] Lienhart R, Maydt J. An extended set of Haar-Like features for rapid object detection [A]. The IEEE International Conference on Image Processing [C]. New York, USA, 2002, 1:900-903.
- [7] Xuezhi Wen, Wei Fang, Yuhui Zheng. Vehicle identification algorithm based on Haar-like features and improved Adaboost classifier Journal of Electron, 2011(5):1121-1126.
- [8] L.G.Valiant. A Theory of the Learnable. Communications of the ACM, November 1984, 1134-1142.
- [9] Freund Y, Schapire RE. Experiments with a New Boosting Algorithm [A]. In Proceeding of the 13th Conference on Machine Learning, Morgan Kaufmann [C]. USA, 1996, 148-156.

Qiu-wei HE, Yu-peng ZHANG, Xing-tian QU\*

## Virtual Assembly Process Simulation for Hybrid Car Battery based on DELMIA

**Abstract:** In view of the disadvantages of low assembly efficiency and poor quality of hybrid car battery, this paper researches on the virtual assembly process simulation technology. This paper analyzes the assembly process of the battery firstly. Then, based on the principle that detachable parts can be also assembled orderly, the assembly sequence and path planning of parts and components are implemented in the assembly process simulation platform DPM of DELMIA software, and the simulation process is simultaneously completed in DPM platform. The assembly process is verified, and the interference detection is carried out. Lastly, the ergonomics assembly process simulation is implemented in the Ergonomics module of DELMIA. The assembly motion setting and planning for workers are completed, the walking route is determined, and the relationship between the assembly simulation process of the battery and action of workers is established. The feasibility of assembly process and the reachability of workers are verified. The virtual assembly simulation process proposed in this paper improves assembly quality and assembly efficiency of hybrid car battery.

**Keywords:** virtual assembly; simulation; DELMIA; hybrid car battery;

### 1 Introduction

The assembly is a bridge between the design and manufacture, the assembly process design directly affects the product quality and production efficiency. Currently, computers are being applied more and more in the assembly process design. The product design, assembly, analysis and detection are carried out in virtual environment, which gets rid of the traditional product design and development process. Virtual assembly technology can shorten the product development time, improve product quality and reduce product cost and price. At present, many research institutes and teaching institutions in developed countries have made a lot of progress in virtual assembly. In Germany, the FRAUNHOFER industry research institute developed a virtual assembly planning system, which can consider the influence of assembly condition, assembly feature and other factors on the assembly, and realize the man-machine interactive

---

\*Corresponding author: Xing-tian QU, College of Mechanical Science and Engineering, Jilin University, Changchun, China, E-mail:quxt@163.com

Qiu-wei HE, Yu-peng ZHANG, College of Mechanical Science and Engineering, Jilin University, Changchun, China

assembly operation and analyze the assembly time and cost [1]. Jung et al. developed the virtual assembly system CODY, which is combined with artificial intelligence technology and virtual reality technology, and the product designers can make products by simple language commands or three-dimensional assembly operation based on knowledge and 3D interactive [2]. Hermansson et al. of Sweden proposed a low-dimensional path planning algorithm for automatically planning and finding a smooth and collision-free mounting of connectors in a wiring harness installation [3]. Garbaya el of France focused on modeling the dynamic behavior of mechanical parts during the execution of virtual assembly operation [4]. In America, The NIST institute developed a kind of virtual assembly design environment named as VADE, which explored the virtual manufacturing in virtual environment through assembly planning and assembly evaluation [5]. The VPL company developed RB2, DIVISION developed the DVS system, AUTODESK company developed CTL [6]. Vyawahare et al. developed a new interaction technique ‘Bimanual Stretched String Control of Haptic Workspace Mapping’ using a unique combination of spatial interaction device in the domain of virtual assembly [7].

The automotive industry of today is focusing on electrified and hybrid solutions, where both conventional combustion engines and battery supplied electrical engines need to fit in an already densely packed vehicle[3]. The clearance of each component must be evaluated with other disciplines and their components. There are some research on the field of path planning [8,9].

In this paper, virtual assembly technology for hybrid car battery is researched. As an important part of the hybrid car, battery is the power supply with the powerful energy. It is not only as a driving power energy, but also provides power to the air conditioning system, power steering system, ignition system, lighting and signal system, wiper and sprinkler, vehicle entertainment music and communications. The design of hybrid car battery, especially the design and verification of assembly process, has always been paid attention to. DELMIA is the digital software developed by French Dassault System, which faces manufacturing process, maintenance process and ergonomic, provides all kinds of definition, simulation and analysis of the manufacturing process, and covers the application of automobile manufacturing, aircraft design, ship manufacturing and other various industry fields.

This paper analyzes battery assembly process, describes assembly process simulation and ergonomics assembly process simulation for hybrid car battery based on DELMIA.

## 2 Hybrid car battery structure and assembly process analysis

The hybrid car battery structure is shown in Figure 1. Overall, the battery is mainly composed of two parts: the front part including part covered by the front cover, the rear part including part covered by the upper cover. The part covered by the front cover

mainly contains blower, junction box and service pin, which is simple to assemble from the scene feedback. There are many parts in the part covered by the upper cover, the structure is more complex, and so the assembly process is complex.

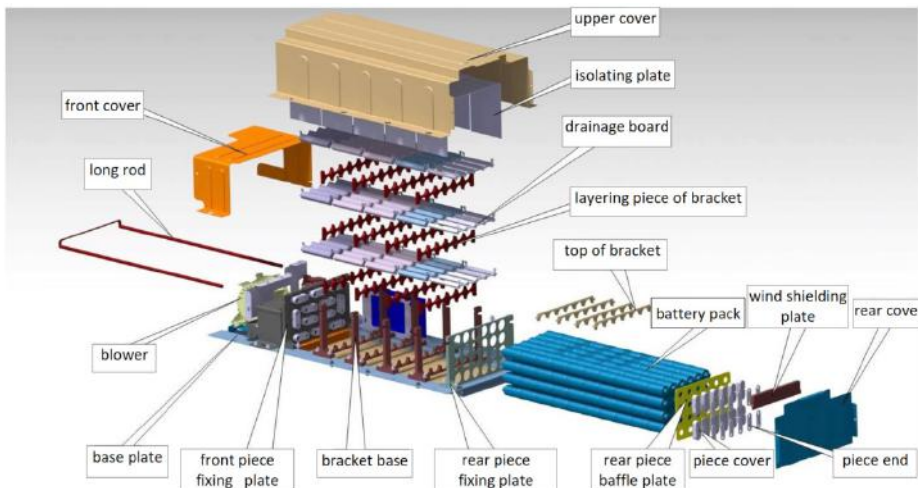


**Figure 1.** Parts decomposition diagram of battery structure.

The hierarchical assembly design is adopted in battery assembly, which is the design concept of assembly oriented to improve the assembly ability of the battery. The hierarchical assembly design can reduce the insertion operation and replace it with placement operation. The number of parts has increased somewhat, but the assembly operation becomes simple, and an assembly operation can be completed basically by only one worker. The bracket plate is divided into three parts of the bracket base, the bracket layering piece and the top of the bracket. A trapezoidal groove is processed on both sides of the bracket layering piece, and the trapezoidal groove is longitudinally inserted through the trapezoidal groove on the bracket base. The trapezoidal groove is processed on both sides of the bracket, and the trapezoidal groove is transversally inserted through the lateral trapezoidal groove on the bracket base. The drainage plate is horizontal, and it is mainly positioned with four positioning plates between two bracket layer pieces. The drainage plate is formed by injection molding, deformation is easily generated, so there is the locating pin hole in the drainage plate to prevent the twist deformation of the drainage plate. The drainage plate which is located between the two layers of the battery pack mainly plays the role of guiding the airflow direction. When assembled, the front and rear fixing plate and the bracket layering pieces are fixed firstly, then the drainage plate is inserted, the baffle plate is installed lastly. The hierarchical assembly of the battery is simple and efficient.

### 3 Virtual Assembly process simulation

In the virtual environment, the assembly process of battery is simulated by DELMIA software, and the rationality of the assembly process is verified. Figure 2 is the simulation flow of hybrid car battery assembly process.

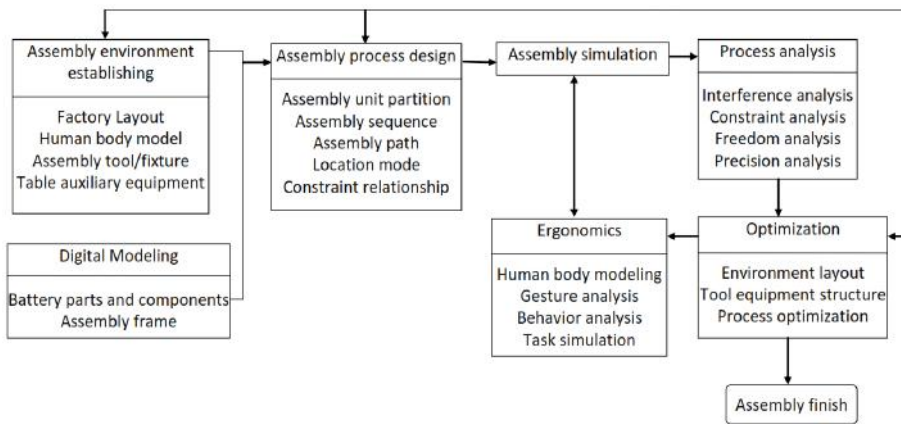


**Figure 2.** The simulation flow of hybrid car battery assembly process.

The process of assembly simulation is shown as follows:

1. Three-dimension modeling of battery components and related resources.

Before assembly process simulation, the battery parts, the 3D entity model and related resources are established in the three-dimensional mapping software firstly, and assembly hierarchy and assembly constraint relations between battery parts and components are determined. In this way, the 3D solid model of the battery parts and components and related resources can be called directly when the assembly process is simulated.

2. Create a virtual assembly environment.

The whole simulation process is carried out in virtual environment. The battery parts and components the 3D solid model of related resources are called in the virtual environment, assembly process documents are established, and the production line and tooling equipment are distributed and so on.

3. Planning of virtual assembly sequence and assembly path.

In the DELMIA assembly process simulation platform, the battery is wholly shown as a product. The location of each part and component is obvious. According to the principle that detachable parts can be also assembled orderly, parts and components of the battery are disassembled, the reverse route of disassembly process is namely the assembly route.

The virtual assembly process of the battery is based on the base plate. The various parts and components of the battery is closed to the base plate from the different space position, and then fixed.

The assembly path of the battery parts and components is created. At the same time, the interference of parts and components is detected to see if there is collision among parts and components. In the process of removing the battery, we get the assembly sequence and assembly path, as shown in Figure 3.

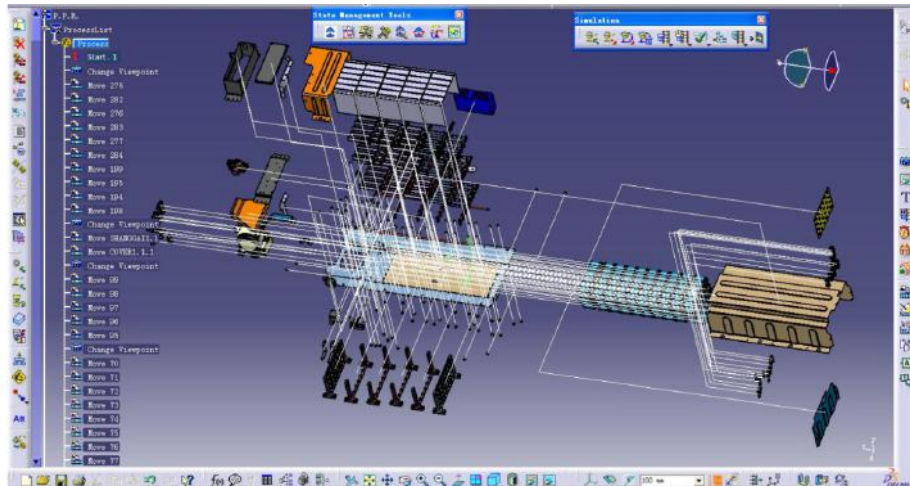


**Figure 3.** The assembly path of battery parts and components.

#### 4. Simulation of assembly process.

The assembly process of battery is simulated in DPM platform of DELMIA software. The simulation includes three processes. Firstly, we initialize the simulation environment. Secondly, the assembly sequence and path are planned. Finally, the assembly process is simulated, and the interference is synchronously detected. The method combining user manual guidance and software automatic search is adopted to plan the battery assembly path. After the assembly process simulation, the relevant reports are generated to guide the actual production process. Figure 4 is the result of the simulation of hybrid car battery assembly process in DELMIA software.

#### 5. Simulation analysis.

The simulation results of hybrid car battery assembly are analyzed. From Figure 3, the assembly simulation process can directly determine the virtual assembly sequence and assembly path. The assembly body explosion diagram also clearly shows the main sub assembly and components structure. If the assembly sequence and path are

not satisfied, it can be modified according to simulation results and actual assembly, until it is satisfied.

The interference detection in the assembly simulation process is carried out by using static, dynamic and movement interference detection method of DELMIA software itself. At the same time, the assembly constrains and assembly error can be detected, and the influence of parts deformation to assembly process can be analyzed.

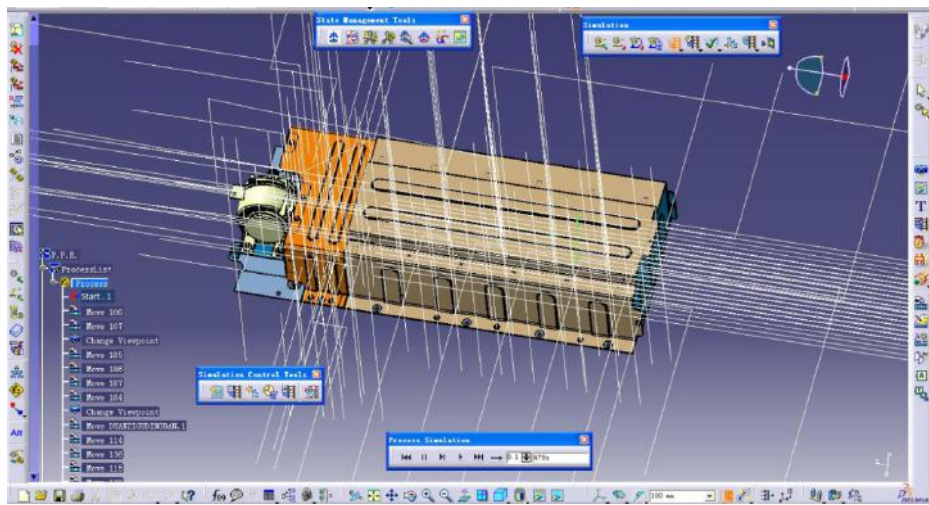


**Figure 4.** The result of assembly process simulation of battery.

#### 4 Ergonomics assembly process simulation

The car battery is assembled with manual assembly, so the staff labor intensity, the commodious operating space and the comfort of gesture become evaluation criteria of assembly process rationality. This work can be completed in the Ergonomics module of DELMIA. In the Ergonomics module, the assembly motion setting and planning for the workers is completed, the walking route is determined, the work task is established and workers assembly process is simulated to analysis labor intensity of workers and assembly reachability. Figure 5 is the ergonomics simulation flow of hybrid car battery assembly process. The 3D solid model of related resources of the battery parts and components are called into DPM platform of DELMIA software firstly. The XY plane is as the datum plane in this paper. Then the contact position and orientation of the products and resources to the floor are determined. In this way, the preparation of the battery assembly is completed, as shown in Figure 6.

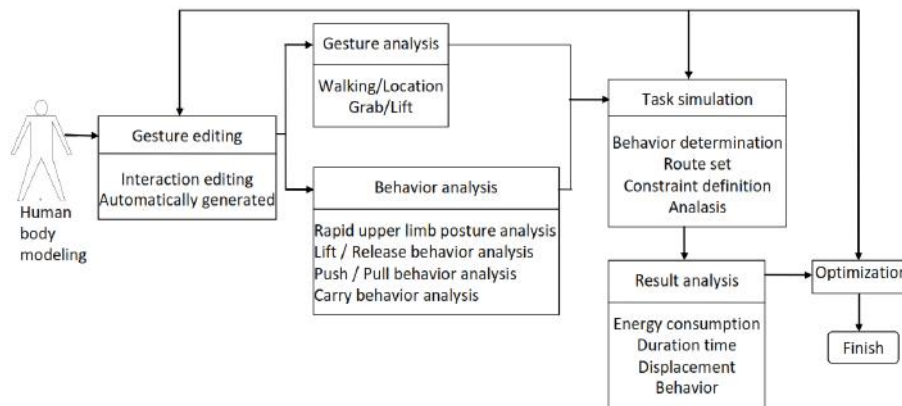


**Figure 5.** The ergonomics simulation flow of hybrid car battery assembly process.

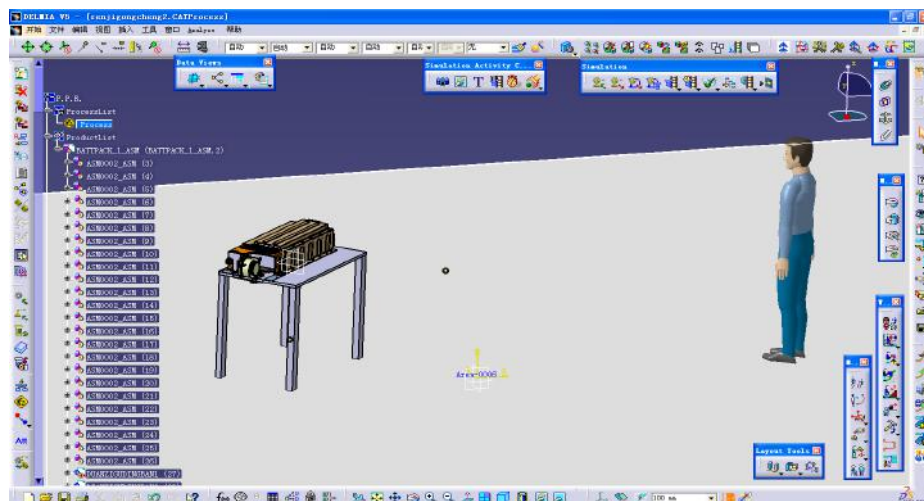


**Figure 6.** The preparation result of ergonomics simulation.

Worker's movement is planned in ergonomics simulation platform (Human Task Simulation) of DELMIA. After getting assembly simulation process of the battery in assembly process simulation platform, the movement of workers are inserted into the assembly process simulation platform to connect the battery simulation assembly process with workers. The walking route of workers is shown in Figure 7. Figure 8 is the result of movement execution.

The reachability of workers movement and commodious operating space are verified by ergonomics assembly process simulation of battery, and the assembly process is reasonable in ergonomics.

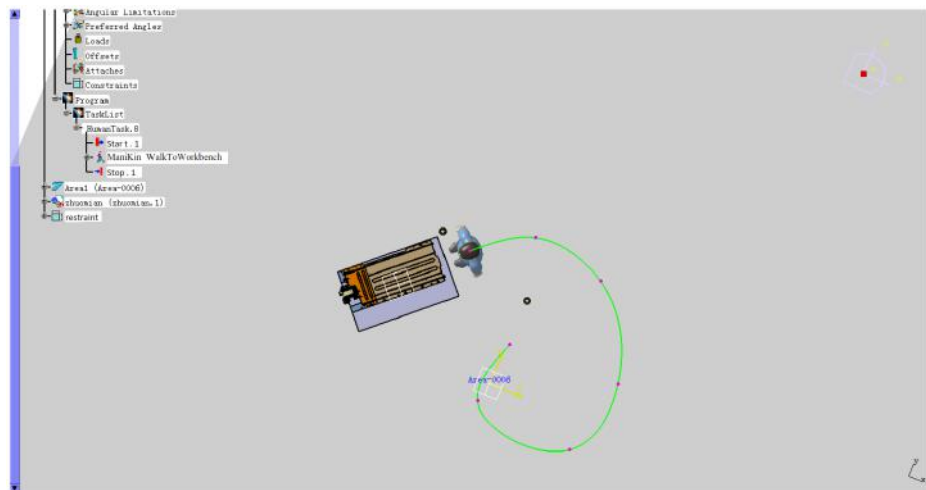


**Figure 7.** The walking route of workers.

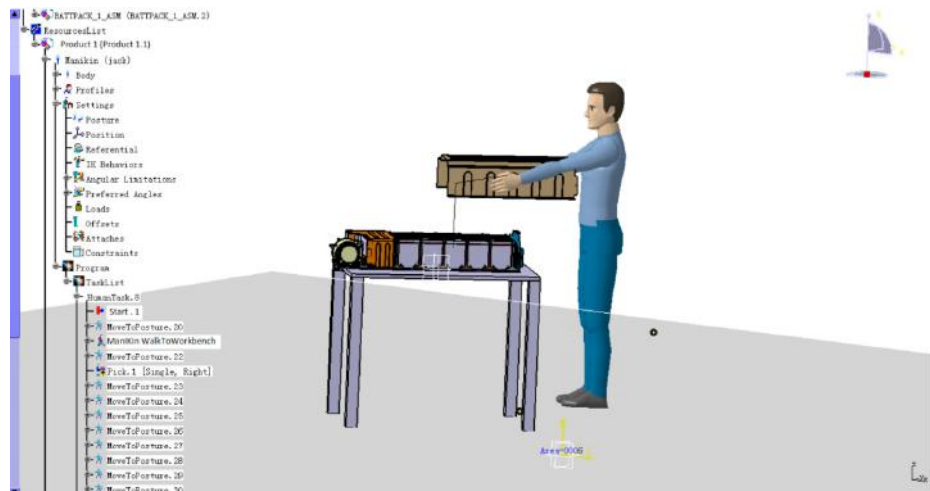


**Figure 8.** The result of movement execution.

## 5 Conclusion

This paper describes virtual assembly process simulation for hybrid car battery. Based on the principle that detachable parts can be also assembled orderly, the assembly sequence and path planning of parts and components are implemented in the assembly process simulation platform DPM of DELMIA software, and the simulation process is simultaneously completed in DPM platform. The assembly process is verified, and the interference detection is carried out.

The ergonomics assembly process simulation is implemented in the Ergonomics module of DELMIA. In the Ergonomics module, the assembly motion setting and planning for the workers are completed, the walking route is determined, and the relationship between the assembly simulation process of the battery and action of workers is established. The feasibility of assembly process and the reachability of workers are verified. The virtual assembly simulation process put forward in this paper improves assembly quality and assembly efficiency of hybrid car battery.

In the future, we will further research on assembly path planning method to realize the automatic and rapid assembly path planning of hybrid car battery.

## References

- [1] B. Schmitz, Virtual reality:On the brink of greatness, Computer Aided Engineering, vol. 12, 1993, pp. 26-32.
- [2] B. Jung, M. Latoschik, and I. Wachsmuth, Knowledge-based assembly simulation for virtual prototype modeling, Proceedings of the 24th Annual Conference of IEEE Industrial Electronics Society, Aachen, Germany, 1998.
- [3] T. Hermansson, R. Bohlin, J. S. Carlson, and R. Söderberg, Automatic assembly path planning for wiring harness installations, Journal of Manufacturing System, vol. 32, 2013, pp. 417-422, 2013.
- [4] S. Garbaya and U. Z. Colado, Modeling dynamic behavior of parts in virtual assembly environment, Proceedings of the ASME/AFM 2009 World Conference on Innovative Virtual Reality, Chalon-sur-Saône, France, 2009.
- [5] S. Jayaram S, H. I. Connacher, and K. W. Lyons, Virtual assembly using virtual reality techniques, Computer Aided Design, vol. 29, 1997, pp. 575-584.
- [6] Q. Peng, F. R. Hal1, and P. M. Lister, Application and evaluation of VR-based CAPP system, Journal of Materials Processing Technology, vol. 107, 2000, pp. 153-159.
- [7] V. S. Vyawahare and R. T. Stone, Evaluation of bimanual stretched string control of haptic workspace mapping for virtual assembly, Proceedings of the ASME 2013 International Mechanical Engineering Congress and Exposition, San Diego, USA, 2013.
- [8] M. Schaub and J. Uthoff, Virtual analysis of compliant parts, The SAE Internation Journal of Materials and Manufacturing, vol. 4, 2011, pp. 799-807.
- [9] SM. LaVille, Planning algorithms, Cambridge University, Press:2006.

Yu-fei WANG, Jian-ming FU\*, Yan LIN, Wei-xia LI

## Information Flow Integrity of ECPS based on Domain Partition

**Abstract:** A smart grid is faced with many security threats, such as false data injection attacks, replay attacks and delay attacks. In this paper, we have constructed an information flow model which abstracts the ECPS workflow as the information flows among nodes, and nodes with a similar function is grouped into the same domain. On account of the above model, we define and clarify the threat model in ECPS. Then, this paper proposes an information flow integrity assurance mechanism, which includes secure communication framework and key management. Encryption algorithms and digital signatures have been used in the mechanism, which share the public-private key pair in the same domain to decrease the complexity of key management. Finally, we analyzed and verified the effectiveness of our mechanism by using a Ukraine power failure event on the transformer substation. After combining the information flow model and the mechanism we proposed, the above three kinds of attacks can be countered and the information such as data, command can be integrated and confidential during the process of information collection and transmission.

**Keywords:** smart grid; cryptography; information flow; integrity; key management

### 1 Introduction

Compared to traditional power grids, smart grids allows a great number of users to access it. And it can monitor energy flow and consumption in real time, which provides support for the efficient use of energy, zone pricing, fault isolation and decision making. The implementation of smart grid is based on Electrical Cyber-Physical System(ECPS), and the prototype of ECPS is a Cyber-Physical System(CPS) [1], which leverages the interaction between a great number of calculating units and physical units, and the transmission of control flow to achieve a real-time monitoring for a physical system.

Smart grids have achieved the industry innovation required by the current age, but also face some security challenges. On one hand, the boundary of smart grid has been widened by the great number of accessed users and distributed power, which increases as the attack surfaces; on the other hand, the critical modules in smart

---

\*Corresponding author: Jian-ming FU, Computer School, Wuhan University,Wuhan 430072, China,  
E-mail: jmfp@whu.edu.cn

Yu-fei WANG, Global Energy Interconnection Research Institute, Beijing 102209, China  
Yan LIN, Wei-xia LI, Computer School, Wuhan University,Wuhan 430072, China

grid often use IP networks to connect each other, and the communication protocol is becoming public and standardized, so there are common threats in these modules as well as in the information system. For example, attackers can tamper with, counterfeit data and issue false commands to destroy the availability, integrity, dependability and controllability of the modules and devices [2]. Smart grids have been exploited by malware in recent years. Stuxnet [3] exploits the virus in a mobile storage medium to diffuse malware to smart grid, which is the malware that first attacked on the infrastructure in industry. Blackenergy [4] is another malware, which can release back doors and special module to issue false commands and delete data on disks, and balckenergy has generated serious threats. For example, the Ukraine power failure event caused power failure in more than half of the region.

Encryption and identity authentication are effective ways to ensure the security of the cyber system in a smart grid [5-8]. However, the key management is a complex problem, including key replacement, key distribution, key security, key operation cost and so on. In order to reduce the complexity of key management, Kim et al. [9] and Wu et al. [10] proposed some ways to decrease the key operation cost and increase the security of key respectively.

All of these work provide some cryptography methods to improve the security of ECPS, but they do not provide a systematical model for ECPS, and they do not consider key management systematically.

In this paper, we have constructed an information flow model of ECPS based on domain partition, such as data collection domain, data processing domain, decision domain, and control domain. According to this model, we have proposed an information flow integrity mechanism based on encryption and digital signature, and each node in same domain shares the same public-private key pair, so the complexity of the key management in smart grid is decreased. This mechanism can counter against false data injection attacks, replay attacks, delay attacks, and ensure that the data and the command are integrated and confidential during the procedure of transmission.

To measure the effectiveness of our information flow integrity mechanism, the Ukraine power failure event on transformer substation is analyzed, and the result shows that our mechanism can effectively defend from these kind of attacks.

The rest of this paper is organized as follows. The next section briefly states related work, and our information flow model has been presented based on domain partition in ECPS in section III. Section IV introduces the information flow integrity mechanism based on encryption and identity authentication. Section V illustrates a case study for our mechanism. Finally, we have given a conclusion and a future direction for work.

## 2 Related Work

A smart grid gives a new mission to the power grid, and its informatization, intelligence, automation propel the revolution of the smart grid infrastructure. At the same time, the security problems in smart grids attract many researchers.

Many warnings concerning the security of smart grid are appearing [2,5,11-13]. And ECPS [2,11,12] is a complex and heterogeneous system, which is formed by the coordination between a cyber system and a physical system. Both of the two systems interdepend with each other, so it is more complex to analyze the security and dependability of ECPS than a single system. The open technologies in ECPS rely on computer systems and communication systems, so there are information security threats to it. How to ensure the availability, integrity and confidentiality of the information flow in ECPS is a key issue. Lots of data are generated during the interactions of a cyber system and a physical system [13], such as real-time measurements, historical data, external events and decisions, and it is also crucial to ensure these data are transmitted efficiently and securely. If internal staff use the picture steganography to carry out illegal information, we should detect the abnormal image [20,21]. Liu Xueyan et al. [5] analyzed the threats in a smart grid from devices, network and data, and proposed some techniques can be applied to smart grid, for instance, intrusion detection, access control and industrial firewall. They also pointed out that key management in a smart grid is a challenge. But there is no solution to the characteristics of ECPS.

To improve the security in a smart grid, researchers have proposed lots of methods. Lu et al. [8] proposed that Advanced Metering Infrastructure(AMI) is a key module in smart grid, and analyzed some common attacks on it, including packet sniffing, data interception, data falsification, data tampering, DDoS attack and so on. Meanwhile, they used a light-weight symmetric encryption algorithm Blom to ensure the integrity and confidentiality of the communication data, which can be used to counter false data injection, replay attack and man-in-the-middle attack, but ZIGBEE-based wireless networks and other protocol frame structures have not yet been proposed. Mo et al. [14] analyzed sources of threats in a smart grid, such as price information, commands, measurements and software. Based on system theory, they built a model for smart grid and its threats, then they used encryption algorithm and identity authentication to achieve confidentiality and entity authentication respectively. However, the physical world is modeled with approximations and is subject to noise, which can result in a deviation of any model to the reality. Therefore, system-theoretic approaches are nondeterministic as compared to information security. Liu et al. [6] described a dynamic approach which dynamically generates a key for sender and receiver in wireless communication, and it increases the difficulty to launch an attack. However, it also increases the complexity of key management. Mike et al. [7] extended the traditional Byzantine fault model to prevent collaborative

exploits. The traditional Byzantine fault model just considers the potential attacks in CPS, but it does not consider that the attacker can intercept and tamper with the data.

Key management is a crucial problem in a smart grid. Kim et al. [9] leveraged a binary tree to manage key search among different nodes, which achieves the security for unicast, multicast and broadcast communication. By using binary tree, the time of querying a shared key decreased from  $O(n^2)$  to  $O(\log_2(n))$ , but this method relies on a third party for identity authentication or key generation. It might cause additional equipment cost and communication traffic. Wu et al. [10] integrated symmetric encryption algorithm and elliptic curve cryptography to dynamically generate key to counter man-in-the-middle attack. In their scheme, they combine both of PKI and a third trusted anchor, which will essentially increase the complication for the smart grid because their protocol at least needs two different kinds of servers for PKI and the trust anchor respectively. Besides, this scheme is not secure against the man-in-the-middle attack.

Compared to some existing work, our work not only counters against false data injection attacks, replay attacks and delay attacks, but also decreases the number of public-private key pairs needed in a smart grid, which is helpful to reduce the complexity of key management.

### 3 Information Flow And Threat Model

A smart grid is composed of four parts: infrastructure layer, measurement layer, information processing layer and decision making layer. The first one locates in the physical system and the last three constitute the cyber system in smart grid.

#### 3.1 Information flow model

The work flow of ECPS can be described as follows: physical sensors collect real-time data from electric equipment components, and then transmit these data to its upper-level component; the upper-level component process these data, and make a decision, and then the decision is transmitted to the control component; finally, the control component will issue the decision to achieve energy management. We abstract the work flow of ECPS into information flow between nodes, and we put nodes which have the similar functionality into a domain, as shown in Figure 1. The information collection domain and control domain form the measurement layer, which achieves the interaction between cyber system and physical system in smart grid; the information processing layer is constituted by data processing domain, and the decision making domain corresponds to the decision making layer.

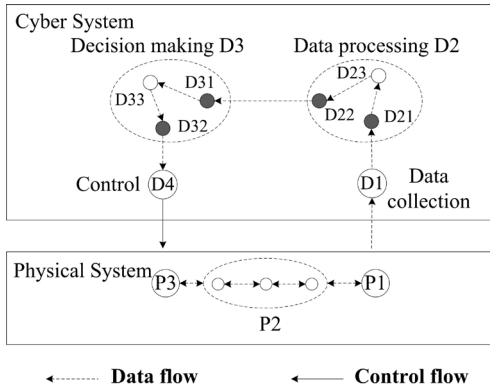


**Figure 1.** Information flow model of ECPS

In order to describe the data flow of ECPS more accurately, we give some definitions as follows:

**Definition 1(ECPS-IFG).** A ECPS-IFG(ECPS Information Flow Graph)= $\langle D, E, \delta \rangle$ . D is the set of domains formed the ECPS; E is the set of data flows between different domains, and  $\delta$  is the data flow function.

**Definition 2(Domain-IFG, D-IFG).** A Domain Information Flow Graph in ECPS can be described as Domain-IFG= $\langle N, E, F \rangle$ . N is the set of nodes a domain has, and there are two kinds of nodes in a domain: boundary node  $N_b$  and internal node  $N_i$ . The responsibility of  $N_b$  is to transmit data, and  $N_i$  is responsible to process data. When there is only one node in a domain, the type of this node is boundary node beside internal node; E is the set of data flows in the domain, and F is the data flow function in the domain.

Given a ECPS-IFG= $\langle D, E, \delta \rangle$ ,  $D_t$  and  $D_j$  are two different domains in the system, the following relations are true:

- the number of nodes in  $D_t$  and  $D_j$  are more than one.

$\exists n_{tbk} \in N_b \in D_t$  makes  $\exists E : n_{tbk} \rightarrow n_{jbr} \in N_b \in D_j$  That is to say, there will be an information flow E from boundary node  $n_{tbk}$  to a boundary node  $n_{jbr}$  in another domain  $D_j$

$\exists n_{ij} \in N_i \in D_t$  makes  $\exists E : n_{ij} \rightarrow n_{tv} \in N_i \in D_t$

That is to say in domain  $D_i$ , there will be information flow E from internal node  $n_{ij}$  to a node  $n_{tv}$ , and  $n_{tv}$  can be a boundary node or an internal node.

- the number of nodes in  $D_i$  is equal to one.

For  $n \in D_i$ ,  $\exists E : n \rightarrow n_{jv} \in D_j$ . When the number of nodes in  $D_j$  is more than one,  $n_{jv} \in N_b$ , that is to say when domain  $D_i$  only has one node, in the function of  $\delta_i$ , the information flow will be transmitted to the node in another domain  $D_j$ , and if the number of nodes in  $D_j$  is more than one, this node must be boundary node.

As shown in Figure 1, the cyber system is composed of four domains: data collection domain  $D_1$ , data processing domain  $D_2$ , decision making domain  $D_3$  and control domain  $D_4$ ; the physical system has three parts: data emission domain  $P_1$ , data processing domain  $P_2$  and command receiving domain  $P_3$ . And there is only one node in domain  $D_1$ ,  $D_4$ ,  $P_1$  and  $P_3$ . the functionality of each node and the information flow in ECPS are described as follows:

1. Node  $P_1$  in data emission domain, gets the information from  $P_2$  and sent it to  $D_1$ .
2. Node  $D_1$  in data collection domain, collects the real-time data from physical system and transmits the data to the boundary node  $D_{21}$  in data processing domain.
3. Boundary node  $D_{21}$  in data processing domain, just transmits the data to the internal node  $D_{23}$ .
4. Internal node  $D_{23}$  in data processing domain, stores and computes the data it received and then transmits it to boundary node  $D_{22}$ .
5. Boundary node  $D_{22}$  in data processing domain, transmits data to the boundary node  $D_{31}$  in decision making domain.
6. Boundary node  $D_{31}$  in decision making domain, transmits data to internal node  $D_{33}$ .
7. Internal node  $D_{33}$  in decision making domain, analyzes the data it received and make some decisions on it. Finally, it will transmit the decision to the boundary node  $D_{32}$ .
8. Boundary node  $D_{32}$  in decision making domain, transmits the decision to control domain.
9. Node  $D_4$  in control domain issues the decision to smart devices.
10. Node  $P_3$  in commands receiving domain, gets the information from  $D_4$  and sent it to  $P_2$ .
11. Node  $P_2$  in data processing domain, gets the commands from  $P_3$  and processes it, then tells physical equipment what to do and how to work.

### 3.2 Threat Model

Some attacks in smart grid can be directly reflected to our information flow model, such as data interception, data tampering and false data injection. According to the information flow model, we define the threat model in ECPS as follows.

1. For any domains in ECPS, attackers can inject false data in it.
2. For the information flow from domain  $D_i$  to domain  $D_j$ , attackers can intercept the datagram transmitted. That is to say, the datagram transmitted between two different domains can be intercepted.
3. Attackers can use the false data and the data intercepted to launch a replay attack or a delay attack to any domains.

Figure 2 shows the situations when false data injection attacks, replay attacks and delay attacks happen.

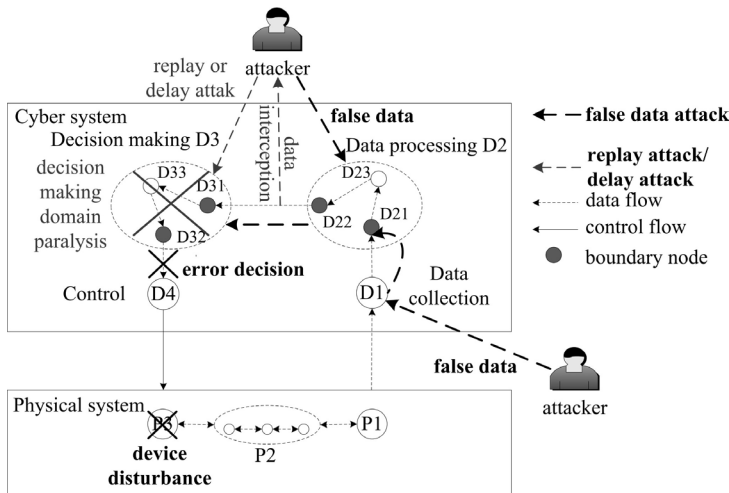


**Figure 2.** Attack model in ECPS

Attackers send a false datagram to the cyber system, or intercept the datagram and then tamper with it, so ECPS cannot perceive the actual state of the physical devices and decision making domain will make an improper or wrong decision. As shown in Figure 2, the attacker injects false data to domain  $D_2$ , which makes the boundary node  $D_{22}$  transmit the false data to the decision making domain. Hence, the wrong decision is issued to the smart device and device disturbance occurs.

A replay attack means attackers intercept the datagram transmitted between two different domains and then send it repeatedly to bypass the identity authentication, even to launch a Denial of Service(DoS) attack. As shown in Figure 2, the attacker intercepts the datagram transmitted from domain  $D_2$  to domain  $D_3$ .

When attackers delay the datagram arriving time between two different domains is called delay attack, which will make the receiver get the obsolete datagram. Shown in Figure 2, when the attacker intercepts the datagram from  $D_2$  to  $D_3$ , he does not send it immediately, but sends it after some time.

On 23rd December, 2015, the Ukraine power sector was attacked, which caused power failure among more than half of the region, and its attack flow is described in Figure 3. Firstly, an email with malware was sent to users in the power sector. When a user clicked this email, the Trojan was run, and a SSH back door and a killdisk module were installed, then with this back door the attacker could issues command to smart devices. In addition, killdisk can delete system data to delay the system recovery time.

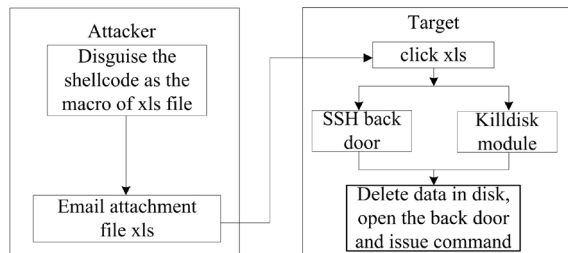


**Figure 3.** Attack flow of Ukraine power sector

From the Ukraine power failure event, we can find that a smart grid now will be under great threat, and there will be heavy losses when attackers issue false command to the electric devices. So it is urgent to ensure the security and dependability of ECPS [4,15,16].

## 4 Information Flow Integrity Mechanism

According to the information flow integrity model and threat model introduced in section III, we propose an information flow integrity mechanism, which includes secure communication framework and key management. This mechanism can ensure that the data transmitted in the ECPS can only be shared by authorized nodes, and it is not counterfeited and tampered with by attackers.

### 4.1 Secure communication framework

As introduced in section III-B, false data injection attack has two parts. One is data interception and modification, and the other one is to inject false data into a domain directly. In order to counter it, we need to use cryptography method to ensure data cannot be divulged and modified during transmission, and to ensure the sender is authorized by using digital signatures.

False data injection attacks can be mitigated by using cryptography methods and digital signatures, but the attacker can intercept the data which is encrypted and signed, and send it repeatedly to cause a DoS attack. So a timestamp is added at the process of computing a digital signature, and the receiver needs to check whether the timestamp is valid after receiving a datagram.

There are two kinds of cryptography methods, symmetric encryption and asymmetric encryption. We use symmetric encryption to achieve confidentiality for data and commands. The data processing domain and decision making domains can use cryptography methods that have a high level of security [22,23], such as AES. For control domains we can use some lightweight encryption methods, such as MIBS [17],

SMS4 [18] and PRESENT [19]. RSA is the standard algorithm used in digital signature, so we use it to achieve identity authentication. The secure communication framework is shown in Figure 4, and the functionality of each node is shown in Table 1.

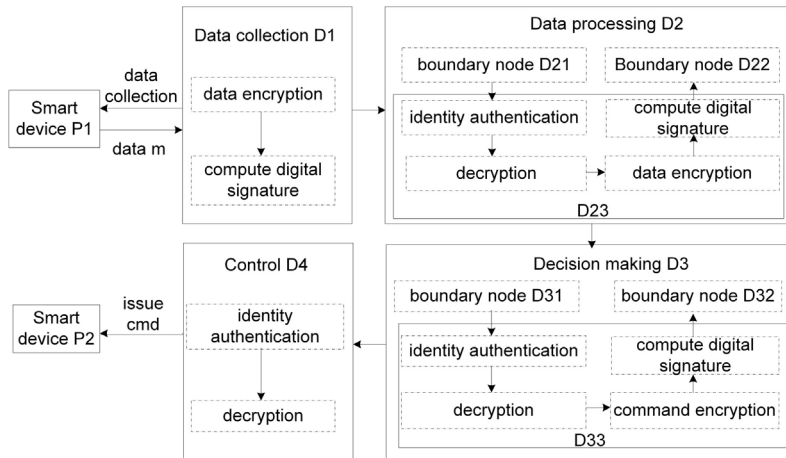


**Figure 4.** ECPS secure communication framework

**Table 1.** Functionality Of Each Node

Node	Functionality
$D_1$	collect real-time data from electric devices, do encryption and digital signature on the data and then send it to boundary node $D_{21}$
$D_{21}$	transmit data to node $D_{23}$
$D_{23}$	signature verification and decryption; then store, compute the data, encrypt and sign the data been operated and transmit the datagram to node $D_{22}$
$D_{22}$	transmit datagram to node $D_{31}$
$D_{31}$	transmit datagram to node $D_{33}$
$D_{33}$	signature Verification and decryption; then make decision, encrypt and sign the decision and transmit the datagram to node $D_{32}$
$D_{32}$	transmit datagram to node $D_4$
$D_4$	signature Verification and decryption; issue decision to smart devices

## 4.2 Key management

Smart grids are a large-scale and heterogeneous network, and the large number of nodes and their connections in it make a great challenge to the encryption key and identity key management. If every node in the information flow model has its own

public-private key pair, the number of keys for ECPS will be very large, and the key management will be very complex. We propose sharing the public-private key pair in a domain to decrease the number of keys, which reduces the complexity of key management. The key management is shown in Figure 5, the responsibility of KDC (Key Distribution Center) is to distribute and manage encryption key, identity key is distributed and managed by CA (Certification Authority). As shown in Figure 5, nodes in data processing domain and decision making domain share the same public-private key pair respectively.

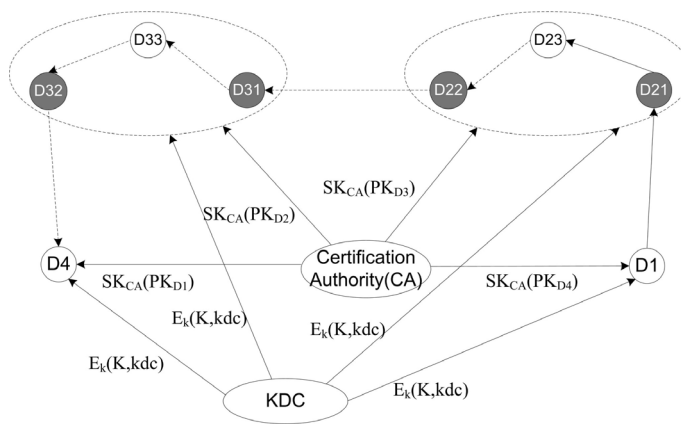


**Figure 5.** Key management in ECPS

Combined with key management, the communication flow in ECPS is described in Figure 6, which contains five steps.

1. KDC distributes an encryption key  $K$  for every domain, and identity key ( $PK_{D_i}$ ,  $SK_{D_i}$ ) for every domain is distributed by CA.
2. Node  $D_i$  encrypts data  $m$  using encryption key  $K$ , then computes its hash value  $h$ . In order to defend against replay attacks and delay attacks, the digital signature for hash value  $h$  and a timestamp  $T$  is computed. Finally, node  $D_i$  transmits the encrypted data, digital signature and its public key certificate to the boundary node in domain  $D_2$ .
3. Internal node  $D_{23}$  in domain  $D_2$  verifies the validity of the public key certificate it receives and uses the public key to get the hash value  $h'$  and timestamp  $T'$  from the digital signature. Then  $D_{23}$  computes the hash value using the encrypted data it received and compares it with  $h'$ . At the same time,  $T'$  is checked whether it is closer to the current time. If both conditions are satisfied, encrypted data is decoded using key  $K$ . Finally node  $D_{23}$  does some operations on data  $m$  and then does the same steps described in step 2).

4. Node  $D_{32}$  does the same operations in step 3, then it will make decision according to the information, and then transmits the encrypted decision and digital signature to the boundary node.
5. Node  $D_4$  verifies the identity of the sender and decrypts the encrypted decision according to steps in step 3, and then delivers the decision (command) to electric devices.

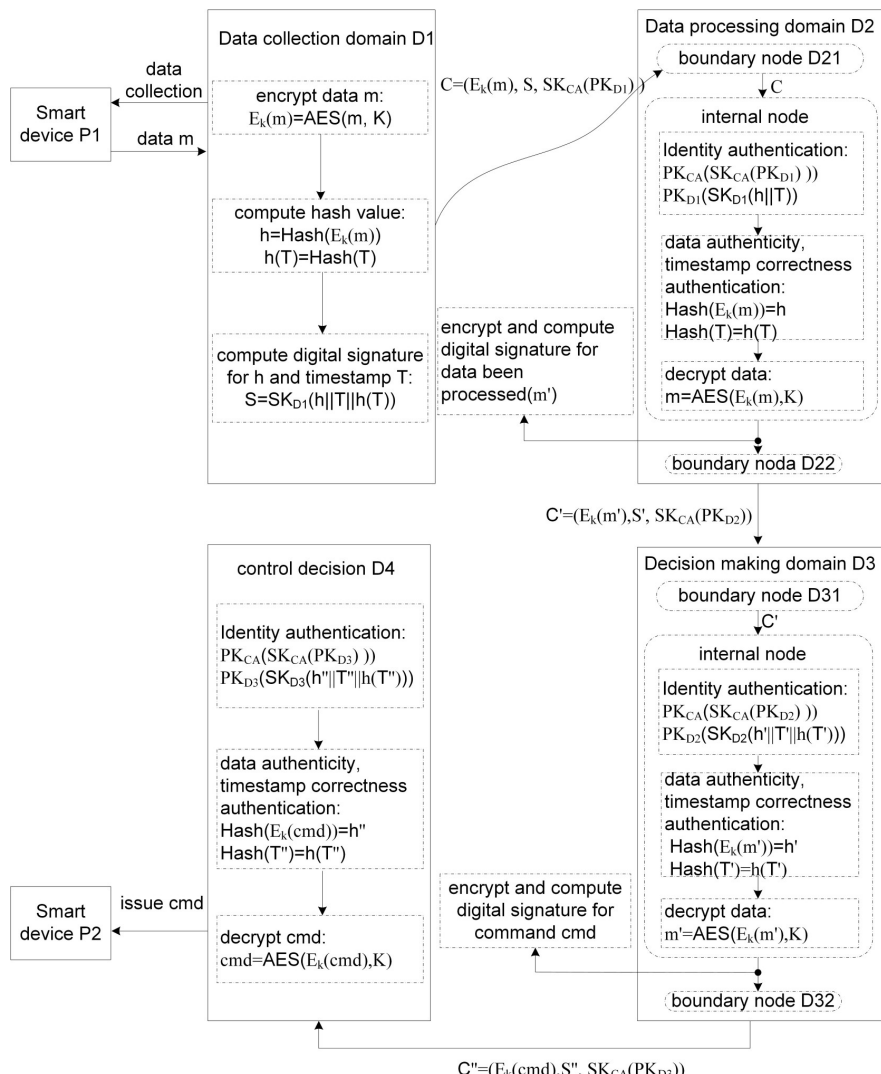
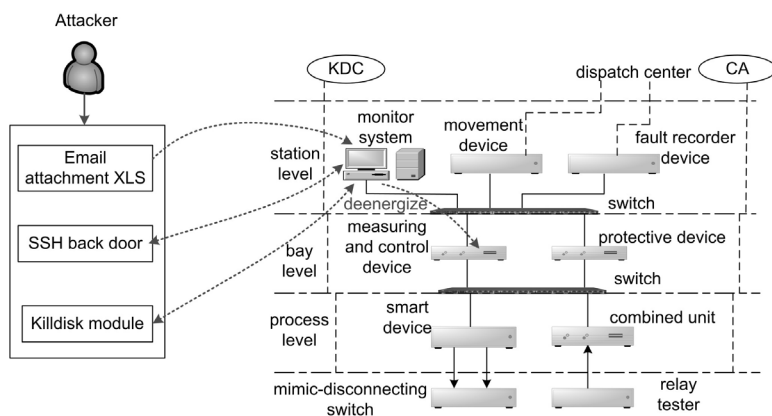


Figure 6. Communication flow combined with key management

## 5 Case Study

In this section, we will introduce how our information flow integrity mechanism can be applied to the Ukraine power failure event and to the transformer substation.

There is a transformer substation, whose architecture is shown in Figure 7. It is composed of station level, bay level and process level. Process level is the lowest level, which controls the electric devices directly; the middle one is a bay level, which is responsible for collecting data and issuing command to smart devices; the station level is the highest one, and data processing, decision making domains are located in this level.



**Figure 7.** Architecture of transformer substation

When collecting data from smart devices, the measuring and control device gets its own encryption key and identity key from KDC and CA, and all the keys are stored in a trusted storage area. Then it uses the encryption key to encrypt the data collected from smart devices, and integrates the current timestamp, the hash value for encrypted data into a data group. Finally, it gets a digital signature using the identity key and the encrypted data, digital signature, and its public key certificate as a payload is transmitted to the process level.

The dispatch center verifies the validity of the public key certificate after it receives the datagram, if it is authorized, it gets the hash value and the timestamp from the digital signature, and compares it with the hash value computed from the encrypted data and checks whether the timestamp is valid. After that, decode the encrypted data and make decisions according to it, such as turning off the power network. Because attackers do not have an encryption key and a private key, they cannot launch a false data injection attack; meanwhile, there is a timestamp, so replay attacks and delay attacks cannot be successful.

When the measuring and control device receives a command, it must verify the identity of the sender. As shown in Figure 6, in the Ukraine power failure event, the attacker controlled the monitor device and let it issue a command to turn off the power network. When the measuring and control device received this command, it will verify the identity of the sender, but now the sender did not have the correct private key, so it cannot bypass the identity authentication, and the attack would fail. Similarly, the attack does not have the encryption key, and it cannot inject false command to turn off the power network.

## 6 Conclusion

An information flow integrity mechanism of ECPS based on domain partition can counter false data injection attack, replay attack, delay attack effectively, and it can reduce the complexity of key management in a smart grid. The data collected or the command must go through a lot of nodes, so it is easy to append digital signatures and timestamps on forward nodes. The receiver can do the inverse operations to the sender to check the digital signatures and timestamps, and detect attacks. In addition, each node can be combined with a log audit to discover traffic anomalies, to collect data anomalies and command anomalies. For example, the control domain can compute the command entropy in a time window and then rely on the difference on the command entropy to detect replay attacks, DOS attacks and false command attacks. Of course, our mechanism cannot counter against side-channel attacks during encryption or decryption. In addition, we may use a novel encryption method to counter against this attack. A smart grid is composed of electricity generation, transmission, distribution and consumption [24], and in the future, we will focus on the attack and the protection on specific object to improve the protection efficiency, and we should improve and apply this mechanism.

**Acknowledgment:** Supported by Science and Technology Project of China State Grid Corp. Research on the key technology of security strategy and information communication support power system (XXB17201400056).

## References

- [1] Rajkumar R R, Lee I, Sha L, et al. Cyber-physical systems: the next computing revolution[C]. Proceedings of the 47th Design Automation Conference, New York, USA. ACM, 2010: 731-736.
- [2] Sridhar S, Hahn A, Govindarasu M. Cyber physical system security for the electric power grid[J]. Proceedings of the IEEE, 2012, 100(1): 210-224.
- [3] Langner R. Stuxnet: Dissecting a cyberwarfare weapon[J]. Security & Privacy, IEEE, 2011, 9(3): 49-51.

- [4] A comprehensive analysis report on Ukraine power system attacks [public edition]. [http://www.360doc.com/content/16/0226/23/30824275\\_537668183.shtml](http://www.360doc.com/content/16/0226/23/30824275_537668183.shtml)
- [5] LIU Xueyan, ZHANG Qiang, LI Zhanming. A Survey on Information Security for Smart Grid. ELECTRIC POWER. 2014;12(4).
- [6] Liu T, Liu Y, Mao Y, et al. A dynamic secret-based encryption scheme for smart grid wireless communication[J]. Smart Grid, IEEE Transactions on, 2014, 5(3): 1175-1182.
- [7] Burmester M, Magkos E, Chrissikopoulos V. Modeling security in cyberphysical systems[J]. International Journal of Critical Infrastructure Protection, 2012, 5(3): 118-126.
- [8] LU Baohui, MA Yonghong. Research on Communication System of Advanced Metering Infrastructure for Smart Grid and Its Data Security Measures. Power System Technology, 2013, 37(8): 2243-2248.
- [9] Kim J Y, Choi H K. An efficient and versatile key management protocol for secure smart grid communications[C]. Wireless Communications and Networking Conference (WCNC), 2012 IEEE, Paris, France. IEEE, 2012: 1823-1828.
- [10] Wu D, Zhou C. Fault-tolerant and scalable key management for smart grid[J]. Smart Grid, IEEE Transactions on, 2011, 2(2): 375-381.
- [11] GAO Kunlun. Security research on Energy Cyber-Physical System[J]. China Information Security, 2013(2): 86-87.
- [12] Wang W, Lu Z. Cyber security in the Smart Grid: Survey and challenges[J]. Computer Networks, 2013, 57(5): 1344-1371.
- [13] Li Renfa, Xie Yong, Li Rui, and Li lang. Survey of Cyber-Physical Systems[J]. Computer Research and Development, 2015, 49(6): 1149-1161.
- [14] Mo Y, Kim T H J, Brancik K, et al. Cyber physical security of a smart grid infrastructure[J]. Proceedings of the IEEE, 2012, 100(1): 195-209.
- [15] TANGYi, WANGQi, NIMing, LIANGYun. Analysis of Cyber Attacks in Cyber Physical Power System[J]. Automation of Electronic Power System. 2016, 40(6):100~104
- [16] Analysis and defence on Ukraine power system attacks. <http://blog.nsfocus.net/ukraine-power-plant-attack-analysis-protection-programs/>
- [17] Wu W, Zhang L. LBlock: a lightweight block cipher[C]. Applied Cryptography and Network Security, Nerja, Spain. Springer Berlin Heidelberg, 2011: 327-344.
- [18] Shi Y, Wei W, He Z. A lightweight white-box symmetric encryption algorithm against node capture for WSNs[J]. Sensors, 2015..
- [19] Bogdanov A, Knudsen L R, Leander G, et al. PRESENT: An ultra-lightweight block cipher[M]. Springer Berlin Heidelberg, 2007.
- [20] MH Memon, JP Li, I Memon, QA Arain. GEO. matching regions: multiple regions of interests using content based image retrieval based on relative locations. Multimedia Tools and Applications, 2016:1-35.
- [21] I Memon, L Chen, A Majid, M Lv, I Hussain. Travel Recommendation Using Geo-tagged Photos in Social Media for Tourist. Wireless Personal Communications, 2015, 80(4):1347-1362.
- [22] I Memon, QA Arain. Dynamic path privacy protection framework for continuous query service over road networks. World Wide Web, p 1-33, August 30, 2016.
- [23] I Memon, I Hussain, R Akhtar, G Chen. Enhanced Privacy and Authentication: An Efficient and Secure Anonymous Communication for Location Based Service Using Asymmetric Cryptography Scheme, 2015.
- [24] FA Mangi, S Xiao, I Memon. Novel design and performance analysis of broadband dual layer circular polarizer based on frequency selective surface for 60 GHZ application. Lecture Notes in Electrical Engineering, v 348, p 319-325, 2016, Wireless Communications, Networking and Applications, Proceedings of WCNA 2014.

Hai-Tao CHEN\*, Hao HU

# Simulating the Time-Domain Response for Monopole Antennas Excited by DC Voltage Source

**Abstract:** When a monopole antenna is connected to or disconnected from a DC voltage source, the process of charge and discharge takes place. The time-domain response for the charge and discharge process is investigated by the finite difference time domain (FDTD) method in this paper. It is shown that a damping oscillation can be excited in the instant when the DC source is turn on or shunt off. By using FFT to analyze the time-domain response oscillation waveform, harmonic modes are observed and some parameters of the antenna, such as resonant frequency, impedance, can be obtained. It is indicated that the time-domain response of the charge and discharge process can be used to measure some parameters of antennas.

**Keywords:** antenna, time-domain response, FDTD

## 1 Introduction

Monopole antennas are widely used as transmitting antennas for high power HF and MF band wireless transmitting systems[ 1,2]. The whip antenna, vertical cage antenna, invert L antenna, T-shape antenna and MF tower antenna, which are very common in communication and broadcast system, can all be seen as a monopole antenna. The performance of the monopole antenna has been investigated so much in the frequency domain, including input impedance, radiation efficiency and broadband. This is because the harmonic source is used so far and wide in radio engineering. With the development of wireless technology, the time-domain performance of antennas has come to be of interest more and more, and there is a great deal of literature discussing this problem [3-6]. In the published research results, however, most focus on the response of antennas for the time-pulse signal.

In this paper, another type of time-domain problem for antennas is studied. What is concerned here is the time response of antennas in the instant when excited sources are open or shunt off. This time response can be named as the charge and discharge process of antennas, as the similar process of capacitors. Since high resonance modes can exist in antennas, the charge and discharge process will excite higher frequency signal which can be radiated to space by antennas. For a high power radio transmitting

---

\*Corresponding author: Hai-Tao CHEN, Antenna Research department, Wuhan Maritime Communication Research Institute, Wuhan, P. R. China., E-mail: hbcht@163.com

Hao HU, Research Project department, Wuhan Maritime Communication Research Institute, Wuhan, P. R. China

system, the effect of this high frequency mode on electromagnetic environment may be notable and should be taken into account by transmitting system designers.

The charge and discharge response of a monopole antenna excited with DC voltage source is analyzed in this paper. A FDTD code is developed to model the charge and discharge process in the instant when the DC voltage source is turned on or shunt off.

## 2 Theoretical model

Considering the charge and discharge process of a monopole antenna excited by DC voltage source shown in Figure 1. Two type of discharge are considered. In Figure 1a, the feed point of the antenna can be connected to the voltage source or the ground by the switch. When the antenna is connected to the source, a charge process is takes place due to the distributed capacitive of the antenna. As a result, there will be electric charge distribution along the antenna. Then, if the switch is connected to the ground, the electric charge stored along the antenna will flow to the ground, which is known as a discharge process. In fact, a monopole antenna working in lower frequency is always matched with a tuning inductor to the transmitter. So another type of discharge is considered in Figure 1b, in which the antenna is connected to the ground by a tuning inductor.

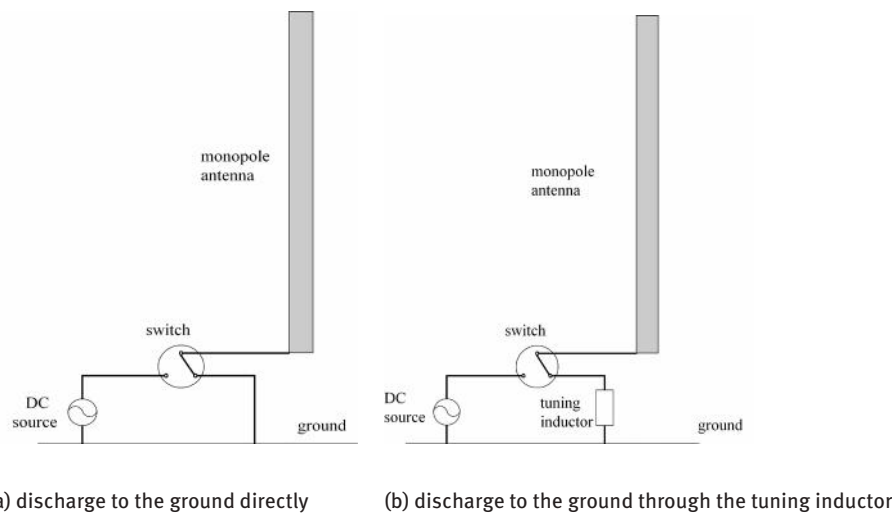


**Figure 1.** The charge and discharge process of the monopole antenna.

The time performance of the antenna is suitable to be simulated by FDTD method [7,8]. The loss which will occur when the antenna current returns through the ground is one of the important factors that effects the performance of the antenna, especially for the antennas which work on a lower frequency. Modeling the effect of the real ground

exactly is very difficult and is not the key point of our research. So the monopole is considered located on the PEC ground and a lumped loaded resistance at feed point is used to represent the losses of the real ground.

### 3 Numerical results and analysis

The charge and discharge performance in time domain is calculated for a whip antenna which height is 19m and radius is 50mm. The ground loss resistance is  $10\Omega$ , and the voltage of the DC source is 1V.

A FDTD code is developed in this work and used to model the time domain response of the monopole antenna. The charge process is shown in Figure 2. It can be seen that the time damping oscillation is excited in the charge process. Due to the loss caused by radiation and ground resistance, the charge oscillation waveform is dampens. Because of the existence of high modes, the oscillation waveform is very complex. In Figure 2, it is observed that the effect of the higher mode is more distinct in the first and second waveforms while the waveforms are approach to the sinusoidal wave with the lapse of time. It can be explained that the total resistance of the antenna increases with the increase of the frequency, and the attenuation of the higher mode is faster than the lower mode.

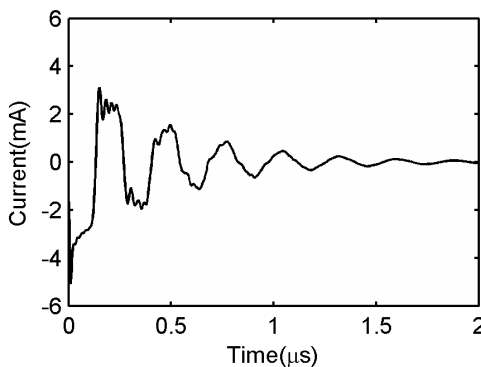


**Figure 2.** Oscillation wave of the charge process for the antenna.

When the Fourier transform to the time oscillation, the spectrum response of the charge can be obtained. The FFT result for the Figure 2 is shown in Figure 3. It can be seen that the first three resonant frequencies are 3.6MHz, 11.2MHz and 18.7MHz, which correspond to the 1st, 3rd and 5th resonant modes respectively. And with the increase of the number of order, the high frequency components decrease progressively. To antennas, the 2nd, 4th and 6th modes belong to the parallel resonant mode of which

resistance is very large. So the signal of even modes is suppressed and can not be observed.

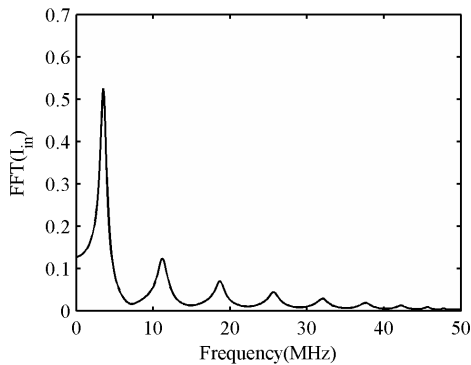


**Figure 3.** Spectrum of the charge process for the antenna

The discharge process of the antenna which is connected to the ground directly is shown in Figure 4. It is obvious that the discharge oscillation waveform is antipode of the charge oscillation waveform shown in Figure 2.

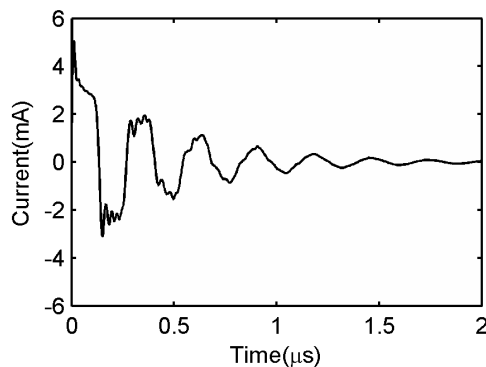


**Figure 4.** Oscillation wave of the discharge process for the antenna

The discharge process of the antenna which is connected to the ground by the tuning helix is shown in Figure 5, where the inductor L is  $6\mu\text{H}$ . It can be seen that the high order modes are decreased much due to the filtering of the tuning coil. The waveform approaches a sinusoidal wave. The FFT result of Figure 5 is shown in Figure 6, in which only the 1st and 3rd resonant modes can be observed and the magnitude of the 3rd mode is much less than the magnitude of the 1st dominant mode. After loaded

with the tuning inductor, the antenna's first resonant frequency is 2.9MHz. The reactance of the  $6\mu\text{H}$  inductor at this frequency is  $109.3\Omega$ , which indicates that the input reactance of the antenna is equal to  $109.3\Omega$  at 2.9MHz.

According to the simulated results of EM software FEKO, the whip antenna shown in figure1 has a self-resonant at 3.7MHz and the input reactance at 2.9MHz is about to  $120\Omega$ , which are approach to the analysis results 3.6MHz and  $109.3\Omega$  from the charge and discharge oscillation waveform respectively. The difference of the results between FEKO and our analysis can be attributed to the difference between the FEKO (MoM) and FDTD method.

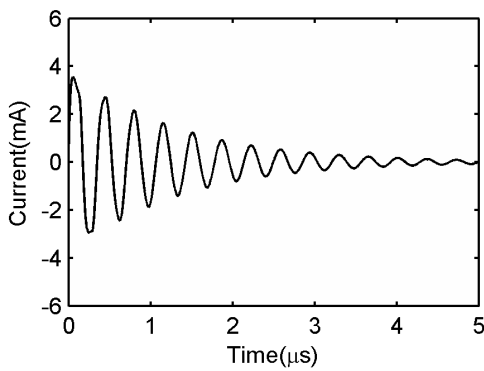


**Figure 5.** Oscillation wave of the discharge process for the antenna connected to the ground by tuning coil.

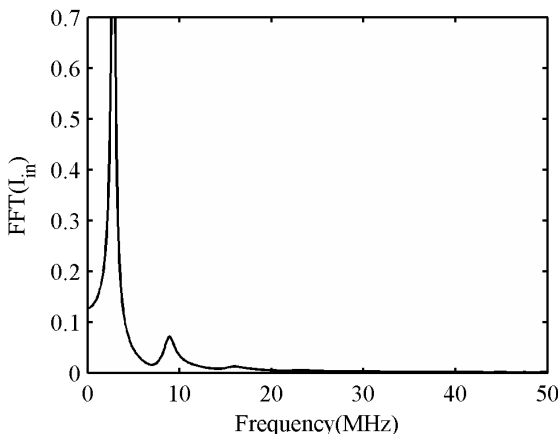


**Figure 6.** Spectrum of the discharge process for the antenna connected to the ground by tuning coil.

## 4 Discussion

The time domain waveform of input current for the monopole antenna excited by DC voltage source has been presented in this paper. And the charge and discharge process can be observed from the waveform, which is in accordance with the expectations. Based on the research of the charge and discharge process of the monopole antenna, two problems should be given attention. The first problem is the effect of the higher modes of the high power transmitting antenna when the transmitter is turned on or shunt off. For constructing a high power broadcast transmitting station, the level of high mode harmonic components is an important parameter and should be reduced as far as possible to reduce the disturbance to the other wireless signals. According to the analysis of this paper, however, the high modes will still be excited strongly even if the technique of suppressing high modes is utilized in transmitter. The duration of high modes depends on the working frequency and Q value of the antenna. The effect of high modes on the electromagnetic environment will not to be neglected for the antenna with very high power, low frequency and high Q value.

Another interesting problem is that the impedance parameters of the antenna may be measured from the charge and discharge oscillation waveform. Although the vector network analyzer (VNA) has been widely used in antenna measurement, the measurement for huge-scale antennas, however, is still difficult because of the high induced voltage on the antenna. Usually, the induced voltage on the very low frequency (VLF) transmitted antenna, such as the Cutler antenna of the U.S. Navy, can exceed 1000V or even more [9,10]. The high induced voltages will breakdown those costly RF instruments if they are connected to the antenna. According to the results of our research, the impedance and resonant frequency can be obtained from the discharge waveform of the antenna. And a high voltage DC source can be adopted to overcome the disturbance of the high induced voltage on the antenna. So it's workable to use a variable tuning inductor to measure the antenna's impedance at different frequency by recording the discharge time oscillation waveform.

## References

- [1] C.A Balanis, *Antenna theory, analysis and design*, 3rd Ed. New York: John Wiley&Sons Inc. 2005.
- [2] Nikolaos K. Uzunoglu, Low- and medium- frequency antennas. chapter 27 of the *Antenna Engineering Handbook*, John L. Volakis, McGraw-Hill, 2007.
- [3] M. Douglas, M. Sullivan, Accurate modeling of thin-wire antenna in the FDTD method, *Microwave and Optical Technology Letters*, vol. 21(4), pp. 261-265, May 1999.
- [4] P. Li, Y. Shi, L. Jiang, and H. Bagci, Transient analysis of lumped circuit networks loaded thin wires by DGTD method, *IEEE Transaction on Antennas and Propagation*, vol. 64(6), pp. 2358-2369, June 2016.
- [5] T. Noda and S. Yokoyama, Thin wire representation in finite difference time domain surge simulation, *IEEE Power Engineering Review*, vol. 22(5), pp. 72, May 2002.

- [6] Poljak, D. and V. Doric, Wire antenna model for transient analysis of simple grounding systems, Part II: The horizontal grounding electrode, *Progress In Electromagnetics Research*, PIER 64, 167–189, 2006.
- [7] Y., H., Lv, *The Numerical Methods of Computational Electromagnetics*. Tsinghua University Press, 2006.
- [8] Dennis M. Sullivan, *Electromagnetics simulation using the FDTD method*, New York: Wiely-IEEE press, 2016.
- [9] Wait, J. R., *VLF Radio Engineering*, Oxford: Pergamon Press, 1967.
- [10] Liu, C., Q.-Z. Liu, L. Zheng, and W. Yu, Numeric calculation of input impedance for a giant VLF T-type antenna array, *Progress In Electromagnetics Research*, PIER 75, 1–10, 2007.

Xiao-long ZHOU, Wei SOHG, Xin-ping LI\*

# Permanent Magnet Brushless DC Motor Driver Base On DSP56F8346

**Abstract:** In this paper, a permanent magnet brushless DC motor drive is designed for smart barrier car. The designed car is, all-digital system, uses direct-axis current zero, vector control strategy, which are based on DSP. System hardware is composed of power boards, power panels and intelligent control boards. A DSP minimum system, it typically uses a current loop and speed loop control structure. A PI regulator is used for current loop control, a PID for speed control loop, to solve the contradiction between fast overshoot, to improve anti-jamming capability, meet the performance requirements.

**Keywords:** permanent magnet brushless DC motor; FOC

## 1 Introduction

This design is based on FREESCALE DSP. the system designed as follow. Once the system is powered and started, the motion parameter is given by uart or a resistor. DSP reads parameter and commutation HALL code start to start the motor running. HALL not only act as a rotor position sensor, but also as a rotor speed sensor. After a rotor rolling DSP calculates the rotor speed and sensing stator (either two-phase) current so that motors can maintain the given speed and desire torque. FOC control algorithm adjusts the q axis voltage output,calculated by PI controller and generate voltage value then through the coordinate transformation and output six SVPWM control signal. The system control chart is Figure 1 [1].

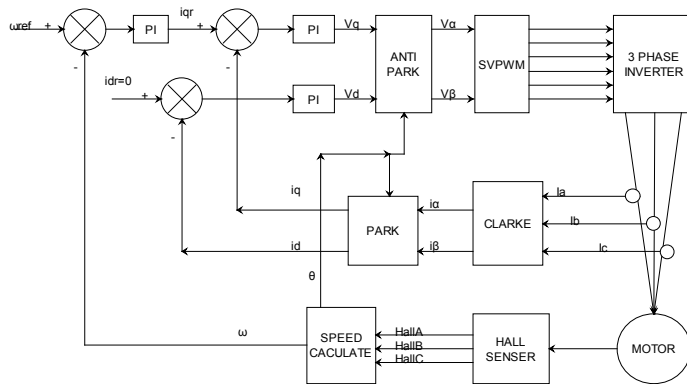
## 2 Control Algorithm

FOC control algorithm achieved by the DSP, which also called vector control. The basic idea is based on vector transformation of coordinate. The current vector is decomposed into two mutually perpendicular to each other independent of the vector  $i_d$ , generates magnet flux, and  $i_q$  generates torque. Now the control method set  $i_d = 0$ , then, the torque is a linear relationship to  $i_q$ <sup>[5]</sup>. A three phase static coordinate system ABC can be converted to static  $\alpha$ - $\beta$  coordinate system by a Clarke transformer, their relationship is shown in equation (1).

---

\*Corresponding author: Xin-ping Li, Shenzhen Institute of Advanced Smart Technology Shenzhen, China, E-mail: 903110232@qq.com

Xiao-long ZHOU, Wei SOHG, State Grid Chongqing Electric Power CO. Electric Power Research Institute, Chongqing, China

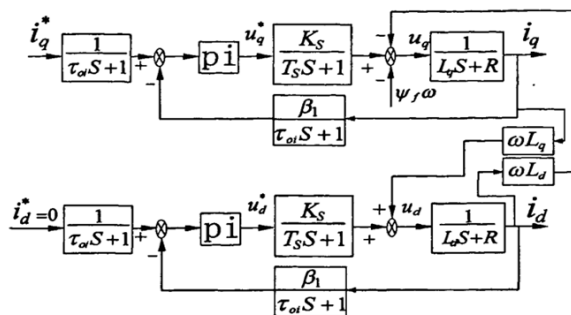
**Figure 1.** System control chart

$$\begin{pmatrix} i_\alpha \\ i_\beta \end{pmatrix} = \sqrt{\frac{2}{3}} \begin{pmatrix} 1 & -\frac{1}{2} & -\frac{1}{2} \\ 0 & \frac{\sqrt{3}}{2} & -\frac{\sqrt{3}}{2} \end{pmatrix} \begin{pmatrix} i_a \\ i_b \\ i_c \end{pmatrix} \quad (1)$$

A Park transformer transfer static  $\alpha\beta\gamma$  coordinate system to rotor d-q coordinate system through the matrix converting is shown in equation (2).

$$\begin{pmatrix} i_d \\ i_q \end{pmatrix} = \begin{pmatrix} \cos \theta & \sin \theta \\ -\sin \theta & \cos \theta \end{pmatrix} \begin{pmatrix} i_\alpha \\ i_\beta \end{pmatrix} \quad (2)$$

Current loop control, motor stator current control, is the key to high-performance basis function. Control accuracy and response speed is major control factor and realized in voltage-mode PWM mode (SVPWM) [3]. Since the current feedback signal with more harmonic components, is necessary to filter links, and given equal time the constant of the filter and the feedback filter time are constant. As equivalent armature circuit resistance and inductance of the first-order inertia link, can be a controlled loop current loop in Figure2,  $\beta_1$  The amplification factor of the current feedback circuit [2].

**Figure 2.** Current loop closed loop transfer function block diagram

A current loop closed-loop transfer function compared with second-standard form, and according to “second order optimal” parameters can be adjusted for the current loop scale factor.

$$K_{pi} = \frac{T_e R}{2T_{\Sigma i} K_s \beta_1} \quad (3)$$

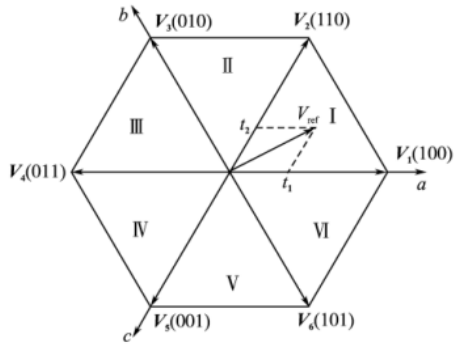


**Figure 3.1:** 6 sectors display

Any given space voltage vector can be represented by eight basic space voltage vector synthesis ( $S_a, S_b, S_c$ ) [4] in Figure 3.1. According to the triangular relationship, each vector can be calculated as follows in Figure 3.2: the reference voltage vector  $V_{ref}$  located within the basic space vectors  $V_1$  and  $V_2$  surrounding a sector. The relationship is represented in equation (4).

$$\begin{cases} T = T_1 + T_2 + T_0 \\ V_{ref} = \frac{T_1}{T} V_1 + \frac{T_2}{T} V_2 \end{cases} \quad (4)$$

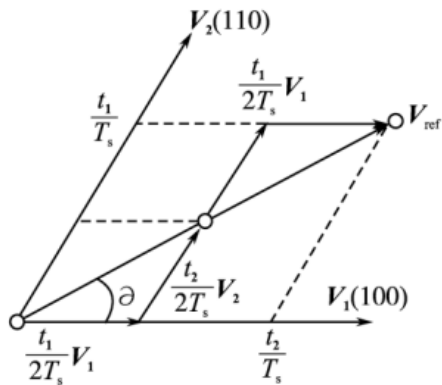


**Figure 3.2.** Triangular relationship

In order to minimize harmonics, the design use 7-segment method.  $T_0 = T_s - T_1 - T_2$  is zero-vector time. Figure 3.3 is a three-arm switching function waveform.

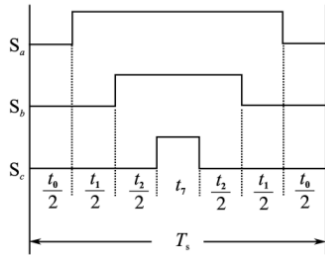


**Figure 3.3.**Three-arm switching function waveform

Respectively,  $T_1$  and  $T_2$  are the space in the cycle time of each station time.  $T_0$  vector is zero vector time. The  $\alpha\beta$  shadow is shown in equation (5).

$$\begin{cases} V_\beta = \frac{T_2}{T} |V_2| \bullet \sin 60^\circ = V_{ref} \bullet \sin \theta \\ V_\alpha = \frac{T_1}{T} |V_1| + \frac{T_2}{T} |V_2| \bullet \cos 60^\circ = V_{ref} \bullet \cos \theta \end{cases} \quad (5)$$

Basic space vector magnitude is  $\sqrt{2/3}U_{dc}$ . According to equation (6), it is possible to obtain an arbitrary voltage vector space, precise control of voltage vector.

$$\begin{cases} T1 = \frac{\sqrt{2}}{U_{dc}} \bullet T \bullet \sin(\frac{\pi}{3} - \theta) \\ T2 = \frac{\sqrt{2}}{U_{dc}} \bullet T \bullet \sin \theta \end{cases} \quad (6)$$

A speed control loop is based on the current loop design [2] and speed loop PI regulator. A speed loop requires a high and fast response speed sampled signal and speed reference signal has increased the time constant  $t$  of filter can then it can be obtained as shown in Figure 4 speed closed-loop system transfer function block diagram:

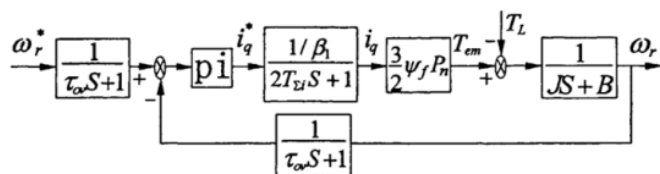


**Figure 4.** Speed closed-loop system transfer function block diagram

After the actual situation simplified, the model calculations can be roughly calculated. The closed loop PI regulator proportional coefficient is  $K_{vp}$ .

$$K_{vp} = \frac{\beta_1 J(h+1)}{3\psi_f P_n h T_{\Sigma_v}} \quad (7)$$

SVPWM control signal is generated by DSP after FOC control, isolated by ACPL-3120 to driver power MOSFET switches which consist of H-bridge by six irf540 so that motor stator windings shaped a rotating magnetic field [5]. The actual circuit is shown in Figure 5.

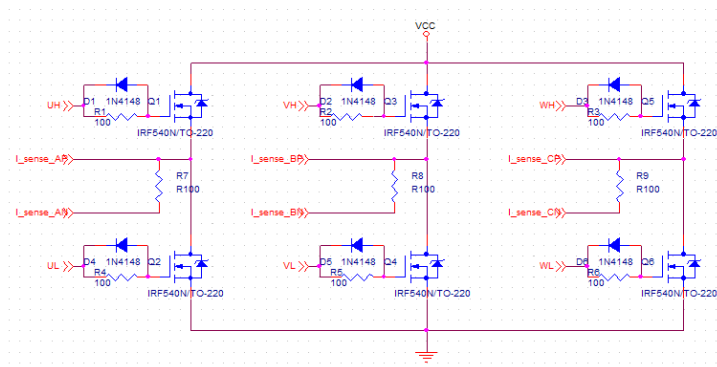


**Figure 5.** SVPWM control H-bridge circuit

The motor stator windings are connected to a structure of star series a resistor to the winding, which act as a current sensor [6]. The body voltage is amplified by AD8656 and isolated by an optocoupler, producing a voltage of 0.3V and connecting to DSP's ADC, which calculates the phase current. Actual current sensing amplifier circuit is shown in Figure 6.

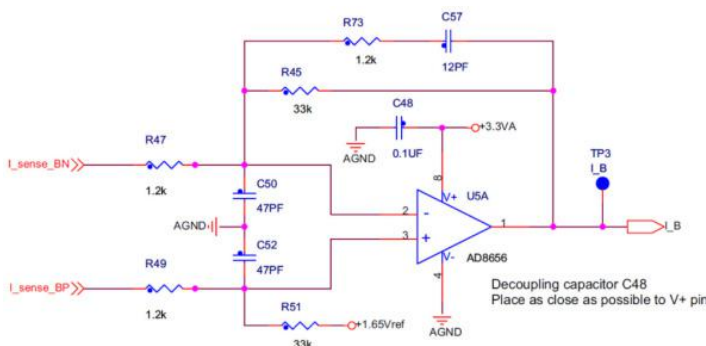


**Figure 6.** Current sensing amplifier circuit

This measurement method can detect stator phase current, quickly and simply, is low cost, and is little influenced by temperature on the measurement accuracy.

### 3 Software design

The main progress is operate in a interrupt. The interrupt procedure is shown in Figure 7.

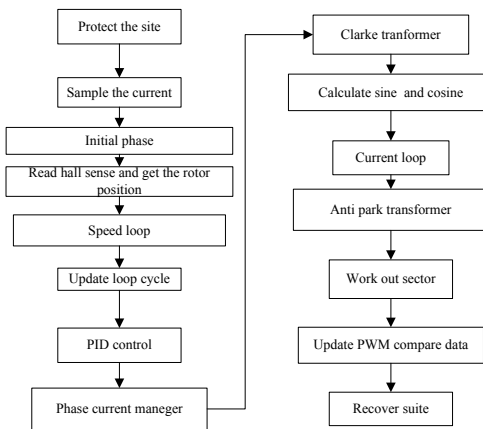


**Figure 7.** System interrupt control

Current feedback [2], through a vector transformation, adjusted by controlling the amount of each PID regulator, requires discrete signals PID controller,

$$U(k) = K_p \left\{ e(k) + \frac{T}{T_i} \sum_{i=0}^{k-1} e(i) + \frac{T_d}{T} [e(k) - e(k-1)] \right\} \quad (8)$$

Into the formula:

$$\begin{aligned} \Delta u(k) &= u(k) - u(k-1) \\ &= K_p \Delta e(k) + K_i e(k) + [\Delta e(k) - \Delta e(k-1)] \end{aligned} \quad (9)$$

Among:

$$\begin{aligned} \Delta e(k) &= e(k) - e(k-1) \\ e(k-1) &= e(k-2) = 0 \end{aligned}$$

At last:

$$\Delta u(k) = A \Delta e(k) - B e(k-1) + C e(k-2) \quad (10)$$

$$A = K_p (1 + T/T_i + T_d/T)$$

$$B = K_p (1 + 2T_d/T) \quad C = K_p (T_d/T)$$

This becomes an incremental PID control [3]. Generally, a computer only needs in the same sample period  $T_s$ , select  $K_p$ ,  $T_d$  and  $T_i$ , determining an output value of the controller, is the amount of time related. Software flow chart is in Figure 8.

SVPWM is determined by the output voltage in  $\alpha\beta$  coordinate system, know output voltage locate in which sector is key point, the decomposed into basic voltage vector. Figure 9 gives SVPWM Sector match algorithm software flow chart.

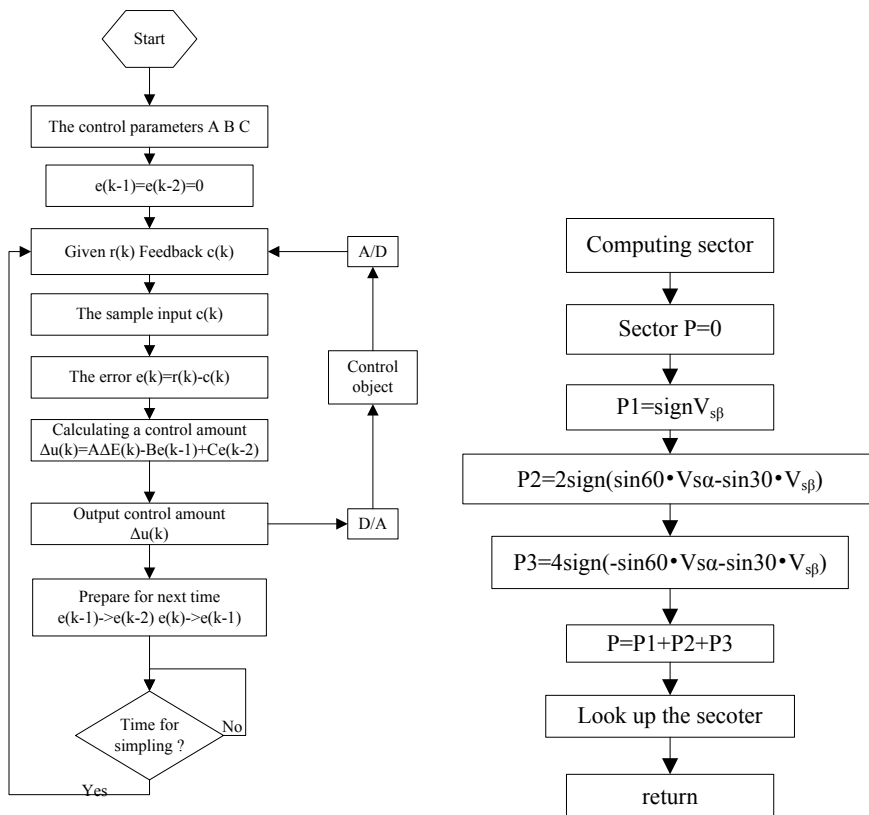


**Figure 8.** Incremental PID control flaw

**Figure 9.** Sector match

## 4 Conclusion

In this paper, we developed a permanent magnet brushless DC motor control system. The whole system is applied to current loop and speed control loop. The results show that the system has better control precision and dynamic response as a follow-up study done a good technical foundation.

## References

- [1] Yu Shuile, The Research on Servo Control System For AC PMSM Based on DSP, Master's degree, Nanjing University of Aeronautics and Astronautics, China 2012, p.35-55.
- [2] Teng Fulin, Research on Position Servo Control System For Permanent magnet Syschronous Motors, PHD, Nanjing University of Aeronautics and Astronautics, China 2009, p.20-55.
- [3] [ZhengJun, Wang Xiaoming, LiXiaoDan Servo System Design of ADSP21990 Based Brushed DC Motor Journal of Liaoning University of Technology(Natural Science Edition) v01.30, NO.6, p. 371-373
- [4] Quan HengLi, Zhang Gang, CHEN Jie, LIU Zhi, Digital Implementation of SVPWM Over-modulation ELECTRIC DRIVE 2010 Vol. 40 No. 5, p. 44-48
- [5] Hendershot JR and T.J.E. Miller, Design of Brushless Permanent-magnet Motors, Magna Physics Publishing and Clarendon Press, 1994
- [6] 3-Phase BLDC Motor Sensorless Control Using MC56F8013, DRM70, Freescale 2005

Qing ZHOU\*, Bang-fei DENG, Cheng-jiang WANG, Qian-bo XIAO,  
Hai-bing ZHANG, Xiang-ming LIU

## The Study on the Power Transmission Line Icing Image Edge Detection based on DTW Measure Cluster Analysis

**Abstract:** As a variety of different types of icing on power lines bring different degrees of harm to the power transmission lines, it is necessary to distinguish between them depending on ice cover feature, in order to adopt different strategies. Edge features are an important feature of power transmission line icing, in this paper for is discussed the image edge feature extraction difficult problem, according to the principles of image segmentation clustering analysis on the image of the sample for the Minkowski metric defects, with dynamic time warping (DTW) as the measure of inter-cluster analysis of samples similarity measure, this paper proposes a method of power transmission line based on DTW measure cluster analysis icing image edge feature extraction, clustering center of all clusters formed as the edge features of the a power transmission line icing image. Finally, experimental results show that this method can extract the power transmission line icing image edge features.

**Keywords:** Transmission Line Icing; DTW measure; Cluster Analysis; Image Edge Detection

### 1 Introduction

Transmission Line Icing is a natural phenomenon, usually in the performance characteristics of icing into sleet, mixing rime, snow and frost and other types of ice, they have different causes. As the presentation of the state of different icing the power system has different level of hazards and the hazard range is not the same, it is necessary to cover the various types of ice out from the image feature extraction, to distinguish between different types of icing, icing for further processing foundation. Image features generally have a color feature, a texture feature, and shape and spatial relations characteristics in different research or applications, a selection of these images is not the same characteristics, and some use a particular feature, and some will use a variety of features, forming a large number of image feature extraction

---

\*Corresponding author: Qing ZHOU, State Grid Chongqing Electric Power CO. Electric Power Research Institute, Chongqing, China, E-mail: hvzhou@163.com

Bang-fei DENG, Qian-bo XIAO, Hai-bing ZHANG, State Grid Chongqing Electric Power CO. Electric Power Research Institute, Chongqing, China

Cheng-jiang WANG, Shenzhen Institute of Advanced Smart Technology Shenzhen, China

Xiang-ming LIU, Honghe University, College of Engineering, Mingzi, China

method [1-4]. Since the transmission line icing single color information compares different types of icing in the texture feature, shape and spatial relationship between features exhibits its own unique characteristics, features integrated edge shape and spatial relationship between the two aspects characteristic, therefore transmission Line ice edge features of the image can be used as a basis for the classification icing process. In this paper, this feature is difficult to extract from the image edge according to the principles of image segmentation clustering analysis using DTW measure as an inter-cluster analysis of samples similarity measure on a proposed power transmission line based on DTW measure cluster analysis icing Edge feature extraction method, the center of all clusters formed as a clustering feature edge power transmission line icing image.

## 2 Image DTW measure

Minkowski distance, which is used to measure the difference between objects is expressed as:

$$dist(\mathbf{X}, \mathbf{Y}) = \left( \sum_{i=1}^n |x_i - y_i|^p \right)^{1/p} \quad (1)$$

Where  $\mathbf{X} = [x_1, x_2, \dots, x_n]$  and  $\mathbf{Y} = [y_1, y_2, \dots, y_n]$ , when  $p = 1, 2, \infty$ , the formula (1) represent Euclidean distance, Manhattan distance and Chebyshev distance. On the basis of the Euclidean distance, cosine distance is defined as:

$$dist(\mathbf{X}, \mathbf{Y}) = \frac{\langle \mathbf{X} \cdot \mathbf{Y} \rangle}{\|\mathbf{X}\| \cdot \|\mathbf{Y}\|} \quad (2)$$

Where  $\langle \cdot \rangle$  represents vector inner-product,  $\|\cdot\|$  represents the vector mode, the formula (2) represents the cosine of the angle between vectors  $\mathbf{X}$  two vectors  $\mathbf{Y}$  in the geometric space. The cosine distance extended to the Pearson correlation coefficient, expressed as:

$$dist(\mathbf{X}, \mathbf{Y}) = \frac{\sum_{i=1}^n (x_i - \bar{x})(y_i - \bar{y})}{\sqrt{\sum_{i=1}^n (x_i - \bar{x})^2} \sqrt{\sum_{i=1}^n (y_i - \bar{y})^2}} \quad (3)$$

Where  $\bar{X}, \bar{Y}$  are the means of vector  $\mathbf{X}$  and vector  $\mathbf{Y}$ .

Usually similarity is defined as the reciprocal of the distance, the greater the distance, the lower the similarity; conversely, the smaller the distance, the higher the similarity. Namely  $sim(\mathbf{X}, \mathbf{Y}) = 1 / dist(\mathbf{X}, \mathbf{Y})$ , it is obvious that  $sim(\mathbf{X}, \mathbf{Y}) = sim(\mathbf{Y}, \mathbf{X})$ . Since Minkowski theory and calculations are very simple, it has a lot of applications in the similarity measure, but the image similarity use of Minkowski is mainly two questions:

- (1) The image translated, the image itself is not changed, but the change of the distance before and after its translation is very large, namely the Minkowski metric cannot be performed on image transforming.

(2) The image is scaled or rotated, but the image itself does not change, namely the Minkowski metric cannot be performed on image scaled or rotation. It will be described using four images, as shown:

Where Figure 1a shows an image of 32x32 pixel size, the white part is the pattern, the pixel value of 255, the other part is black background, the pixel value is 0; Figure 1b is that Figure 1a moved the white pattern down and right by 5 units of pixels; white pattern in Figure 1c is that Figure 1a zoom out by 0.8 and rotated 45 degrees; Figure 1d is white pattern of rectangle. According to common sense, we can observe in Figure 1a, b and c have the same shape, it should have a high similarity, but in Figure 1d should be low similarity.

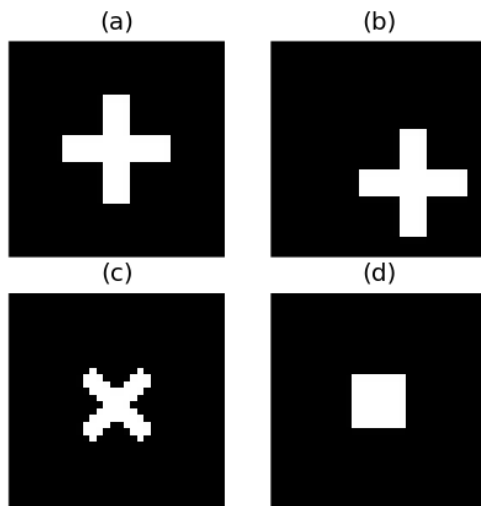


**Figure 1.** The images of illustrating the similarity measure

With Minkowski distance as similarity measure, which  $p = 2$ , Formula as follows:

$$dist(u, v) = \sqrt{\sum_{i=0}^{31} \sum_{j=0}^{31} (img_u[i, j] - img_v[i, j])^2} \quad (4)$$

Where  $img_u$  and  $img_v$  are data matrixes of image  $u$  and  $v$ ,  $img_u[i, j]$  and  $img_v[i, j]$  are the pixel values of the image  $u$  and  $v$  in  $i$ -th row and  $j$ -th column. According to the formula, we calculated the results, as shown in Table 1.

**Table 1.** The Euclidean distance of image a, b, c and d

<i>dist (u,v)/32</i>	a	b	c	d
a	0.000	12.649	10.583	8.944
b	12.649	0.000	12.083	12.247
c	10.583	12.083	0.000	5.657
d	8.944	12.247	5.657	0.000

From the table, it shows that:

- 1) With  $di\ st\ (a, d) < di\ st\ (a, c) < di\ st\ (a, b)$ , the similarity would be  $si\ m(a, d) > si\ m(a, c) > si\ m(a, b)$  between Figure 1a, 1b, 1c and 1d, namely Figure 1a is the most similar to Figure 1d than others. However, we observe that they should not be the most similar, the conclusion is unreasonable;
- 2) With  $di\ st\ (d, b) < di\ st\ (a, b)$ , the similarity would be  $si\ m(d, b) > si\ m(a, b)$ , that Figure 1d is more similar to Figure 1b than Figure 1a. The conclusion is unreasonable too.
- 3) With  $di\ st\ (d, c) < di\ st\ (a, c)$  and  $di\ st\ (d, c) < di\ st\ (b, c)$ , the similarity would be  $si\ m(d, c) > si\ m(a, c)$  and  $si\ m(d, c) > si\ m(b, c)$ , that Figure 1 (c) is most similar to Figure 1 (d) than others. So the conclusion is unreasonable too.

Since described above defects of Minkowski distance as the image similarity measure, paper introduce DTW measure, which was originally used for audio signal identification and now has been applied in many fields [5-9]. If there are two vectors  $\mathbf{x} = [x_1, x_2, \dots, x_i, \dots, x_m]$  and  $\mathbf{y} = [y_1, y_2, \dots, y_j, \dots, y_n]$ , which length with  $m$  and  $n$ , it can construct  $M \in R^{m \times n}$ :

$$M = \begin{bmatrix} d(x_1, y_1) & \dots & d(x_1, y_j) & \dots & d(x_1, y_n) \\ \vdots & \ddots & \vdots & \ddots & \vdots \\ d(x_i, y_1) & \dots & d(x_i, y_j) & \dots & d(x_i, y_n) \\ \vdots & \ddots & \vdots & \ddots & \vdots \\ d(x_m, y_1) & \dots & d(x_m, y_j) & \dots & d(x_m, y_n) \end{bmatrix} \quad (5)$$

Where  $d(x_i, y_j)$  is the distance between the i-th and j-th component of  $\mathbf{x}$  and  $\mathbf{y}$ , which usually been named base distance. It defines a set of contiguous matrix elements in the matrix M collection:

$$W = \{w_1, w_2, \dots, w_i, \dots, w_k\} \quad (6)$$

If the elements meet the boundary, continuity and monotonicity requirement, it can be called a path. There are many path met the conditions, commonly used dynamic programming to find a path, it can be calculated by the following formula:

$$\begin{cases} \gamma(1,1) = d(x_1, y_1) \\ \gamma(i,j) = d(x_i, y_j) + \min\{\gamma(i-1, j), \gamma(i-1, j-1), \gamma(i, j-1)\} \\ dist(\mathbf{x}, \mathbf{y}) = \gamma(m, n) \end{cases} \quad (7)$$

Where  $\gamma(i, j)$  is the distance between i-th and j-th component of  $\mathbf{x}$  and  $\mathbf{y}$ , the  $\gamma(m, n)$  is the distance between  $\mathbf{x}$  and  $\mathbf{y}$ .

With defined  $d(x_i, y_j) = |x_i - y_j|$ , this paper calculate the distances of image a, b, c and d by DTW distance measure, where the image matrix of 32x32 expanded to a vector with 1024 length row by row, as shown in Table 2.

**Table 2.** The DTW distance of image a, b, c and d

dist(u,v)	a	b	c	d
a	0	0	255	8160
b	0	0	255	8160
c	255	255	0	4345
d	8160	8160	4345	0

From the table, it shows that:

- 1) With  $sim(a, b) > sim(a, c) > sim(a, d)$ , Figure 1 (a) would be similar to (b) and (c) than (d);
- 2) with  $sim(b, a) > sim(b, c) > sim(b, d)$ , Figure 1 (b) would be similar to (a) and (c) than (d);
- 3) with  $sim(c, a) = sim(c, b) > sim(c, d)$ , Figure 1 (c) would be similar to (a) and (b) than (d).

As it can be seen from the above analysis, the DTW distance measure can be resolved image similarity problem of image translation, image scaling and image rotation in Minkowski distance measure.

### 3 The image cluster analysis based on DTW measure

In various clustering algorithms, the k-means clustering algorithm has been widely used, which is simple in principle and able to solve most clustering tasks. It uses Euclidean distance to measure the similarity between objects, whose cluster center is the average value of each cluster. It should make changes in k-means clustering algorithm that the DTW distance been done the similarity between objects, as shown:

With a set of images  $\mathbf{V} = \{V^1, V^2, \dots, V^n\}$ , the  $V^1, V^2, \dots, V^n$  are the vectors of images expanded row by row or column by column. Given the definition:

$$E = \sum_{i=1}^k \sum_{j=1}^{c_i} dist(V_i^j, v_i) \quad (10)$$

Where  $V_i^j$  is the  $j$ -th object of  $i$ -th cluster,  $V_i$  is the center of  $i$ -th cluster,  $K$  is the number of clusters,  $C_i$  is the number of objects of  $i$ -th cluster, obviously  $C_1 + C_2 + \dots + C_k = n$ . The cluster analysis task is to find a cluster partition, so that the formula (10) to obtain the minimum. The steps as follows:

- 1) Initialization, according to the number of clusters, it randomly selects  $K$  elements in set  $\mathbf{V}$ , as the initial center of  $k$  clusters  $\{V_1, V_2 \dots V_k\}$ .
- 2) Element partition, calculating the distances  $\{dist(v^j, v_1) dist(v^j, v_2) \dots dist(v^j, v_k)\}$  between element  $v^j$  and the centers  $\{V_1, V_2 \dots V_k\}$ , the element  $v^j$  and the center with minimum distance belong to the same cluster. A cluster partition would be  $\{v_1^1, v_1^2 \dots v_1^{c_1} \dots v_i^1, v_i^2 \dots v_i^{c_i} \dots v_k^1, v_k^2 \dots v_k^{c_k}\}$ , where  $V_i^j$  is the  $j$ -th object of  $i$ -th cluster.
- 3) Center update, it find out the object  $V_i$  in each cluster  $\{v_1^1, v_1^2 \dots v_i^j \dots v_k^{c_k}\}$  such that the  $\sum_{j=1}^c dist(v_i^j, v_i)$  obtain a minimum value.
- 4) Repeat steps (2) and (3) such that  $\{V_1, V_2 \dots V_k\}$  is not changed so far. The similar is high within the same cluster, otherwise is low.

## 4 The Icing Image Edge Detection

With the size of image being  $w \times h$ , the width of image is  $w$  and the height of image is  $h$ , so the image can be as a matrix with  $\mathbf{A} \in R^{h \times w}$ . With the size of feature image being  $m \times n$ , it can build a sliding 2D-window with the size of  $m \times n$ . The image is divided into  $(w - m + 1) \times (h - n + 1)$  overlapping images with the size of  $m \times n$ , so the image defined in the  $i$ -th row and  $j$ -th column of matrix  $\mathbf{A}$  as shown:

$$\mathbf{S}_{(i,j)} = \mathbf{A}[i : i + m, j : j + n] \quad (8)$$

Where  $i \in [1, h - n + 1]$ ,  $j \in [1, w - m + 1]$ , the  $\mathbf{A}[i : i + m, j : j + n]$  was constituted by elements of  $i$ -th to  $i+m$ -th rows and  $j$ -th to  $j+n$ -th columns in the matrix  $\mathbf{A}$ , abbreviated as  $\mathbf{S}_{(i,j)}$ .

These images with size of  $m \times n$  can be expand into a vector with length of  $m \times n$  row by row or column by column, abbreviated as  $\mathbf{V}_{(i,j)}$ . The vectors are order marked  $\mathbf{V} = \mathbf{V}_{(1,1)}, \mathbf{V}^2 = \mathbf{V}_{(1,2)}, \dots, \mathbf{V}^{w-m+1} = \mathbf{V}_{(1,w-m+1)}, \mathbf{V}^{w-m+1+1} = \mathbf{V}_{(2,1)}$ ,

$\mathbf{V}^{w-m+1+2} = \mathbf{V}_{(2,2)}, \dots, \mathbf{V}^{w-m+1+w-m+1} = \mathbf{V}_{(2,w-m+1)}, \dots, \mathbf{V}^{(w-m+1)(h-n+1)} = \mathbf{V}_{(h-n+1,w-m+1)}$ , abbreviated as:

$$\mathbf{V} = \{\mathbf{V}^1 \mathbf{V}^2 \dots \mathbf{V}^{(w-m+1)(h-n+1)}\} \quad (9)$$

With the elements of  $\mathbf{V}$  as cluster analysis objects and the cluster analysis algorithm determined according to the formula (10), the images' similarity is high

within the same cluster, otherwise is low. When the center of each cluster is extracted, these centers can be used as image feature.

In most cases, the size of the image is generally higher, compared to the size of the sliding window is generally small, so the number of sub-images formed by division is large; especially the use of DTW distance as the similarity measure, the calculation improves accuracy, but also an enormous amount of calculation, to ensure accuracy to reduce the number of objects involved in cluster analysis it is the most direct and effective way of reducing the amount of computation. In one image, not all pixels are feature, most of them are redundant, the paper builds a collection of images using the image corner feature, to greatly reduce the amount of computing cluster analysis. The image corner is generally defined as the intersection of two sides, the local neighborhood with two boundaries and direction of the different regions, which and the nature of the image edge features a close to nature, there are a lot of corner extraction methods, which reduce the number of objects involved in the calculation of clustering methods for many applications [10-13], the paper also use this method to reduce calculation.

## 5 Experiment

There are two transmission line icing images, having different edge features, as shown:

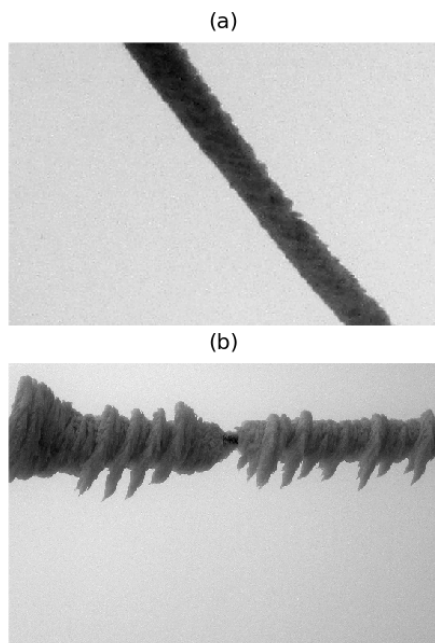


**Figure 2.** The Transmission Line Icing images

Where the size of images being 542x358, Figure 2a and b, respectively, using ORB [14] to find their corners, respectively 81 and 189 corners, their position in the Figure 3, as shown below.

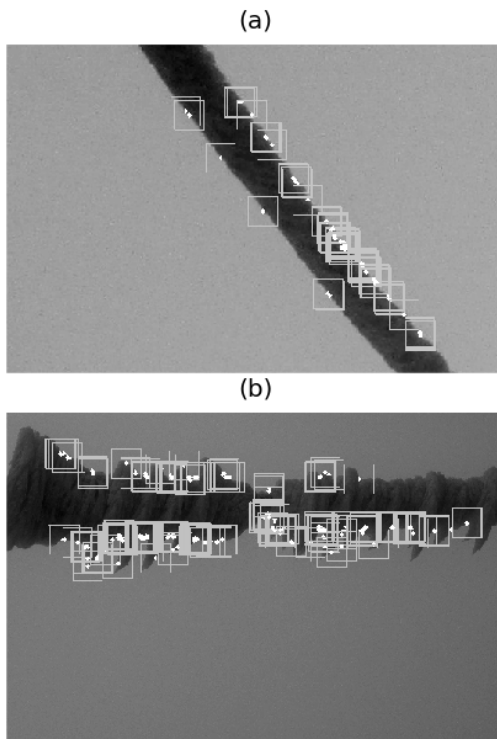


**Figure 3.** The ORB corner of the transmission line icing images

It can be seen from the Figure 3 that the ORB corner are at the edge of covered ice part and background part, getting 81 and 189 images respectively with these corners as the center which width and height are 32 pixels. When the number of clusters is set to 16, after the DTW measure cluster analysis were obtained 16 cluster centers, as shown:

The Figure 4a images can be seen are smooth, may represent the edge feature of the Figure 2a; the dramatic changes of the Figure 4b images in shape can be observed, can represent the edge feature of the Figure 2b.

(a)



(b)

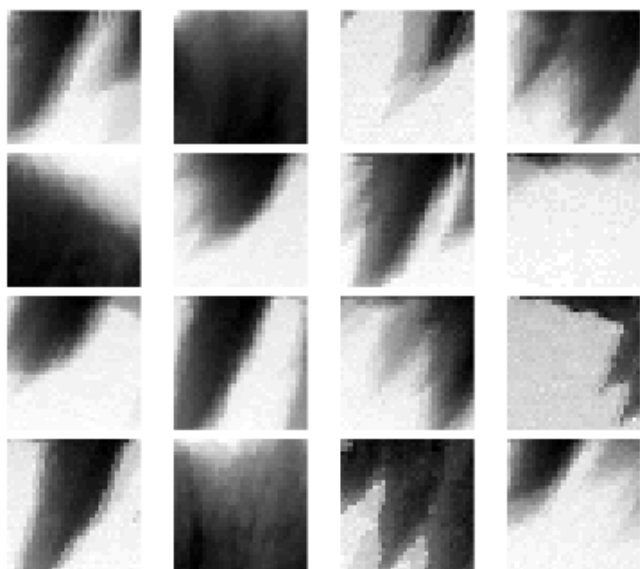


**Figure 4.** the cluster centers of the transmission line icing images

## 6 Conclusion

In this paper, the image edge feature extraction difficult problem is discussed, according to the principles of image segmentation clustering analysis using DTW measure as an inter-cluster analysis of samples similarity measure is proposed a method of power transmission line based on DTW measure cluster analysis icing image edge detection, the clusters center be formed as the edge feature of the power transmission line icing image. Finally, through experiment that the transmission line icing images having different edge features show that this method can effectively extract power transmission line icing image edge features.

## References

- [1] Lowe D G. Lowe, D.G.: Distinctive Image Features from Scale-Invariant Key-points. *Int. J. Comput. Vision* 60(2), 91-110[J]. International Journal of Computer Vision, 2004, 60(2):91---110.
- [2] Lowe D G. Distinctive Image Features from Scale-Invariant Keypoints[J]. International Journal of Computer Vision, 2004, 60(60):91-110.
- [3] Yu N, Qiu T, Bi F, et al. Image Features Extraction and Fusion Based on Joint Sparse Representation[J]. *IEEE Journal of Selected Topics in Signal Processing*, 2011, 5(5):1074-1082.
- [4] Nan-Nan Y U, Qiu T S, Feng B I. Medical image features extraction and fusion based on K-SVD[J]. *Journal of Dalian University of Technology*, 2012.
- [5] Jeong Y S, Jeong M K, Omitaomu O A. Weighted dynamic time warping for time series classification[J]. *Pattern Recognition*, 2011, 44(9):2231-2240.
- [6] Petitjean F, Ketterlin A, Gançarski P. A global averaging method for dynamic time warping, with applications to clustering[J]. *Pattern Recognition*, 2011, 44(3):678-693.
- [7] Forestier G, Lalys F, Riffaud L. Classification of surgical processes using dynamic time warping. [J]. *Journal of Biomedical Informatics*, 2012, 45(2):255-64.
- [8] Yu D, Yu X, Hu Q, et al. Dynamic time warping constraint learning for large margin nearest neighbor classification[J]. *Information Sciences*, 2011, 181(13):2787-2796.
- [9] Sempena S, Maulidevi N U, Aryan P R. Human action recognition using Dynamic Time Warping[C]. *International Conference on Electrical Engineering & Informatics*. IEEE, 2011:1-5.
- [10] Derpanis K G. The Harris Corner Detector[J]. *Symposium Svenska Slöskapet Fr Bildanalys*, 2004.
- [11] Antonopoulos P, Nikolaidis N, Pitas I. Hierarchical Face Clustering using SIFT Image Features[C]. IEEE, 2007:325-329.
- [12] Bay H, Tuytelaars T, Gool L V. SURF: Speeded Up Robust Features[J]. *Computer Vision & Image Understanding*, 2006, 110(3):404-417.
- [13] Mahmoudi M, Sapiro G. Fast image and video denoising via nonlocal means of similar neighborhoods[J]. *IEEE Signal Processing Letters*, 2010, 12(12):839--842.
- [14] Wang G, Tian J. License plate localization in complex scenes based on oriented FAST and rotated BRIEF feature[J]. *Journal of Electronic Imaging*, 2015, 24(5).